

AD-A261 949



DARPA Advanced High Current Density Cathodes for
Defense Applications: Development Phase

Final Report

Contract Number N00014-90-C-2118

Project Number 01-0624-07-0857

Report Number SAIC-93/1018

March 1, 1993



Science Applications International Corporation

An Employee-Owned Company

DTIC
ELECTE
MAR 26 1993
S E D

DISTRIBUTION STATEMENT

Approved for public release
Distribution Unlimited

93-06061



336128

~~03~~

1710 Goodridge Drive, P.O. Box 1303, McLean, Virginia 22102 (703) 821-4300

Other SAIC Offices: Albuquerque, Boston, Colorado Springs, Dayton, Huntsville, Las Vegas, Los Angeles, Oak Ridge, Orlando, Palo Alto, San Diego, Seattle, and Tucson

98 3 24 004

DARPA Advanced High Current Density Cathodes for Defense Applications: Development Phase

FINAL REPORT

Contract Number N00014-90-C-2118
Project Number 01-0624-07-0857
Report Number SAIC-93/1018

March 1, 1993

Statement A per telecon
Dr. Joel Schmur NRL Code 6090
Washington, DC 20375-5000

NWW 3/26/93

Accession For	
NTIS CRA&I	<input checked="" type="checkbox"/>
DTIC TAB	<input checked="" type="checkbox"/>
Unannounced	<input type="checkbox"/>
Justification	
By	
Distribution /	
Availability Codes	
Dist	Avail and/or Special
A-1	

Submitted to:

DARPA

DTIC QUALITY INSPECTED 1

Submitted by:

Science Applications International Corporation
Applied Physics Operation
1710 Goodridge Drive
McLean, Virginia 22102

Table of Contents

1	Executive Summary	1
2	Design and Analysis of Advanced Microstructure Cathodes	6
2.1	Analytical Formulations.....	6
2.1.1	Quantum Field Emission from 3-D Structures	6
2.1.2	Thermal Limitations	14
2.1.3	Brightness Effects on FEL Performance.....	23
2.2	Computational Formulations	31
2.2.1	Solid Needle Geometry - "Type 1"	34
2.2.2	Hollow Cylinder Geometry - "Type 2"	38
2.2.3	Comparisons of Performance Potential: "Type 1" vs. "Type 2"	43
3	Fabrication of Eutectic Composite Cathodes	51
3.1	Growth and Fabrication of Si-TaSi ₂	51
3.1.1	Si-TaSi ₂ Boule Growth	51
3.1.2	Etching of Si-TaSi ₂	55
3.1.3	Metallization of Si-TaSi ₂	57
3.1.4	Patterned Contacts.....	58
3.1.5	Removal of Surface Oxides.....	59
3.2	Initial Testing and Screening of Cathodes	61
3.3	Growth of Other Eutectics	61
3.4	Fabrication Optimizations for Si-TaSi ₂	62
4	Testing of Tubule Microstructure Cathodes and Eutectic Composite Cathodes.....	64
4.1	DC Test Stand	64
4.2	DC I-V Characteristics	68
4.2.1	DC Characterization: Tubule Cathodes.....	70
4.2.2	DC Characterization: Eutectic Cathodes	76
4.2.3	DC Characterization: Filter Paper Template Tubule Cathodes	85
4.2.4	DC Characterization: Microlithographic Tubule Cathodes.....	87
4.3	"Pepper-pot" Emittance Apparatus	89
4.4	Initial Emittance Measurements	90
4.5	Lifetime Test Apparatus.....	91
4.6	Vacuum Sensitivity Tests	92
4.7	Impurity Sensitivity Tests	92
4.8	Lifetime Tests	93
4.9	AC Test Stand	95
4.10	AC I-V Characteristics	98
4.11	Slit-Wire Emittance Apparatus	100
4.12	DC/AC Fine Emittance Measurements	102
5	Applications Evaluation.....	103
5.1	FEL and Ubitron Applications	103
5.2	Aegis CFA Startup Application	104
5.3	Long Pulse RKA Application	108

5.4	Laser Driven FEA Applications - Accelerators	108
5.5	Laser Driven FEA Applications - Compact Wideband Microwave Amplification	112
5.6	High Pressure FEA Operation - Fluorescent Backlights	113
5.7	High Pressure FEA Operation - Thin Film Processing	114
6	Summary of Milestone Achievements	115
7	Conclusions	118
Appendix A:	Publications.....	A1
Appendix B:	FEAT Code Listing	B1
	TPIC Code Listing	
Appendix C:	Final Report-GTEL.....	C1

List of Figures

- 2.1: The geometry of the prolate ellipsoid of revolution that is used for these calculations.
- 2.2: $\langle\beta\rangle$ parameterized vs. I_{tip} for $J_{max} = 10^{10}, 10^8$, and 10^6 A/cm^2 . The independent variable is the applied field E_0 , which varies over a range of 50-350 kV/cm. The tip height is $h=10 \mu\text{m}$ and the tip radius of curvature is $r_c=100 \text{ \AA}$.
- 2.3: $\langle\beta\rangle$ parameterized vs I_{tip} for the same values of J_{max} and tip height as in the previous graph, but with a tip radius of curvature $r_c=25 \text{ \AA}$. Note that observable changes in $\langle\beta\rangle$ occur for tip currents starting at $\sim 1 \mu\text{A}$, and large changes may occur for tip currents $\sim 10 \mu\text{A}$.
- 2.4: $\langle\beta\rangle$ plotted vs E_0 for the same data as plotted in Fig. 2.2. Note that in the absence of any accounting for materials limitations, as in the case of $J_{max}=10^{10} \text{ A/cm}^2$, $\langle\beta\rangle$ evidences a linear decrease with increasing field. The inclusion of some accounting for the refilling time of vacated states generates a faster falloff for $\langle\beta\rangle$, in this case appearing bilinear in nature.
- 2.5: $\langle\beta\rangle$ plotted vs E_0 for the same data as plotted in Fig. 2.3.
- 2.6: $\alpha I/r_c^2$ parameterized vs. I_{tip} for $J_{max} = 10^{10}, 10^8$, and 10^6 A/cm^2 , and $r_c=100 \text{ \AA}$. The independent variable is the applied field E_0 , which varies over a range of 100-350 kV/cm. Note that $\alpha I/r_c^2$ is not constant, is not equal to π , and is increasing while $\langle\beta\rangle$ is decreasing. This is true even for $J_{max} = 10^{10} \text{ A/cm}^2$, where $J_{eff} = J_{FN}$ to within $<1\%$.
- 2.7: The geometry for the 1-D steady state thermal calculation. Ohmic heating is distributed throughout the tip volume, and the perfect heat sink at $T=T_0$ is at $x=0$. Cooling due to radiation losses or the Nottingham effect is neglected, as are any variations in k_t or ρ_e .
- 2.8: The geometry used for the calculation of the steady state temperature profile for a solid cone (Type 1) structure.
- 2.9: Different steady state temperature profiles for the convergent cone geometry as a function of the cone angle θ_0 . Note that the results have been scaled in order to fit all the data on the same plot. Note also that the horizontal axis has been defined as $x=h-r$ rather than just r : the tip of the emitter is at the right of the plot, the base at the left.

- 2.10: The approximate time dependent temperature profile for a 1-D emitter structure. For these calculations $f=10\text{GHz}$, $a_0=1\text{cm}^2/\text{sec}$, $h=10\mu\text{m}$. For this combination of parameters the value of $\tau_p^0 \sim 400\text{ns}$.
- 2.11: Graph of the growth rate versus frequency for the fundamental and third harmonic interactions.
- 2.12: Variation of the normalized growth rates at the fundamental and third harmonic with the axial momentum spread.
- 2.13: The grid structure used in FEAT and TPIC is optimized to provide extreme resolution where the field gradients are largest - near the tip - and not waste resolution where the field gradients are small. Properly matching between successive grid structures is essential if reliable results are to be achieved in a reasonable time.
- 2.14: The geometry of the Type 1 tip. The shank of the emitter is $1\mu\text{m}$ in diameter. The tip terminates in a spherical cap of radius of curvature r_c , which is matched to the shank by a 22.5° tapered section.
- 2.15(a): The equipotential plot output from a run of the FEAT code.
- 2.15(b): A contour plot for the magnitude of E_y , showing the large compression near the tip apex.
- 2.15(c): The output listing from the FEAT code for Figs. (a) and (b).
- 2.16(a): Output from a TPIC run for a Type 1 tip. This plot shows the trajectories of electrons emitted from the tip. The emission occurs from only a very small area near the tip apex.
- 2.16(b): A plot from the same TPIC run as 2.16(a) showing the phase space contours used to evaluate emittance and brightness.
- 2.17: A composite Fowler-Nordheim I - V characteristic obtained from a series of TPIC runs. The geometry is Type 1 with $r_c=25\text{\AA}$. Note the saturation rollover at high fields. Such an effect might normally be misinterpreted as "current hogging."
- 2.18: The geometry of the Type 2 tip. The mean diameter of the hollow cylinder is $0.5\mu\text{m}$. The tip terminates in a rounded square wall with a radius of curvature r_c . The thickness of the cylinder wall is given by Δr .
- 2.19(a): The equipotential plot output from a run of the FEAT code for a Type 2 structure.
- 2.19(b): A contour plot for the magnitude of E_y , showing the large compression near the outer edge of the tip.
- 2.19(c): The output listing from the FEAT code for Figs. (a) and (b).

- 2.20(a): Output from a TPIC run for a Type 2 tip. This plot shows the trajectories of electrons emitted from the tip. The emission occurs from only a very small area near the tip apex.
- 2.20(b): A plot from the same TPIC run as 2.20(a) showing the phase space contours used to evaluate emittance and brightness.
- 2.21: A composite Fowler-Nordheim I - V characteristic obtained from a series of TPIC runs. The structure is Type 2 with $r_c=150\text{\AA}$. In contrast with the Type 1 structure that evidenced saturation, the Type 2 structures typically do not show saturation for tip currents that are thermally realizable.
- 2.22: A plot of the values for single tip current obtained from TPIC runs at various values for the refilling time parameter Δt_{xtal} at constant applied electric field using the field solves from FEAT for the A012 geometry.
- 2.23: A plot of the values of the single tip currents obtained from TPIC and FEAT for four tip geometries: open circle, Type 1, $h=10\mu\text{m}$, $r_c=25\text{\AA}$; open triangle, Type 1, $h=10\mu\text{m}$, $r_c=100\text{\AA}$; solid triangle, Type 2, $h=15\mu\text{m}$, $\Delta r=300\text{\AA}$, $r_c=150\text{\AA}$; solid circle, Type 2, $h=15\mu\text{m}$, $\Delta r=600\text{\AA}$, $r_c=150\text{\AA}$. In all cases $\Delta t_{\text{xtal}}=10^{-17}\text{ sec}$.
- 2.24: The same data as in Fig. 2.23 but with a value of 10^{-13} sec for Δt_{xtal} .
- 2.25: A plot of the values for $\delta\theta$ obtained from TPIC runs at various applied electric fields using the field solves from FEAT for four tip geometries. $\Delta t_{\text{xtal}}=10^{-17}\text{sec}$.
- 2.26: A plot of the values for $\delta\theta$ obtained from TPIC runs at various applied electric fields using the field solves from FEAT for four tip geometries. $\Delta t_{\text{xtal}}=10^{-13}\text{sec}$.
- 2.27: A plot of the values for $\gamma\beta(\delta\theta)$ obtained from TPIC runs at various applied electric fields using the field solves from FEAT for four tip geometries. $\Delta t_{\text{xtal}}=10^{-17}\text{sec}$.
- 2.28: A plot of the values for B_n obtained from TPIC runs at various applied electric fields using the field solves from FEAT for four tip geometries. $\Delta t_{\text{xtal}}=10^{-17}\text{sec}$.
- 2.29: A plot of the values for B_n obtained from TPIC runs at various applied electric fields using the field solves from FEAT for four tip geometries. $\Delta t_{\text{xtal}}=10^{-13}\text{sec}$.
- 2.30: A plot of the values for single tip brightness $B_n^{(1)}$ obtained from TPIC runs at various applied electric fields using the field solves from FEAT. $\Delta t_{\text{xtal}}=10^{-17}\text{sec}$.
- 2.31: A plot of the values for single tip brightness $B_n^{(1)}$ obtained from TPIC runs at various applied electric fields using the field solves from FEAT. $\Delta t_{\text{xtal}}=10^{-13}\text{sec}$.
- 3.1: A photograph of a typical Si-TaSi₂ boule used for the eutectic advanced cathode materials in this project. The seed for the boule is at right in the photograph.

- 3.2: An SEM micrograph of the surface of a polished Si-TaSi₂ wafer. Note the irregular distribution, the cellular structure of rod distributions, and the non-circular cross-section of most rods.
- 3.3: An SEM micrograph of the surface of a polished and etched Ge-TiGe₂ wafer taken from a Bridgeman grown boule (left) as compared with the same material grown Czochralski (right).
- 3.4: An illustration of the effect of different rod diameters on the height of the emitter structures after selective etching.
- 3.5: An illustration of a two step etch process to optimize the distribution of tip heights despite a distribution in rod diameters.
- 3.6: A schematic diagram of the patterned contact on a Si-TaSi₂ FEA.
- 3.7: An XPS spectrum of the Ta peaks for an as-processed Si-TaSi₂ cathode.
- 3.8: The XPS spectrum of an as-processed Si-TaSi₂ cathode after Ar-ion milling of the surface. Note the absence of the oxidized Ta signal.
- 3.9: An SEM micrograph of cathode GTE 32-2. This cathode is fabricated from a Si-WSi₂ eutectic, and evidences a more blade-like structure to the emitters.
- 4.1: The DC test stand used to measure the initial *I-V* characteristics of the advanced cathode materials. Vacuum was provided originally by a combination of sorption and vac-ion pumps. Maximum vacuum and turnaround time have both been improved by the substitution of a dry rough pump/turbopump/cryopump system.
- 4.2: The geometry of the microanode electrode structure. This assembly allows for the more selective characterization of emission from the cathode emitter.
- 4.3: The axial field profile produced at the surface of the cathode emitter by the full radiused microanode at a distance of 1.0mm. The dashed line is the relative vacuum field emission current for an applied voltage of 15kV and a field enhancement factor $\beta=500$.
- 4.4: Chart recorder data for the startup of a tubule cathode.
- 4.5: Chart recorder data for the initial conditioning of the cathode shown in Fig. 4.4. Note that the voltage necessary to drive emission has fallen significantly.
- 4.6: A plot of the microanode current vs. the amplitude of the sawtooth voltage. The data is taken from a single sawtooth cycle on G12-G.
- 4.7: A Fowler-Nordheim style plot of the data from the sawtooth in Fig. 4.6. Note the hysteresis in the data.
- 4.8: The sawtooth voltage (upper) and corresponding microanode current averaged over 32 successive pulses in run 1 of cathode G12-E.

- 4.9: The Fowler-Nordheim plot for the average data from Run 2 and Run 5, as given in the *Appl. Phys. Lett.* publication. Note that while the data lie very close to each other, the sensitivity of the linear fit yields substantial variations in " α " and " β ".
- 4.10: The calculated field enhancement factor for three different shapes of tubule structure as a function of tubule height.
- 4.11: A plot of the microanode current (thin line) vs. the amplitude of the sawtooth voltage (dark line). The data are taken from an average over 32 successive pulses.
- 4.12: A plot of the microanode current vs. the amplitude of the sawtooth voltage. The data are taken from an envelope over 32 successive pulses.
- 4.13: The Fowler-Nordheim plot of the data in Fig. 4.11. Note the relative lack of hysteresis compared to the same data for a tubule cathode.
- 4.14: The Fowler-Nordheim plot for the average data from several different runs of several different cathodes, as given in the *Appl. Phys. Lett.* publication.
- 4.15: A plot of the calculated maximum field enhancement factor as a function of tip height for several tip radii of curvature. Note that $\beta=500$ with $h=10\mu\text{m}$ corresponds to $r_c \leq 100\text{\AA}$.
- 4.16: A plot of several successive TPIC runs with a $10\mu\text{m}$ tall Type 1 structure with a tip radius of curvature of 100\AA . The standard analysis of this data yields " β "=340 and " α "= 32nm^2 per tip.
- 4.17: A Fowler-Nordheim plot (upper) and the voltage and current traces corresponding to it (lower) for the cathode RPI.
- 4.18: A SEM image of a microlithographically prepared tubule cathode. The shape of the structures led to the nickname "TMI"s.
- 4.19: A Fowler-Nordheim plot (upper) and the voltage and current traces corresponding to it (lower) for the cathode LC117.
- 4.20: The schematic drawing of the system used to perform the coarse emittance measurements. This assembly mates to the bottom of the DC test stand and provides a viewable phosphor image of the witness beamlets formed from the replaceable screen.
- 4.21: The screen apertures the incident electron beam into several "beamlets." Each of these beamlets spreads according to its own distribution function of v_{\perp} . This distribution can be deconvolved from the image of the beamlet on the phosphor plate.
- 4.22: A spot image of the Si-TaSi₂ cathode #23-3, as measured by the coarse emittance measurement apparatus. The aperture disk has a single, on-center aperture of $\sim 0.3\text{mm}$ diameter. The aperture plate thickness is $\sim 1\text{mm}$.

- 4.23: A schematic drawing of the close spaced Pierce focused electron gun used for the pulsed high current experiments. The cathode is mounted in the cylindrical aperture in the electrode on the left. The beam is electrostatically focused through the anode structure on the right and subsequently either dumped in a collector structure or further diagnosed.
- 4.24: The modified cathode electrode structure for an improved AC gun design. The cathode is mounted through the back of the structure, and presses up against an anodized aperture in the front face of the electrode structure. This design removes the effects of the cathode wafer edges and allows a uniform wafer size to be used in designs for a wide range of generated electron beam diameters.
- 4.25: A pulse waveform from a Si-TaSi₂ eutectic cathode during an 8 hour run at 10Hz. The uppermost waveform is the current through the gun. The leading trace is the voltage on the gun, and can also be distinguished by the HF hash as it reaches peak and the cathode turns on. The middle trace is the total current, which takes into account the gun current and the current through the shunt. The values for the voltage, beam current, and minimum average beam current density are shown in the figure.
- 4.26: A schematic drawing of the slit wire emittance measurement system constructed for this project. The various parameters of the apparatus are discussed in the text.
- 5.1: The apparatus used in the modification of the DC test stand for the investigation of the application of the advanced cathode materials to the emission startup problem of the Aegis CFA tube.
- 5.2: The peak jitter measured by Litton for the modified and standard CFA tubes. The graph shows the results of a series of measurements over several hundred samples.
- 5.3: The rms jitter measured by Litton for the modified and standard CFA tubes. The graph shows the results of a series of measurements over several hundred samples.
- 5.4: The schematic layout of the emitter strip in the CFA cathode. The depth of the slot and the thickness of the emitter strip determine the setback of the emitters from the nominal surface of the cathode.
- 5.5: A SEM image of the Si-TaSi₂ emitter in the CFA. Note the small particulates. These are sand particles sifted out of the CFA tube by the emitter. The sand is introduced into the emitter during a preparation phase, and is evidently not completely removed.
- 5.6: The experimental setup used for the fast pulse laser experiments.
- 5.7: The CVR (solid line, upper) and pyroelectric laser detector (dashed line, lower) signals for an applied DC bias of 30kV/cm. The slow tail on the pyroelectric detector is a result of near-saturation of the detector. The actual laser pulse is

nearly symmetric, and the rise of the pyroelectric detector signal is indicative of its shape.

- 5.8: The schematic design for a FEA RF amplifier with inherent opto-isolation of the input and output stages. This design is based on the observed laser driven operation of the field emitters and uses demonstrated or off-the-shelf technology in all its components.

List of Tables

- 4.1: A summary of the tungsten cathodes tested in this project.
- 4.2: The analyzed data for cathode GI2-E and GI2-G.
- 4.3: A summary of the eutectic cathodes tested in this project.
- 4.4: The analyzed data for the 5-series cathodes.
- 4.5: The filter paper template cathodes tested in this project.
- 4.6: The microlithographic cathodes tested in this project.
- 4.7: A summary of the major lifetime data for this project.
- 4.8: The parameters for the HV modulator used in the AC gun experiments.

1 Executive Summary

This project was initiated to design, develop, test, and evaluate advanced cathode materials as electron beam sources. These cathode materials produce macroscopic electron beams via quantum field emission from a large density of emission sites. Our initial calculations and experimental data indicated that these materials would be capable of stable DC operation, high current density ($J > 200 \text{ A/cm}^2$), extremely high beam brightnesses (normalized brightness $B_n > 10^7 \text{ A/cm}^2\text{-rad}^2$), operation in poor vacuum (pressures $\sim 5 \times 10^{-5} \text{ Torr}$), and operational DC lifetimes greater than 1000 hours. This combination of capabilities would improve the operational characteristics of existing devices and enable new devices spanning a wide range of DOD applications.

There were two principal paths for the fabrication of the advanced cathode materials: (1) aligned composites of metallized self assembling bio-molecular microstructures called tubules, and (2) directionally solidified semiconductor-metal eutectic composites, predominantly Si-TaSi₂. Our initial calculations and data suggested that the tubule-based cathode approach would be superior to the eutectic composite cathode approach because of the nature of the tip microgeometry (hollow cylinders versus conical rods) and the larger parameter space available for optimization (including metal composition, density of emitter sites, and matrix composition). The eutectic composite materials were included as a backup option to the principal thrust of the self assembled tubule composites.

The advanced cathode materials developed under this project have now been tested in a variety of configurations and devices. Most of the performance milestones set forth in the original proposal have been met. In addition, several performance milestones not contemplated in the original proposal have been demonstrated. The sum of these achievements is reflected in the incorporation of the advanced cathode materials into follow-on efforts funded by DARPA, the US Army, the US Air Force, DOD industry, and commercial industry, and several additional pending proposed efforts.

The principal achievements of the advanced cathode materials to date can be summarized as:

- Long pulse average current density of 75 A/cm^2 over a 0.12" diameter area.
- Long pulse, repetitive operation of a 162 kW field emission array electron gun ($V = 27 \text{ kV}$, $I = 6 \text{ A}$, 0.12" diameter cathode). This is the highest power operation of a field emission array cathode by a factor of 10^5 .

- Detailed characterizations of cathode performance that show excellent agreement with theory and numerical simulation.
- Operation of several cathodes over 100 hours.
- Operation for over 100 hours in an oxygen background gas at $>10^{-6}$ Torr: removed from test while still running.
- Operation for over 400 hours in a Crossed-Field Amplifier (CFA) tube for the Navy Aegis radar, with significant improvement in performance: removed from test while still running.
- Operation in an argon background at ~ 1 Torr for >100 hours; demonstrated that operation under these conditions is dramatically different from vacuum operation.
- Brightness measurements of a non-optimized cathode structure in agreement with numerical simulations of the same structure.
- Demonstration of laser driven field emission using the electric field of the optical wave including:
 - macro-pulse modulation frequencies ~ 200 MHz,
 - optical modulation frequency of ~ 1000 THz (linearly polarized Nd:YAG),
 - scaling of field emission parameters appears to be the same as for DC operation.

This list represents a brief summary of some of the capabilities of the advanced cathode materials developed under this project. What such a list cannot convey is the detail of understanding that has been developed in terms of the properties of the advanced cathode materials, the fabrication and optimization processing, and the design of their incorporation into a given application.

During the course of this short term, fast paced development project, the wide range of available parameters for the tubule composite cathode approach proved to be more of a liability instead of a strength. Reproducible control of the parameters of the fabricated tubule composite cathodes was more difficult than anticipated. These stumbling blocks appeared unexpectedly throughout the various steps of the fabrication process. The fabrication of the lipid tubules, the deposition of the metal film, the incorporation of the metallized tubules into a uniformly distributed aligned composite, the selective removal of the matrix material -- all phases proved to be difficult to control to the necessary degree indicated by the calculations and experiments. Several alternative approaches were undertaken to fabricate the hollow cylinder array structure, replacing some elements of the tubule cathode fabrication process with other process steps. In the short time available, these alternatives did not succeed in breaking through the performance limitations observed with the tubule cathodes.

On the other hand, the performance of the Si-TaSi₂ eutectic materials far outstripped anticipations. Initial concerns regarding the tailorability of the tip shape, electrical contact to and physical mounting of the emitter wafer, and the emission startup difficulties were all successfully addressed. The application opportunities were further expanded by the development of additional capabilities, including the addressing of a cathode wafer in a pixelized format, the incorporation of a device quality Si epilayer on the wafer backplane, the protection of the emitter tips from an oxygen background, and several process developments that dramatically improved performance reproducibility and even allowed the resuscitation of some cathodes that had been intentionally "killed."

Limited program funds and project duration demanded a downselection of fabrication approaches to focus those resources on achieving the necessary cathode performance. While we still believe the arrays of hollow cylinder microstructures may be the penultimate performance winner, the existing performance differential between the eutectic approach and the self-assembling tubule composite approach (and its variations) forced that process to select the Si-TaSi₂ material option. The experience gained from the tubule composite fabrication process control has found its way into several other projects unrelated to advanced cathode materials. Further fabrication optimizations in those projects may, in turn, address the performance shortfalls experienced in this project.

The development of the advanced cathode materials accomplished in this project has directly led to follow-on projects for their incorporation into electron beam driven devices for the DOD, other government agencies, and commercial industry. As can be seen from the list below, the application arena is diverse and the degree of technology transfer to the user communities is extensive:

- The FEL application originally described in the proposal continues to be a promising use of the advanced cathode materials due to their ease of use, potential for high brightness, and now laser-synchronized emission. The principal interest in FELs is for medical and materials processing applications, which are presently primarily funded by SDIO and DOE. We have met with the DOE and they have expressed significant interest in following this aspect of the cathode performance.
- The ubitron and other microwave tube applications described in the proposal were highlighted at the 1992 Tri-Service/NASA cathode workshop. Parties having expressed interest in the cathodes and now in the process of testing them for use in

their microwave systems include Varian, Litton, and Raytheon, all of whom are major tube manufacturers for the DOD.

- A particularly novel application of the advanced cathode materials is as a startup primer for the Aegis CFA tube. Emitters were installed in a production CFA at Litton's facility in Williamsport, PA, and tested head-to-head against a standard tube. The modified tube demonstrated a factor of 10 to 1000 improvement in pulse jitter. The Navy subsequently de-emphasized CFA jitter in favor of low noise performance, but recent measurements by Varian suggest that low noise and low jitter may be interdependent. Varian has recently requested emitters for installation in their CFAs.
- As part of the Army's overall HPM efforts, the advanced cathode materials were selected as the electron source for General Dynamics' long pulse relativistic klystron amplifier development. Cutbacks in the program have resulted in the cancellation of that effort after the initial phase. The required cathode performance has already been demonstrated.
- The demonstration of laser driven field emitter array performance has profound implications for compact, high energy accelerator applications. For both advanced accelerator concepts and more conventional RF accelerator concepts, the availability of a compact, low cost method for extracting picosecond electron beams is extremely important. We have met with the DOE and they have expressed significant interest in pursuing this area. We are also investigating the potential for applying these advanced accelerator concepts to medical techniques, particularly aimed at reducing the size and weight of the required physical plant.
- The demonstration of laser driven FEA operation also has implications for DARPA's vacuum microelectronic RF amplifier program. Calculations indicate that commercial semiconductor lasers have more than sufficient power to effectively gate FEAs. These semiconductor lasers are routinely modulated in the GHz frequency range, and would therefore trivially provide the desired modulation frequency for the FEAs. Perhaps a more significant advantage is the isolation of the input from the output in such a device scheme. Such isolation is typically very difficult to achieve in stripline microwave systems and can dramatically increase the overall robustness of the microwave system.
- An application with very large potential impact has been the incorporation of the FEAs into fluorescent discharge tubes. The original driver for this work was the need for a night vision compatible, full sunlight readable LCD displays for the Army's Comanche helicopter. Initial measurements of the FEA performance have

demonstrated outstanding performance, and suggest the possibility of a much more widespread application of FEAs in this role. The efficiency of these fluorescent backlights has led to further investigations into their commercial value and their potential for a variety of applications where a white-hot cathode element is undesirable.

- Another large impact application of the higher pressure operation of these advanced cathode materials is a new DARPA sponsored project for the reduction of hazardous waste generation through the use of advanced thin film coatings. The advanced cathode materials play a central role in this project, allowing the optimization and scale-up of an experimental process for the efficient ion beam assisted deposition of wear resistance inorganic thin films.

A number of these application arenas were anticipated at the time of the proposal for this project. Other large impact application arenas were not anticipated because the performance capabilities they are based on had not been contemplated.

In summary, if the object of this project was the focused development of advanced high current density cathodes with the intent of radically improving existing technological capabilities or enabling the investigation of entirely new ones, then we have been successful. The assertion that advancements in cathode technology will act as a fulcrum for striking new developments is proven by the brief list of technology startups given above. The only shortfall worth noting is that the project that spawned these advancements may have paced too quickly: development programs for the incorporation of newly available technologies typically take 12 to 24 months to initiate. As scheduled, the majority of technological achievements in this project were not demonstrated until well into the second year. This left the potential for a 6 to 18 month gap between the technology and product phases. In retrospect, a more prudent project schedule would have specified an optional six month follow-on to bridge to the DOD product phase.

2 Design and Analysis of Advanced Microstructure Cathodes

In this section we discuss the work performed on the design and analysis of advanced microstructure cathodes such as the advanced cathode materials. This work has taken the form of both analytical and computational formulations for understanding and optimizing the operational characteristics of the FEAs. The analytical work concentrated on the thermal limitations of various structures, the theory of quantum field emission from three dimensional structures (for simplicity limited to structures with prolate spheroidal shape), and the beam brightness requirements for various operational regimes of the targeted free electron laser application. The numerical work concentrated on the emission simulations of realistic microemitter structures with the goals of understanding and optimizing the observed emission behavior for both the solid rod (Type 1) and hollow cylinder (Type 2) structures.

2.1 Analytical Formulations

In this subsection we first cover the analytical formulation of quantum field emission from three dimensional structures. This represents a modification to the canonical use of Fowler-Nordheim field emission for the analysis of data and design of optimized structures. The need for this focus was originally suggested by results of the numerical simulations covered in the next subsection. Next we discuss the thermal limitations of the structures and how these limitations affect the design of the advanced cathode materials. Finally, we discuss the theoretical aspects of beam brightness limitations of FEL performance.

2.1.1 Quantum Field Emission from 3-D Structures

The majority of this work has been published in Applied Physics Letters, Vol. 60, No. 17, pp. 2065-2067, 27 April 1992. A copy of this publication is included in Appendix A. The motivation for this analytical investigation was an insight, gained from working with the FEAT simulation code discussed later in this section, that the field enhancement factor and effective emission area for a sharp emitter tip would change as a function of the applied field. This change is due to the combination of the extremely nonlinear nature of quantum field emission and the rapidly varying electric field profile in the vicinity of the emitter tip apex.

The advanced cathode materials are moderately uniform, irregular arrays of classical field emitters. Each emitter tip is much like a tungsten filament used in an SEM. As

classical field emitters, the local current density is described by Fowler-Nordheim field emission¹

$$J_{FN} = \frac{A(\beta E)^2}{\phi t^2(y)} \exp\left(-B \frac{\phi^{3/2} v(y)}{\beta E}\right) \quad \text{A/cm}^2,$$

where A and B are constants, ϕ is the work function of the emission material, E is the applied electric field, β is the field enhancement factor due to local geometry, and $t(y)$ and $v(y)$ are very weak functions of the work function and electric field (a more detailed description of this equation is given later). As can be seen from the $\beta^2 E^2 \exp(-\kappa/\beta E)$ dependence of the current density J_{FN} , this type of emission is very sensitive to the electric field at the emission surface. To achieve the high local electric fields necessary for the quantum field emission process, field emitter arrays like the advanced cathode materials must have emitters with sharp tips: typical tip radii of curvature are in the range of 10-600Å.

The analysis of the emission characteristics of these highly sharpened tips continues to be based on the theoretical work of Fowler and Nordheim. That calculation assumes a one-dimensional problem where all quantities vary only with the distance from the emission surface or their depth within it, and also assumes that the state from which an electron is emitted is instantaneously refilled. Furthermore, the typical extension of the Fowler-Nordheim theory that is used to analyze the current-voltage (I - V) characteristics of arrays of sharp tips assumes that the field enhancement factor, β , and the tip emission area, α , are constant and independent of the applied field E . Our analysis demonstrated that the parameters α and β are not constants, and that when a simple account of realistic material properties is included, the variation of α and β can be pronounced for sharp tips operating at currents of 1--100μA. Not including this variation can result in both incorrect calculation of the performance potential for a given microstructure design and erroneous interpretation of the measured data from an existing structure.

The typical technique^{2,3} employed to characterize an array of field emitting tips is to measure the I - V characteristic of the array and from that data to deduce the field enhancement factor, β , and an effective emission area, α , of the array in operation. This procedure is based on the assumption that the local tip current density is governed by quantum field emission as derived by Fowler and Nordheim,

$$J_{FN} = \frac{A(\beta E)^2}{\phi t^2(y)} \exp\left(-B \frac{\phi^{3/2} v(y)}{\beta E}\right) \quad \text{A/cm}^2,$$

where J_{FN} is the local current density, $A=1.54 \times 10^{-6}$, $B=6.87 \times 10^7$, $y=3.79 \times 10^{-4} (\beta E)^{1/2}/\phi$, $t^2(y) \cong 1.1$, $v(y) \cong 0.95 - y^2$, E is the applied electric field in V/cm, β is the field

enhancement factor due to local geometry, and ϕ is the work function in eV of the surface emission material. Precise values for $t^2(y)$ and $v(y)$ are tabulated in the literature.^{4,5} The next step in this process is the assertion that $I=J_{FN}\alpha$. With this, a plot of $\ln(I/V^2)$ against $1/V$ will be well fit by a straight line, and the slope and intercept of this line can be used to find α and β of the tips in the array. The measured β is used to infer a weighted average for the radius of curvature of those tips participating in the emission process. Similarly, the value for α is used to infer an average emitting area per tip in the array. The emitting area per tip is further often assumed⁶ to be of the order of πR_c^2 , where R_c is the inferred radius of curvature of the operating tips. A gross discrepancy is often found between the value for R_c inferred from α and that from β . This discrepancy has been resolved typically by postulating either that only a few of the tips in the array are participating in the emission,⁷ or that the emission emanates from isolated surface protrusions or dielectric inclusions on the tip surface.⁸

While both of these deficiencies may be present in the field emitter array, the analysis just described does not address the variation in field enhancement factor over the surface of a tip, nor the consequences this has for the variation in the profile of the emitted current density. Because the local emitted current density must vary from its peak value at some region near the apex, to essentially zero at other regions still close to the apex, the assumption that β is constant over the region of emission is clearly in error. More precisely, the error lies in the assumption that β for the tip as an emitting region is the same as the value for β_0 at the apex of the tip. The value for β obtained from the analysis of the data from a single tip represents a local current weighted average over the tip surface,

$$\langle \beta \rangle = \frac{1}{I_{tip}} \int_S \beta(x) J_{FN}(x) dS.$$

In the case of an array of many tips, this average must be extended over the entire array.

For a prolate half ellipsoid of revolution on a flat surface immersed in a paraxial electric field (see Fig. 2.1), Kosmahl⁹ has calculated the potential to be

$$\Phi(\eta, \xi) = -E_0 c_2 \xi \eta \left[1 - \left(\left(\ln \frac{\eta+1}{\eta-1} - \frac{2}{\eta} \right) \middle/ \left(\ln \frac{\eta_0+1}{\eta_0-1} - \frac{2}{\eta_0} \right) \right) \right]$$

where η and $\xi = \cos \phi$ are the ellipsoidal coordinates given by

$$z = c_2 \xi \eta,$$

$$\frac{r^2}{c_2^2(\eta^2-1)} + \frac{z^2}{c_2^2 \eta^2} = 1,$$

$c_2 = \sqrt{h^2 - b^2}$, h is the ellipsoid semi-major axis and the height of the tip, b is the ellipsoid semi-minor axis, E_0 is the uniform applied field far from the ellipsoid surface, and $\eta = \eta_0 = h/c_2$ prescribes the surface of the ellipsoid. The radius of curvature at the apex of the ellipsoid is equal to $r_c = b^2/h$. Following some straightforward math the tip average field enhancement factor is given by,

$$\langle \beta \rangle = \frac{1}{I_{tip}} \beta_0 \int 2\pi c_2^2 \xi \sqrt{(\eta_0^2 - 1)(\eta_0^2 - \xi^2)} J_{FN}(\beta(\xi)) d\xi.$$

While the tip current I_{tip} is given by

$$I_{tip} = \int 2\pi c_2^2 (\eta_0^2 - \xi^2) J_{FN}(\beta(\xi)) d\xi.$$

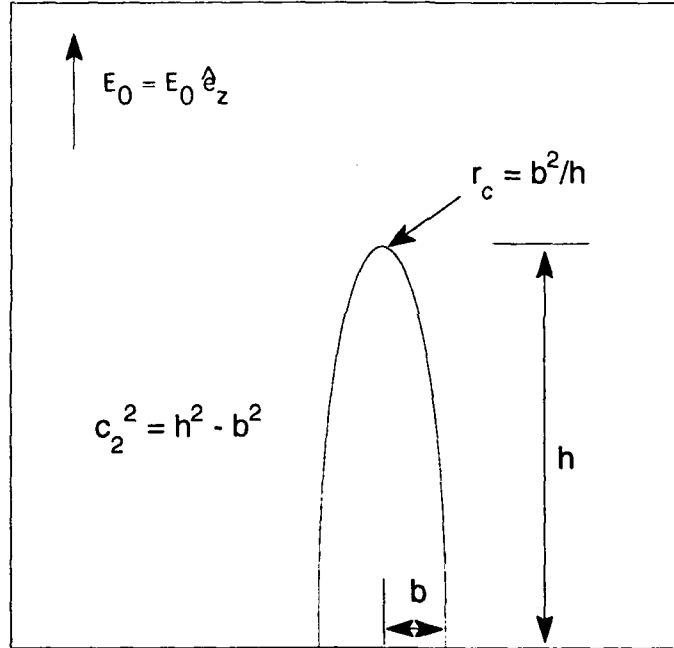


FIGURE 2.1: The geometry of the prolate ellipsoid of revolution that is used for these calculations.

The non-constant nature of α and $\langle \beta \rangle$ are evident from a cursory inspection of the previous two equations. For small values of the applied field, only a very small region near the apex of the tip emits any appreciable current, and the value for $\langle \beta \rangle$ will be very close to the value of β_0 . Similarly, the actual emitting area will be quite small. In order to be consistent, an appropriate definition for the emitting area is

$$\alpha_1 = I_{tip}/J_{FN}(\langle \beta \rangle)$$

where the notation α_1 is used to distinguish the quantity from that derived from an I - V characteristic.

A final point in this analysis is a basic attempt to account for some simple materials issues that must be considered when dealing with very sharp tips and significant tip currents ($I_{tip} \sim 1-100\mu A$). The calculation of J_{FN} assumes a certain density of electron states at the Fermi level of the tip material, and calculates a transition probability per unit time for the tunneling of such a bound electron to a vacuum state outside the tip material. Once such an electron is emitted, subsequent emission must either await the repopulation of the original state or must occur from other, perhaps more tightly bound, energy levels. For sharp tips and high fields, the local values of J_{FN} can easily be greater than $10^8 A/cm^2$ while the integrated tip current I_{tip} is only $1-100\mu A$. Thermal issues aside, a local current density of $10^8 A/cm^2$ corresponds to the emission of an electron per $1nm^2$ every 160fs, while $10^{10} A/cm^2$ corresponds to an electron every 1.6fs. Emission from energy levels that are more bound than the Fermi level is strongly attenuated, as can be seen by the dependence of J_{FN} on the work function, ϕ . The potential effect of this depletion can be considered by forcing a fixed, minimum time interval for the repopulation of an emitted state, Δt_{xtal} . The time interval between successive emission events is then $\Delta t = \Delta t_{xtal} + \Delta t_{FN}$. In terms of the local current density, such a limit takes the form

$$(1/J_{eff}) = (1/J_{max}) + (1/J_{FN}) ,$$

where J_{max} is some value associated with the properties of the emitter material. With this modification to the local current density, the quantities $\langle\beta\rangle$, I_{tip} , and α_1 become

$$\langle\beta\rangle = \frac{1}{I_{tip}} \beta_0 \int 2\pi c_2^2 \xi \sqrt{(\eta_0^2 - 1)(\eta_0^2 - \xi^2)} J_{eff}(\beta(\xi)) d\xi .$$

$$I_{tip} = \int 2\pi c_2^2 (\eta_0^2 - \xi^2) J_{eff}(\beta(\xi)) d\xi .$$

$$\alpha_1 = I_{tip}/J_{eff}(\langle\beta\rangle) .$$

The results of this analysis are shown in Figs. 2.2 through 2.6, where $\langle\beta\rangle$ and α_1 are plotted against I_{tip} or E_0 for $J_{max} = 10^6$, 10^8 , and $10^{10} A/cm^2$. The work function used in these calculations is $\phi = 5eV$. While the falloff in $\langle\beta\rangle$ is noticeable in the case of $r_c = 100\text{\AA}$, it is quite pronounced for $r_c = 25\text{\AA}$. For the case of $J_{max} = 10^8 A/cm^2$, the falloff in $\langle\beta\rangle$ from its peak value to its value at $I_{tip} = 100\mu A$ is about 10% in the case of $r_c = 100\text{\AA}$, while it is about 35% in the case of $r_c = 25\text{\AA}$. Even with minimal influence from $J_{max} = 10^{10} A/cm^2$ the value of $\langle\beta\rangle$ decreases by 10% in the case of $r_c = 25\text{\AA}$. Perhaps more pronounced is the variation of α_1 shown in Fig. 2.6 for $r_c = 100\text{\AA}$. As can be seen in the figure, the source of the decrease in the value of $\langle\beta\rangle$ evidenced in Figs. 2.2 and 2.4 is the activation of more of the tip area, and correspondingly increasing the contribution

to $\langle\beta\rangle$ from points farther away from the tip apex. This effect is more pronounced for the sharper tip with $r_c=25\text{\AA}$.

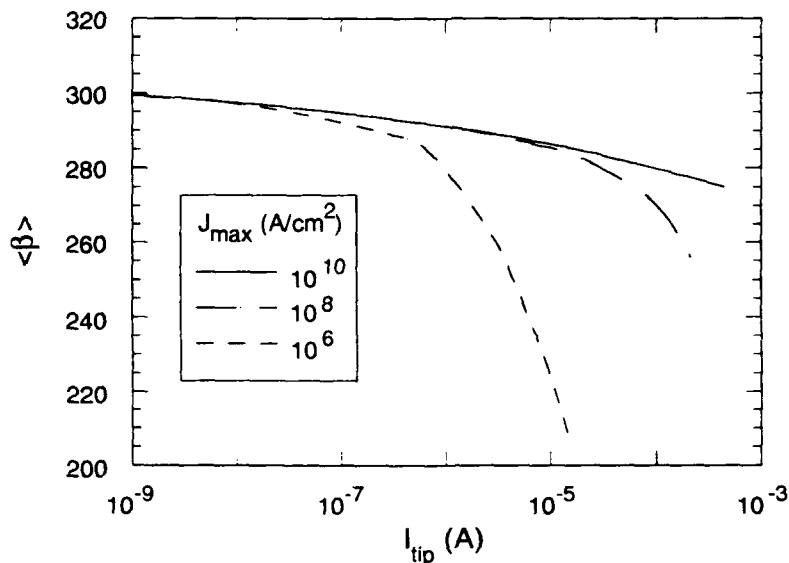


FIGURE 2.2: $\langle\beta\rangle$ parameterized vs. I_{tip} for $J_{max} = 10^{10}, 10^8$, and 10^6 A/cm^2 . The independent variable is the applied field E_0 , which varies over a range of 50-350 kV/cm. The tip height is $h=10\mu\text{m}$ and the tip radius of curvature is $r_c=100\text{\AA}$.

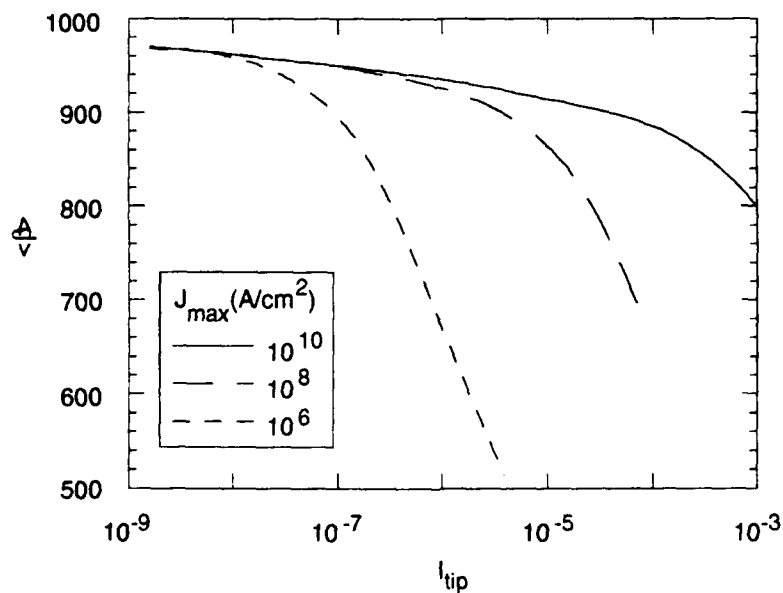


FIGURE 2.3: $\langle\beta\rangle$ parameterized vs I_{tip} for the same values of J_{max} and tip height as in the previous graph, but with a tip radius of curvature $r_c=25\text{\AA}$. Note that observable changes in $\langle\beta\rangle$ occur for tip currents starting at $\sim 1\mu\text{A}$, and large changes may occur for tip currents $\sim 10\mu\text{A}$.

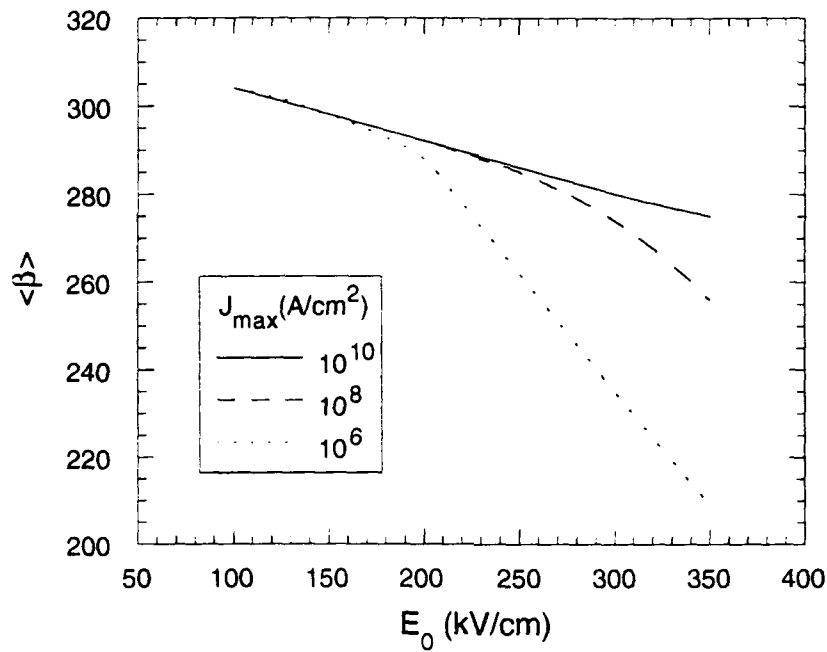


FIGURE 2.4: $\langle \beta \rangle$ plotted vs E_0 for the same data as plotted in Fig. 2.2. Note that in the absence of any accounting for materials limitations, as in the case of $J_{\max}=10^{10}$ A/cm 2 , $\langle \beta \rangle$ evidences a linear decrease with increasing field. The inclusion of some accounting for the refilling time of vacated states generates a faster falloff for $\langle \beta \rangle$, in this case appearing bilinear in nature.

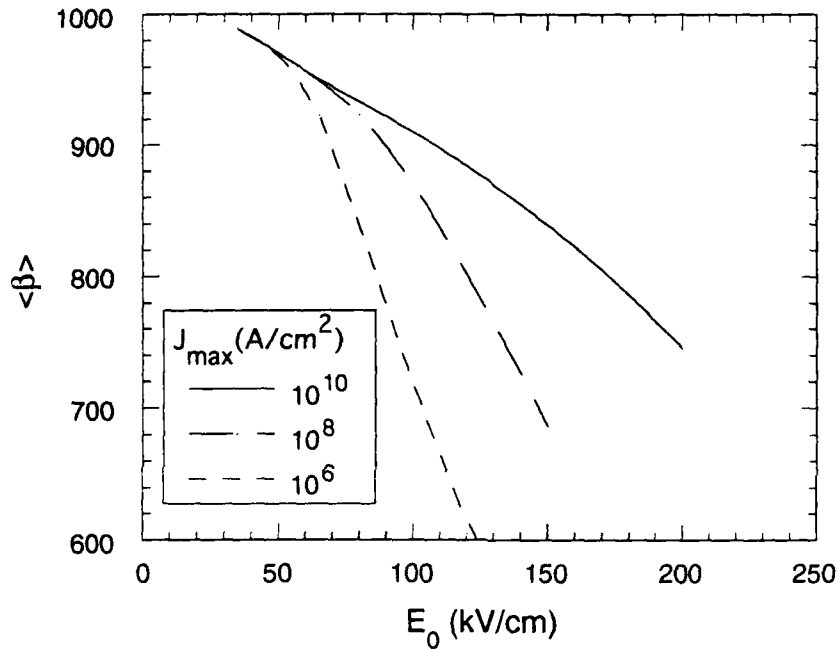


FIGURE 2.5: $\langle \beta \rangle$ plotted vs E_0 for the same data as plotted in Fig. 2.3.

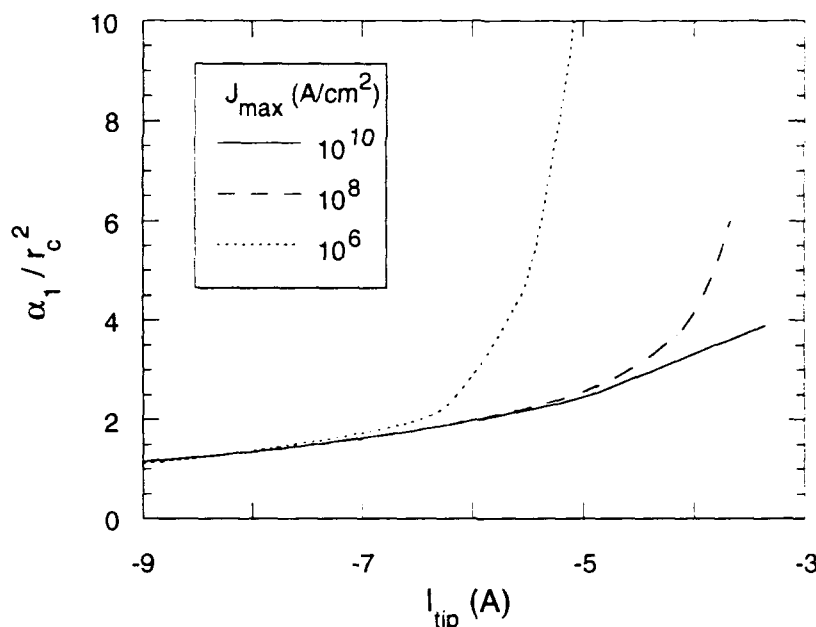


FIGURE 2.6: α_1/r_c^2 parameterized vs. I_{tip} for $J_{max} = 10^{10}$, 10^8 , and 10^6 A/cm², and $r_c = 100$ Å. The independent variable is the applied field E_0 , which varies over a range of 100-350 kV/cm. Note that α_1/r_c^2 is not constant, is not equal to π , and is increasing while $\langle\beta\rangle$ is decreasing. This is true even for $J_{max} = 10^{10}$ A/cm², where $J_{eff} = J_{FN}$ to within <1%.

The conventional analysis of the I - V characteristic for this same data would incorrectly suggest a decrease in the participating emission area and an increase in the average field enhancement factor of those tips contributing - a phenomenon more commonly termed "current hogging." The Fowler-Nordheim I - V characteristic ($\ln(I/E^2)$ vs. $1/E$) of the tip emission when J_{max} has an appreciable effect evidences a flatter slope for higher fields and tip currents, due to the saturation of some areas on the tip. The usual analysis of this data would indicate both an increase in the average field enhancement factor and a decrease in the emission area, when in fact exactly the opposite is occurring.

The conclusion reached from this analysis is that the operation of sharp tips as vacuum field emission electron sources is necessarily a dynamic process, with the tip field enhancement factor and effective tip emission area both being functions of the applied electric field. This dynamic behavior is due to the nature of the tip as a distributed area with varying local field enhancement as a function of position on the tip. If a limit to the maximum local emission density is imposed, the variation of $\langle\beta\rangle$

and α_1 can be large. The variation increases substantially for tips with radii of curvature less than 100 Å.

These results have their greatest effect on those applications that have sought the use of sharp tips ($r_c < 100$ Å), at large currents ($I_{tip} > 10$ μA), and in particular those that depend on the assumed dynamic behavior of a field emitter array in an amplifier configuration. The geometry of the prolate ellipsoid of revolution is a rough match to the "Type 1" solid rod geometry of the eutectic composite field emitter arrays. The analytical formulation of the coordinate system necessary to address some approximation to the "Type 2" hollow cylinder geometry of the tubule composite field emitter arrays is formidable, and so we have started with the less difficult system. One obvious advantage of the tubule composite cathode geometry is borne out in the simulations discussed later: the emitting area at the top of an individual emitter structure is much larger for a hollow cylinder than for a solid rod. The dramatic falloffs in $\langle \beta \rangle$ therefore occur at much higher total tip currents, and high current, high brightness operation is more readily achieved.

2.1.2 Thermal Limitations

The list of potential applications of FEAs such as the advanced cathode materials includes flat panel displays, high power switches, and RF amplifiers. The power requirements that these applications place on the emitter structures are wide ranging and depend on the application of interest. Flat panel displays may require average array power densities of $< 1 \text{ W/cm}^2$, while high power switches may require power densities $> 1 \text{ MW/cm}^2$ for short durations. These electrical power requirements drive the thermal loading of the emission structure, as well as the collector structure. The dynamics and capabilities of electron beam collectors have been covered extensively elsewhere. This subsection is concerned with the time-average and time-dependent thermodynamic response of the emitter structures.^{10,11}

Several types of structures have been implemented for use as field emission arrays. The list of emitter microstructure types includes pyramids, wedges, cones, hollow right circular cylinders, and hollow cone-shaped cylinders. Some of these structures are similar in topology. In some cases, the electrical topology is different from the thermal topology inasmuch as a smaller material volume than is available for thermally sinking the generated Ohmic heating may be carrying the electrical current. Such a case is not considered in the analytical formulations here, but these calculations can be extended to accommodate that situation.

We first consider the time-independent heat equation and its solution as a function of the geometry of the emitter structure. These calculations indicate an advantage of the conical convergent type emitter geometries over the hollow, right circular cylinder, non-convergent type structure. This analysis indicates that a modification to the tubule cathode structure would be desirable, where the hollow center of the cylinder is filled up to some height with thermally and electrically conductive material. We then look at the fully time-dependent heat equation and develop closed-form solutions for both the hollow right circular cylinder and the solid cone. Relevant approximations are applied to these exact solutions in order to extract the general thermodynamic properties without the need for the full solution. We close with a discussion of the thermal limitations these calculations suggest, and the implications of those limitations for high frequency devices, high power devices, and optimized emitter structure design.

The heat equation with a distributed Ohmic thermal source is given by

$$c\rho_m \frac{\partial T}{\partial t} = \nabla \cdot (k_t \nabla T) + J^2 \rho_e .$$

This equation can also be written in the form

$$\frac{\partial T}{\partial t} - \frac{k_t}{c\rho_m} \nabla^2 T = \frac{J^2 \rho_e}{c\rho_m} .$$

Here T is the temperature function, t is time, k_t is the thermal conductivity, c is the specific heat, ρ_m is the mass density, ρ_e is the electrical resistivity, and J is the local current density. Note that J could be a function of space, that additional source terms could be added, and that boundary conditions can be applied to account for sources and sinks of heat that occur in a very small volume. The case of the equilibrium solution is taken by setting

$$\frac{\partial T}{\partial t} = 0 ,$$

resulting in Poisson's equation, $-\nabla^2 T = (\text{source})$.

Consider a right circular cylinder with constant wall thickness (see Fig. 2.7), for which the source deposition term is a constant. Assuming there is no heat transport other than a perfect heat sink at the base of the emitter structure, the temperature profile of the emitter structure is one dimensional in nature. This case is appropriate for a tubule cathode wherein all of the composite matrix in the center of the tubule has been removed or where that matrix material is neither a good electrical or thermal conductor. The 1-D heat equation becomes

$$\frac{d^2T}{dx^2} = - \frac{I^2 \rho_e}{k_t}.$$

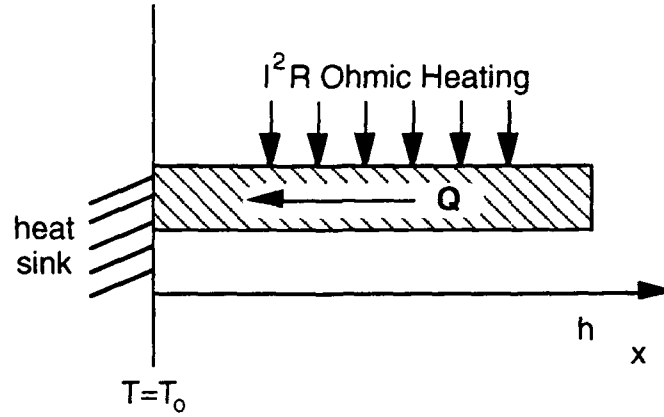


FIGURE 2.7: The geometry for the 1-D steady state thermal calculation. Ohmic heating is distributed throughout the tip volume, and the perfect heat sink at $T=T_0$ is at $x=0$. Cooling due to radiation losses or the Nottingham effect is neglected, as are any variations in k_t or ρ_e .

At equilibrium, assuming the radiated heat is negligible, the total heat generated in the emitter tip must flow through the thermal sink boundary at $x=0$ into the reservoir. In these calculations only the Ohmic heating due to the transfer of current through the tip structure is considered. The boundary condition on dT/dx is then given by

$$\left. \frac{dT}{dx} \right|_{x=0} = \frac{I^2 \rho_e}{k_t} h.$$

This boundary condition, plus $T=T_0$ at $x=0$, gives the maximum temperature at the top of the tip $x=h$

$$T_{max} = \frac{I^2 \rho_e}{2 k_t} h^2 + T_0.$$

Including the effect of other heat sources or sinks in the vicinity of the emitter tip and is accomplished by modifying the boundary condition on dT/dx . Labeling this additional power source or sink as U_{tip} gives us

$$\left. \frac{dT}{dx} \right|_{x=0} = \frac{I^2 \rho_e}{k_t} h + \frac{U_{tip}}{k_t}$$

at the emitter base, while at the emitter tip

$$\left. \frac{dT}{dx} \right|_{x=h} = \frac{U_{tip}}{k_t},$$

which modifies the previous result for the maximum temperature at the emitter tip apex

$$T_{max} = \frac{1}{2} \frac{J^2 \rho_e}{k_t} h^2 + \frac{U_{tip}}{k_t} h + T_0.$$

These calculations do not consider the variation of k_t or ρ_e with temperature. The results are therefore limited in validity to temperature variations that are small enough so that variations in k_t or ρ_e are negligible. The various materials that have been used as substrates for field emitters have a wide range of values for k_t and ρ_e . Considering a poor metal such as steel, or a good metal such as copper, these values might range $\rho_e = 2\text{--}100\mu\Omega\text{-cm}$, $k_t = 0.1\text{--}4\text{W/cm}^\circ\text{K}$. If those structures fabricated from doped silicon are included, the range of resistivities increases to $\rho_e = 2\text{--}10^9\mu\Omega\text{-cm}$.

Applying this calculation to the specific example of a tubule structure, we take a cylinder with a radius to the wall center of $R_0 = 0.25\mu\text{m}$, a wall thickness of $\Delta r = 0.05\mu\text{m}$, and neglect the convergence of the current to the outermost lip of the cylinder at the top of the emitter. This gives $J = I(\mu\text{A}) \times 1.6 \times 10^3 \text{ (A/cm}^2\text{)}$, and taking $\rho_e = 100\mu\Omega\text{-cm}$ and $k_t = 0.1\text{W/cm}^\circ\text{K}$ gives a maximum for the product of the tip height and tip current of

$$I(\mu\text{A}) \times h(\mu\text{m}) \leq 6 \times 10^3.$$

For a tip height of $20\mu\text{m}$ this gives a maximum tip current of $\sim 300\mu\text{A}$. For the case of a tubule with the properties of bulk copper, this factor increases by approximately $\times 14$. It should be noted that the use of bulk values for ρ_e and k_t of the tubule material is probably unrealistic: thin film coatings typically demonstrate electrical and thermal properties well below the properties of the same material in bulk form.

A calculation of the steady state limits for a convergent conical geometry is more relevant to the cone-shaped tips of the Type 1 structure. This is also the more typical shape for field emitters fabricated from microlithographic techniques. The geometry for the calculation is shown in Fig. 2.8. For a conical emitter with half-angle θ_0 , tip diameter $r_i \sin \theta_0$, and base diameter $r_o \sin \theta_0$, the local current density is

$$J = \frac{I}{\pi r^2} \frac{1}{\sin^2 \theta_0}.$$

With this driving source the time-independent heat equation is expressed in spherical coordinates,

$$\frac{1}{r} \frac{d^2}{dr^2}(rT) = - \frac{\rho_e I^2}{\pi^2 k_t \sin^4 \theta_0} \frac{1}{r^4}.$$

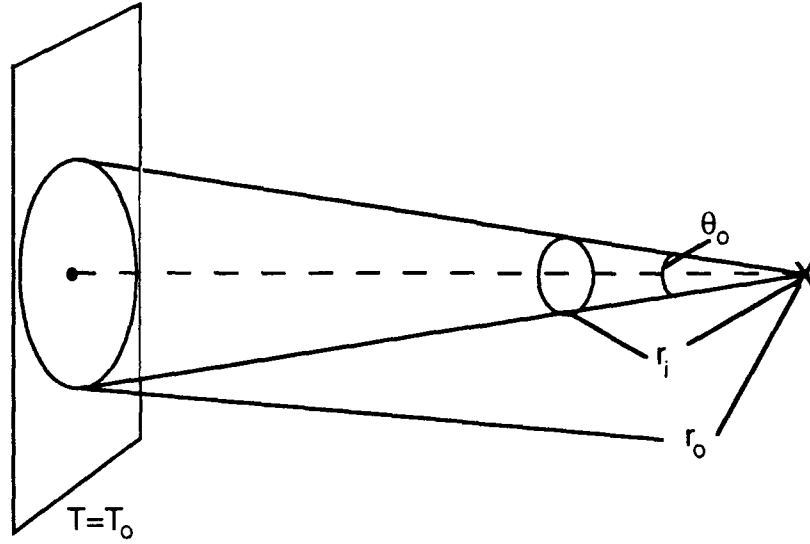


FIGURE 2.8: The geometry used for the calculation of the steady state temperature profile for a solid cone (Type 1) structure.

This equation has a solution of the same form as for the linear geometry and the temperature profile is given by

$$T(r) = \frac{\rho_e I^2}{\pi^2 k_t \sin^4 \theta_0} \frac{1}{2} \left\{ \left(\frac{1}{r_i} - \frac{1}{r_o} \right)^2 - \left(\frac{1}{r_i} - \frac{1}{r} \right)^2 \right\} + T_0$$

where the boundary conditions

$$T(r_o) = T_0 ; \frac{dT}{dr}(r_i) = 0$$

have been applied. A sample temperature profile given by this equation is shown in Fig. 2.9. Evaluating this function at $r=r_i$ gives a maximum temperature at the tip of

$$T(r_i) = \frac{\rho_e I^2}{\pi^2 k_t \sin^4 \theta_0} \frac{1}{2} \left(\frac{1}{r_i} - \frac{1}{r_o} \right)^2 + T_0.$$

Defining the height of the cone as $h=r_o - r_i$, this can be rewritten as

$$\Delta T = T(r_i) - T_0 = \frac{\rho_e I^2}{\pi^2 k_t \sin^4 \theta_0} \frac{1}{2} \left(\frac{h}{r_i r_o} \right)^2$$

or further

$$\Delta T = \frac{1}{2} \frac{\rho_e}{k_t} \frac{I^2}{(\pi r_i^2 \sin^2 \theta_0)(\pi r_o^2 \sin^2 \theta_0)} h^2 = \frac{1}{2} \frac{\rho_e}{k_t} \cdot I_{tip} \cdot I_{base} \cdot h^2 .$$

As in the previous calculation for a non-convergent geometry, additional sources or sinks of energy local to a small area near the tip can be accounted for by judicious use of

the boundary conditions on dT/dr , and the resulting modification in the coefficients in the equation for $T(r)$.

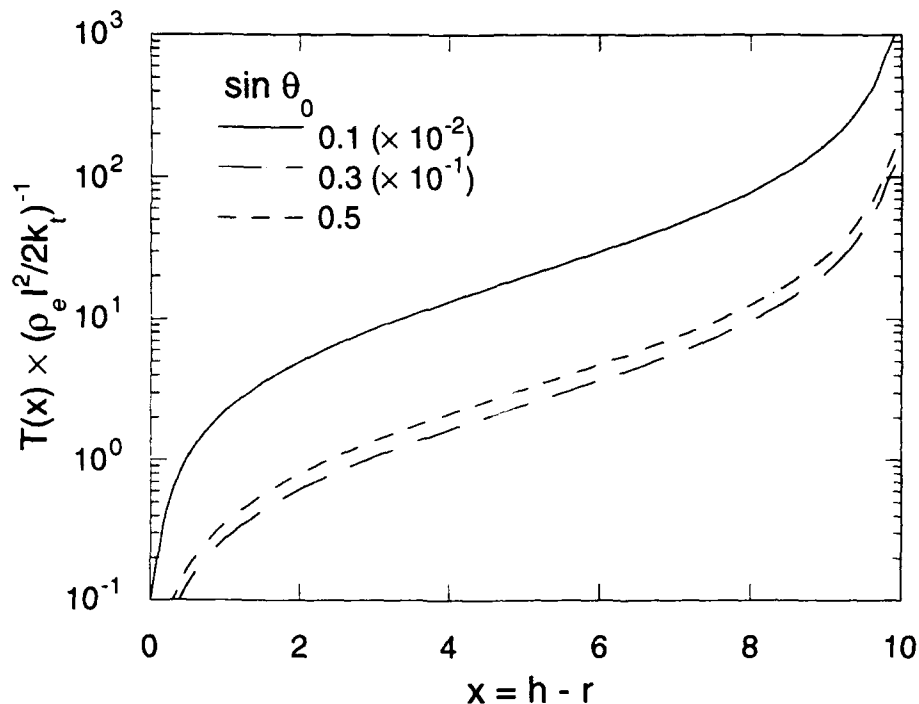


FIGURE 2.9: Different steady state temperature profiles for the convergent cone geometry as a function of the cone angle θ_0 . Note that the results have been scaled in order to fit all the data on the same plot. Note also that the horizontal axis has been defined as $x=h-r$ rather than just r : the tip of the emitter is at the right of the plot, the base at the left.

The analysis has so far been limited to steady-state equilibrium, which is relevant for DC or very long pulse operation of the advanced cathode materials. Every application of these materials is subject to variations in the applied field, either because of noise in the driving system or because the system itself is repetitively pulsed as in a radar. A key question of interest is the time scale over which the structures come to equilibrium, and how this interval is related to the geometry and materials characteristics of the structure.

The time dependent heat equation with sources can be written as,

$$\frac{c_v \rho_m}{k_t} \frac{\partial T}{\partial t} - \nabla^2 T = \frac{j^2(x,t) \rho_e}{k_t} \equiv f(x,t) ,$$

where the units of $f(x,t)$ are $^{\circ}\text{K}\cdot\text{cm}^{-2}$. For an arbitrary driving function $f(x,t)$, this equation can be solved by Duhamell's principle.¹² Start with the homogeneous equation

$$\frac{c_v \rho_m}{k_t} \frac{\partial T}{\partial t} - \nabla^2 T = 0 ,$$

and separate $T(x,t) = v(x)\Theta(t)$, giving

$$\frac{c_v \rho_m}{k_t} \frac{1}{\Theta} \frac{\partial \Theta}{\partial t} = \frac{1}{v} \nabla^2 v = -k^2.$$

Because the first part of this equation depends only on time, and the second part only on space, both parts must be independently equal to a constant, $-k^2$. The time equation becomes

$$\frac{\partial \Theta}{\partial t} + k^2 a_0 \Theta = 0$$

where $a_0 \equiv k_t / c_v \rho_m$. Note that a_0 has units of cm^2/sec . Similarly, the spatial equation becomes

$$\nabla^2 v + k^2 v = 0 .$$

The solution to the temporal equation is straightforward,

$$\Theta = e^{-k^2 a_0 t} .$$

The solution to the spatial equation requires the specification of the boundary conditions as well as the geometry, and will provide an eigenvalue equation for k^2 . Given the eigenfunctions of the spatial equation, v_n , and the eigenvalues, k_n , the solution to the inhomogeneous equation is

$$T(x,t) = \sum_{n=0}^{\infty} \left[\int_0^t f_n(\tau) e^{-k_n^2 a_0 (t-\tau)} d\tau \right] v_n(x) ,$$

where the f_n are given by

$$f_n(\tau) = a_0 \int_V f(x,t) v_n(x) dx ,$$

and the orthonormality condition on the v_n is given by

$$\int_V v_n(x) v_m(x) dx = \delta_{nm} .$$

It is easily verified that the above series solution for $T(x,t)$ indeed solves the given inhomogeneous heat equation.

Application of this methodology to the case of the 1-D non-convergent geometry of a tubule-like tip gives us the spatial homogeneous equation

$$\nabla^2 v + k^2 v = 0 ,$$

with the boundary conditions

$$v(0) = 0$$

$$\left. \frac{dv}{dx} \right|_{x=h} = 0$$

and the solution for the v_n, k_n , are:

$$v_n(x) = \sqrt{\frac{2}{h}} \sin(k_n x) ; k_n = \frac{n + \frac{1}{2}}{h} \pi .$$

Further, assume a driving current of the form $J(x,t) = J_{max} \sin(kx - \omega t)$, giving

$$f(x,t) = C_0 \sin^2(kx - \omega t)$$

$$f_n(\tau) = a_0 \sqrt{\frac{2}{h}} \int_0^h C_0 \sin^2(kx - \omega \tau) \sin(k_n x) dx .$$

The various necessary integrals can be found in the tables, leading to the final expression for the complete time dependent temperature profile for a tubule-like structure in the case where the driving current is sinusoidal, with frequency ω and wavenumber k , and also with the restriction that the driving wavenumber is not resonant with any of the natural wavenumbers of the system, $k_n \neq 2k$:

$$\begin{aligned} T(x,t) = & a_0 \frac{J_0^2 \rho_e}{k_t} \frac{2}{h} \sum_{n=0}^{\infty} \sin(k_n x) \left\{ \frac{1}{4} \left[\left(\frac{\sin(2k + k_n)h}{2k + k_n} - \frac{\sin(2k - k_n)h}{2k - k_n} \right) \right. \right. \\ & \left. \left(\frac{a_0 k_n^2 \sin(2\omega t) - 2\omega \cos(2\omega t) + 2\omega e^{-k_n^2 a_0 t}}{(a_0 k_n^2)^2 + 4\omega^2} \right) \right] \\ & + \frac{1}{4} \left[\left(\frac{\cos(2k + k_n)h}{2k + k_n} - \frac{\cos(2k - k_n)h}{2k - k_n} + \frac{2k_n}{4k^2 - k_n^2} \right) \right. \\ & \left. \left(\frac{a_0 k_n^2 \cos(2\omega t) + 2\omega \sin(2\omega t) - a_0 k_n^2 e^{-k_n^2 a_0 t}}{(a_0 k_n^2)^2 + 4\omega^2} \right) \right] \\ & \left. + \frac{1}{2k_n} \left(\frac{1 - e^{-k_n^2 a_0 t}}{a_0 k_n^2} \right) \right\} . \end{aligned}$$

With the assumption $k_n \gg 2k$, many of the terms in the above equation cancel or can be dropped. Note that for structures that protrude $h \sim 25 \mu\text{m}$ above the thermal sink backplate, the assumption $k_n \gg 2k$ corresponds to Fourier components of the driving currents with wavelengths $\lambda \gg 200 \mu\text{m}$. This long wavelength assumption $k_n \gg 2k$ is then satisfied for driving current frequencies up to at least 100GHz ($\lambda \sim 3\text{mm}$), and the equation reduces to

$$T(x,t) = a_0 \frac{J_0^2 \rho_e}{k_t} \frac{2}{h} \sum_{n=0}^{\infty} \left\{ \frac{\sin(k_n x)}{2k_n} \times \left[\frac{1 - e^{-k_n^2 a_0 t}}{a_0 k_n^2} - \frac{a_0 k_n^2 \cos(2\omega t) + 2\omega \sin(2\omega t) - a_0 k_n^2 e^{-k_n^2 a_0 t}}{(a_0 k_n^2)^2 + 4\omega^2} \right] \right\}.$$

Further simplification is possible depending on the relative magnitudes of t , ω , and $a_0 k_0^2$. For most materials of interest, $a_0 \sim 0.1\text{-}6\text{cm}^2/\text{sec}$. For emitter structures in the range of heights $1\text{-}10\mu\text{m}$, $a_0 k_0^2 \sim 10^5\text{-}10^9\text{sec}^{-1}$. The frequency has already been restricted to $\omega < 2\pi \times 100\text{ GHz}$.

For the case where $\omega \gg a_0 k_0^2$ and $t \rightarrow \infty$, the summation further reduces to

$$T(x,t) = \left(\frac{J_0}{\sqrt{2}} \right)^2 \frac{\rho_e}{k_t} 2h^2 \sum_{n=0}^{\infty} \frac{\sin(k_n x)}{k_n^3 h^3}.$$

This equation can be compared with the quadratic equation obtained for the steady state 1-D case, and indeed it is found that they are equivalent upon the substitution of the r.m.s. current ($J_0/\sqrt{2}$) for the dc current J_0 .

The timescale for the evolution to the steady state solution can also be extracted from the fully time dependent series solution. Again, assume the wavelength of the driving current to be long compared to the scale size of the structure, $k_n \gg 2k$. Additionally, consider times t such that $\omega t \sim 0$, assume $4\omega^2 \ll (a_0 k_n^2)^2$, but do not assume any strict relationship between t and $\tau_r^n = (a_0 k_n^2)^{-1}$. Under these conditions, the full series expression can be approximated by

$$T(x,t) = \left(\frac{J_0}{\sqrt{2}} \right)^2 \frac{\rho_e}{k_t} 2h^2 \sum_{n=0}^{\infty} \frac{\sin(k_n x)}{k_n^3 h^3} (1 - e^{-k_n^2 a_0 t}).$$

As n gets large, τ_r^n decreases, and the longest e-folding time is for the $n=0$ term when

$$\tau_r^0 = \frac{1}{a_0 k_0^2} = \frac{c_v \rho_m}{k_t} \frac{4h^2}{\pi^2}.$$

The dominant spatial term in the approximate time dependent summation is the $n=0$ term; the $n=1$ term is smaller by a factor of 3^3 while the $n=2$ term is smaller by a factor of 5^3 . For times $t \ll \tau_r^0$, the temperature rise in the emitter structure is significantly less than the temperature rise in the steady state case. Similarly, the shape of the temperature profile is modified for these short times. An example of this evolution is shown in Fig. 2.10, where $T(x,t)$ is plotted for various values of t/τ_r^0 . Note that the scale

has been magnified for the shortest timescale case. The magnitude of τ_r^0 is determined by the material properties of the emitter structure, and the size scale of the structure. For most structure scales and most materials of interest, $\tau_r^0 \sim 0.1\text{-}100\mu\text{sec}$.

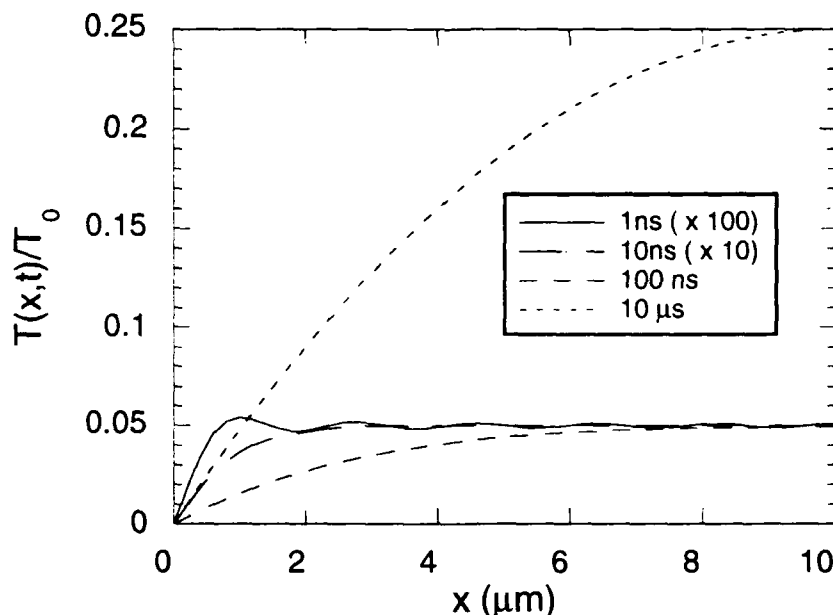


FIGURE 2.10: The approximate time dependent temperature profile for a 1-D emitter structure. For these calculations $f=10\text{GHz}$, $a_0=1\text{cm}^2/\text{sec}$, $h=10\mu\text{m}$. For this combination of parameters the value of $\tau_p^0 \sim 400\text{ns}$.

2.1.3 Brightness Effects on FEL Performance

One of the primary applications of interest for the advanced cathode materials has been as an electron source for free electron lasers for materials processing. An important issue in the generation of coherent radiation at short wavelengths from the free electron laser (FEL) is the effect of a beam thermal spread on the interaction. Indeed, in many cases, the thermal spread available from various electron beam sources constitutes the essential limiting factor for many FEL applications. The thermal spread of an electron beam generated from the advanced cathode materials can be estimated from numerical simulations and measured experimentally. These two analyses then provide a measure of the parameter space of FEL operation available with the advanced cathode materials.

The results of this work are presented in detail in the publication attached in Appendix A, "Thermal Effects on the Linear Gain in Free-Electron Lasers." In this

paper, we address the question of the effect of an axial energy spread upon the linear gain of the FEL at both the fundamental resonance frequency and at harmonics of the fundamental. Coherent harmonic radiation is an important approach to the reduction in the beam energy required to achieve short wavelength operation, and has been observed in the laboratory over a wide spectral range. The question of the effect of beam thermal spread upon the gain at the harmonics, therefore, is of particular importance because reducing the required beam energy has a large impact on the affordability and utility of FELs.

Theoretical analyses of harmonic radiation in FELs have dealt with both the linear⁵⁻⁷ and nonlinear⁸⁻¹³ interactions. Results of these analyses indicate that substantial gains and efficiencies are possible for the harmonic interactions, but that the sensitivity of the interaction to the thermal spread increases with harmonic number. Hence, the beam quality required for coherent emission rises dramatically at the higher harmonics.

Our purpose was to develop a unified formulation of thermal effects on the linear gain in both the Compton and Raman regimes in a planar wiggler geometry. An industrial FEL will almost necessarily run CW (constant-wave) as opposed to pulsed: CW helical wigglers are difficult to build and offer no maintenance access to the interior, whereas CW planar wigglers have already seen extensive application. The differentiation between the Compton and Raman regimes is an analytical artifact corresponding to the approximation of either a single particle or collective beam interaction. In reality, the transition between these two regimes is gradual and continuous and many design configurations that might be considered lie in this transition region. A valid formulation for the effects of thermal spread that is independent of the Compton or Raman approximation is therefore desirable.

We assume that the beam is monoenergetic but characterized by a pitch-angle spread, and treat both the fundamental and harmonic interactions subject to an idealized one-dimensional approximation. This implies that the transverse velocity associated with the pitch-angle spread be much less than the wiggler-induced transverse oscillation. The effect of the pitch angle spread is twofold. In the first place, the resultant axial energy spread acts to degrade the interaction, and a general thermal function describing this effect is derived for the fundamental and the harmonics. In the second place, the pitch angle spread induces an oscillation in the axial velocity that can also act to excite harmonic radiation.

The physical configuration we consider is that of a relativistic electron beam propagating through an idealized one-dimensional planar wiggler. The representation for a planar wiggler in the idealized limit is given by

$$\mathbf{B}_w = B_w \hat{\mathbf{e}}_y \sin k_w z .$$

Since x and y are ignorable coordinates in the idealized representation for the wiggler fields, these components of the canonical momenta [denoted by P_x and P_y] are constants of the motion. In addition, the total energy is also a conserved quantity. As a result, the single-particle orbits are given by

$$p_x = P_x + p_w \cos k_w z ,$$

$$p_y = P_y ,$$

$$p_z = \sqrt{P_{\parallel}^2 - \frac{1}{2} p_w^2 \cos 2k_w z - 2 p_w P_x \cos k_w z}$$

where

$$P_{\parallel}^2 \equiv p^2 - \frac{1}{2} p_w^2 - P_x^2 - P_y^2$$

where $\gamma \equiv (1 + p^2/m_e^2 c^2)^{1/2}$ is the relativistic factor corresponding to the total electron energy and momentum p , $p_w \equiv \gamma m_e v_w$, $v_w \equiv -\Omega_w/k_w$ is the wiggler-induced velocity, and $\Omega_w \equiv |eB_w/\gamma m_e c|$. Since P_y is constant, the magnitude of the transverse wiggler-induced velocity oscillates at the wiggler period. This results in an oscillation in the axial momentum and velocity as well, which broadens the wave-particle resonance, and gives rise to harmonic interactions. The assumption of small displacements from the symmetry axis is equivalent to the condition that $|v_w/v_{\parallel}| \ll 1$, and we assume as well that $|V_{\perp}/v_w| \ll 1$.

The dispersion equation in the idealized one-dimensional representation is found in the context of a linearized Vlasov-Maxwell formalism. The Vlasov equation in the combined wiggler and electromagnetic fields is

$$\left[\frac{\partial}{\partial t} + \mathbf{v} \cdot \nabla - e \left(\delta \mathbf{E}(z,t) + \frac{1}{c} \mathbf{v} \times [\mathbf{B}_w(z) + \delta \mathbf{B}(z,t)] \right) \cdot \nabla_{\mathbf{p}} \right] f_b(z, \mathbf{p}, t) = 0 ,$$

where $f_b(z, \mathbf{p}, t)$ is the distribution function of the electron beam, $\delta \mathbf{E}(z,t)$ and $\delta \mathbf{B}(z,t)$ denote the fluctuating electric and magnetic fields of the wave. The Vlasov equation is linearized by expanding the distribution in powers of the fluctuating fields. We write $f_b(z, \mathbf{p}, t) = F_b(z, \mathbf{p}) + \delta f_b(z, \mathbf{p}, t)$ where F_b and δf_b are the equilibrium and perturbed

components of the distribution, and it is assumed that $|\delta f_b| \ll |F_b|$. The equilibrium distribution can be expressed as a function of the constants of the motion in the form $F_b(z, \mathbf{p}) = F_b(P_x, P_y, p)$. Correct to first order in the fluctuation fields, the perturbed distribution satisfies

$$\delta f_b(z, \mathbf{p}, \tau(z)) = e \int_0^z \frac{dz'}{v_z(z')} \left[\delta \mathbf{E}(z, \tau(z')) + \frac{1}{c} \mathbf{v}(z') \times \delta \mathbf{B}(z, \tau(z')) \right] \cdot \nabla_{\mathbf{p}} F_b$$

over the unperturbed trajectories with the assumption that the perturbations are negligibly small at time $t = 0$. We treat spatial growth and adopt Lagrangian coordinates in which $\mathbf{v}(z)$ denotes the unperturbed velocity of an electron as a function of the axial position, and

$$\tau \equiv t_0 + \int_0^z \frac{dz'}{v_z(z')}$$

The Vlasov equation is solved in conjunction with Maxwell's equations. We choose to deal with the scalar $\delta\phi(z, t)$ and vector potentials $\delta\mathbf{A}_{\perp}(z, t)$ in the Coulomb gauge. In terms of this representation, Maxwell's equations are

$$\left(\nabla^2 - \frac{i}{c^2} \frac{\partial^2}{\partial t^2} \right) \delta \mathbf{A}_{\perp} = - \frac{4\pi}{c} \delta \mathbf{J}_{\perp} ,$$

and

$$\frac{\partial^2}{\partial t \partial z} \delta \phi = 4\pi dJ_z .$$

The source current is given in terms of the perturbed distribution function as follows

$$\delta \mathbf{J}(z, t) = - \frac{e}{m_e} \int d^3p \frac{1}{\gamma} \mathbf{p} \delta f_b(z, \mathbf{p}, t) .$$

Since the FEL operates by means of an axial bunching mechanism, it is the axial velocity spread that is most important. As a consequence, we assume the beam to be monoenergetic but with a pitch angle spread. The effect of the pitch angle spread is to include velocity spreads in both the axial and transverse directions, and may be described by a distribution function of the form¹⁵

$$F_b(P_x, P_y, p) = n_b \frac{\exp(-P_\perp^2/\Delta P^2)}{\pi \Delta P^2} \frac{p_z}{p} \delta(p-p_0) ,$$

where n_b denotes the bulk ambient density, $P_\perp^2 \equiv P_x^2 + P_y^2$, and ΔP represents the thermal spread.

The interaction occurs for plane waves polarized in the direction of the wiggler-induced oscillation. Using a Floquet analysis for periodic systems, we express the vector and scalar potentials for a wave with angular frequency ω as

$$\begin{bmatrix} \delta \mathbf{A}(z, t) \\ \delta \phi(z, t) \end{bmatrix} = \frac{1}{2} \sum_{n=-\infty}^{\infty} \begin{bmatrix} \delta \hat{A}_n \hat{\mathbf{e}}_x \\ \delta \hat{\phi}_n \end{bmatrix} \exp(ik_n z - i\omega t) + \text{c.c.} ,$$

where $k_n = k + nk_w$. The perturbed distribution function, therefore, takes the form

$$\delta f_b(z, \mathbf{p}) = \frac{e}{2c} \left[D_x \frac{\partial}{\partial P_x} + D_z \frac{\partial}{\partial p} \right] F_b(P_x, P_y, p) ,$$

where the orbit integrals are defined as [where $\tau(z, z') \equiv \tau(z) - \tau(z')$]

$$D_x \equiv -\delta \hat{A}(z) + \delta \hat{A}(0) \exp(i\omega \tau(z, 0)) ,$$

$$D_z \equiv \frac{1}{p} \int_0^z dz' \frac{\exp(i\omega \tau(z, z'))}{v_z(z')} \left[-cpz(z') \frac{\partial}{\partial z'} \delta \hat{\phi}(z') + i\omega p_x(z') \delta \hat{A}(z') \right] .$$

The orbit integrals D_x and D_z , which appear in the source currents, represent an integration over the unperturbed electron trajectories. In particular, we observe that the Lagrangian time variable characteristic of the electron trajectories is of the approximate form

$$\tau(z) \equiv t_0 + \frac{z}{V_{||}} + \frac{P_x}{P_{||}} \frac{v_w}{V_{||}} \frac{1}{k_w V_{||}} \sin k_w z + \frac{v_w^2}{8V_{||}^2} \frac{1}{k_w V_{||}} \sin 2k_w z \quad ,$$

where it is assumed that both $v_w < V_{||}$ and $P_x < P_{||}$. The existence of a nonvanishing canonical momentum introduces an oscillation at the wiggler period into the trajectory.

The dominant contribution of the axial thermal spread occurs within the resonance condition, and we restrict the analysis to the resonance associated with the Doppler upshift in frequency and restrict the analysis to a specific harmonic [i.e., for fixed l and m]. After some lengthy but straightforward manipulations,⁷ the dispersion equation may be written as

$$\left[(\omega - k_{n+l+2m} V_{||})^2 - \frac{\omega_b^2}{\gamma_0 \gamma_{||}^2} T_l(\zeta_{n+l+2m}) \right] \left(\omega^2 - c^2 k_{n+l+2m}^2 - \frac{\omega_b^2}{\gamma_0} \right) \\ \equiv - \frac{v_w^2}{4c^2} \frac{\omega_b^2}{\gamma_0} K_m^{(+)}(b_2) T_l(\zeta_{n+l+2m}) \left(\omega^2 - c^2 k_{n+l+2m}^2 - \frac{\omega_b^2}{\gamma_0} T_l(\zeta_{n+l+2m}) \right) ,$$

where $K_m^{(+)}(x) \equiv [J_m(x) - J_{m+1}(x)]^2$, J_n denotes the regular Bessel function of the first kind, $b_2 \equiv (\omega/k_w V_{||})(v_w^2/8V_{||}^2)$,

$$T_l(\zeta) \equiv \frac{\zeta^2}{2\pi} \int_0^{2\pi} d\phi \int_0^\infty dz \exp(-z) \frac{J_l^2(b_1)}{(z + \zeta)^2} ,$$

$$\zeta_{n+l+2m} \equiv \frac{\gamma_0^2 m_e^2}{\Delta P_2} \left(\frac{\omega^2}{k_{n+l+2m}^2} - v_{||}^2 \right) ,$$

and

$$b_1 \equiv \frac{\omega}{k_w V_{||}} \frac{v_w}{V_{||}} \frac{\Delta P}{P_{||}} z^{1/2} \cos \phi \quad .$$

The effect of the pitch angle spread on the axial velocity is the source of the l th harmonic contribution, which has the effect of modifying the thermal function T_l . In order to describe this effect in more detail, we assume that $b_1 \ll 1$, which is valid as long as $P_\perp \ll P_{||}$. As a result, we expand the Bessel function to lowest order in b_1 , and obtain

$$T_l(\zeta) \equiv \frac{(2l)!}{(l!)^4} \left(\frac{v_{tw}}{2v_{||}} \right)^{2l} \left(\frac{\omega}{k_w v_{||}} \right)^{2l} \left(\frac{\Delta P}{p_{||}} \right)^{2l} \left((-1)^l \zeta^{l+1} [1 - (\zeta + l) \exp(\zeta) E_1(\zeta)] + U_l(\zeta) \right),$$

where

$$U_l(\zeta) \equiv \begin{cases} 0 & ; l < 2 \\ \sum_{k=2}^l \sum_{n=0}^{k-2} \beta \frac{(-1)^{k-n} l! n! \zeta^{l-n}}{k! (l-k)! (k-2-n)!} & l \geq 2 \end{cases}$$

The dispersion equation is solved numerically for the fundamental and the third harmonic. In general, strong harmonic amplification requires a relatively large oscillation in the axial velocity; hence, the growth rate at the harmonics increases rapidly with Ω_w / ck_w . The analysis of cases in which Ω_w / ck_w is greater than unity requires a fully three-dimensional analysis. We restrict the numerical analysis herein to the case for which $\Omega_w / ck_w = 1$, which is at the fringe of the range of validity, and serves to clearly illustrate the relationship of the harmonics to the fundamental. In addition, we shall assume that $\gamma_0 = 2.957$ and $\omega_b / ck_w = 0.1$ as well. The magnitude of the growth rate is plotted versus frequency in Fig. 2.11 for the fundamental and third harmonic. The fundamental exhibits a peak growth rate of $|\text{Im } k| / k_w \approx 0.065$ at $\omega / ck_w \approx 1.55$. In contrast, the magnitude of the growth rate at the third harmonic is $|\text{Im } k| / k_w \approx 0.012$ at $\omega / ck_w \approx 4.80$. Observe that both the magnitude and bandwidth of the harmonic are reduced relative to the fundamental.

The effect of the thermal spread is shown in Fig. 2.12. Here we plot the normalized growth rate [the ratio of the maximum growth rate for a specific value of $\Delta P / p_0$ to the maximum growth rate for $\Delta P / p_0 = 0$] versus $\Delta P / p_0$. Thermal effects become important on the fundamental when $\Delta v_{||} / v_{||} \approx |\text{Im } k| / (k_w + \text{Re } k) \approx 0.025$, which corresponds to $\Delta P / p_0 \approx 22\%$ [recall that $\Delta v_{||} / v_{||} \approx \Delta P^2 / 2p_0^2$]. This is in substantial agreement with the results shown. For the harmonics, thermal effects become important at a much reduced thermal spread;^{7,8} specifically, when $\Delta v_{||} / v_{||} \approx |\text{Im } k| / [(1+2m)k_w + \text{Re } k]$. For the third harmonic in the present example, $\Delta v_{||} / v_{||} \approx |\text{Im } k| / (3k_w + \text{Re } k) \approx 0.0015$. This corresponds to $\Delta P / p_0 \approx 5.5\%$, which is also in good agreement with the calculation.

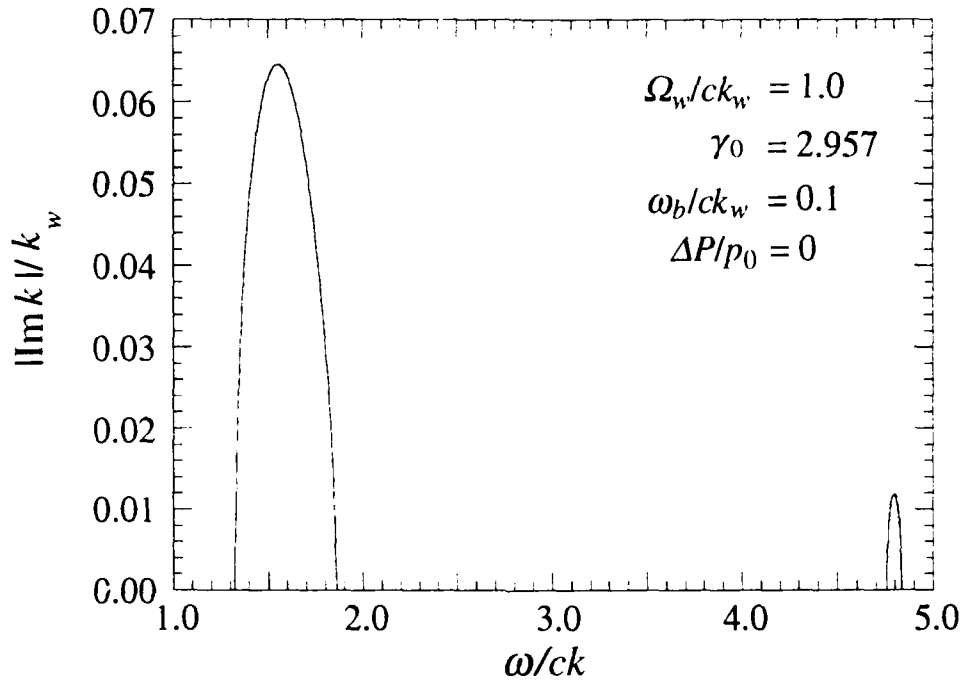


FIGURE 2.11: Graph of the growth rate versus frequency for the fundamental and third harmonic interactions.

The conclusions from the analysis are consistent with those found previously on the basis of an analytic model of thermal effects due to an energy spread and a nonlinear simulation using the pitch angle spread model.^{12,13} Specifically, that the gain at the harmonics is more sensitive to the effects of a thermal spread than is the fundamental. In particular, the thermal effect becomes important when $\Delta v_{||}/v_{||} \approx |\text{Im } k| / [(1+2m)k_w + \text{Re } k]$. In addition, it is clear that the thermal effect itself can give rise to amplification at the even as well as odd harmonics. However, this process requires a large energy spread that will result in relatively low growth rates, and is not likely to be of practical use.

Indeed, for many classes of electron beam, the source of the axial energy spread is predominantly the pitch angle spread rather than a spread in the total energy. For example, electron beams produced by MIG and Pierce guns are accelerated by voltages of up to several MeV and focused, prior to injection into the interaction region, either by shaped electric or magnetic fields. The coils and/or electrodes that produce the external fields in these guns must be carefully designed in order to offset the effects of the self-electric and magnetic fields of the beam. While the accelerating voltage may vary over

the duration of the beam pulse, the electrons are instantaneously characterized by a largely monoenergetic distribution. However, the focusing process itself gives rise to a pitch angle spread due to a variety of causes [such as field imperfections, shot noise, and self-field effects of the beam]. Similar effects are found in a variety of accelerating mechanisms, and the description of the axial energy spread as arising from a pitch angle distribution, rather than a spread in the total energy, is appropriate to a wide range of FEL designs.

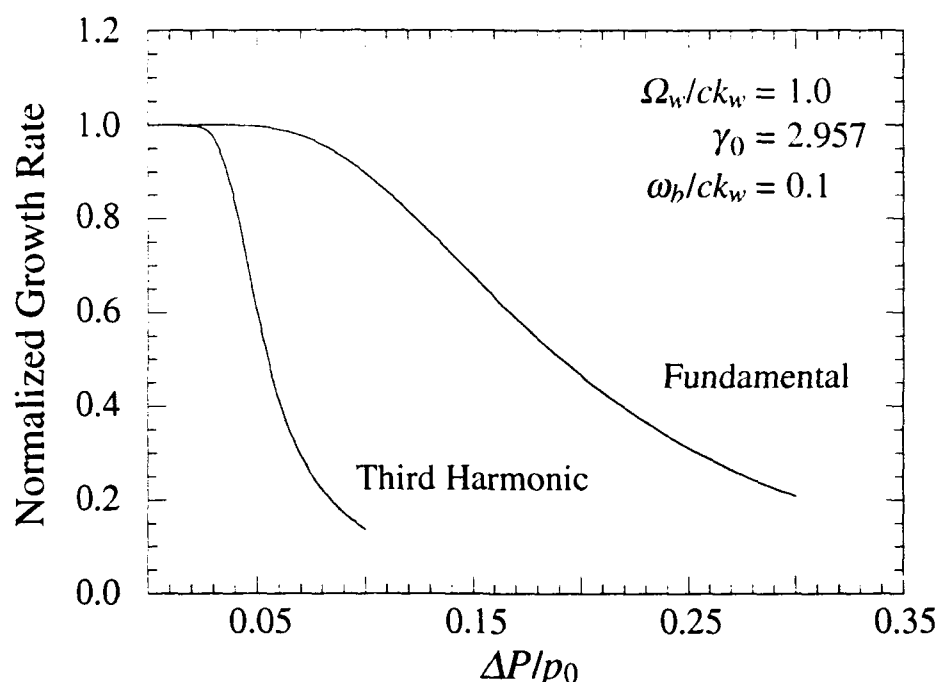


FIGURE 2.12: Variation of the normalized growth rates at the fundamental and third harmonic with the axial momentum spread.

2.2 Computational Formulations

There have been continuing questions regarding the applicability of the 1-D Fowler-Nordheim quantum field emission calculations to the highly 3-D nature of field emission array tips, be they gated as in the case of those fabricated at SRI by Spindt et al., or ungated as in the case of the advanced cathode materials developed under this project. In either case the electric fields required to generate significant field emitted currents are produced by the combination of an applied electric field and a local field enhancement due to the geometry of the field emitter tip. As was shown in Section

2.1.1, this field enhancement factor varies as a function of position on the tip. The calculation covered in Section 2.1.1 is limited to a geometry that allows a relatively straightforward analytical solution. More accurate depictions of the field emitter geometry and subsequent calculations of not only field emitted currents but also transverse velocity distributions (e.g., emittance and beam thermal spread) require the use of detailed numerical simulations.

Existing numerical simulation tools were not capable of accurately resolving the tip radius of curvature of a field emitter structure ($r_c \sim 100 \text{ \AA}$) while at the same time encompassing the boundary of the electrode structure ($h \sim 10 \mu\text{m}$). Given the azimuthal symmetry of both the tubule and eutectic emitter structures, only a 2-D model was required. A nested-grid structure was used to define the problem in order not to waste large amounts of computing time resolving areas where the feature sizes and fields were not rapidly changing, and instead focus that power on the vicinity of the emitter tip. For all the calculations performed in this project, the grid nesting was three deep, as shown in Fig. 2.13. The resolution of the smallest (innermost) grid was typically $\Delta x = 2.5 \text{ \AA}$, $\Delta y = 8 \text{ \AA}$. For the largest (outermost) grid these values were typically $\Delta x = 0.01 \mu\text{m}$, $\Delta y = 0.04 \mu\text{m}$. All three grids typically used 500 cells in the x and y directions.

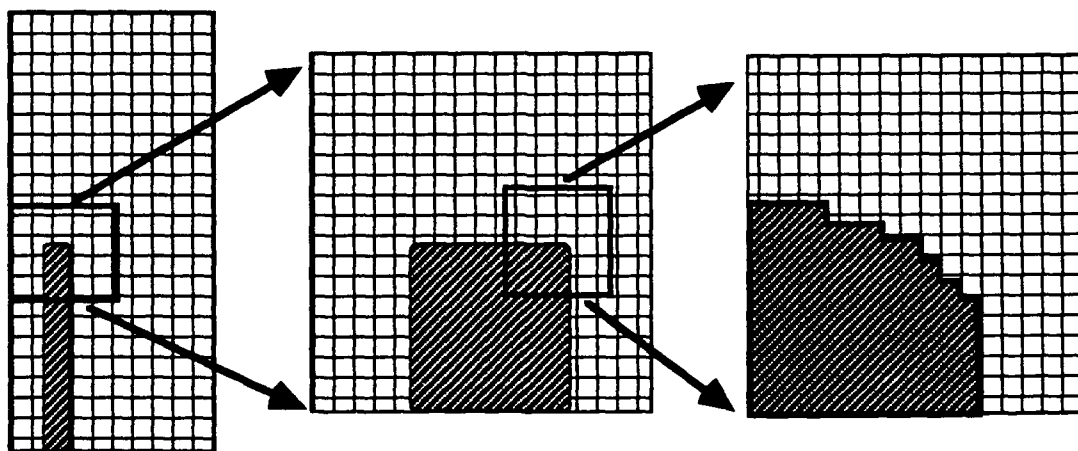


FIGURE 2.13: The grid structure used in FEAT and TPIC is optimized to provide extreme resolution where the field gradients are largest - near the tip - and not waste resolution where the field gradients are small. Properly matching between successive grid structures is essential if reliable results are to be achieved in a reasonable time.

The numerical simulations are broken into two parts covered by two separate codes: FEAT (Field Emitter Array Tip) and TPIC (Tip Particle In Cell). Complete listings of

both of these codes are given in Appendix B. FEAT solves for the electric potential distribution for a unit-applied macroscopic field, typically $1\text{V}/\mu\text{m}$. FEAT takes as inputs various descriptors of the structure dimensions and the dimensions and positions of the nested grid structures. Calculation of a solution on a triply nested 500 by 500 grid takes on the order of 20 CPU minutes on a IBM RS6000/320. TPIC takes as inputs a storage file with the field solve from a FEAT run, as well as various input parameters for the emission algorithm, including the applied voltage and Δt_{xtal} . TPIC then calculates the trajectories of test particles emitted from the structure surface and weighted by the local emission algorithm. The remainder of this subsection discusses some of the details of the calculations in FEAT and TPIC.

FEAT calculates a solution to Poisson's equation, $\nabla^2 \Phi = 0$, with appropriate boundary conditions to obtain the local electric field at all points on the surface of the field emitter structure. In cylindrical coordinates Poisson's equation is

$$\nabla^2 \Phi = \frac{1}{r} \frac{\partial}{\partial r} \left(r \frac{\partial \Phi}{\partial r} \right) + \frac{\partial^2 \Phi}{\partial z^2} = 0 .$$

The volume of interest is discretized as discussed above, creating a finite-difference mesh. On this mesh the elements of Poisson's equation become linear equations:

$$\begin{aligned} \frac{\partial^2 \Phi}{\partial z^2} &\rightarrow \frac{\Phi(i,j+1) - 2\Phi(i,j) + \Phi(i,j-1)}{(\Delta z)^2} , \\ \frac{\partial \Phi}{\partial r} &\rightarrow \frac{\Phi(i+1,j) - \Phi(i-1,j)}{2\Delta r} . \end{aligned}$$

The emitter region is masked off in stairstep fashion, leaving a discreteness to the emitter surface typically on the order of $2.5\text{-}10\text{\AA}$. All of the boundaries describing the centerline axis, cathode and anode planes, and emitter structure, combine with the finite element description of Poisson's equation to form a system of simultaneous linear equations. FEAT uses a numerical method termed ADI (for alternating - direction - implicit) to solve this system of equations to whatever accuracy is desired. The electric field is subsequently found from $E = -\nabla \Phi$.

The solution found in FEAT explicitly ignores the space-charge of the emitted beamlet. Given the formula for the Child-Langmuir space charge limited current in a parallel plate diode,

$$J_{\text{Ch-L}} = 2.335 \times 10^{-6} \frac{E^{3/2}}{d^{1/2}} \quad (\text{A/cm}^2) ,$$

we can estimate the range of validity of the FEAT code. In this equation E is the electric field in units of V/cm and d is the diode spacing in units of cm . For a surface electric

field of $\sim 10^8$ V/cm with a scale length of 100\AA , the local value for $J_{Ch-L} \sim 3 \times 10^9$ A/cm² -- well in excess of all but those calculations that ignore materials limitations associated with Δt_{xtal} . Space charge effects are in general only important when $J \geq 0.3 J_{Ch-L}$.

The particle pusher TPIC uses the field solve from FEAT and emits particles based on the value of the electric field local to tip location. This field is the unit field from FEAT multiplied by some constant equivalent to varying the voltage on a close-spaced diode. The particles are emitted from the local cells according to strict 1-D Fowler Nordheim field emission - this process is assumed to valid over the small incremental volumes that make up each simulation cell. The emission algorithm accepts as one of its inputs a value for Δt_{xtal} , and follows the process for calculating J_{eff} outlined in Section 2.1.1. The field that is used for the local cell emission calculation may or may not be smoothed over surface - the implications of smoothing or not smoothing over a surface that is rough on the size scale of 2.5\AA must be considered. On the one hand, realistic emitter tips are hardly smooth to subatomic dimensions. On the other hand, neither are they perfect conductors that instantaneously screen out the electric field: the electric field undoubtedly penetrates the material a few monolayers. The parameter "NS" in the input to TPIC controls the number of nearest neighbor smoothing cycles that are performed on the electric field before the emission algorithm proceeds. Most of our data runs are taken with NS=5, which produced a "bumpy" but not "jagged" field on the scale size of individual cells. Runs were also made varying NS to investigate the effect on the results.

2.2.1 Solid Needle Geometry - "Type 1"

One of the two geometries with masking templates already set up in FEAT and TPIC is the solid needle or "Type 1" geometry. This geometry is essentially that of the eutectic emitters investigated in this project, and the details of the shape are shown in Fig. 2.14. The emitter is an on-axis rod with a $1\mu\text{m}$ diameter. The tip of the emitter has a radius of curvature, r_c , which matches to a 22.5° taper out to the full $1\mu\text{m}$ diameter shank. The height, h , of the emitter is measured to the top of the spherical terminating cap.

A set of code outputs from a FEAT run for a Type 1 tip is shown in Fig. 2.15. These outputs include an equipotential plot in Fig. 2.15(a), magnitude of E plots in Figs. 2.15(b), and the brief output listing in Fig. 2.15(c). Note the dramatic compression of the equipotentials near the apex of the structure. It is this compression of the equipotentials that generates the field enhancement, allowing the fields necessary for

substantial field emitted currents locally while still operating with relatively modest average fields.

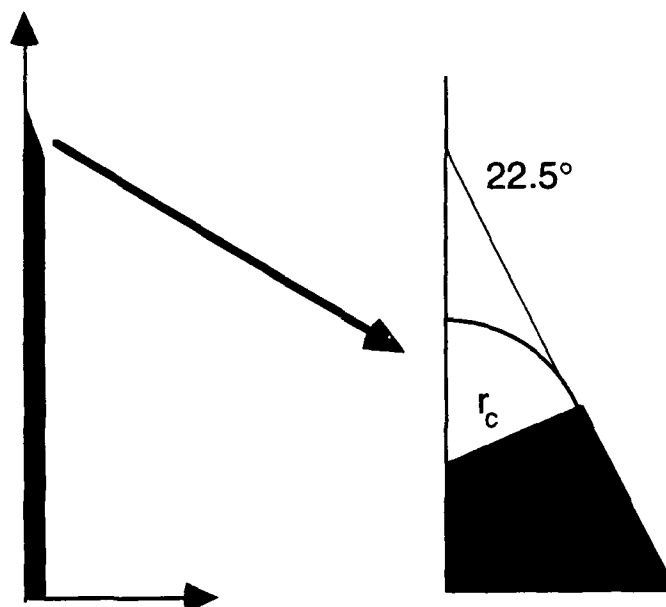


FIGURE 2.14: The geometry of the Type 1 tip. The shank of the emitter is $1\mu\text{m}$ in diameter. The tip terminates in a spherical cap of radius of curvature r_c , which is matched to the shank by a 22.5° tapered section.

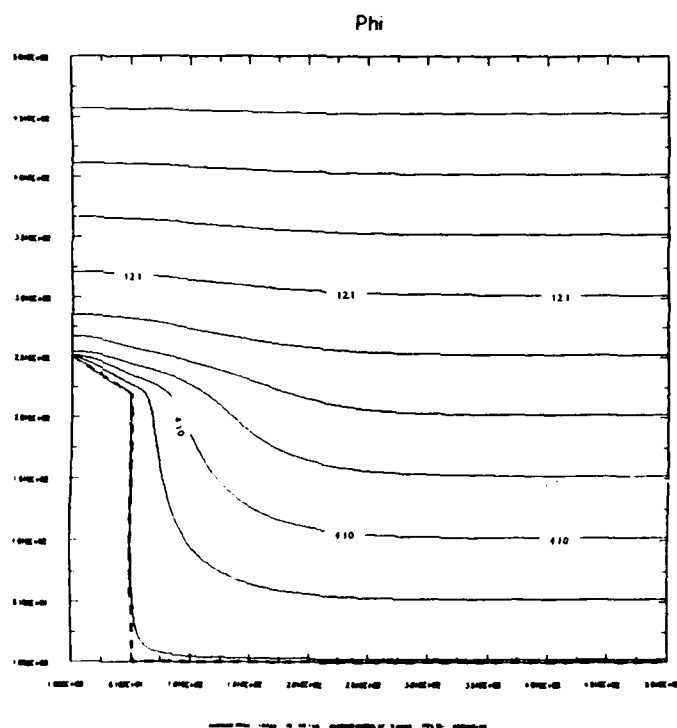


FIGURE 2.15(a): The equipotential plot output from a run of the FEAT code.

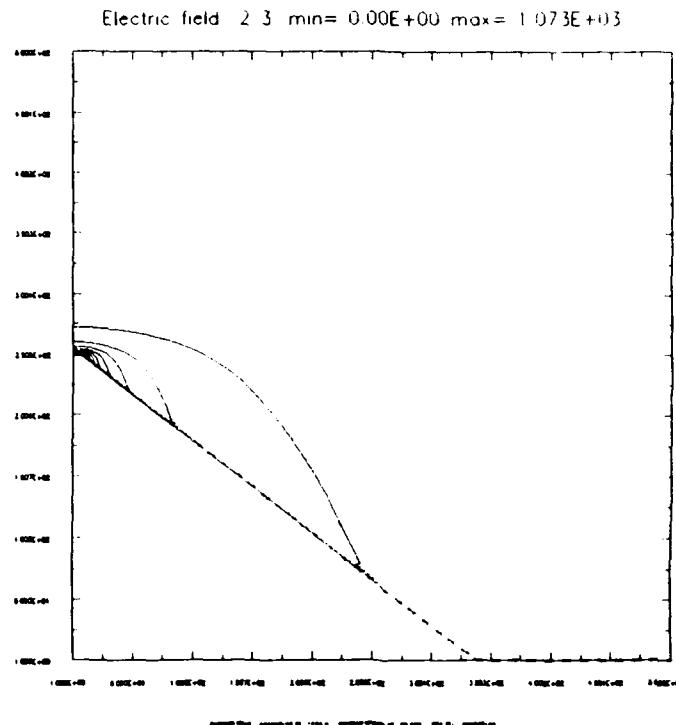


FIGURE 2.15(b): A contour plot for the magnitude of E_y , showing the large compression near the tip apex.

```

relx= 1.000E-02 rely= 4.000E-02
relxf= 1.000E-01 relyf= 4.000E-01
relxfr= 1.000E-04 relyfr= 3.000E-04
nxlcl.2 nyfcl.2 1 51 226 276 1.00E+01 1.00E+01 1.51E-05
nxfl.2 nyfl.2 1 126 201 301 4.00E+00 5.00E+00 1.24E-05
radd,height,width,angle 1.00E-02 1.00E-01 5.00E-01 1.93E-01
nxi,neta 501 501
nxi,neta 501 501
xi,xh,yi,yh 0.000 0.000 5.000 0.000 0.000 0.0 9.0 9.3 20.0 11.0 10.1
ni20,nj10 51 250
c it sumerr errmx
c it sumerr errmx
f it sumerr errmx
f it sumerr errmx
ff it sumerr errmx
ff it sumerr errmx
max Electric field 16 250 4.721E+02 1.750E-03 9.999E+00
f it sumerr errmx
f it sumerr errmx
max Electric field 1 251 5.310E+02 0.000E+00 1.000E+01
c it sumerr errmx
c it sumerr errmx
max Electric field 1 100 2.110E+03 5.118E+00 51 221
c it sumerr errmx
max Electric field 1 251 5.310E+02 0.000E+00 1.000E+01
ff it sumerr errmx
ff it sumerr errmx
max Electric field 16 250 4.635E+02 1.750E-03 9.999E+00
f it sumerr errmx
f it sumerr errmx
max Electric field 1 251 5.434E+02 0.000E+00 1.000E+01
c it sumerr errmx
c it sumerr errmx
max Electric field 2 251 7.300E+01 1.000E-02 1.000E+01
f it sumerr errmx
f it sumerr errmx
max Electric field 1 251 5.434E+02 0.000E+00 1.000E+01
ff it sumerr errmx
ff it sumerr errmx
max Electric field 16 250 4.597E+02 1.750E-03 9.999E+00
CPU (min)= 40.71

```

FIGURE 2.15(c): The output listing from the FEAT code for Figs. (a)-(c)

The TPIC code is used subsequent to the FEAT code while varying the applied average electric field, the value for Δt_{xtal} , and the number of smoothing iterations

applied to the surface fields prior to calculating the emission parameters. A sample output from a single TPIC run is shown in Fig. 2.16. A series of TPIC runs can be used to calculate a theoretical I - V characteristic: a Fowler-Nordheim type plot of some such characteristics is shown in Fig. 2.17. Using the combined FEAT and TPIC codes in this manner is extremely useful in the investigation of different mechanisms that might be responsible for various effects sometimes observed in experimental data.

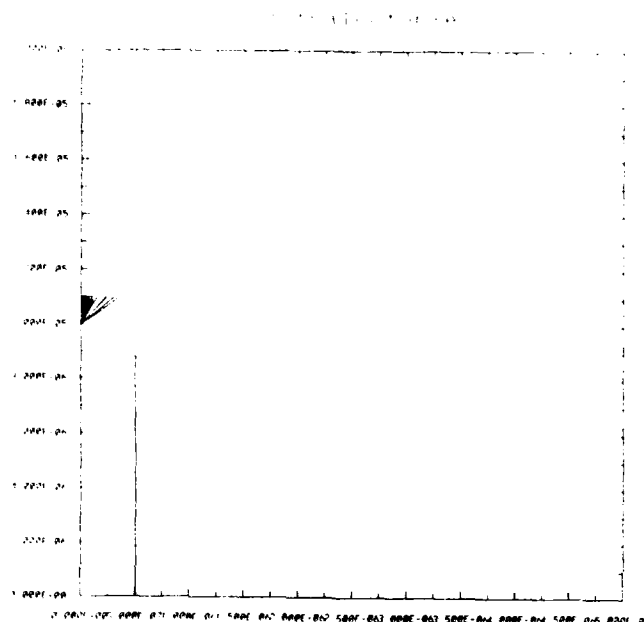


FIGURE 2.16(a): Output from a TPIC run for a Type 1 tip. This plot shows the trajectories of electrons emitted from the tip. The emission occurs from only a very small area near the tip apex.

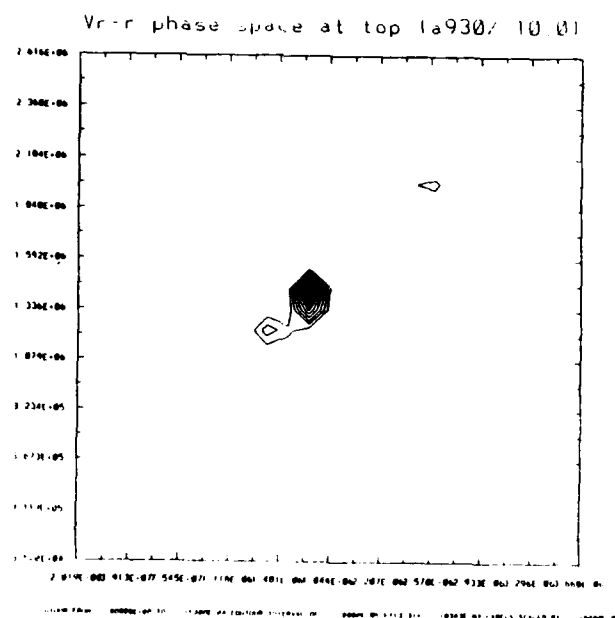


FIGURE 2.16(b): A plot from the same TPIC run as 2.16(a) showing the phase space contours used to evaluate emittance and brightness.

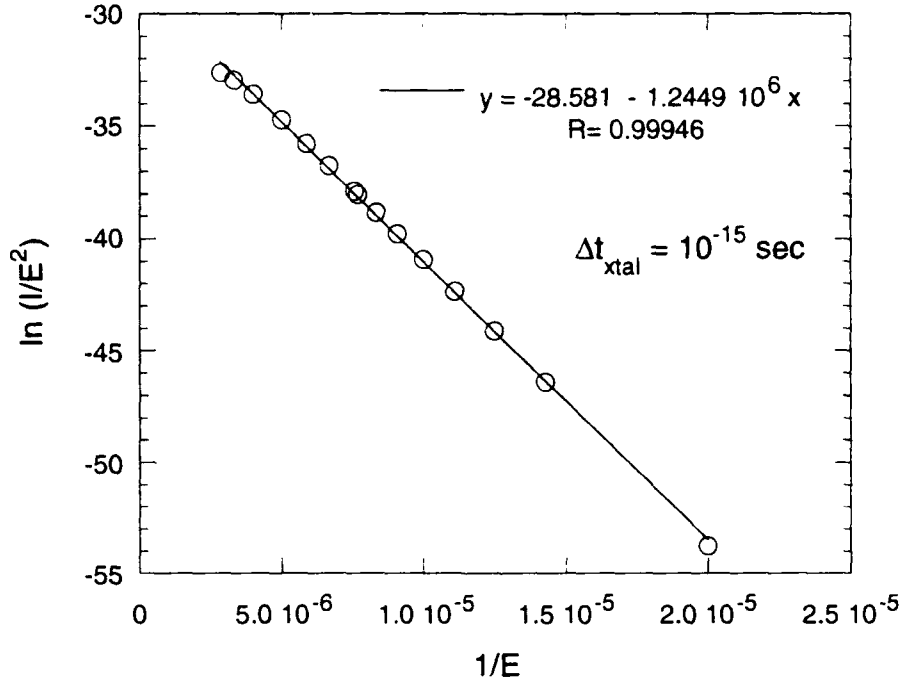


FIGURE 2.17: A composite Fowler-Nordheim I - V characteristic obtained from a series of TPIC runs. The geometry is Type 1 with $r_c=25\text{\AA}$. Note the saturation rollover at high fields. Such an effect might normally be misinterpreted as "current hogging."

2.2.2 Hollow Cylinder Geometry - "Type 2"

The second of the two geometries with masking templates already set up in FEAT and TPIC is the hollow cylinder or "Type 2" geometry. This geometry is essentially that of the tubule composite emitters investigated in this project, and the details of the shape are shown in Fig. 2.18. The emitter is a on-axis hollow cylinder with a $0.5\mu\text{m}$ mean diameter and a wall thickness of Δr . The cylinder wall at the tip of the emitter has a radius of curvature, r_c , which is limited by the nature of the structure to $r_c \leq \Delta r/2$. The height, h , of the emitter is measured to the top of the cylinder.

A set of code outputs from a FEAT run for a Type 2 tip is shown in Fig. 2.19. These outputs include an equipotential plot in Fig. 2.19(a), magnitude of E plots in Figs. 2.19(b) and (c), and the brief output listing in Fig. 2.19(d). Note the compression of the equipotentials near the apex of the structure, and the asymmetry of this compression between the inside and outside walls of the cylinder. It is this compression of the equipotentials that generates the field enhancement, allowing the fields necessary for substantial field emitted currents locally while still operating with relatively modest average fields. The substantially larger field compression on the outer edge of the

cylinder indicates that most of the emission will be confined to this area, and that the inner edge will contribute little, if any, to the performance of the cathode.

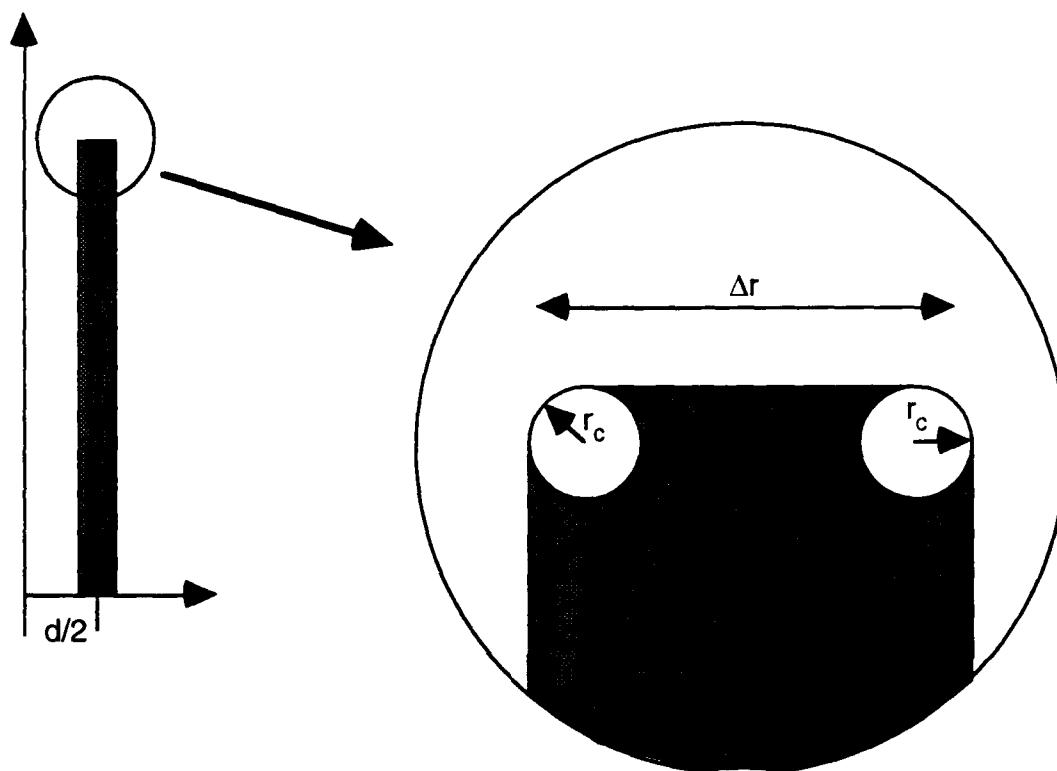


FIGURE 2.13: The geometry of the Type 2 tip. The mean diameter of the hollow cylinder is $0.5\mu\text{m}$. The tip terminates in a rounded square wall with a radius of curvature r_c . The thickness of the cylinder wall is given by Δr .

The lack of any significant emission from all but the outer lip of the cylinder apex mitigates the advantages of this type of structure. This effect might be minimized by controlling the details of the shape of the top of the cylindrical tip, and investigating a more tapered termination. This thought was pursued in part by the fabrication of microlithographically defined cylindrical field emitter arrays by NRL and SAIC, but fabrication problems associated with the metal deposition limited the efficacy of this approach.

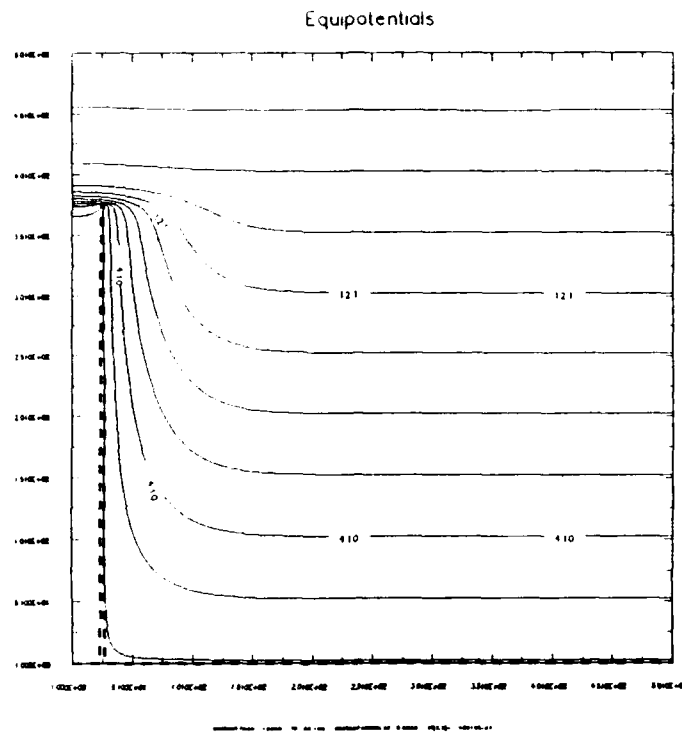


FIGURE 2.19(a): The equipotential plot output from a run of the FEAT code for a Type 2 structure.

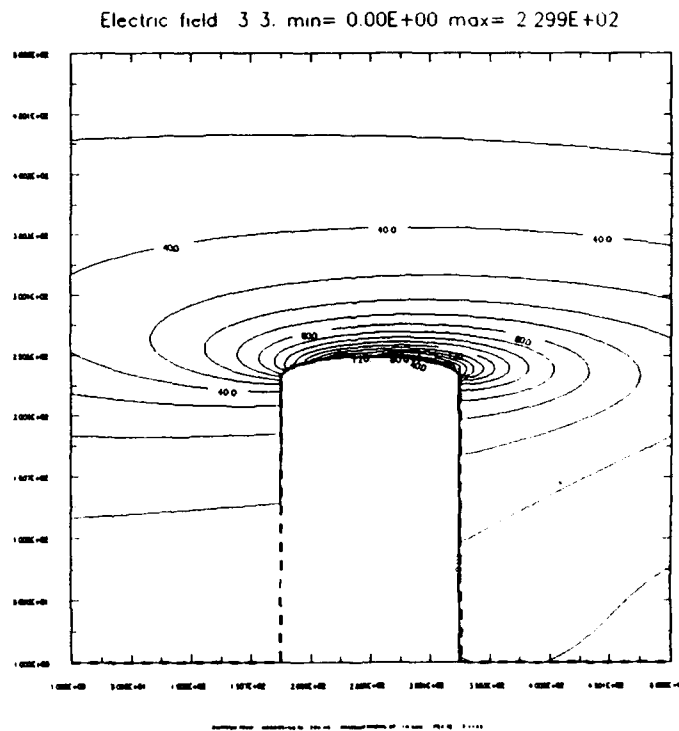


FIGURE 2.19(b): A contour plot for the magnitude of E , showing the large compression near the outer edge of the tip.

```

relx= 1.000E-02 rely= 4.000E-02
relxr= 1.000E-03 relyr= 4.000E-03
relxrf= 2.000E-04 relyrf= 8.000E-04
nxfcl,3 nxfcl,3 1 51 351 401 1.00E-01 1.00E-01 1.00E-05
nxfcl,3 nxfcl,3 201 301 201 301 5.00E-00 5.00E-00 1.00E-05
xmas,ymas 1.00E-01 1.00E-01 1.00E-00 1.00E-01 rmas 1.00E-02
x1,neta 501 31
xl,xh,yl,yn 1.000 1.000 1.000 5.000 1.000 1.000 14.0 14.0 14.0 14.0 14.0
nifl,nif2 njl 25 27 376
it sumerr errmx 1 1 0.317E+05 1.485E+02 27 377
it sumerr errmx 100 1.022E+03 1.000E+02 2 386
nifl,nif2 njlf 236 265 250
it sumerr errmx 1 1 0.142E+03 6.000E+01 266 248
it sumerr errmx 100 1.052E+02 1.000E+02 248 265
max Electric field 261 250 1.088E+02 1.600E+01 1.500E+01
nifl,nif2 njlff 176 325 250
it sumerr errmx 1 1 0.257E+02 7.000E+01 274 250
it sumerr errmx 100 1.075E+01 1.000E+02 254 265
max Electric field 275 250 1.061E+02 1.048E+01 1.500E+01
nifl,nif2 njlf 236 265 250
it sumerr errmx 1 1 0.646E+01 8.122E+02 367 201
it sumerr errmx 100 6.851E+01 7.320E+04 2 362
max Electric field 261 250 1.747E+02 1.600E+01 1.500E+01
nifl,nif2 njl 25 27 376
it sumerr errmx 1 1 1.046E+01 1.064E+01 29 351
it sumerr errmx 100 9.532E+02 1.742E+02 93 329
max Electric field 27 376 9.141E+01 1.000E+01 1.500E+01
nifl,nif2 njlf 236 265 250
it sumerr errmx 1 1 0.058E+02 6.000E+00 500 2
it sumerr errmx 100 9.530E+01 1.147E+03 426 19
max Electric field 261 250 1.747E+02 1.600E+01 1.500E+01
nifl,nif2 njlff 176 325 250
it sumerr errmx 1 1 6.292E+01 1.659E+01 500 2
it sumerr errmx 2 100 1.822E+01 1.097E+04 250 270
max Electric field 275 250 2.022E+02 2.548E+01 1.500E+01
nifl,nif2 njlf 236 265 250
it sumerr errmx 2 1 9.316E+01 6.993E+02 301 202
it sumerr errmx 2 100 6.667E+01 7.141E+04 2 359
max Electric field 261 250 1.715E+02 1.600E+01 1.500E+01
nifl,nif2 njl 25 27 376
it sumerr errmx 2 1 1.058E+03 2.105E+00 51 352
it sumerr errmx 2 100 7.374E+02 1.076E+02 104 320
max Electric field 27 376 9.158E+01 1.000E+01 1.500E+01
nifl,nif2 njlf 236 265 250
it sumerr errmx 2 1 1.010E+03 1.801E+00 500 2
it sumerr errmx 2 100 8.789E+01 1.216E+03 421 20
max Electric field 261 250 1.715E+02 1.600E+01 1.500E+01
nifl,nif2 njlff 176 325 250
it sumerr errmx 3 1 6.040E+01 1.268E+01 500 2
it sumerr errmx 3 100 1.357E+01 2.222E+04 256 272
max Electric field 275 250 2.299E+02 2.548E+01 1.500E+01
CPU (min)= 42.40

```

FIGURE 2.19(c): The output listing from the FEAT code for Figs. (a) and (b).

As is the case for the Type 1 structure, the TPIC code is used subsequent to the FEAT code while varying the applied average electric field, the value for Δt_{xtal} , and the number of smoothing iterations applied to the surface fields prior to calculating the emission parameters. A sample output from a single TPIC run is shown in Fig. 2.20. Note that the emission is almost exclusively from the outer edge of the cylinder. Moreover, note that this results in trajectories with a larger transverse component than in the case of the Type 1 structure. A series of TPIC runs can be used to calculate a theoretical I - V characteristic. A Fowler-Nordheim type plot of some such characteristics is shown in Fig. 2.21.

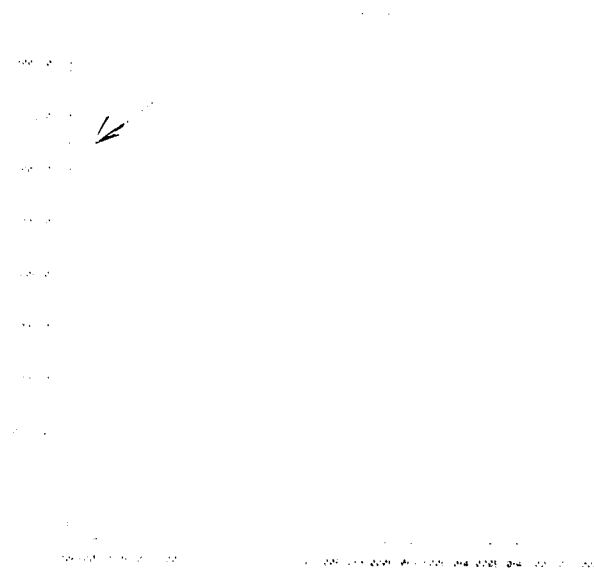


FIGURE 2.20(a): Output from a TPIC run for a Type 2 tip. This plot shows the trajectories of electrons emitted from the tip. The emission occurs from only a very small area near the tip apex.

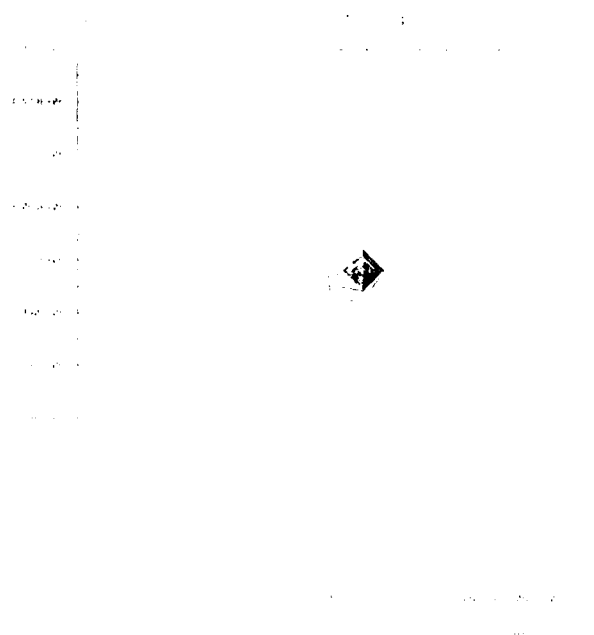


FIGURE 2.20(b): A plot from the same TPIC run as 2.20(a) showing the phase space contours used to evaluate emittance and brightness.

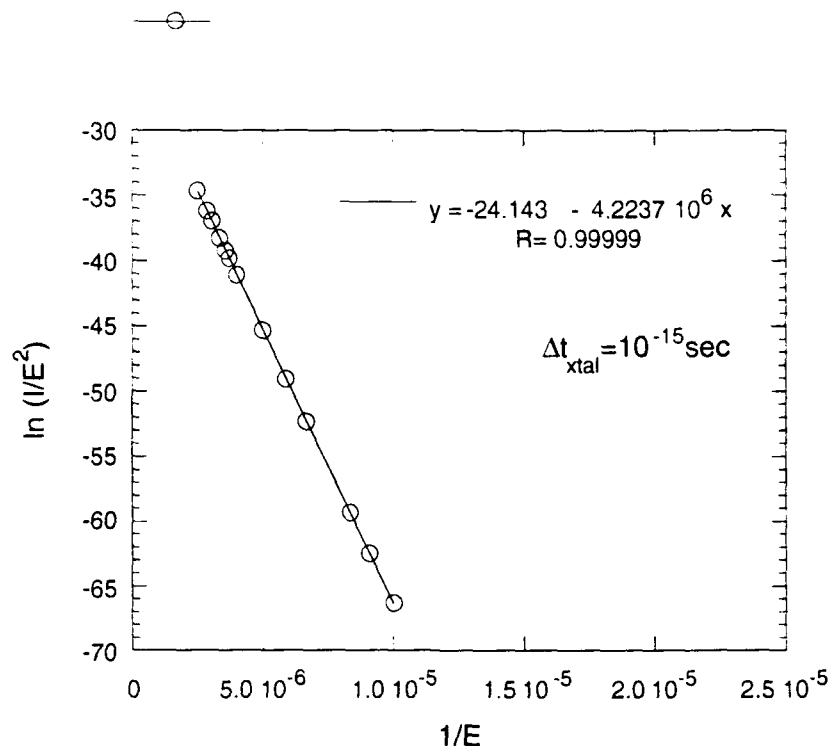


FIGURE 2.21: A composite Fowler-Nordheim I - V characteristic obtained from a series of TPIC runs. The structure is Type 2 with $r_c=150\text{\AA}$. In contrast with the Type 1 structure that evidenced saturation, the Type 2 structures typically do not show saturation for tip currents that are thermally realizable.

2.2.3 Comparisons of Performance Potential: "Type 1" vs "Type 2"

The FEAT and TPIC codes are valuable tools for the analysis of the complex data obtained in the laboratory and for the investigation of design possibilities for optimized structures. Several series of comparisons were calculated for this project with both of these purposes in mind. The general issue of emitter material selection was investigated in terms of the total current and brightness limitations due to the effect of the parameter Δt_{xtal} . The Type 1 and Type 2 structures also evidence difference performance limitations with respect to high current density operation. These have been investigated in some detail and a summary of those results is presented here.

The selection of an appropriate emitter material is essential to attaining high current density operation. As can be seen in Fig. 2.22, the current from a sharp ($r_c=25\text{\AA}$) Type 1 emitter begins to fall precipitously for $\Delta t_{xtal} > 10^{-15}$ sec. The value of Δt_{xtal} for which the emitter current begins to rapidly fall off is dependent on the maximum Fowler-Nordheim field emission density on the surface. This determines an average time interval per unit area for a field emission event. The greater the local current density, the shorter is this time interval. When the refilling time, Δt_{xtal} , is of the same order as this time interval, we observe a significant reduction in the emitted current. The use of

Δt_{xtal} in the simulations is an ad hoc attempt to observe the effect of materials limitations on the refilling time of surface states that have been emptied by the emission process. Clearly, one would expect good conductors to evidence significantly lower values for this refilling time than poor conductors or semiconductors. A detailed materials-characteristics based calculation might be able to better define anticipated ranges for Δt_{xtal} for the most commonly used emitter materials such as doped-Si, Mo, W, diamond, or TaSi₂.

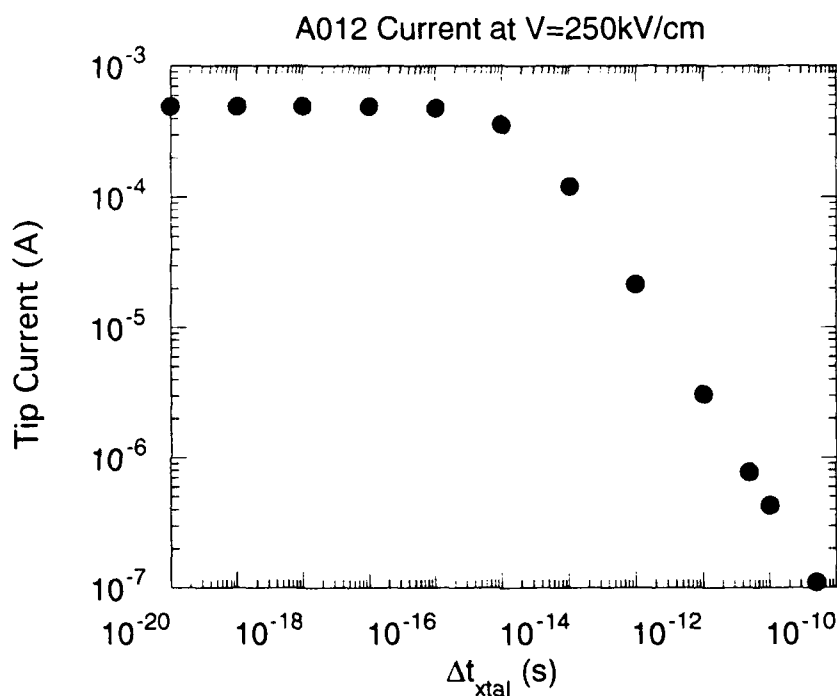


FIGURE 2.22: A plot of the values for single tip current obtained from TPIC runs at various values for the refilling time parameter Δt_{xtal} at constant applied electric field, using the field solves from FEAT for the A012 geometry.

High current operation is clearly more favorable with a material that we would anticipate to have a low value for Δt_{xtal} . What is seen in Figs. 2.23 and 2.24, however, is that the effect of Δt_{xtal} is more or less severe depending on the geometry of the emitter. The difference is easily understood by noting that the structures with more field enhancement and less "emitting area" begin to feel the effects of Δt_{xtal} at much lower applied fields and total emitted currents, because the peak local current density in these cases has already grown quite large.

Similar effects are observed in the relative performance of the different structures with respect to both edge brightness and single tip brightness. The beamlet spreading

angle, $\delta\theta$, can be seen in Figs. 2.25 and 2.26 to remain fairly constant except when saturation effects take effect. At its largest, this effect is only a factor of two in the emittance, corresponding to a factor of four in the brightness. Given the large changes in the single tip currents, these dominate and the brightness evidences the same saturation characteristics.

The beam brightness is an important attribute for some applications of interest. For applications where significant current is required, the edge brightness B_n is the relevant measure of performance. As can be seen in Figs. 2.28 and 2.29, the maximum available brightness with a given structure can be strongly affected by the material characteristics associated with Δt_{xtal} . This is most pronounced in the case of the Type 1 structures, due to their much larger field enhancement factor and relatively small emission areas. For materials with $\Delta t_{xtal} = 10^{-17}$ sec, $B_n > 10^6$ A/cm²-rad² appears feasible. If Δt_{xtal} falls to 10^{-13} sec, the upper limit for B_n decreases to just slightly over 10^4 A/cm²-rad².

The situation would seem to imply the Type 2 structures to be superior to the Type 1 structures in the case of "imperfect" materials. This story is not complete, however, without considering some of the circuit ramifications of the lower field enhancement factors associated with the Type 2 structures covered in these simulations. The requirement for higher average fields is a direct result of the lower β values for the Type 2 structures. This places a greater stress on the overall system to accommodate those field stresses in terms of the insulators and surface treatments necessary to prevent flashover or emission from unwanted areas. It similarly results in greater stored energy in the electrode structure, resulting in greater damage in the event of a fault such as flashover or an anode flare resulting from uncontrolled emission.

Finally, the Type 2 structures investigated here are perfectly azimuthally uniform. This is clearly unrealistic for the structures available to this project experimentally. Small irregularities in the structure of the top ring of the cylinder will result in local "hot spots," which will limit absolute performance. Still, the potential boon in terms of available emitting area makes the Type 2 structures an attractive high current option.

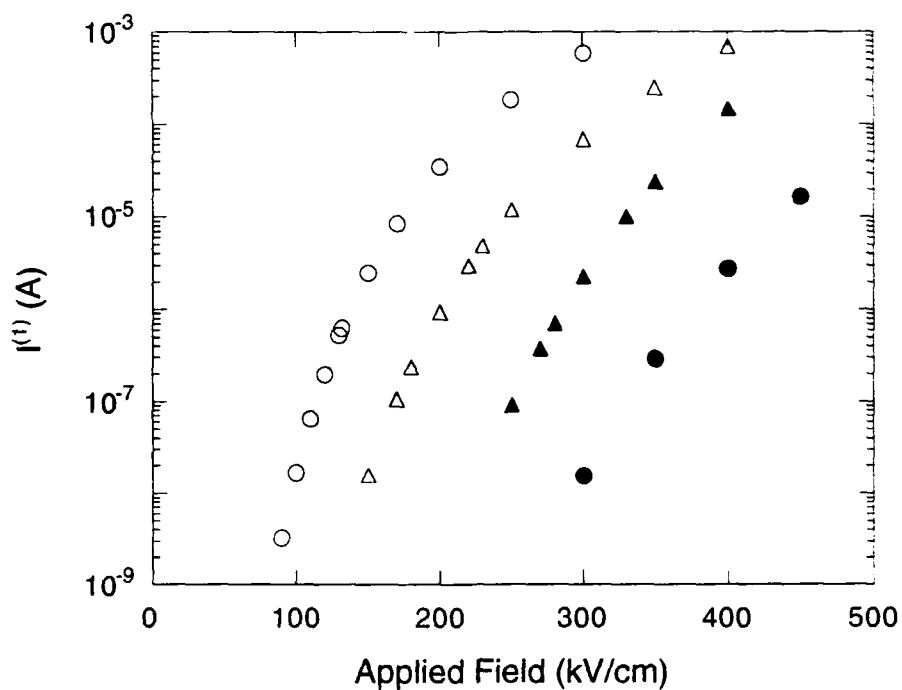


FIGURE 2.23: A plot of the values of the single tip currents obtained from TPIC and FEAT for four tip geometries: open circle, Type 1, $h=10\mu\text{m}$, $r_c=25\text{\AA}$; open triangle, Type 1, $h=10\mu\text{m}$, $r_c=100\text{\AA}$; solid triangle, Type 2, $h=15\mu\text{m}$, $\Delta r=300\text{\AA}$, $r_c=150\text{\AA}$; solid circle, Type 2, $h=15\mu\text{m}$, $\Delta r=600\text{\AA}$, $r_c=150\text{\AA}$. In all cases $\Delta t_{\text{xtal}}=10^{-17}$ sec.

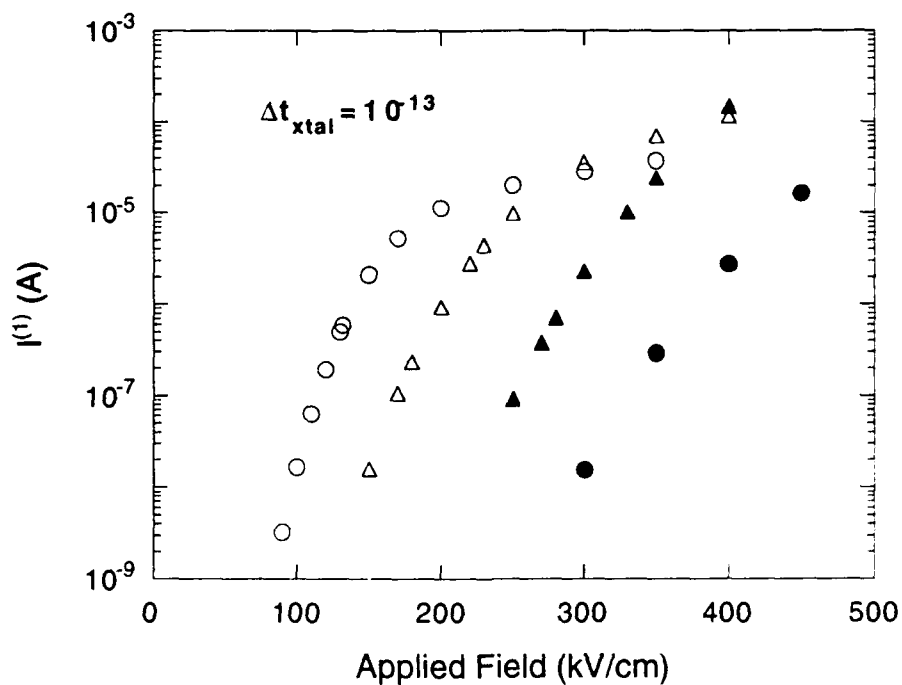


FIGURE 2.24: The same data as in Fig. 2.23 but with a value of 10^{-13} sec for Δt_{xtal} .

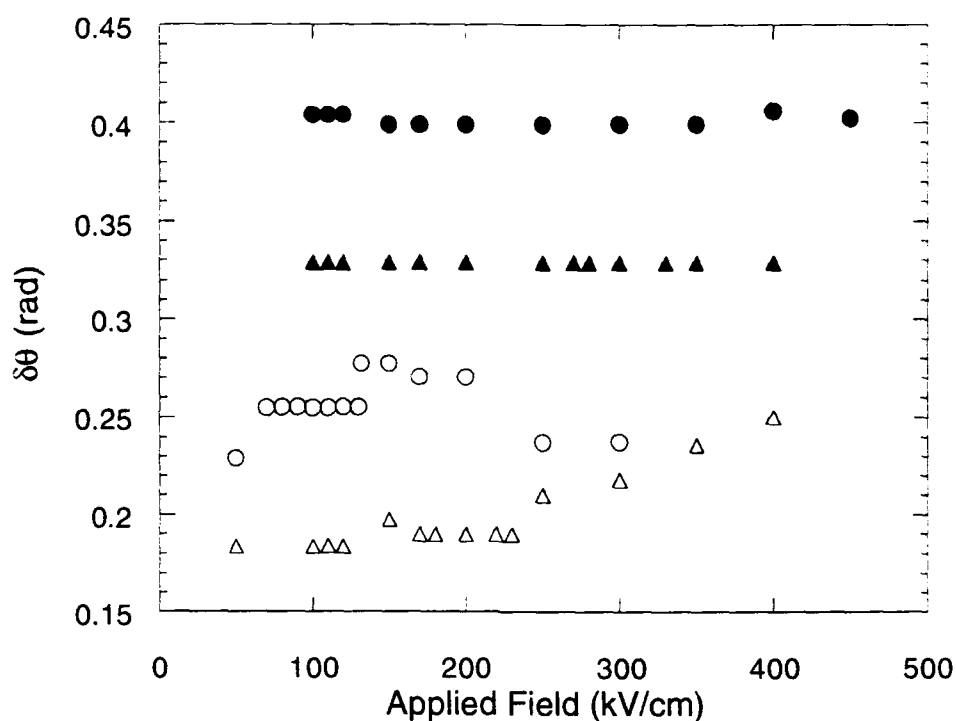


FIGURE 2.25: A plot of the values for $\delta\theta$ obtained from TPIC runs at various applied electric fields using the field solves from FEAT for four tip geometries. $\Delta t_{\text{xtal}} = 10^{-17}$ sec.

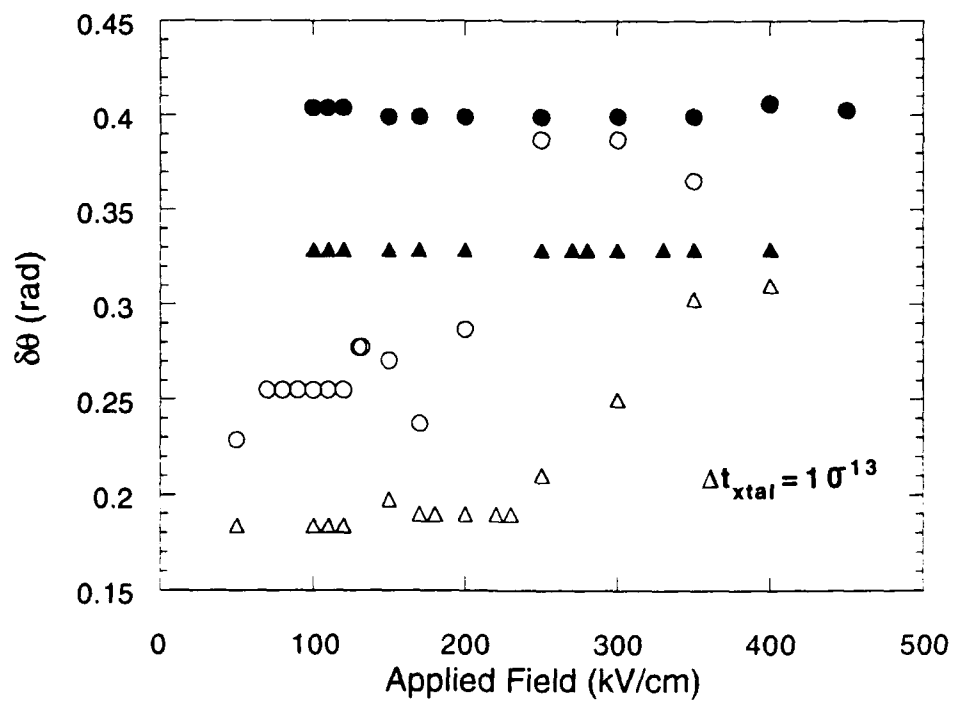


FIGURE 2.26: A plot of the values for $\delta\theta$ obtained from TPIC runs at various applied electric fields using the field solves from FEAT for four tip geometries. $\Delta t_{\text{xtal}} = 10^{-13}$ sec.

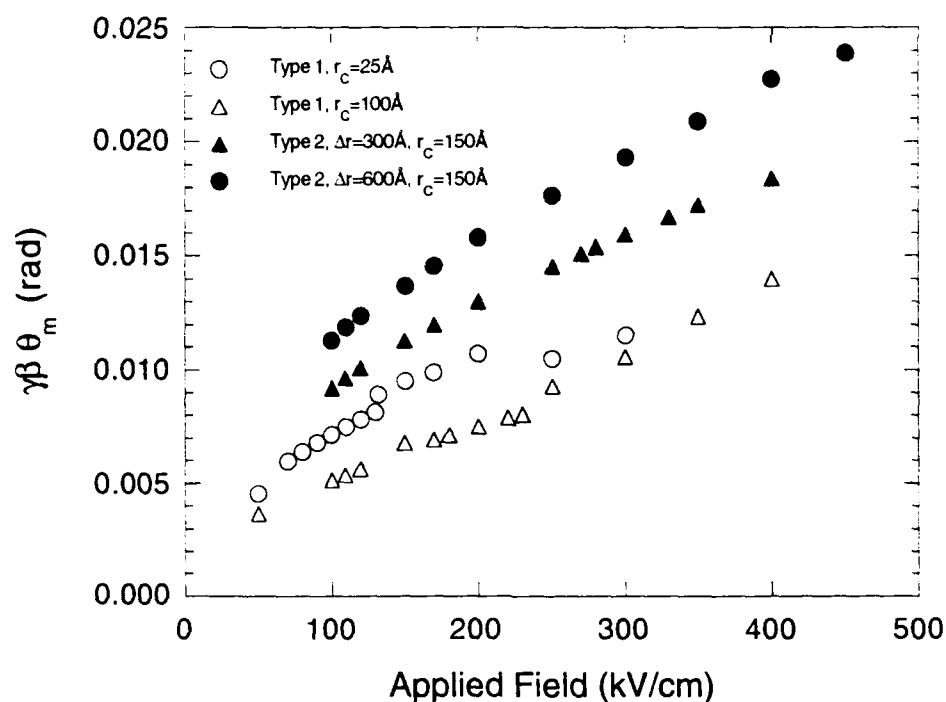


FIGURE 2.27: A plot of the values for $\gamma\beta(\delta\theta)$ obtained from TPIC runs at various applied electric fields using the field solves from FEAT for four tip geometries. $\Delta t_{\text{xtal}}=10^{-17}\text{sec}$.

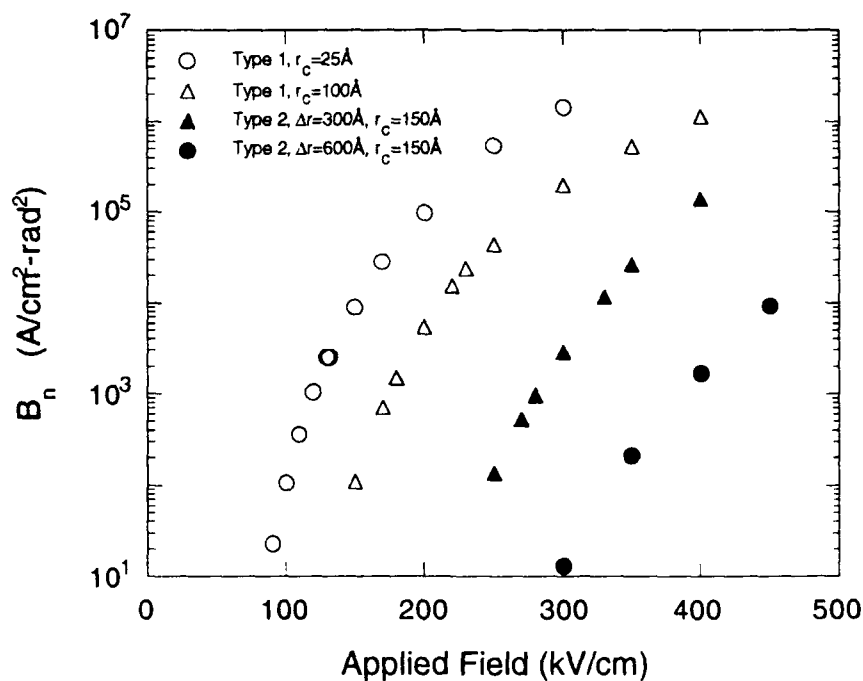


FIGURE 2.28: A plot of the values for B_n obtained from TPIC runs at various applied electric fields using the field solves from FEAT for four tip geometries. $\Delta t_{\text{xtal}}=10^{-17}\text{sec}$.

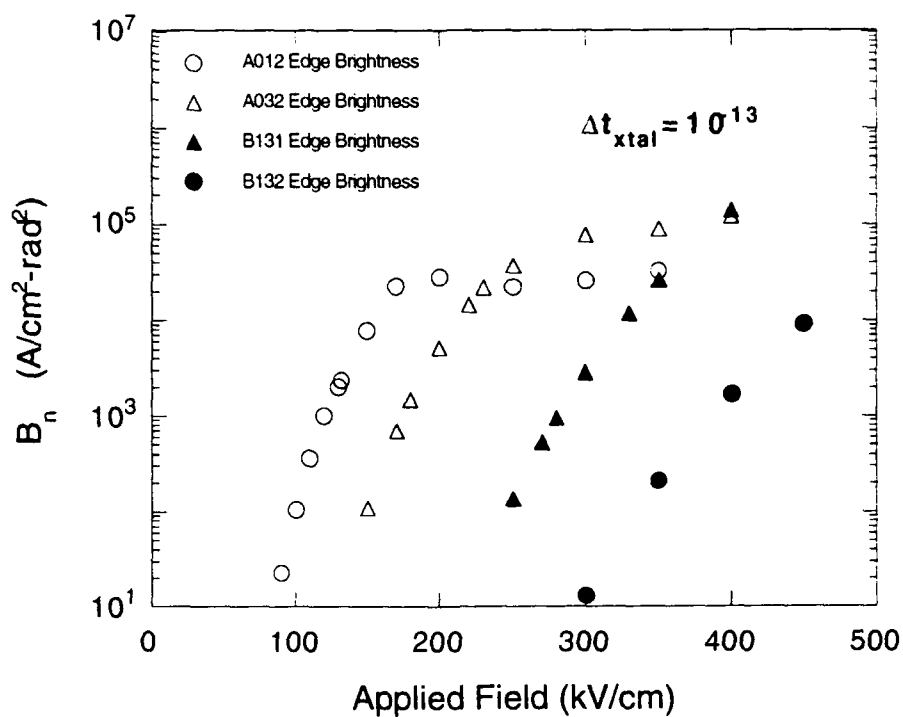


FIGURE 2.29: A plot of the values for B_n obtained from TPIC runs at various applied electric fields using the field solves from FEAT for four tip geometries. $\Delta t_{\text{xtal}}=10^{-13}\text{sec}$.

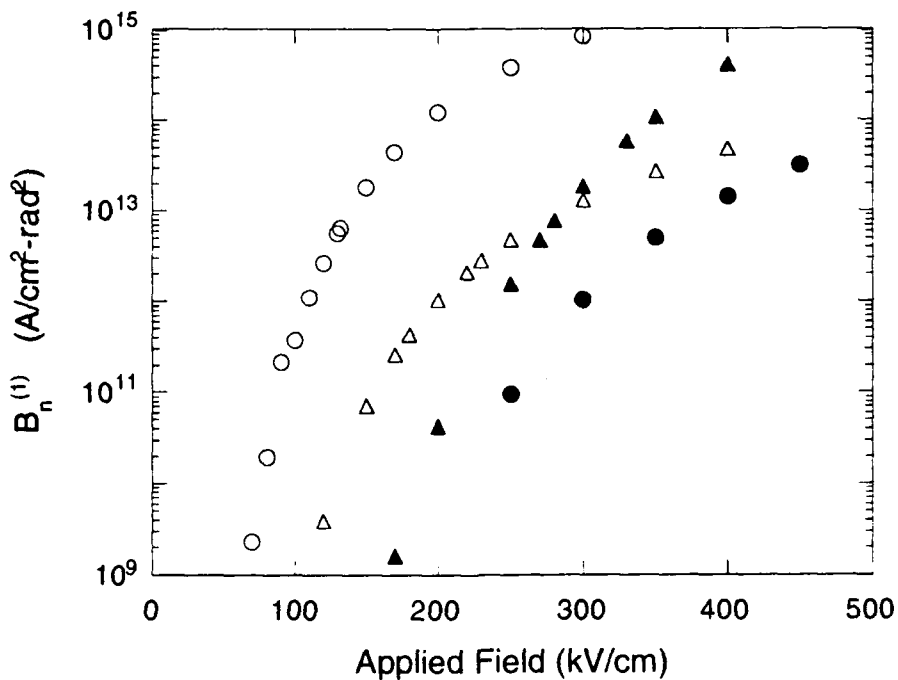


FIGURE 2.30: A plot of the values for single tip brightness $B_n^{(1)}$ obtained from TPIC runs at various applied electric fields using the field solves from FEAT. $\Delta t_{\text{xtal}}=10^{-17}\text{sec}$.

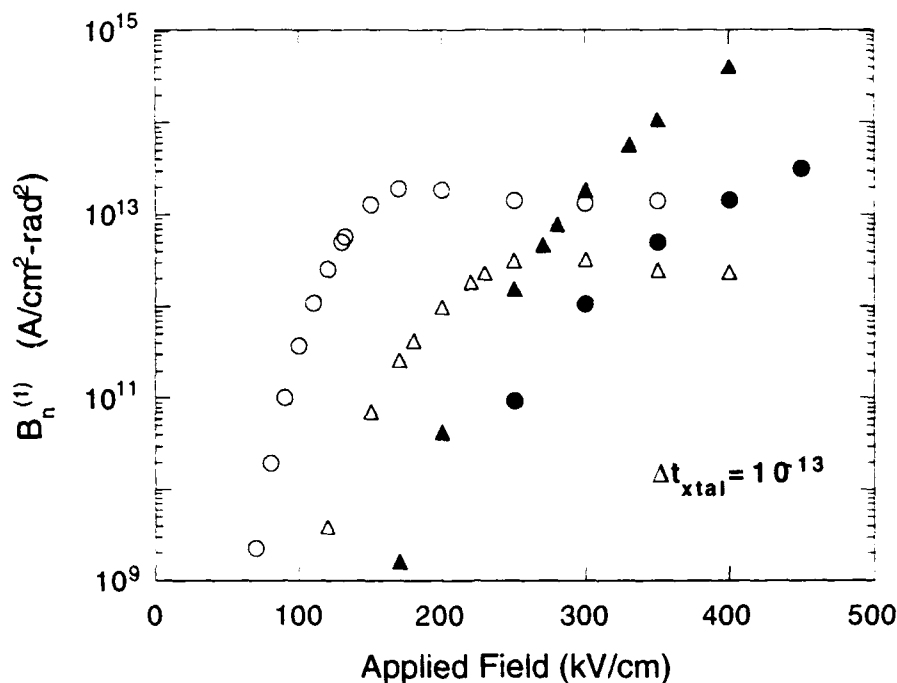


FIGURE 2.31: A plot of the values for single tip brightness $B_n^{(1)}$ obtained from TPIC runs at various applied electric fields using the field solves from FEAT. $\Delta t_{\text{xtal}} = 10^{-13} \text{sec}$.

1. R.H. Fowler and L. Nordheim, Proc. R. Soc. London A **119**, 173 (1928).
2. C.A. Spindt, I. Brodie, L. Humphrey, and E.R. Westerberg, J. Appl. Phys. **47**, 5248 (1976).
3. G.A. Farral in "Vacuum Arcs, Theory and Application," J.M. Lafferty, Ed., Ch. 2 (John Wiley & Sons, New York, NY: 1980).
4. H.C. Miller, J. Franklin Inst. **282**, 382 (1966).
5. H.C. Miller, J. Franklin Inst. **287**, 347 (1969).
6. H.G. Kosmahl, IEEE Trans. Elec. Dev. **36**, 2728(1989).
7. D.F. Howell, R.D. Groves, R.A. Lee, C. Patel, and H.A. Williams, Tech. Digest of Int. Electron Devices Mtg., Washington, D.C., 525 (IEEE, Piscataway, NJ, 1989).
8. C.A. Spindt, et al., ibid (1976).
9. H.G. Kosmahl, IEEE Trans. Elec. Dev. **38**, 1534 (1991).
10. Hinshelwood
11. Mesyats
12. E.C. Zachmanoglou and D.W. Thoe, in "Introduction to Partial Differential Equations with Applications," pub. The Williams and Wilkins Co., 428 E. Preston St., Balt. MD, (1976), p. 352.

3 Fabrication of Eutectic Composite Cathodes

The eutectic composite cathodes used in this project were fabricated predominantly by the principal subcontractor for this effort, GTE Laboratories Incorporated of Waltham, MA. Their final report to SAIC is included as Appendix C. It is unfortunate that during the course of our efforts, GTE decided to consolidate their business to telecommunications and away from lighting products: the laboratory at GTEL that was so ably supporting our efforts was in support of the lighting division and was disbanded. SAIC has acquired a small reserve supply of the Si-TaSi₂ material in boule form as a part of this project: we have also acquired a roughly equal supply using internal funds. The combination of these two sources is hoped to be sufficient until SAIC can establish its own growth capability. With the aid of former GTEL staff, this is in progress and we anticipate boule material to be available as of June 1993.

The tubule composite cathodes used in this project were fabricated by the Center for Biomolecular Science and Engineering, Code 6090, of the Naval Research Laboratory in Washington DC. In the evaluation of their performance as cathodes, substantial design modifications were suggested, and various design and fabrication compromises were attempted following meetings with NRL scientists and engineers.

3.1 Growth and Fabrication of Si-TaSi₂

The Si-TaSi₂ advanced cathode materials are fabricated by the etching of wafers sliced from boules grown from the melt. This section discusses the growth, etching, and fabrication of electrical contacts on the backplane of Si-TaSi₂ cathodes. All of the boules for this project were grown by GTEL at their Waltham, MA facility. Efforts with respect to subsequent processing steps have been pursued at both SAIC and GTEL.

3.1.1 Si-TaSi₂ Boule Growth

The Si-TaSi₂ material used in this project was grown from the melt by the Czochralski technique. The charge is composed of P-doped Wacker float zone Si with a carrier concentration in the $\sim 10^{14} \text{ cm}^{-3}$ or less and Gallard-Schlessinger float zone Ta of 99.996% purity. The charge is melted in a quartz crucible surrounded by a graphite susceptor. The Si seed used in the growth process was produced by growing from the same system. During growth, ultra-high purity Ar is flowed through the quartz chamber. The seed and crucible rotation are independently controlled. After a soaking period of three hours at 1600°C, the melt temperature is reduced to $\sim 1450^\circ\text{C}$ and the Si seed is lowered and contacted with the melt, given time to equilibrate, and then pulled

up at the fixed rate of 20 cm/hr. The composite boule solidifies as the seed is pulled. This process of directional solidification yields the eutectic rod-like microstructure with the rods oriented along the growth direction.

A single-crystal Si matrix is required for a variety of reasons, including the reproducible production of a smooth surface with uniform emitter height and the use of device quality Si-epilayers as the wafer backplane. Growth of a single-crystal matrix eutectic depends primarily on using the exact eutectic composition and minimizing impurities. The composition control is quite difficult due to the loss of Si as SiO during the soaking period and the melt back of the quartz crucible and the seed. With experience in balancing these two effects, composite boules with a single-crystal matrix can be routinely grown.

A photograph of a typical single-crystal matrix $\langle 111 \rangle$ boule is shown in Fig. 3.1. Note that the diameter of the boules used in this project are all on the order of 2-5 cm, and 5-8 cm in length. The eutectic microstructure in a typical transverse section is shown in Fig. 3.2. The figure shows that the rods in the eutectic are neither arranged in a regular array nor distributed in a strictly random pattern, but instead exhibit a cellular structure. The interrod spacing in the cell walls is less than the average interrod spacing. Note also that the rod shape is not generally circular, but instead shows a more random cross section. Given the uniformity of spacing when averaged over an area of $100\mu\text{m}$ square, the variations and correlations of the interrod spacing are not expected to have a significant effect on the macroscale performance of the cathodes. On the other hand, as will be discussed in the next subsection, variations in the cross-section of the metal rods have a direct effect in limiting the uniformity of the final etched structure.

Thermal and forced convection currents are always produced by the seed/crucible rotation and the asymmetrical thermal distribution in the melt in a Czochralski crystal growth system. This in turn causes temperature fluctuations and growth rate variations at the solid-liquid interface, and the rod density distribution can become nonuniform. An analysis of this effect was investigated by counting the rod density in a square $85\mu\text{m} \times 85\mu\text{m}$ as a function of position along the boule diameter for boules grown under different conditions. In one particular case, modifying the growth conditions from crucible and seed counter-rotation of ± 6 rpm to a stationary seed and crucible rotation of 12 rpm resulted in a decrease in the lateral variation in rod density of 30%.

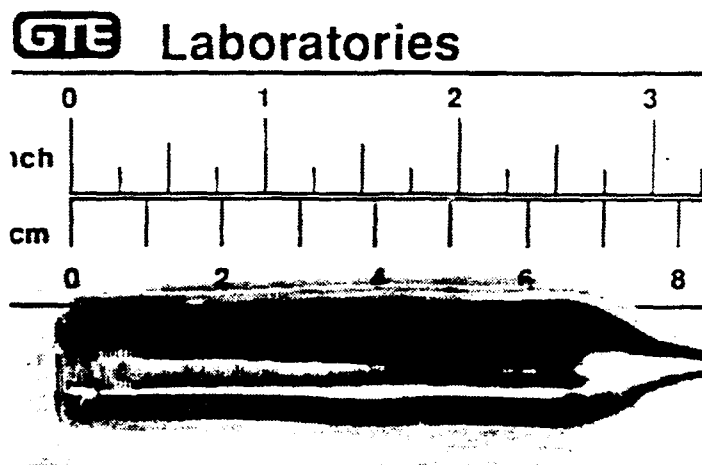


FIGURE 3.1: A photograph of a typical Si-TaSi₂ boule used for the eutectic advanced cathode materials in this project. The seed for the boule is at right in the photograph.

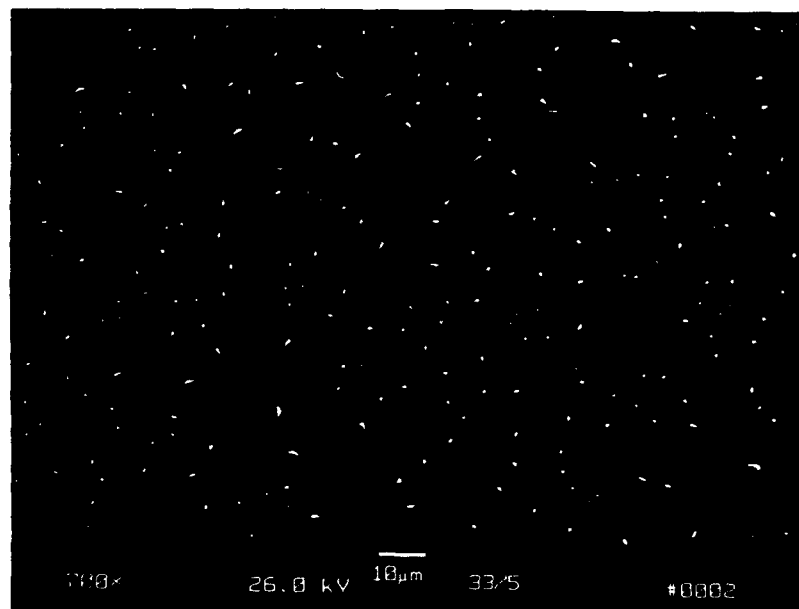


FIGURE 3.2: An SEM micrograph of the surface of a polished Si-TaSi₂ wafer. Note the irregular distribution, the cellular structure of rod distributions, and the non-circular cross-section of most rods.

Optimization of the growth conditions will require much greater statistics than were available with the few boules grown during this project. Such improvements as that discussed above are indicative of what might be expected. A particular interest may be the investigation of Bridgeman growth of the Si-TaSi₂ eutectic: Bridgeman grown Ge-TiGe₂ evidences a far superior microstructure to Czochralski grown Ge-TiGe₂, as seen in Fig. 3.3. The microstructure of the Ge-TiGe₂ and Si-TaSi₂ eutectics is similar, and obtaining uniform and circular rod cross-sections would have a beneficial effect on cathode performance. The Ge-TiGe₂ system itself is undesirable as a cathode material due to the low melting temperatures of the constituents. An alternative approach is the scaling of the growth to larger diameter systems such as 3-inch or 4-inch boule diameters. Conventional Si processing has noted significant increases in wafer quality as systems are scaled to larger diameter, and the cost of Bridgeman growth as compared to Czochralski growth will drive the use of Czochralski systems whenever cost is a driving factor in an application.

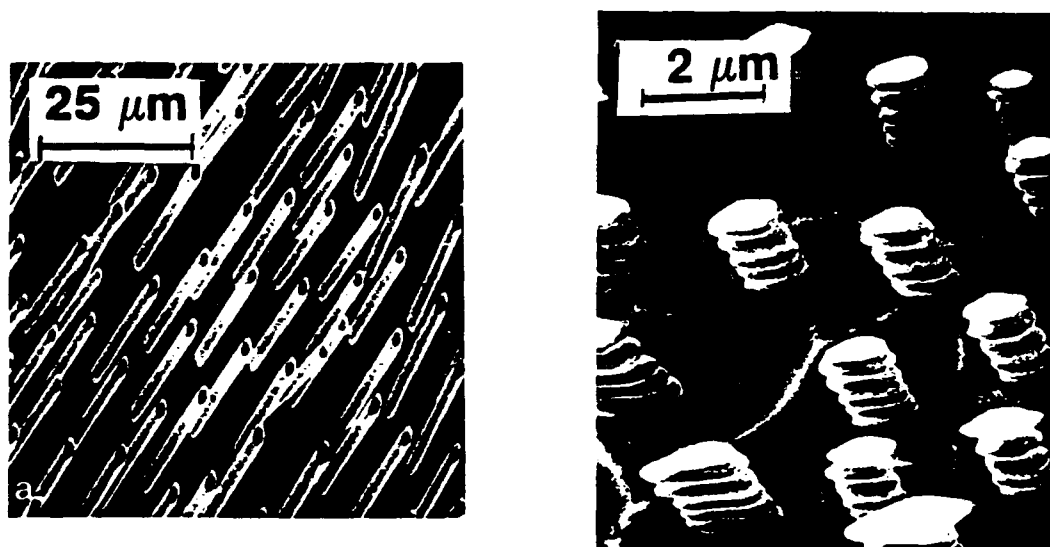


FIGURE 3.3: An SEM micrograph of the surface of a polished and etched Ge-TiGe₂ wafer taken from a Bridgeman grown boule (left) as compared with the same material grown Czochralski (right).

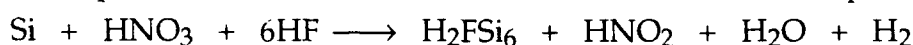
Table 4.3 is a summary of the cathode wafers and Si-TaSi₂ boules that were fabricated during the course of this project. Some cathodes were tested by GTEL, though most were tested by SAIC. All cathodes were fabricated from eight boules. Boules TaSi₂-40, 47, and 84 were grown at seed and crucible counterrotation at 6 rpm; boules TaSi₂-86, 87, 90, 91, and 92 were grown with crucible rotation only at 12 rpm. Boules 40 and 47 have a p-type Si matrix, while all the rest have n-type. Boule TaSi₂-91

has a polycrystalline Si matrix grown at 30 cm/hr instead of 20 cm/hr to increase the rod density.

3.1.2 Etching of Si-TaSi₂

An important step in the fabrication of FEAs from the Si-TaSi₂ eutectic is the etching back of the Si matrix to expose the TaSi₂ rods. This process is typically also used to sharpen the emitter rods as they are exposed. The etching process is based on wet chemical techniques using either a modified CP4 solution or a sodium hypochlorite solution. The CP4 solution is composed of hydrofluoric, nitric, and acetic acids, and in general the chemical reaction of this solution with Si proceeds as follows:

- Si is oxidized by nitric acid to form SiO₂
- The oxidation products are reacted with HF to form the soluble complex H₂FSi₆:



Acetic acid is used as a diluent. Although water can also be used for this purpose, acetic acid is preferred because using this diluent results in less dissociation of the nitric acid and hence in a higher concentration of the undissociated species. This preserves the oxidizing power of the nitric acid for a wider range of dilution than if water is used. Therefore the oxidizing power of the etchant tends to remain relatively constant during its operating life. The etching rate will depend on the removal reaction of SiO₂ by HF and hence depend directly on HF concentration in the etchant.

The etching process used to reveal the silicide emitter rods for the FEA application must also produce a smooth Si surface and uniform emitter height. Initially, a number of etchants with different composition were used to etch the composite wafers. Wafers were cut from the boule perpendicular to the growth axis, chemically polished to obtain a mirror surface finish, and then etched in solutions of (X:HF + Y:HNO₃ + 3:CH₃COOH) where X/Y was varied from 0.1 to 0.6. Increasing the HF/HNO₃ ratio is found to produce deep etch pits and a non-uniform Si substrate. Use of a solution with a lower HF/HNO₃ ratio improves the smoothness of the Si substrate. However, significantly decreasing this ratio causes the cathode surface to heavily oxidize and become very cloudy. This heavy surface oxide may be amenable to subsequent removal processes. The solution of (1:HF + 10:HNO₃ + 3:CH₃COOH) is typically used as an optimized etchant.

Further experiments have been performed to investigate the influence of etching temperature on the surface morphology. Wafers were etched in the (1:10:3) optimized solution at room temperature, and at 8°C, 4°C, 0°C, and -20°C by the use of either ice baths or dry ice - isopropanol baths. The surface morphology of the Si substrate

improves with decreasing temperature, becoming essentially flat at around 4°C. The speed and selectivity of the etch also change, producing slightly taller emitter tips at a slower rate as the bath temperature is decreased.

The etch selectivity between the Si and TaSi₂, combined with the cross-sectional morphology of the TaSi₂ rods, determines the emitter tip height and distribution of heights. The (1:10:3) etchant does attack the silicide, albeit at a much slower rate than the Si matrix. For a etchant temperature of 5°C, GTEL found etch rates for the Si matrix of ~0.5µm/min while for the TaSi₂ the etch rate was approximately 20 times smaller at ~0.025µm/min. With an average TaSi₂ rod diameter of 1µm, an etching time of 20min is required to etch half the diameter of the rods, resulting in an emitter height of ~10µm.

Rods with variable cross-sectional shapes and with different minimum through-the-center thicknesses will produce emitter tips of different heights. With a single selective etch, the relative difference in tip height will be equal to the relative difference in rod thickness. This effect is shown in Fig. 3.4. Very uniform emitter arrays therefore require very uniform diameter and cross-sectional morphology rods. An alternative is to use a two step etch process, where the first etch has a very low selection ratio, such as 2:1, and the second etch only acts on the Si matrix. The relative variation in heights is then produced only by the first step, which only acts over the first 1-2µm in tip height. If the variation in rod thickness is 30%, then this step produces a variation in emitter height of 30% or 0.3µm for 1µm tall tips. The second step does not etch the TaSi₂ rods at all, but instead etches the Si matrix an additional 9µm. The relative tip height variation is now 0.3µm out of 10µm, or 3% - a large improvement. This process is illustrated in Fig. 3.5.

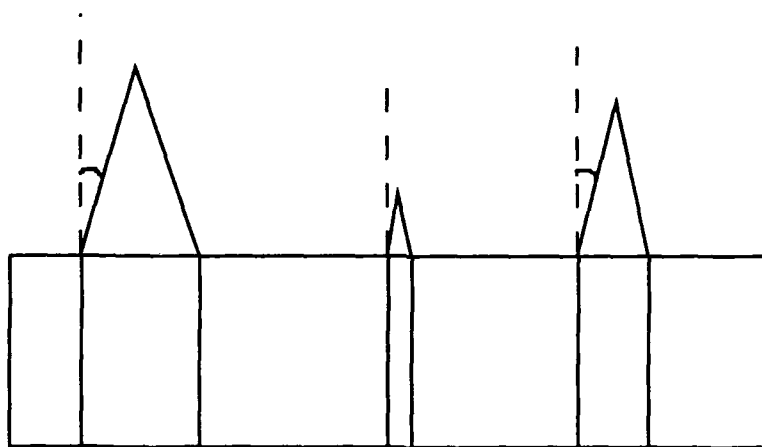


FIGURE 3.4: An illustration of the effect of different rod diameters on the height of the emitter structures after selective etching.

The need for etchants with different selectivities extends beyond those available with the (1:10:3) CP4 solution at different temperatures. To obtain less than 10 μ m emitter tip heights, etchants with selectivity ratios between Si and TaSi₂ smaller than 20 are necessary. It is known that the addition of sulfuric acid will accelerate the etching rate of TaSi₂. As a result, a number of etchants with various concentrations of sulfuric acid were developed to obtain different rod heights of less than 10 μ m. Selectivity ratios of much greater than 20:1 can be obtained by using an etchant composed of (1:5% NaOCl + 1:40% NaOH) at 85°C. This etch process removes only Si; however, it is an anisotropic etch, and maintaining a smooth Si surface requires a high quality single-crystal matrix. With a polycrystalline matrix, the wafer surface is composed of multigrain orientations that are etched at different rates. Polycrystalline wafers exposed to the NaOCl/NaOH etch therefore evidence very rough surfaces. Another option for precision applications is the use of RIE processes to accurately remove the Si matrix while leaving the TaSi₂ emitters unaffected. No RIE was performed during this project.

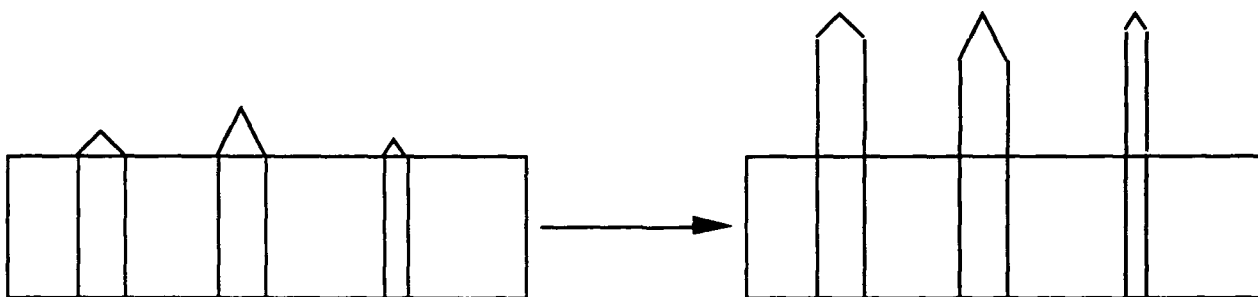


FIGURE 3.5: An illustration of a two step etch process to optimize the distribution of tip heights despite a distribution in rod diameters.

3.1.3 Metallization of Si-TaSi₂

Cathodes with thickness of 0.025 cm in many shapes and sizes such as 1/8 in. round, 3/8 in. round, 1 mm \times 15 mm rectangular, and 5 mm \times 5 mm square used in this project for testing were cored and cut from 1 in. diameter boule material. Both sides of the wafers were lapped with alumina powder and finally polished with colloidal silica gel to get a mirror-like surface.

The first two batches of Si-TaSi₂ cathodes received from GTEL for testing used cathode wafers that were bonded to an OFHC stub with Ag paint. Emission testing on these cathodes (see the next section) clearly indicated a problem with the electrical contact between the stub and the emitter rods. A new metallization for the back side contact was subsequently developed based on a standard Si metallization process. In

the process used here, prior to etching but following an HF dip to remove surface oxides on the wafer, one side of the wafer is successively coated with evaporated films of Ti (50nm), Ni (150nm), and Au (500 nm), and then annealed at 350°C for 15 minutes. This process produces very good contact to the TaSi₂ rods. The cathodes are then etched to produce the shaped emitter tips.

Ultra-high vacuum levels required for some microwave tube devices typically use a high temperature (~500°C) bakeout. The above process for the cathode contact and subsequent mounting with solder are incompatible with such elevated temperatures. A metal brazing process was developed for fabrication of contacted cathodes for such applications. One piece of the brazing alloy InCuSil (61.5% Ag + 24% Cu + 14.5% In) with exactly the same size cathode wafer and W stub is sandwiched between the cathode wafer and W stub. This assembly is placed inside a vacuum furnace with the W stub sitting on the brazing alloy piece and wafer, so that its weight can push down the brazing metal when it is melted to adhere to the wafer and the W stub. The vacuum level during the brazing process is about 10⁻⁵ Torr. The temperature of the furnace is increased to 750°C at a ramping rate of 20°C/min and maintained at 750°C for 10 minutes, then cooled down to room temperature by free falling. This process also produced good contact to the TaSi₂ rods. The cathode wafer is then etched to reveal the TaSi₂ emitters. This etching process is also simply performed because the W stub and brazing alloy are not attacked by the etching solutions.

3.1.4 Patterned Contacts

Patterned metal contacts on the back side of Si-TaSi₂ eutectic composite cathode wafers were fabricated to create multiple, individually addressable emission areas on the cathode. This arrangement allows the use of this type of cathode in display applications or the simple fabrication of emission arrays of complex shape, as might be required for a distributed cathode microwave amplifier where the electron source is directly coupled to the waveguide.

The structure is shown in Fig. 3.6. First, a dielectric silicon nitride layer with thickness of 1-2µm and 1µm thick Al layer are deposited on the backside of the wafer. Holes corresponding to the desired emitter areas are defined in the dielectric layer by photolithography and etching using the Al layer as an etching mask in the plasma etching process for silicon nitride. The Al etch mask layer is removed by etching in the solution of (18:H₃PO₄ + 1:HNO₃ + 2:H₂O) for five minutes. Metallization with Ti/Ni/Au as discussed previously is applied to the entire back surface, but electrical

contact is only made to the areas in the holes. The wafer is then etched in the usual manner to form the emitter elements on the front surface of the wafer.

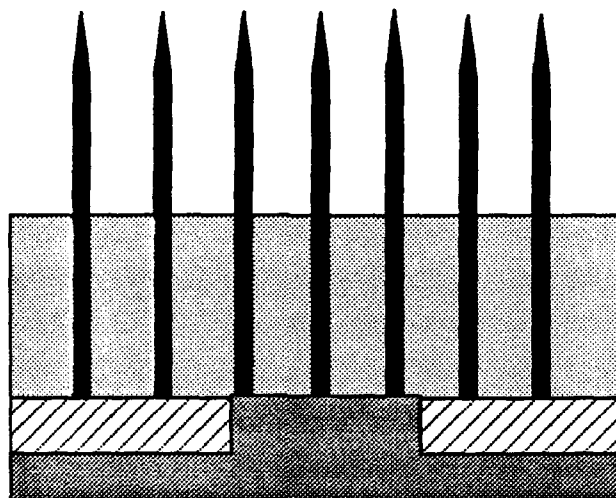


FIGURE 3.6: A schematic diagram of the patterned contact on a Si-TaSi₂ FEA.

An important aspect of the patterned contact to the backplane of the Si-TaSi₂ wafer is the use of the embedded radial Shottky barrier that isolates all the tips from the matrix and from one another. Were it not for these isolating barriers, the drive current would radially bleed out from the backplane contacts and the emission image would be uniform, rather than a replication of the patterned backplane contacts. The fact that the image is a direct replica of the contact pattern is an indication of the relative isolation that can be achieved. This has important implications for devices that would use the backplane as an addressing matrix.

3.1.5 Removal of Surface Oxides

The etch process used to expose the emitter tips leaves a thin oxide on the emitter structures as a result of the nitric acid etch component. The presence of this oxide has been documented by XPS measurements of the Ta spectrum of an "as-processed" cathode (see Fig. 3.7). Initial cathode operation was demonstrated without removal of this oxide layer, and the initial phase of turn-on evidenced a multitude of miniature arcs and unstable periods of emission. Over a period of several minutes this instability would evanesce into more stable operation. The observation of the thin surface oxide on the "as-processed" cathodes led to the hypothesis that this layer was responsible for the initial period of instability during operation. An Ar-ion mill was used in-situ in the XPS to remove the etch-oxide. The XPS spectrum of such a "cleaned" cathode is shown

in Fig. 3.8. Turn-on and burn-in of new cathodes was much easier and more reliable with the oxide-stripped cathodes.

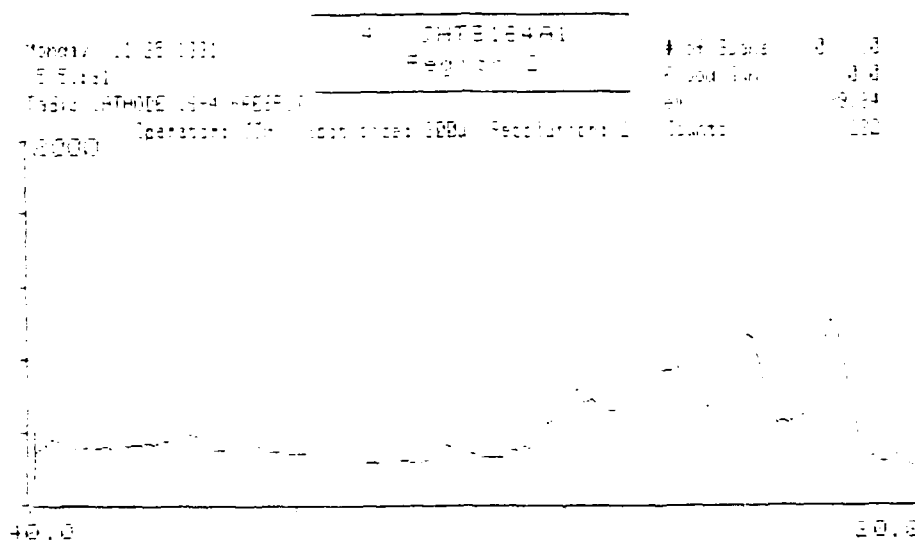


FIGURE 3.7: An XPS spectrum of the Ta peaks for an as-processed Si-TaSi₂ cathode.

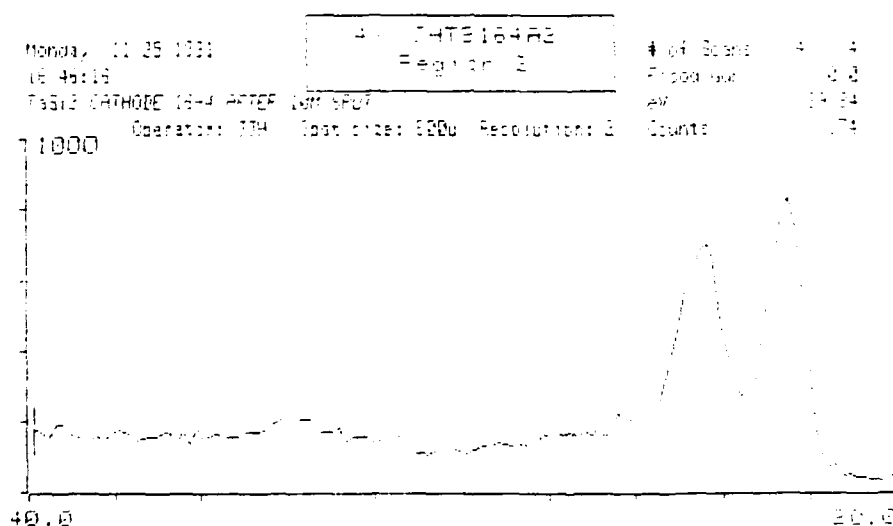


FIGURE 3.8: The XPS spectrum of an as-processed Si-TaSi₂ cathode after Ar-ion milling of the surface. Note the absence of the oxidized Ta signal.

The use of the Ar-ion milling technique was sufficient for the relatively low numbers of cathodes required for this project, but this technique would be unwieldy and expensive for some of the targeted downstream applications. As part of an SAIC Internal Research and Development (IRAD) project, an alternative technique was developed using a directional Ar-plasma. Verification of the equivalence of the two techniques was performed by comparing the XPS spectra of cathodes prepared with

both techniques. The Ar-plasma technique is compatible with high-volume, low-cost requirements and does not require expensive, sophisticated equipment.

3.2 Initial Testing and Screening of Cathodes

The experimental operational data obtained in this project are given in Section 4. All of the Si-TaSi₂ cathodes received during the first ~14 months of this project were rapidly run through an initial set of experimental characterizations to roughly gauge their performance characteristics. These initial characterizations typically included an SEM examination, followed by a measurement of the initial turn-on characteristics over a period of a few hours. These initial data were immediately communicated back to the personnel at GTEL for adjustment of their ongoing fabrication efforts. Given the initial characterizations, more detailed experimental plans were formulated that typically included longer (10-100 hour) burn-in and characterization periods.

3.3 Growth of Other Eutectics

The family of semiconductor-metal eutectic composites is rich in transition metal silicides. A number of these are shown in the attached appendix of GTEL's final report Fig. 4, showing SEM micrographs of Si-eutectics of Ta, W, Nb, Zr, Cr, and Co. Four cathode wafers were fabricated from a Si-WSi₂ polycrystalline boule using the same etching technique as for Si-TaSi₂. An SEM of one of these cathodes is shown in Fig. 3.9. The tips were extremely sharp, as can be seen in the figure.

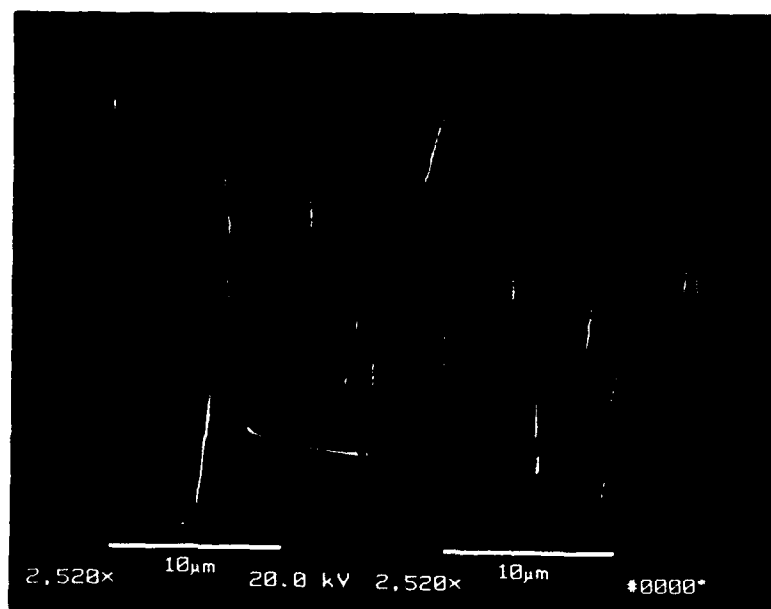


FIGURE 3.9: An SEM micrograph of cathode GTE 32-2. This cathode is fabricated from a Si-WSi₂ eutectic, and evidences a more blade-like structure to the emitters.

The characterization of these cathodes will be presented in Section 4. To summarize those results here, the cathodes turned on at reasonably low voltages but evidenced a tendency to rapidly degrade in time. Post-test examination with an SEM showed what was interpreted as significant thermal damage to the structures. This could be due to a variety of causes. The conductivity of WSi_2 , both thermal and electrical, could be significantly poorer than those of TaSi_2 . The relative work functions are also unknown, but the reasonable voltages for turn-on suggest that they are close. Finally, the Si-WSi_2 boule from which the wafers were cut was polycrystalline. In general, our experience with the Si-TaSi_2 material would lead us to expect that the WSi_2 emitter rods would likewise be polycrystalline. Operation with polycrystalline TaSi_2 tips in our standard eutectic composite evidenced greater thermal instability than single crystal material, though not to the extent found with the WSi_2 . Finally, another contributory factor may be related to the chemical stability of WSi_2 relative to TaSi_2 .

3.4 Fabrication Optimizations for Si-TaSi_2

Various optimizations were attempted with the Si-TaSi_2 structure fabrication technique. A desire to be able to operate the cathodes at high current in harsh vacuum conditions led to the optimization of the process of coating the cathodes with thin layers of gold. A desire to lower the effective work function of the emitter tips extrapolated these coating operations to include various low work function materials. The work on cylindrical emitter structures took an interesting twist with the development of a technique for fabricating W-tubule structures using the Si-TaSi_2 cathodes as a deposition template. Finally, in a combined method, these W-tubule arrays were coated with LaB_6 . All of these efforts shared the same goal of optimizing cathode performance using the Si-TaSi_2 emitters as a starting point.

Several of the downstream application opportunities require the ability to operate in an oxygen environment. Both the Aegis CFA microwave tube application and the oxygen ion gun application need electron sources compatible with operation in oxygen pressures of 5×10^{-6} to 1 Torr. Our earlier experiments with coating the complete structures with gold, at that time to short out the Schottky barriers between the tips and the matrix, suggested the use of the noble metal coating to prevent oxidation. Successful operation at high currents required the removal of the process oxide layer prior to the deposition of the gold coating. These experiments are described in detail in the Applied Physics Letters article by Hickman et al. attached in Appendix A.

A series of experiments was focused on the deposition of low work function coatings over the emitter structures in order to lower the required operating voltages and fields.

The deposition technique applied in this case was to use foils of the desired deposition material in a parallel plate Edwards sputter coater. Foils of Ta, Nb, and Mo were employed in an attempt to rationally modify the work function of the emitter surface. The difficulty in this case was the deposition process itself: accurate deposition of these high temperature materials was difficult in a system intended to be depositing gold. Measurements with the "coated" cathodes did not indicate any dramatic success. This is probably attributable to the deposition process used and the resultant character of the coatings.

In an interesting twist, the Si-TaSi₂ cathodes were used as a template for the fabrication of W-tubule arrays. This process is described in detail in the final report from GTEL in Appendix C and will only be summarized here. A Si-TaSi₂ cathode is processed as usual to produce the 10μm tall emitter array. This is then coated with a 0.1μm thick W layer by CVD. A 10μm thick photoresist layer is deposited, and 1-2μm of this photoresist is removed to expose the tips of the rods. The W on the tips of the rods is selectively etched away with a solution of (KH₂PO₄, KOH, K₃Fe(CN)₆, H₂O) to reveal the TaSi₂ tips underneath the W. The TaSi₂ is etched down into the W coating with HF, leaving W microtubes. Finally, the photoresist layer is rinsed off. The only difficulty with this technique is the relative unevenness of the resultant W microtubule tips. A variety of possibilities exist that might significantly improve this technique.

Testing of these microstructures by GTEL and SAIC indicated rather poor performance. This is consistent with the work function of W and the relatively rounded shapes produced by the technique, both of which led to the use of very high fields to produce emission. GTEL did successfully deposit a 100Å layer of LaB₆ over the W-tubules to reduce their work function, and observed the desired effect of the 3eV work function of LaB₆ as compared to the 4.5eV of W. After some initial testing, GTEL found the coating to be relatively fragile during some operation instabilities.

4 Testing of Tubule Microstructure Cathodes and Eutectic Composite Cathodes

The testing of the tubule and eutectic cathodes was carried out using successively sophisticated apparatus with improving accuracy. These measurements included *I-V* characterizations, emission uniformity measurements, emittance measurements, lifetime measurements, characterization of operation in varying background gases and pressures, and detailed materials characterizations of the cathodes throughout all stages of all types of tests. The materials characterizations included scanning electron microscopy (SEM), x-ray photoelectron spectroscopy (XPS), and scanning Auger microprobe (SAM). The nature of the emitter materials was always found to play a leading role in the operation of the cathodes.

This section is divided into subsections describing the apparatus and measurements. In some cases, open literature publications included in Appendix A provide enough detail that only brief summaries will be provided here. Other areas in preparation for publication in the open literature will be covered in much greater detail. Finally, some areas are of limited interest and will only be covered in this report.

4.1 DC Test Stand

The workhorse of the cathode characterization apparatus is the DC test stand. This apparatus could be configured in several different ways depending on the desired information and the nature of the cathode. A general configuration is shown in Fig. 4.1. Note that the anode can be changed both in terms of materials and geometry. OFHC copper, graphite, aluminum, and phosphor-glass were used as anode materials for different measurements. A configuration using a "full" anode is shown in the figure; a "microanode" was also used that consisted of a 1/8" diameter OFHC copper pin with a full-radiused termination.

The cathode electrode is fabricated from aluminum with a cylindrical hole machined on center to accommodate the cathodes on their mounts. The cathodes are typically mounted on either 3/8" or 1/8" diameter OFHC copper stubs. Different holders can be interchanged into the test stand to fit different sized cathodes. The face of the cathode electrode is anodized to a thickness of 0.002" to inhibit emission from any area other than the cathode. The quality of the anodizing is a key factor in determining the maximum electric field strength available for testing purposes. The anodizing for these experiments was always performed by Duralectra Inc., of Natick, MA. The surface of

the aluminum holder is prepared to a "32" finish prior to shipment to Duralectra for anodizing.

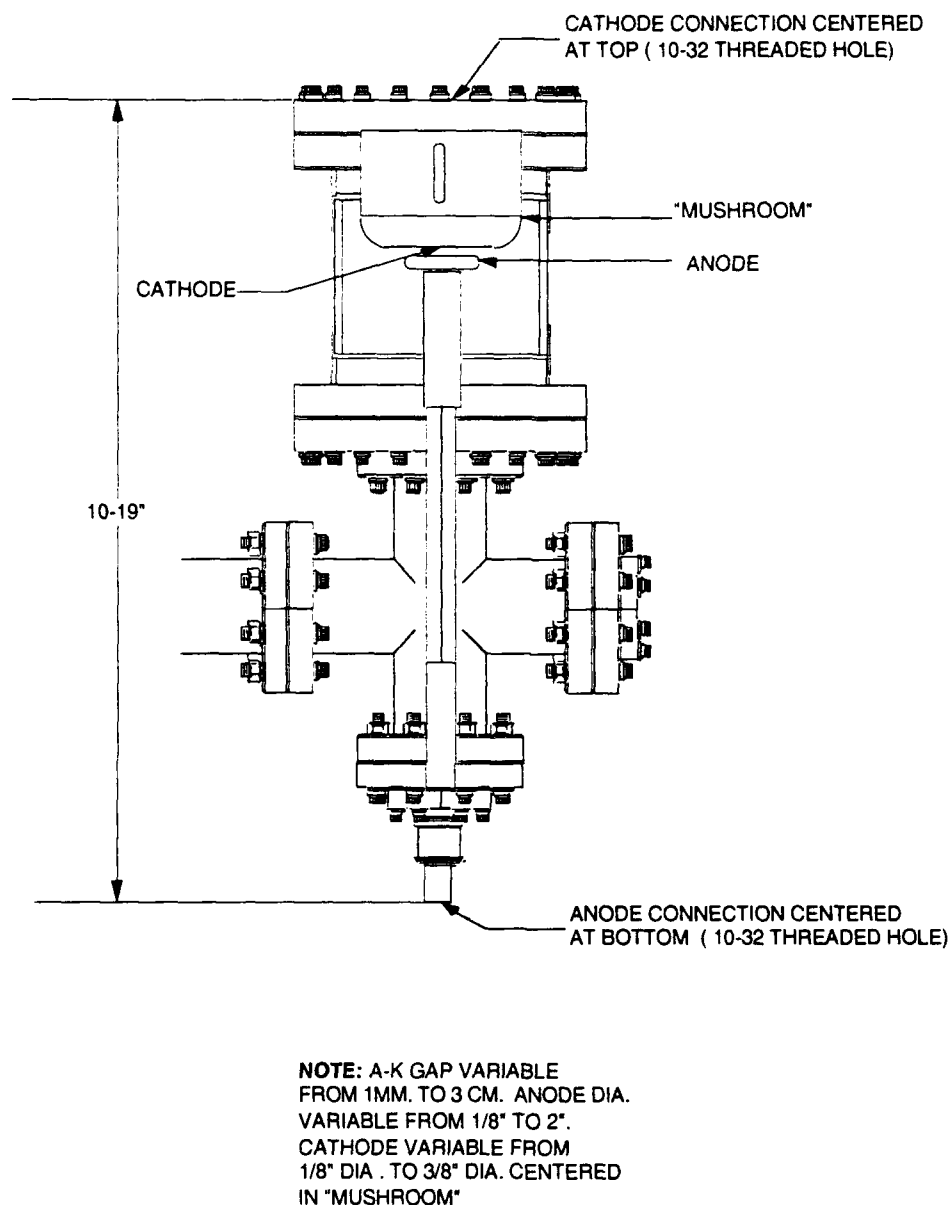


FIGURE 4.1: The DC test stand used to measure the initial *I-V* characteristics of the advanced cathode materials. Vacuum was provided originally by a combination of sorption and vac-ion pumps. Maximum vacuum and turnaround time have both been improved by the substitution of a dry rough pump/turbopump/cryopump system.

The anode electrode is mounted directly opposite the cathode emitter and was varied in material and geometry over the course of our experiments. A full anode structure consisted of a solid ~1" diameter cylinder with a highly polished flat face and rounded edges to reduce edge field enhancement. Full anodes fabricated from OFHC copper and POCO graphite were used in our experiments. A drawback to the use of a

full anode is the sensitivity of the measurements to emission from the portion of the cathode near the edge of the emitter. Small fabrication imperfections or mounting misalignments could lead to edge emission dominating everything else. Over time, the proper techniques to prevent this from occurring have been developed, and include "breaking" the edge of the emitter and using a slight (~ 0.003 ") setback to electrically hide the emitter edge.

An alternative anode structure developed early in our experimentation is shown in Fig. 4.2. A 0.125" diameter OFHC copper rod, with the end nearest the emitter fully radiused and the other end mounted in a larger anode "sink," is used to select a smaller emission area near the center of the emitter and away from the cathode edges. This is the anode structure used for obtaining most of the low-current I - V characterization data.

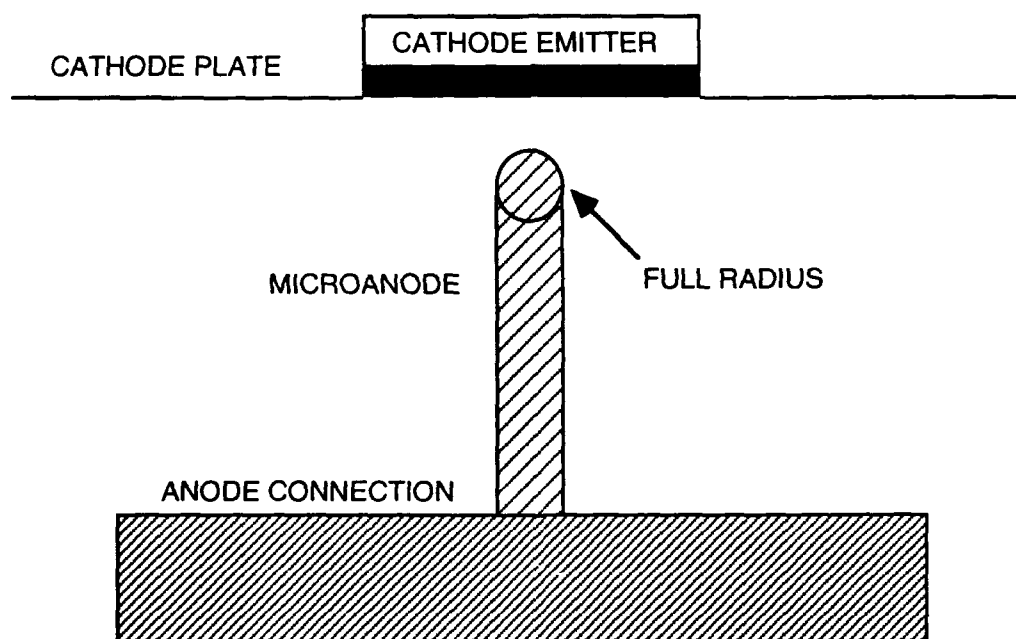


FIGURE 4.2: The geometry of the microanode electrode structure. This assembly allows for the more selective characterization of emission from the cathode emitter.

The field profile produced by the microanode electrode structure is shown in Fig. 4.3. Note that the field is non-uniform and falls off rapidly away from the axis of the anode structure. The details of the radial field profile depend on the separation of the end of the microanode from the cathode emitter face. The field profile shown in the figure is calculated for a 1mm K-A separation. The effective area under intense fields in this configuration is approximately 0.04cm^2 . This corresponds to the area where the fields are within $\sim 80\%$ of their maximum value. Due to the highly nonlinear nature of

vacuum field emission, this corresponds to approximately the 5% point for the emitted currents.

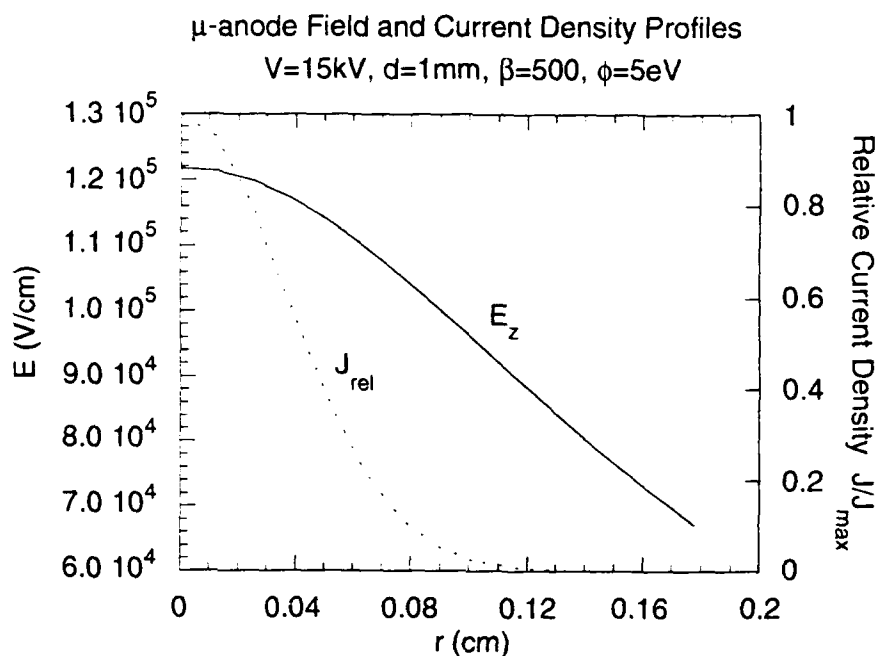


FIGURE 4.3: The axial field profile produced at the surface of the cathode emitter by the full radiused microanode at a distance of 1.0mm. The dashed line is the relative vacuum field emission current for an applied voltage of 15kV and a field enhancement factor $\beta=500$.

The cathode mount for most of the early measurements has already been described as an anodized aluminum plate as shown in Fig. 4.1. The only significant modification to this structure was the mounting of the cathode assembly on a linear motion feedthrough to allow continuous variation of the K-A gap distance. This modification was put in place during the testing of the microlithographically defined tubule structures in order to reliably achieve reproducible gap spacings on the order of 0.5mm.

The vacuum for the DC test stand was typically in the range of $1\text{--}7 \times 10^{-6}$ torr, though measurements were taken over the range of 1×10^{-8} to 1×10^{-4} . The vacuum system was initially comprised of twin sorption pumps and a 60l/s Vacion pump. This vacuum system gradually evolved to its present state of a dry rough pump, turbopump, cryopump staged system. These modifications have resulted in dramatically increased turn-around time: initially an entire day was required to pump the chamber from atmosphere to 10^{-6} torr--this process is now accomplished in less than 15 minutes. This rapid turnaround time was found to be necessary to allow rapid test-examine-test cycling of the emitter structures.

One of the intermediate incarnations of the vacuum system used a cold-trapped rough pump as the roughing system and the cryopump as the high vacuum system. This worked well with one exception: the cathode materials were found to be very sensitive to minute amounts of hydrocarbons that would successfully make it back through the cold trap. Even a high vacuum clean of the vacuum components between every pump cycle proved insufficient to prevent small amounts of oil from backstreaming. These hydrocarbons would plate out on the cathode structures and be readily detected by either Auger or XPS. This eventually required the complete replacement of the pumping unit in the cryopump to remove trapped oils from that system.

4.2 DC *I-V* Characteristics

The testing and characterization of the advanced cathode materials almost always started with a hand operated microanode experiment to observe initial current emission. Following the initial observation of emission, the DC power supply (15kV, 1.5mA max) is put on a remote driver, which modulates the applied DC voltage in a sawtooth waveform. The period of the sawtooth voltage waveform is varied between eight and thirty seconds, and the amplitude is varied to maintain an approximate duty cycle of ten percent.

Over a period of about one hour, the voltage required to maintain a peak current of 30-100 μ A in the sawtooth cycle typically decreases. During the lifetime runs described later, this decrease was observed to continue for anywhere from 25 to 75 hours, over which the *I-V* characteristic could be observed to change dramatically. Most of the voltage decrease would typically be observed in the first few hours. Subsequent changes in the *I-V* characteristic typically occurred in the relative shape and duty cycle of the current waveform.

The voltage and current can be monitored in a variety of different ways. During startup and conditioning, the signals are monitored on a two-channel chart recorder. Examples of this type of data are shown in Figs. 4.4 and 4.5. More detailed data are acquired by dropping the signals onto a Tektronix DSA 602 digital oscilloscope and subsequently analyzing the data on a 386PC computer. This analysis can straightforwardly provide the typical " α " and " β " parameters often used to characterize field emitter performance. The analyzed data presented here are obtained with the voltage always on the decreasing side of the sawtooth waveform. For reasons that may be related to short term thermal effects, the reproducibility of the data on the decreasing

side of the voltage waveform was better than that from the increasing side of the sawtooth.

DC I - V characteristic data were obtained for tubule cathodes, eutectic cathodes, microlithographically defined tubule cathodes, and tubule-like cathodes produced using a filter-paper template approach. Data summaries for all four types of cathodes will be presented separately.

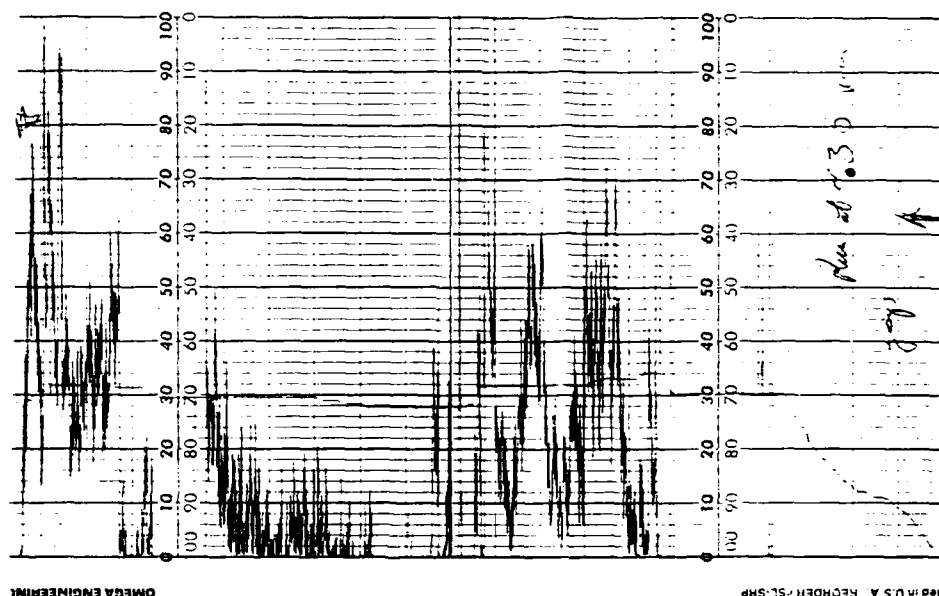


FIGURE 4.4: Chart recorder data for the startup of a tubule cathode.

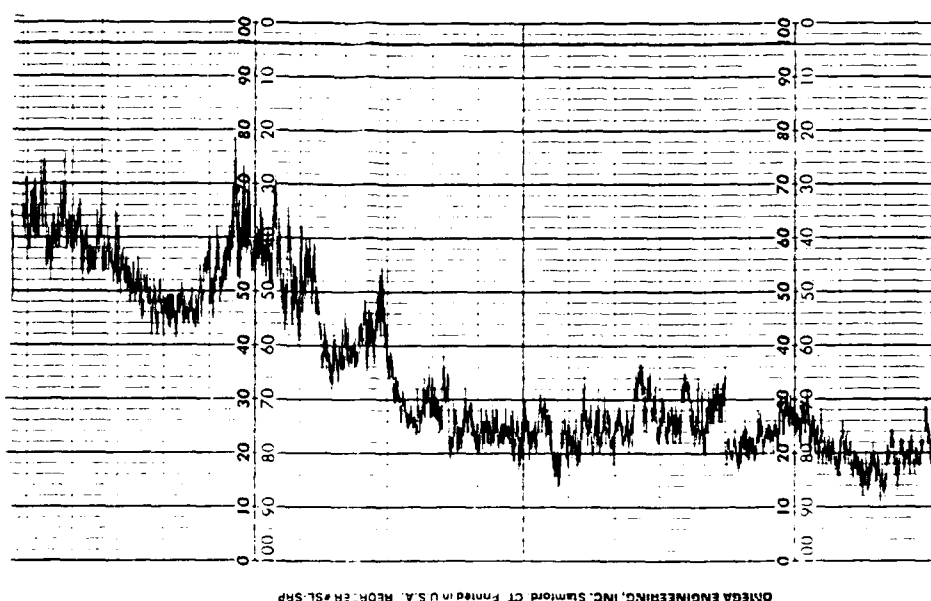


FIGURE 4.5: Chart recorder data for the initial conditioning of the cathode shown in Fig. 4.4. Note that the voltage necessary to drive emission has fallen significantly.

4.2.1 DC Characterization: Tubule Cathodes

A total of approximately 110 different cathodes supplied by NRL were tested over a period of eighteen months. Of these, 69 were structures fabricated from DC_{8,9}PC lipid tubules or structures intended as tubule analogs for process investigations. A summary of the cathodes tested in this project is given in Table 4.1. As can be seen from the table, all phases of the tubule cathode fabrication produced cathodes that did not emit.

All of the tubule cathodes that successfully emitted current required a 150Å coating of gold to be deposited over the cathode surface. This coating was necessary both to provide an emission surface and a conducting path to the emitter tips. The fabrication process used to create the tubule cathode microstructure resulted in oxidized Ni tubules embedded in a non-conducting epoxy substrate. Attempts to ensure that the tubules would go through this thin epoxy base and contact a conducting underlayer uniformly failed. Oxidized Ni is both a poor emitter with a high work function and a poor conductor. The deposition of the thin film Au overcoat was the only remedy used in this project.

Table 4.1: A summary of the tubule cathodes tested in this project.

#	DESIGNATION	DATE REC'D	EMISSION	COMMENTS
1	Q5	7/90	YES	CYCOM fiber
2	Q6	7/90	YES	CYCOM fiber
3	C6	8/90	NO	0.5% Ni by wt., Au coated; poor etch
4	C8	8/90	NO	0.5% Ni by wt., Au coated; poor etch
5	#2	10/90	NO	low density
6	#3	10/90	NO	low density
7	TL1	10/90	NO	
8	TL2	10/90	NO	
9	TL3	10/90	NO	
10	TL4	10/90	NO	
11	GM3A	10/90	NO	
12	GM3C	10/90	NO	
13	GM3F	10/90	NO	
14	GM3G	10/90	NO	
15	GM3H	10/90	NO	
16	W1	11/90	NO	
17	W2	11/90	YES	low current, edge only, 5min life
18	W3	11/90	YES	arcing, then stable
19	W4	11/90	YES	low current, arcing
20	W5	12/90	NO	
21	W7	12/90	NO	
22	W8	12/90	NO	

23	W3A	12/90	YES	stable emission only at low currents
24	W3C	12/90	YES	slowly died
25	W3D	12/90	YES	stable emission only at low currents
26	GI1	2/91	NO	no tubes
27	GI2	2/91	NO	no tubes
28	GI3	2/91	NO	
29	GI4	2/91	NO	sample charges up in SEM
30	GI2A	3/91	YES	arcing only
31	GI2B	3/91	NO	emitter corners detached
32	GI2C	3/91	YES	arcing from one corner of emitter
33	GI2D	3/91	NO	arcing only
34	GI2E	3/91	YES	lots of data
35	GI2F	3/91	YES	lots of data
36	GI2G	3/91	YES	lots of data
37	GI2H	3/91	NO	
38	GI2I	3/91	NO	
39	GI2J	3/91	NO	
40	GI3A	6/91	YES	unstable, arcing
41	GI3B	6/91	YES	run ~2hrs
42	GI3C	6/91	YES	unstable, arcing
43	GI3D	6/91	NO	arcing only
44	GI3E	6/91	NO	arcing only
45	GI3F	6/91	NO	arcing only
46	GI4A	8/91	NO	arcing only
47	GI4B	8/91	NO	arcing only
48	GI4C	8/91	NO	arcing only
49	GI4D	8/91	YES	few seconds of life only
50	GI4E	8/91	NO	arcing only
51	GI4F	8/91	NO	one arc; cathode detached from stub
52	GI4G	8/91	YES	consistent emission; run >1hour
53	GI4H	8/91	NO	arcing only
54	GI4I	8/91	YES	unstable; run over 40min.
55	GI4J	8/91	YES	gradually died over 1.5hr
56	GI4K	8/91	YES	rel. low voltage, arcing goes uncontr.,
57	GI4L	8/91	YES	5min, then arc, then gone
58	GI5A	8/91	NO	one arc
59	GI5B	8/91	NO	
60	GI5C	8/91	NO	uncontrollable arcing
61	GI5D	8/91	NO	
62	GI5E	8/91	NO	
63	GI5F	8/91	NO	cathode detached from stub
64	GI5G	8/91	NO	not run - SEM showed no tips
65	GI5H	8/91	YES	current low, run ~0.5hr
66	GI5I	8/91	YES	10min., then uncontrollable arcing
67	GI5J	8/91	YES	erratic, heavy arcing
68	GI5K	8/91	YES	brief run only
69	GI5L	8/91	YES	brief run, then wild arcing

Of the 69 cathodes tested, 27 emitted in a fashion that could be described as stable field emission over an interval of at least a few minutes. The majority of the characterization data came from a smaller subset of perhaps five cathodes that were run extensively enough to acquire detailed digitized data on the DSA 602. An example of the detail of the data available under these circumstances is shown in Figs. 4.6 - 4.9 for datasets taken with cathodes GI2E and GI2G. These cathodes are those covered in detail in the article in Appendix A, Appl. Phys. Lett., Vol. 60, No. 13, pp. 1556-1558 (1992).

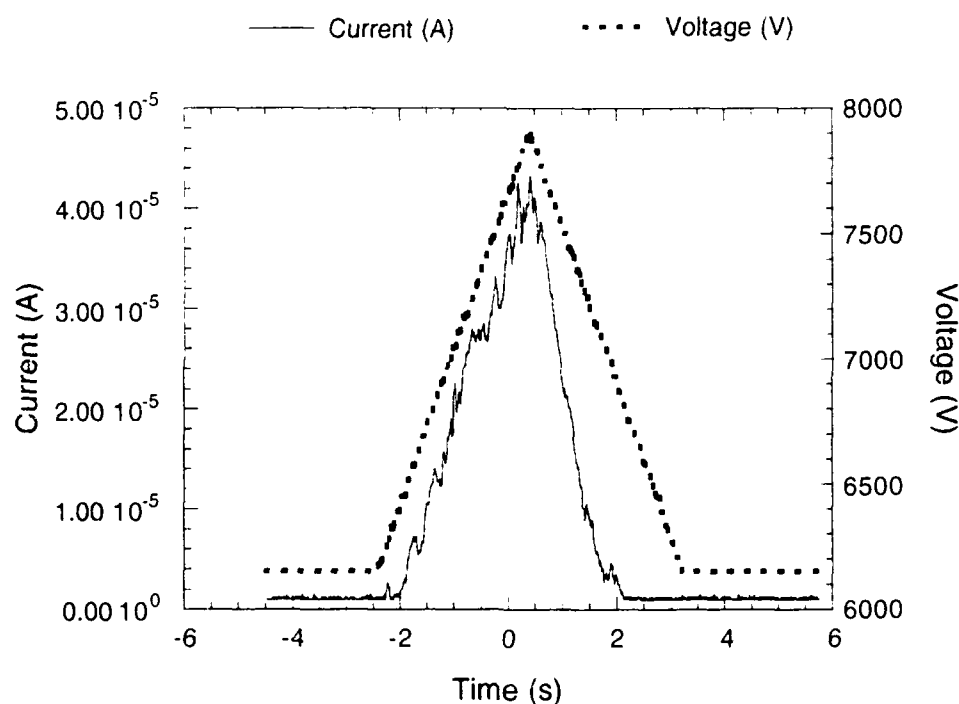


FIGURE 4.6: A plot of the microanode current vs. the amplitude of the sawtooth voltage. The data is taken from a single sawtooth cycle on GI2-G.

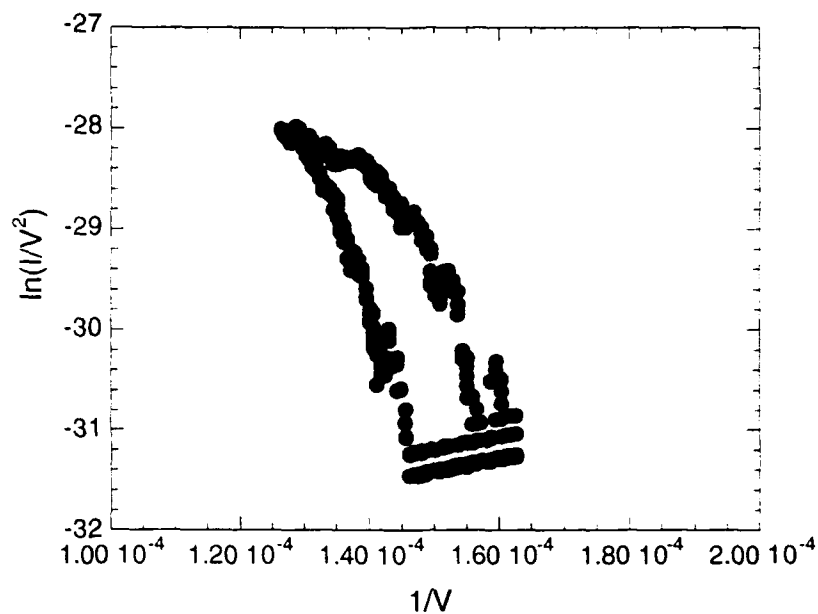


FIGURE 4.7: A Fowler-Nordheim style plot of the data from the sawtooth in Fig. 4.6. Note the hysteresis in the data.

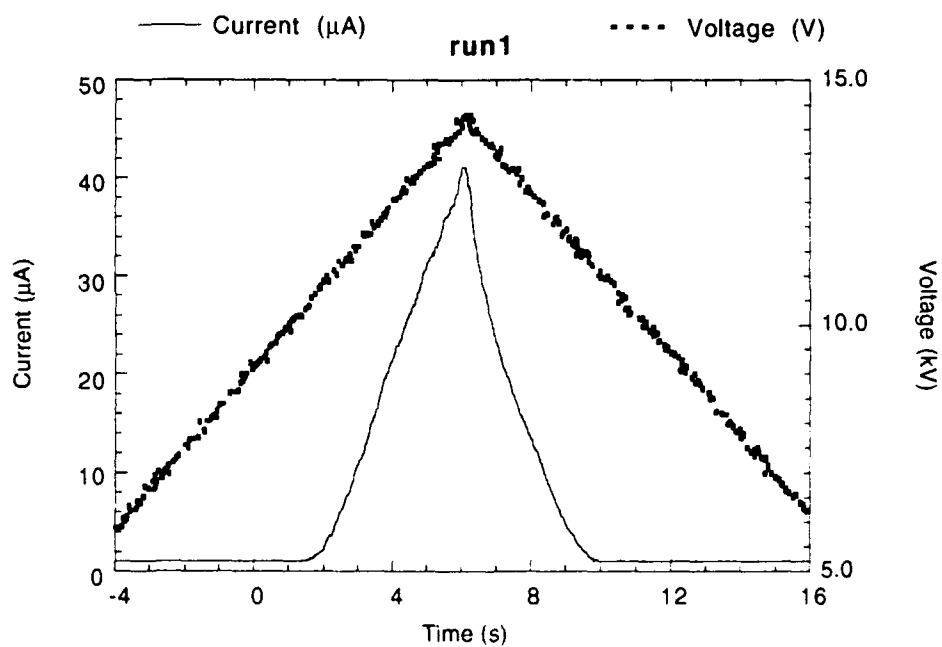


FIGURE 4.8: The sawtooth voltage (upper) and corresponding microanode current averaged over 32 successive pulses in run 1 of cathode GI2-E.

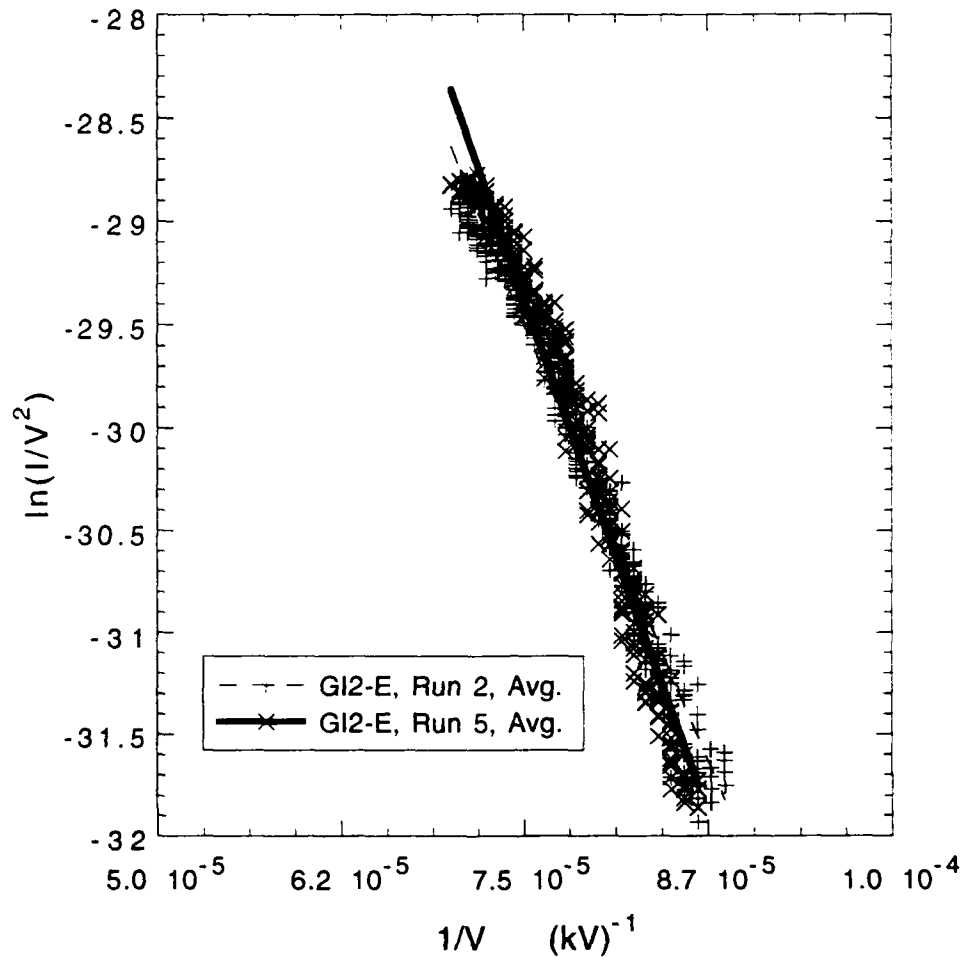


FIGURE 4.9: The Fowler-Nordheim plot for the average data from Run 2 and Run 5, as given in the Appl. Phys. Lett. publication. Note that while the data lie very close to each other, the sensitivity of the linear fit yields substantial variations in " α " and " β ."

The analysis of the data from cathodes GI2-E and GI2-G yields additional information as to the nature of the emission. The typical analysis to extract the apparent field enhancement factor and emission area has been covered in detail in Section 2. For ease of reference, the results of the standard analysis of the data from GI2-E and GI2-G given in the Appl. Phys. Lett. article are reproduced in Table 4.2.

Several things should be noted about the results in Table 4.2. First, both cathodes have been etched to produce $\sim 15\mu\text{m}$ tall tubes and then coated with 500\AA of gold. The numerical models in Section 2 can be used to calculate the field enhancement for these structures, assuming perfectly smooth cylinders with walls of varying thickness. A plot of the field enhancement factor as a function of height for two such cases is shown in

Table 4.2: The analyzed data for cathode GI2-E and GI2-G.

Test Sequence	$\ln a$	b (kV)	β	α (10^{-8} cm ²)
GI2-E Run 1, Avg.	-13.65	204	429	1.06
GI2-E Run 2, Avg.	-15.45	206	471	0.0506
GI2-E Run 5, Avg.	-10.67	245	357	10.4
GI2-G Run 1, Rep No. 2	-2.53	199	440	23,500
GI2-G Run 1, Rep No. 10	-7.93	156	561	65.3
GI2-G Run 1, Rep No. 21	-9.33	146	600	14.1

Fig. 4.10. Note that for $\sim 15\mu\text{m}$ tall emitters the nominal field enhancement factor is in the range 150-250. This differs from the observed results in Table 4.2 by a factor of 2-4. Fig. 4.10. Note that for $\sim 15\mu\text{m}$ tall emitters the nominal field enhancement factor is in the range 150-250. This differs from the observed results in Table 4.2 by a factor of 2-4. This is precisely the result so often cited in the early work of Spindt et al., corresponding to the additional field enhancement of small protruberances distributed over the surface of the emitter. High resolution SEMs of the emitters justify this supposition: the emitter surfaces produced by the electroless deposition-coated, tubule composite fabrication process are rough and grainy.

The rough and grainy nature of the emitter structure has a deleterious effect on the available emission area because only the high spots of the "pebbles" participate in the emission process. The parameter " α " is sensitive and variable under the best of circumstances. The data in Table 4.2, however, evidence a six order of magnitude variation in this parameter (though only three orders of magnitude in any given cathode). This is a strong indicator of the changing status of the details of the emitter tip shape as a function of time. The thin film gold overcoat is a relatively low melting point material and is probably field forming at the most modest of currents.

Finally, note that for the successive pulse data for cathode GI2-G, from cycle number 2 to cycle number 21 the field enhancement factor uniformly increases and the emission area uniformly decreases. The continuance of this trend over time for this type of structure indicates that it may have limited high current utility. This is in contrast to the data presented next for the eutectic cathodes where precisely the opposite happens during the "conditioning" phase. The mechanism does not appear to be uniform or

long lasting, as evidenced by the average data for cathode GI2-E, which shows a more random trend with time.

In summary, the DC characterization of the tubule cathodes demonstrated their capability to act as field emitter arrays. The reproducibility of the data was generally poor, and could be considered a reflection of the difficulty in producing reproducible cathode structures with the fabrication technique that was employed. The overall yield of usable cathode structures did not improve significantly with time: typically only a third to a half of the cathode structures received from NRL emitted at all, and less than 10% of the structures emitted stably for times approaching one hour. This dramatically limited the amount of experimentation, characterization, and measurements that could be performed with the tubule cathodes.

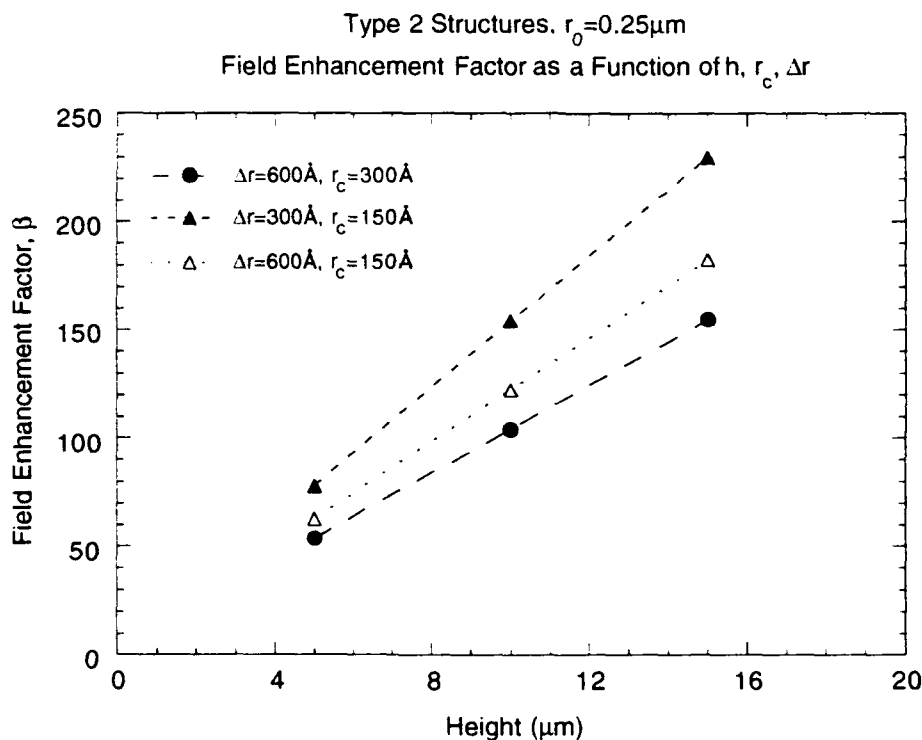


FIGURE 4.10: The calculated field enhancement factor for three different shapes of tubule structure as a function of tubule height.

4.2.2 DC Characterization: Eutectic Cathodes

A total of approximately 250 different cathode wafers and two Si-TaSi₂ crystal boules were produced by GTEL for this effort. Of these, XX were tested in the DC test stand during the initial test phase of the project. The remainder were used in AC tests described later in this report, used as test samples for a variety of technology transfer

and transition opportunities as described later in this report, or remain in stock at SAIC with the intent of use in subsequent government efforts.

Neither the initial nor the second initial series of cathodes received from GTEL emitted. This effect was traced to the silver-polyamide paste that was used to bond the cathode wafers to the copper stub. Previous work (D.A. Kirkpatrick, U.S. Pat. No. 5,138,220) had established that mere contact to this silicon matrix was insufficient to attain emission: the radial Schottky barriers implicit between the TaSi₂ rods and the Si matrix isolate the rods from the matrix. The nature of the silver-polyamide paste made contact to the emitter rods unlikely. After initial experiments with the 23-series of wafers, we applied the same technique of a gold overcoat that was used earlier to short out the Schottky barriers and make contact to the tips. At this point, sustained emission was achieved.

The incorporation of this learning into the fabrication process was delayed one series in the fabrication line due to the timing of the experiments and the preparation of cathodes at GTEL. Starting with the 4-series emitters, the backplane of the emitter wafers was coated with successive layers of Ti-Ni-Au and annealed for 15 minutes at 350°C. This allowed the Ti-Ni layer to diffuse into the TaSi₂ and Si portions, making intimate contact to what we believe is all of the tips.

The next step was the development of the etch process to produce ~10μm tall emitters on a flat Si matrix substrate, which was accomplished in the 5-series of emitters. This was rapidly reproduced in both the 6-series and 7-series of emitters. The 6-series was the first attempt at 0.125" diameter cathodes that would be applied in the higher current density experiments in the lifetime and AC test stands. The 7-series cathodes featured a patterned backplane contact (see Section 3) and unequivocally demonstrated the application of the Schottky barrier isolation of the emitters to the problem of addressability.

All during these efforts, the initial startup of the cathode emitters continued to be an interesting experience. Invariably significant arcs would occur during startup, often damaging areas of the cathode. Various artistic techniques were developed in an attempt to minimize the damage to the emitters during this phase. Detailed investigations of the surface chemistry of the "as received" emitters revealed a remnant oxide of the emitter tips. This oxide was removed *in situ* by bombardment from an Ar-ion gun. Subsequent improvements to this technique were developed for commercial applications under an SAIC IR&D project. The removal of the oxide prior to operation dramatically reduces the likelihood of damage during startup, and is an essential

development for both the improved device yield and a number of downstream applications. This is detailed in the publication attached in Appendix A, Appl. Phys. Lett. Vol. 61, No. 21, pp. 2518-2520 (1992).

It should be noted that except for checks of various performance parameters, following the 100% yields of the 5-, 6-, and 7-series, DC I-V characterization of the eutectic cathodes was used predominantly as a baseline measurement. Except for cathodes that have been physically damaged or mistreated, there has been a 100% emission yield since the 5-series. This is not to say that all of the cathodes have performed exactly as desired - as will be detailed later, several cathodes were damaged or destroyed in various subsequent tests without ever being characterized DC to any detail. The low current DC operation was instead taken for granted as we progressed to more stringent performance requirements.

Table 4.3: A summary of the eutectic cathodes tested in this project.

#	I.D.	REC'D	h (μ m)	EMIT?	COMMENTS
1	19-1	8/90	5-8	NO	Ag-polyimide cement mount
2	19-2	8/90	5-8	NO	Ag-polyimide cement mount
3	19-3	8/90	5-8	NO	Ag-polyimide cement mount
4	19-4	8/90	5-8	N/Y	Ag-polyimide cement mount/ Au overcoat
5	19-5	8/90	5-8	NO	Ag-polyimide cement mount
6	23-1	9/90	10-20	N/Y	Ag-polyimide cement mount/ Au overcoat
7	23-2	9/90	10-20	NO	Ag-polyimide cement mount
8	23-3	9/90	10-20	N/Y	Ag-polyimide cement mount/ Au overcoat
9	23-4	9/90	15-30	Y	Ag-polyimide cement mount/ Au overcoat
10	23-5	9/90	15-30	N/Y	Ag-polyimide cement mount/ Au overcoat
11	3-1	11/90	20	Y	Ti/Ni/Au; uneven wafer
12	3-2	11/90	20	Y	Ti/Ni/Au; uneven wafer
13	3-3	11/90	20	Y	Ti/Ni/Au
14	3-4	11/90	20	Y	Ti/Ni/Au
15	3-5	11/90	20	Y	Ti/Ni/Au
16	4-1	1/91	15-20	NA	Ti/Ni/Au
17	4-2	1/91	15-20	NA	Ti/Ni/Au
18	4-3	1/91	15-20	NA	Ti/Ni/Au
19	4-4	1/91	15-20	NA	Ti/Ni/Au
20	4-5	1/91	15-20	Y	Ti/Ni/Au
21	5-1	3/91	8-9	Y	Ti/Ni/Au; long CFA test run (100 hrs)
22	5-2	3/91	8-9	Y	Ti/Ni/Au
23	5-3	3/91	8-9	Y	Ti/Ni/Au
24	5-4	3/91	8-9	Y	Ti/Ni/Au
25	5-5	3/91	8-9	Y	Ti/Ni/Au
26	6-1	3/91	8-9	Y	Ti/Ni/Au; 0.125" diam
27	6-2	3/91	8-9	Y	Ti/Ni/Au; 0.125" diam

28	6-3	3/91	8-9	Y	Ti/Ni/Au; 0.125" diam
29	6-4	3/91	8-9	Y	Ti/Ni/Au; 0.125" diam
30	6-5	3/91	8-9	Y	Ti/Ni/Au; 0.125" diam
31	7-1	3/91	8-9	Y	Ti/Ni/Au; patterned contact
32	7-2	3/91	8-9	Y	Ti/Ni/Au; patterned contact; 100 hr run
33	7-3	3/91	8-9	Y	Ti/Ni/Au; patterned contact
34	7-4	3/91	8-9	Y	Ti/Ni/Au; patterned contact
35	9-1	5/91	8-9	NA	AC Pulsed expts
36	9-2	5/91	8-9	NA	AC Pulsed expts
37	9-3	5/91	8-9	NA	AC Pulsed expts
38	9-4	5/91	8-9	NA	AC Pulsed expts
39	9-5	5/91	8-9	NA	AC Pulsed expts
40	9-6	5/91	8-9	NA	AC Pulsed expts
41	8-7	5/91	8-9	NA	AC Pulsed expts
42	9-8	5/91	8-9	NA	AC Pulsed expts
43	9-9	5/91	8-9	NA	AC Pulsed expts
44	9-10	5/91	8-9	NA	AC Pulsed expts
45	10-1	5/91	15-25	Y	
46	10-2	5/91	15-25	Y	
47	10-3	5/91	15-25	Y	
48	10-4	5/91	15-25	Y	
49	10-5	5/91	15-25	Y	
50	11-1	7/91	8-9	NA	AC Pulsed expts
51	11-2	7/91	8-9	NA	AC Pulsed expts
52	11-3	7/91	8-9	NA	AC Pulsed expts
53	11-4	7/91	8-9	NA	AC Pulsed expts
54	11-5	7/91	8-9	NA	AC Pulsed expts
55	13-1	8/91			W-tubules
56	13-2	8/91			W-tubules
57	13-3	8/91			W-tubules
58	14-1	9/91	~25	Y	CFA rectangles
59	14-2	9/91	~25	Y	CFA rectangles
60	14-3	9/91	~25	Y	CFA rectangles
61	14-4	9/91	~25	Y	CFA rectangles
62	14-5	9/91	~25	Y	CFA rectangles
63	14-6	9/91	~25	Y	CFA rectangles
64	15-1	10/91	8-9		processing tests
65	15-2	10/91	8-9		processing tests
66	15-3	10/91	8-9		processing tests
67	15-4	10/91	8-9		processing tests
68	15-5	10/91	8-9		processing tests
69	16-1	10/91	~25		CFA rectangles
70	16-2	10/91	~25		CFA rectangles
71	16-3	10/91	~25		CFA rectangles
72	16-4	10/91	~25		CFA rectangles
73	16-5	10/91	~25		CFA rectangles
74	16-6	10/91	~25		CFA rectangles
75	18-1	12/91	8-9		InCuSil/W braze
76	18-2	12/91	8-9		InCuSil/W braze

77	30-1	2/92	8-9		0.125"
78	30-2	2/92	8-9		0.125"
79	30-3	2/92	8-9		0.125"
80	30-4	2/92	8-9		0.125"
81	30-5	2/92	8-9		0.125"
82	31-1	2/92	8-9		sent to BNL for laser expt.
83	31-2	2/92	8-9		sent to W&M
84	31-3	2/92	8-9		sent to Raytheon for testing
85	31-4	2/92	8-9		sent to Raytheon for testing
86	31-5	2/92	8-9		
87	S-1	2/92	8-9	ion	5mm squares
88	S-2	2/92	8-9	ion	5mm squares
89	S-3	2/92	8-9	ion	5mm squares
90	S-4	2/92	8-9	ion	5mm squares
91	32-1	2/92	8	Y	Si-WSi;
92	32-2	2/92	8	Y	Si-WSi;
93	32-3	2/92	8	Y	Si-WSi;
94	32-4	2/92	8	Y	Si-WSi;
95	33-1	2/92			not etched; sent to BNL as control
96	33-2	2/92			laser expt; sent to BNL for confirm.
97	33-3	2/92			xfered to DARPA/env. project
98	33-4	2/92			xfered to DARPA/env. project
99	33-5	2/92			xfered to DARPA/env. project
100	33-6	2/92			xfered to DARPA/env. project
101	33-7	2/92			xfered to DARPA/env. project
102	33-8	2/92			xfered to DARPA/env. project
103	33-9	2/92			xfered to DARPA/env. project
104	33-10	2/92			xfered to DARPA/env. project
105	33-11	2/92			xfered to DARPA/env. project
106	33-12	2/92			in laser expt.
107	33-13	2/92			xfered to DARPA/env. project
108	33-14	2/92			sent to W&M for laser expt.
109	33-15	2/92			sent to W&M for laser expt.
110-121	34-1 to 34-12	2/92			0.125" diam; used in gated cathode fab. expts.
122	35-1	5/92	8-9		del. to Silicon Video for DARPA displays
123	35-2	5/92	8-9		del. to Silicon Video for DARPA displays
124-138	35-3 to 35-17	5/92			xfered to DARPA / env. project
139-156	36-1 to 36-18	5/92			xfered to DARPA/ env. project
157-228	37-1 to 37-72	5/92			in use for μ -wave switch project w/ VARIAN
229-263	1 boule single	5/92			35 wafers assumed; xfered to DARPA / env.
264-298	1 boule poly	5/92			35 wafers assumed; xfered to DARPA / env.

Of the 298 cathodes, wafers, or boule/wafers received, 30 of the first 34 cathodes were tested and characterized in the DC test stand, and 25 emitted in a fashion that could be described as stable field emission over an interval of at least a few minutes. The characterization data came from a large set of cathodes from the 23-, 3-, 4-, 5-, 6-, and 7-series that was run extensively to acquire detailed digitized data on the DSA 602. Several of these cathodes were run over 100 hours. An example of the detail of the data available under these circumstances is shown in Figs. 4.11 - 4.13 for a dataset taken with cathode 5-5. This cathode is one of those covered in detail in the article in Appendix A, Appl. Phys. Lett., Vol. 59, No. 17, pp. 2094-2096 (1991). The summary data given in the figure in the article are reproduced in Fig. 4.14.

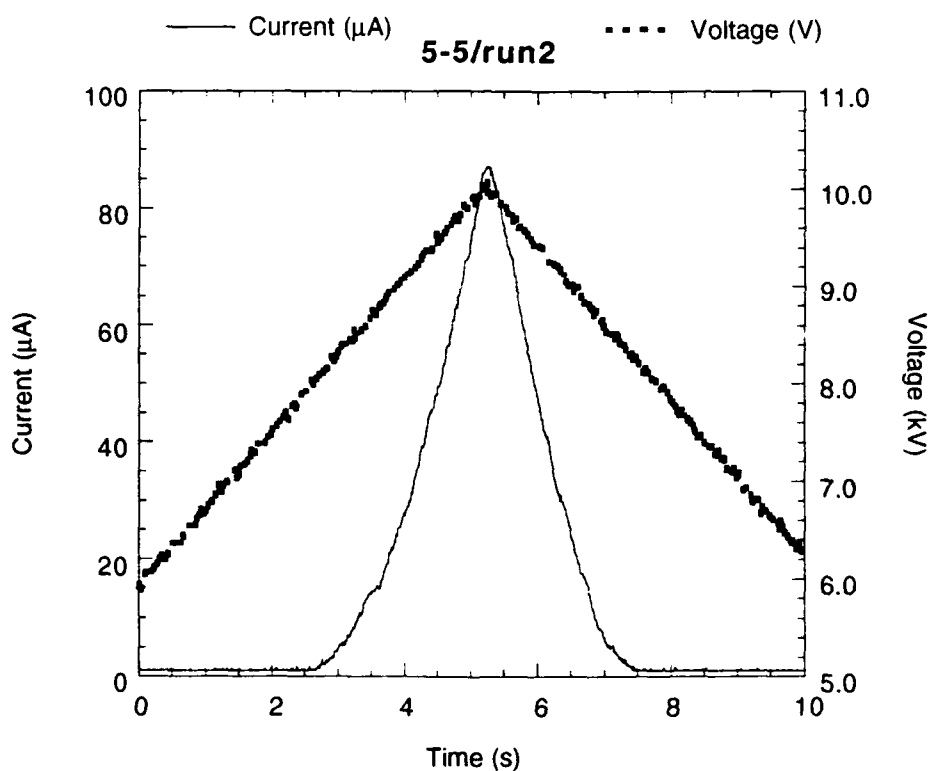


FIGURE 4.11: A plot of the microanode current (thin line) vs. the amplitude of the sawtooth voltage (dark line). The data are taken from an average over 32 successive pulses.

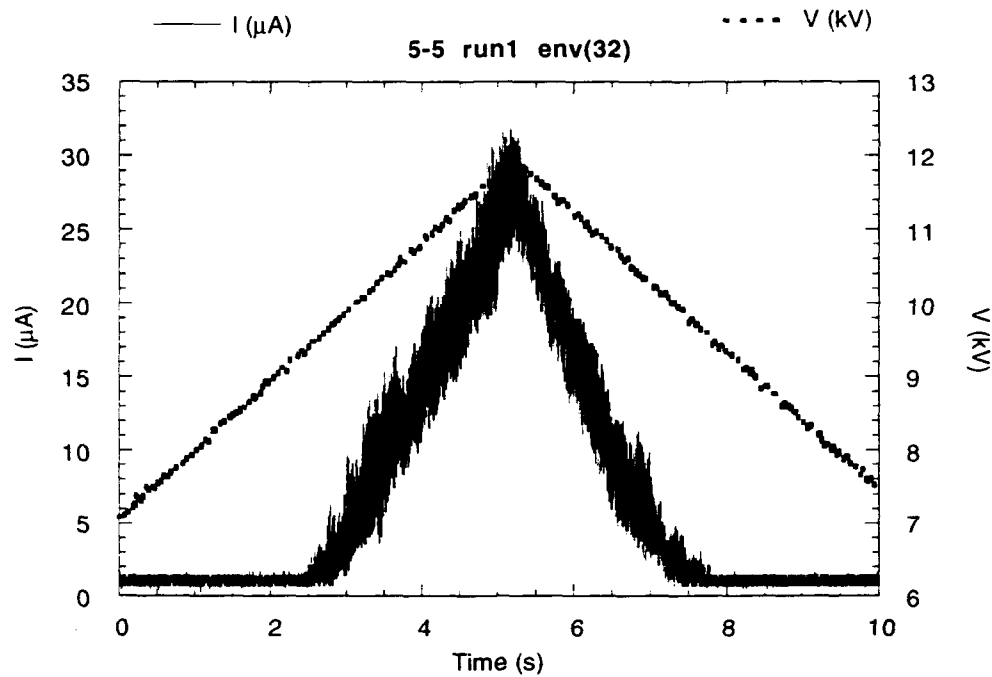


FIGURE 4.12: A plot of the microanode current vs. the amplitude of the sawtooth voltage. The data are taken from an envelope over 32 successive pulses.

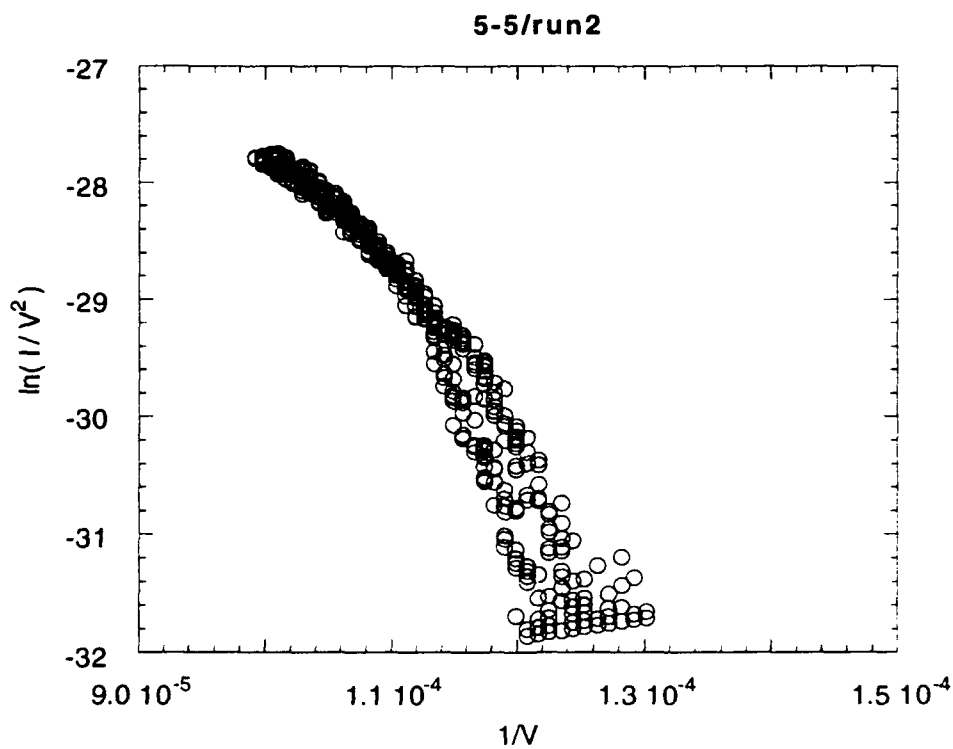


FIGURE 4.13: The Fowler-Nordheim plot of the data in Fig. 4.11. Note the relative lack of hysteresis compared to the same data for a tubule cathode.

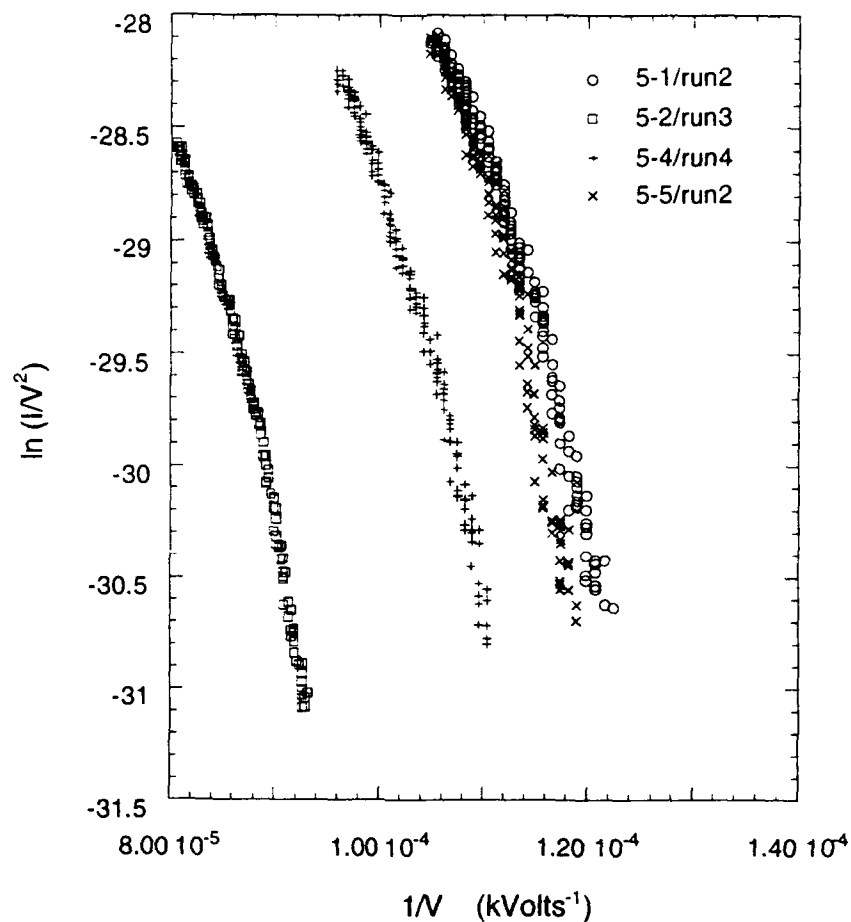


FIGURE 4.14: The Fowler-Nordheim plot for the average data from several different runs of several different cathodes, as given in the Appl. Phys. Lett. publication.

The analysis of the data from the 5-series cathodes as presented in the Appl. Phys. Lett. article yields additional information as to the nature of the emission. For ease of reference, the results of the standard analysis of the data from the 5-series cathodes are reproduced below:

Table 4.4: The analyzed data for the 5-series cathodes.

Test Sequence	β'	β	α (nm ²)
5-1, Run 2	4770	573	1.3×10^6
5-2, Run 3	3670	440	1.3×10^6
5-4, Run 4	4510	541	6.5×10^5
5-5, Run 2	4030	484	3.3×10^7

Several things should be noted about the results in Table 4.4. First, all the cathodes feature 8-9 μm tall tips and are bare TaSi₂. Cathode 5-3 was coated with gold and was left out of this analysis. The numerical models in Section 2 can be used to calculate the field enhancement for these structures, while varying the tip radius of curvature and emitter height. A plot of the maximum field enhancement factor as a function of height for several tip radii of curvature is shown in Fig. 4.15. Note that for $\sim 10\mu\text{m}$ tall emitters with a 100 \AA tip radius of curvature, the nominal field enhancement factor β_0 is ~ 350 . This agrees fairly well with the results of Table 4.4. More importantly, a TPIC set of simulations using the 10 μm tall, $r_c=100\text{\AA}$ simulation structure yields an " α " per tip of 32nm². For the prolate ellipsoid calculation discussed in Section 2, this value for " α " per tip is about 110 for $r_c=100\text{\AA}$ while " β " falls to ~ 300 . All the evidence points towards almost uniform emission from tips with r_c in the range of 50-100 \AA .

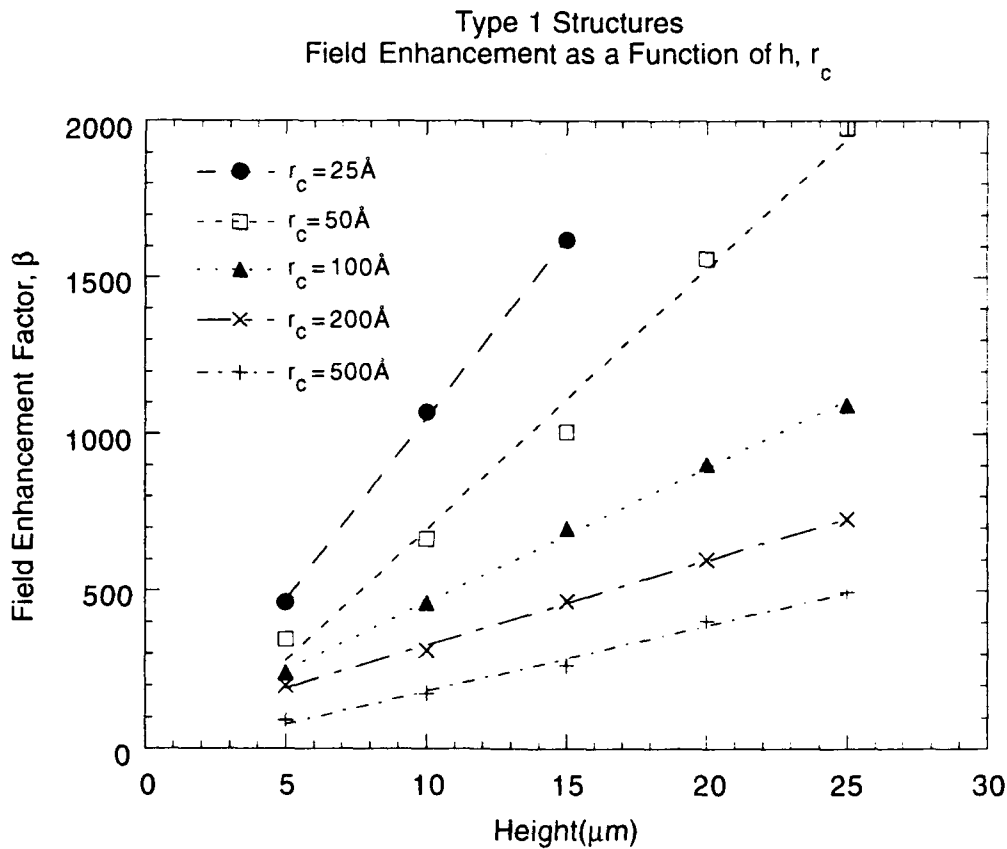


FIGURE 4.15: A plot of the calculated maximum field enhancement factor as a function of tip height for several tip radii of curvature. Note that $\beta=350$ with $h=10\mu\text{m}$ corresponds to $r_c=100\text{\AA}$.

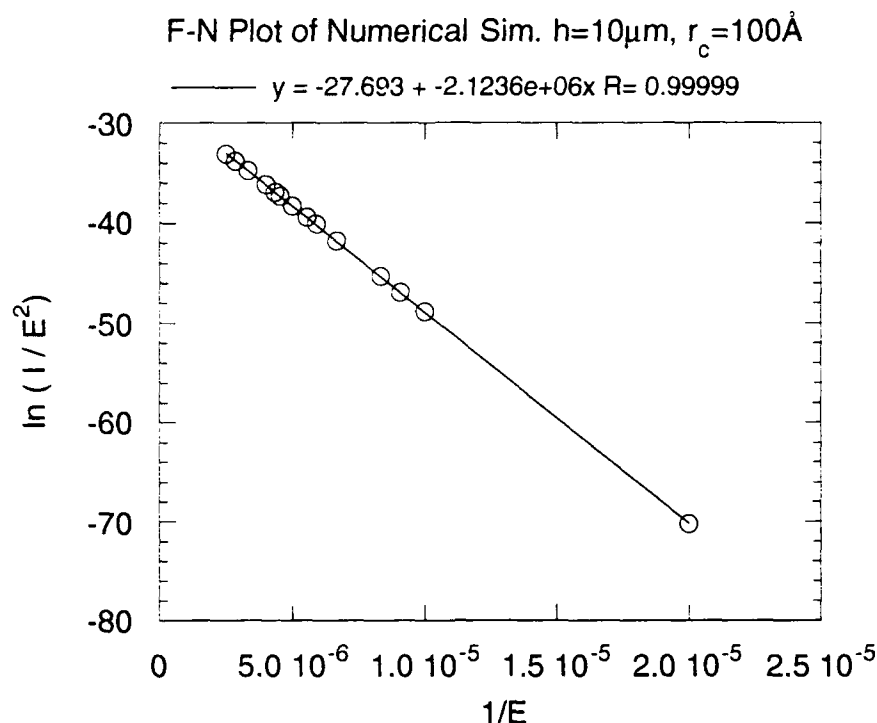


FIGURE 4.16: A plot of several successive TPIC runs with a $10\mu\text{m}$ tall Type 1 structure with a tip radius of curvature of 100\AA . The standard analysis of this data yields " β "= 340 and " α "= 32nm^2 per tip.

An important difference between the performance of the eutectic emitters and the tubule emitters is the agreement between theory and measurement. The characterization of the eutectic emitters indicates that the majority of the emitter tips are participating in the emission process. This tendency towards uniform emission is further borne out by subsequent measurements with a phosphor system. The long life of the eutectic emitters is also in stark contrast to the data obtained with the tubule cathodes. Finally, the yield of working emitters took several positive steps forward to the point where the baseline operation of the eutectic cathodes is now taken for granted. This was essential to making the further progress called for in the project milestones.

4.2.3 DC Characterization: Filter Paper Template Tubule Cathodes

Cathodes fabricated by an extrusion technique using PCTE filter paper as a negative template were delivered to SAIC for testing by NRL Code 6090. These cathodes can be thought of as tubule cathodes with an alternative fabrication process. The cathodes did demonstrate emission, but were unable to do so for periods in excess of one hour. A listing of the filter paper template tubule cathodes received for testing, and their status, is given below.

Table 4.5: The filter paper template cathodes tested in this project.

#	DESIGNATION	DATE REC'D	EMISSION	COMMENTS
1	RPA	3/91	NO	very dense emitters
2	RPB	3/91	NO	sparse emitter coverage
3	RPC	3/91	NO	sparse and peeking NOT TESTED
4	RPD	3/91	NO	too much Au NOT TESTED
5	RPE	3/91	NO	too much Au NOT TESTED
6	RPF	3/91	NO	hard to find tips
7	RPC	3/91	YES	dense emitters w/ heavy Au
8	RPH	3/91	NO	dense emitters w/ heavy Au
9	RPI	10/90	YES	

A total of nine cathodes were inspected and/or tested, of which two emitted. Several additional undesignated cathodes were also inspected but were not found to be promising as candidates for emitters. A sample of the emission data from RPI is shown in Fig. 4.17. The overall performance of this cathode could be favorably compared with the tubule cathode GI2-E, though the field enhancement factor for the PCTE filter paper cathode was about a factor of two higher.

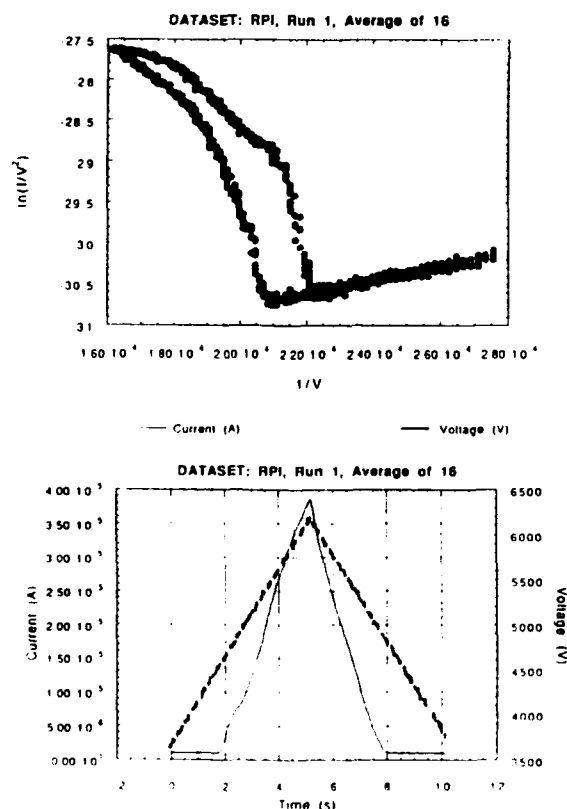


FIGURE 4.17: A Fowler-Nordheim plot (upper) and the voltage and current traces corresponding to it (lower) for the cathode RPI.

4.2.4 DC Characterization: Microlithographic Tubule Cathodes

Another fabrication effort that produced emitter samples tested by SAIC in this project used proprietary chemistry at NRL to microlithographically produce tubule-like structures. An SEM image of one such sample is shown in Fig. 4.18, and the details of the fabrication are outlined in the attached publication in Appendix A, "Ungated Vacuum Field Emission from Ordered Arrays of Microlithographically Defined Cylinders." A brief synopsis of those emitters tested to some detail is given in Table 4.6.

Table 4.6: The microlithographic cathodes tested in this project.

#	DESIGNATION	DATE REC'D	EMISSION	COMMENTS
1	JJ-1A	3/91	NO	
2	JJ-1B	3/91	NO	
3	JJ-3A	3/91	YES	small gap, fields $\geq 200\text{kV/cm}$
4	LC117	3/91	YES	small gap, field $> 150\text{kV/cm}$
5	2MMA B1	5/91	YES	small gap, field $> 150\text{kV/cm}$
6	A-1	5/91	YES	small gap, field $> 150\text{kV/cm}$
7	A-2	5/91	YES	small gap, field $\sim 100\text{kV/cm}$
8	C1	5/91	YES	small gap, field $\sim 100\text{kV/cm}$
9	C2	5/91	YES	small gap, field $\sim 200\text{kV/cm}$
10	D1	5/91	NO	
11	B1	6/91	YES	video tape - corner emission
12	A1	6/91	YES	video tape
13	E9	9/91	NO	
14	E10	9/91	NO	
15	E11	9/91	YES	$\sim 150\text{-}200\text{kV/cm}$ turn on
16	E10/2	9/91	YES	$\sim 150\text{-}200\text{kV/cm}$ turn on

The microlithographic cathodes tested in this project were only started as a fabrication effort at NRL during the last 12 months of the project. In the very controlled environment in which they could be fabricated, the distribution of the cylindrical structures could be well defined. It proved to be more difficult to fabricate uniform structures across the arrays, and more difficult still to produce structures with uniform egg-shell tops (e.g., without fluting or high points). The emitters had difficulty sustaining emission without arcing and damaging themselves: several good SEM images of destroyed emitters are included in the publication. These emitters suffered from many of the same drawbacks as the tubule cathodes and the filter paper template cathodes: an inability to perform for long times or at substantial emission currents without being destroyed.



FIGURE 4.18: A SEM image of a microlithographically prepared tubule cathode. The shape of the structures led to the nickname "TMI"s.

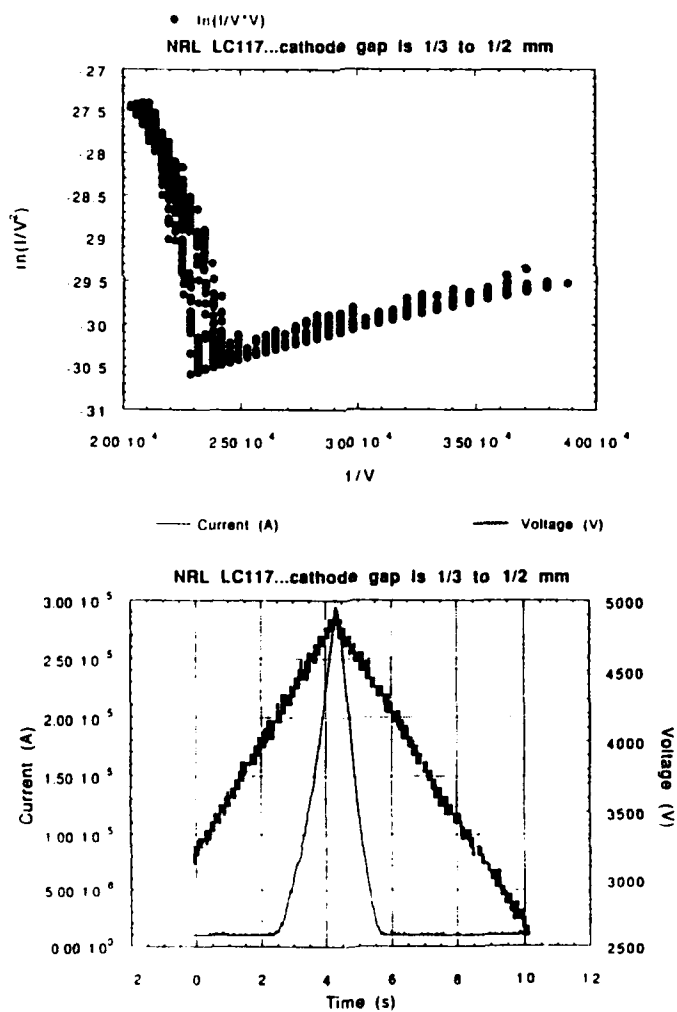


FIGURE 4.19: A Fowler-Nordheim plot (upper) and the voltage and current traces corresponding to it (lower) for the cathode LC117.

4.3 "Pepper-pot" Emittance Apparatus

The "pepper pot" emittance apparatus is used to provide a coarse measurement of the transverse momentum spread present in an electron beam. The basic apparatus is shown in Fig. 4.20. This long tube fits to the apparatus of the DC test stand, with the plate at the left forming a "full anode" structure. This plate is drilled through with a pattern of several small holes that aperture the electron beam incident from the left of the figure into several smaller "beamlets" traveling down the tube and to the right. These beamlets spread ballistically, with their local spreading angle determined by the transverse momentum spread of the beam at the point of the original aperture. This is shown graphically in Fig. 4.21. The apertures must be chosen to be of a small enough size such that the anticipated spreading due to transverse momentum is much larger than any spreading due to the space charge in the beam.

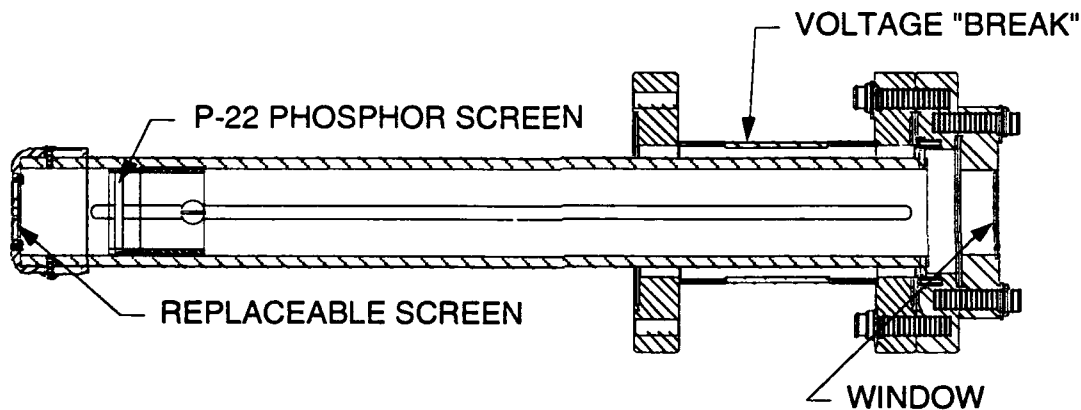


FIGURE 4.20: The schematic drawing of the system used to perform the coarse emittance measurements. This assembly mates to the bottom of the DC test stand and provides a viewable phosphor image of the witness beamlets formed from the replaceable screen.

The image on the phosphor screen created by the incident beamlet current can be observed through the glass plate at the rightmost end of the tube. The distance between the aperture disk and the phosphor plate can be continuously varied between about 3cm and 30cm. If the aperture disk is removed, the phosphor plate can be moved directly up to the level of the anode and can be used to directly image the emission uniformity. Several aperture disks are available with one to several aperture holes of varying sizes. The size of the image spot on the phosphor is divided by the distance between the phosphor and the aperture disk to determine the beamlet spreading angle $\delta\theta$. This angle is equivalent to v_{\perp}/v_z for small angles, and can be directly compared to values anticipated from the numerical simulations.

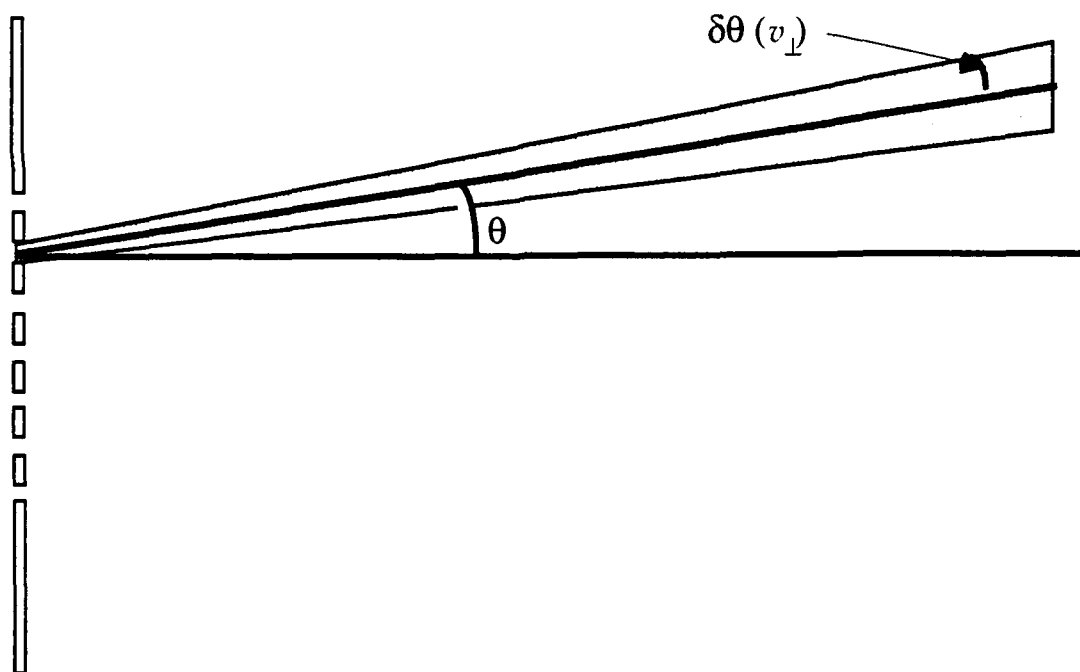


FIGURE 4.21: The screen apertures the incident electron beam into several "beamlets." Each of these beamlets spreads according to its own distribution function of v_{\perp} . This distribution can be deconvolved from the image of the beamlet on the phosphor plate.

4.4 Initial Emittance Measurements

Initial measurements of the emittance from an advanced cathode material source were carried out with cathode GTE-23-3, as described in the article attached in Appendix A, "High brightness electron beam sources for FEL applications," Nucl. Inst. and Meth. A (1992). These measurements indicated a normalized beam spreading angle of $\gamma\beta\delta\theta \sim 7\text{mrad}$. Here $\gamma = (1 + (eV/mc^2))$, and the value for β is given by $\beta = (v/c) = \sqrt{1 - (1/\gamma^2)}$, where v is the velocity of the electrons and c is the speed of light.

The observed value for $\gamma\beta\delta\theta$ is in good agreement with the results of the numerical simulations in Section 2. The cathode 23-3 features tips with heights of 10-20 μm , whereas the simulation results assume a tip height of 10 μm . Still, the predicted value for a 100 \AA radius of curvature tip is approximately 7mrad for an applied macroscopic field of 100kV/cm, as is the case for the data presented in the publication. A reproduction of this data is shown in Fig. 4.22.

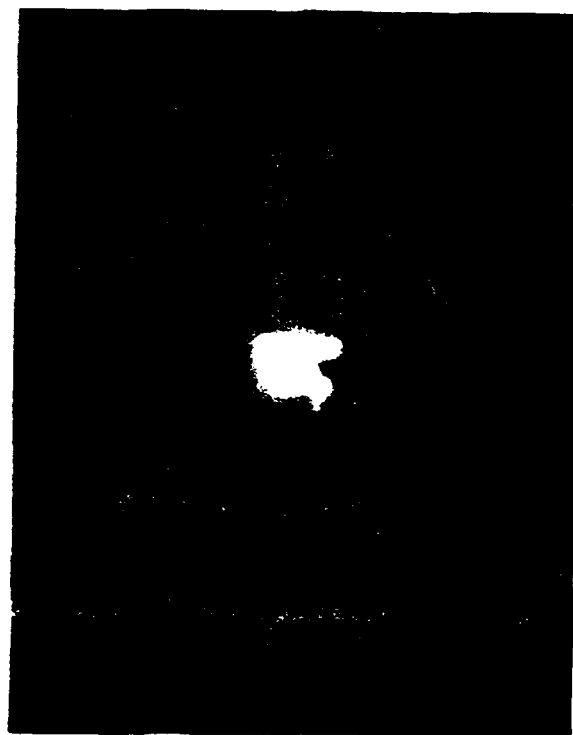


FIGURE 4.22: A spot image of the Si-TaSi₂ cathode #23-3, as measured by the coarse emittance measurement apparatus. The aperture disk has a single, on-center aperture of ~0.3mm diameter. The aperture plate thickness is ~1mm.

4.5 Lifetime Test Apparatus

The lifetime test apparatus is a duplication of the DC I-V characterization apparatus, but with protection circuitry on the driving voltages added to prevent prolonged overcurrents in the event of a self-sustaining arc. The two channel chart recorder was expressly set aside for long timescale runs (> 24 hours continuous) and dedicated to this apparatus. In addition, precision gate valves and leak valves were added to the vacuum system to provide for both the vacuum and impurity sensitivity tests.

It was originally contemplated that the lifetime test apparatus would be a stand-alone system pumped by one of several Vacion pumps available. The dynamics of the lifetime tests and the demands that were placed on that system for measuring lifetime under a variety of conditions made the use of ion pumps unfeasible. Ion pumps are designed for use only in closed, high vacuum systems, and are not intended for use in a system with an intentional leak pressure of oxygen.

4.6 Vacuum Sensitivity Tests

Several measurements were carried out to characterize the performance of the emitters as a function of the emitter pressure. Due to their prolonged robustness, the majority of these measurements were carried out with the eutectic cathodes. The high quality vacuum available in the lifetime test apparatus is ideal for these types of measurements, in that it can provide a dynamic range of vacuum from 1×10^{-8} torr to 1 torr. This range is accomplished by the use of ultrahigh vacuum fittings and variable gate valves. On a few occasions, after the system had been closed for a prolonged period of time, vacuum readings of $5-7 \times 10^{-9}$ torr have been achieved during measurements.

Most of the data presented in this section on DC characterization of the emitter performance were taken with vacuum pressures in the range of 1 - 7×10^{-6} torr. Several series of measurements were taken after allowing the vacuum system to pump the chamber to pressures into the 10^{-8} to 10^{-7} ranges with no observed change in performance. A degradation in performance with increasing pressure was not noted until the pressure reached the 5×10^{-5} to 1×10^{-4} torr pressure range. This range is well beyond the range of interest for most of the applications investigated in this project, and detailed characterizations of the performance in this regime were not carried out. Following the completion of this project, several applications with interests in this pressure range have come to our attention and we are currently investigating them.

4.7 Impurity Sensitivity Tests

Impurity sensitivity tests were carried out with various gases being intentionally leaked into the vacuum chamber; some gases were also inadvertently leaked as a result of shortcomings of some of the vacuum systems used at various stages of the early DC characterization experiments. The gases actively leaked into the vacuum chamber to specific background pressures included air, argon, and oxygen. Their effect on the overall performance of the emitters was gauged in terms of *I-V* characteristic deterioration and shortened lifetime.

The inadvertent impurity tests occurred as a result of the previously mentioned phenomenon of minute amounts of oil backstreaming through what were thought were protected vacuum systems. Eliminating all traces of this oil from the vacuum systems required repeated efforts over an extended time period of six months or more. Originally, we realized that something was getting into the system after noticing sooty,

black deposits on the microanode structure. Subsequent XPS of the cathodes involved showed extensive carbon deposits all over the cathode surface. During this phase, maximum cathode lifetimes for the eutectic cathodes were limited to a few tens of hours. This limit was imposed by a combination of our patience, the number of cathodes in the queue for testing, and a slow degradation of the performance -- probably due to the large buildups of carbon on the cathode surface. The resolution of this issue coincided with the demonstration of 100hr lifetime runs in vacuum and in 5×10^{-6} torr oxygen.

The cathodes were intentionally run in oxygen backgrounds as demonstration of their viability in the Aegis Cross-Field Amplifier microwave tube. These tests were carried out on cathodes that had been etched, stripped of their surface oxide, and subsequently coated with gold. None of these cathodes ceased operating during any of the experiments, some of which exceeded 100 hours in length. As a check on the utility of the gold coating, an uncoated cathode was operated under the same conditions and died after a few tens of hours of running. Subsequent XPS characterization of the dead cathode indicated severe tip material oxidation.

Cathodes have also been operated in argon and argon-mercury environments in conjunction with an internal SAIC development for high brightness LCD display backlights. Operation of the backlights under conditions of approximately 1-fTorr is dramatically different from the more conventional high vacuum requirements associated with FEAs. Cathodes are also being operated in Varian proprietary microwave devices where the cathodes are exposed to chlorine and water vapor. Varian has investigated a number of other FEA technologies and none have been able to survive under their conditions. The coated and modified eutectic cathodes supplied to Varian have not evidenced a single failure to date. Clearly, while this latter point is just a matter of time and numbers, the eutectic emitters have already outperformed the harsh atmosphere performance of all other FEA technologies by a large factor in several ways.

The operation of the advanced cathode materials in unique environments is one of their most unanticipated properties. It continues to be an area of active exploration, and is one focus of a new DARPA project in advanced, environmentally benign manufacturing technologies.

4.8 Lifetime Tests

As we have mentioned previously, several cathodes were subjected to lifetime measurements. In the case of all of the cathodes except the eutectics, these lifetime

measurements were effectively carried out during the phosphor characterization of their emission uniformity. In all cases, the measured low current lifetime for the tubule, filter paper template, and microlithographic cylinder cathodes was less than a few hours. It was pointed out earlier that this short lifetime effectively precluded any further significant performance characterization of these types of cathodes.

Several of the eutectic cathodes were run for extended periods of time, either explicitly or implicitly as cathode lifetime measurements. These runs are summarized in Table 4.7. As shown in the table, long duration runs with the eutectic cathodes took place as early as six months into the project, and runs of over 100 hours took place within the first year.

The long life run of an advanced cathode material priming element in the Aegis CFA tube at Litton's plant in Williamsport, PA, was terminated because nothing was changing. The improved performance of the CFA was so remarkably stable that the Litton staff stopped the experiments and opened the tube to investigate -- fully expecting that the emitter had been destroyed in the first few minutes. However, on examination of the emitter showed absolutely NO operational damage. The only damage evident was clearly due to handling of the emitter structure during mounting in the tube. Indeed, the emitter structure had collected several microscopic particles of what was later found to be sand. These particles had been introduced into the tube during a sandblasting cleaning phase used in the assembly, and the emitter acted like a microscopic broom in capturing them. Clear evidence of emission by the eutectic array could be seen in the shapes of the tips--typical for what we had observed on "conditioned" emitters run at SAIC.

Finally, three cathodes were installed at the College of William and Mary during an investigation of surface ion emission and laser driven field emission. During the initial experiments, the staff at William and Mary covered the range of performance parameters already discussed, and characterized in detail the nature of ion species coming off the surface of the cathode. Follow-on experiments characterized the emitter performance when irradiated with a long pulse low power Nd:YAG laser, as a complement to similar experiments performed at SAIC and discussed later in this section. The total number of hours run on the cathode is estimated to be ~1000. The cathode was finally destroyed by an experimental mishap unrelated to normal operation.

Table 4.7: A summary of the major lifetime data for this project.

Cathode	Conditions	Duration (hours)
3-3	Gold coated- microanode run then used for imaging system tests.	22+ [Dec 1990]
3-4	Gold coated - microanode run then run in imaging system	70+ [Jan 4-7 1991]
5-2	Several hours of vacuum data (20+) then 30+ additional hours oxygen CFA tests, turned off while still operating	50+ (30+ in O ₂) [May 1991]
5-1	Several hours of vacuum data (20+) then gold coated and long oxygen run (5 days); cathode "dead" at end of O ₂ run.	140+ (120+ in O ₂) [May 1991]
7-2	Patterned backplane cathode; Ar ion etched then Au coated; run in oxygen CFA test for 100 hrs; test terminated while still fully running	100+ (100+ in O ₂ and still functioning) [June 1991]
16-3	Installed in CFA at Litton. Full power test in operating Aegis CFA.	>450 [Feb. 1992]
31-2	Installed in W&M experimental apparatus	~1000 (est.)

4.9 AC Test Stand

The AC test stand is a Pierce focused electron gun that employs shaped electrode structures to compensate for the self electric field of the generated electron beam, and to produce a solid, laminar beam. The design also seeks to minimize the variation of the applied field across the surface of the cathode. The SLAC EGUN code was modified to accept a larger grid structure to resolve the field in detail near the cathode surface; this code was then used as a design tool. The important thing to note here is that the emission law governing the advanced cathode materials is dramatically different from that which describes the more conventional thermionic sources. In particular, the change in emission current density is much more sensitive to the applied electric field. As a consequence, "tuning in" on the desired design parameters and geometry can be an exasperating challenge.

The AC gun designed and fabricated for this effort is shown schematically in Fig. 4.23. Vacuum is provided by either a 45 l/s or 60 l/s Vacion pump, with rough pumping provided by a dry roughing pump and dry turbopump system. Typical operating vacuum pressures were in the range of 10^{-7} - 10^{-8} Torr. The cathode on its stub is mounted in the cylindrical aperture in the shaped, anodized aluminum cathode

holder. The cathode flange is pin-aligned to the clear glass electrical standoff, which in turn is pinned to the anode structure.

During the initial tests of the system, it was discovered that extreme care must be taken in the assembly of this mechanical system to ensure precise alignment of the cathode and anode. Small misalignments produce non-centered field maxima and diverging field lines, which in turn produce concentrated emission from the cathode in undesired directions. This emission typically impacts somewhere on the anode structure, most often on or just beyond the inner edge of the aperture in the anode face. The extremely high power density in the incident electron beam ($V \sim 25\text{kV}$, $J \sim 100\text{A/cm}^2$, $P \sim 2.5\text{MW/cm}^2$) rapidly produces an anode flare, which propagates back to the cathode and drives a short. At this point, the remaining energy in the modulator pulse dumps through the cathode, destroying the emitter on a timescale of less than a microsecond. The protections on the modulator prevent a following pulse from getting out, but the damage has been done. The results of this extreme sensitivity were discovered immediately. The nature of the sensitivity and our first steps towards its resolution followed the sacrifice of numerous cathodes.

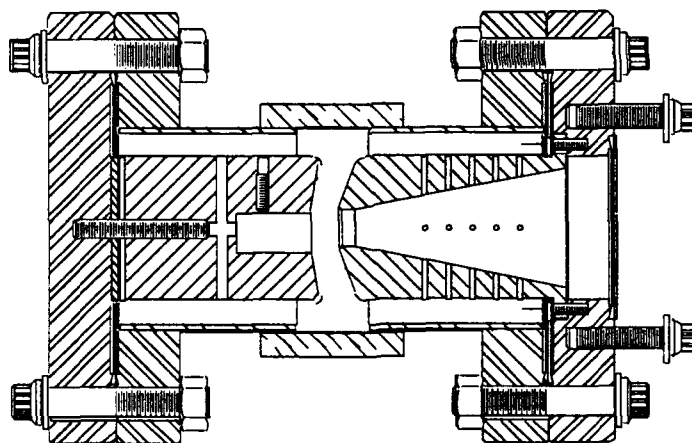


FIGURE 4.23: A schematic drawing of the close spaced Pierce focused electron gun used for the pulsed high current experiments. The cathode is mounted in the cylindrical aperture in the electrode on the left. The beam is electrostatically focused through the anode structure on the right and subsequently either dumped in a collector structure or further diagnosed.

Four complete cathode and anode system structures were fabricated for the AC gun shown in Fig. 4.23. Primary and backup pieces for accommodating 0.375" diameter cathodes were fabricated as shown. As a result of EGUN design runs, additional cathodes and anodes were fabricated for 0.125" diameter emitters using a smaller A-K gap distance. With an applied voltage maximum of 45 kV, the maximum field available in the 0.375" diameter cathode system was $\sim 120\text{ kV/cm}$. The maximum field available

in the 0.125" diameter cathode system was $\sim 350\text{kV/cm}$. A practical limit in this latter case is the long pulse breakdown of the anodizing coating, which occurs at $\sim 280\text{-}300\text{ kV/cm}$.

The pulse modulator used for these experiments was custom built for SAIC's ACT Laboratory by Fiore Industries of Albuquerque, NM. A brief summary of its characteristics is given in Table 4.8. The most important characteristic of the modulator design is its capability to operate over a wide range of dynamic loads. It must be noted that the impedance of the advanced cathode materials in the AC electron gun can change from effectively infinite to $\sim 10\text{ k}\Omega$ on a timescale of nanoseconds. This requires that the circuitry involved in the modulator and its path to the AC gun be designed to damp out fast reflections and oscillations in order to prevent damage to the modulator or large voltage fluctuations at the gun.

Table 4.8: The parameters for the HV modulator used in the AC gun experiments.

Voltage	0-50 kV
Current	0-10 A
Pulse Width	0.1 - 10 μs
Repetition Rate	0.01 Hz to 1kHz and single-shot
Overshoot	$\leq 2.0\%$
Duty Factor	$\leq 0.1\%$
Ripple	$\leq \pm 3.0\%$
Pulse to Pulse Jitter	$\leq 100\text{ ns}$
Risetime	Variable, $\leq 1\mu\text{s min.}$
Burst mode	5 pulses at 20kHz

Following our initial testing results, which are described in the next section, a modified design was prepared that is less susceptible to misalignment during assembly. This assembly is shown in Fig. 4.24. The cathode element is mounted from behind the cathode aperture in this scheme, avoiding the exposure of the cathode edges. These edges cause a highly localized field enhancement, which is very difficult to control. The mounting scheme in this improved design allows a controlled set back of the cathode from the shaping electrode plane. This set-back further promotes uniformity of emission from the cathode element. Another advantage of this type of construction is

its amenability to variations in the diameter of the emitter region without the necessity of processing the cathode itself to this same size. This also allows the use of square or irregularly shaped cathodes to produce cylindrical beams, giving us a much higher device yield.

The availability of variable sized beams is very important if this technology is to access the widest range of applications. In fact, low current ($I < 1\text{A}$) applications dominate the application arena, but high current density ($J > 10\text{A}/\text{cm}^2$) is often coupled with these lower current requirements. Cutting small cylindrical elements precisely circular and 0.050" in diameter is unnecessarily costly and difficult. Finally, the smaller diameter emission areas are compatible with smaller cathode-anode gap spacings and therefore lower applied voltages for the same electric field of $\sim 200\text{kV}/\text{cm}$. This allows the use of precision power supplies rather than the more costly, bulky, pulse modulator systems.

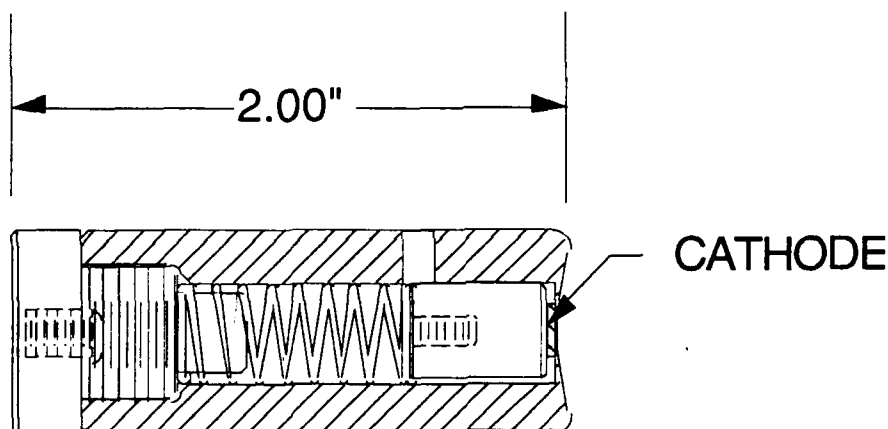


FIGURE 4.24: The modified cathode electrode structure for an improved AC gun design. The cathode is mounted through the back of the structure, and presses up against an anodized aperture in the front face of the electrode structure. This design removes the effects of the cathode wafer edges and allows a uniform wafer size to be used in designs for a wide range of generated electron beam diameters.

4.10 AC I - V Characteristics

The AC I - V characteristics were only measured for the eutectic advanced cathode materials. Lifetime and survivability issues precluded the investigation of the other cathode materials under development. As described in the previous subsection, the measurement of the advanced cathode materials under pulsed high power conditions proved very difficult. As was shown later in the project, the advanced cathode materials can respond to field fluctuations as fast as 10^{-15}s . This speed of signal is

fundamentally unmeasurable with electronic instrumentation. More importantly, this speed of response indicates that the cathodes are much faster and more sensitive measurements of high frequency spike noise in the driving voltage waveform than any characterization tool available.

Once an understanding of this sensitivity developed, the essential component in driving the cathodes with high power pulses was the careful elimination of any capacity for voltage spikes to find their way to the cathode. This included parallel and series circuits designed to load any high frequencies and a partially matched resistive load ($R \sim 7k\Omega$) for loading the output of the modulator. These precautions were gradually put in place. Finally, a small series resistance was added to the cathode side of the gun to slow down the charging cycle of the gun structure capacitance.

The various efforts in this area culminated in the ~ 8 hour, 10Hz run of a 0.125" diameter cathode; a pulse from this run is shown in Fig. 4.25. This cathode had first been conditioned in a DC test stand for more than 50 hours. The operating pressure during the 8 hour run was approximately 5×10^{-7} torr. This had increased from the nominal base pressure of less than 1×10^{-7} torr during the run, probably due to the heat output of the beam dump. The figure shows a pulse from approximately mid-way through the run. Note that there is a small signal at the leading edge of the beam current signal in the figure: this corresponds to the capacitive charging current during the rise of the voltage pulse, and is always present regardless of emission. The electron beam is on for approximately $1.2\mu s$ with a peak current of 6A, corresponding to a minimum current density of $75A/cm^2$. The accelerating voltage is 27 kV, which combined with the beam current and current density yields a beam power of 162 kW and a beam power density of $2MW/cm^2$. These are both records for field emitters.

The intense power in these experiments precluded running with greater repetition rate, due to the heat being generated and the gradual rise in vacuum pressure. The stability of the cathode was satisfactory considering the conditions: at this point on the I - V characteristic the current is scaling as $\sim V^{1/2}$. With the pulse to pulse reproducibility of the modulator at $\pm 3\%$, this yields a $\pm 40\%$ variation in the expected current. In order to maintain a reasonable safety factor the voltages in the experiment were not increased beyond what is shown in the figure.

The experimental conditions would be more optimum under the conditions designed for the second AC gun structure shown in Fig. 4.24. This gun would operate at lower voltages and currents, and could therefore be pulsed at much higher repetition rates. Furthermore, the stability of pulse power supplies at the $< 20kV$ level is much

greater than that of the high power modulator used for these experiments. Typical numbers for these types of solid state switching supplies are stabilities of better than 10^{-5} . Difficulties in the fabrication of the structure shown in Fig. 4.24 precluded us from performing experiments under these improved conditions during this project. Due to the demand for pulsed electron sources with these more modest voltage and current demands, we intend to continue pursuing these improvements with internal SAIC funds.

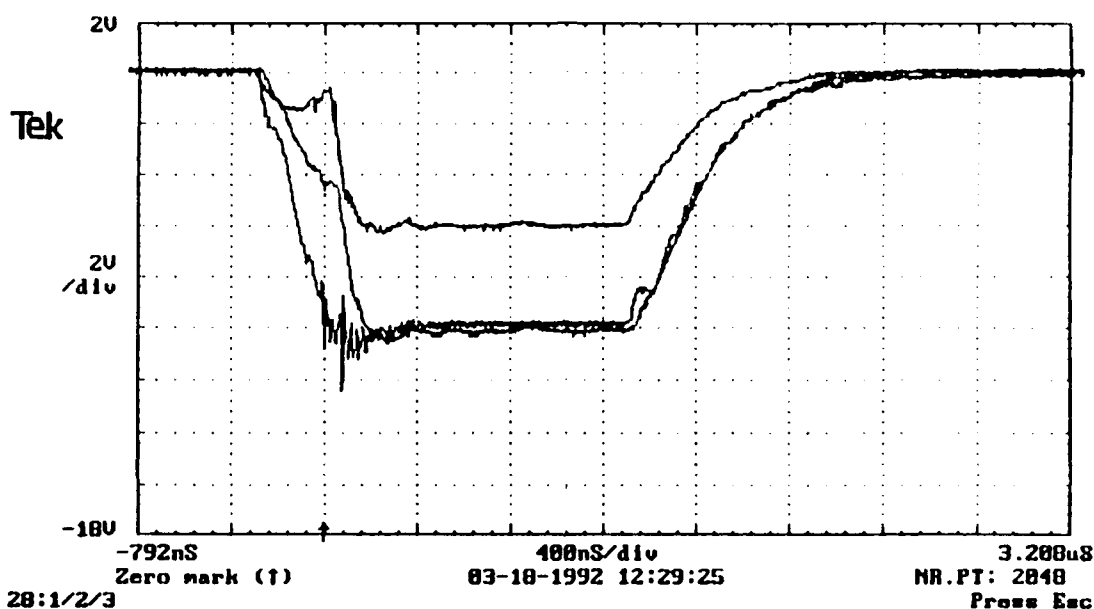


FIGURE 4.25: A pulse waveform from a Si-TaSi₂ eutectic cathode during an 8 hour run at 10Hz. The uppermost waveform is the current through the gun. The leading trace is the voltage on the gun, and can also be distinguished by the HF hash as it reaches peak and the cathode turns on. The middle trace is the total current, which takes into account the gun current and the current through the shunt. The values for the voltage, beam current, and minimum average beam current density are shown in the figure.

4.11 Slit-Wire Emittance Apparatus

The schematic of the slit-wire emittance measurement apparatus constructed for this project is shown in Fig. 4.26. The principle of the measurement is essentially the same as that for the coarse emittance measurement: aperture the incident beam to define the position of the electron source, then characterize the beam section after it has free-space drifted for a known distance. However, rather than measuring the divergence of an individual or set of spots, the slit-wire emittance system characterizes a linear section of the beam and integrates over the other ignorable coordinate. For a complete theoretical

description as to the merits of this approach, see the treatise by J.D. Lawson "The Physics of Charged Particle Beams," (Oxford University, Oxford, U.K., 1977).

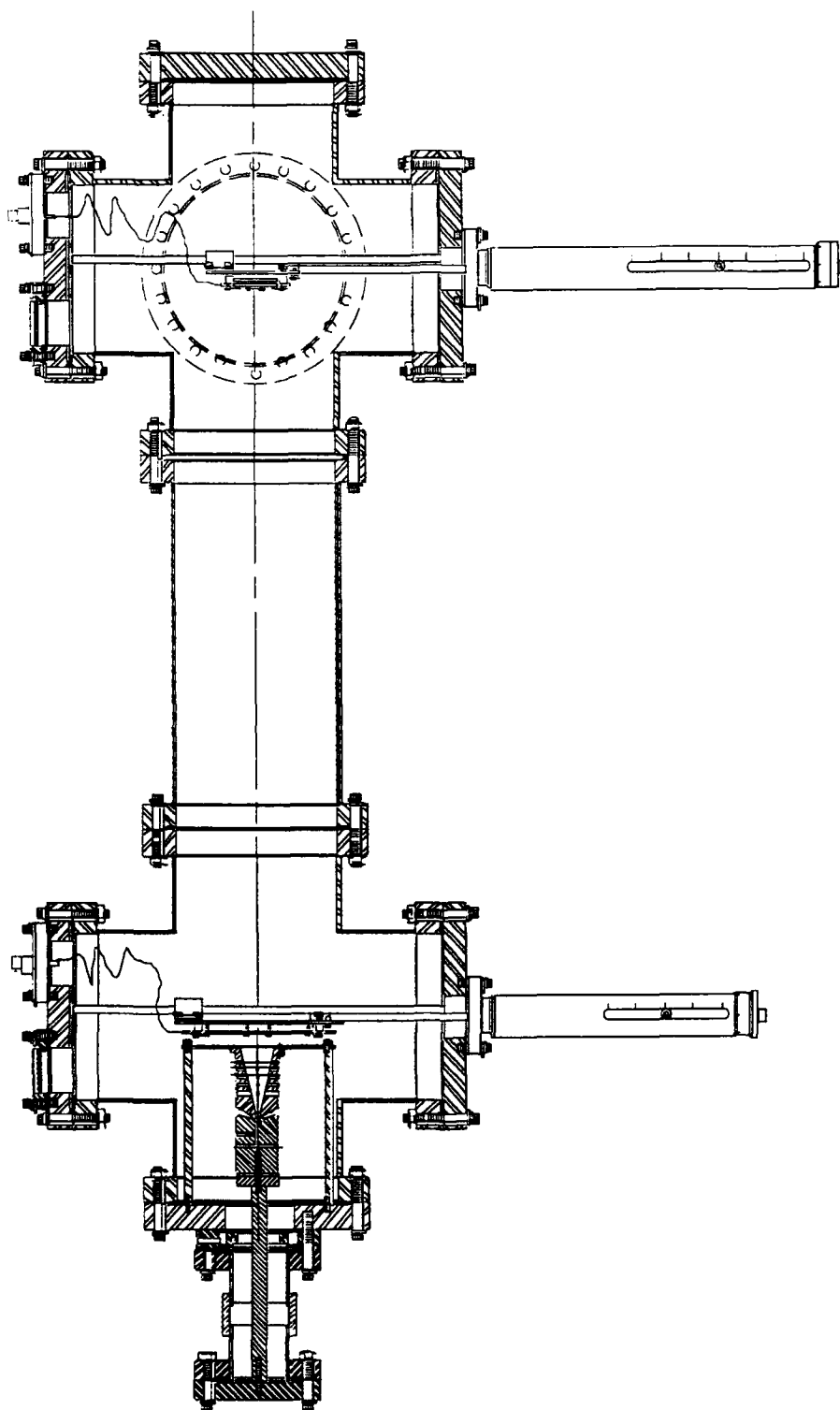


FIGURE 4.26: A schematic drawing of the slit wire emittance measurement system constructed for this project. The various parameters of the apparatus are discussed in the text.

The chamber for the slit-wire apparatus is constructed from two 8-inch diameter 5-way high vacuum crosses, either directly joined or separated by an 8-inch diameter drift section that is an additional 13 inches long. The drift section is shown at its largest in Fig. 4.26. Two Varian Vacion pumps are mounted on the fifth, out-of-plane port on the five-way crosses and provide ultra-high vacuum. Both the aperture and receiving wire are mounted on precision linear feedthroughs, and both the current intercepted by the aperture plate and that intercepted by the receiving wire are monitored. There can further be a bias applied to the receiving wire to prevent secondary electron aliasing of the received current. The diameter of the receiving wire and the long drift section are sufficient to exceed the 0.2 mrad resolution in $\delta\theta$ necessary to define beam brightnesses in excess of $10^7 \text{A/cm}^2 \text{rad}^2$ with a beam current density of 100A/cm^2 . The demonstrated base pressure of less than 1×10^{-7} torr is sufficient to guarantee that collisional scattering will not broaden the signal nor alias the received current.

4.12 DC/AC Fine Emittance Measurements

The emittance apparatus was fully checked out as a stand alone system but was not used to measure the beam parameters during this project. During the course of the project, the issue of beam brightness for pulsed experiments was superceded by: (1) the drive for demonstrations of high cathode current density and long life operation, and (2) the issue of ultra-fast pulsing (e.g., sub-ns) of the advanced cathode materials and the resultant beam brightness under those conditions.

5 Applications Evaluation

A primary focus of this project was the evaluation of and transition to applications. Several application concepts were set forth in the project proposal, including ubitron microwave amplifier tubes, microwave amplifiers for satellite communications applications, direct processing of semiconductors through addressed e-beam lithography, and harmonic FELs for advanced manufacturing technologies. As unexpected properties of the advanced cathode materials were discovered during the course of the project, we began to focus on several other application areas. These included using the cathode materials as a emission primer in the Aegis radar CFA tube to reduce jitter, as a long pulse high current density cathode for a Relativistic Klystron Amplifier (RKA) for a classified Army project, and as a laser-driven field emitter for RF accelerator applications including SDI, synchrotron light sources, and UV FELs. The cathodes' unique ability to operate in harsh background gases has led to transitions in backlights for military displays, commercial lighting requirements, and thin film processing for environmentally benign manufacturing alternatives. This list is by no means exhaustive, and a large number of patents are in preparation to protect these technologies.

5.1 FEL and Ubitron Applications

The FEL and ubitron application potential of the advanced cathode materials is significant. The high cost of the accelerator and beam power dictates the use of a harmonic interaction as an economical path to a short wavelength FEL for laser manufacturing. In simplest terms, for a given frequency of light, using a harmonic interaction reduces the voltage requirement on the accelerator by the square root of the harmonic number. For instance, approximately the same frequency of light can be generated by a system operating at the fundamental interaction and 20MV acceleration, as a system operating at the third harmonic and ~11.5MV. A 20MV electrostatic accelerator is large and costly, and presently is not very viable in an industrial environment. By contrast, a 11.5MV electrostatic accelerator is more within the scope of industrial applications.

As was shown in Section 2, the use of a harmonic interaction in the FEL enhances the FEL's sensitivity to beam brightness. In the low gain regime, the spatial growth rate of the FEL scales approximately as I/γ^3 , where I is the beam current and γ is the relativistic factor. Assuming the two cases are using the same prime power in the beam, $\gamma \times I = \text{constant}$; in these two cases, the spatial growth rate for the fundamental

interaction is different by a factor of $1/\gamma^4$, favoring the lower voltage interaction. This nominally leads to a difference in growth rates of a factor of $3^2 = 9$, but the differential in the peak growth rates between the fundamental and third harmonic interactions compensates for this to make the growth rates equal to within a factor of two.

The beam brightness requirement for the lower voltage, higher harmonic interaction is increased due to both the larger current and smaller beam momentum spread requirements. These factors combined lead to an increase in the beam brightness requirement of approximately a factor of 30. There is also a requirement for increased beam current and current density. For IR wavelengths, these increased requirements are at the edge of, or beyond, the capabilities of thermionic cathodes. They are within the capabilities of laser photocathodes, but laser photocathodes necessarily operate under pulsed conditions unsuited to manufacturing operations. The advanced cathode materials appear to be capable of the same brightnesses as present photocathode technology, but without the rapid pulsed operation requirement.

The ubitron interaction is nothing more than a low voltage FEL interaction, with the resultant difference in the relevant approximations. The applicability of the advanced cathode materials to the ubitron is the same as for almost any microwave tube: increased available current density, greater ease of use, and greater robustness in operational environments. The downside that has been discovered in this project, through only partially addressed, is the sensitivity of the emission from the advanced cathode materials to very fast fluctuations in the applied voltage. This would require some additional care in the design and fabrication of the power supplies used to drive the microwave tubes. The relative benefits of the advanced cathode materials must be weighed against the increased power supply complexity on a case by case basis.

5.2 Aegis CFA Startup Application

The application of the advanced cathode materials to the problem of CFA startup was brought to our attention by the CFA projects at Litton, Varian, and Raytheon. The problem to be addressed was the pulse to pulse jitter of the turn-on of the CFA microwave tube, which was limiting the performance of the Aegis radar system. Following a presentation to the Litton CFA team, Litton requested and received permission to modify a line CFA tube for inserting a Si-TaSi₂ cathode strip into the CFA cathode. The intent was to use the eutectic emitter's capability for emission at very low fields and provide "priming" electrons for the CFA tube's secondary emission cathode. Several questions had to be addressed, including the survival of the emitters in the CFA

tube O₂ environment and their operation under the intense fields and circulating electron currents in the high power device.

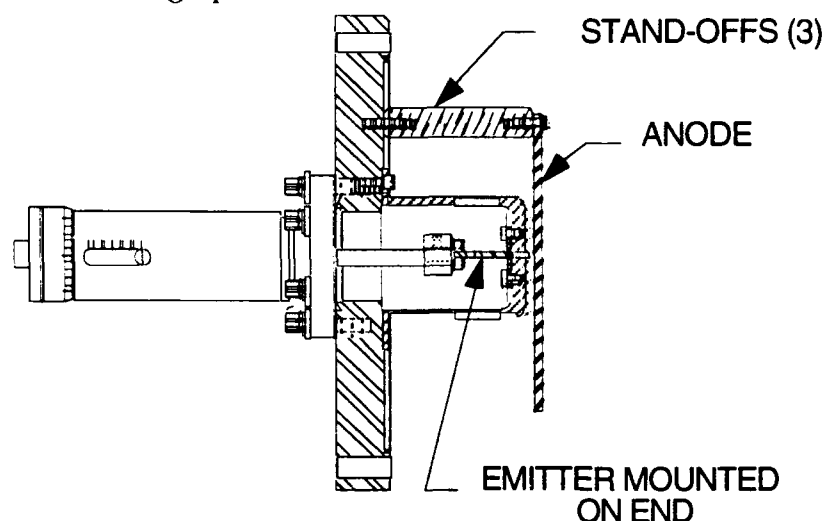


FIGURE 5.1: The apparatus used in the modification of the DC test stand for the investigation of the application of the advanced cathode materials to the emission startup problem of the Aegis CFA tube.

Before the installation of a field emitter into the CFA, experimental tests were performed on the emitters as a verification of suitability. These tests consisted of a eutectic field emitter, shaped for installation into a CFA, being placed in a dc test stand. This stand had provisions for the controlled injection of oxygen into the evacuated test chamber. The eutectic field emitter was recessed into a slot in an anodized aluminum electrode, which in turn was placed at a distance from a parallel plate copper anode equal to that of the A-K gap of the CFA. The depth of the emitter relative to the surface of the electrode was controlled by a linear motion feedthrough (Fig. 5.1). This arrangement allowed the cathode to be tested in a controlled oxygen environment at different recess depths. Through this process, it was found that at a .006" recess and 10-15 kV applied voltage, 0.3 to 3 μ amps of current could be reliably drawn from the tips. The system pressure was maintained at 5×10^{-6} torr, under continuous injection of oxygen. Subsequent analysis of the test emitters showed that no surface damage was caused by operation in this manner.

A series of emitters was prepared and shipped to Litton for installation in the modified tube. Litton installed one emitter in a test tube with guidance from SAIC. This tube was then run through a full series of acceptance tests for shipment to the Navy, and these tests were run side-by-side with a standard production tube (i.e., one without a FEA primer). The FEA primed tube repeatedly outperformed its unmodified twin with respect to pulse to pulse jitter. Measurement results, shown in Figs. 5.2 and

5.3, indicate that the peak jitter was reduced by a factor of 30 and the rms jitter was reduced by a factor of 20. Both of these improvements reflect only a first effort, and optimization of the mounting geometry can probably improve the performance substantially.

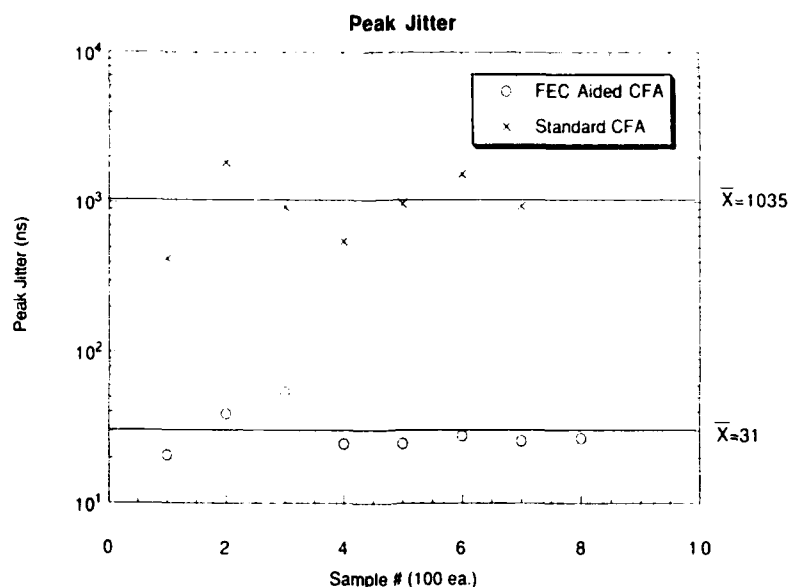


FIGURE 5.2: The peak jitter measured by Litton for the modified and standard CFA tubes. The graph shows the results of a series of measurements over several hundred samples.

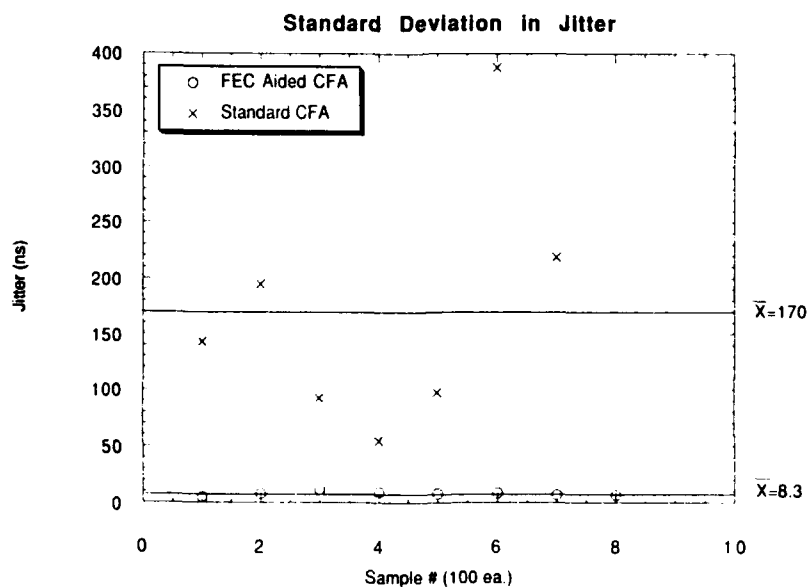


FIGURE 5.3: The rms jitter measured by Litton for the modified and standard CFA tubes. The graph shows the results of a series of measurements over several hundred samples.

The geometry of the CFA cathode with the strip included is shown in Fig. 5.4. The cathode was run under these conditions for >450 hours, at which point the tube was removed from the test and opened. The entire cathode assembly was removed and sent to SAIC for inspection. A tape of this inspection was made and sent to NAVSEA at Crane, IN, Litton, and DARPA. The inspection clearly shows no electrical damage to the emitter. A SEM micrograph of the emitter is shown in Fig. 5.5.

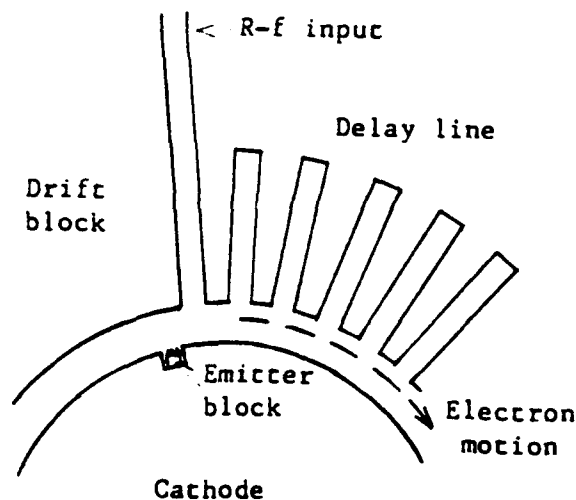


FIGURE 5.4: The schematic layout of the emitter strip in the CFA cathode. The depth of the slot and the thickness of the emitter strip determine the setback of the emitters from the nominal surface of the cathode.

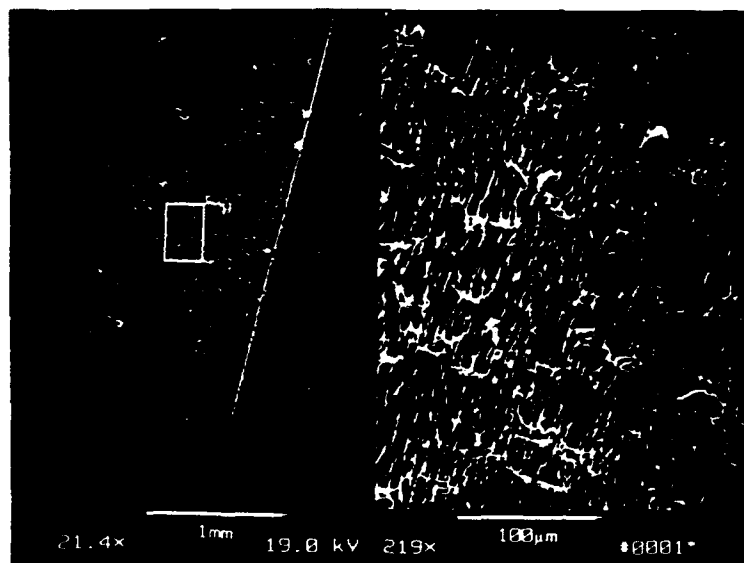


FIGURE 5.5: A SEM image of the Si-TaSi₂ emitter in the CFA. Note the small particulates. These are sand particles sifted out of the CFA tube by the emitter. The sand is introduced into the emitter during a preparation phase, and is evidently not completely removed.

5.3 Long Pulse RKA Application

The eutectic emitters were selected as candidate cathode material for an experimental development project at General Dynamics' Missile Systems Division that looks at long pulse relativistic klystron amplifiers. The sponsor for this project is the U.S. Army and the prime contract number is DAAL-92-C-0039. The beam requirements are $V \sim 450\text{--}600\text{ kV}$, $I \sim 1\text{--}3\text{ kA}$, in a hollow beam with $R_0 \sim 0.9\text{ cm}$ and $\Delta r \sim 0.1\text{ mm}$. The pulse length was to be $1\mu\text{s}$ with a repetition rate of less than 1 Hz .

General Dynamics had originally designed their experiment around the use of an experimental thermionic gun to be fabricated by Varian. That design intended to use a 200:1 compression ratio using convergent magnetic fields. The cathode current density for the thermionic emitter was constrained to 10 A/cm^2 due to the large size of the cathode. This allowed a maximum of 2 kA/cm^2 in the beam, as opposed to the $2\text{--}6\text{ kA/cm}^2$ desired by GD for the experimental plan.

The experiment team at GD was informed of the advanced cathode material technology following a briefing to their Army sponsors, and rapidly sought to change their experimental plan to include the new cathodes. Phase 1 of our project plan has been completed, during which a design with only 70:1 compression ratio was found to be capable of providing the full range of current densities of interest to GD. This much lower compression ratio results in a simpler magnetic design and lower beam temperature in the interaction region. The electrical design and vacuum requirements are also considerably relaxed from the previous thermionic cathode design. A report of this design is in preparation and has been forwarded to the prime (since purchased by Hughes Missile Systems).

Unfortunately, the driving interest in the final product has been relaxed and funding has been severely constrained. Despite the obvious promise of the design, we do not anticipate the second and third phases of our effort to be funded. GD has downscoped their effort to focus on short pulse experiments that do not require the long pulse capability. We continue to mutually seek further funding for the construction and testing of the design.

5.4 Laser Driven FEA Applications - Accelerators

Several experiments early in the development of the advanced cathode materials led us to question the nature of the field emission phenomenon. The investigations into the analysis of field emission from 3-D structures in Section 2 is one example. Additional experiments were carried out in collaboration with LANL to investigate the operation of

a eutectic emitter in a $\sim 3\text{GHz}$ RF cavity. Though not conclusive, these measurements strongly indicated identical operation at 3GHz as was found at DC. In addition, several sources stressed the need for an alternative ultra-fast pulsed electron source other than photocathodes. This led us to consider the use of a fast pulse IR laser as the emission “catalyst” with the advanced cathode materials.

The experimental setup is shown in Fig. 5.6. A 20mJ , 8 ns , linearly polarized Nd:YAG laser operating in the fundamental at $1.064\mu\text{m}$ wavelength is passed through a beam expander and then incident on a eutectic cathode. The incident angle of the laser light is within $5\text{-}10^\circ$ of grazing. The polarization of the electric field in the laser light is into and out of the cathode face. An anode is located opposite the cathode, with a small DC bias field applied to close the circuit should emission occur. The anode is tied to a 0.2 ns response time current viewing resistor (CVR) with an impedance of $\sim 0.2\Omega$. The CVR nominally should drive a high impedance load; however, this results in signal ringing. Instead, the CVR signal cable is terminated in 50Ω , which reduces the signal amplitude by 50% . After striking the cathode, the remaining laser light is incident on a fast pyroelectric detector via a beamsplitter. This signal is used to trigger data acquisition and measures the time duration of the light pulse.

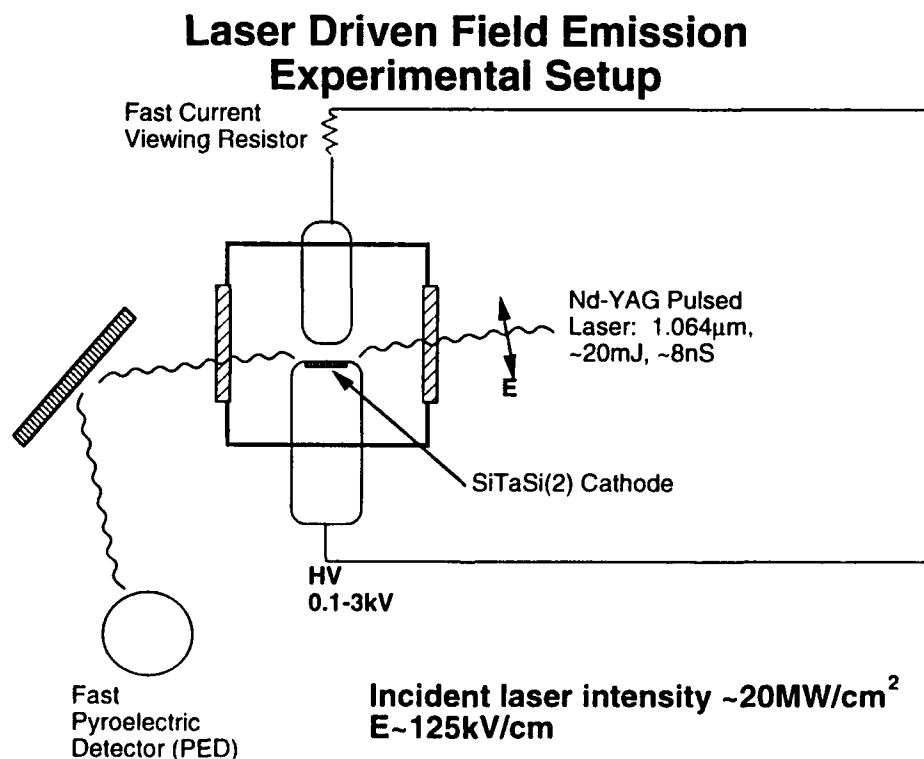


FIGURE 5.6: The experimental setup used for the fast pulse laser experiments.

Under these illumination conditions, three types of emission are possible: thermally excited field emission due to the heating up of the field emitter tips by the laser light, photon assisted field emission where the incident photons create an excited electron distribution with a modified work function of $\phi' = \phi - h\nu$, and laser driven field emission where the fast oscillatory electric field of the laser is sufficient to drive field emission from the tips. The fortune of this experiment is that these three types of emission are readily separable with at most two measurements. Thermal enhancement of the emission will have a long time profile: the thermal decay time of these emitter structures can be readily calculated, as in Section 2, and is $\sim 100\text{ns}$. Both of the other mechanisms will have emission profiles equal to or shorter than the laser pulse. If a short pulse is seen, the remaining two types of emission can be distinguished by rotating the polarization of the laser. The laser driven field emission case should be sensitive to the direction of polarization, the photon pumped distribution case should not.

A Si-TaSi₂ cathode with $\sim 10\mu\text{m}$ tall tips was plasma etched, coated with a thin layer of gold, and mounted in the laser stand. Vacuum is provided by a Vacion pump, and the chamber was allowed to pump down to the low 10^{-7} torr range. The cathode-anode gap was then reduced to $\sim 1\text{mm}$ by means of a linear motion feedthrough, and the cathode was conditioned DC for ~ 50 hours. The laser was then pulsed while applying varying DC bias levels to the system. The laser power does fluctuate somewhat from pulse to pulse, but otherwise the only variation in the incident laser intensity was the presence or absence of the beam expander in the optical path. With it in, the peak electric field is estimated to be $\sim 125\text{kV/cm}$. With it removed, this value increases to greater than 400kV/cm . These latter fields are too strong and result in severe damage to the cathode. An example of the data with the beam expander in is shown in Fig. 5.7, clearly showing the fast response of the emitter.

The data in Fig. 5.7 clearly demonstrate that the emission is not due to thermal excitation of the tip: there is no evidence of a $\sim 100\text{ns}$ decay time. Therefore, the only remaining possibilities are photon-assisted field emission and laser field driven emission. The polarization of the laser was rotated through 90° and the measurement series was repeated. The laser electric field is now polarized parallel to the cathode face. No emission was observed. The signal-to-noise available in the initial measurements is at least a factor of 10. The sensitivity of the laser driven emission to laser polarity clearly indicates that the source of the emission is the electric field of the laser.

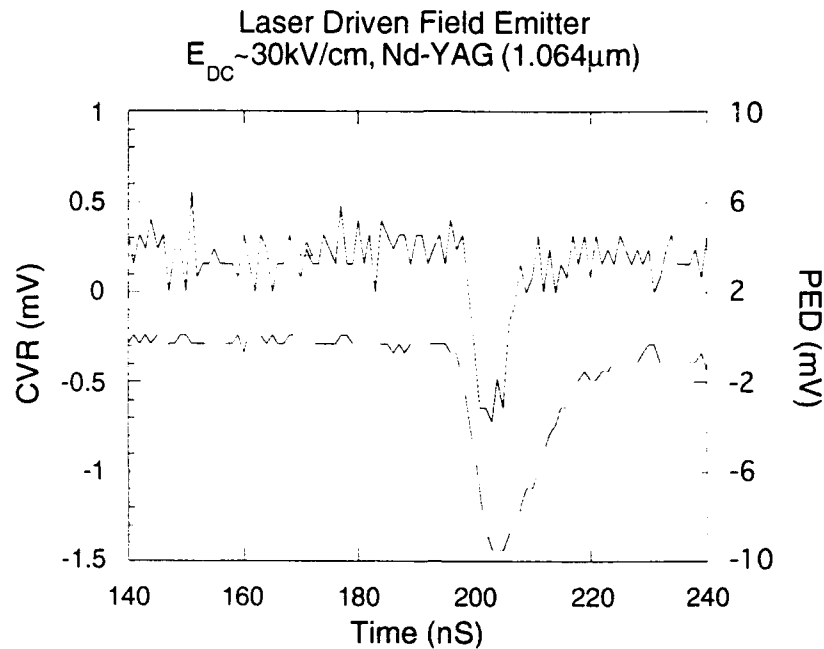


FIGURE 5.7: The CVR (solid line, upper) and pyroelectric laser detector (dashed line, lower) signals for an applied DC bias of 30kV/cm. The slow tail on the pyroelectric detector is a result of near-saturation of the detector. The actual laser pulse is nearly symmetric, and the rise of the pyroelectric detector signal is indicative of its shape.

The implications of this proof-of-concept experiment are profound:

- First, the 5ns pulse width in Fig. 5.7 is an immediate demonstration of 100MHz macromodulation of the pulse from an ungated field emission cathode. This pulse width is ~50% shorter than the pulse width of the driving laser. Shorter pulse lasers are commonly available: ~ps duration Nd:YAG lasers are available off the shelf. This immediately provides for macromodulation of ~500GHz.
- Second, the modulation is provided by NIR photons with an energy of ~1eV. Photocathodes typically operate with VUV photons with tripled or quadrupled Nd:YAG light, dramatically raising the cost of the injection system. NIR photons are also available from semiconductor lasers at the same and greater intensities than were used in this experiment. These lasers-on-a-chip have been directly modulated to ~20GHz. Such a modulated laser driven FEA RF amplifier would have the very desirable aspect of isolation between input and output.
- Third, the emission from the tips is being modulated by the fast oscillatory laser field. For ~1 μm light, the period of this oscillation is ~3fs. The emission occurs only when the amplitude is near the peak of the sinusoid and only for the portion that is oriented in the correct direction. This corresponds to emission bursts of ~0.6fs. With

the proper construction, these bursts could be made uniform across the cathode surface to create coherent electron emission - with a bunch frequency of 1000THz.

- Finally, the implication of such ultrashort emission durations is to completely invalidate the assumptions of the Fowler-Nordheim emission model - yet the emission characterization parameters obtained from DC characterizations appear to give us reasonable estimates of the performance at 1000THz. This is all the more exciting when one notes that the emission duration is approximately the same order as the classical orbit of an electron around an atom, as well as close to the inverse of the plasma frequency for the near-Fermi level density of electrons in the tip.

An FEA RF amplifier based on this process has been suggested to Dr. Hui at DARPA/DSO as part of the Vacuum Microelectronics Program. This potential is described in some detail in the next subsection. A basic investigation of the emission mechanism and the applicability of this technique to various accelerator needs is being proposed to the Department of Energy's Advanced Accelerator Concepts office, and we anticipate project funding to commence by late summer 1993.

5.5 Laser Driven FEA Applications - Compact Wideband Microwave Amplification

The advanced cathode materials' capacity to be modulated with the electric field of intense laser light can be applied to the RF generation area as a compact means for wideband microwave amplification. A potential project aimed at rapidly developing this capability of the advanced cathode materials has been discussed with the manager of DARPA's Vacuum Micro-electronics Program, Dr. B. Hui. Due to funding limitations in that program, we have not been encouraged to submit a formal proposal at this time. The basic outline of the potential in this regard is outlined here for future reference.

The setup is shown in Fig. 5.8. A semiconductor laser operating at $\sim 1.3\mu\text{m}$ is driven by a modulated RF signal at the input stage. The modulated laser output then drives a biased FEA to provide a modulated beam current. The modulated beam current can then be used to drive either a stripline output or a microwave extraction cavity. The laser chip has a forward drop, which can be provided by an inductively isolated DC bias. This bias should also be used to run the laser some portion of the way up its I - V curve to improve overall RF efficiency. The RF input is capacitively coupled into the laser bias: modulation in commercial off-the-shelf devices is available to $\sim 2\text{GHz}$, while research devices have been modulated to $\sim 20\text{GHz}$. The laser output is multimode from a $1\mu\text{m}$ tall by $100\mu\text{m}$ wide strip that is aligned to the position of the FEA. The FEA array

itself is a 50 wide by 3 deep array on 2 μ m centers, providing 150 emitters in the useful region of the laser light.

This type of FEA RF amplifier will necessarily be lower in efficiency than a purely electrically gated FEA RF amplifier. For one particular design configuration that has been investigated in some detail, the efficiency of the laser driven system is typically 85-90% of the efficiency of the electrically gated system. The return for this investment of lost efficiency is the complete electrical isolation of the FEA "output" from the RF input. We believe this isolation is an important benefit from the standpoint of the overall microwave system design.

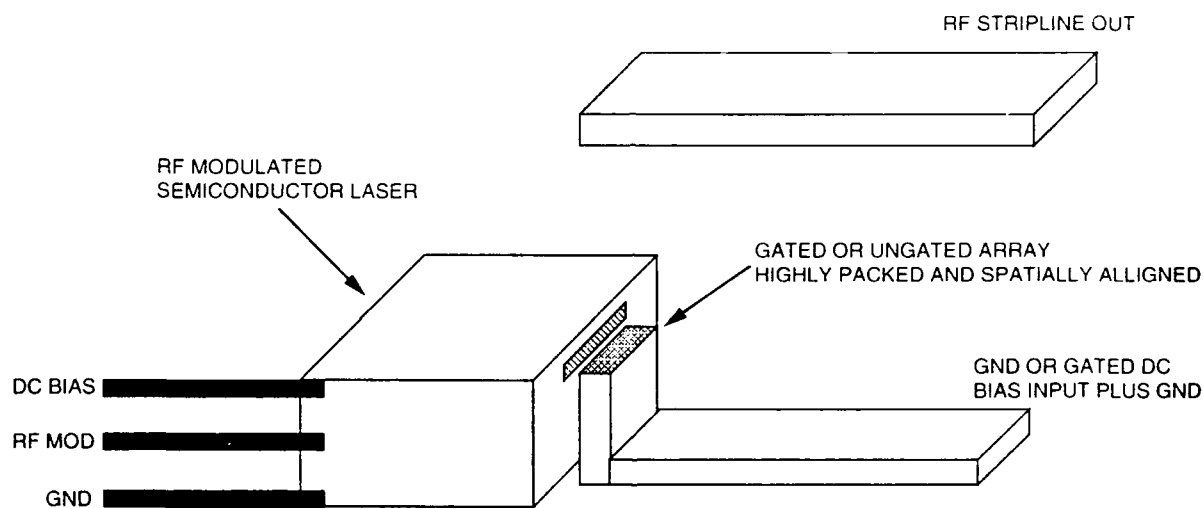


FIGURE 5.8: The schematic design for a FEA RF amplifier with inherent opto-isolation of the input and output stages. This design is based on the observed laser driven operation of the field emitters and uses demonstrated or off-the-shelf technology in all its components.

5.6 High Pressure FEA Operation - Fluorescent Backlights

The robustness of the advanced cathode materials attracted the attention of several applications arenas, including that of display technology. Engineers from SAI-Technology were made aware of the advanced cathode technology through internal communication, and expressed an interest in potential cathode use in fluorescent backlighting for military displays. Funding from IR&D was provided for the investigation of the eutectic emitter operation in standard discharge gases of Argon at ~7 torr.

The emitters have proved to be a significant success in this area and have attracted the attention of a wide variety of commercial and military applications industries. As a result of our investigations, numerous patents have been submitted or are in preparation. The performance of the advanced cathode materials in this application can be described as completely unexpected. A significant SAIC IR&D effort has been initiated to protect and commercialize this technology during the near term. Military applications of interest include avionics displays and visual low observable techniques. Other applications include conventional lighting, UV treatment of waste water, and a wide variety of communications and electronics devices. A demonstration of this technology was provided under proprietary disclosure limitations to the government at the 1992 DARPA Vacuum Microelectronics Program Review held at NRL.

5.7 High Pressure FEA Operation - Thin Film Processing

The capacity for the advanced cathode materials to operate in relatively high pressures of background gases has led to a follow-on DARPA/DSO effort for hazardous waste reduction using advanced coating technologies. In the context of this effort, the advanced cathode materials are being used to provide an advanced oxygen ion source, with longer life and 30-50 times higher ion current densities than are available with existing state-of-the-art technologies. This ion source is used as part of an advanced coating process for the economical deposition of wear resistant coatings. These coatings, and the process used to deposit them, are completely environmentally benign and offer a "green" alternative to a wide variety of military coatings needs. The key element in this development is the ability of the advanced cathode materials to operate for long times at relatively high current density in an oxygen environment - a capability not found in any other emission technology.

6 Summary of Milestone Achievements

There were twelve milestones specified in the original proposal. These are listed below, followed by comments relating to the completion or non-completion of the milestone during the execution of the project. This is followed by a listing of other major milestones not originally specified but demonstrated as "targets of opportunity" with respect to stated DARPA, DoD, or service interests.

The major milestones for this project were modified slightly from those in the proposal with the consent of the sponsor. The modifications reflect only changes due to equipment limitations.

Month 2. Completion of DC test stand assembly. Capabilities will include 15kW average power, with maximum current of 0.6A, and voltage ripple less than 0.1%. **Completed on schedule.**

Month 4. Demonstration of Fowler-Nordheim field emission behavior for the eutectic and tubule microstructure cathodes. Measurement and comparison of the effective field enhancement factor and effective emission area for the two structures. **Completed. Eutectic emitters on schedule. Tubule emitters in Month 9.**

Month 6. Achievement of stable cathode current densities $J > 2\text{A}/\text{cm}^2$. This to be achieved with the DC test stand, with a total cathode current in the range 0.5A. **Completed on schedule. Used microanode and 50mA current due to ripple of large DC supply.**

Month 6. Completion of assembly of lifetime test stand. Capabilities will include 15kW average power, maximum current of 0.6A, vacuum pressure from 10^{-8} - 10^{-4} torr, and with capacity for backfilling with gases such as Nitrogen, Argon, Sulfur-Hexafluoride, and Carbon Dioxide. **Completed on schedule. Concentrated on Oxygen, Nitrogen, Argon.**

Month 12. Completion of assembly of the AC test stand. Capabilities to include 1MW peak power, 25kV, 40A, pulse length variable from 0.5 - 5 μsec , maximum pulse repetition rate greater than 1kHz (limited by 0.2% duty cycle). **Completed on schedule. Capabilities modified to 0.5MW peak power, 45kV, 10A, pulse lengths from 0.1-10 μs , maximum PRF of 1kHz or 20kHz burst mode, 0.1% duty.**

Month 12. Achievement of cathode current densities $J \sim 20 - 50 \text{ A/cm}^2$. This to be achieved with the AC or DC test stand, with a total cathode current in the range 0.5 - 5A. **Completed in month 18 w/ use of AC pulser and eutectic emitters.**

Month 15. Completion of assembly of the slit-wire emittance measurement system. Emittance measurement system to be compatible with existing DC and AC test stands, and capable of resolving velocity spread angles of $\delta\theta < 0.1 \text{ mrad}$. **Completed in month 20.**

Month 18. Achievement of cathode current densities $J > 100 \text{ A/cm}^2$. This to be achieved with the AC test stand, with a total current less than 40A, or with the DC test stand, with a total current in the range 0.2 - 0.6A. **Effectively completed in month 21 w/ achievement of 75 A/cm^2 pulsed currents described in Section 4.**

Month 21. Achievement of cathode beam brightness $B_n > 10^6 \text{ A/cm}^2\text{-rad}^2$. This to be achieved with the AC test stand, with a total current less than 40A, or with the DC test stand, with a total current in the range 0.2 - 0.6A. **Effectively completed in month 21 w/ achievement of 75 A/cm^2 pulsed currents described in Section 4, earlier coarse emittance measurements, and scaling indicated by computer simulation. Importance of direct demonstration superceded by other targets of opportunity.**

Month 22. Demonstration of lifetime $> 100 \text{ hours}$ with $J > 20 \text{ A/cm}^2$ and vacuum pressure $\sim 10^{-6} \text{ Torr}$. This to be achieved with the DC test stand, with a total cathode current in the range 0.2 - 0.6A. **Completed ahead of schedule at 1 A/cm^2 , on schedule w/ respect to CFA tests at Litton.**

Month 24. Achievement of cathode current densities $J > 200 \text{ A/cm}^2$. This to be achieved with the AC test stand, with a total current less than 40A, or with the DC test stand, with a total current in the range 0.2 - 0.6A. **Not completed. Potentially implied by laser results.**

Month 24. Achievement of cathode beam brightness $B_n > 10^7 \text{ A/cm}^2\text{-rad}^2$. This to be achieved with the AC test stand, with a total current less than 40A, or with the DC test stand, with a total current in the range 0.2 - 0.6A. **Not completed. Potentially implied by laser results. De-emphasized as a result of applications evaluations and other transition targets of opportunity.**

In all, nine of the twelve original milestones were achieved and three remained beyond the demonstrated capabilities. These latter three were, in a sense, overtaken by events: the technology transition opportunities that had presented themselves did not feature these milestones as significant achievements. Rather, other performance goals were set forth as targets of opportunity for transition of this technology into applications arenas. Some of these unanticipated milestones included:

Demonstration of prolonged operational lifetime in oxygen. This achievement allowed the operation of the advanced cathode materials in both the CFA and the proposed advanced oxygen ion source in the upcoming DARPA "green" manufacturing project.

Demonstration of prolonged and high current operation at ~torr background pressures. This achievement, performed on IR&D to conserve project funds, allowed the transition of this technology into the lighting, display, and several other applications areas.

Demonstration of laser field driven emission. This achievement was essential for the consideration of the cathode materials in any of the ongoing FEL projects. They viewed the demonstration of short pulse operation as more important than brightness measurements. As a further result, however we may have opened a Pandora's box of optically driven FEA applications.

In retrospect, the achievements attained in this project were those necessary to develop, demonstrate, and transition the technology to applications. That some of those latter milestones were not achieved is more an indication of our inability to project those applications of greater importance than an indication of any shortcoming on the part of the cathode materials. The successful transition to applications can now be looked to for providing the "technology pull" in these areas, rather than any substantial continuing need for a basic "technology push."

7 Conclusions

This project successfully developed and initiated the transition of an advanced, high current density cathode technology. The advanced cathode materials developed under this project have now been tested in a variety of configurations and devices. Most of the performance milestones set forth in the original proposal have been met. In addition, several performance milestones not contemplated in the original proposal have been demonstrated. The sum of these achievements is reflected in the incorporation of the advanced cathode materials into follow-on efforts funded by DARPA, the US Army, the US Air Force, DOD industry, and commercial industry, and several additional pending proposed efforts.

A wide range of cathode fabrication techniques were attempted and evaluated during the course of this project including self-assembled biomolecular tubule based structures, semiconductor-metal eutectic composite structures, PCTE filter paper template structures, and microlithographically defined cylinders. All of these techniques but the eutectic approach used an electroless deposition process to provide the conducting metal structure that served as the emitter. Difficulties with the deposition process limited the electrical and thermal conductivity that could be achieved in these structures. The eutectic option features a high conductivity (thermal and electrical) emitter material which is also refractory, with a melting point exceeding 2000°C. The resistivity of the electroless coatings used in the tubule process may make those materials more advantageous for applications where energy dissipation is important, such as packaging and noise suppression.

This development effort succeeded in large part due to the fact that it was driven by the needs of applications and transition demonstrations. Fundamental science issues were addressed in the beginning of the project, and issues that could not be addressed in this timeframe were postponed or resulted in downselections away from these uncertainties. These unresolved issues continue to be addressed at a background level of effort and in parallel with the primary production, application, and transition efforts. One unanticipated difficulty arose from the short timeframe available for the execution of the transitions. Secondary sponsors required greater depth of demonstrated capability and longer lead times to start follow-on efforts than had been allowed for. In the future, a one year follow-on option to aid in these transitions is recommended.

Appendix A

Publications

Measurements of Vacuum Field Emission From Bio-Molecular and Semiconductor-Metal Eutectic Composite Microstructures

Douglas A. Kirkpatrick, Paul E. Schoen, W. B. Stockton, R. Price, S. Baral, Brian E. Kahn, Joel M. Schnur, Mark Levinson, and Brian M. Ditchek

Abstract— We present designs, calculations, and initial data from a program investigating the use of bio-molecular and eutectic composite microstructures as vacuum field emission cathodes. Calculations, supported by the initial data, indicate that these electron sources should be capable of macroscopic beam current densities $J \geq 100 \text{ A/cm}^2$ without the formation of a surface plasma. The absence of a plasma allows these cathodes to operate as a long-pulse to dc electron sources.

These composite materials are processed to produce surface structures which consist of rod-like tips protruding from a uniform base, where the protruding rods are $\sim 0.5 \mu\text{m}$ in diameter by $\sim 10 \mu\text{m}$ tall, with an average surface density of $> 10^6$ tips/cm². Such structures are essentially microanalogs of the velvet cathodes which have found widespread use in the exploding field-emission cathode domain. However, unlike the velvet cathodes, the aim of the present research is the controlling of the surface emission and preventing the formation of surface plasma. The present designs seek to avoid the formation of surface plasma by forcing the current emitted from the tips to transit a thin layer of silicon. The natural high-field current-limiting nature of the silicon serves to prevent the ablation of the tip structure and the subsequent formation of cathode plasma.

Initial data obtained with these microstructures has demonstrated Fowler–Nordheim characteristic emission. With a final surface coating of amorphous, p-doped silicon, the bio-molecular composite cathodes have demonstrated stable dc (10 s, $\pm 10\%$ p-p) current densities of $\sim 100 \text{ mA/cm}^2$, and the eutectic composites cathodes have demonstrated similarly stable dc current densities of $\sim 1 \text{ A/cm}^2$. It is anticipated that using crystalline or polycrystalline n-type silicon coatings can increase these values to greater than 100 A/cm^2 .

I. INTRODUCTION

THE need for high current density, high brightness, survivable cathodes is driven by several applications of interest, including microwave sources [1], [2] for use in radars, communications, and ECRH heating of fusion plasmas, high-power fast switches [3], high gradient accelerators [4], and electron beam processing of materials [5]. Those properties which constitute the ideal electron source vary from application to

application. For some, the capability to operate for long pulses at high current density is the most significant improvement. For others, it is not so much the highest current densities that would be available, as it is a combination of a modest increase in the available current density combined with an increase in the operational lifetime.

The existing technology for electron beam sources can be broken down into four groups: (i) thermionic cathodes, (ii) laser-driven photo-cathodes, (iii) classical field emission cathodes, and (iv) exploding or plasma field emission cathodes. The existing state-of-the-art can be summarized as follows:

- 1) Thermionic cathodes use a thermally activated, low work function material to act as an electron beam source. Older technologies simply used a barium-oxide coating which was painted on the desired emission surface. New technologies use a porous dispenser matrix to gradually deliver a scandate compound to the cathode surface. Commercially available technology delivers 20 A/cm^2 for lifetimes longer than 1000 h, but requires vacuum pressures less than 10^{-7} torr and has a long list of materials that will chemically poison the surface even at that level. Notably excluded materials include hydrocarbons, fluorocarbons, and stainless steel. Research cathodes [6] have produced cathode current densities as high as 140 A/cm^2 , but these require even higher vacuum standards and have problems with beam quality, reproducibility, and lifetime. All of these cathodes require a heater element to maintain the cathode surface at an elevated temperature anywhere between 900 and 2200°C .
- 2) Laser-driven photo-cathodes [7], [8] use an intense pulse of light to photo-eject electrons from a low work function (typically cesiated) surface. They can produce very high instantaneous current densities ($> 60 \text{ kA/cm}^2$), albeit for very short times. They require very high vacuum, with vacuum pressures in the range of 10^{-9} torr or less. Other approaches, using bare metals such as copper, operate in a slightly poorer vacuum (10^{-8} torr), but have a considerably poorer efficiency of conversion of the laser light.
- 3) Vacuum field emission cathodes are typically tungsten fibers and are predominantly used in scanning electron microscopes. They produce an electron beam by classical Fowler–Nordheim quantum tunneling of electrons

Manuscript received February 1, 1991; revised April 16, 1991. This work was supported by the Defense Advanced Research Projects Agency, and by the Office of Naval Technology.

D. A. Kirkpatrick is with Science Applications International Corporation, McLean, VA 22102.

P. E. Schoen, W. B. Stockton, R. Price, S. Baral, B. E. Kahn, and J. M. Schnur are with the Naval Research Laboratory, Washington DC 20375.

M. Levinson, and B. M. Ditchek are with GTE Laboratories Incorporated, Waltham, MA 02254.

IEEE Log Number 9102536.

from near the Fermi level into the vacuum. The large electric field that is required is obtained from the very large field enhancements near a sharp point. Beam brightness is very high, since the beam is essentially produced by a point-emitter. The current density is very high, but this is a single-tip emitter and therefore the total current is very low. The ability to expand this type of device to a multitip emission surface, while also maintaining internal thermo-electric stability, is the intention of our development project. Other researchers [9]–[13] are pursuing the same objective using microlithographic approaches which produce "gated" arrays of small pyramids or cones.

- 4) Exploding or plasma field emission cathodes [14] are the cornerstone of the extremely high pulsed power regime. Cathode current densities in excess of 1 MA/cm² have been demonstrated. They tolerate moderate-to-poor vacuum quite well. The quality of the electron beam is not high, but high-quality beams may be obtained by passing the electrons through an emittance filter. This may reduce the beam current to 1% of its initial value, but one still has a high current beam that is now also a high quality beam. The truly significant drawback to these cathodes is their inherent inability to operate for long pulses (> 1 μ s) or at a high repetition rate (> 10 Hz).

The basic limitations for these four types of electron beam sources dictates which is used for a specific application. Most existing technology utilizes thermionic emitters. Some high-power research experiments use plasma field emission cathodes because of their high instantaneous power capability and their ease of operation. Classical field emission cathodes are almost exclusively used in SEM's, and laser photo-cathodes are still mostly in a research phase.

The class of thermionic emitters is the dominant segment of the electron-beam-source pie, because of its dc and long pulse capability. All radars, all RF sources that drive RF linacs, all conventional tubes, and almost all of the commercial electron source demand is currently utilizing thermionic cathodes. Almost any application which requires substantial average power capability must use a thermionic emitter.

Applications that require high quality, high current electron beams are also limited by the thermionic emitters. The normalized electron beam brightness is defined as:

$$B_n = \frac{I}{\pi^2 \epsilon_n^2} = \frac{J}{\pi(\gamma\beta\delta\theta)^2} \quad (1)$$

where J is the cathode current density in A/cm², $\gamma = 1 + (eV/m_0c^2)$ is the relativistic factor, $\beta = v/c$ is the electron velocity normalized to the speed of light, and $\delta\theta = v_{\perp}/v_{\parallel}$ is the FWHM in the transverse velocity spread angle of the electron beam distribution. The maximum beam brightness available from a thermionic emitter is theoretically on the order of 10⁸ A/cm²-rad². But achieving a high beam current density in addition to this beam brightness demands magnetic compression of the emitted beam. Creating very accurate magnetic fields over any substantial area is extremely difficult,

and this limits the practically available brightness for a ~ 1 A beam using a thermionic emitter to $\sim 10^6$ A/cm²-rad².

A device that is most significantly affected by electron beam brightness is the free-electron laser (FEL). For the FEL, it is the brightness of the electron beam which determines the characteristics of the device. The minimum operational wavelength is determined by the electron beam emittance, $\epsilon_n = (1/\pi)\sqrt{I/B_n}$,

$$\lambda_{rad} > \pi \epsilon_n. \quad (2)$$

Given a desired operational wavelength, the electron beam brightness determines how much beam current can participate in the interaction. This in turn determines whether the interaction will be high gain, low gain, or no gain. Existing technology for thermionic emitters makes 10 μ m about the transition wavelength for the high gain to low gain regimes, and optical wavelengths in the blue the transition from the low gain to no-gain regimes. Increasing the available beam brightness shifts these transition points to shorter wavelengths.

The other major category of electron sources—explosive or plasma field emission cathodes—is limited in pulse length to approximately 1 μ s due to the inherent presence of an expanding cathode plasma. A significant advantage to these cathodes is their relative insensitivity to the vacuum environment. They operate quite well in vacuum of 10⁻⁴ torr, and do not poison. This makes them ideal electron beam sources for experimental apparatus that do not require long pulse or repetitively pulsed capability. They are also inexpensive and do not require any special handling.

The advanced cathode materials presented here could potentially combine the advantages of both thermionic and plasma field emission cathodes. Like the thermionic cathodes, they have the capability to operate in dc or be repetitively pulsed. Like the plasma field emission cathodes, they are inexpensive, require minimal care in handling, operate well in moderate vacuum, and do not poison. They do not require a heater nor its associated power supply. Cathode current densities $J > 200$ A/cm² and brightness $B_n > 10^7$ A/cm²-rad² appear possible.

II. THEORY AND BACKGROUND

All high current density cathodes share some fundamental properties. The Child–Langmuir space-charge-limited current density

$$J = 2.34 \times 10^{-6} \frac{V^{3/2}}{d^2} \quad (3)$$

governs the maximum current density which can be drawn from an infinite parallel plate diode with cathode–anode separation of d and applied voltage V . This current density is obtained by calculating the point at which the cathode surface is completely shielded from the applied electric field. This shielding effect is due to the electron cloud of the generated electron beam. The presence of background plasma due to ionization by the electron beam modifies this result upwards. For high vacuum systems (pressure < 10⁻⁷ torr) this effect is negligible. For more moderate vacuums, the precise effect depends on the degree of ionization and can be greater than

a factor of two. Another aspect of the self-electric fields associated with high current density cathodes is the design of electron guns to use them. An electron gun operating near the Child–Langmuir limit necessarily experiences a substantial modification of its electric field structure during the turn-on phase of the electron beam. Unless the electron gun is designed to be dominated by an externally applied magnetic field, this places a high degree of difficulty on the electron gun design. Plasma field emission cathodes, almost by definition, operate at the Child–Langmuir limited current.

The advanced cathode materials are a moderately uniform, irregular array of classical field emitters. Each emitter tip is much like a tungsten filament used in a SEM. As classical field emitters, the Fowler–Nordheim emission current is given by:

$$J = \frac{A(\beta E)^2}{\phi t^2(y)} \exp\left(-B \frac{\phi^{3/2} r(y)}{\beta E}\right) \text{ A/cm}^2 \quad (4)$$

where A and B are constants, ϕ is the work function of the emission material, E is the applied electric field, β is the field enhancement factor due to local geometry, and $t(y)$ and $r(y)$ are very weak functions of the work function and electric field (values for these constants and coefficients are given in the next section). As can be seen from the $\beta^2 E^2 \exp(-\alpha/\beta E)$ dependence of the current density J , this type of emission is very sensitive to the electric field at the emission surface. For a 5-eV work function material and an applied electric field of 30 kV/cm, an increase in the field enhancement factor β from 2000 to 5000 results in a two order of magnitude increase in the emission density. Clearly, operation of this type of cathode near the Child–Langmuir limit would be unstable. If this can be engineered, for some devices it may be desirable. If not, then another means of limiting the cathode current density must be used. In the advanced cathode materials discussed here, external current-limiting circuits or nonlinear current saturation effects in certain types of semiconductors are used to limit the emission density.

The advanced cathode materials are open, ungated field emission arrays which utilize a high density of emission sites across macroscopic areas to achieve macroscopic current densities. The emission sites are typically rods or spikes protruding from a background matrix (see Fig. 1). The electric field enhancement associated with the rod or spike length, its aspect ratio, and the radius of curvature of its tip must be large in order to achieve the $10^7 - 10^8$ V/cm field magnitudes necessary to drive significant quantum field emission. Microtip currents of $\sim 10 - 100$ μA are achievable with fields in this range, depending on the work function of the surface materials and the effective emitting area. In order to arrive at macroscopic current densities of ~ 100 A/cm², it is necessary to pack $10^6 - 10^7$ tips/cm². This implies a tip-to-tip spacing of less than 10 μm , and through the field enhancement requirement, consequently requires a tip or edge radius of curvature less than ~ 200 Å.

There are several ways to achieve this combination of parameters. Microlithographic techniques of fabricating many-tip arrays have been eminently successful. Within this general class of techniques, several processes and refinements exist. Attempts to extend this technique to million-tip arrays have

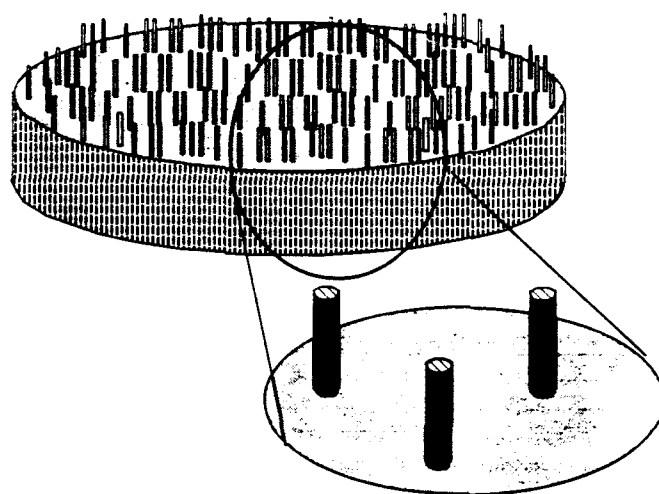


Fig. 1. Recent advances in materials engineering allow the fabrication of the advanced cathode materials. These new electron sources require surfaces with a large density of protrusions which generate very high local electric fields. Composite materials fabricated with the self-assembling bio-molecular microstructures form arrays like that shown here, with a random, moderately uniform distribution of right-circular hollow cylinders.

not been successful. A recurring problem is the nonuniformity of the radius of curvature of the tip emitters. In addition, these microlithographically prepared emitters have required very clean high vacuum, and can fail catastrophically through a shorting of the local gate electrode.

Unlike the microlithographically prepared, gated field emitter arrays, the cathode materials reported here use microstructure templates and current limiting surface coatings to generate stable Fowler–Nordheim-type classical field emission. SEM images of two such microstructures are shown in Figs. 2 and 3. The first material, shown in Fig. 2, is derived from a diacetylenic lipid (DC_{8,9}PC) that forms tubule-like structures [15]–[19]. This approach has already produced a uniform, irregular array of 0.4 μm -diam, 10 μm -tall right circular cylinders protruding from a gold-sputtered background surface and separated by an average of about 10 μm . An alternate means to achieve a similar cathode-surface micromorphology is shown in Fig. 3. This material is a silicon–tantalum–disilicide eutectic composite [20]–[22]. The protruding sharp, pointed rods are the minority tantalum–disilicide. This material is a good electrical conductor. The matrix is a poly-crystalline rod of silicon. The silicon matrix has been etched preferentially to produce the structure shown.

Past and ongoing investigations into gated field emitter structures at SRI by Spindt *et al.* also suggest the potential and utility of our approach. They have successfully demonstrated individual emitter tip currents as high as 500 μA without the formation of plasma or catastrophic failure of the structure [23]. The geometric properties of their tip structure are very similar to those we measure for our own. The major difference between our approaches are the fabrication technique and the presence or absence of a nearby ($\Delta x = 1$ μm) gate electrode.

An estimate of the advanced cathode material performance requires evaluation of the Fowler–Nordheim emission density and the effective emission area. For the sake of brevity, this

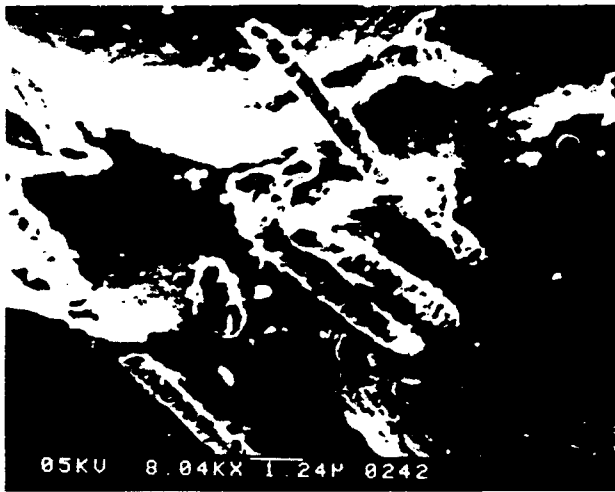


Fig. 2. A scanning electron microscope image of the biologically derived cathode surface shows the high density of emitters necessary to generate substantial macroscopic beam currents. Note the size scale.

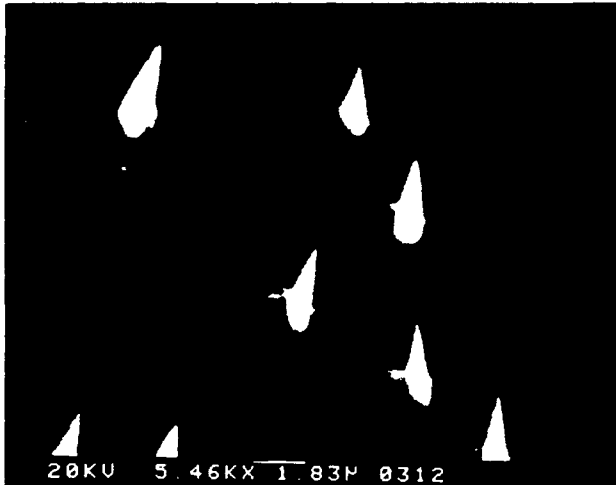


Fig. 3. A scanning electron microscope image of the semiconductor-metal eutectic composite cathode surface shows the high density of emission sites available with this material. The emitters tips are acute tetrahedral structures, as compared to the cylindrical emitter tips obtained with the biological materials. Note the size scale.

calculation is performed here for the case of the tubule cathode. Application to the eutectic cathode is straightforward. The Fowler–Nordheim emission density is given by:

$$J = \frac{A(\beta E)^2}{\phi t^2(y)} \exp\left(-B \frac{\phi^{3/2} v(y)}{\beta E}\right) \text{ A/cm}^2 \quad (5)$$

where $A = 1.54 \times 10^{-6}$, $B = 6.8 \times 10^7$, $y = 3.79 \times 10^{-4}(\beta^{1/2}/\phi)$, $t^2(y) = 1.1$, $v(y) = 0.95 - y^2$, E is the applied electric field in V/cm, β is the field enhancement factor due to local geometry, and ϕ is the work function in electronvolts of the surface emission material. For $\beta E = 1.5 \times 10^8$ V/cm and a work function of 5 eV, $J = 3.6 \times 10^9$ A/cm². When the effective emission area reduction factor is taken into account, this corresponds to 291 μ A per tip. For an enhanced electric field value of $\beta E = 0.6 \times 10^8$ V/cm, this is reduced to less than 1 μ A per tip.

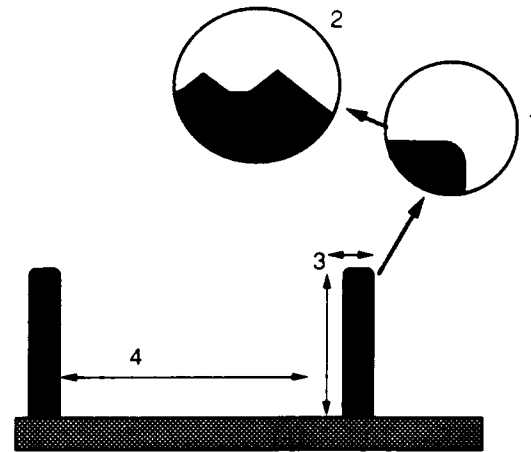


Fig. 4. The sources of electric field enhancement and degradation for our structures: (1) the radius of curvature of the exposed tip; (2) atomic scale surface protrusions; (3) the height and width of the exposed tip; and (4) the presence of other tips.

The effective electric field value of $\beta E = 0.6 - 1.5 \times 10^8$ V/cm requires substantial field enhancement to obtain, given a desired starting value of 20 kV/cm. For the structure shown in Fig. 1, there are three sources of field enhancement and one source of field suppression. Considering the tubule cathode structure shown in Fig. 4, the three sources of enhancement are: (i) the edge radius of curvature of the exposed tip, (ii) atomic scale surface roughness of the material on this edge, and (iii) the height and aspect ratio of the exposed tip. This calculated field enhancement is an over-estimate due to the nature of the calculation for item (iii), which assumes a single isolated tip on a flat surface. An estimate of the effect of neighboring tips on this calculation can be made by comparing the field gradient at the geometric middle between two emitter tips. These enhancement factors are calculated as follows:

- 1) *Radius of curvature of the exposed tip*: approximate the calculation as that of the field enhancement due to two concentric spheres, with radii R_{tip} and $\Delta x/2$ (see Fig. 5). With a nominal voltage V_A applied between the two spheres, the electric field at the inner sphere is

$$E(R_{in}) = \frac{V_A}{R_{out} - R_{in}} \times \frac{R_{out}}{R_{in}}$$

which corresponds to a field enhancement factor $R_{out}/R_{in} = \frac{1}{2}\Delta x/R_{tip}$. For a tip radius of 500 Å and tip separation of 10 μ m, this gives an enhancement factor of 100. Reduction of the emitter tip radius to 100 Å increases this factor to 500. SEM micrographs of the emitter surface place an upper limit of 200 Å on the edge radius of curvature.

- 2) *Atomic-scale surface roughness*: measurements by Spindt *et al.* at SRI have observed a field enhancement effect attributed to atomic-scale surface roughness. This enhancement factor is observed to be approximately 3, but with the additional aspect that the effective emission area is dramatically reduced by a factor of 10000.
- 3) *Height and aspect ratio of the exposed tip*: the field structure surrounding a Lorentzian-like surface bump

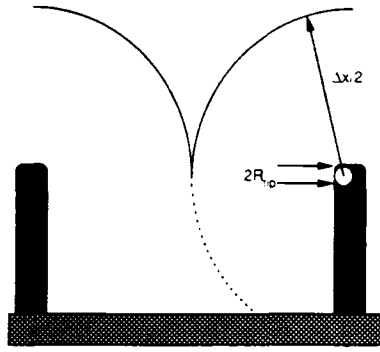


Fig. 5. The field enhancement due to the radius of curvature of the exposed tip. The approximation used is that of two concentric spheres, with radii R_{tip} and $\Delta x/2$.

has been calculated to be [24]:

$$E_x + iE_y = \frac{-iE_0[x - i(y + b)]}{\{[x - i(y + b)]^2 + a^2\}^{1/2}} \quad (6)$$

where a and b are conformally mapped parameters from the height and width of the bump:

$$b \approx (w/3.464) \left[1 + \frac{w}{3.464h} \right]; \quad a \approx h + \frac{w}{3.464}. \quad (7)$$

An estimate of the Lorentzian profile that closely fits the borders of the exposed emitter in the neighborhood of the tip gives $w \sim 4 \times R_{cyl}$. For a single protrusion of height $h = 10 \mu\text{m}$ and width $w = 2 \mu\text{m}$, we have $a \sim 10$, $b \sim 0.56$, and letting $\delta = b/a$:

$$\begin{aligned} E_y &\approx iE_0 \times \left\{ \frac{(b + h)}{[a^2 - (b + h)^2]^{1/2}} \right\} \\ &\approx E_0 \times \frac{1}{\sqrt{2}} \frac{1}{\delta} \sqrt{1 + \delta} \\ &\approx E_0 \times 10 \end{aligned} \quad (8)$$

giving us a field enhancement factor of about 10.

- 4) *Degradation of 3) due to neighboring tips*: the error incurred by neglecting the presence of other tips in the calculation of the previous enhancement factor can be estimated by calculating E_x , the transverse field component, at a distance from the one tip corresponding to the midpoint between two tips. A fully accurate many-tip calculation would clearly give $E_x = 0$. Again, using the field structure above for $x = 5 \mu\text{m}$, $y = 10 \mu\text{m}$ we calculate $E_x/|E| = 0.1$. Therefore we estimate our calculation of the enhancement factor in 3) to be too large by about 10%.

The complete enhancement factor can be approximated by multiplying together the individual enhancement factors for the edge radius of curvature, microsurface protrusions, the tip aspect ratio, and the presence of other tips:

$$\beta = (250) \times (3) \times (10) \times (0.9) = 6750 \quad (9)$$

and the local electric field is:

$$E_k = E_0 \times \beta = (20 \text{ kV/cm}) \times 6750 = 1.35 \times 10^8 \text{ V/cm} \quad (10)$$

giving us the higher end of the $0.6 - 1.5 \times 10^8 \text{ V/cm}$ -enhanced electric field quoted previously.

The last element of the design is the method used to limit the current at the emitter tips. This limiting is necessary to avoid current runaway at the tips. In the case of the gated field emitter arrays studied by Spindt *et al.*, the current limiting is achieved by mounting the emitter tips on a doped silicon crystal. This approach is also possible here, where electrical contact would be made to the emitter tips from the back of the composite array. Another possibility, that which has been explored in the initial research, is to coat the emission surface itself with a coating of silicon. This approach has the advantage that the current limiting occurs at the emitter tip, and therefore each tip is protected. In the approach where the emitter tips are mounted on a macroscopic silicon crystal, the current limiting is more macroscopic and current "hogging" can occur. The primary drawbacks to the thin-film limiter approach are verifying the integrity of the thin film, and also the open question of the current-limiting capability of a thin film. These are questions which are presently being addressed.

The expectations for high beam brightness from these cathode materials are based on the analogy with velvet or felt cathodes. Measurements with velvet cathodes have shown that the dominant source of electron beam emittance is that due to the surface roughness. Given our cathode surface structure, we anticipate that this will also be the dominant source of electron beam emittance for the advanced cathode materials. For a surface with a roughness of characteristic height h and width w (in 100's of μm) and for a cathode not operating in the space-charge-limited regime, the maximum normalized spread angle is calculated to be [24]:

$$\gamma\beta\delta\theta_{\text{max}} = 0.15\sqrt{E_0} \frac{h}{(h^2 + w^2)^{1/4}} \quad (11)$$

where E_0 is the applied macroscopic electric field in MeV/cm. This maximum in the perpendicular electron velocity occurs for electrons emitted from about 40% down the side of the characteristic bump. In our case, however, the electron emission is occurring at or near the top of the protrusion. This reduces the maximum normalized spread angle to:

$$\gamma\beta\delta\theta_{\text{max}} = 0.05\sqrt{E_0} \frac{h}{(h^2 + w^2)^{1/4}}. \quad (12)$$

For our parameters of $h = 10 \mu\text{m}$, $w = 0.4 \mu\text{m}$, and $E_0 = 20 \text{ kV/cm}$, we obtain $\gamma\beta\delta\theta_{\text{max}} = 2.2 \text{ mrad}$. This leads to a normalized brightness of:

$$\begin{aligned} B_n &= \frac{I}{\pi^2 \epsilon_n^2} = \frac{I}{\pi r^2} \frac{1}{\pi (\gamma\beta\delta\theta_{\text{max}})^2} = \frac{1}{\pi} \frac{200 \text{ A/cm}^2}{(2.2 \text{ mrad})^2} \\ &= 1.3 \times 10^7 \text{ A/cm}^2 - \text{rad}^2. \end{aligned} \quad (13)$$

This brightness exceeds presently available parameters by approximately one to two orders of magnitude.

The expectations for long operational lifetime stem from two sources. First and foremost are the lifetime measurements already performed by Spindt *et al.* on their gated field emitter arrays. In cases where the gate electrode did not fail, lifetimes well in excess of 1000 h have been demonstrated. The other

lifetime limitation is taken from calculations of the surface erosion due to back-ion bombardment. The rate of erosion is governed by several parameters, including the electron beam voltage, the background vacuum pressure, the surface material, and the electron gun structure itself. The highest rate of surface erosion occurs for ions striking the cathode surface with energies around 1 keV. At this energy the probability for sputtering is the highest. Well above this energy, the ions pass through the surface structure with very little probability of interaction. Well below this energy, the ions possess too little energy to do sputtering damage. Clearly, a gun design would want to minimize the number of ~ 1 keV ions that are allowed to track to the cathode surface. Taking as a minimum a layer of thickness 1 mm for the volume creating ~ 1 keV ions, a background pressure of 10^{-6} torr, and a 1-1 ion-sputtering ratio, less than 1 μm of surface material is lost in greater than 1000 h of exposure.

III. EXPERIMENTS AND RESULTS

Experiments to date have focused on the demonstration of low turn-on macroscopic electric fields, the fabrication of the suitable surface microstructure, and measurements of the $I-V$ characteristics. Experiments are in progress to measure the resultant beam emittance, the uniformity of turn-on across the cathode surface, and the cathode lifetime. Results of these experiments will be used to optimize the cathode material performance.

The cathode measurements presented here used a simple parallel-plate cathode-anode geometry as shown in Figs. 6 and 7. The processed emitters are mounted on either aluminum or OFHC copper stubs, which in turn are mounted in an anodized aluminum cathode holder. The exposed surface of the cathode holder is anodized to prevent unwanted emission from the aluminum surface, while the sides of the cylindrical hole are left uncoated to facilitate good electrical and thermal contact with the aluminum cathode holder. The entire cathode assembly is mounted in a cathode test stand and is placed opposite a long, OFHC copper-cone beam collector that is held at ground potential. The outside of the cone is covered with refrigeration tubing, which flows water for cooling the collector. The face of the cone is covered with a stainless-steel plate, which has a hole cut through the center to facilitate passage of the electron beam. The plate is to ensure an approximately planar field structure in the cathode-anode gap. A calibrated current-viewing resistor monitors the current in the ground return from the anode. The vacuum is provided by a cold-trapped diffusion pump and was typically in the range $2-5 \times 10^{-5}$ torr. All of the test results presented here are dc measurements.

Proof-of-principle tests were performed with the cathode emitter shown previously in Fig. 2. That surface was coated with successive 50 Å layers of gold and amorphous silicon. Application of a macroscopic 20 kV/cm electric field produced a measured current density of 38 mA/cm² for a duration of 10 s. Subsequent inspection of the cathode surface with a SEM showed no observable damage due to the emission. Using the simple template as the cathode emitter with no coatings of

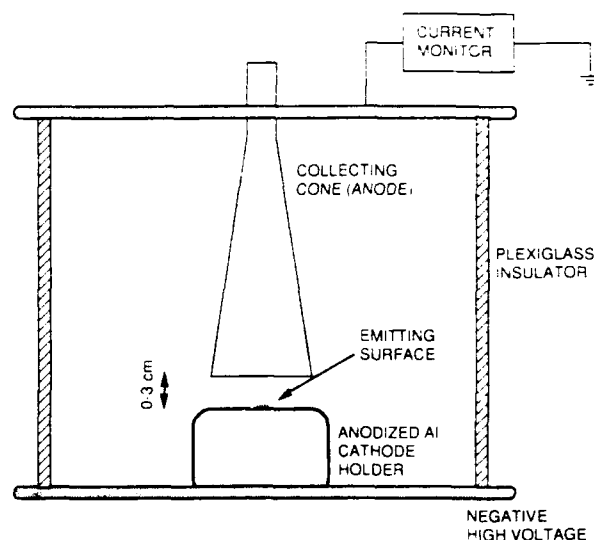


Fig. 6. A sketch of the test setup used to measure the performance of the advanced cathode materials.

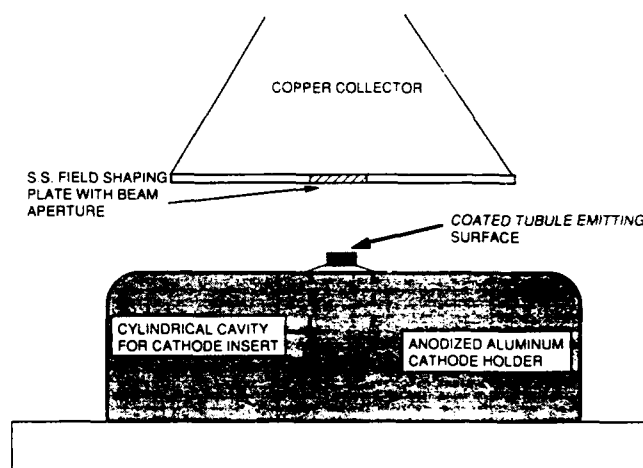


Fig. 7. The cathode materials are mounted on an aluminum or copper stub that is inserted into an anodized cathode holder. An aperture in the anode faceplate opposite the emitter position is used to allow for passage of the beam electrons.

gold or silicon produced no observable emission. With only the gold coating, the cathode was observed to form an unstable plasma discharge at approximately the same 20 kV/cm.

For the case of the silicon-tantalum-disilicide emitter shown in Fig. 3, the application of macroscopic electric fields as high as 45 kV/cm failed to produce any measurable emission. Subsequent coating of the surface with a 50 Å coating of gold produced an unstable plasma discharge at approximately the 20 kV/cm applied field. Subsequent coating of this surface with 50 Å of amorphous silicon produced approximately 10 mA/cm² for an applied electric field of 20 kV/cm, and approximately 1 A/cm² for an applied field of 15 kV/cm. The cathode emission surface was approximately 0.7 cm² in area, and the latter current density measurement corresponded to a total emission current of approximately 0.7 A. Due to limitations of the available power supply, this was achieved with an RC charge-discharge circuit. The measurements were

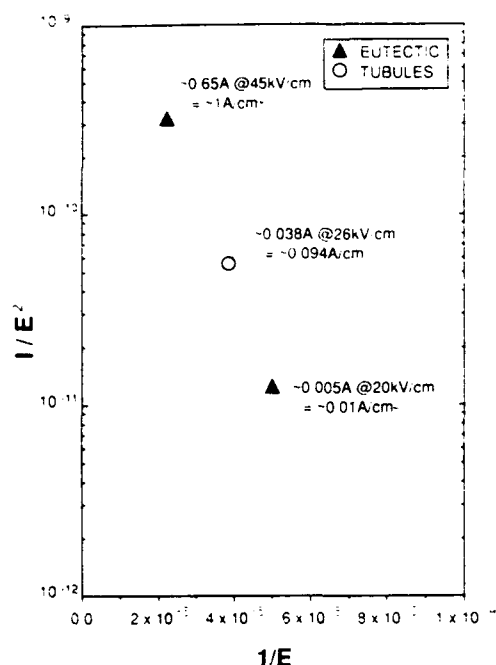


Fig. 8. A summary of the performance of our proof-of-principle emitter structures.

therefore made with an effectively varying voltage (22 – 18 kV) over a decay time of about 10 s. Due to the variational nature of the voltage and the crudeness of the measurement technique, these current measurements may have an error as large as 50%. The measurements do, however, serve as proof of principle of the utility of the microstructures as field-emitter templates. These data for both the eutectic composite cathode as well as the tubule composite cathode are shown in Fig. 8.

Our measurements are proceeding with the development of an improved testing apparatus. In addition, alternative processing schemes are being developed to optimize the resultant surface micromorphology of both the eutectic-composite and tubule-composite cathode materials. The approaches involve optimized etching procedures and, in the case of the tubule cathode, alternative matrix materials more suitable to post-composite processing.

REFERENCES

- [1] C. W. Roberson, *Proc. Soc. Photo-Opt. Int. Eng.*, vol. 453, p. 320, 1983.
- [2] D. A. Kirkpatrick, G. Bekefi, A. C. DiRienzo, H. P. Freund, and A. K. Ganguly, *Phys. Fluids B*, vol. 1, p. 1511, 1989; see also, *Vacuum Arcs, Theory and Application*, J. M. Lafferty, Ed., New York, Wiley, 1980.
- [3] J. LeDuff, in *Proc. Lin. Acc. Conf.* (Newport News, VA), 1988, p. 285; see also, *The New York Times*, p. D1, June 20, 1990.
- [4] R. E. Thomas, J. W. Gibson, G. A. Haas, and R. H. Abrams, *IEEE Trans. Electron Devices*, vol. 37, p. 850, 1990.
- [5] R. L. Sheffield, E. R. Gray, and J. S. Fraser, *Nucl. Instrum. Meth.*, vol. A272, p. 222, 1988.
- [6] C. Santord and N. C. MacDonald, *J. Vac. Sci. Technol.*, vol. B6, p. 2005, 1988.
- [7] C. A. Spindt, K. R. Shoulders, and L. N. Heynick, U.S. Patents 3755704, 1973, and 3812559, 1974.
- [8] C. A. Spindt, I. Brodie, L. Humphrey, and E. R. Westerberg, *J. Appl. Phys.*, vol. 47, p. 5248, 1976.
- [9] C. A. Spindt, C. E. Holland, and R. D. Stowell, *Appl. Surf. Sci.*, vol. 16, p. 268, 1983.
- [10] G. J. Campisi and H. F. Gray, *Mater. Res. Soc. Symp. Proc.*, vol. 76, p. 67, 1987.

- [11] H. H. Busta, R. R. Shaddock, and W. J. Orvis, *IEEE Trans. Electron Devices*, vol. 36, p. 2679, 1989.
- [12] D. D. Hinshelwood, Naval Res. Lab., Washington, DC, Memo. Rep. No. 5492, 1985.
- [13] P. Yager and P. E. Schoen, *Mol. Cryst. Liq. Cryst.*, vol. 106, p. 371, 1984.
- [14] P. Yager, P. E. Schoen, C. Davies, R. Price, and A. Singh, *Biophys. J.*, vol. 48, p. 899, 1985.
- [15] J. M. Schnur *et al.*, *Thin Solid Films*, vol. 152, p. 181, 1987.
- [16] J. H. Georger *et al.*, *J. Amer. Chem. Soc.*, vol. 109, p. 6169, 1987.
- [17] F. Behroozi *et al.*, *J. Appl. Phys.*, to be published.
- [18] B. M. Ditchek, T. R. Middleton, P. G. Rossoni, and B. G. Yacobi, *Appl. Phys. Lett.*, vol. 52, p. 1147, 1988.
- [19] M. Levinson, B. M. Ditchek, and B. G. Yacobi, *Appl. Phys. Lett.*, vol. 50, p. 1906, 1987.
- [20] B. M. Ditchek and M. Levinson, *Appl. Phys. Lett.*, vol. 49, p. 1656, 1986.
- [21] C. A. Spindt, private communication.
- [22] Y. Y. Lau, *J. Appl. Phys.*, vol. 61, p. 36, 1987.

Douglas A. Kirkpatrick was born in Paris, France, in 1959. He received the B.S. degree in physics and mathematics from the College of William and Mary, Williamsburg, VA, in 1980, and the Ph.D. degree in physics from the Massachusetts Institute of Technology, Cambridge, in 1988.

After his studies at MIT he joined Science Applications International Corporation, McLean, VA, where he is a Research Scientist with the Applied Physics Operation. His research interests include advanced cathode materials, free electron lasers, electron-beam dynamics, electron-beam generation, gyrotrons, and plasma-filled microwave devices.

Paul E. Schoen was born in Evanston, IL, in 1942. He received the B.A. degree with a major in physics from Rockhurst College, Kansas City, MO, and continued his education in physics at The Johns Hopkins University, Baltimore, MD, obtaining the Ph.D. in 1971.

He pursued postdoctoral studies at the University of Kent, Canterbury, England, investigating cryogenic fluids by optical spectroscopy, and at SUNY, Stony Brook, Long Island, NY, performing Raman spectroscopy with organic liquids and proteins. He joined the staff of the Naval Research Laboratory, Washington, DC, in 1975, where he has worked with polymers, surface phenomena, lithography, membrane lipids, and applications of biologically derived microstructures.

W. B. Stockton, photograph and biography not available at the time of publication.

R. Price, photograph and biography not available at the time of publication.

S. Baral, photograph and biography not available at the time of publication.

Brian E. Kahn was born in New York in 1957. He received the B.S. degree in botany from the University of Wisconsin at Madison in 1980.

After spending six years at the National Museum of Natural History in the Smithsonian Institution, he joined Geo-Centers, Inc., for whom he is a Microscopist at the Naval Research Laboratory's Center for Bio Molecular Science and Engineering.

Joel M. Schnur was born in Washington, DC, in 1945. He studied physics and chemistry at Rutgers College and Georgetown University, receiving the A.B. degree in 1966, the M.S. degree in 1969, and the Ph.D. degree in 1971.

He then furthered his education with postdoctoral fellowships at the Naval Research Laboratory, the Istituto di Fisica, Parma, Italy, and the Université de Paris, Sud until 1973. These fellowships were supported by a National Academy of Science Fellowship. He returned to the United States in 1973 to accept a position in the Optical Sciences Division of the Naval Research Laboratory, Washington, DC. Between 1973 and 1983 he pursued research in the area of advanced spectroscopies applied to the study of complex organic materials. In 1983 he was awarded a Professor Associe at the Université of Paris VI. In 1984 he became Head of a newly formed group in Bio Molecular Engineering. He is now the Director of the Center for Bio Molecular Science and Engineering at the NRL. His research interests include self-assembly, picosecond spectroscopy, liquid crystals, biomaterials, and advanced material development.

Mark Levinson received the S.B. and Sc.D. degrees in materials science from the Massachusetts Institute of Technology in 1972 and 1978, respectively.

Following a postdoctoral fellowship at the University of Geneva, Switzerland, he was a Member of the Technical Staff at AT&T Bell Laboratories,

Murray Hill, NJ, from 1979 to 1985. In 1985 he joined GTE Laboratories, Waltham, MA, where he is a Principal Member of the Technical Staff. His research has concerned semiconductor defect physics, integrated circuit process development, high temperature superconductors, novel semiconductor-metal eutectic composite materials and devices, vacuum microelectronics, and flat-panel displays. He is an author of over 50 papers in refereed journals and holds four U.S. patents.

Brian M. Ditchek received the B.E. degree from the State University of New York at Stony Brook in 1973, and the Ph.D. degree in materials science and engineering from Northwestern University in 1977.

He has held the positions of Postdoctoral Associate for the National Bureau of Standards from 1977 to 1978, and Research Scientist at Martin Marietta Laboratories from 1978 to 1981. Since 1981 he has been at GTE Laboratories, Waltham, MA, where he is currently Manager of the Electronic Materials Department. He has performed research in many areas, including silicon-metal silicide eutectic composite material, single crystal and epitaxial silicides, and eutectic composite devices.

Thermal Effects on the Linear Gain in Free-Electron Lasers

H. P. Freund, R. C. Davidson, and D. A. Kirkpatrick

Abstract—The effect of an axial energy spread on the linearized gain in free-electron lasers is considered for configurations which employ both helical and planar wiggler fields. The analysis includes collective effects and is valid for either the Raman or high-gain Compton regimes. A thermal function is obtained which applies to both the helical and planar wiggler configurations at the fundamental, and which is generalized to treat the thermal effect on the harmonics for a planar wiggler. It is assumed that the displacement of the electron beam from the axis of symmetry for a helical wiggler, or the plane of symmetry for a planar wiggler, is much less than the wiggler period, and an idealized one-dimensional model is considered. The electron-beam model used to describe the axial energy spread is based upon the assumption of a monoenergetic beam which exhibits a pitch angle spread. This is described in the analysis by the inclusion of nonvanishing components of the canonical momenta in the single-particle trajectories of the electrons, and the specific distribution used is that of a Gaussian spread in the canonical momenta. The linearized Vlasov-Maxwell equations are then used to derive the dispersion equations, including collective Raman effects, for both the helical and planar wigglers. The analysis treats the interaction at the fundamental resonance frequency in the case of the helical wiggler, and a general thermal function is derived which describes the effect of the axial energy spread. The planar wiggler configuration admits interactions at odd harmonics as well as the fundamental, and a general dispersion equation is derived which includes the thermal effect at each harmonic as well as the fundamental. In addition, the nonvanishing canonical momenta results in an oscillation in the axial velocity at the wiggler period which gives rise to emission at all harmonics. This effect is included in the analysis for the planar wiggler configuration.

I. INTRODUCTION

AN IMPORTANT issue in the generation of coherent radiation at short wavelengths from the free-electron laser (FEL) is the effect of a beam thermal spread on the interaction. Indeed, in many cases, the thermal spread available from various electron-beam sources constitutes the essential limiting factor for many FEL applications. In this paper, we address the question of the effect of an axial energy spread upon the linear gain of the FEL at *both* the fundamental resonance frequency and at harmon-

ics of the fundamental. Coherent harmonic radiation is an important approach to the reduction in the beam energy required to achieve short-wavelength operation, and has been observed in the laboratory over a wide spectral range [1]–[5]. The question of the effect of beam thermal spread upon the gain at the harmonics, therefore, is of particular importance.

Theoretical analyses of harmonic radiation in FELs have dealt with both the linear [6]–[9] and nonlinear [10]–[16] interactions. Results of these analyses indicate that substantial gains and efficiencies are possible for the harmonic interactions, but that the sensitivity of the interaction to the beam thermal spread increases with harmonic number. Hence, the beam quality required for coherent emission rises dramatically at the higher harmonic numbers. Analytical formulations of the interaction which include thermal effects have considered both a distribution in the pitch angle spread [8] and the axial velocity, typically specified by a Gaussian [9], [17]. In the former case dealing with the pitch-angle spread, the effect of three-dimensional wiggler geometry has been included via betatron oscillations arising from the wiggler inhomogeneity; however, the analysis is restricted to the low-gain Compton regime. The formulations in the latter case describe a beam with an energy spread but a vanishing emittance (or pitch-angle spread), and treat either harmonic emission from a planar wiggler configuration in the high-gain Compton regime [9] or the fundamental interaction in a variety of operating regimes [17]. In addition, nonlinear analyses and simulation of both the fundamental and harmonic interactions for a planar wiggler configuration in the high-gain Compton regime in three dimensions have been presented [10], [12], [14] which include both the effects of a pitch-angle spread (for a monoenergetic beam) and the wiggler inhomogeneity.

In contrast with the preceding work, our purpose in this paper is to develop a unified formulation of thermal effects on the linear gain in both the high-gain Compton and collective Raman regimes. We assume that the beam is monoenergetic but characterized by a pitch-angle spread, and treat both the fundamental (for both helical and planar wigglers) and harmonic (for a planar wiggler) interactions. In order to treat this problem analytically, we shall impose an idealized one-dimensional approximation in which we neglect the wiggler inhomogeneity, and treat the pitch-angle spread by the inclusion of nonvanishing

Manuscript received January 7, 1991; revised March 10, 1991. This work was supported by the Defense Advanced Research Projects Agency under Contract N00014-90C-2118.

H. P. Freund and D. A. Kirkpatrick are with Science Applications International Corp., McLean, VA 22102.

R. C. Davidson is with Science Applications International Corp., McLean, VA 22102, on leave from Princeton Plasma Physics Laboratory, Princeton University, Princeton, NJ 08543.

IEEE Log Number 9103648.

canonical momenta in the single-particle trajectories. As such, we assume that the electron displacements from either the axis (helical wiggler) or plane (planar wiggler) of symmetry are much smaller than a wiggler period. In practical terms, this implies that the bulk transverse velocity associated with the pitch-angle spread be much less than the wiggler-induced transverse oscillation.

The effect of the pitch-angle spread is twofold. In the first place, the resultant axial energy spread acts to degrade the interaction, and a general thermal function which describes this effect for both the helical and planar wigglers is derived for the interaction at the fundamental resonance. The effect of the axial energy spread on the odd harmonics excited in planar wiggler configurations is also described, and a generalized thermal function is derived for the linear gain at the harmonics. In the second place, the pitch angle spread induces an oscillation in the axial velocity which can also act to excite harmonic radiation, and this is treated for the case of a planar wiggler.

Indeed, for many classes of electron beam, the source of the axial energy spread is predominantly the pitch-angle spread rather than a spread in the total energy. For example, electron beams produced by MIG and Pierce guns are accelerated by voltages of up to several mega-electronvolts and focused, prior to injection into the interaction region, either by shaped electric or magnetic fields. The coils and/or electrodes which produce the external fields in these guns must be carefully designed in order to offset the effects of the self-electric and magnetic fields of the beam. While the accelerating voltage may vary over the duration of the beam pulse, the electrons are instantaneously characterized by a largely monoenergetic distribution. However, the focussing process itself gives rise to a pitch-angle spread due to a variety of causes (such as field imperfections, shot noise, and self-field effects of the beam). Similar effects are found in a variety of accelerating mechanisms, and the description of the axial energy spread as arising from a pitch-angle distribution, rather than a spread in the total energy, is appropriate to a wide range of FEL designs.

The organization of the paper is as follows. A summary of the single-particle orbits in both helical and planar wigglers is given in Section II. The general formalism used to derive the linear growth rates for helical and planar wigglers is described in Section III. Sections IV and V include the linear stability analyses for the helical and planar wigglers, respectively. In the case of helical wigglers, the effect of an axial energy spread is included only upon the growth rate at the fundamental. In this case a general thermal function is derived which describes the axial thermal effect upon the instability. In the case of planar wigglers, the analysis includes the effect of the axial energy spread upon the fundamental and the harmonics. Here we observe that one effect of the axial energy spread derived by means of a nonvanishing canonical momentum is to give rise to growth at both even and odd harmonics. A summary and discussion is given in Section VI.

II. SINGLE-PARTICLE ORBITS

The physical configurations we consider in this paper are those of a relativistic electron beam propagating through either a helical or a planar wiggler within the context of the idealized, one-dimensional limit. As such, we implicitly assume that the displacements of the electron beam from the axis or plane of symmetry are much smaller than the wiggler period (i.e., $k_w r \ll 1$). The helical wiggler field is assumed to be generated by a bifilar helical current winding which produces a field of the form

$$\mathbf{B}_w = B_w(\hat{e}_t \cos k_w z + \hat{e}_\phi \sin k_w z) \quad (1)$$

in the idealized limit, where B_w denotes the wiggler amplitude, and k_w is the wiggler wavenumber ($\equiv 2\pi/\lambda_w$, where λ_w is the wiggler period). The representation for a planar wiggler in the idealized limit is given by

$$\mathbf{B}_w = B_w \hat{e}_x \sin k_w z. \quad (2)$$

Since x and y are ignorable coordinates in the idealized representation for the wiggler fields, these components of the canonical momenta (denoted by P_x and P_y) are constants of the motion. In addition, the total energy is also a conserved quantity. As a result, the single-particle orbits in a helical wiggler are given by

$$p_x = P_x + p_w \cos k_w z \quad (3)$$

$$p_y = P_y + p_w \sin k_w z \quad (4)$$

and

$$p_z = \sqrt{P^2 - 2p_w(P_x \cos k_w z + P_y \sin k_w z)} \quad (5)$$

where $\gamma \equiv (1 + p^2/m_e^2 c^2)^{1/2}$ is the relativistic factor corresponding to the total electron energy and momentum p , $p_w \equiv \gamma m_e v_w$, $v_w \equiv -\Omega_w/k_w$ is the wiggler-induced velocity, $\Omega_w \equiv |eB_w/\gamma m_e c|$, m_e is the electron mass, c is the speed of light *in vacuo*, and $P^2 \equiv p^2 - p_w^2 - P_x^2 - P_y^2$ defines the bulk axial momentum. Observe that the magnitude of both the transverse and axial components of the velocity are constant in the limit in which both P_x and P_y vanish, and the orbit describes a helix which is in phase with the wiggler field and characterized by an axial momentum $p_z \equiv (p^2 - p_w^2)^{1/2}$.

The single-particle orbits in the idealized planar wiggler are given by (3) for the x component of the momentum

$$p_x = P_x \quad (6)$$

and

$$p_z = \sqrt{P^2 - \frac{1}{2}p_w^2 \cos 2k_w z - 2p_w P_x \cos k_w z} \quad (7)$$

where

$$P^2 \equiv p^2 - \frac{1}{2}p_w^2 - P_x^2 - P_y^2 \quad (8)$$

for a planar wiggler. Since the y component of the momentum is constant, the magnitude of the transverse wiggler-induced velocity in a planar wiggler oscillates at the wiggler period. This results in an oscillation in the axial

momentum and velocity as well, which broadens the wave-particle resonance, and gives rise to harmonic interactions. In addition, the principal resonance and coupling coefficient are determined by the bulk transverse velocity $\langle v_{\perp} \rangle = v_w / \sqrt{2}$. This reduces the effective wiggler field with respect to the helical wiggler.

The assumption of small displacements from either the symmetry axis (for a helical wiggler) or plane (for a planar wiggler) is equivalent to the condition that $|v_w/v| \ll 1$. It is also evident from (5) and (8) that the existence of a nonvanishing canonical momentum introduces an oscillation into the axial velocity in the case of both helical and planar wigglers, which can also give rise to harmonic emission when $V_- \approx v_w$, where $V_- \equiv (P_x^2 + P_y^2)^{1/2} / \gamma m_e$ is the velocity which corresponds to the transverse canonical momenta. In most FEL experiments, however, $V_- \ll v_w$, and the effect of a nonvanishing canonical momentum is largely on the broadening of the wave-particle resonance and the consequent degradation of the interaction strength. It should be remarked that this inequality is identical to that required in order to neglect the effect of betatron oscillations and wiggler inhomogeneities. Hence, in the remainder of this paper we will discuss the effect of the axial momentum spread due to a nonvanishing canonical momentum on the gain at the fundamental in both helical and planar wiggler FEL's, and on the gain in planar wiggler FEL's at harmonics of the fundamental.

III. GENERAL FORMULATION

In this section, we derive the general formalism for obtaining the linearized dispersion equation for the FEL in the idealized one-dimensional representation within the context of a linearized Vlasov-Maxwell formalism. The Vlasov equation in the combined wiggler and electromagnetic fields is

$$\left[\frac{\partial}{\partial t} + \mathbf{v} \cdot \nabla - e \left(\delta \mathbf{E}(z, t) + \frac{1}{c} \mathbf{v} \times [\mathbf{B}_w(z) + \delta \mathbf{B}(z, t)] \right) \cdot \nabla_p \right] f_b(z, \mathbf{p}, t) = 0 \quad (9)$$

where $f_b(z, \mathbf{p}, t)$ is the distribution function of the electron beam, $\delta \mathbf{E}(z, t)$ and $\delta \mathbf{B}(z, t)$ denote the fluctuating electric and magnetic fields of the wave, and

$$\nabla_p \equiv \hat{e}_x \frac{\partial}{\partial p_x} + \hat{e}_y \frac{\partial}{\partial p_y} + \hat{e}_z \frac{\partial}{\partial p_z} \quad (10)$$

The Vlasov equation is linearized by expanding the distribution in powers of the fluctuating fields. To this end we write $f_b(z, \mathbf{p}, t) = F_b(z, \mathbf{p}) + \delta f_b(z, \mathbf{p}, t)$ where F_b and δf_b are the equilibrium and perturbed components of the distribution, and it is assumed that the perturbed distribution is of the order of the fluctuating fields and $|\delta f_b| \ll |F_b|$. The equilibrium distribution must satisfy the lowest order Vlasov equation

$$\left[\frac{\partial}{\partial t} + \mathbf{v} \cdot \nabla - \frac{e}{c} \mathbf{v} \times \mathbf{B}_w(z) \cdot \nabla_p \right] F_b(z, \mathbf{p}) = 0. \quad (11)$$

This is satisfied for any equilibrium distribution which is a function of the constants of the motion. As discussed in Section II, these constants are the total energy (or momentum) as well as the canonical momenta for both helical and planar wigglers in the one-dimensional representation; hence, we may express the equilibrium distribution in the form $F_b(z, \mathbf{p}) = F_b(P_x, P_y, p)$. Correct to first order in the fluctuation fields, the perturbed distribution satisfies

$$\left[\frac{\partial}{\partial t} + \mathbf{v} \cdot \nabla - \frac{e}{c} \mathbf{v} \times \mathbf{B}_w(z) \cdot \nabla_p \right] \delta f_b(z, \mathbf{p}, t) = e \left(\delta \mathbf{E}(z, t) + \frac{1}{c} \mathbf{v} \times \delta \mathbf{B}(z, t) \right) \cdot \nabla_p F_b. \quad (12)$$

The perturbed Vlasov equation may be solved by the method of characteristics in which we integrate

$$\delta f_b(z, \mathbf{p}, \tau(z)) = e \int_0^z \frac{dz'}{v_z(z')} \left[\delta \mathbf{E}(z, \tau(z')) + \frac{1}{c} \mathbf{v}(z') \times \delta \mathbf{B}(z, \tau(z')) \right] \cdot \nabla_p F_b \quad (13)$$

over the unperturbed trajectories under the assumption that the perturbations are negligibly small at time $t = 0$. Observe that we treat the case of spatial growth and have adopted Lagrangian coordinates in which $\mathbf{r}'(z)$ denotes the unperturbed velocity of an electron as a function of the axial position, and

$$\tau(z) \equiv t_0 + \int_0^z \frac{dz'}{v_z(z')} \quad (14)$$

represents the time it takes an electron to reach a particular axial position after crossing the $z = 0$ plane at time t_0 .

The solution to the perturbed Vlasov equation is solved in conjunction with Maxwell's equations. We choose to deal with the scalar $\delta \varphi(z, t)$ and vector potentials $\delta \mathbf{A}_{\perp}(z, t)$ in the Coulomb gauge. Note that since we treat a one-dimensional model, the scalar and vector potentials describe plane waves. Hence, the vector potential represents a purely transverse electromagnetic wave. In terms of this representation, Maxwell's equations are

$$\left(\nabla^2 - \frac{1}{c^2} \frac{\partial^2}{\partial t^2} \right) \delta \mathbf{A}_{\perp} = -\frac{4\pi}{c} \delta \mathbf{J}_{\perp} \quad (15)$$

and

$$\frac{\partial^2}{\partial t \partial z} \delta \varphi = 4\pi \delta J_z. \quad (16)$$

Observe that the scalar potential is described in terms of the z component of Ampere's Law rather than with Poisson's equation. The perturbed source current is given in terms of the perturbed distribution function as follows:

$$\delta \mathbf{J}(z, t) = -\frac{e}{m_e} \int d^3p \frac{1}{\gamma} \mathbf{p} \delta f_b(z, \mathbf{p}, t). \quad (17)$$

The dispersion equation governing the growth and/or damping of the electromagnetic field is obtained by the simultaneous solution of (13), (15), and (16).

Since the FEL operates by means of an axial bunching mechanism, it is the axial velocity spread which is most important. As a consequence, in the treatment of thermal effects on the linear stability properties we shall impose the simplification that the electron beam is monoenergetic but exhibits a pitch-angle spread. The effect of the pitch-angle spread is to include velocity spreads in both the axial and transverse directions, and may be described by a distribution function of the form [18]

$$F_b(P_x, P_y, p) = n_b G_{\perp}(P_x, P_y) \frac{p_z}{p} \delta(p - p_0) \quad (18)$$

where n_b denotes the bulk ambient density, and $G_{\perp}(P_x, P_y)$ represents the transverse distribution. For convenience we shall assume that this transverse distribution takes the form of a Gaussian

$$G_{\perp}(P_x, P_y) = \frac{1}{\pi \Delta P^2} \exp(-P_{\perp}^2 / \Delta P^2) \quad (19)$$

where $P_{\perp}^2 \equiv P_x^2 + P_y^2$, and ΔP represents the thermal spread. An alternate distribution which includes the effects of both emittance and Betatron oscillations has also been developed [19].

IV. HELICAL WIGGLER CONFIGURATIONS

In treating the case of a helical wiggler under the assumption of plane-wave solutions, the vector and scalar potentials for a wave with angular frequency ω are of the form

$$\delta \mathbf{A}_{\perp}(z, t) = \frac{1}{2} \delta \hat{\mathbf{A}}_{\perp}(z) \exp(-i\omega t) + \text{c.c.} \quad (20)$$

and

$$\delta \varphi(z, t) = \frac{1}{2} \delta \hat{\varphi}(z) \exp(-i\omega t) + \text{c.c.} \quad (21)$$

After transformation to the basis

$$\hat{\mathbf{e}}_{\pm} \equiv \frac{1}{2} (\hat{\mathbf{e}}_x \pm i \hat{\mathbf{e}}_y) \quad (22)$$

which is convenient for the description of left- and right-hand circularly polarized electromagnetic waves, the perturbed distribution function can be written as

$$\delta f_b(z, \mathbf{p}, \tau(z)) \equiv \delta \hat{f}_b(z, \mathbf{p}) \exp(-i\omega \tau(z)) + \text{c.c.} \quad (23)$$

where

$$\begin{aligned} \delta \hat{f}_b(z, \mathbf{p}) = & \frac{e}{2c} \left[D_+ \left(\frac{\partial}{\partial P_x} + i \frac{\partial}{\partial P_y} \right) \right. \\ & + D_- \left(\frac{\partial}{\partial P_x} - i \frac{\partial}{\partial P_y} \right) + D_z \frac{\partial}{\partial p} \Big] \\ & \cdot F_b(P_x, P_y, p). \end{aligned} \quad (24)$$

The orbit integrals in (24) are defined as

$$D_{\pm} \equiv \int_0^z dz' \frac{\exp(i\omega \tau(z, z'))}{v_z(z')} \left(i\omega - v_z(z') \frac{\partial}{\partial z'} \right) \delta \hat{A}_{\pm}(z') \quad (25)$$

and

$$\begin{aligned} D_z = & \frac{1}{p} \int_0^z dz' \frac{\exp(i\omega \tau(z, z'))}{v_z(z')} \\ & \times \left(-c p_z(z') \frac{\partial}{\partial z'} \delta \hat{\varphi}(z') \right. \\ & \left. + i\omega [p_-(z') \delta \hat{A}_+(z') + p_+(z') \delta \hat{A}_-(z')] \right) \end{aligned} \quad (26)$$

where $p_{\pm} \equiv p_x \mp p_y$, $\tau(z, z') \equiv \tau(z) - \tau(z')$, and

$$\delta \hat{A}_{\pm} \equiv \frac{1}{2} (\delta \hat{A}_x \mp i \delta \hat{A}_y) \quad (27)$$

denotes the amplitudes of the circularly polarized electromagnetic waves.

The source current

$$\begin{aligned} \delta \mathbf{J}(z, t) = & [\delta \hat{J}_+(z) \hat{\mathbf{e}}_+ + \delta \hat{J}_-(z) \hat{\mathbf{e}}_- + \delta \hat{J}_z(z) \hat{\mathbf{e}}_z] \\ & \cdot \exp(-i\omega t) + \text{c.c.} \end{aligned} \quad (28)$$

is determined by means of the perturbed distribution as follows:

$$\begin{pmatrix} \delta \hat{J}_+(z) \\ \delta \hat{J}_-(z) \end{pmatrix} = -\frac{e}{m_e} \int dP_x dP_y dp \frac{p}{\gamma p_z} \delta \hat{f}_b(z, \mathbf{p}) \begin{pmatrix} p_+ \\ p_- \end{pmatrix}. \quad (29)$$

The interaction principally couples the space-charge and right-hand circularly polarized modes; hence, we neglect the left-hand circular polarization state. Therefore, the orbit integrals can be written as

$$D_{\pm} = \delta \hat{A}_{\pm}(0) \exp(i\omega \tau(z, 0)) - \delta \hat{A}_{\pm}(z) \quad (30)$$

and

$$\begin{aligned} D_z = & \frac{\gamma m_e c}{p} \int_0^z dz' \exp[i\omega \tau(z, z')] \\ & \cdot \left[-\frac{\partial}{\partial z'} \delta \hat{\varphi}(z') + \frac{i\omega}{c} \frac{p_-}{p_z} \delta \hat{A}_+(z') \right]. \end{aligned} \quad (31)$$

The Lagrangian time coordinate which appears in the orbit integrals can be evaluated using the single-particle trajectories in (3)–(5), and we obtain

$$\begin{aligned} \tau(z, z') = & \frac{\gamma m_e}{P_{\parallel}} \left[(z - z') - \frac{p_w P_x}{k_w P_{\parallel}^2} \right. \\ & \cdot (\sin k_w z - \sin k_w z') \\ & \left. + \frac{p_w P_y}{k_w P_{\parallel}^2} (\cos k_w z - \cos k_w z') \right] \end{aligned} \quad (32)$$

correct to terms of order in $p_w^2 P_{x,y}^2 / P_{\parallel}^4$. In the evaluation of the source currents, we substitute for the perturbed distribution function and integrate by parts in P_x and P_y .

Hence

$$\delta \hat{J}_+(z) = \frac{e^2}{2m_e c} \int dP_x dP_y dp \frac{p}{\gamma p_z} \left[\left(2 + \frac{p_+ p_-}{p_z^2} \right) D_+ + p_+ \left(\frac{\partial}{\partial P_x} + i \frac{\partial}{\partial P_y} \right) D_+ - p_+ D_z \frac{\partial}{\partial p} \right] F_b(P_x, P_y, p) \quad (33)$$

and

$$\delta \hat{J}_z(z) = \frac{e^2}{2m_e c} \int dP_x dP_y dp \frac{p}{\gamma} \left[\left(\frac{\partial}{\partial P_x} + i \frac{\partial}{\partial P_y} \right) D_+ - D_z \frac{\partial}{\partial p} \right] F_b(P_x, P_y, p) \quad (34)$$

where we observe that from the single-particle trajectories

$$\left(\frac{\partial}{\partial P_x} + i \frac{\partial}{\partial P_y} \right) p_+ = 2 \quad (35)$$

and

$$\left(\frac{\partial}{\partial P_x} + i \frac{\partial}{\partial P_y} \right) p_z = -\frac{p_-}{p_z} \quad (36)$$

The orbit integrals may be evaluated using the single-particle trajectories. We retain only the lowest order contributions due to P_x and P_y in the steady-state trajectories; hence, these contributions appear principally in the resonance condition. We consider the high-gain regime in which

$$\delta \hat{A}_+(z) = \delta \hat{A}_+(0) \exp(-ik_+ z)$$

and

$$\delta \hat{\phi}(z) = \delta \hat{\phi}(0) \exp(-ikz). \quad (37)$$

Under these conditions, the axial orbit integral can be approximated as

$$D_z \equiv \frac{\gamma m_e}{p} \left[\delta \hat{\phi}(z') \frac{kv_{\parallel}}{\omega - kV_{\parallel}} - \frac{v_w}{c} \delta \hat{A}_+(z') \exp(ik_w z') \frac{\omega}{\omega - (k + k_w)V_{\parallel}} \right] \quad (38)$$

where $V_{\parallel} \equiv P_{\parallel}/\gamma_0 m_e$ is the axial velocity corresponding to the generalized steady-state trajectory. In addition, we retain only the term which varies as $\exp(ik_+ z)$ in D_+ . Hence, the source currents can be written as

$$\begin{aligned} \delta \hat{J}_+(z) &\equiv -\frac{e^2}{m_e c} \delta \hat{A}_+(z) \int dP_x dP_y dp \left[\frac{p}{\gamma p_{\parallel}} \left(1 + \frac{\beta_w^2}{2} \right) \right. \\ &\quad \left. - \frac{\beta_w^2}{2} \frac{\omega m_e v_{\parallel}}{\omega - kV_{\parallel}} \frac{\partial}{\partial p} \right] F_b(P_x, P_y, p) \\ &\quad - \frac{e^2}{2m_e} p_w \delta \hat{\phi}(z) \exp(-ik_w z) \int dP_x dP_y dp \\ &\quad \cdot \frac{k}{\gamma(\omega - kV_{\parallel})} \frac{\partial}{\partial p} F_b(P_x, P_y, p), \end{aligned} \quad (39)$$

and

$$\begin{aligned} \delta \hat{J}_z(z) &\equiv \frac{e^2}{2m_e c} p_w \delta \hat{A}_+(z) \exp(ik_w z) \int dP_x dP_y dp \\ &\quad \cdot \frac{\omega}{\gamma(\omega - kV_{\parallel})} \frac{\partial}{\partial p} F_b(P_x, P_y, p) \\ &\quad - \frac{e^2}{2m_e} \delta \hat{\phi}(z) \int dP_x dP_y dp \frac{m_e k v_{\parallel}}{\omega - kV_{\parallel}} \frac{\partial}{\partial p} \\ &\quad \cdot F_b(P_x, P_y, p) \end{aligned} \quad (40)$$

$\gamma_0 \equiv (1 + p_0^2/m_e^2 c^2)^{1/2}$, $v_{\parallel} \equiv (p_0^2 - p_w^2)/\gamma_0 m_e$, and $\beta_w^2 \equiv v_w^2/v_{\parallel}^2$. Note that v_{\parallel} and v_w now denote the axial and transverse velocities for the steady-state trajectory corresponding to γ_0 .

The derivatives of the distribution with respect to p which appear in the above expressions for the source currents may be integrated by parts and the results substituted into Maxwell's equations to give

$$\begin{aligned} &\left[\omega^2 - k_+^2 c^2 - \frac{\omega_b^2}{\gamma_0} \left(1 - \frac{v_w^2}{c^2} \frac{\omega^2 - k^2 c^2}{(\omega - kv_{\parallel})^2} T(\zeta) \right) \right] \delta \hat{A}_+(0) \\ &= -\frac{\omega_b^2}{2\gamma_0} \frac{v_w}{c} \frac{ck(ck - \omega\beta_{\parallel})}{(\omega - kv_{\parallel})^2} T(\zeta) \delta \hat{\phi}(0) \end{aligned} \quad (41)$$

and

$$\begin{aligned} &\left[(\omega - kv_{\parallel})^2 - \frac{\omega_b^2}{\gamma_0 \gamma_{\parallel}^2} T(\zeta) \right] \delta \hat{\phi}(0) \\ &= -\frac{\omega_b^2}{\gamma_0} \frac{v_w}{c} \left(1 - \frac{\omega}{ck} \beta_{\parallel} \right) T(\zeta) \delta \hat{A}_+(0) \end{aligned} \quad (42)$$

where we identify $k = k_+ + k_w$ from the wavenumber matching condition, $\beta_{\parallel} \equiv v_{\parallel}/c$, $\gamma_{\parallel}^2 \equiv (1 - v_{\parallel}^2/c^2)^{-1}$, and $T(\zeta)$ defines the thermal function which arises from the Gaussian distribution in the canonical momenta. This thermal function is defined as

$$T(\zeta) \equiv \zeta [1 - \zeta \exp(\zeta) E_1(\zeta)] \quad (43)$$

for the argument

$$\zeta \equiv \frac{\gamma_0^2 m_e^2}{\Delta P^2} \left(\frac{\omega^2}{k^2} - v_{\parallel}^2 \right) \quad (44)$$

where

$$E_1(\zeta) \equiv \int_{\zeta}^{\infty} dt \frac{\exp(-t)}{t} \quad (45)$$

denotes the exponential integral function defined over the domain $|\arg \zeta| < \pi$.

The dispersion equation which results from this formulation is

$$\begin{aligned} &\left[(\omega - kv_{\parallel})^2 - \frac{\omega_b^2}{\gamma_0 \gamma_{\parallel}^2} T(\zeta) \right] \left[\omega^2 - k_+^2 c^2 - \frac{\omega_b^2}{\gamma_0} \right] \\ &= -\frac{\omega_b^2}{2\gamma_0} \frac{v_w^2}{c^2} T(\zeta) \left[\omega^2 - k^2 c^2 - \frac{\omega_b^2}{\gamma_0} T(\zeta) \right] \end{aligned} \quad (46)$$

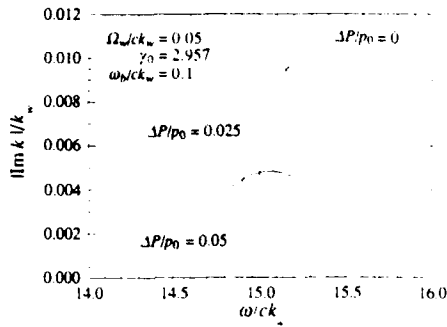


Fig. 1. Graph of the magnitude of the growth rate versus frequency for $\Delta P/p_0 = 0.025$, and 0.05 , and $\Omega_w/ck_w = 0.05$, $\gamma_0 = 2.957$, and $\omega_b/ck_w = 0.1$.

correct to lowest nontrivial order in v_w/c . In order to verify that this dispersion equation reproduces that found in the idealized beam limit, we observe that $\lim_{\Delta P \rightarrow 0} |\zeta| = \infty$. Expanding the exponential integral function in the asymptotic limit, therefore, we find that $\lim_{\Delta P \rightarrow 0} T(\zeta) = 1$ and that the ideal beam dispersion equation is recovered. Thermal effects become dominant whenever $\text{Im } k/(\text{Re } k + k_w) \approx \Delta v_{\parallel}/v_{\parallel}$, where the wavenumber is to be evaluated at the peak growth rate in the ideal beam limit. On the basis of the perturbed trajectories, it is clear that $\Delta v_{\parallel}/v_{\parallel} \approx \Delta P^2/2p_0^2$; hence, thermal effects are important when

$$\frac{\delta P^2}{p_{\parallel}^2} \approx \frac{\sqrt{3}}{2\gamma_{\parallel}^2} \left(\frac{\beta_w^2}{2\beta_{\parallel}^2} - \frac{\omega_b^2}{\gamma_0 k_w^2 v_{\parallel}^2} \right)^{1/3} \quad (47)$$

in the high-gain Compton regime, and

$$\frac{\Delta P^2}{p_{\parallel}^2} \approx \frac{\beta_w}{2\gamma_{\parallel}^2 \beta_{\parallel}} \sqrt{\frac{\omega_b}{\gamma_0^{1/2} ck_w}} \quad (48)$$

in the collective Raman regime.

The effect of the thermal spread on the linear growth rate is threefold. In the first place, the wider range of axial velocities introduced thereby results in a broader resonance condition in which the unstable frequency band increases. In the second place, the fact that the bulk axial velocity decreases means that the center frequency of the gain band also decreases. In the third place, the peak growth rate decreases with increasing ΔP . Each of these properties is illustrated in Fig. 1 in which we solve (46) numerically for the growth rate, and plot the magnitude of the growth rate as a function of the frequency for $\Omega_w/ck_w = 0.05$, $\gamma_0 = 2.957$, and $\omega_b/ck_w = 0.1$. Observe that the growth rate peaks for $|\text{Im } k|/k_w \approx 0.011$ in the absence of the thermal spread, and decreases by over 100% as the thermal spread increases to $\Delta P/p_0 = 5\%$.

The detailed variation in the peak growth rate and the frequency corresponding to peak growth as a function of ΔP is illustrated in Fig. 2. As shown in the figure, the peak growth rate remains relatively constant for $\Delta P/p_0 < 2\%$ and decreases rapidly thereafter. As a consequence, thermal effects become dominant for $\Delta P/p_0 \geq 3\%$. We expect that for thermal effects to be important

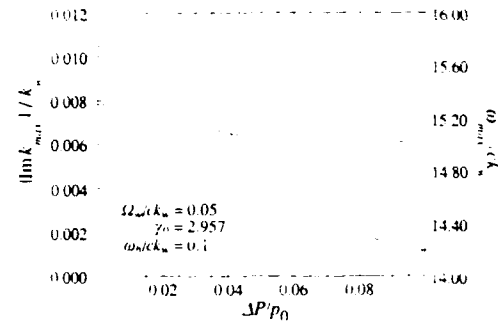


Fig. 2. Graph of the magnitude of the maximum growth rate (solid line) and the corresponding frequency (dashed line) as a function of $\Delta P/p_0$ for $\Omega_w/ck_w = 0.05$, $\gamma_0 = 2.957$, and $\omega_b/ck_w = 0.1$.

$\Delta v_{\parallel}/v_{\parallel} \approx \text{Im } k/(k_w + \text{Re } k) \approx 0.067\%$ (where $\text{Im } k/k_w \approx 0.011$ and $\text{Re } k/k_w \approx 15.4$ at peak growth) for this example. This yields an estimate of $\Delta P/p_0 \approx 3.7\%$, which is in reasonable agreement with the numerical solution for the growth rate shown in the figure. The frequency at which peak growth is found drops approximately 2% over this range.

V. PLANAR WIGGLER CONFIGURATIONS

In this case, the interaction occurs principally for plane waves polarized in the direction of the wiggler-induced oscillation, and the vector and scalar potentials for a wave with angular frequency ω are of the form

$$\delta A(z, t) = \frac{1}{2} \delta \hat{A}(z) \hat{e}_x \exp(-i\omega t) + \text{c.c.} \quad (49)$$

and

$$\delta \varphi(z, t) = \frac{1}{2} \delta \hat{\varphi}(z) \exp(-i\omega t) + \text{c.c.} \quad (50)$$

The analysis is similar to that described for the helical wiggler configuration. As in the case of the helical wiggler analysis, the perturbed distribution function takes the form

$$\delta f_b(z, p) = \frac{e}{2c} \left[D_x \frac{\partial}{\partial p_x} + D_z \frac{\partial}{\partial p} \right] F_b(P_x, P_y, p) \quad (51)$$

where the orbit integrals are defined as

$$D_x \equiv \int_0^z dz' \frac{\exp(-i\omega\tau(z, z'))}{v_z(z')} \left(i\omega - v_z(z') \frac{\partial}{\partial z'} \right) \delta \hat{A}(z') \quad (52)$$

and

$$D_z \equiv \frac{1}{p} \int_0^z dz' \frac{\exp(i\omega\tau(z, z'))}{v_z(z')} \cdot \left[-cp_z(z') \frac{\partial}{\partial z'} \delta \hat{\varphi}(z') + i\omega p_z(z') \delta \hat{A}(z') \right] \quad (53)$$

$\tau(z, z') \equiv \tau(z) - \tau(z')$. Observe that D_x may be integrated directly to give

$$D_x = -\delta \hat{A}(z) + \delta \hat{A}(0) \exp(i\omega\tau(z, 0)). \quad (54)$$

The source current

$$\delta J(z, t) = [\delta \hat{J}_x(z) \hat{e}_x + \delta \hat{J}_z(z) \hat{e}_z] \exp(-i\omega t) + \text{c.c.} \quad (55)$$

is determined by integration over the perturbed distribution

$$\delta \hat{J}(z) = -\frac{e}{m_e} \int dP_x dP_y dp \frac{p}{\gamma} \delta \hat{f}_b \left[\frac{p}{p_z} \hat{e}_x + \hat{e}_z \right]. \quad (56)$$

Substitution of the perturbed distribution yields, after integration by parts over P_x ,

$$\delta \hat{J}_x(z) = \frac{e}{m_e} \int dP_x dP_y dp \frac{p}{\gamma} \left[\frac{\partial}{\partial P_x} \left(\frac{p_x}{p_z} D_x \right) - \frac{p_x}{p_z} D_z \frac{\partial}{\partial p} \right] \cdot F_b(P_x, P_y, p) \quad (57)$$

and

$$\delta \hat{J}_z(z) = \frac{e}{m_e} \int dP_x dP_y dp \frac{p}{\gamma} \left[\frac{\partial}{\partial P_x} D_x - D_z \frac{\partial}{\partial p} \right] \cdot F_b(P_x, P_y, p). \quad (58)$$

The orbit integrals D_x and D_z which appear in the source currents represent an integration over the unperturbed electron trajectories in the planar wiggler. The characteristic trajectories in a planar wiggler differ from those in a helical wiggler in that the magnitudes of the axial and transverse velocity components are not constant but, rather, oscillate at harmonics of the wiggler period. This, in turn, introduces harmonic components into the dynamics of the interaction. In particular, we observe that in a planar wiggler the Lagrangian time variable characteristic of the electron trajectories is of the approximate form

$$\tau(z) \cong t_0 + \frac{z}{V_{\parallel}} + \frac{P_x v_w}{P_{\parallel} V_{\parallel} k_w V_{\parallel}} \sin k_w z + \frac{v_w^2}{8V_{\parallel}^2} \frac{1}{k_w V_{\parallel}} \sin 2k_w z \quad (59)$$

where it is assumed that both $v_w < V_{\parallel}$ and $P_x < P_{\parallel}$. Observe that existence of a nonvanishing canonical momentum introduces an oscillation at the wiggler period into the trajectory.

We express the vector and scalar potentials by application of Floquet's theorem for periodic systems in the form

$$\delta \hat{A}(z) = \sum_{n=-\infty}^{\infty} \delta \hat{A}_n \exp(ik_n z) \quad (60)$$

and

$$\delta \hat{\varphi}(z) = \sum_{n=-\infty}^{\infty} \delta \hat{\varphi}_n \exp(ik_n z) \quad (61)$$

where $k_n = k + nk_w$. Since the gain is exponential in this regime, we may neglect the initial value contributions to the orbit integrals. In the analysis of the thermal regime the dominant contribution of the axial thermal spread occurs within the resonance condition. Hence, if we restrict

the analysis to the resonance associated with the Doppler upshift in frequency then the source currents can be expressed in the form

$$\begin{aligned} \delta \hat{J}_x(z) \cong & -\frac{\omega_b^2}{8\pi\gamma_0 c} \sum_{n=-\infty}^{\infty} \delta \hat{A}_n \exp(ik_n z) \\ & \times \left(1 - \frac{v_w^2}{4c^2} \sum_{l,m=-\infty}^{\infty} K_m^{(+)}(b_2) \right. \\ & \cdot \int \int dP_x dP_y G_{\perp}(P_x, P_y) J_l^2(b_1) \\ & \cdot \frac{\omega^2 - c^2 k_{n+l+2m+1}^2}{(\omega - k_{n+l+2m+1} V_{\parallel})^2} \Big) \\ & + \frac{\omega_b^2}{16\pi\gamma_0} \sum_{n,l,m=-\infty}^{\infty} k_n \delta \hat{\varphi}_n \exp(ik_{n-1} z) J_m(b_2) \\ & \cdot [J_m(b_2) - J_{m+1}(b_2)] \\ & \times \int \int dP_x dP_y G_{\perp}(P_x, P_y) J_l^2(b_1) \\ & \cdot \frac{v_w \left(k_{n+l+2m} - \omega \frac{v_{\parallel}}{c^2} \right)}{(\omega - k_{n+l+2m} V_{\parallel})^2} \end{aligned} \quad (62)$$

and

$$\begin{aligned} \delta \hat{J}_z \cong & \frac{\omega_b^2}{8\pi\gamma_0 \gamma_{\parallel}} \sum_{n,m=-\infty}^{\infty} k_n \delta \hat{\varphi}_n \exp(ik_n z) J_m^2(b_2) \\ & \times \int \int dP_x dP_y G_{\perp}(P_x, P_y) J_l^2(b_1) \\ & \cdot \frac{\omega}{(\omega - k_{n+l+2m} V_{\parallel})^2} \\ & - \frac{\omega_b^2}{16\pi\gamma_0 c} \sum_{n,l,m=-\infty}^{\infty} \delta \hat{A}_{n-1} \exp(ik_n z) J_m(b_2) \\ & \cdot [J_m(b_2) - J_{m+1}(b_2)] \\ & \times \int \int dP_x dP_y G_{\perp}(P_x, P_y) J_l^2(b_1) \\ & \cdot \frac{v_w \left(k_{n+l+2m} - \omega \frac{v_{\parallel}}{c^2} \right)}{(\omega - k_{n+l+2m} V_{\parallel})^2} \end{aligned} \quad (63)$$

where V_{\parallel} and v_{\parallel} are the bulk axial velocities with and without the pitch angle spread, respectively, and J_l denotes the regular Bessel function of the first kind. In addition

$$b_1 \equiv \frac{\omega}{k_w V_{\parallel}} \frac{v_w}{V_{\parallel}} \frac{P_x}{P_{\parallel}} \quad (64)$$

$$b_2 \equiv \frac{\omega}{k_w V_{\parallel}} \frac{v_w^2}{8V_{\parallel}^2} \quad (65)$$

$$K_m^{(+)}(b_2) \equiv [J_m(b_2) - J_{m+1}(b_2)]^2 \quad (66)$$

and we have made use of the Bessel function relations

$$\frac{2n}{x} J_n(x) \equiv J_{n-1}(x) + J_{n+1}(x) \quad (67)$$

$$\exp(ib \sin \theta) = \sum_{n=-\infty}^{\infty} J_n(b) \exp(in\theta). \quad (68)$$

The integrals over the canonical momenta in (62) and (63) may be evaluated using the transverse distribution function, and we find that in the limit in which $P_{\perp} \ll p_{\parallel}$

$$\iint dP_x dP_y G_{\perp}(P_x, P_y) \frac{J_l^2(b_1)}{(\omega - k v_{\parallel})^2} \equiv \frac{T_l(\zeta)}{(\omega - k v_{\parallel})^2} \quad (69)$$

where

$$T_l(\zeta) \equiv \frac{\zeta^2}{2\pi} \int_0^{2\pi} d\phi \int_0^{\infty} dz \exp(-z) \frac{J_l^2(b_1)}{(z + \zeta)^2} \quad (70)$$

$$\zeta \equiv \frac{\gamma_0^2 m_e^2}{\Delta P^2} \left(\frac{\omega^2}{k^2} - v_{\parallel}^2 \right) \quad (71)$$

and we write that

$$b_1 = \frac{\omega}{k_w v_{\parallel}} \frac{v_w}{v_{\parallel}} \frac{\Delta P}{p_{\parallel}} z^{1/2} \cos \phi. \quad (72)$$

If we now select a specific harmonic (i.e., for fixed l and m), then the coupled mode equations may be written as

$$\begin{aligned} & \left[(\omega - k_{n+l+2m} v_{\parallel})^2 - \frac{\omega_b^2}{\gamma_0 \gamma_{\parallel}^2} T_l(\zeta_{n+l+2m}) \right] \delta \hat{\varphi}_n J_m(b_2) \\ & \equiv - \frac{\omega_b^2}{\gamma_0 k_n} \frac{v_w}{2c} \delta \hat{A}_{n-1} T_l(\zeta_{n+l+2m}) \left(k_{n+l+2m} - \omega \frac{v_{\parallel}}{c^2} \right) \\ & \cdot [J_m(b_2) - J_{m+1}(b_2)] \end{aligned} \quad (73)$$

and

$$\begin{aligned} & \left[\omega^2 - c^2 k_{n-1}^2 - \frac{\omega_b^2}{\gamma_0} \left(1 - \frac{v_w^2}{4c^2} K_m^{(+)}(b_2) \right. \right. \\ & \cdot \left. \left. \frac{\omega^2 - k_{n+l+2m}^2 c^2}{(\omega - k_{n+l+2m} v_{\parallel})^2} T_l(\zeta_{n+l+2m}) \right) \right] \delta \hat{A}_{n-1} \\ & \equiv - \frac{\omega_b^2}{2\gamma_0} \frac{k_n v_w}{(\omega - k_{n+l+2m} v_{\parallel})^2} \delta \hat{\varphi}_n T_l(\zeta_{n+l+2m}) \\ & \times \left(k_{n+l+2m} - \omega \frac{v_{\parallel}}{c^2} \right) J_m(b_2) [J_m(b_2) - J_{m+1}(b_2)] \end{aligned} \quad (74)$$

where

$$\zeta_{n+l+2m} \equiv \frac{\gamma_0^2 m_e^2}{\Delta P^2} \left(\frac{\omega^2}{k_{n+l+2m}^2} - v_{\parallel}^2 \right). \quad (75)$$

The dispersion equation is found by requiring that the determinant of the coefficients vanishes. Therefore, for a specific choice of harmonic interaction, the dispersion

equation which results is expressed as a straightforward generalization of that found in the cold beam limit: specifically

$$\begin{aligned} & \left[(\omega - k_{n+l+2m} v_{\parallel})^2 - \frac{\omega_b^2}{\gamma_0 \gamma_{\parallel}^2} T_l(\zeta_{n+l+2m}) \right] \\ & \cdot \left(\omega^2 - c^2 k_{n-1}^2 - \frac{\omega_b^2}{\gamma_0} \right) \\ & \equiv - \frac{v_w^2}{4c^2} \frac{\omega_b^2}{\gamma_0} K_m^{(+)}(b_2) T_l(\zeta_{n+l+2m}) \\ & \cdot \left(\omega^2 - c^2 k_{n+l+2m}^2 - \frac{\omega_b^2}{\gamma_0} T_l(\zeta_{n+l+2m}) \right). \end{aligned} \quad (76)$$

This dispersion equation which includes the effect of an axial energy spread for a planar configuration is similar to that found for the corresponding case for a helical wiggler geometry. The differences are as stated previously in that 1) the wiggler amplitude is replaced by the root-mean-square (rms) value, 2) the oscillation in the axial velocity introduces modifications in $K_m^{(\pm)}(b_2)$ and $J_l^2(b_1)$, and 3) harmonic amplification is found in the one-dimensional formulation. The effect of the pitch-angle spread on the axial velocity is the source of the l th harmonic contribution, which has the effect of modifying the thermal function T_l . In order to describe this effect in more detail, we assume that $b_1 \ll 1$ which is valid as long as $P_{\perp} \ll p_{\parallel}$. As a result, we expand

$$J_l(b_1) \equiv \frac{1}{(l!)^2} \left(\frac{v_w}{2v_{\parallel}} \right)^{2l} \left(\frac{\omega}{k_w v_{\parallel}} \right)^{2l} \left(\frac{\Delta P}{p_{\parallel}} \right)^{2l} z^l \cos^{2l} \phi. \quad (77)$$

As a consequence

$$\begin{aligned} T_l(\zeta) & \equiv \frac{(2l)!}{(l!)^4} \left(\frac{v_w}{2v_{\parallel}} \right)^{2l} \left(\frac{\omega}{k_w v_{\parallel}} \right)^{2l} \left(\frac{\Delta P}{p_{\parallel}} \right)^{2l} \zeta^2 \\ & \cdot \exp(\zeta) \int_{\zeta}^{\infty} dt \frac{\exp(-t)}{t^2} (t - \zeta)^l. \end{aligned} \quad (78)$$

As in the case of the helical wiggler, the thermal function may be expressed in terms of the exponential integral function. To this end we observe that

$$\begin{aligned} & \zeta^2 \exp(\zeta) \int_{\zeta}^{\infty} dt \frac{\exp(-t)}{t^2} (t - \zeta)^l \\ & = (-1)^l \zeta^{l+1} [1 - (\zeta + l) \\ & \cdot \exp(\zeta) E_1(\zeta)] + U_l(\zeta) \end{aligned} \quad (79)$$

where

$$\begin{aligned} U_l(\zeta) & \equiv 0, & l < 2 \\ & \sum_{k=2}^l \sum_{n=0}^{k-2} \frac{(-1)^{k-n} l! n! \zeta^{l-n}}{k! (l-k)! (k-2-n)!}, & l \geq 2. \end{aligned} \quad (80)$$

As a consequence

$$T_l(\zeta) \equiv \frac{(2l)!}{(l!)^4} \left(\frac{v_w}{2v_0} \right)^{2l} \left(\frac{\omega}{k_w v_0} \right)^{2l} \left(\frac{\Delta P}{p_0} \right)^{2l} \cdot \{(-1)^l \zeta^{l+1} [1 - (\zeta + l)] \cdot \exp(\zeta) E_l(\zeta) + U_l(\zeta)\}. \quad (81)$$

We observe that for $l = 0$ the planar wiggler thermal function reduces to that found for the helical wiggler (43), i.e.,

$$T_0(\zeta) \equiv \zeta [1 - \zeta \exp(\zeta) E_1(\zeta)]. \quad (82)$$

This will reproduce a thermal response for the interaction at the fundamental which is similar to that found for the helical geometry

The general dispersion equation (76) has been solved numerically for a case which illustrates the relative growth of the fundamental and the third harmonic. In general, strong harmonic amplification requires a relatively large oscillation in the axial velocity; hence, the growth rate at the harmonics increases rapidly with $\Omega_w/c k_w$. Indeed, the growth rate at the harmonics as predicted by (76) can be larger than that at the fundamental when $\Omega_w/c k_w$ exceeds unity. However, this is an unjustifiable conclusion based upon the present type of formulation. It is important to bear in mind that the analysis cannot be applied for arbitrarily large values of this parameter because 1) the idealized one-dimensional model breaks down when the displacement of the electrons from the plane of symmetry becomes large, and 2) the Lagrangian time coordinate (14) has been integrated in (59) under the assumption that $v_w \ll v_0$. Therefore, the analysis of cases in which $\Omega_w/c k_w$ is greater than unity requires a fully three-dimensional analysis. We restrict the numerical analysis herein to the case for which $\Omega_w/c k_w = 1$. This is a physically interesting case which is at the fringe of the range of validity of the formulation, and will serve to clearly illustrate the relationship of the harmonics to the fundamental. In addition, we shall assume that $\gamma_0 = 2.957$ and $\omega_b/c k_w = 0.1$ as well. It should also be remarked that in order for the thermal effects to result in substantial growth at the even harmonics, $\Delta P/p_0$ must be of the order of unity as well. Since this is unreasonably high for any well-designed experiment, we shall ignore this effect henceforth, and concentrate on the emission at the odd harmonics.

The magnitude of the growth rate is plotted as a function of frequency in Fig. 3 for the fundamental and the third harmonic. The fundamental exhibits a peak growth rate of $|\text{Im } k|/k_w \approx 0.065$ at a normalized frequency of $\omega/c k_w \approx 1.55$. In contrast, the magnitude of the growth rate at the third harmonic is $|\text{Im } k|/k_w \approx 0.012$ at a frequency of $\omega/c k_w \approx 4.80$. Observe that both the magnitude and bandwidth of the harmonic is reduced relative to the fundamental.

The effect of the thermal spread on the fundamental and the third harmonic is shown in Fig. 4. Here we plot the normalized growth rate (defined as the ratio of the maxi-

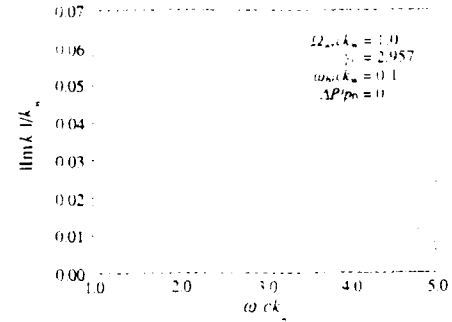


Fig. 3. Graph of the growth rate versus frequency for the fundamental and third harmonic interactions.

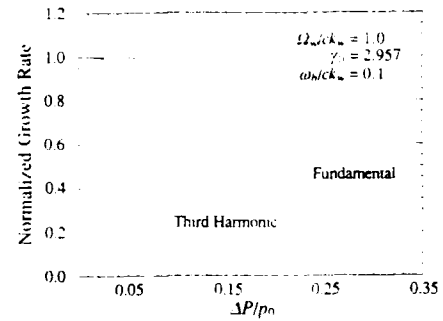


Fig. 4. Variation of the normalized growth rates at the fundamental and third harmonic with the axial momentum spread.

imum growth rate for a specific value of $\Delta P/p_0$ to the maximum growth rate for $\Delta P/p_0 = 0$) as a function of $\Delta P/p_0$ for the fundamental and third harmonic. Observe that thermal effects are expected to become important on the fundamental when $\Delta v_0/v_0 \approx |\text{Im } k|/(k_w + \text{Re } k) \approx 0.025$, which corresponds to $\Delta P/p_0 \approx 22\%$ (recall that $\Delta v_0/v_0 \approx \Delta P^2/2p_0^2$). This is in substantial agreement with the results shown in the figure. For the case of the harmonics, thermal effects are expected to become important at a much reduced thermal spread [7], [10]; specifically, when $\Delta v_0/v_0 \approx |\text{Im } k|/[(1 + 2m)k_w + \text{Re } k]$. For the third harmonic in the present example $\Delta v_0/v_0 \approx |\text{Im } k|/(3k_w + \text{Re } k) \approx 0.0015$. This corresponds to $\Delta P/p_0 \approx 5.5\%$, which is also in good agreement with the calculation.

VI. SUMMARY AND DISCUSSION

In this paper, we have developed a self-consistent formulation of the linear gain in both helical and planar wiggler configurations in the presence of an axial energy spread derived from a beam pitch-angle spread. Such a beam may be thought of as monoenergetic but with a non-vanishing emittance. The analysis included collective Raman effects for both the helical and planar wiggler systems, and described the gain at harmonics in the case of a planar wiggler. General dispersion equations were derived, and solved numerically, for each wiggler configuration which included a general thermal function which described the effect of the pitch-angle spread.

The conclusions from the analysis are consistent with those found previously on the basis of an analytic model of thermal effects due to an energy spread [7] and a nonlinear simulation using the pitch-angle spread model [13], [14]. Specifically, that the gain at the harmonics is more sensitive to the effects of a thermal spread than is the fundamental. In particular, the thermal effect becomes important when $\Delta v/v_0 \approx |\text{Im } k|/(1 + 2m)k_w + \text{Re } k|$. In addition, it is clear that the thermal effect itself can give rise to amplification at the even as well as odd harmonics. However, this process requires a large energy spread which will result in relatively low growth rates, and is not likely to be of practical use.

REFERENCES

- [1] B. Girard, Y. Lapierre, J. M. Ortega, C. Bazin, M. Billardon, P. Ellaume, M. Bergher, M. Velghe, and Y. Petroff, "Optical frequency multiplication by an optical klystron," *Phys. Rev. Lett.*, vol. 53, pp. 2405-2408, 1984.
- [2] S. V. Benson and J. M. J. Madey, "Demonstration of harmonic lasing in a free electron laser," in *Proc., Int. Conf. Lasers '88*, R. C. Sze and F. J. Duarte, Eds., McLean, VA: STS Press, 1989, pp. 189-195.
- [3] D. J. Bamford and D. A. G. Deacon, "Measurement of the coherent harmonic emission from a free electron laser oscillator," *Phys. Rev. Lett.*, vol. 62, pp. 1106-1109, 1989.
- [4] S. V. Benson and J. M. J. Madey, "Demonstration of harmonic lasing in a free electron laser," *Phys. Rev. A*, vol. 39, pp. 1579-1581, 1989.
- [5] R. W. Warren, L. C. Haynes, D. W. Feldman, W. E. Stein, and S. J. Gitomer, "Lasing on the third harmonic," *Nucl. Instrum. Methods*, vol. A296, pp. 84-88, 1990.
- [6] W. B. Colson, "The nonlinear wave equation for higher harmonics in free-electron lasers," *IEEE J. Quantum Electron.*, vol. QE-17, pp. 1417-1426, 1981.
- [7] R. C. Davidson and W. A. McMullin, "Intense free electron laser harmonic generation in a longitudinal magnetic wiggler," *Phys. Fluids*, vol. 26, pp. 840-847, 1983.
- [8] W. B. Colson, G. Dattoli, and F. Ciocci, "Angular-gain spectrum of free-electron lasers," *Phys. Rev. A*, vol. 31, pp. 828-842, 1985.
- [9] R. C. Davidson, "Kinetic description of harmonic instabilities in a planar wiggler free electron laser," *Phys. Fluids*, vol. 29, pp. 267-274, 1986.
- [10] A. K. Ganguly and H. P. Freund, "Nonlinear analysis of free-electron laser amplifiers in three-dimensions," *Phys. Rev. A*, vol. 32, pp. 2275-2286, 1985.
- [11] M. J. Schmitt and C. J. Elliot, "Even-harmonic generation in free electron lasers," *Phys. Rev. A*, vol. 34, pp. 4843-4850, 1986.
- [12] H. P. Freund, C. L. Chang, and H. Bluem, "Harmonic generation in free electron lasers," *Phys. Rev. A*, vol. 36, pp. 3218-3221, 1987.
- [13] M. J. Schmitt and C. J. Elliot, "The effects of harmonic wiggler field components on free electron laser operation," *IEEE J. Quantum Electron.*, vol. QE-23, pp. 1552-1557, 1987.
- [14] H. Bluem, H. P. Freund, and C. L. Chang, "Harmonic content in a planar wiggler based free electron laser amplifier," *Nucl. Instrum. Methods*, vol. A272, pp. 579-585, 1988.
- [15] M. J. Schmitt, C. J. Elliot, and B. E. Newman, "Harmonic power implications on free electron laser mirror design," *Nucl. Instrum. Methods*, vol. A272, pp. 586-589, 1988.
- [16] H. P. Freund, H. Bluem, and C. L. Chang, "Nonlinear theory and design of a harmonic ubitron-free electron laser," *Nucl. Instrum. Methods*, vol. A285, pp. 169-175, 1989.
- [17] E. Jerby and A. Gover, "Investigation of the gain regimes and gain parameters of the free electron laser dispersion equation," *IEEE J. Quantum Electron.*, vol. QE-21, pp. 1041-1058, 1985.
- [18] C. W. Roberson, Y. Y. Lau, and H. P. Freund, "Emittance, brightness, free electron laser beam quality, and the scaled thermal velocity," in *High-Brightness Accelerators*, A. K. Hyder, M. F. Rose, and A. H. Guenter, Eds., New York: Plenum, 1986, pp. 627-646.
- [19] E. Jerby, "The axial-velocity distribution function and the longitudinal susceptibility of an e-beam in a planar wiggler free-electron laser," *Nucl. Instrum. Methods*, vol. A272, pp. 457-466, 1988.

H. P. Freund, photograph and biography not available at the time of publication.

R. C. Davidson, photograph and biography not available at the time of publication.

D. A. Kirkpatrick, photograph and biography not available at the time of publication.

Analysis of field emission from three-dimensional structures

D. A. Kirkpatrick, A. Mankofsky, and K. T. Tsang
Science Applications International Corporation, McLean, Virginia 22102

(Received 27 December 1991; accepted for publication 18 February 1992)

An analysis of the field emission from emitter tips with the geometry of a prolate ellipsoid of revolution indicates that the field enhancement factor, β , and effective emission area, α , are not constant but instead depend on the applied field. The added complexity of a materials related limit on the minimum time for transition of an electron from the solid into the vacuum is also examined in the analysis. The calculated variations of α and β are as large as 35%, and in some instances could result in erroneous interpretation of measured current-voltage (I - V) characteristic data.

The quantum-field emission of electrons from sharp points immersed in a strong electric field is a well-known process, and devices based on vacuum field emission are found throughout the sciences.¹ More recently, large arrays of vacuum field emission tips have been developed in the field of vacuum microelectronics, potentially leading to low voltage high efficiency rf sources,² high beam brightness cathode materials,³ and a myriad of other applications. Many advances in fabrication technology have led to the capability to fabricate arrays of microscopic tips several microns tall and with final tip radii of curvature in the range of 1–10 nm.

The analysis of the emission characteristics of these highly sharpened tips continues to be based on the theoretical work of Fowler and Nordheim.⁴ That calculation assumes a one-dimensional problem where all quantities vary only with the distance from the emission surface or their depth within it, and also assumes that the state from which an electron is emitted is instantaneously refilled. Furthermore, the typical extension of the Fowler-Nordheim theory that is used to analyze the current-voltage (I - V) characteristics of arrays of sharp tips assumes that the field enhancement factor, β , and the tip emission area, α , are constant and independent of the applied field E . The analysis in this letter demonstrates that the parameters α and β are not constants, and that when a simple account of realistic material properties is included, the variation of α and β can be pronounced for sharp tips operating at currents of 1–100 μ A.

The typical technique^{5–9} employed to characterize an array of field emitting tips is to measure the I - V characteristic of the array and from that data to deduce the field enhancement factor, β , and an effective emission area, α , of the array in operation. This procedure is based on the assumption that the local tip current density is governed by quantum-field emission as derived by Fowler and Nordheim,

$$J_{\text{FN}} = \frac{A(\beta E)^2}{\phi r^2(y)} \exp \left(-B \frac{\phi^{3/2} v(y)}{\beta E} \right) \text{A/cm}^2 \quad (1)$$

where J_{FN} is the local current density, $A = 1.54 \times 10^{-6}$, $B = 6.87 \times 10^7$, $y = 3.79 \times 10^{-4}[(\beta E)^{1/2}/\phi]$, $r^2(y) \approx 1.1$, $v(y) \approx 0.95 - y^2$, E is the applied electric field in V/cm, β

is the field enhancement factor due to local geometry, and ϕ is the work function in eV of the surface emission material. Precise values for $r^2(y)$ and $v(y)$ are tabulated in the literature.^{10,11} The next step in this process is the assertion that $I = J_{\text{FN}}\alpha$. With this, a plot of $\ln(I/V^2)$ against $1/V$ will be well fit by a straight line, and the slope and intercept of this line can be used to find α and β of the tips in the array. The measured β is used to infer a weighted average for the radius of curvature of those tips participating in the emission process. Similarly, the value for α is used to infer an average emitting area per tip in the array. An additional assumption, often made,¹² is that the emitting area per tip is of the order of πR_c^2 , where R_c is the inferred radius of curvature of the operating tips. A gross discrepancy is often found^{8,13} between the value for R_c inferred from α and that from β . This discrepancy has been resolved typically by postulating either that only a few of the tips in the array are participating in the emission, or that the emission emanates from isolated surface protrusions or dielectric inclusions on the tip surface.

While both of these deficiencies may be present in the field-emitter array, the analysis just described does not address the variation in field enhancement factor over the surface of a tip, nor the consequences this has for the variation in the profile of the emitted current density. Because the local emitted current density must vary from its peak value at some region near the apex, to essentially zero at other regions still close to the apex, the assumption that β is constant over the region of emission is clearly in error. More precisely, the error lies in the assumption that β for the tip as an emitting region is the same as the value for β_0 at the apex of the tip. The value for β obtained from the analysis of the data from a single tip represents a local current weighted average over the tip surface,

$$\langle \beta \rangle = \frac{1}{I_{\text{tip}}} \int_S \beta(\mathbf{x}) J_{\text{FN}}(\mathbf{x}) dS. \quad (2)$$

In the case of an array of many tips, this average must be extended over the entire array.

For a prolate half ellipsoid of revolution on a flat surface immersed in a paraxial electric field (see Fig. 1), Kosmahl¹⁴ has calculated the potential to be

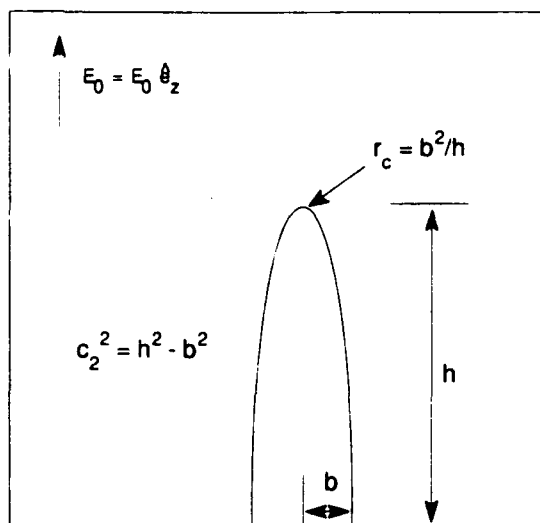


FIG. 1. The geometry of the prolate ellipsoid of revolution that is used for these calculations.

$\Phi(\eta, \xi)$

$$= -E_0 c_2 \xi \eta \left[1 - \left(\ln \frac{\eta + 1}{\eta - 1} - \frac{2}{\eta} \ln \frac{\eta_0 + 1}{\eta_0 - 1} - \frac{2}{\eta_0} \right) \right] \quad (3)$$

where η and $\xi = \cos \phi$ are the ellipsoidal coordinates given by

$$z = c_2 \xi \eta, \quad (4)$$

$$\frac{r^2}{c_2^2(\eta^2 - 1)} + \frac{z^2}{c_2^2 \eta^2} = 1, \quad (5)$$

$c_2 = \sqrt{h^2 - b^2}$, h is the ellipsoid semi-major axis and the height of the tip, b is the ellipsoid semi-minor axis, E_0 is the uniform applied field far from the ellipsoid surface, and $\eta = \eta_0 = h/c_2$ prescribes the surface of the ellipsoid. The radius of curvature at the apex of the ellipsoid is equal to $r_c = b^2/h$. The field at the surface of the ellipsoid is found from

$$E(\eta, \xi) = -\frac{1}{c^2} \sqrt{\frac{\eta^2 - 1}{\eta^2 - \xi^2}} \frac{\partial \Phi}{\partial \eta} \quad (6)$$

evaluated at $\eta = \eta_0$. Applied to the previous equation this gives,

$$E(\eta_0, \xi) = \beta_0 E_0 \xi \sqrt{\frac{\eta_0^2 - 1}{\eta_0^2 - \xi^2}} \quad (7)$$

where

$$\beta_0 = \frac{2}{\eta_0(\eta_0^2 - 1)} \frac{1}{\ln \left(\frac{\eta_0 + 1}{\eta_0 - 1} \right) - \frac{2}{\eta_0}} \quad (8)$$

is the magnitude of the field enhancement factor at the apex of the tip. The element of area, dS , on the surface of the ellipsoid $\eta = \eta_0$ is given by

$$dS = 2\pi c_2^2 (\eta_0^2 - \xi^2) d\xi. \quad (9)$$

The tip average field enhancement factor $\langle \beta \rangle$, and the tip current, I_{tip} , are therefore given by,

$$\langle \beta \rangle = \frac{1}{I_{\text{tip}}} \beta_0 \int 2\pi c_2^2 \xi \sqrt{(\eta_0^2 - 1)(\eta_0^2 - \xi^2)} J_{\text{FN}}[\beta(\xi)] d\xi, \quad (10)$$

$$I_{\text{tip}} = \int 2\pi c_2^2 (\eta_0^2 - \xi^2) J_{\text{FN}}[\beta(\xi)] d\xi. \quad (11)$$

The nonconstant nature of α and $\langle \beta \rangle$ are evident from inspection of these equations. For small values of the applied field, only a very small region near the apex of the tip emits any appreciable current, and the value for $\langle \beta \rangle$ will be very close to the value of β_0 . Similarly, the actual emitting area will be quite small. In order to be consistent, an appropriate definition for the emitting area is

$$\alpha_1 = I_{\text{tip}} / J_{\text{FN}}(\langle \beta \rangle) \quad (12)$$

where the notation α_1 is used to distinguish the quantity from that derived from an I - V characteristic.

A final point in the present analysis is a basic attempt to account for some simple materials issues that must be dealt with when dealing with very sharp tips and significant tip currents ($I_{\text{tips}} \sim 1$ – $100 \mu\text{A}$). The calculation of J_{FN} assumes a certain density of electron states at the Fermi level of the tip material, and calculates a transition probability per unit time for the tunneling of such a bound electron to a vacuum state outside the tip material. Once such an electron is emitted, subsequent emission must either await the repopulation of the original state or must occur from other, perhaps more tightly bound energy levels. For sharp tips and high fields, the local values of J_{FN} can easily be greater than 10^8 A/cm^2 while the integrated tip current I_{tip} is only 1 – $100 \mu\text{A}$. Thermal issues aside, a local current density of 10^8 A/cm^2 corresponds to the emission of an electron per 1 nm^2 every 160 fs , while 10^{10} A/cm^2 corresponds to an electron every 1.6 fs . Emission from energy levels that are more bound than the Fermi level is strongly attenuated, as can be seen by the dependence of J_{FN} on the work function, ϕ . The potential effect of this depletion can be considered by forcing a fixed, minimum time interval for the repopulation of an emitted state, Δt_{xtal} . The time interval between successive emission events is then $\Delta t = \Delta t_{\text{xtal}} + \Delta t_{\text{F1}}$. In terms of the local current density such a limit takes the form

$$(1/J_{\text{eff}}) = (1/J_{\text{max}}) + (1/J_{\text{FN}}) \quad (13)$$

where J_{max} is some value associated with the properties of the emitter material. With this modification to the local current density, the quantities $\langle \beta \rangle$, I_{tip} , and α_1 become

$$\langle \beta \rangle = \frac{1}{I_{\text{tip}}} \beta \int 2\pi c_2^2 \xi \sqrt{(\eta_0^2 - 1)(\eta_0^2 - \xi^2)} J_{\text{eff}}[\beta(\xi)] d\xi, \quad (14)$$

$$I_{\text{tip}} = \int 2\pi c_2^2 (\eta_0^2 - \xi^2) J_{\text{eff}}[\beta(\xi)] d\xi. \quad (15)$$

$$\alpha_1 = I_{\text{tip}} / J_{\text{eff}}(\langle \beta \rangle). \quad (16)$$

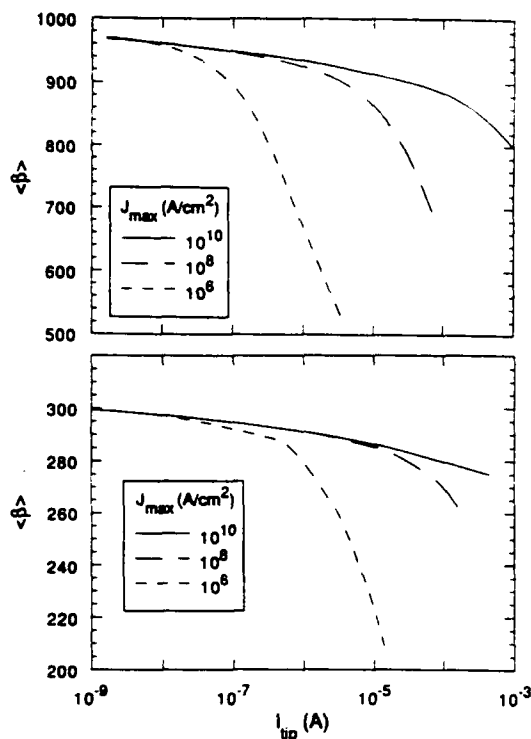


FIG. 2. $\langle \beta \rangle$ parametrized vs I_{tip} for $J_{\text{max}} = 10^{10}$, 10^8 , and 10^6 A/cm². The independent variable is the applied field E_0 , which varies over a range of 50–350 kV/cm. The tip height in both cases is $h = 10 \mu\text{m}$. The tip radius of curvature in the upper plot is $r_c = 25 \text{ \AA}$, while in the lower plot $r_c = 100 \text{ \AA}$. Note that the indexing of the vertical axes does not start at $\langle \beta \rangle = 0$.

The results of this analysis are shown in Figs. 2 and 3, where $\langle \beta \rangle$ and α_1 are plotted against I_{tip} for $J_{\text{max}} = 10^6$, 10^8 , and 10^{10} A/cm². The work function used in these calculations is $\phi = 5 \text{ eV}$. While the falloff in $\langle \beta \rangle$ is noticeable in the case of $r_c = 100 \text{ \AA}$, it is quite pronounced for $r_c = 25 \text{ \AA}$. For the case of $J_{\text{max}} = 10^8 \text{ A/cm}^2$, the falloff in $\langle \beta \rangle$ from its peak value to its value at $I_{\text{tip}} = 100 \mu\text{A}$ is about 10% in the case of $r_c = 100 \text{ \AA}$, while it is about 35%

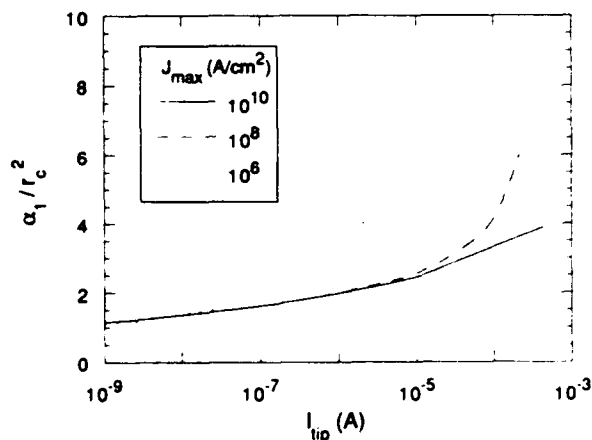


FIG. 3. α_1/r_c^2 parameterized vs I_{tip} for $J_{\text{max}} = 10^{10}$, 10^8 , and 10^6 A/cm^2 , and $r_c = 100 \text{ \AA}$. The independent variable is the applied field E_0 , which varies over a range of 100–350 kV/cm. Note that α_1/r_c^2 is not constant, is not equal to π , and is increasing while $\langle \beta \rangle$ is decreasing. This is true even for $J_{\text{max}} = 10^{10} \text{ A/cm}^2$, where $J_{\text{eff}} = J_{\text{FN}}$ to within $< 1\%$.

in the case of $r_c = 25 \text{ \AA}$. Even with minimal influence from $J_{\text{max}} = 10^{10} \text{ A/cm}^2$ the value of $\langle \beta \rangle$ decreases by 10% in the case of $r_c = 25 \text{ \AA}$. Perhaps more pronounced is the variation of α_1 shown in Fig. 3 for $r_c = 100 \text{ \AA}$. As can be seen in the figure, the source of the decrease in the value of $\langle \beta \rangle$ is the activation of more of the tip area, and correspondingly increasing the contribution to $\langle \beta \rangle$ from points farther away from the tip apex.

Yet, an analysis of the I - V characteristic for this same data would incorrectly suggest a decrease in the participating emission area and an increase in the average field enhancement factor of those tips contributing a phenomenon more commonly termed "current hogging." The Fowler-Nordheim I - V characteristic [$\ln(I/E^2)$ vs $1/E$] of the tip emission when J_{max} has an appreciable effect evidences a flatter slope for higher fields and tip currents, due to the saturation of some areas on the tip. The usual analysis of this data would indicate both an increase in the average field enhancement factor and a decrease in the emission area, when in fact exactly the opposite is occurring.

In conclusion, the operation of sharp tips as vacuum field emission electron sources is necessarily a dynamic process, with the tip field enhancement factor and effective tip emission area both being functions of the applied electric field. This dynamic behavior is due to the nature of the tip as a distributed area with varying local field enhancement as a function of position on the tip. If a limit to the maximum local emission density is imposed, the variation of $\langle \beta \rangle$ and α_1 can be large. The variation increases substantially for tips with radii of curvature less than 100 \AA . These results have their greatest effect on those applications that have sought the use of sharp tips ($r_c < 100 \text{ \AA}$), at large currents ($I_{\text{tip}} > 10 \mu\text{A}$), and in particular those that depend on the assumed dynamic behavior of a field-emitter array in an amplifier configuration.

This work was supported by the Defense Advanced Research Projects Agency.

¹D. Rugar and P. Hansma, *Physics Today* **43**, 23 (1990).

²A. K. Ganguly, P. M. Phillips, and H. F. Gray, *J. Appl. Phys.* **67**, 7098 (1990).

³D. A. Kirkpatrick, G. L. Bergeron, M. A. Czarnaski, R. C. Davidson, H. P. Freund, J. J. Hickman, A. Mankofsky, K. T. Tsang, J. M. Schnur, M. Levinson, and B. M. Ditchek, *Nucl. Instrum. Methods A* (1991) (accepted for publication).

⁴R. H. Fowler and L. Nordheim, *Proc. R. Soc. London A* **119**, 173 (1928).

⁵D. Alpert, D. A. Lee, E. M. Lyman, and H. E. Tomaschke, *J. Vac. Sci. Technol.* **1**, 35 (1964).

⁶H. Tomaschke and D. Alpert, *J. Appl. Phys.* **38**, 881 (1967).

⁷G. A. Farral, *J. Appl. Phys.* **41**, 563 (1970).

⁸C. A. Spindt, I. Brodie, L. Humphrey, and E. R. Westerberg, *J. Appl. Phys.* **47**, 5248 (1976).

⁹G. A. Farral, in *Vacuum Arcs, Theory and Application*, edited by J. M. Lafferty (Wiley, New York, 1980), Ch. 2.

¹⁰H. C. Miller, *J. Franklin Inst.* **282**, 382 (1966).

¹¹H. C. Miller, *J. Franklin Inst.* **287**, 347 (1969).

¹²H. G. Kosmahl, *IEEE Trans. Elec. Dev.* **36**, 2728 (1989).

¹³D. F. Howell, R. D. Groves, R. A. Lee, C. Patel, and H. A. Williams, *Technical Digest of the International Electron Devices Meeting, Washington, D.C.* (IEEE, Piscataway, NJ, 1989), p. 525.

¹⁴H. G. Kosmahl, *IEEE Trans. Electron Devices* **38**, 1534 (1991).

Demonstration of vacuum field emission from a self-assembling biomolecular microstructure composite

D. A. Kirkpatrick, G. L. Bergeron, M. A. Czarnaski, and J. J. Hickman
Science Applications International Corporation, 1710 Goodridge Drive, MS 2-3-1, McLean, Virginia 22102

G. M. Chow,^{a)} R. Price, B. L. Ratna,^{b)} P. E. Schoen,
W. B. Stockton, S. Baral,^{a)} A. C. Ting,^{c)} and J. M. Schnur
Center for Biomolecular Science and Engineering, Code 6090, Naval Research Laboratory, Washington, DC 20375-5000

(Received 18 December 1991; accepted for publication 3 February 1992)

We report the first demonstration of vacuum field emission from an electron source fabricated from self-assembling biomolecular composite microstructures. Diacetylenic lipid DC_{8,9}PC is used to form hollow, 0.5 μm diam, > 50 μm long, tubelike structures that are subsequently plated with metal and formed into an aligned composite in an epoxy matrix. The composite material is thin-sectioned across the axis of alignment and then etched to expose the plated tubules. The sharp edges of the exposed metal tubules produce a very large local electric field enhancement, allowing for the vacuum field emission of significant current densities at relatively low applied macroscopic fields (<60–80 kV/cm).

In this letter we present the initial demonstration of vacuum field emission from a cathode fabricated from self-assembling biomolecular microstructure composites. The array of shapes and sizes of biomolecular microstructures available for incorporation into physical systems is extremely diverse and potentially very useful.¹ In the field emission arrays described here, the surface micromorphology is produced by using biologically derived hollow cylinders, called tubules,^{2,3} as templates for metal deposition, and then forming an aligned composite of these metal microstructures.^{4–6} The diversity of biomolecular microstructures, particularly the biotechnology for using them as templates for the deposition of a variety of materials, has broad interest from the standpoint of electron beam source materials, control and detection of electromagnetic radiation, controlled release mechanisms, and microelectronics. The structures we discuss here may provide a means to achieve electron beam brightness in excess of 10^6 A/cm² rad² from an ungated field emission cathode.

The generation of macroscopic electron beam currents through vacuum field emission from a large number of emission sites requires a surface with a complex microstructure. To date, the fabrication of surfaces suitable to this task has been dominated by microlithographic techniques^{7–10} that employ a nearby gate electrode. In these processes, masks are used in conjunction with etching or deposition techniques to produce arrays of μm scale cones or wedges recessed only a few μm from an aperture in a gate structure. The microstructure composite cathode materials described here do not use such an electrode configuration, and are similar in this respect to more conventional electron source materials. The structure of an array of microscopic hollow cylinders protruding a uniform distance from a base electrode has not been investigated with other fabrication techniques, and may be preferred over an

array of pyramids or cones because of the generated field structure and the larger available emission area.

The cathode structure considered in this letter is made possible by the recent discovery of micron size scale tubules.^{2,5} The tubules are hollow, have typical dimensions of 0.5 μm diam and lengths from 50 to over 200 μm . They can be electrolessly plated with a variety of metals, including copper, nickel, gold, iron, cobalt, and permalloy.¹¹ The coating covers both the inside and outside surfaces of the tubules, including the ends. Tubules coated with ferromagnetic metals can be aligned in an external magnetic field, allowing the fabrication of composites of aligned tubules in a host matrix.

The process of quantum field emission from a one-dimensional cold-cathode system is described by the Fowler–Nordheim¹² field emission current density

$$J_{\text{FN}} = \frac{A(\beta E)^2}{\phi r^2(y)} \exp\left(-B \frac{\phi^{3/2} v(y)}{\beta E}\right) \text{ A/cm}^2, \quad (1)$$

where $A = 1.54 \times 10^{-6}$, $B = 6.87 \times 10^7$, $y = 3.79 \times 10^{-4} [(\beta E)^{1/2}/\phi]$, $r^2(y) \approx 1.1$, $v(y) \approx 0.95 - y^2$, E is the applied electric field in V/cm, β is the field enhancement factor due to local geometry, and ϕ is the work function in eV of the surface emission material. Precise values for $r^2(y)$ and $v(y)$ are tabulated in the literature.^{13,14} This type of emission is very sensitive to the local electric field, βE . For $\beta E = 100$ MV/cm and a work function of 5.1 eV, $J_{\text{FN}} = 3.90 \times 10^8$ A/cm². For $\beta E = 30$ MV/cm, J_{FN} is reduced to 1.17 A/cm². The current density available from this type of cathode is clearly dependent on the local electric field at the emission site. Achieving steady-state fields on the order of 10^8 V/cm is not possible without the use of structures that significantly enhance the local electric field.

The necessary local enhancement of the applied electric field is produced by the geometry of the exposed tubules: their height, inner radius, and outer radius, the average spacing between nearest neighbors, the radius of curvature of the metal wall at the edge of the exposed

^{a)}Geo-Centers Inc., Newton Center, MA 02159.

^{b)}Georgetown University, Washington, DC.

^{c)}Beam Physics Branch, Code 4790, Naval Research Laboratory.

hollow cylinder, and the character of the surface in the vicinity of the exposed edge. Detailed numerical simulations¹⁵ of the electrostatic field in the vicinity of the hollow cylindrical structure have shown that field enhancement factors in the range $\beta = 150$ –250 are readily achieved with the $0.5\text{ }\mu\text{m}$ diam tubules protruding a height $h = 10$ – $15\text{ }\mu\text{m}$ above the base surface. The intrinsic surface roughness of the electrolessly deposited metal film that makes up the outer tubule surface would probably increase this nominal enhancement factor by an additional factor of 2–4, yielding an expected range in the enhancement factor of $\beta = 300$ –1000.

The measurements reported here use tubules that are self-assembled from the diacetylenic lipid 1,2-bis (10,12 tricosadiynoyl)-sn-glycero-3-phosphocoline ($\text{DC}_{8,9}\text{PC}$).¹⁶ Following formation the tubules are catalyzed with a commercial Pd/Sn catalyst, and then electrolessly plated with Ni. The Ni-coated tubules are dispersed in low-viscosity epoxy Epon 815/Ancamide 507B and aligned in a $\sim 500\text{ G}$ magnetic field. Following polymerization, the composite is cut across its alignment axis into thin $50\text{ }\mu\text{m}$ slices using a microtome. The thin section of tubules and epoxy is etched in an oxygen plasma on one side to a depth of $\sim 5\text{ }\mu\text{m}$. The oxygen plasma etching procedure selectively removes the epoxy but not the metal tubule structures (however, the metal tubules are oxidized). This etched surface is then coated with a $\sim 0.01\text{ }\mu\text{m}$ coating of gold, followed by a 1 – $5\text{ }\mu\text{m}$ coating of silver. The silver and gold coated face of the section is soldered to a copper stub with a low-temperature indium alloy solder (Indalloy). Next, the exposed epoxy face of the section is oxygen plasma etched to expose the embedded tubule microstructures to a height of $\sim 15\text{ }\mu\text{m}$. A $500\text{ }\text{\AA}$ coating of gold is sputter deposited over the resultant structure, which is used as a template. This final gold coating acts as both the emission surface and the electrical contact to the protruding microstructures. A scanning-electron micrograph of a finished emitter microstructure is shown in Fig. 1.

The measurements are taken by placing the resultant cathode, mounted on its copper stub, into a cylindrical hole centered in an anodized aluminum cathode holder. The exposed surface of the cathode holder is anodized to prevent unwanted emission from the aluminum surface, while the sides of the cylindrical hole are left uncoated to facilitate good electrical and thermal contact with the aluminum cathode holder. The entire cathode assembly is mounted in a cathode test stand, opposite a 3 mm diameter OFHC copper rod that acts as an anode structure. The end of this anode rod is rounded to a full radius to reduce field enhancement in the vicinity of the anode structure. The diameter of the anode is much less than the diameter of the cathode surface in order to localize the area on the cathode surface that is subject to the large applied field, and to avoid the possibility that the measured emission would emanate from areas other than the microcomposite cathode array structure. For all these data, the vacuum pressure is in the range 1 – 7×10^{-6} Torr. The vacuum system uses a sorption pump and a cryopump to maintain a clean, oil-free environment.



Ni tubules in epoxy, plasma etched.

1 μm SEM

FIG. 1. A scanning electron micrograph of an etched tubule composite surface. The tubules project out of the host epoxy matrix a distance of approximately $2\text{ }\mu\text{m}$, and end at a sharp right angle. A cathode composite microstructure suitable for emission testing is additionally etched to expose the tubule microstructures to a depth of $\sim 10\text{ }\mu\text{m}$.

The results of several sets of measurements from two cathodes, GI2-E, and GI2-G, are shown in Fig. 2 where we plot $\ln(I/V^2)$ against $1/V$. If we define β' by $\beta'V = \beta E$, assume that $v(y) \approx 0.95 - y^2$, and let the total current I be expressed as $I = J\alpha$, then Eq. (1) can be rewritten as

$$\ln(I/V^2) = \ln\left(\alpha \frac{A\beta'^2}{\phi r^2(y)}\right) + \frac{B(3.79 \times 10^{-4})^2}{\phi^{1/2}} - \frac{0.95B\phi^{3/2}}{\beta'} \frac{1}{V}. \quad (2)$$

As can be seen from Eq. (2), an array of Fowler–

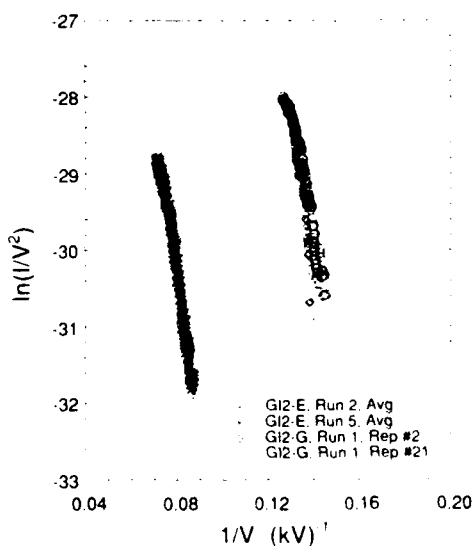


FIG. 2. A Fowler–Nordheim plot of the cathode performance for the cathodes GI2-E and GI2-G. The data shown here correspond to the data runs shown in Table I.

TABLE I. A summary of the data for the cathodes GI2-E and GI2-G. The values for β' , β , and α are calculated using a work function $\phi = 5$ eV

Test sequence	$\ln a$	b (kV)	β' (cm ⁻¹)	$\beta \approx \beta' d$	α (10 ⁻⁵ cm ⁻²)
GI2-E, Run 1, Avg.	-13.65	204	3577	429	1.06
GI2-E, Run 2, Avg.	-15.45	206	3923	471	0.0506
GI2-E, Run 5, Avg.	-10.67	245	2978	357	10.4
GI2-G, Run 1, Rep. No. 2	-2.53	199	3667	440	23 500
GI2-G, Run 1, Rep. No. 10	-7.93	156	4677	561	65.3
GI2-G, Run 1, Rep. No. 21	-9.33	146	4998	600	14.1

Nordheim quantum field emitters yields a straight-line characteristic when plotted as is shown in Fig. 2. Assuming the emission surface work function ϕ is approximately known,⁸ the slope and intercept of this plot yield β' and the apparent emission area, α . The intercept, slope, β' , β , and α obtained from the data shown in Fig. 2 are shown in Table I.

The I - V characteristic data shown in Fig. 2 are obtained by applying a sawtooth voltage waveform to the cathode test stand, and measuring the resultant circuit current. The period of the sawtooth waveform is varied between 8 and 30 s and the amplitude is varied to maintain an approximate duty cycle of 10%. All of the data shown represent measurements taken after an initial conditioning phase. This conditioning is typically comprised of cycling the cathode through an initial I - V characteristic over a period of an hour.

Both cathodes demonstrated initial emission ($I > 1$ μ A) for applied voltages $V_0 < 10$ kV, corresponding to an applied electric field of $E < 60$ –80 kV/cm. The maximum emitted currents are limited to the order of 50 μ A by reducing the amplitude of the applied sawtooth voltage waveform. As an additional check that the measured emission indeed emanates from the tubule microstructures, the tubule array was physically removed from the sample GI2-E and the now tubule-free sample reinserted in the test stand. Up to applied fields of 130 kV/cm no emission is observed. The sensitivity of this measurement is 0.3 μ A.

It has been well established that the presence of adsorbed atoms can affect the emission characteristics.¹⁷ It is also true that estimating α to within a factor of 3 requires¹⁸ a precision of $\pm 10\%$ in the measurement of β' . The tabulated values for α shown in Table I should therefore be considered only for comparison of the different cathode datasets, and not as an absolute measure. Note that using the absolute values for α yields current densities as large as 10^5 A/cm².

The values tabulated in Table I correspond to a least-squares fit to the data, where for consistency only those data occurring on the fall of the voltage waveform are selected. By comparison, the reproducibility and the scatter are poorer for the data on the rise of the voltage waveform. Due to the long timescale nature of the applied waveform ($\tau \sim 8$ –30 s) and the thermal and electrical limitations of the thin gold coating being used to make contact, this difference may be due to a variation in the temperature at the emitter tip during the application of the voltage pulse.

In conclusion, we have presented measurements of vacuum field emission from an ungated field emitter array fabricated from a composite of self-assembling biomolecular microstructures. Microstructure composite materials offer an interesting alternative to microlithographic techniques for the achievement of complex surface micromorphologies. Complex biological systems and organic molecules, in particular self-assembling biomolecular microstructures, offer a wide variety of microstructure geometries potentially useful for application in physical systems. The hollow, thin walled, high-aspect ratio tubule microstructures discussed here provide a surface micromorphology well suited to the generation of high current, high brightness electron beams. An identical structure would be difficult to generate using existing microlithographic techniques.

This work was supported by the Defense Advanced Research Projects Agency, and by the Office of Naval Technology.

- ¹ B. P. Gaber, J. M. Schnur, and D. Chapman, Eds. *Biotechnological Applications of Lipid Microstructures* (Plenum, New York, 1988).
- ² P. Yager and P. E. Schoen, *Mol. Cryst. Liq. Cryst.* **106**, 371 (1984).
- ³ P. Yager, P. E. Schoen, C. Davies, R. "rice, and A. Singh, *Biophys. J.* **48**, 899 (1985).
- ⁴ J. H. Georger, A. Singh, R. R. Price, J. M. Schnur, P. Yager, and P. Schoen, *J. Am. Chem. Soc.* **109**, 6169 (1987).
- ⁵ J. M. Schnur, R. Price, P. Schoen, P. Yager, J. M. Calvert, J. Georger, and A. Singh, *Thin Solid Films* **152**, 181 (1987).
- ⁶ F. Behrooz, M. Orman, R. Reese, W. Stockton, J. Calvert, F. Rockford, and P. Schoen, *J. Appl. Phys.* **68**, 3688 (1990).
- ⁷ C. A. Spindt, K. R. Shoulders, and L. N. Heynick, *U. S. Patents* 3 755 704 (1973), and 3 812 559 (1974).
- ⁸ C. A. Spindt, I. Brodie, L. Humphrey, and E. R. Westerberg, *J. Appl. Phys.* **47**, 5248 (1976).
- ⁹ C. A. Spindt, C. E. Holland, and R. D. Stowell, *Appl. Surf. Sci.* **16**, 268 (1983).
- ¹⁰ H. F. Gray, G. J. Campisi, and R. F. Greene, in *Proceedings of International Electron Devices Meeting*, Los Angeles, CA, 1986, (IEEE, Piscataway, NJ, 1986), p. 776.
- ¹¹ J. M. Schnur, P. Schoen, P. Yager, J. M. Calvert, J. Georger, and R. Price, *U. S. Patent* 4,911, 891 (1990).
- ¹² W. P. Dyke and W. W. Dolan, in *Advances in Electronics and Electron Physics* (Academic, New York, 1956), Vol. 8, p. 89.
- ¹³ H. C. Miller, *J. Franklin Inst.* **282**, 382 (1966).
- ¹⁴ H. C. Miller, *J. Franklin Inst.* **287**, 347 (1969).
- ¹⁵ A. Mankofsky and K. T. Tsang (private communication).
- ¹⁶ A. Singh and J. M. Schnur, *Synth. Commun.* **16**, 847 (1986).
- ¹⁷ C. B. Duke and M. E. Alferieff, *J. Chem. Phys.* **46**, 923 (1967).

Surface composition of Si-TaSi₂ eutectic cathodes and its effect on vacuum field emission

James J. Hickman, George Bergeron, Mark Czarnaski, and Douglas A. Kirkpatrick
Science Applications International Corporation, 1710 Goodridge Drive, McLean, Virginia 22102

(Received 8 June 1992; accepted for publication 15 September 1992)

Our research shows that the presence of an oxide layer on the surface of a field emission cathode is deleterious to its performance and that, for successful operation, removal of this layer is necessary before overcoating with another material. We further show that once the surface oxide is removed, cathodes can be protected with a Au overcoat and run in harsh environments. We have demonstrated stable emission for a Au-coated Si-TaSi₂ cathode for over 100 h in an O₂ atmosphere at 5×10^{-6} Torr.

The process of vacuum field emission from a sharp tip or an array of sharp tips has been subject to renewed interest as a result of recent advances in microlithographic fabrication techniques.¹ This has led to a wide variety of cathode microstructures.²⁻⁵ The reason for renewed interest is that field emission array technology has potential application in areas as diverse as flat panel displays, RF power amplifiers, and microrobotics.¹ However, much of this microfabrication technology is based upon Si where surface oxides can result from etching techniques, secondary processing techniques, or exposure to the ambient atmosphere. Until it was addressed recently in a theoretical paper,⁶ this oxide layer had been ignored when emitter performance was considered and evaluated. A different field emission system based on a Si-TaSi₂ eutectic has been reported that also suffers from the presence of an oxide layer on the TaSi₂ emitter tips.⁷ We demonstrate here that removal of a surface oxide layer followed by subsequent reoxidation will turn a Si-TaSi₂ vacuum field emission array on and off for repeated cycles.

We have also shown that when the oxide layer in the Si-TaSi₂ cathodes is overcoated with a metal, such as gold, high currents cannot be maintained without destruction of the array structure. Previous reports have shown sustained current only at very low current densities when cathodes are overcoated with a metal,^{8,9} or have indicated that channels must be created in the insulating overlayer to facilitate emission at high current densities.¹⁰⁻¹² We hypothesized that the oxide was simply establishing a high impedance boundary on the cathode surface, which would explain the observed failures. We have shown that by first removing the oxide layer and then overcoating the structures with Au, we can sustain high current densities from the array in an atmosphere of pure O₂ at 5×10^{-6} Torr for over 100 h with no damage to the Au-coated TaSi₂ tips.

We have previously reported the apparatus test conditions used to evaluate cathode performance.⁷ Cathode arrays were fabricated from Si-TaSi₂ eutectic composite material¹³ that had been etched in a buffered HNO₃/HF acid solution to expose and sharpen the TaSi₂ fibers. In general, the chemically etched cathodes had extremely variable turn-on behavior, and if stable emission was achieved, it was only after extensive conditioning. Scanning electron microscopy (SEM) and either x-ray photoelectron spectroscopy (XPS) or Auger electron spectroscopy (AES)

were used to examine the cathode surface composition before and after each emission test. The surface composition of an individual chemically etched TaSi₂ tip is shown in Fig. 1(a). In all cathodes examined, an oxide layer was present whose thickness depended upon the chemical etch used during cathode fabrication. The oxide layer was removed by *in situ* Ar⁺ ion milling of the surface in the XPS or AES spectrometer followed by spectroscopic reexamination of the cathode [Fig. 1(b)]. The cathode was then removed and transferred to the test apparatus within a short time. XPS analysis indicated that during this transfer, the surface of the Si matrix reoxidized but the TaSi₂ rods did not to any great extent. The cleaned cathodes exhibited turn on at macroscopic fields $E_0 \times 130$ kV/cm and sustained emission at fields of ~ 80 kV/cm, which is typical for a well-conditioned, 10- μ m-tall Si-TaSi₂ cathode. The local electric field at the emitter tips is greater than the macroscopic E_0 due to the applied voltage and test structure by the field enhancement factor β , which is approximately 450 for these cathodes.⁷ The cathodes were removed from the test apparatus, placed in a rf plasma generator, and oxidized in an O₂ plasma for 10 min at 40 W. These cathodes were then reexamined by XPS or AES. Using these measurements we can estimate, by assuming uniform coverage, that the oxide layer is approximately 15–30-Å thick. Following the oxygen plasma etch, turn on was not achieved even with applied E fields of over 300 kV/cm. These steps of oxide removal and subsequent reoxidation were repeated with several cathodes. Since the sensitivity of the Fowler-Nordheim field emitted current to the work function of the emitter material is well documented,^{14,15} one can view this in a simplified way as an increase and decrease of the apparent work function at the field emission tips.

Another problem faced with many types of cathodes, particularly arrays of cathodes, is that they cannot be reused once they cease to emit. A desirable property would be a method to extend the lifetime of a cathode. To this end, we were able to regenerate a Si-TaSi₂ eutectic cathode that had emitted for over 100 h before failure. Typical parameters for these 100 h tests are current density ~ 3 mA/cm², current ~ 30 μ A, and an average current per tip of ~ 3 nA. Figure 2(a) shows a high resolution XPS scan of the Ta region, demonstrating extensive oxidation has occurred at the surface of the TaSi₂ rods. A survey spec-

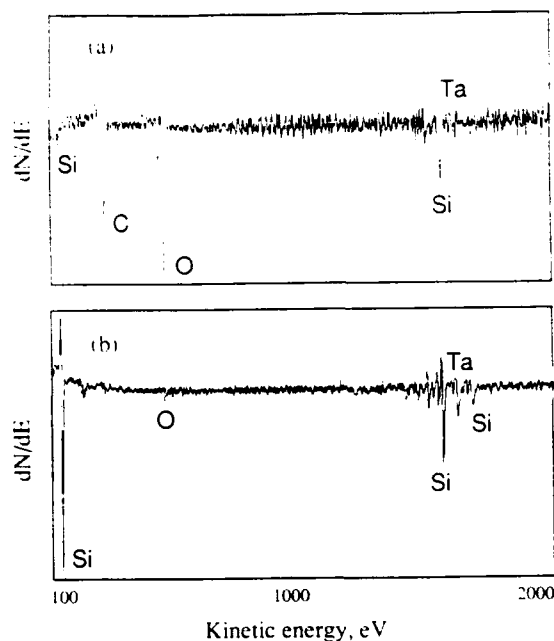


FIG. 1. We used AES to examine individual tips of a cathode as received and after Ar ion cleaning. (a) Survey spectra of a TaSi₂ tip indicating large amounts of oxide on the surface before ion milling. This cathode did not turn on at fields up to 300 kV/cm. (b) Survey scan of a TaSi₂ tip after ion Ar sputtering the cathode *in situ*. Virtually no oxide remains. When tested again, this cathode ran at a field of 100 kV/cm.

trum (data not shown) indicated large amounts of carbon as well, despite operation at 1×10^{-6} Torr in an oil-free, cryopumped environment. The contamination is probably due to residual air interacting with the cathode surface. This cathode was then *in situ* Ar⁺ ion milled and reexamined by XPS. Figure 2(b) shows complete elimination of peaks due to tantalum oxide. Testing of this cathode then demonstrated operation at applied fields E_0 equal to the lowest we had observed during its 100 h test (previously achieved after > 20 h of conditioning). It is possible that the conditioning process, which has been reported necessary in most previous work for optimal performance,^{2,4,16} is due in part to the *in situ* removal of surface oxidation products and contamination. This implies that careful interface preparation may eliminate conditioning steps or, at the very least, lessen their duration.

The second point we addressed was the effect of an oxide between the underlying TaSi₂ cathode tip and an Au overcoat on the subsequent emission at high current densities. We took the cathode that had been regenerated, as shown in Fig. 2(b), and oxidized it to a depth of 15–30 Å on the cathode surface [Fig. 2(c)]. We then sputter-deposited 500 Å of Au over the oxide and tested for emission. This step lowered the apparent work function of the oxidized tips (the work function of TaSi₂ is approximately the same as that of Au) and turn on was achieved at ~100 kV/cm. However, we observed arcing accompanied by large fluctuations in current. After 3 h of running, we removed the cathode and examined it by SEM and AES. The SEM indicated that tips had been broken and removed, and craters were present on the cathode surface, most

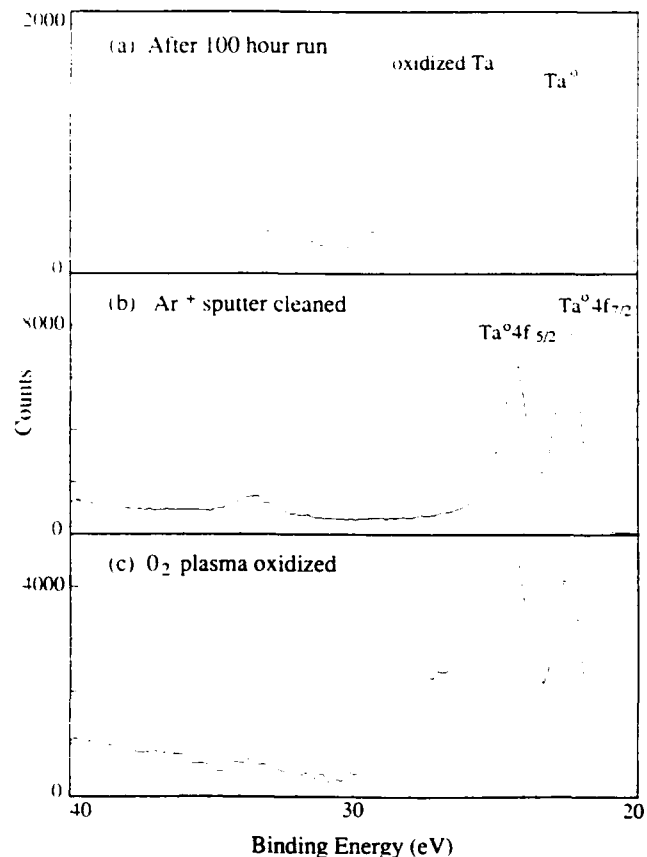


FIG. 2. (a) High resolution XPS spectra of the Ta region of a Si-TaSi₂ cathode that ceased to emit after 100 h of testing. (b) The Ta region of the same cathode after Ar⁺ ion milling. After oxide removal, the cathode ran at a field of 80 kV/cm, which was its peak performance during its 100 h run. (c) The Ta region after reoxidation in an O₂ plasma. The similarity of the spectra in (a) and (c) supports our claim that we could approximate the failure modes.

likely a result of tip explosions. Examination of AES element maps for Ta, Si, and Au showed that the Au had been removed from a number of tips and that oxide was underneath these areas. These measurements with Au-coated, oxidized cathodes were repeated with several cathodes. It is known that Au will not adhere well to a SiO₂ surface in the absence of an adhesion layer of Cr or Ti, so the observation that Au spalled from the Si matrix under thermal stress was not unexpected. Possible mechanisms for the removal of the Au from the TaSi₂ rods include field stress leading to a vacuum arc, or thermal instability of the emission through the Au thin film, which might also lead to arcing.

To test the theory that the oxide was responsible for the destructive behavior, we took another cathode that had not previously been tested, removed the surface oxide by Ar⁺ ion milling the surface, and then overcoated it with Au. We filled the test apparatus with a background pressure of 5×10^{-6} Torr pure O₂ and tested the cathode. This cathode ran for over 100 h with a sustained emission of 100 mA/cm² with an applied field of 80 kV/cm². It showed no signs of arcing during the test process. Examination by SEM [Fig. 3(a)] showed intact tips. The Au is again spalled from the Si substrate as expected, due to the absence of

SEM at 3000X



Au Auger element map



Si Auger element map



SEM at 322X



FIG. 3. SEMs and Auger element maps of a cathode where all oxide on the tips was removed, an overcoat of 300 Å of Au applied, and then run for over 100 h in a background O_2 pressure of 5×10^{-6} Torr. (Top left) SEM micrograph of area analyzed by Auger element mapping. (Top right) Au map showing Au still on the tips. The Au has spalled from the Si matrix; however, this was to be expected because Au does not adhere to SiO_2 . (Bottom right) Si map indicating Si is not showing through the tips. An O map indicated O associated with the Si but not with the tips. (Bottom left) Large area SEM showing the tips are still there after running 100 h in an O_2 atmosphere.

an adhesion layer. AES examination of the surface showed Au on all the tips [Fig. 3(b)], and little or no evidence of the underlying Si [Fig. 3(c)], or Ta (data not shown) from the cathode structures. This is consistent with our assertion that the oxide layer must be removed from the $TaSi_2$ before metal overcoating to maintain cathode integrity. If this is not done, capacitive breakdown or thermal meltdown results after short periods of running. The presence of an insulating oxide or a nonconducting region under the overlayer sets up a resistive and/or capacitive junction in the vacuum field emission circuit. Thus, when high current densities are achieved, capacitive breakdown results, which produces arcing and destruction of the overlayer, or if the oxide layer acts as a resistor, heating takes place which melts the array. In either case, destruction of the vacuum field emission cathode results. Not only is this undesirable for the preservation of cathode geometry but also for the overlayer's ability to protect the underlying surface in a harsh environment.

We have shown that the performance of Si- $TaSi_2$ eutectic cathode arrays is directly affected by the presence of a surface oxide layer on the $TaSi_2$ tips. Removal of the oxide formed during the chemical etch step of fabrication leads to improved cathode characteristics. Similarly, removal of the oxide before overcoating with a low work function material such as Au prevents catastrophic failure at low current density. Au-coated cathodes that have been

treated to remove any surface oxide possess the remarkable ability to emit for extended periods (> 100 h) in an O_2 atmosphere at 5×10^{-6} Torr.

This work was supported by the Defense Advanced Research Projects Agency. We would also like to thank the Chemistry Division at the Naval Research Laboratory for use of their surface analysis facilities.

¹T. Utsumi, IEEE Trans. Electron Devices ED-38, 2276 (1991).

²C. A. Spindt, I. Brodie, L. Humphrey, and E. R. Westerberg, J. Appl. Phys. 47, 5248 (1976).

³J. K. Cochran, A. T. Chapman, D. N. Hill, and K. J. Lee, J. Mater. Res. 2, 322 (1987).

⁴H. E. Cline, J. Appl. Phys. 41, 76 (1970).

⁵H. F. Gray and G. J. Campisi, Mater. Res. Soc. Proc. 76, 25 (1987).

⁶G. Yang, K. K. Chin, and R. B. Marcus, IEEE Trans. Electron Devices ED-38, 2373 (1991).

⁷D. A. Kirkpatrick, G. L. Bergeron, M. A. Czarnaski, J. J. Hickman, M. Levinson, Q. V. Nguyen, and B. M. Ditchek, Appl. Phys. Lett. 59, 2094 (1991).

⁸D. W. Branstor and D. Stephani, IEEE Trans. Electron Devices ED-38, 2329 (1991).

⁹R. B. Marcus, T. S. Ravi, T. Gmitter, H. H. Busta, J. T. Niccum, K. K. Chin, and D. Liu, IEEE Trans. Electron Devices ED-38, 2289 (1991).

¹⁰M. S. Mousa, Surf. Sci. 231, 142 (1990).

¹¹S. Bajic, M. S. Mousa, and R. V. Latham, Colloq. Phys. C 8, 79 (1989).

¹²Y. Yankelevitch, Y. Barengolts, and M. Khaskelberg, in Ref. 12, p. 73.

¹³B. M. Ditchek and M. Levinson, Appl. Phys. Lett. 49, 1656 (1986).

¹⁴C. B. Duke and M. E. Alferieff, J. Chem. Phys. 46, 923 (1967).

¹⁵G. A. Haas and R. E. Thomas, J. Appl. Phys. 48, 86 (1977).

¹⁶E. A. Adler, Z. Bardai, R. Forman, D. M. Goebel, R. T. Longo, and M. Sokolich, IEEE Trans. Electron Devices ED-38, 2304 (1991).

UNGATED VACUUM FIELD EMISSION FROM ORDERED ARRAYS OF MICROLITHOGRAPHICALLY DEFINED CYLINDERS

JAMES J. HICKMAN*, J. H. GEORGER**, M. ANDERSON**, G. L. BERGERON*,
AND D. A. KIRKPATRICK*

*Science Applications International Corp., 1710 Goodridge Drive, McLean, VA 22102

**GEO-Centers, Inc., Fort Washington, MD 20744

ABSTRACT

A new process has been developed which allows electroless metal deposition on ordered arrays of resist structures with high aspect ratios (10-25 μm tall x 0.5-13 μm diameter). The fabricated structures have demonstrated ungated vacuum field emission at fields of 80-300 kV/cm in background pressures of 5×10^{-6} torr. The surface composition and interface contamination relate directly to cathode performance. Cathode performance can be optimized by controlling the chemistry at these interfaces. X-ray Photoelectron Spectroscopy depth profiles, Scanning Auger Electron Spectroscopy, and Scanning Electron Microscopy have been used to characterize this system. These structures have potential vacuum microelectronics applications such as addressable electron emitters for flat panel displays.

INTRODUCTION

Recently there has been a large amount of interest in vacuum field emission from arrays of sharp tips [1]. Among the potential applications of this technology are vacuum microelectronics [2], flat panel displays [3], and RF devices [4]. Another geometry has recently been reported that makes use of metal-coated biologically derived cylinders [5,6]. Numerical modeling has shown that electron beam brightness for a hollow cylinder geometry could be superior to that of a sharp tip at higher current densities [6]. However, problems with the biologically derived cylinders fabrication process severely limits their performance [7]. In addition to addressing those fabrication process issues, the approach discussed in this paper allows for the fabrication of a wide range of tip geometries and sizes. This detailed control of the emitter shape may be most important where high degrees of uniformity are required, such as in a flat panel display.

A novel metallization technique has recently been developed that allows ordered arrays of hollow metal cylinders with high aspect ratios [8]. A representative example of these structures is pictured in Figure 1. The dimensions to date are 5-25 μm tall x 0.5-13 μm in diameter. Because this is a microfabrication process, the many difficulties associated with using tubules are avoided. We demonstrate here that these structures will emit but their performance and lifetime is largely dependent

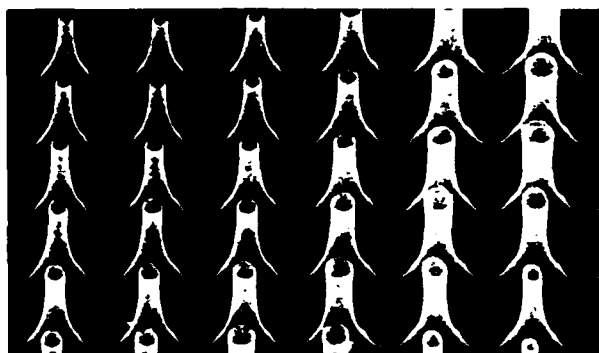


Figure 1. An SEM micrograph of an array of hollow cylinder Ni microstructures. The scaling factor is 10 $\mu\text{m}/\text{cm}$.

on the structure at the interfaces. We have previously demonstrated that the presence of a surface oxide is deleterious to performance of a eutectic cathode [9]. We show that if the interfaces are conductive, sustained DC emission is observed without destruction of the array.

The Fowler-Nordheim [9] field emission current density, J_{FN} , describes the process of quantum field emission from a one-dimensional cold-cathode system,

$$J_{FN} = \frac{A(\beta E)^2}{\phi t^2(y)} \exp \left(-B \frac{\phi^{3/2} v(y)}{\beta E} \right) \text{ A/cm}^2 \quad (1)$$

where $A = 1.54 \times 10^{-6}$, $B = 6.87 \times 10^7$, $y = 3.79 \times 10^{-4}((\beta E)^{1/2}/\phi)$, $t^2(y) \approx 1.1$, $v(y) = 0.95 - y^2$, β is the field enhancement factor due to local geometry, E is the applied electric field in V/cm, and ϕ is the work function in eV of the surface emission material. The current density generated from this type of cathode is dependent on the local electric field at the emission site.

Hollow cylinders can be used to produce a local enhancement of the applied electric field whose magnitude is dependent upon cylinder height, the average spacing between nearest neighbors, the radius of curvature of the metal wall at the edge of the exposed hollow cylinder, and the nature of the surface near the exposed edge. Detailed numerical simulations [6] of the electrostatic field in the vicinity of a hollow cylindrical structure have shown that field enhancement factors in the range $\beta = 150$ -250 could be readily achieved with a cylinder of diameter 0.5 μm and a height $h = 10$ -15 μm . It is probable that the enhancement factor could be increased an additional 2- to 4-fold by the inherent surface roughness of the electrolessly deposited metal film that makes up the outer cylinder surface, yielding an enhancement factor in the range $\beta = 300$ -1000.

The hollow nature of the protruding tubule microstructures also provides an electrostatic lensing effect for the emitted electrons: the thinner the tubule wall, the greater the self-focusing effect of the structure, and the more collimated the emitted beam. For suitably fabricated structures, with thin wall thicknesses near the emission tip, normalized electron beam brightnesses well in excess of $10^6 \text{ A/cm}^2\text{-rad}^2$ can be achieved [6].

Experimental

Thin film photoresists were fabricated with two different commercially available resists onto flat substrates such as silicon wafers or other optically flat materials. AZ4400 and AZ4903 from Hoechst AG Corp, were spun on 3 inch antimony doped silicon wafers on a vacuum chuck. To produce resist films with homogeneous thicknesses of 10 μm or greater, single and multiple 3-4K spins of AZ4903 and AZ4400 resists were used. A chrome-on-fused-silica mask was then placed in contact with the resist in a deep UV SUSS MJ3B contact printer and exposed with the correct dosage of light to clear the exposed regions of the photoresist after development with an alkaline solution. This procedure should result in resist posts that are the height of the resist thickness, with their center-to-center spacing, tip, and base diameters dictated by the mask feature spacing and size.

After development, the resist posts were metallized by first selectively catalyzing the side walls and surface of the substrate with a palladium/tin colloid for 5 min, then accelerating the catalyst with 50 mg/L of PdCl_2 in 1 M HCl for 4 min. After rinsing, the substrate was placed in a 10% Niposit 468 electroless plating bath at pH 7 and 25°C for 40-50 min then rinsed with deionized water. This resulted in photoresist posts plated with ~ 800 -1000 Å of NiB on the bottom of the sidewalls tapering to ~ 100 Å at the top of the structures, but none on top of the photoresist. The area between the posts was plated to ~ 800 -1000 Å as well. Following metallization, the photoresist was removed by placing the substrate in acetone for 1 min followed by rinsing with water. The metal microcylinder arrays were cut into individual arrays and then mounted on copper stubs with silver paint for emission testing. The test apparatus and conditions have been described previously [11].

XPS spectra were obtained on a SSX-100 spectrometer (Surface Science Instruments) equipped with a concentric hemispherical analyzer. The instrument was operated in a fixed analyzer transmission mode using a monochromatic Al K α X-ray source. The pass energy was 50 eV with a 600 μ m spot size. The take-off angle was 35° and the normal operating pressure was approximately 10⁻⁹ torr. AES was performed on a PHI 660 Scanning Auger Microprobe. A 15 kV beam at 20 nA was used for the scanning electron micrograph (SEM) images, Auger element surveys, and single element maps.

Results and Discussion

The initial microcylinder arrays were fabricated on antimony doped silicon wafers. These structures were mounted on copper stubs, sputtered with gold and tested for field emission. Emission from structures with a turn-on field of 300 kV/cm with a field enhancement of ~ 300 was achieved with 17 μ m tall x 2 μ m tip diameter structures. The results of this measurement are shown in Figure 2 where $\ln(I/V^2)$ is plotted against $1/V$. However, emission from these structures was destructive resulting in melting and ejection of the structures from the surface of the substrate.

Figure 3 (top left) shows an SEM of the metal micro-structures after field emission testing. Figure 3 also shows AES element maps for Au, Ni, and Si. The Au has clearly spalled from the Ni, and where structures have been removed, Si is clearly visible.

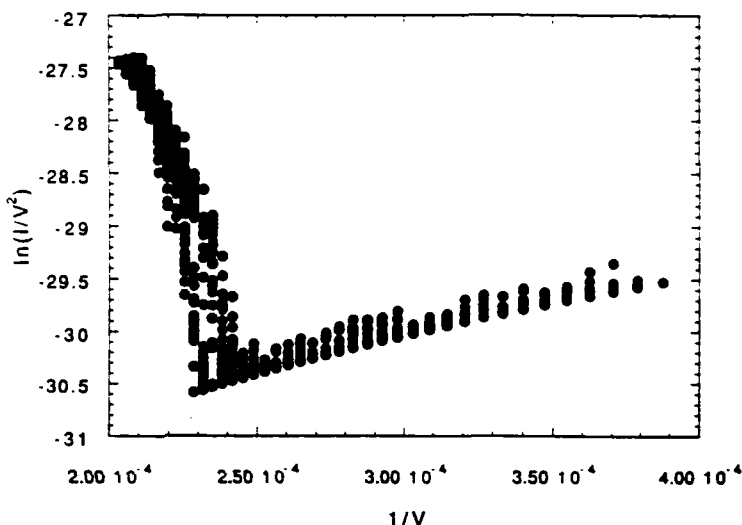


Figure 2. Fowler-Nordheim plot of cathode LC-117

To investigate the reasons for the destruction of the array, the wafer from which LC-117 was cut was examined by an XPS depth profile. Figure 4 indicates that there would have been oxides present at the Ni surface as well as the nickel-silicon interface. After coating with Au, this would have created two resistor or capacitor junctions in the structures. Previous work on Si-TaSi₂ cathodes has demonstrated that oxide interfaces on the TaSi₂ tips causes melting and destruction of the structures during field emission testing [9]. The destructive melting and ejection of the microstructures is likely due to oxide layers which can cause resistive heating or capacitive breakdown at the metal oxide interfaces resulting in melting and thermal stress.

In order to eliminate the oxide interfaces in the microcylinder arrays the following changes in their fabrication were adopted. To make better electrical contact to the silicon substrate, the silicon oxide was removed. This was accomplished by first removing the oxide with an HF dip and then evaporating ~ 500 Å of titanium onto the wafer surface which reacts with any remaining oxide. Next ~ 1500 Å of nickel was evaporated onto the titanium in situ. The nickel acts as a diffusion barrier so that the gold film which follows cannot diffuse into the silicon and form a detrimental silicide. Gold was then evaporated onto the nickel to inhibit oxidation of the nickel and form a good final electrical contact. The substrate was then annealed at 350°C for 15 min to accelerate the titanium reaction with the remaining interfacial oxygen and to promote interdiffusion of the metal interfaces.

Wafers with the Ti/Ni/Au overcoat described above were then processed as described previously to form 10-12 μ m tall microcylinders with 1-3 μ m wide tip diameters. Immediately following the removal of the photoresist the substrate was

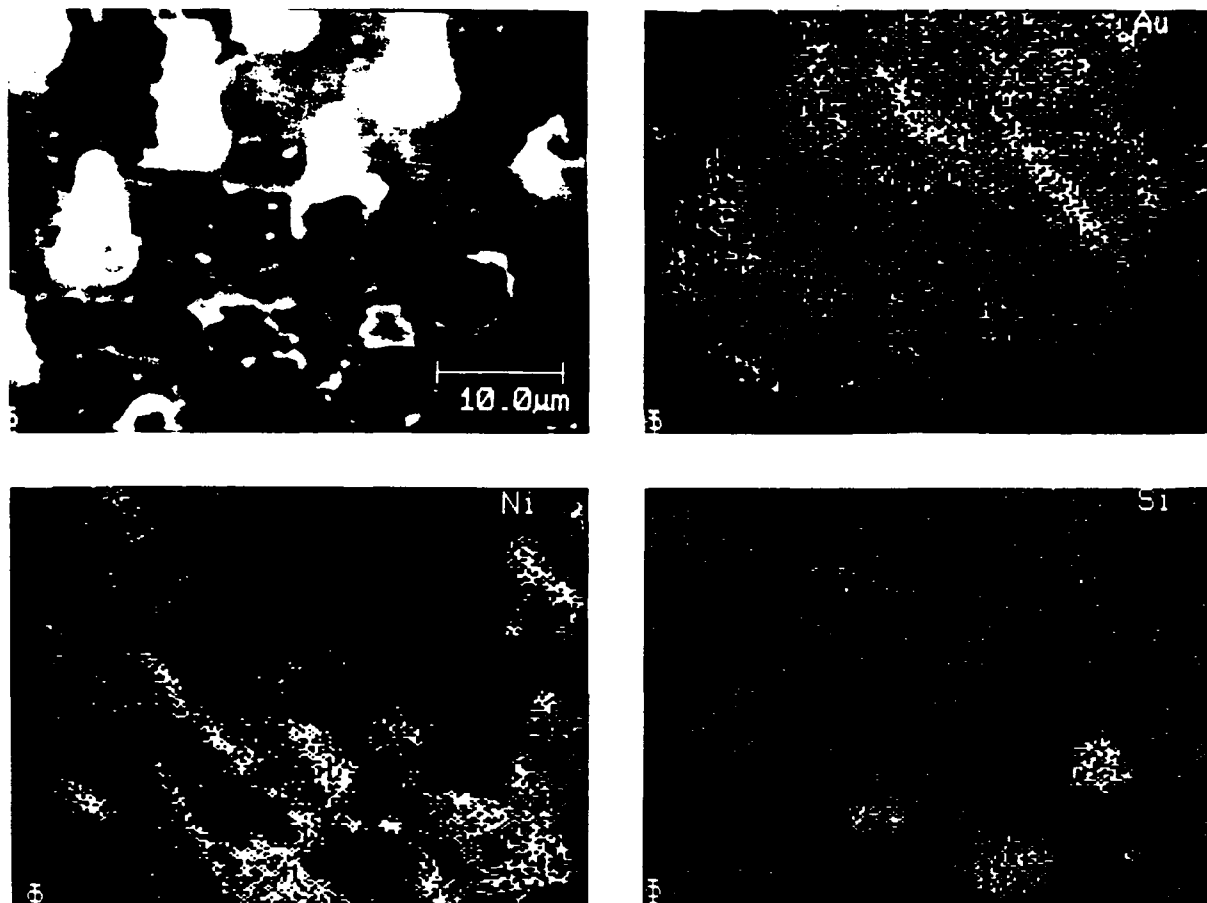


Figure 3. Surface analysis of cathode LC-117 after running 2 hrs DC. (Top left) SEM of a typical area from the emitter which indicates extensive spalling of the Au from the Ni surface as well as ejection of the structures from the surface. (Top right) AES Au element map. (Bottom left) Ni element map. (Bottom right) Si element map which shows location of ejected towers.

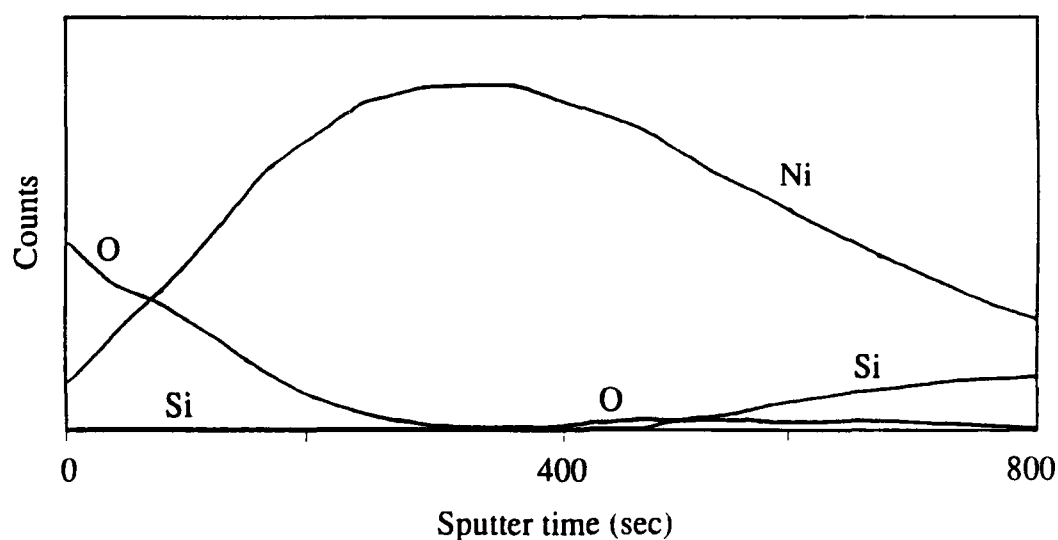


Figure 4. XPS depth profile of a flat region of the wafer from which cathode LC-117 was cut. The elements Ni, O, and Si were recorded while sputtering with a 3 kV Ar⁺ beam.

annealed at 300°C for 10 min to promote diffusion of the Ni, Sn, and Pd metals into the gold surface and to reduce nickel oxide penetration into the underlying metallic

Ni. The mounted arrays were then etched with an argon or hydrogen etch to remove any nickel oxide and were then sputtered in situ with ~ 200 Å of gold. Other mounted arrays went through the etching step alone and were then immediately transferred into the field emission test stands. All microcylinder arrays fabricated using the procedures described above demonstrated stable DC field enhanced emission with turn-on fields of 80-300 kV/cm and currents in the 50 μ A range as shown in Table I.

Table I: Tested Lithographic Cathodes

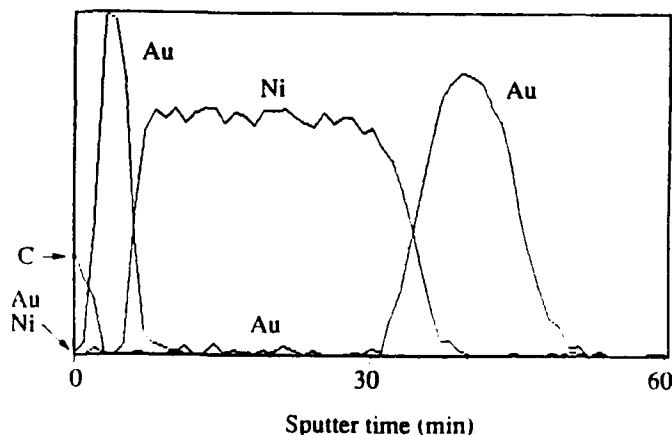
ID	Metal(s)	Turn-on Field (kV/cm)	Running Field (kV/cm)
LC-C1	Ni	110	80
LC-C2	Ni	330	215
LC-B2	Ni	240	180
LC-B1	Ni/Au	120	135
LC-A1	Ni/Au	270	100
LC-A2	Ni/Au	315	170
LC-117	Ni/Au	180	150

Figure 5 shows an array of Ni cylinders that were coated with 200 Å of Au and run for 2 hrs DC; no evidence of major degradation is visible. Figure 6 shows an XPS depth profile revealing little, if any, oxides at the interfaces. Both the gold coated and uncoated arrays emitted which is the first demonstration of emission from nickel-coated microstructures of any kind. One array was also tested using a P-22 phosphor coated glass screen as the anode which was imaged through a video camera, which demonstrated that the emission was primarily from the metal microstructures. This leads to the possibility of emission from patterned addressable arrays.

Figure 5. SEM micrograph of a Au-coated Ni array after 2 hrs of DC operation. The boxes indicate where AES survey scans were conducted.



Figure 6. AES depth profile of the cathode in Figure 5. Because AES gives much higher lateral resolution than XPS, this depth profile was performed on the cathode previously tested. The elements Ni, C, Au, and O were monitored while sputtering with a 4 kV Ar⁺ beam. No detectable O signal was seen throughout the structure.



If one assumes that the entire array was aligned with the anode, the fact that the structure has demonstrated stable nondestructive electron emission at 50 μA indicates that current densities of at least 1-3 mA/cm^2 have been achieved. The variability of the fields required for turn-on and emission from these cathodes was probably due to the variation of the metal thickness at the rim of the cathodes. AES survey scans indicated that these walls could be $< 100 \text{ \AA}$ in thickness. Arrays that were etched but did not receive a gold overcoat initially showed that the nickel oxide had been removed, but over a period of days a new oxide formed that was detrimental to the emission efficiency of the array.

This work demonstrates that stable electron emissive surfaces can be fabricated using non-conventional optical lithography and selective metallization techniques. Highly regular arrays of microstructures with high aspect ratios have been produced, allowing us to control the packing density and microstructure geometry. Further optimization of the process for improved field emission properties is underway with the fabrication of new test masks which are designed to optimize the fabrication of 10 and 20-25 μm tall microstructures over 3mm diameter areas, as well as masks to determine the effect of packing density and tip diameters on the emission properties of these arrays.

References

1. T. Utsumi, IEEE Trans. Electron Devices 38, 2276 (1991).
2. C.A. Spindt, I. Brodie, L. Humphrey, and E.R. Westerberg, J. Appl. Phys. 47, 5248 (1976).
3. C.A. Spindt, C.E. Holland, I. Brodie, J.B. Mooney, and E.R. Westerberg, IEEE Trans. Electron Devices 36, 225 (1989).
4. A.K. Ganguly, P.M. Phillips, and H.F. Gray, J. Appl. Phys 67, 7098 (1990).
5. D.A. Kirkpatrick, G.L. Bergeron, M.A. Czarnaski, J.J. Hickman, G.M. Chow, R. Price, B.L. Ratna, P.E. Schoen, W.B. Stockton, S. Baral, A.C. Ting, and J.M. Schnur, Appl. Phys. Lett. 60, 1556 (1992).
6. D.A. Kirkpatrick, G.L. Bergeron, M.A. Czarnaski, R.C. Davidson, H.P. Freund, J.J. Hickman, A. Mankofsky, K.T. Tsang, J.M. Schnur, M. Levinson, and B.M. Ditchek, in Nuclear Instruments and Methods in Physics Research, (Elsevier Science Publishers, New York, 1991), p. 1.
7. G.M. Chow, W.B. Stockton, R. Price, S. Baral, A.C. Ting, B.R. Ratna, P.E. Schoen, J.M. Schnur, G.L. Bergeron, M.A. Czarnaski, J.J. Hickman, and D.A. Kirkpatrick, accepted for publication in J. Mater. Sci. Eng.
8. J.H. Georger, Jr., M.L. Rebbert, M.A. Anderson, D. Park, J.J. Hickman, J.M. Calvert, C.S. Dulcey, and M.C. Peckerar, submitted for publication in Proc. Mater. Res. Soc., San Francisco, April 1992.
9. J.J. Hickman, G. Bergeron, M. Czarnaski, and D. A. Kirkpatrick, submitted to Appl. Phys. Lett.
10. R.H. Fowler and L. Nordheim, Proc. R. Soc. London A. 119, 173 (1928).
11. D.A. Kirkpatrick, G.L. Bergeron, M.A. Czarnaski, J.J. Hickman, M. Levinson, Q.V. Nguyen, and B.M. Ditchek, Appl. Phys. Lett. 59, 2094 (1991).

If one assumes that the entire array was aligned with the anode, the fact that the structure has demonstrated stable nondestructive electron emission at 50 μA indicates that current densities of at least 1-3 mA/cm^2 have been achieved. The variability of the fields required for turn-on and emission from these cathodes was probably due to the variation of the metal thickness at the rim of the cathodes. AES survey scans indicated that these walls could be $< 100 \text{ \AA}$ in thickness. Arrays that were etched but did not receive a gold overcoat initially showed that the nickel oxide had been removed, but over a period of days a new oxide formed that was detrimental to the emission efficiency of the array.

This work demonstrates that stable electron emissive surfaces can be fabricated using non-conventional optical lithography and selective metallization techniques. Highly regular arrays of microstructures with high aspect ratios have been produced, allowing us to control the packing density and microstructure geometry. Further optimization of the process for improved field emission properties is underway with the fabrication of new test masks which are designed to optimize the fabrication of 10 and 20-25 μm tall microstructures over 3mm diameter areas, as well as masks to determine the effect of packing density and tip diameters on the emission properties of these arrays.

Acknowledgements

This work was supported by the Defense Advanced Research Projects Agency. The authors would also like to thank the Naval Research Laboratories for fabricating the structures and use of facilities.

References

1. T. Utsumi, IEEE Trans. Electron Devices 38, 2276 (1991).
2. C.A. Spindt, I. Brodie, L. Humphrey, and E.R. Westerberg, J. Appl. Phys. 47, 5248 (1976).
3. C.A. Spindt, C.E. Holland, I. Brodie, J.B. Mooney, and E.R. Westerberg, IEEE Trans. Electron Devices 36, 225 (1989).
4. A.K. Ganguly, P.M. Phillips, and H.F. Gray, J. Appl. Phys 67, 7098 (1990).
5. D.A. Kirkpatrick, G.L. Bergeron, M.A. Czarnaski, J.J. Hickman, G.M. Chow, R. Price, B.L. Ratna, P.E. Schoen, W.B. Stockton, S. Baral, A.C. Ting, and J.M. Schnur, Appl. Phys. Lett. 60, 1556 (1992).
6. D.A. Kirkpatrick, G.L. Bergeron, M.A. Czarnaski, R.C. Davidson, H.P. Freund, J.J. Hickman, A. Mankofsky, K.T. Tsang, J.M. Schnur, M. Levinson, and B.M. Ditchek, in Nuclear Instruments and Methods in Physics Research, (Elsevier Science Publishers, New York, 1991), p. 1.
7. G.M. Chow, W.B. Stockton, R. Price, S. Baral, A.C. Ting, B.R. Ratna, P.E. Schoen, J.M. Schnur, G.L. Bergeron, M.A. Czarnaski, J.J. Hickman, and D.A. Kirkpatrick, accepted for publication in J. Mater. Sci. Eng.
8. J.H. Georger, Jr., M.L. Rebbert, M.A. Anderson, D. Park, J.J. Hickman, J.M. Calvert, C.S. Dulcey, and M.C. Peckerar, submitted for publication in Proc. Mater. Res. Soc., San Francisco, April 1992.
9. J.J. Hickman, G. Bergeron, M. Czarnaski, and D. A. Kirkpatrick, submitted to Appl. Phys. Lett.
10. R.H. Fowler and L. Nordheim, Proc. R. Soc. London A. 119, 173 (1928).
11. D.A. Kirkpatrick, G.L. Bergeron, M.A. Czarnaski, J.J. Hickman, M. Levinson, Q.V. Nauven, and B.M. Ditchek. Appl. Phys. Lett 59 2004 (1991)

High brightness electron beam sources for FEL applications *

D.A. Kirkpatrick ^a, G.L. Bergeron ^a, M.A. Czarnaski ^a, R.C. Davidson ^a, H.P. Freund ^a,
J.J. Hickman ^a, A. Mankofsky ^a, K.T. Tsang ^a, J.M. Schnur ^b, M. Levinson ^b and B.M.
Ditchek ^c

^a Science Applications International Corporation, 1710 Goodridge Drive, McLean, VA 22102, USA

^b Naval Research Laboratory, Code 6090, Washington DC 20375-5000, USA

^c GTE Laboratories, 40 Sylvan Rd., Waltham, MA 02254, USA

A new generation of field emitter array (FEA) cathode materials is under development at SAIC, in collaboration with NRL and GTE Laboratories. The emitter structures under consideration consist of large area ($\sim 1 \text{ cm}^2$) arrays of large numbers ($\sim 10^6$) of microscopic field emitting tips. The structures can be fabricated so as to choose an emitter tip microstructure that is a solid cone, a hollow cylinder, or a variety of other shapes. These microstructures evidence very high local field enhancement factors, controllable from a factor of ~ 200 to > 2000 . This large local field enhancement allows quantum field emission of significant current from the large area array while the applied macroscopic electric field is still quite low ($\sim 20 \text{ kV/cm}$). Single-tip, noninteracting particle, multigrid simulations indicate that beam brightnesses $B_n = I/\pi^2 \epsilon_n^2 > 10^{10} \text{ A/cm}^2 \text{ rad}^2$ may be possible. Beams with such high brightnesses allow for a greatly expanded field of FEL applications, including high gain and harmonic operation in the FIR wavelength regime. Experiments have so far demonstrated DC average current densities $> 1 \text{ A/cm}^2$, uniform emission, and improved characteristics when run for long periods of time ($> 100 \text{ h}$, DC). Our present efforts are concentrated on optimizing the available cathode current density, measuring the actual beam brightness, and including self-field and 3-D effects in the numerical simulations.

The need for high brightness electron beams for use in free electron lasers is well known and understood. The basic relation between the electron beam emittance and the minimum wavelength for gain, $\epsilon < \lambda_{\text{rad}}/\pi$, coupled with the scaling of laser efficiency and gain with electron beam current, results in the electron beam brightness being one of the limiting parameters for FEL performance. In this paper the normalized electron beam brightness is defined to be $B_n \equiv I/\pi^2 \epsilon_n^2$, where I is the electron beam current and ϵ_n is the normalized electron beam emittance, $\epsilon_n \equiv \gamma\beta(A_\phi/\pi)$, and A_ϕ is the transverse phase space area occupied by the beam. Depending on the method used to define the phase space occupied by the beam, the emittance and brightness can be defined as "edge" or "rms" quantities. FEL performance would significantly benefit from the availability of inexpensive, robust, and reliable electron beam sources with edge brightness in excess of $B_n \sim 10^{10} \text{ A/cm}^2 \text{ rad}^2$.

Advanced cathode materials formed from arrays of microscopically sharp tips may provide an alternative to other approaches. These advanced cathode materials are formed from composite materials and can be pro-

cessed to yield a high density ($\sim 10^6 \text{ cm}^{-2}$) of microscopic field emitting tips. One approach uses a composite of self-assembled biomolecular microstructures that resemble hollow soda straws [1], while a second approach uses a semiconductor-metal eutectic composite material [2]. In the first approach, an aligned composite of the metallized biomolecular microparticles is etched to reveal a random and moderately uniform array of hollow, cylindrical microstructures protruding 10–20 μm above the base. The second approach uses wafers cut from a crystal-grown Si-TaSi₂ eutectic composite, then the Si matrix material is preferentially etched to reveal the metal TaSi₂ rods. The degree of chemical selectivity of the etch determines the eventual height of the TaSi₂ emitter rods; this can be varied to achieve exposed emitter heights anywhere from 1–60 μm . An example of a Si-TaSi₂ cathode is shown in fig. 1.

The performance to date of the advanced cathode materials has been documented elsewhere [4–6]. Although the hollow cylinder microstructure geometry may eventually prove superior, difficulties with the biomolecular microstructure composite cathode fabrication process has severely limited their performance. The Si-TaSi₂ eutectic composite cathodes, on the other hand, have proven to be robust and reliable. Experi-

* Work supported by the Defense Advanced Research Projects Agency.

ments with 1 cm diameter cathodes have so far demonstrated DC average current densities $> 1 \text{ A/cm}^2$, uniform emission over the entire cathode face, improved characteristics when run for long periods of time, and I - V characteristics consistent with the observed microstructure.

The Si-TaSi₂ material has so far been processed to produce two different types of cathode structures: a high field enhancement cathode array structure, where the tip heights are $> 20 \text{ }\mu\text{m}$, but where the matrix substrate is significantly pitted and varying in depth; and a moderate field enhancement cathode array structure where the tip heights are all 8–9 μm and where the matrix floor is almost perfectly flat. In both cases the average tip-to-tip separation is about 8 μm . The high field enhancement cathode structures evidence field enhancement factors $\beta > 2000$ ($E_{\text{tip}} = \beta E_{\text{applied}}$), and have turned on as low as 20 kV/cm. The moderate field enhancement structures evidence $\beta \sim 500$.

Numerical simulations of the emission from single tips with the microstructure of the advanced cathode materials indicate that normalized electron beam brightnesses $B_n > 10^6 \text{ A/cm}^2 \text{ rad}^2$ should be attainable with the achievement of macroscopic current densities of $J \sim 100 \text{ A/cm}^2$. Furthermore, single-tip brightness well in excess of 10^{10} A/cm^2 appear feasible. The numerical simulations use a nested, multiple grid, implicit Laplace solver to calculate the electric

field structure given the microtip geometry. The cell size of the highest resolution grid is typically 4 Å. A Fowler–Nordheim emission law is applied [7], and the noninteracting particles are propagated through the field solve to a witness plate for distant from the emission surface. The single tip brightness is calculated as $B_n^{(1)} = I^{(1)}/\pi^2(\epsilon_n^{(1)})^2$, where $I^{(1)}$ is the single tip current, $\epsilon_n^{(1)}$ is the normalized single tip emittance given by $\gamma\beta A_{\text{ps}}^{(1)}/\pi$, and $A_{\text{ps}}^{(1)}$ is the phase space area of the single beamlet. The beam brightness is calculated as $B_n = J/\pi(\gamma\beta\theta_m^{(1)})^2$, where J is the macroscopic cathode current density given by $N_{\text{tip}}I^{(1)}$, N_{tip} is the areal density of emitter tips, and $\theta_m^{(1)}$ is the trajectory angle such that 90% of the current from the single tip is emitted into trajectories with trajectory angles less than $\theta_m^{(1)}$. This difference in definitions between single tip brightness, $B_n^{(1)}$, and beam brightness, B_n , is equivalent to assuming the possibility of refocussing a single beamlet, and no such possibility in the case of an array of 10^6 random beamlets.

Unlike analytical solutions of the effect of a protrusion on emitted electron beam trajectories in the space-charge limited or temperature-limited regime [3], the highly nonlinear dependence of quantum field emission on the applied field results in the electron emission from these microtips being confined to a very small region near the tip apex. This concentration of the emission near the tip and away from the sides of the emitter structure results in the electrons acquiring

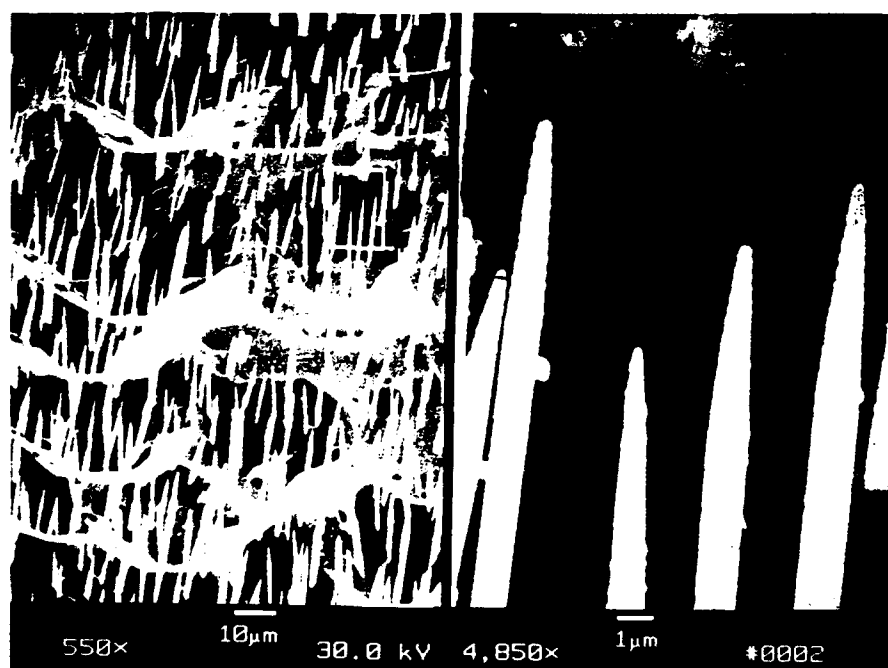


Fig. 1. A scanning electron microscope image of a Si-TaSi₂ emitter structure. The exposed rods are the minority TaSi₂ material, while the matrix is single-crystal Si. The rods exhibit tip radii of curvature on the order of or less than 20 nm.

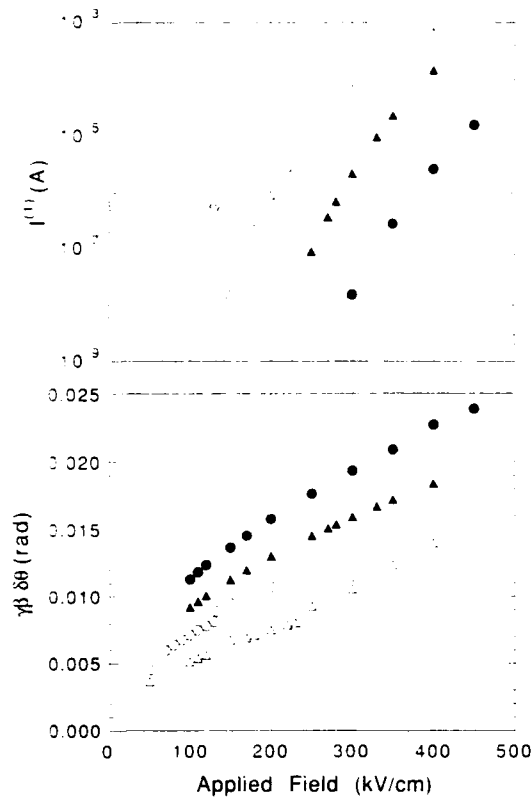


Fig. 2. The calculated value for the single tip current $I^{(1)}$ (top), and the beamlet spreading angle $\gamma\beta\theta_m$ (bottom) as a function of applied macroscopic electric field for several structure geometries. Open circle: pointed rod type structure, 10 μm tall, 1 μm diameter at the base, 2.5 nm tip radius of curvature. Open triangle: pointed rod type structure, 10 μm tall, 1 μm diameter at the base, 10 nm tip radius curvature. Solid triangle: hollow cylinder structure, 15 μm tall, 0.5 μm constant mean diameter, wall thickness 30 nm, edge radius of curvature of 15 nm. Solid circle: hollow cylinder structure, 15 μm constant mean diameter, wall thickness 60 nm, edge radius of curvature of 15 nm.

less transverse momentum, and the value for $\gamma\beta\theta_m^{(1)}$ in this case is at least a factor of two smaller than in the thermionic case calculated by Lau [3]. The more significant difference these cathode arrays present is the capability for current densities on the order of 100 A/cm^2 , and the very nonlinear dependence of the current on the applied field. The values for $I^{(1)}$ and $\gamma\beta\theta_m^{(1)}$ observed for four different structures over a large range of applied electric field is shown in fig. 2. Note that for $I^{(1)} = 100 \mu\text{A}$ and a density of emitter tips of 10^6 cm^{-2} the macroscopic current density is 100 A/cm^2 .

Initial experiments have been performed to measure the value of $\gamma\beta\theta_m$ for the Si-TaSi₂ cathode structures. These first measurements have used a high field enhancement type cathode, such as is shown in fig. 1.

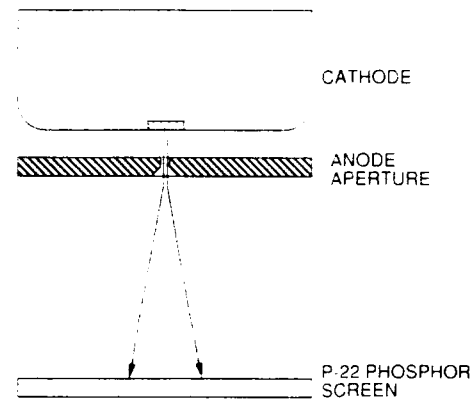


Fig. 3. A crude single-aperture emittance measurement apparatus, used to obtain the image in fig. 4.

It is anticipated that the larger tip height as well as the significant undulations of the matrix base will lead to a value for $\gamma\beta\theta_m$ that is a factor of 2–4 times greater than the value for the moderate field enhancement type cathode structures. These latter type Si-TaSi₂ cathode structures features 8–9 μm tall emitter structures on a microscopically flat substrate. The object of these measurements is to place a bracket on the cath-

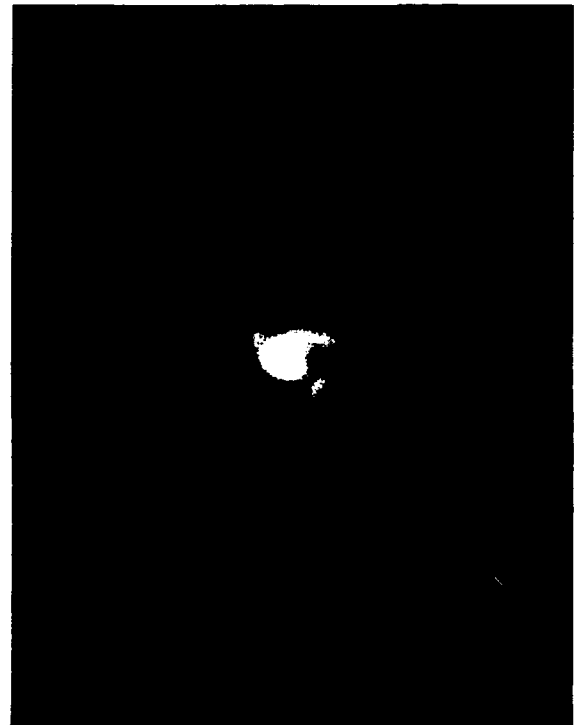


Fig. 4. A spot image of a Si-TaSi₂ cathode as measured by the apparatus in fig. 3. The spot size corresponds to a beamlet divergence angle of $\delta\theta \sim 30 \text{ mrad}$. The peak applied voltage is 10 kV, yielding a normalized divergence angle $\gamma\beta\delta\theta \sim 7 \text{ mrad}$.

ode performance in order to optimize a detailed emittance measurement apparatus planned for the near future. The initial apparatus, a simple single-aperture beamlet witness measurement, is shown in fig. 3. The cathode-anode aperture gap is set at ~ 1 mm, and the applied voltage is a 10 kV peak triangle wave with a period of approximately ten seconds. A 0.5 s exposure of the phosphor image at the peak of the voltage pulse is shown in fig. 4. The measured spot size corresponds to $\gamma\beta\delta\theta \approx 7$ mrad.

Given the dependence of $\gamma\beta\theta_m$ on applied electric field observed in the numerical simulations, and the measured value of $\gamma\beta\theta_m \approx 7$ mrad, a beam brightness of $B_n = 10^6$ A/cm² rad² from a nonoptimized structure such as shown in fig. 1 would require a cathode current density of $J \sim 500$ A/cm². If the more regular structures of the moderate field enhancement type cathodes indeed produce a value for $\gamma\beta\theta_m$ a factor of 2–4 lower than that measured for the high field enhancement cathode structures, the same beam brightness of 10^6 would require a cathode current density of $J \sim 30$ –120 A/cm². Please note that the simulation results shown in fig. 2 represent nonoptimized microstructure with respect to the detailed tip geometry, and more detailed inspection of the actual tip shape is required for the in order to achieve a closer correspondence between the simulations and the measured cathode performance.

The measurements to date have been limited in current, current density, and applied voltage. A 500

kW peak power modulator will be on-line for use in the cathode testing in the near future, which should allow for testing the cathode structures to macroscopic current densities greater than 100 A/cm² and total currents of 10 A. Similarly, a high resolution slit-wire emittance measurement apparatus is in construction and should come on-line at approximately the same time. At present, given the promising results to date, this apparatus is designed to measure normalized beam brightnesses greater than 10^7 A/cm² rad².

References

- [1] J.M. Schnur, R. Price, P. Schoen, P. Yager, J.M. Calvert, J. Georger and A. Singh, *Thin Solid Films* 152 (1987) 181.
- [2] B.M. Ditchek and M. Levinson, *Appl. Phys. Lett.* 49 (1986) 1656.
- [3] Y.Y. Lau, *J. Appl. Phys.* 61 (1987) 36.
- [4] D.A. Kirkpatrick, P.E. Schoen, W.B. Stockton, R. Price, S. Baral, B. Kahn, J.M. Schnur, M. Levinson and B.M. Ditchek, *IEEE Trans. Plasma Sci.* 19 (1991) 749.
- [5] D.A. Kirkpatrick, G.L. Bergeron, M.A. Czarnaski, J.J. Hickman, M. Levinson, Q.V. Nguyen and B.M. Ditchek, *Appl. Phys. Lett.* 59 (1991) 2094.
- [6] D.A. Kirkpatrick, G.L. Bergeron, M.A. Czarnaski, J.J. Hickman, G.M. Chow, R. Price, B.L. Ratna, P.E. Schoen, W.B. Stockton, S. Baral, A.C. Ting and J.M. Schnur, submitted for publication.
- [7] R.H. Fowler and L. Nordheim, *Proc. R. Soc. London* A119 (1928) 173.

Thermal effects on the gain in free-electron lasers

H.P. Freund, R.C. Davidson¹ and D.A. Kirkpatrick

Science Applications International Corp., McLean, VA 22102, USA

The effect of an axial energy spread on the linearized gain in free-electron lasers is considered for planar wiggler configurations in both the Raman and high-gain Compton regimes in the idealized one-dimensional limit. A thermal function is obtained by a linearized Vlasov-Maxwell analysis which applies to both the fundamental and the harmonics. The electron beam is assumed to be monoenergetic with a pitch angle spread, and is described by the inclusion of nonvanishing canonical momenta by means of a Gaussian distribution. The planar wiggler configuration admits interactions at odd harmonics as well as the fundamental, and a general dispersion equation is derived which includes the thermal effect at each harmonic as well as the fundamental.

An important issue in the generation of coherent radiation at short wavelengths from the free-electron laser (FEL) is the effect of a beam thermal spread. The thermal spread available from various electron beam sources is an essential limiting factor for many FEL applications. In this paper, we address the effect of an axial energy spread on the linear gain of the FEL at both the fundamental and harmonics. Harmonic radiation is important in the reduction in the energy required to achieve short wavelength operation, and has been observed in the laboratory over a wide spectral range [1-4]. The effect of beam thermal spread upon the gain at the harmonics, therefore, is of particular importance.

Theoretical analyses of harmonic radiation in FELs have dealt with both the linear [5-7] and nonlinear [8-13] interactions. Results of these analyses indicate that substantial gains and efficiencies are possible for the harmonic interactions, but that the sensitivity of the interaction to the thermal spread increases with harmonic number. Hence, the beam quality required for coherent emission rises dramatically at the higher harmonics.

Our purpose in this paper is to develop a unified formulation of thermal effects on the linear gain in both the Compton and Raman regimes in a planar wiggler geometry. We assume that the beam is monoenergetic but characterized by a pitch-angle spread, and treat both the fundamental and harmonic interactions subject to an idealized one-dimensional approximation. This implies that the transverse velocity associ-

ated with the pitch-angle spread must be less than the wiggler-induced transverse oscillation.

The effect of the pitch angle spread is twofold. In the first place, the resultant axial energy spread acts to degrade the interaction, and a general thermal function which describes this effect is derived for the fundamental and the harmonics. In the second place, the pitch angle spread induces an oscillation in the axial velocity which can also act to excite harmonic radiation.

The physical configuration we consider is that of a relativistic electron beam propagating through an idealized one-dimensional planar wiggler. The representation for a planar wiggler in the idealized limit is given by

$$B_w = B_w e_i \sin k_w z. \quad (1)$$

Since x and y are ignorable coordinates in the idealized representation for the wiggler fields, these components of the canonical momenta [denoted by P_x and P_y] are constants of the motion. In addition, the total energy is also a conserved quantity. As a result, the single-particle orbits are given by

$$p_x = P_x + p_w \cos k_w z, \quad (2)$$

$$p_y = P_y, \quad (3)$$

$$p_z = \left(P^2 - \frac{1}{2} p_w^2 \cos 2k_w z - 2p_w P_x \cos k_w z \right)^{1/2}, \quad (4)$$

where

$$P^2 \equiv p^2 - \frac{1}{2} p_w^2 = P_x^2 + P_y^2, \quad (5)$$

where $\gamma \equiv (1 + p^2/m_e^2 c^2)^{1/2}$ is the relativistic factor corresponding to the total electron energy and momentum p , $p_w \equiv \gamma m_e v_w$, $v_w \equiv -\Omega_w/k_w$ is the wiggler-induced velocity, and $\Omega_w \equiv eB_w/\gamma m_e c$. Since P_x is constant, the magnitude of the transverse wiggler-in-

¹ Permanent address: Princeton Plasma Physics Laboratory, Princeton University, P.O. Box 451, Princeton, NJ 08543, USA.

duced velocity oscillates at the wiggler period. This results in an oscillation in the axial momentum and velocity as well, which broadens the wave-particle resonance, and gives rise to harmonic interactions. The assumption of small displacements from the symmetry axis is equivalent to the condition that $|V_w/v_w| \ll 1$, and we assume as well that $|V_-/v_w| \ll 1$.

The dispersion equation in the idealized one-dimensional representation is found in the context of a linearized Vlasov-Maxwell formalism. The Vlasov equation in the combined wiggler and electromagnetic fields is

$$\left[\frac{\partial}{\partial t} + v \cdot \nabla - e \left(\delta E(z, t) + \frac{1}{c} v [B_w(z) + \delta B(z, t)] \right) \cdot \nabla_p \right] f_b(z, p, t) = 0, \quad (6)$$

where $f_b(z, p, t)$ is the distribution function of the electron beam, $\delta E(z, t)$ and $\delta B(z, t)$ denote the fluctuating electric and magnetic fields of the wave. The Vlasov equation is linearized by expanding the distribution in powers of the fluctuating fields. We write $f_b(z, p, t) = F_b(z, p) + \delta f_b(z, p, t)$ where F_b and δf_b are the equilibrium and perturbed components of the distribution, and it is assumed that $|\delta f_b| \ll |F_b|$. The equilibrium distribution can be expressed as a function of the constants of the motion in the form $F_b(z, p) = F_b(P_r, P_v, p)$. Correct to first order in the fluctuation fields, the perturbed distribution satisfies

$$\begin{aligned} \delta f_b(z, p, \tau(z)) \\ = e \int_0^z \frac{dz'}{v_z(z')} \left[\delta E(z, \tau(z')) \right. \\ \left. + \frac{1}{c} v(z') \delta B(z, \tau(z')) \right] \cdot \nabla_p F_b \end{aligned} \quad (7)$$

over the unperturbed trajectories under the assumption that the perturbations are negligibly small at time $t = 0$. We treat spatial growth and adopt Lagrangian coordinates in which $v(z)$ denotes the unperturbed velocity of an electron as a function of the axial position, and

$$\tau(z) \equiv t_0 + \int_0^z \frac{dz'}{v_z(z')}. \quad (8)$$

The Vlasov equation is solved in conjunction with Maxwell's equations. We choose to deal with the scalar $\delta \phi(z, t)$ and vector potentials $\delta \mathbf{A}_\perp(z, t)$ in the Coulomb gauge. In terms of this representation, Maxwell's equations are

$$\left(\nabla^2 - \frac{1}{c^2} \frac{\partial^2}{\partial t^2} \right) \delta \mathbf{A}_\perp = -\frac{4\pi}{c} \delta \mathbf{J}_\perp, \quad (9)$$

and

$$\frac{\partial^2}{\partial t \partial z} \delta \phi = 4\pi \delta J_z. \quad (10)$$

The source current is given in terms of the perturbed distribution function as follows

$$\delta \mathbf{J}(z, t) = -\frac{e}{m_e} \int d^3p \frac{1}{\gamma} p \delta f_b(z, p, t). \quad (11)$$

Since the FEL operates by means of an axial bunching mechanism, it is the axial velocity spread which is most important. As a consequence, we assume the beam to be monoenergetic but with a pitch angle spread. The effect of the pitch angle spread is to include velocity spreads in both the axial and transverse directions, and may be described by a distribution function of the form [15]

$$F_b(P_r, P_v, p) = n_b \frac{\exp(-P_\perp^2/\Delta P^2)}{\pi \Delta P^2} \frac{p_z}{p} \delta(p - p_0), \quad (12)$$

where n_b denotes the bulk ambient density, $P_\perp^2 \equiv P_r^2 + P_v^2$, and ΔP represents the thermal spread.

The interaction occurs for plane waves polarized in the direction of the wiggler-induced oscillation. Using a Floquet analysis for periodic systems, we express the vector and scalar potentials for a wave with angular frequency ω as

$$\begin{aligned} \begin{bmatrix} \delta \mathbf{A}(z, t) \\ \delta \phi(z, t) \end{bmatrix} = \frac{1}{2} \sum_{n=-\infty}^{\infty} \begin{bmatrix} \delta \hat{A}_n \hat{e}_\perp \\ \delta \hat{\phi}_n \end{bmatrix} \exp(ik_n z - i\omega t) \\ + \text{c.c.}, \end{aligned} \quad (13)$$

where $k_n = k + nk_w$. The perturbed distribution function, therefore, takes the form

$$\delta \hat{f}_b(z, p) = \frac{e}{2c} \left[D_\perp \frac{\partial}{\partial P_r} + D_z \frac{\partial}{\partial p} \right] F_b(P_r, P_v, p), \quad (14)$$

where the orbit integrals are defined as (where $\tau(z, z') \equiv \tau(z) - \tau(z')$)

$$D_\perp \equiv -\delta \hat{A}(z) + \delta \hat{A}(0) \exp(i\omega \tau(z, 0)), \quad (15)$$

$$\begin{aligned} D_z \equiv \frac{1}{p} \int_0^z dz' \frac{\exp(i\omega \tau(z, z'))}{v_z(z')} \\ \times \left[-cp_z(z') \frac{\partial}{\partial z'} \delta \hat{\phi}(z') + i\omega p_r(z') \delta \hat{A}(z') \right]. \end{aligned} \quad (16)$$

The orbit integrals D_\perp and D_z which appear in the source currents represent an integration over the unperturbed electron trajectories. In particular, we ob-

serve that the Lagrangian time variable characteristic of the electron trajectories is of the approximate form

$$\tau(z) \equiv t_0 + \frac{z}{V} + \frac{P_1}{P} \frac{v_w}{V} \frac{1}{k_w V} \sin k_w z - \frac{v_w^2}{8V^2} \frac{1}{k_w V} \sin 2k_w z, \quad (17)$$

where it is assumed that both $v_w < V$ and $P_1 < P$. The existence of a nonvanishing canonical momentum introduces an oscillation at the wiggler period into the trajectory.

The dominant contribution of the axial thermal spread occurs within the resonance condition, and we restrict the analysis to the resonance associated with the Doppler upshift in frequency and restrict the analysis to a specific harmonic (i.e., for fixed l and m). After some lengthy but straightforward manipulations [7], the dispersion equation may be written as

$$\left[(\omega - k_{n+l+2m} v_w)^2 - \frac{\omega_b^2}{\gamma_0 \gamma_1} T_l(\zeta_{n+l+2m}) \right] \times \left(\omega^2 - c^2 k_{n+l+2m}^2 - \frac{\omega_b^2}{\gamma_0} \right) \equiv - \frac{v_w^2}{4c^2} \frac{\omega_b^2}{\gamma_0} K_m^{(1)}(b_2) T_l(\zeta_{n+l+2m}) \times \left(\omega^2 - c^2 k_{n+l+2m}^2 - \frac{\omega_b^2}{\gamma_0} T_l(\zeta_{n+l+2m}) \right), \quad (18)$$

where $K_m^{(1)}(x) \equiv [J_m(x) - J_{m-1}(x)]^2$, J_n denotes the regular Bessel function of the first kind, $b_2 \equiv (\omega/k_w V)(v_w^2/8V^2)$,

$$T_l(\zeta) \equiv \frac{\zeta^2}{2\pi} \int_0^{2\pi} d\phi \int_0^\infty dz \exp(-z) \frac{J_l^2(b_1)}{(z+\zeta)^2}, \quad (19)$$

$$\zeta_{n+l+2m} \equiv \frac{\gamma_0^2 m_c^2}{\Delta P^2} \left(\frac{\omega^2}{k_{n+l+2m}^2} - v^2 \right), \text{ and} \quad (20)$$

$$b_1 \equiv \frac{\omega}{k_w v} \frac{v_w}{V} \frac{\Delta P}{p_0} z^{1/2} \cos \phi. \quad (21)$$

The effect of the pitch angle spread on the axial velocity is the source of the l th harmonic contribution, which has the effect of modifying the thermal function T_l . In order to describe this effect in more detail, we assume that $b_1 \ll 1$ which is valid as long as $P_1 \ll P$. As a result, we expand the Bessel function to lowest order in b_1 , and obtain

$$T_l(\zeta) \equiv \frac{(2l)!}{(l!)^4} \left(\frac{v_w}{2V} \right)^{2l} \left(\frac{\omega}{k_w v} \right)^{2l} \left(\frac{\Delta P}{p_0} \right)^{2l} \times \left\{ (-1)^l \zeta^{l-1} [1 - (\zeta+l) \exp(\zeta) E_1(\zeta)] + U_l(\zeta) \right\}, \quad (22)$$

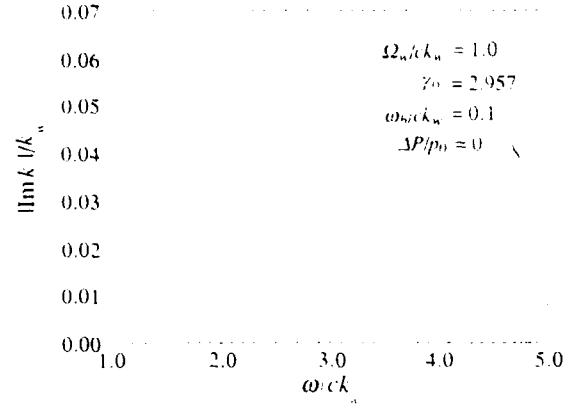


Fig. 1. Graph of the growth rate versus frequency for the fundamental and third harmonic interactions.

where

$$U_l(\zeta) \equiv \begin{cases} 0, & l < 2; \\ \sum_{k=2}^l \sum_{n=0}^{k-2} \frac{(-1)^{k-n} l! n! \zeta^{l-n}}{k! (l-k)! (k-2-n)!}, & l \geq 2. \end{cases} \quad (23)$$

The dispersion equation is solved numerically for the fundamental and the third harmonic. In general, strong harmonic amplification requires a relatively large oscillation in the axial velocity; hence, the growth rate at the harmonics increases rapidly with $\Omega_w/c k_w$. The analysis of cases in which $\Omega_w/c k_w$ is greater than unity requires a fully three-dimensional analysis. We restrict the numerical analysis herein to the case for which $\Omega_w/c k_w = 1$ which is at the fringe of the range of validity, and serves to clearly illustrate the relationship of the harmonics to the fundamental. In addition, we shall assume that $\gamma_0 = 2.957$ and $\omega_b/c k_w = 0.1$ as well. The magnitude of the growth rate is plotted versus frequency in fig. 1 for the fundamental and third harmonic. The fundamental exhibits a peak growth rate of $|\text{Im } k|/k_w \approx 0.065$ at $\omega/c k_w \approx 1.55$. In contrast, the magnitude of the growth rate at the third harmonic is $|\text{Im } k|/k_w \approx 0.012$ at $\omega/c k_w \approx 4.80$. Observe that both the magnitude and bandwidth of the harmonic is reduced relative to the fundamental.

The effect of the thermal spread is shown in fig. 2. Here we plot the normalized growth rate (the ratio of the maximum growth rate for a specific value of $\Delta P/p_0$ to the maximum growth rate for $\Delta P/p_0 = 0$) versus $\Delta P/p_0$. Thermal effects become important on the fundamental when $\Delta v/v \approx |\text{Im } k|/(k_w - \text{Re } k) \approx 0.025$, which corresponds to $\Delta P/p_0 \approx 22\%$ [observe that $\Delta v/v \approx \Delta P^2/2p_0^2$]. This is in substantial agreement with the results shown. For the harmonics, thermal effects become important at a much reduced thermal spread: [7,8] specifically, when $\Delta v/v \approx$

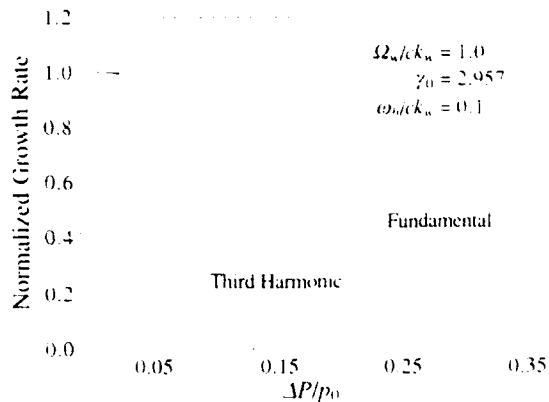


Fig. 2. Variation of the normalized growth rates at the fundamental and third harmonic with the axial momentum spread.

$\text{Im } k \approx [(1 + 2m)k_a + \text{Re } k]$. For the third harmonic in the present example $\Delta\epsilon/\epsilon \approx \text{Im } k \approx (3k_a + \text{Re } k) \approx 0.0015$. This corresponds to $\Delta P/p_0 \approx 5.5\%$, which is also in good agreement with the calculation.

The conclusions from the analysis are consistent with those found previously on the basis of an analytic model of thermal effects due to an energy spread and a nonlinear simulation using the pitch angle spread mode [12,13]. Specifically, that the gain at the harmonics is more sensitive to the effects of a thermal spread than is the fundamental. In particular, the thermal effect becomes important when $\Delta\epsilon/\epsilon \approx |\text{Im } k|/[(1 + 2m)k_a + \text{Re } k]$. In addition, it is clear that the thermal effect itself can give rise to amplification at the even as well as odd harmonics. However, this process requires a large energy spread which will result in relatively low growth rates, and is not likely to be of practical use.

Acknowledgements

This work was supported by the Defence Advanced Research Projects Agency under contract No. N00014-90C-2118.

References

- [1] B. Girard, Y. Lاپierre, J.M. Ortega, C. Bazin, M. Billardon, P. Ellaume, M. Bergher, M. Velghe and Y. Petrot, *Phys. Rev. Lett.* 53 (1984) 2405.
- [2] D.J. Bamford and D.A.G. Deacon, *Phys. Rev. Lett.* 62 (1989) 1106.
- [3] S.V. Benson and J.M.J. Madey, *Phys. Rev.* A39 (1989) 1579.
- [4] R.W. Warren, L.C. Haynes, D.W. Feldman, W.E. Stein and S.J. Gitomer, *Nucl. Instr. and Meth.* A296 (1990) 84.
- [5] W.B. Colson, *IEEE J. Quantum Electron.* QE-17 (1981) 1417.
- [6] R.C. Davidson *Phys. Fluids* 29 (1986) 267.
- [7] H.P. Freund, R.C. Davidson and D.A. Kirkpatrick, *IEEE J. Quantum Electron.* QE-27 (1991) 2550.
- [8] A.K. Ganguly and H.P. Freund, *Phys. Rev.* A32 (1985) 2275.
- [9] M.J. Schmitt and C.J. Elliott, *Phys. Rev.* A34 (1986) 4843.
- [10] H.P. Freund, C.L. Chang and H. Bluem, *Phys. Rev.* A36 (1987) 3218.
- [11] M.J. Schmitt and C.J. Elliott, *IEEE J. Quantum Electron.* QE-23 (1987) 1552.
- [12] M.J. Schmitt, C.J. Elliott and B.E. Newnam, *Nucl. Instr. and Meth.* A272 (1988) 586.
- [13] H.P. Freund, H. Bluem and C.L. Chang, *Nucl. Instr. and Meth.* A285 (1989) 169.
- [14] E. Jerby and A. Gover, *IEEE J. Quantum Electron.* QE-21 (1985) 1041.
- [15] C.W. Roberson, Y.Y. Lau and H.P. Freund, in: *High-Brightness Accelerators*, eds. A.K. Hyder, M.F. Rose and A.H. Guenter (Plenum, New York, 1986) p. 627.

Fabrication of biologically based microstructure composites for vacuum field emission

G. M. Chow*, W. B. Stockton**, R. Price, S. Baral***, A. C. Ting†, B. R. Ratna††, P. E. Shoen and J. M. Schnur

Center for Bio/Molecular Science and Engineering, Code 6090, Naval Research Laboratory, Washington, DC 20375 (USA)

G. L. Bergeron, M. A. Czarnaski, J. J. Hickman and D. A. Kirkpatrick

Science Applications International Corporation, 1710 Goodridge Drive, McLean, VA 22102 (USA)

Received April 1, 1992

Abstract

A multidisciplinary approach to the fabrication of biologically based microstructure composites for vacuum field emission is described. Diacetylenic lipid 1,2-bis(10,12-tricosadiynoyl)-sn-glycero-3-phosphocholine (DC_{29}PC) was self-assembled to form hollow cylindrical tubules approximately $0.5\ \mu\text{m}$ in average diameter and $50\text{--}80\ \mu\text{m}$ long. Following the deposition of nickel on the inner and outer tubule surfaces by an electroless plating method, the nickel-plated tubules were magnetically aligned in an epoxy matrix to form a composite material. Subsequent selective removal of the matrix provided a composite base template of oriented exposed tubules. The tubule template was coated with a thin sputtered gold film to provide the surface electrical contact. The resultant microstructures demonstrated vacuum field emission of current $I > 10\ \mu\text{A}$ at relatively low applied macroscopic electric fields (about $60\text{--}150\ \text{kV cm}^{-1}$).

1. Introduction

There has been an increasing interest in using a biology-related approach to fabricate advanced materials and composites of ultrafine microstructures with interesting properties and morphologies [1]. Nanoscale single and multicomponent particles have been synthesized using self-assembled phospholipid vesicles which act as individual reaction cages [2-4]. Tubules, hollow cylinders with average diameter of about $0.5\ \mu\text{m}$ and about $50\text{--}80\ \mu\text{m}$ long, have also been synthesized by the self-assembly of the diacetylenic lipid 1,2-bis(10,12-tricosadiynoyl)-sn-glycero-3-phosphocholine (DC_{29}PC) [5, 6]. We used an

electroless plating method to metallize the hollow tubules [7]. In this method, colloidal Pd-Sn catalyst particles were attached onto the surface of the tubules which were suspended in an aqueous dispersion. The catalysts had a palladium-rich core surrounded by a shell of hydrolyzed tin chloride. An "acceleration" process, which served to remove the protective shell and to expose the catalytic center, was used to prepare the tubules for plating. A commercial electroless plating solution (Niposit 468, Shipley), consisting of nickel ions, chelating agent, pH buffer and reductant was added to the tubule suspension, resulting in deposition of a thin Ni-B layer on both the inner and the outer surfaces of the tubules. The boron content of the Niposit 468 plating bath was less than 0.5 wt.%. After the plating was complete, the lipid was removed as much as possible from the metal tubules by repeated solvent extraction using acetone.

The metallized tubules have potential applications as controlled delivery vehicles [8], and as dielectric [9, 10] and magnetic materials [11-13]. Also, we have recently demonstrated [14] that the coated tubules can serve as ungated vacuum field emission cathode structures.

In order to generate a macroscopic electron beam

*Formerly also at Geo-Centers, Inc., Fort Washington, MD 20744, USA.

**Present address: Department of Materials Science and Engineering, Massachusetts Institute of Technology, Cambridge, MA 02139, USA.

***Also at Geo-Centers, Inc., Fort Washington, MD 20744, USA.

†Code 4790, Naval Research Laboratory, Washington, DC 20375, USA.

††Also at Georgetown Medical School, Georgetown University, Washington, DC 20007, USA.

current from many emission sites, a complex surface microstructure is necessary. Conventionally, micro-lithography [15–17] is used to fabricate surfaces with arrays of micro-scale cones or pyramids recessed only a few microns from an aperture in a gate structure. In our work [14], the emission sites are oriented hollow cylindrical tubules protruding about 3–15 μm from a base electrode. Although the tubule cathodes are not oriented in a well-defined array, the exposed tubule microstructures may provide a larger emission area than cone or pyramid structures. Local enhancement of the applied electric field is not achieved through the proximity of a nearby gate electrode but rather from the geometry of the protruding microstructures. For such a configuration, a steady state local field of approximately 10^8 V cm^{-1} may be obtained. This local field enhancement will be affected by factors such as the height-to-diameter ratio (aspect ratio) of the tubules, the radius of curvature and the thickness of metal coating at the edge of exposed tubules, and the average intertubule spacing and the tubule surface topography. Theoretically, the hollow nature of the tubules is expected to provide an electrostatic lensing effect which acts to focus the electrons [18]. The tubule cathodes operate well in a background vacuum pressure of 10^{-5} Torr or less in a steady state d.c. condition.

In this paper, we describe an approach for fabricating the vacuum field emission cathode structures using the phospholipid tubules. The electroless nickel-coated tubules were characterized by transmission electron microscopy (TEM), scanning electron microscopy (SEM), Auger electron spectroscopy and X-ray photoelectron spectroscopy (XPS). Qualitative correlation of the coating properties of the tubule cathode microstructures and their field emission behavior is discussed.

2. Experimental details

Electroless nickel-plated tubules, suspended in acetone, were mixed with epoxy resin to form a composite. Epoxy resin was chosen as the matrix material for the tubule composite because of its ease in processing and molding, and its appropriate viscosity and curing rate for tubule dispersion and alignment without settling. Typically, nickel-coated tubules of weight fractions ranging from 0.25 to 1.0% were mixed with Epon 815 (70 wt.%) resin. Acetone was removed by rotary evaporation, followed by addition of the curing agent Ancamide 507B (30 wt.%). The tubule-epoxy mixture was maintained at 60–65 $^{\circ}\text{C}$ during mixing and solvent removal. Agitation was avoided to minimize the aggregation of the nickel tubules. The nickel tubule-epoxy

mixture was cast into a cylindrical mold and then placed in a magnetic field density of approximately 500 G for axial alignment of the tubules at room temperature. The initial viscosity of the epoxy matrix under these circumstances allowed for the movement and therefore the alignment of the tubules to occur in less than 10 min. The resin curing rate was observed to be faster than the gravitational settling rate of the coated tubules, so that tubule settling was not a problem. The tubule-epoxy composite mixture cured at room temperature in air in approximately 24 h. The composite was black whereas the epoxy blank (without nickel tubules) was translucent.

Thin sections, about 50 μm thick, were obtained by cutting the composite perpendicular to the alignment axis using a microtome. The sections were then etched in an oxygen plasma by using a parallel-plate anisotropic plasma configuration to remove selectively the outer few microns of the epoxy. The exposed surface was coated sequentially with layers of evaporated gold (about 200 \AA) followed by silver (about 2000 \AA). This Au/Ag film, although not essential, served as an interface for the Indalloy solder bonding of the tubule composite section onto the copper emission test stub. The exposed epoxy face was subsequently etched in an anisotropic oxygen plasma for times ranging from 2 to 8 h at a power of 65 W and a pressure of 150 mTorr, in order to vary the lengths of the exposed tubules.

The resultant microstructure templates mounted on the copper stub were placed into a cylindrical hole centered in an anodized aluminum cathode holder. A microanode was used to ensure that the emission came only from the localized area of the tubule cathode surface. The vacuum pressure was maintained in the 10^{-6} – 10^{-5} Torr range by a cryopump. After the initial emission testing, the same sample was sputter coated with about 500 \AA of gold and retested for emission. A summary of the fabrication procedure is shown schematically in Fig. 1.

3. Results and discussion

The epoxy matrix was selectively removed by an oxygen plasma etch to expose the oriented metallized tubules. Typically, the different plasma etching times yielded templates with tubules protruding 3–15 μm from the composite base. There was always a height distribution of the exposed tubules. This height distribution was caused by the original length distribution of the tubules and breaking of the tubules during the subsequent processing steps. Because of the height distribution, it is difficult to correlate quantitatively the tubule protrusion height with the plasma etching times. A typical appearance of the exposed tubule templates

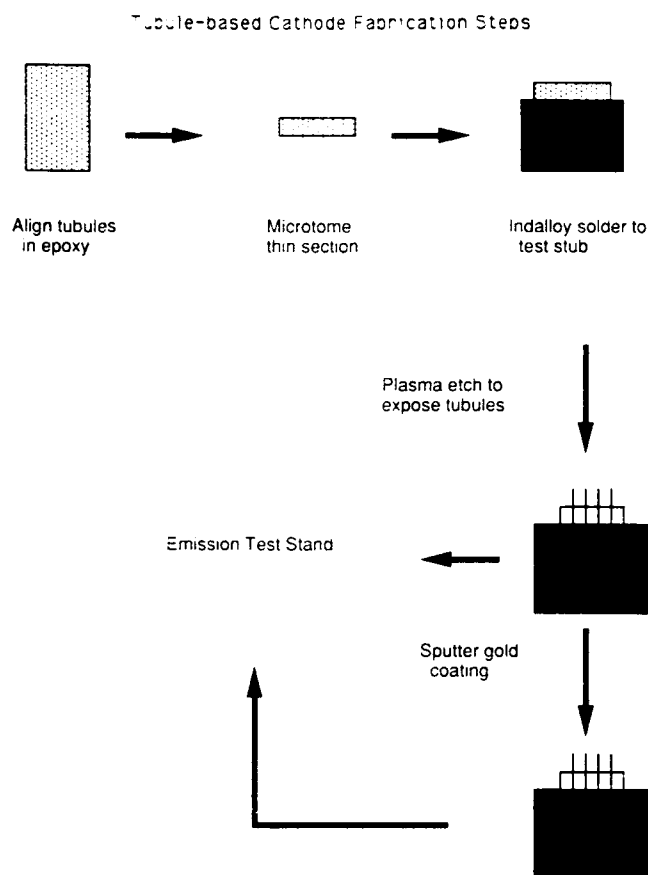


Fig. 1. A schematic diagram of the fabrication of the tubule cathode microstructures.

is shown in Fig. 2(a). There were more aggregated tubules when a higher tubule concentration was used in the composite (Fig. 2(b)). In either case, both individual and aggregated tubules were found. The aggregation of the tubules could have occurred during any steps of the fabrication: tubule formation, electroless metallization and/or composite casting. Although surfactants were intentionally added to the electroless plating bath for tubule metallization, the aggregation problem could not be completely eliminated. The templates showed severe charging when examined by XPS, indicating that the exposed tubules were also oxidized during the plasma etch removal of the epoxy matrix. The templates were subsequently coated with gold by sputtering to obtain a final tubule cathode microstructure.

The quantum field emission from a one-dimensional cold-cathode system is described by the field emission current density equation of Fowler and Nordheim [19]. The available current density for the tubule cathode depended on the local electric field at the emission site. The local field is expected to be enhanced as a result of the morphology and size of the tubule, when the thin metal coating is electrically conductive. For the tubule

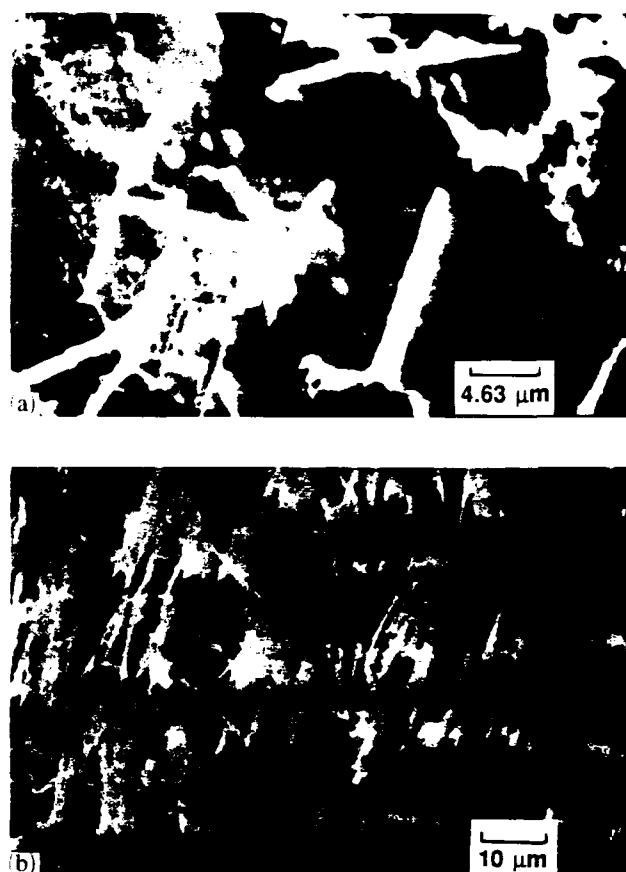


Fig. 2. SEM micrographs of the tubule templates obtained after the oxygen plasma etch of the tubule composite: (a) less aggregated tubules; (b) more aggregated tubules.

templates produced after the plasma etch, no emission was observed because of the highly oxidized surface. However, when the tubule templates were coated with sputtered gold (approximately 500 Å thick), some coated tubules demonstrated emission. Initial emission was observed for tubule cathodes for applied electric fields in the range 60–80 kV cm⁻¹. The maximum emitted currents were limited by controlling the applied field in order to avoid the thermal stress on the gold film. Currents up to 300 μA were measured. It has been estimated that local current densities as large as 10⁵ A cm⁻² were produced [14]. An example of the voltage waveform, current waveform and resultant current-voltage (*I-V*) characteristic is shown in Fig. 3. There was an asymmetry of the current waveform with respect to the rise and fall of the applied voltage, and also a hysteresis in the *I-V* characteristic. This behavior was noted in all the cathodes tested to date and is currently being studied. It was also observed that samples containing taller tubule cathodes started initial emission at a lower turn-on field than those with shorter tubule cathodes. The minimum height for emission to occur was about 6 μm.

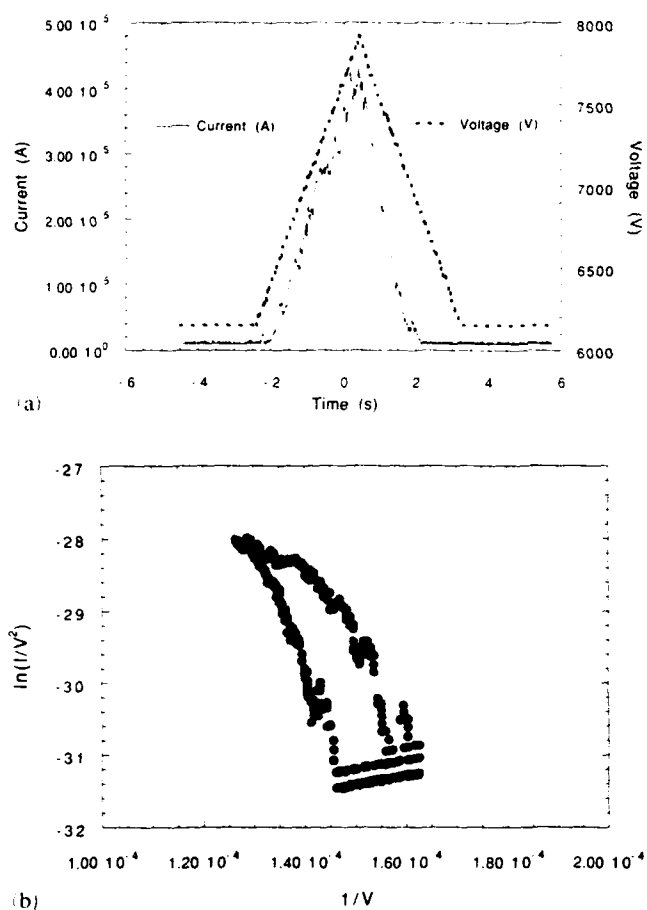


Fig. 3. The voltage waveform, current waveform and resultant I - V characteristics of an emissive tubule cathode sample.

For the aggregated tubule cathode microstructures, the local field enhancement is expected to be small because of the mutual shielding of the tubules in the same bundle and also because of the decrease in the effective edge for emission. Therefore, in the sample shown in Fig. 2(b), the observed emission is believed to arise from only the individual conducting tubules having the favorable local field enhancement. The height variation of individual tubules also plays an important role. Individual protruding tubules having uniform height can turn on at the same applied voltage. However, the non-uniformity of tubule height may cause the taller tubules to emit electrons while the shorter tubules still do not emit because of the difference in field enhancement factors. Applying a larger field in the hope of obtaining emission from the shorter tubules instead resulted in the melting and ablation of the taller structures. Under these circumstances, arcing occurred during the emission measurements. Emission tests showed that from the same parent composite some samples demonstrated emission whereas some did not. This may possibly be caused by the heterogeneity in exposed tubule heights and alignment that

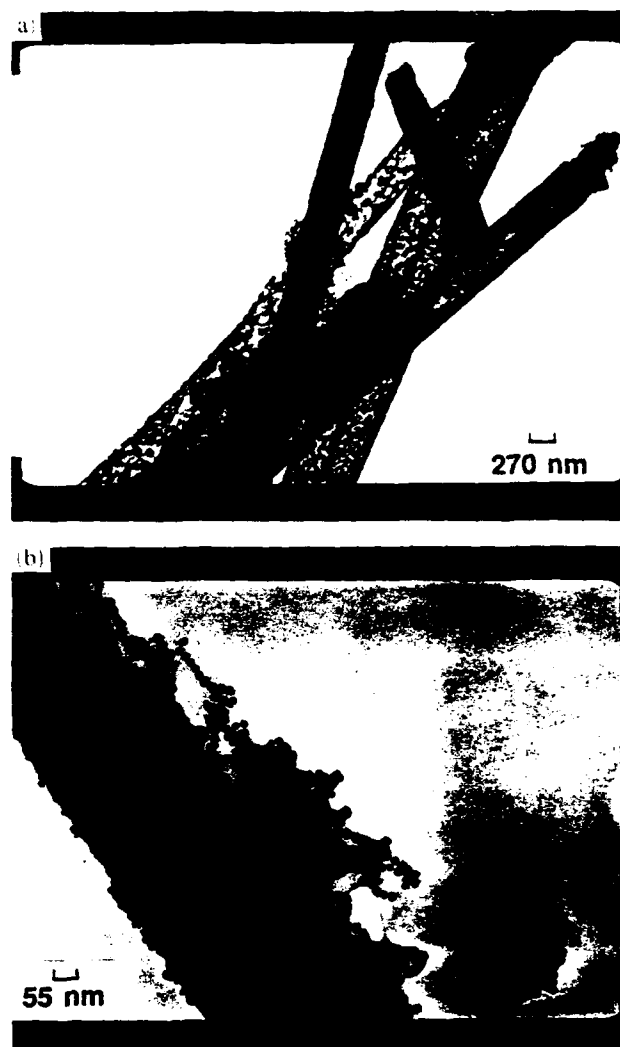


Fig. 4. TEM micrographs showing typical nickel-plated tubules: (a) non-uniform plating; (b) plated tubules with aggregated particles.

occurred in different thin sections of the same composite. A baseline reference of the emission results will need to be established in order to compare the emission data with various parameters of the tubule cathodes.

4. Current fabrication issues

Currently, the nickel crystallite size of the electroless-plated tubules was found to be in the range 30–45 Å by both dark-field TEM and X-ray diffraction. The coating thickness (typically a few hundred ångströms) and uniformity often varied for tubules from the same batch, as shown in Fig. 4. We also observed the formation of aggregated particles. Selected-area electron diffraction analysis revealed that the aggregated particles were SnO_2 and were often coated with nickel. The

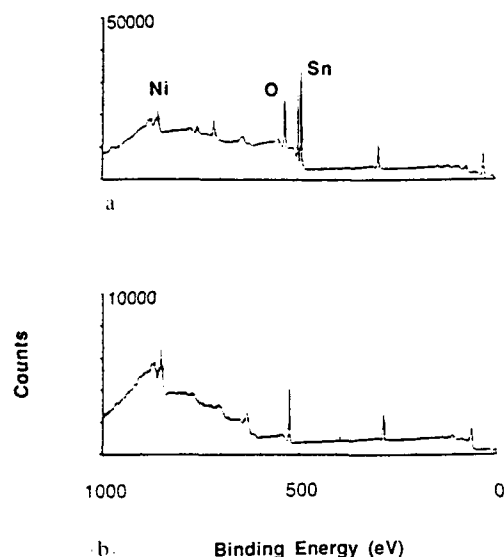


Fig. 5. XPS survey spectra of the electroless plated nickel: (a) tubules plated in the atmosphere; (b) tubules plated under an argon environment.

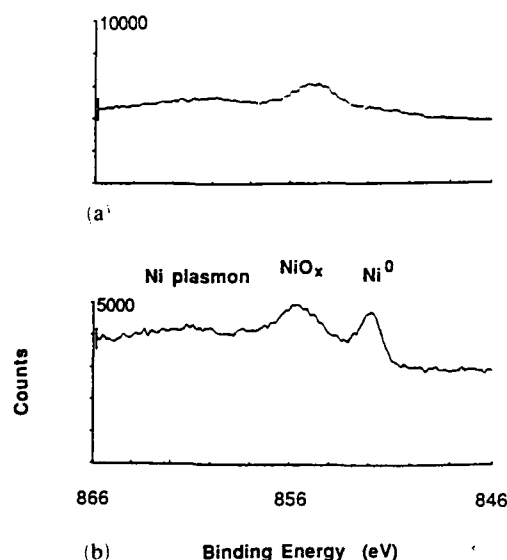


Fig. 6. XPS high resolution scans of the nickel regions of the samples shown in Fig. 5: (a) tubules plated in the atmosphere; (b) tubules plated under an argon environment.

formation of aggregated particles was probably caused by the difficulties of complete removal of free catalysts (not bound to a tubule surface) from the solvent in the plating process. These extraneous microstructures were eventually incorporated into the epoxy matrix.

XPS of tubules plated and handled in air exhibited the surface compositions seen in Fig. 5(a). As can be seen, large amounts of tin and oxygen were on the surface. A high resolution scan of the Ni 2p_{3/2} region (Fig. 6(a)) indicated that the surface was composed entirely of nickel oxide. Boron was detected as

expected from using this electroless plating bath. An Auger depth profile analysis of individual tubules indicated that all the surface was oxidized and smaller amounts of oxide were found throughout the sample. This is attributed to the porous nature of the electroless metal film which allowed rapid oxidation of the entire coating to occur. However, plating of the tubules in an argon atmosphere resulted in much less surface oxide (Figs. 5(b) and 6(b)). Since electron diffraction did not show oxide lines, the oxides are believed to be amorphous. Handling of the tubules in air is necessary at this time for the cathode fabrication and the oxide formation is inevitable. However, there was still enough ferromagnetic nickel on the tubule surfaces to allow them to be magnetically aligned during the composite casting. The subsequent removal of the epoxy matrix to obtain the exposed tubules using an oxygen plasma etch unavoidably oxidized the nickel tubules, leaving an electrically insulating template.

Although the electroless-coated nickel tubules may serve as templates for the fabrication of the final tubule cathode structures by gold coating optimization, this template approach causes the advantage of thin wall and sharp edge tubule to be compromised because of the additional gold thickness on both inner and outer surfaces of the hollow tubules.

It was also observed that often the gold-coated tubule cathodes were ablated during the emission measurements. It is known that the maximum current density that can be sustained by the tubule conductive coating without causing the thermal breakdown is proportional to $(T_m \kappa / \rho_e)^{1/2}$ [20], where T_m is the melting temperature, κ the thermal conductivity and ρ_e the electrical resistivity of the coating. For conducting metals, the thermal conductivity is inversely proportional to its electrical resistivity. Normally, sputtered films have crystallite dimensions of less than 100 Å. For the sputtered gold film on the tubule templates, the resistivity is expected to be large owing to the small crystallite size and the small thickness. The current density that can be safely sustained by these gold-coated tubule cathodes was therefore not very large. Resistive heating of the gold film by the applied voltage during emission tests may lead to its cracking and delaminating, because of the large difference between the coefficients of thermal expansion of the gold film and the insulating epoxy matrix. Eventually, the gold coating melts when enough heat is accumulated owing to the poor thermal conduction.

Future work may aim at the production of electrically and thermally conductive tubules via the electroless metallization technique and, if possible, a suitable matrix with good thermal but poor electrical properties and which might be subsequently removed by a process which does not oxidize the tubule surface.

5. Summary

We have reported a multidisciplinary approach to fabricating cathode microstructures derived from hollow phospholipid tubules. The tubules were plated with nickel using electroless plating and were cast in an epoxy matrix to form an oriented composite. Subsequent selective removal of the epoxy provided a composite template with oriented exposed tubules. The template was sputter coated with gold to provide the electrical conductivity of the exposed tubules. The final gold-coated tubule cathode microstructures demonstrated vacuum field emission. Current fabrication issues are briefly discussed.

Acknowledgments

We thank Dr. S. Qadri for the X-ray diffraction work. We also thank the Defense Advanced Research Projects Agency for support of this work.

References

- 1 D. R. Ulrich, *J. Non-Cryst. Solids*, **121** (1990) 465.
- 2 S. Mann and J. P. Hannington, *J. Colloid. Interface Sci.*, **122** (1988) 326.
- 3 S. Bhandarkar and A. Bose, *J. Colloid Interface Sci.*, **139** (1990) 541.
- 4 H. Liu, G. L. Graff, M. Hyde, M. Sarikaya and I. A. Aksay, in *Materials Synthesis Based Biological Processes, Materials Research Society Symp. Proc.*, **218** (1991) 115.
- 5 P. Yager and P. E. Schoen, *Mol. Cryst. Liq. Cryst.*, **106** (1984) 371.
- 6 J. M. Schnur, R. Price, P. Schoen, P. Yager, J. M. Calvert, J. Georger and A. Singh, *Thin Solid Films*, **152** (1987) 181.
- 7 J. M. Schnur, P. E. Schoen, P. Yager, J. M. Calvert, J. H. Georger and R. Price, *US Patent 4,911,981* March 27, 1990.
- 8 R. Price, M. Patchan and B. P. Gaber, *Proc. 7th Int. Conf. on Encapsulation and Controlled Release, Glasgow, 1990*, University of Strathclyde, Glasgow, 1990, p. 36.
- 9 F. Behroozi, M. Orman, R. Reese, W. Stockton, J. Calvert, F. Rachford and P. Schoen, *J. Appl. Phys.*, **68** (1990) 3688.
- 10 W. Stockton, J. Lodge, F. Rachford, M. Orman, F. Falcos and P. Schoen, *J. Appl. Phys.*, **70** (1991) 4679.
- 11 J. J. Krebs, M. Rubinstein, P. Lubitz, M. Z. Harford, S. Baral, R. Shashidhar, Y. S. Ho, G. M. Chow and S. Qadri, *J. Appl. Phys.*, **70** (1991) 6404.
- 12 C. Rosenblatt, P. Yager and P. Schoen, *Biophys. J.*, **52** (1987) 295.
- 13 Z. Li, C. Rosenblatt, P. Yager and P. Schoen, *Biophys. J.*, **54** (1988) 209.
- 14 D. A. Kirkpatrick, G. L. Bergeron, M. A. Czarnaski, J. J. Hickman, G. M. Chow, R. Price, B. R. Ratna, P. E. Schoen, W. B. Stockton, S. Baral, A. C. Ting and J. M. Schnur, *Appl. Phys. Lett.*, **60** (1992) 1556.
- 15 C. A. Spindt, K. R. Shoulders and L. N. Heynick, *US Patent 3,755,704*, 1973; *US Patent 3,812,559*, 1974.
- 16 C. A. Spindt, C. E. Holland and R. D. Stowell, *Appl. Surf. Sci.*, **16** (1983) 268.
- 17 H. F. Gray, G. J. Campisi and R. F. Greene, *Proc. Int. Electron Devices Meet., Washington, DC, 1989*, IEEE, New York, 1989, p. 776.
- 18 D. Kirkpatrick, unpublished results, 1991.
- 19 R. H. Fowler and L. Nordheim, *Proc. R. Soc. London, Ser. A*, **119** (1928) 173.
- 20 R. B. Miller, *An Introduction to the Physics of Intense Charged Particle Beams*, Plenum, New York, 1982, p. 37.

Jitter Suppression in a CFA by the Use of a Field Emitter Array

Rodney Vaughan, Ken Ramacher

Litton Electron Devices Division

and

George Bergeron

S.A.I.C., McLean, VA

Abstract

A cold-cathode Cross-Field Amplifier (CFA) was built with a 1.5-million-point field emitter array embedded in the cathode just before the start of the active region of the tube. The intention was to reduce jitter, which is a severe problem in these tubes at very low pulse repetition frequencies. Peak jitter at 1 Hz p.r.f. was reduced by two orders of magnitude on average, compared to a control tube built without the array; rms jitter was reduced by one order of magnitude. Reasons for this difference are discussed.

Introduction (RV)

The cold-cathode Cross-Field Amplifier (CFA) depends entirely on secondary emission for the beam current. There is generally no intentional priming source to start the secondary emission process, but some natural sources evidently exist, since the tubes do start. The starting is, however, subject to delays which range from nanoseconds up to seconds, and in one recorded case several minutes. When the delays are in the nanosecond to microsecond range they are called jitter, when longer, they are called delayed starting.

Since jitter affects the range accuracy of a radar using CFAs, it is important to control jitter at a very low level, and 1 nanosec has been the goal, corresponding to approximately 1 foot.

Earlier work had shown that, at a p.r.f. above about 10 Hz the jitter problem is less severe. Once a tube has started, electron storage after each pulse is effective in starting the next pulse with low jitter, but this storage is only effective for at most 100 millise.

Experimental tubes with thermionic filaments embedded in the cathode had shown that the amount of priming current required for jitter suppression even at the lowest p.r.f. was exceedingly small, about 2 nanoAmp; in more meaningful terms, about 10 electrons must be emitted in the critical 1 nanosec period. The cathode filament was not considered a solution for operational tubes, because it required a power supply floating at full pulse voltage.

In the absence of any artificial source, the jitter of the "natural" priming sources (which are discussed further below) fluctuates wildly from the nanosecond to the microsecond range at 1 Hz p.r.f.

Since the required current was so small, it appeared possible that a field emitter might be able to supply it; it would have the advantage of needing no power supply. At this time we at Litton became aware of the TaSi₂ field emitter arrays developed by SAIC (described in more detail below). There were concerns that either the array

might destroy the CFA by causing uncontrollable arcing, or the tube might destroy the array by the intense back bombardment characteristic of all cross-field devices. There seemed to be no way to answer either question except by actual trial, so arrangements were made for SAIC to supply some test pieces, and for Litton to build and test a CFA containing one; a parallel tube was built with no array as a control.

Field Emitter Array (GB)

The field emitters used in the CFA experiments consist of a semiconductor-metal eutectic composite of nearly-parallel fibers of the metallic TaSi₂ phase embedded in single-crystal Si matrix (Si-TaSi₂)⁽¹⁾. Each fiber is about 1 μ m in diameter and is continuous throughout the matrix. The density of the fibers is about 1 million per square centimeter, with an average fiber-to-fiber spacing of about 8-10 μ m. These composites are produced using a Czochralski growth technique, and wafers are sliced from the resulting boule, normal to the growth of the fibers (2). Using standard semiconductor processing technology, the wafers are diced and polished to produce the blanks from which the final cathodes are made. A Ti-Ni-Au layer is evaporated on one side of the blank, providing electrical contact to the TaSi₂ fibers within the matrix. By selective chemical etching of the Si and TaSi₂, the fibers can be exposed and sharpened to controlled heights and tip angles. For the CFA application, the Si base was etched back to expose tips of about 30 - 50 μ m in height (Figure 1). By virtue of the operating characteristics of the field emitters (1), this process yields a required electric field of about 20 kV/cm for device turn-on. Because the CFA is run with an oxygen background, special consideration was given to protecting the tips from oxidation (3). A thin film of gold was sputtered onto the top surface of the emitter, covering both the Si matrix and the TaSi₂ tips.

Before the installation of a field emitter into the CFA, experimental tests were performed on the emitters as a verification of suitability. These tests consisted of a eutectic field emitter, shaped for installation into a CFA, being placed in a dc test stand. This stand had provision for the controlled injection of oxygen into the evacuated test chamber. The eutectic field emitter was recessed in a slot in an anodized aluminum electrode, which in turn was placed at a distance from a parallel plate copper anode equal to that of the A-K gap in the CFA. The depth of the emitter relative to the surface of the electrode was controlled by a linear motion feedthrough (Figure 2). This arrangement allowed the cathode to be tested in a controlled oxygen environment at different

recess depths. Through this process, it was found that at a 0.006" recess depth and 10 - 15 kV applied voltage, 0.3 to 3 μ Amp of current could be reliably drawn from the tips. The system pressure was maintained at 5×10^{-6} Torr, under continuous injection of oxygen. Subsequent analysis of the test emitters showed that no surface damage was caused by operation in this manner.

Construction of CFA (KR)

The tests were carried out in a standard L-4826 CFA, which was rebuilt with a 0.05" wide 0.03" deep groove machined in the cathode and positioned just at the end of the drift region at the input end of the tube (Figure 3). The field emitter block was placed in this groove and held in place by tungsten clips secured with watchmaker's screws; the clips crushed about 75,000 tips at each end, but this was a minor loss; it was decided to use this mechanical fixturing for a first trial because it was not known what brazing procedure would be compatible with the array and the cathode. The operating duty cycle was limited to 0.003 to compensate for the poorer thermal contact. The emitter tips were approximately 0.006" below the adjacent shoulders of the slot.

The tube was standard in all other respects and was put through the normal processing and exhaust procedures. The comparison tube was a standard L-4826 built at the same time.

Test results (KR)

After initial aging, both tubes were tested for jitter at 1 Hz p.r.f. and showed the usual low values: jitter is a problem which normally does not appear until after a few tens of hours of operation. The tubes were run on life test at 0.003 duty, and retested for 1 Hz jitter at approximately 50, 100, 200 and 400 hours (the comparison tube was not tested at 400 hours because it met all the test requirements and was shipped at 200 hours; 1 Hz jitter performance is a goal but not a requirement). Each test consisted of 14 measurements of peak and rms jitter in 100-pulse samples, at oxygen pressure levels covering approximately a 15:1 range. There was no apparent correlation between the jitter and the oxygen level in any of the tests. Table 1 shows the minimum and maximum jitter values from the 14 readings taken on each tube at each test time.

Table 1
Summary of jitter test results

hours	f.e. tube #1004R1		comparison tube #100417	
	peak	rms	peak	rms
0	not rec.	0.76-1.27	not rec.	0.93-4.75
50	12-40	2.26-7.38	96-3150	18.5-642
100	25-28	2.83-10.9	4-30	0.78-4.4
180	21-55	4.75-12.1	424-1854	55-388
425	16-34	2.49-8.74	not rec.	not rec.

Each entry shows the range of jitter values (in nanoseconds) observed in 14 measurements at different oxygen levels.

After the 425-hour test the f.e. tube was cut open, and the entire cathode assembly was sent to SAIC for examination, taking as much care as possible to avoid any spurious contamination. There had been no degradation of tube performance at the time it was taken off test.

Post mortem (GB)

After the tests in the actual CFA were completed, the entire cathode assembly was mounted for surface evaluation via scanning electron microscopy. This examination revealed that, while most tips were undamaged, there was evidence of mechanical breakage of tips in some areas. Arcing damage, which exhibits itself in the form of melted tips and craters in the Si substrate, was not found, but normal rounding caused by field forming was. An unexpected amount of particulate matter in the form of "dust" was found on the emitter surface. This dust was apparently the cause of the slight mechanical damage, as if the particles had been accelerated into the surface of the emitter, knocking over tips as they hit. These particles were also found over the entire surface of the CFA cathode. After SEM inspection of the assembly, the emitter was removed from the cathode and examined using Auger Electron Spectroscopy (AES) to determine the composition of the dust: it was found to be composed of Cu and Mo spheres that did not appear to be cross-contaminating (4).

Discussion of results (RV)

The tests laid to rest the concerns that the array might either promote arcing or be destroyed by electron bombardment: neither of these happened in 425 hours of testing at 0.003 duty.

The field emitter reduced the peak jitter by about 2 orders of magnitude, from several microseconds down to the 30 nanosecond region, and did so consistently in all the tests, as shown in Table 1. The comparison tube was wildly inconsistent, usually showing peak jitter up to 3 microseconds: but on the test at 100 hours the comparison tube was *better* than the field-emitter tube. This was not an isolated fluke, because the sequence of jitter tests at 14 different oxygen levels takes more than 30 minutes to perform (at one pulse per second, data acquisition is very slow), and the comparison tube remained "good" throughout this period; but it was "bad" 50 hours earlier and 80 hours later. Evidently the "natural" priming mechanisms on which a normal tube depends can change dramatically during life, for either better or worse, but cannot be relied upon.

The rms jitter was also reduced by the field emitter, but only by about one order of magnitude. Clearly, the field emitter tube still has the natural priming sources available, and on many pulses one of these sources will have started the tube sometime within the first 25 nanoseconds, thus pre-empting the field emitter. But if no start has occurred in this period, the field emitter steps in and clamps a limit of about 30 nanoseconds on the delay. Thus, the peak jitter is hard-limited by the field emitter, while the rms jitter reflects the continued presence of

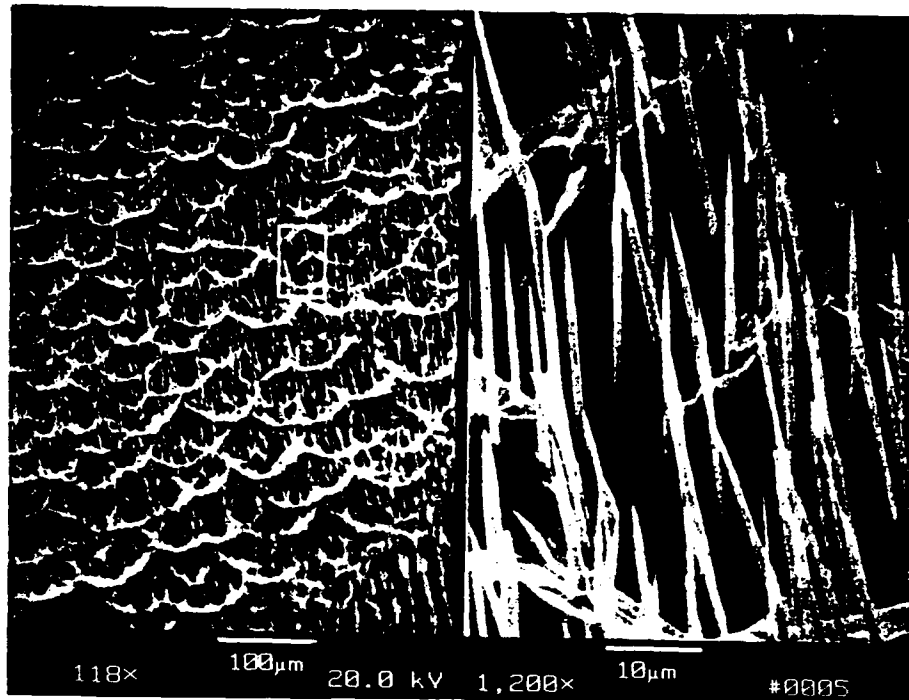


Figure 1: SEM photomicrograph of typical CFA emitter

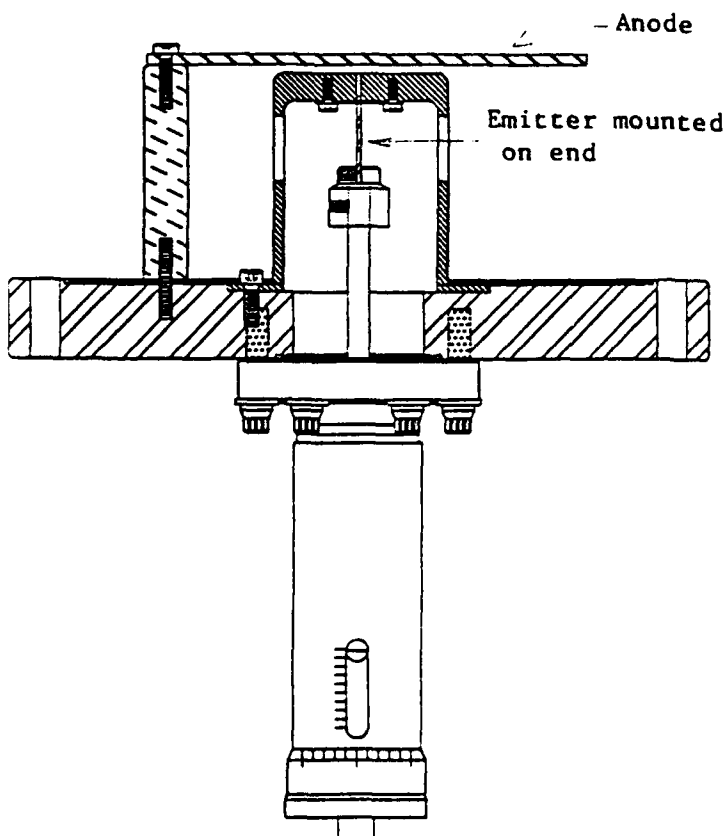


Figure 2: Pre-insertion test set-up

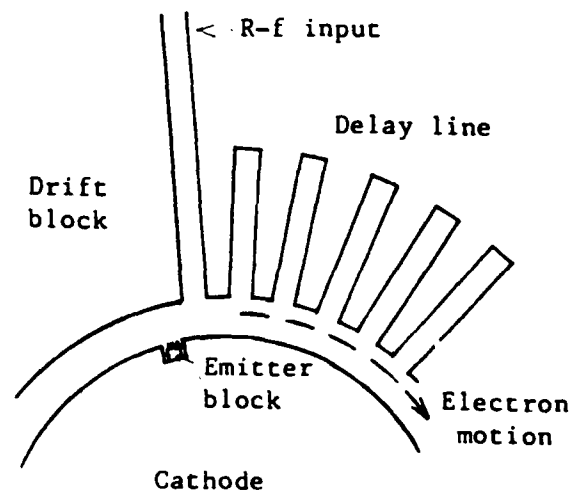


Figure 3: Position of emitter block in CFA

other priming sources.

What these other sources are is still not clear; possibilities include unintended field emitters (whisker growth), residual radioactivity, electron storage from the preceding pulse, cosmic rays, etc. The behavior of the comparison tube at the 100 hour test means that these natural mechanisms must include at least one that is effective at the 10 nanosecond level and can last for an hour or more, but does not typically last 50 hours: whisker growth with subsequent burn-off seems a likely candidate, but we have no direct evidence for it. Residual radioactivity and electron storage would be expected to be much more consistent, while cosmic rays are too transient to explain the observation.

It is not clear why the hard limit imposed by the field emitter was as high as 30 nanosec. From the SAIC measurements, the available current was in the 1 μ amp range, 500 times larger than the 2 nanoamps that the cathode filament experiment had shown to be sufficient to reduce jitter to less than 1 nanosecond. Thus the field emitter *ought*, by this reasoning, to have brought the jitter down to 1 nsec or less, with a large margin of safety. Why did it stop at 30 nsec? One possibility is that we did not put it in the best position: because of the concern about damage, it was placed near the end of the drift region, where the electron bombardment is expected to be much less intense. Now that we know that the array is relatively robust, we should try placing it under the beginning of the delay line; it will receive more electron bombardment there, but will be injecting electrons at a more favorable point, where they will be immediately accelerated into cathode-impacting trajectories. But it is also possible that the real difference between the cathode filament and the field emitter performances is that the filament provided its 2 nanoAmps continuously, while the field emitter provides its 1 microAmp only in pulses, each starting when the cathode voltage pulse is almost up to its peak value. With the aid of the magnetic field, and of any residual inter-pulse anode-cathode voltage -- even a few Volts -- the filament *could* be storing electrons all around the interaction space during the interpulse period. The ungated field emitter has no such storage capability; we may need to consider a gated emitter that can be gated on prior to the cathode pulse, so that some storage can occur; but this carries the penalty that a floating power supply for the gating electrode is then required.

In short, we achieved 2 orders of magnitude improvement, but do not really understand why we did not get 3 orders.

The observation by SAIC of spherical Cu and Mo balls on the cathode is intriguing; we had anticipated bombardment by electrons and by ions, but not a cannonade of micro-birdshot; the sizes were reported as "roughly 10 μ m diameter on down." Crude calculations indicate that a 10 μ m-size Cu or Mo crystallite detached from the anode into the electron stream would rise in temperature more than 500° C per μ sec. Either material could therefore reach its melting point within the 6 μ sec pulse length, accounting for the spherical shape. Smaller particles will melt more rapidly, the rate of rise of temperature being inversely proportional to the diameter.

Above the melting temperature the particle may emit thermionically more than it is bombarded; in addition, the effective secondary emission ratio for a Moly sphere remains above unity up to about 4 kV, because of the increase in δ for oblique impacts, as determined by numerically integrating Vaughan's equations, (5) and (7), as modified by the work of Shih and Hor (6); consequently it acquires positive charge and is accelerated into the cathode. The transit time to the cathode will be tens of μ sec at least; this is more than the pulse length, so that the bombardment by beam electrons has now ceased, and the sphere can re-solidify before it hits the cathode. All this is highly speculative, because the state of charge acquired by the sphere is hard to guess, let alone determine, but the unsplattered spheres are real.

References:

- [1] D.A.Kirkpatrick, G.L.Bergeron, M.A.Czarnaski, J.J.Hickman, Mark Levinson, Q.V.Nguyen and B.M.Ditchek, Appl. Phys. Lett. 59 (1991) 2094.
- [2] B.M.Ditchek and M.Levinson, Appl. Phys. Lett. 49 (1986) 1656.
- [3] J.J.Hickman, G.Bergeron, M.Czarnaski and D.A.Kirkpatrick, submitted to Appl. Phys Lett.
- [4] J.J.Hickman, private communication.
- [5] R.Vaughan, "A New Formula for Secondary Emission Yield", IEEE Trans. Electron Devices, ED 36 #9, Sept. 1989.
- [6] A.Shih and C.Hor, "Secondary Emission Properties as a Function of the Electron Incidence Angle", submitted to IEEE Trans. Electron Devices.
- [7] R.Vaughan, "Secondary Emission Formulas", submitted to IEEE Trans. Electron Devices; this is a revision of (5) based on the measurements reported in (6).

Appendix B

FEAT Code Listing

```

1      program feat
2      c
3      c=====
4      c
5      c.... FEAT: Nested multigrid ADI Laplace solver with internal structure.
6      c
7      c.... Kang Tsang (tsang@mclapo.saic.com)
8      c.... Alan Mankofsky (alan@mclapo.saic.com)
9      c
10     c.... SAIC Applied Physics Operation
11     c.... McLean, VA 22102
12     c
13     c.... January 1990: original version
14     c.... May 1991: multiple geometries (ntype):
15     c.... type 1 geometry: solid cathode structure at cylindrical axis
16     c.... type 2 geometry: hollow cylindrical cathode structure
17     c
18     c=====
19     c
20     common /ccom/ lab,meshfile,dumpfile,diagfile,id,ivers,ascfile
21     character*80 lab
22     character* 8 meshfile,dumpfile,diagfile,id8,ascfile
23     character* 4 id,mode
24     character* 7 ivers
25     common /flags/ debug,resume,ntype,dump
26     logical debug,resume,dump
27     c
28     ivers="25Mar91"
29     c
30     c.... Send banner.
31     write (6,10) ivers
32     10 format(/" FEAT v.",a7/)
33     c
34     c.... Get execute line.
35     narg=iargc()
36     c
37     if (narg.eq.0) then
38         id="test"
39         mode="mesh"
40     elseif (narg.eq.1) then
41         call getarg(1,id)
42         mode="mesh"
43     elseif (narg.eq.2) then
44         call getarg(1,id)
45         call getarg(2,mode)
46         if (mode.ne."mesh" .and. mode.ne."dump" .and. mode.ne."gen")
47             then
48                 write (6,20)
49                 20 format("Mode bad!")
50                 stop
51             endif
52     else
53         write (6,30)
54         30 format("Bad execute line!")
55         stop
56     endif
57     c
58     c.... Form file names, etc.
59     id8=id//" "
60     c
61     meshfile=id//".msh"
62     dumpfile=id//".dmp"
63     diagfile=id//".dia"
64     ascfile=id//".asc"

```

```
65      c
66      c.... Get run parameters.
67          call getinput
68      c
69      c.... Open data file.
70          if (mode.eq."mesh") then
71              write (6,40) meshfile
72          40      format("Opening mesh file ",a8,".")
73              open (22,file=meshfile,status='unknown',form='formatted')
74          elseif (mode.eq."dump") then
75              write (6,50) dumpfile
76          50      format("Opening dump file ",a8,".")
77              open (22,file=dumpfile,status='unknown',form='unformatted')
78          endif
79      c
80      c.... Read file header.
81          if(mode.ne."gen")call readhdr(mode)
82      c
83      c.... Set derived dimensions.
84          call setdims
85      c
86          if (debug) open(23,file=diagfile,status='unknown',
87                          form='formatted')
88          call genmsh
89          write(6,51)
90          51      format("Mesh generated.")
91      c
92      c.... Read KL mesh.
93          if(mode.ne."gen")call readmesh(mode)
94      c
95      c.... Read solution if dump mode.
96          if (mode.eq."dump") then
97              call readsoln
98          endif
99      c
100     c.... Close data file.
101         if (mode.ne."gen") close(22)
102     c
103     c.... Initialize NCAR graphics.
104         call opngks
105     c
106     c.... Solve if necessary.
107         if (mode.ne."dump" .or. (mode.eq."dump" .and. resume)) then
108             if(ntype.eq.1)then
109                 call fcadi1
110             elseif(ntype.eq.2)then
111                 call fcadi2
112             endif
113         c.... Write dump for next time.
114             if (dump) call wrdump
115         endif
116     c
117     c.... Terminate NCAR graphics.
118         call clsgks
119     c
120     c.... Timing.
121         icpu=mclock()
122         write (6,100) 1.e-2*float(icpu)/60.
123         write (23,100) 1.e-2*float(icpu)/60.
124     100     format("CPU (min)=",f8.2)
125         if (debug) close(23)
126     c
127     c.... Done.
128     c
```

```
129      stop
130      c
131      c.... Error trap.
132      c
133      900  write (6,910)
134      910  format("Cannot open data file!")
135      stop
136      c
137      end
```

```
1      block data
2
3      c
4      include 'global.h'
5
6      c
7      data eps/.1e-9/,ck/1.e-5/
8      data itmax/2/,itmx/100/,height/10./,width/0.5/,angle/22.5/
9      data volts/20.0/,radc/.01/,ntype/1/
10     data debug/.true./,newlevs/.false./,nclevs/24/
11     data resume/.false./,dump/.false./
12     data xl/0.,0.,0./,xh/5.,0.5,.125/,yl/.0,9.,9.8/,yh/20.,11.,10.2/
13     data fuzzfc/1.e-5/,fuzzff/1.e-5/
14
15     c
16     data xmas/.23,.27/,ymas/0.0,10.0/
17
18     c
19     data aclevs/0.1,0.2,0.3,0.4,0.5,0.6,0.7,0.8,0.9,1.0,
20     .          2.0,3.0,4.0,5.0,6.0,7.0,8.0,9.0,10.0,20.0,
21     .          30.0,40.0,50.0,60.0/
22
23     c
24     end
```

```

1      subroutine cadil(it1)
2
3      c
4      c.... ADI for coarse grid; excludes fine-grid region.
5      c.... Communicates with fine-grid through the boundary.
6      c.... Neumann condition at i=1 & nxi with d(phi) / d(x) = 0; cylindrical.
7      c.... Dirichlet condition at j=1 & neta.
8      c
9      include 'global.h'
10     c
11     rdelyx=dely/delx
12     rdlyx2=rdelyx**2
13     aa1=2.*rdlyx2
14     aa2=-2.*(rdlyx2+1.)
15     aa3=4.*rdlyx2
16     aa4=-2.*(2.*rdlyx2+1.)
17
18     c
19     do 9000 it=1,itmx
20     c
21     errmx=0.
22     sumerr=0.
23
24     c
25     c.... Y-sweep for i = 1.
26     c
27     do 300 j=nyfc2,netaml
28     erry(j)=aa3*phi(2,j)+phi(1,j+1)+phi(1,j-1)+aa4*phi(1,j)
29     erra=abs(erry(j))
30     if(erra .gt. errmx)then
31         errmx=err
32         iermx=1
33         jermx=j
34     endif
35     300 sumerr=sumerr+err
36     bet(nyfc2)=aa4
37     dp(nyfc2)=-erry(nyfc2)/aa4
38     do 301 j=nyfc2+1,netaml
39     gam(j)=1./bet(j-1)
40     bet(j)=aa4-gam(j)
41     301 dp(j)=(-erry(j)-dp(j-1))/bet(j)
42     do 302 j=netam2,nyfc2,-1
43     dp(j)=dp(j)-gam(j+1)*dp(j+1)
44     do 303 j=nyfc2,netaml
45     phi(1,j)=phi(1,j)+dp(j)
46     c
47     c.... Y-sweep for 1 < i < nil.
48     c
49     do 110 i=2,nxfc2-1
50     if(mj1p1(i).lt.nxfc1)then
51     bet(mj1p1(i))=aa2
52     do 109 j=mj1p2(i),nyfc1
53     gam(j)=1./bet(j-1)
54     109 bet(j)=aa2-gam(j)
55     do 111 j=mj1p1(i),nyfc1
56     erry(j)=ryxm(i)*phi(i-1,j)+ryxp(i)*phi(i+1,j)
57     +phi(i,j+1)+phi(i,j-1)+aa2*phi(i,j)
58     erra=abs(erry(j))
59     if(erra .gt. errmx)then
60         errmx=err
61         iermx=i
62         jermx=j
63     endif
64     111 sumerr=sumerr+err
65     dp(mj1p1(i))=-erry(mj1p1(i))/aa2
66     do 112 j=mj1p2(i),nyfc1
67     dp(j)=(-erry(j)-dp(j-1))/bet(j)

```



```

65      do 113 j=nyfc1-1,mj1p1(i),-1
66      113      dp(j)=dp(j)-gam(j+1)*dp(j+1)
67      do 114 j=mj1p1(i),nyfc1
68      114      phi(i,j)=phi(i,j)+dp(j)
69      endif
70      110      continue
71      c
72      bet(nyfc2)=aa2
73      do 309 j=nyfc2+1,netam1
74      gam(j)=1./bet(j-1)
75      309      bet(j)=aa2-gam(j)
76      do 310 i=2,nxfc2-1
77      do 311 j=nyfc2,netam1
78      erry(j)=ryxm(i)*phi(i-1,j)+ryxp(i)*phi(i+1,j)
79      +phi(i,j+1)+phi(i,j-1)+aa2*phi(i,j)
80      erra=abs(erry(j))
81      if(erra .gt. errmx)then
82          errmx=erra
83          iermx=i
84          jermx=j
85      endif
86      311      sumerr=sumerr+erra
87      dp(nyfc2)=-erry(nyfc2)/aa2
88      do 312 j=nyfc2+1,netam1
89      312      dp(j)=(-erry(j)-dp(j-1))/bet(j)
90      do 313 j=netam2,nyfc2,-1
91      313      dp(j)=dp(j)-gam(j+1)*dp(j+1)
92      do 314 j=nyfc2,netam1
93      314      phi(i,j)=phi(i,j)+dp(j)
94      310      continue
95      c
96      c.... Y-sweep for nxfc2 =< i < nxi.
97      c
98      bet(2)=aa2
99      do 509 j=3,netam1
100      gam(j)=1./bet(j-1)
101      509      bet(j)=aa2-gam(j)
102      do 520 i=nxfc2,nxim1
103      do 521 j=2,netam1
104      erry(j)=ryxm(i)*phi(i-1,j)+ryxp(i)*phi(i+1,j)
105      +phi(i,j+1)+phi(i,j-1)+aa2*phi(i,j)
106      erra=abs(erry(j))
107      if(erra .gt. errmx)then
108          errmx=erra
109          iermx=i
110          jermx=j
111      endif
112      521      sumerr=sumerr+erra
113      dp(2)=-erry(2)/aa2
114      do 522 j=3,netam1
115      522      dp(j)=(-erry(j)-dp(j-1))/bet(j)
116      do 523 j=netam2,2,-1
117      523      dp(j)=dp(j)-gam(j+1)*dp(j+1)
118      do 524 j=2,netam1
119      524      phi(i,j)=phi(i,j)+dp(j)
120      520      continue
121      c
122      c.... Y-sweep for i = nxi.
123      c
124      do 130 j=2,netam1
125      erry(j)=aal*phi(nxim1,j)+phi(nxi,j+1)+phi(nxi,j-1)+aa2*phi(nxi,j)
126      erra=abs(erry(j))
127      if(erra .gt. errmx)then
128          errmx=erra

```

```

129         iermx=nxi
130         jermx=j
131     endif
132     sumerr=sumerr+erra
133     dp(2)=-erry(2)/aa2
134     do 131 j=3,netam1
135     131 dp(j)=(-erry(j)-dp(j-1))/bet(j)
136     do 132 j=netam2,2,-1
137     132 dp(j)=dp(j)-gam(j+1)*dp(j+1)
138     do 133 j=2,netam1
139     133 phi(nxi,j)=phi(nxi,j)+dp(j)
140 c
141 c.... X-sweep for nyfc2 <= j < neta.
142 c
143     bet(1)=aa4
144     gam(2)=aa3/bet(1)
145     bet(2)=aa2-ryxm(2)*gam(2)
146     do 199 i=3,nxim1
147     199 gam(i)=ryxp(i)/bet(i-1)
148     bet(i)=aa2-gam(i)*ryxm(i)
149     gam(nxi)=ryxp(nxi)/bet(nxim1)
150     bet(nxi)=aa2-aal*gam(nxi)
151     do 201 j=netam1,nyfc2,-1
152     201 errx(1)=aa3*phi(2,j)+phi(1,j+1)+phi(1,j-1)+aa4*phi(1,j)
153     sumerr=sumerr+abs(errx(1))
154     do 202 i=2,nxim1
155     202 errx(i)=ryxm(i)*phi(i-1,j)+ryxp(i)*phi(i+1,j)
156     +phi(i,j+1)+phi(i,j-1)+aa2*phi(i,j)
157     sumerr=sumerr+abs(errx(i))
158     errx(nxi)=aal*phi(nxim1,j)+phi(nxi,j+1)+phi(nxi,j-1)+aa2*
159     phi(nxi,j)
160     sumerr=sumerr+abs(errx(nxi))
161     dp(1)=-errx(1)/aa4
162     do 203 i=2,nxim1
163     203 dp(i)=(-errx(i)-ryxm(i)*dp(i-1))/bet(i)
164     dp(nxi)=(-errx(nxi)-aal*dp(nxim1))/bet(nxi)
165     do 204 i=nxim1,1,-1
166     204 dp(i)=dp(i)-gam(i+1)*dp(i+1)
167     do 205 i=1,nxi
168     205 phi(i,j)=phi(i,j)+dp(i)
169     201 continue
170 c
171 c.... X-sweep for nyfc1 >= j > 1.
172 c
173     bet(nxfc2)=aa2
174     do 419 i=nxyc2+1,nxim1
175     419 gam(i)=ryxp(i)/bet(i-1)
176     bet(i)=aa2-gam(i)*ryxm(i)
177     gam(nxi)=ryxp(nxi)/bet(nxim1)
178     bet(nxi)=aa2-aal*gam(nxi)
179     do 441 j=nyfc2-1,nyfc1+1,-1
180     441 do 422 i=nxyc2,nxim1
181     422 errx(i)=ryxm(i)*phi(i-1,j)+ryxp(i)*phi(i+1,j)
182     +phi(i,j+1)+phi(i,j-1)+aa2*phi(i,j)
183     sumerr=sumerr+abs(errx(i))
184     errx(nxi)=aal*phi(nxim1,j)+phi(nxi,j+1)+phi(nxi,j-1)+aa2*
185     phi(nxi,j)
186     sumerr=sumerr+abs(errx(nxi))
187     dp(nxyc2)=-errx(nxyc2)/aa2
188     do 423 i=nxyc2+1,nxi
189     423 dp(i)=(-errx(i)-ryxm(i)*dp(i-1))/bet(i)
190     do 424 i=nxim1,nxyc2,-1
191     424 dp(i)=dp(i)-gam(i+1)*dp(i+1)
192     do 425 i=nxyc2,nxi

```

```

193      425 phi(i,j)=phi(i,j)+dp(i)
194      441 continue
195      c
196      do 221 j=nyfc1,2,-1
197      bet(mi2p1(j))=aa2
198      do 219 i=mi2p2(j),nxim1
199      gam(i)=ryxp(i)/bet(i-1)
200      219 bet(i)=aa2-gam(i)*ryxm(i)
201      gam(nxi)=ryxp(nxi)/bet(nxim1)
202      bet(nxi)=aa2-aal*gam(nxi)
203      do 222 i=mi2p1(j),nxim1
204      errx(i)=ryxm(i)*phi(i-1,j)+ryxp(i)*phi(i+1,j)
205      +phi(i,j+1)+phi(i,j-1)+aa2*phi(i,j)
206      222 sumerr=sumerr+abs(errx(i))
207      errx(nxi)=aal*phi(nxim1,j)+phi(nxi,j+1)+phi(nxi,j-1)+aa2*
208      phi(nxi,j)
209      sumerr=sumerr+abs(errx(nxi))
210      dp(mi2p1(j))=-errx(mi2p1(j))/aa2
211      do 223 i=mi2p2(j),nxi
212      223 dp(i)=(-errx(i)-ryxm(i)*dp(i-1))/bet(i)
213      do 224 i=nxim1,mi2p1(j),-1
214      224 dp(i)=dp(i)-gam(i+1)*dp(i+1)
215      do 225 i=mi2p1(j),nxi
216      225 phi(i,j)=phi(i,j)+dp(i)
217      221 continue
218      c
219      if (it.eq.itmx .or. it .eq. 1) then
220      write(6,901)it1,it,sumerr,errmx,iermx,jermx
221      write(23,901)it1,it,sumerr,errmx,iermx,jermx
222      endif
223      901 format('c it sumerr errmx ',2i6,1pe11.3,e11.3,2i4)
224      c
225      9000 continue
226      c
227      c.... Calculate electric field.
228      emx=0.
229      do 10 i=1,nxim1
230      do 10 j=1,netam1
231      by=.5*(phi(i,j)+phi(i+1,j)-phi(i,j+1)-phi(i+1,j+1))/dely
232      bx=.5*(phi(i,j+1)+phi(i,j)-phi(i+1,j+1)-phi(i+1,j))/delx
233      ex(i,j)=bx
234      ey(i,j)=by
235      eec(i,j)=sqrt(bx**2+by**2)
236      if(eec(i,j) .gt. emx)then
237      emx=eec(i,j)
238      iemx=i
239      jemx=j
240      endif
241      10 continue
242      write (6,200)iemx,jemx,emx,x(iemx),y(jemx)
243      write (23,200)iemx,jemx,emx,x(iemx),y(jemx)
244      200 format('max Electric field ',2i4,1pe11.3,2e11.3)
245      c
246      return
247      end

```

```

1      subroutine cadi10
2
3      c
4      c.... ADI for coarse grid, covering the whole region at beginning.
5      c.... Neumann condition at i=1 & nxi with d(phi) / d(x) = 0; cylindrical.
6      c.... Dirichlet condition at j=1 & neta.
7      c
8      include 'global.h'
9      c
10     c.... Find coarse-grid constants.
11     c
12     do 451 i=1,nxi
13     451   mj1(i)=1
14     do 452 i=1,nxi
15     do 442 j=2,neta
16     if(mask(i,j) .ne. 1)goto 443
17     442   continue
18     443   mj1(i)=j-1
19     452   continue
20     do 453 i=1,nxi
21     mj1p1(i)=mj1(i)+1
22     453   mj1p2(i)=mj1(i)+2
23     nj10=1
24     do 454 i=1,nxi
25     if(mj1(i).gt.nj10)nj10=mj1(i)
26     nj10p1=nj10+1
27     nj10p2=nj10+2
28     c
29     do 346 j=1,neta
30     do 344 i=1,nxi
31     if(mask(i,j) .ne. 1)goto 345
32     344   continue
33     345   mi2(j)=i-1
34     mi2p1(j)=mi2(j)+1
35     mi2p2(j)=mi2(j)+2
36     346   continue
37     ni20=mi2(1)
38     write(6,349)ni20,nj10
39     write(23,349)ni20,nj10
40     349   format('ni20,nj10 ',2i4)
41     c
42     if(resume)return
43     c
44     c.... Initialize phi.
45     c
46     do 1000 i=1,nxi
47     phi(i,1)=0.
48     1000   phi(i,neta)=volts
49     do 1003 i=1,nxi
50     do 1003 j=mj1p1(i),netaml
51     1003   phi(i,j)=(phi(i,mj1(i))*(neta-j)+phi(i,neta)*(j-mj1(i)))/
52     . float(neta-mj1(i))
53     c
54     1004   rdelyx=dely/delx
55     rdlyx2=rdelyx**2
56     aa1=2.*rdlyx2
57     aa2=-2.*(rdlyx2+1.)
58     aa3=4.*rdlyx2
59     aa4=-2.*(2.*rdlyx2+1.)
60     c
61     do 9000 it=1,itmx
62     c
63     errmx=0.
64     sumerr=0.

```

```

65      c.... Y-sweep for i = 1.
66      c
67          do 100 j=mjlp1(1),netaml
68              erry(j)=aa3*phi(2,j)+phi(1,j+1)+phi(1,j-1)+aa4*phi(1,j)
69              erra=abs(erry(j))
70              if(erra .gt. errmx)then
71                  errmx=erra
72                  iermx=1
73                  jermx=j
74              endif
75      100      sumerr=sumerr+erra
76              bet(mjlp1(1))=aa4
77              dp(mjlp1(1))=-erry(mjlp1(1))/aa4
78              do 101 j=mjlp2(1),netaml
79                  gam(j)=1./bet(j-1)
80                  bet(j)=aa4-gam(j)
81      101      dp(j)=(-erry(j)-dp(j-1))/bet(j)
82              do 102 j=netam2,mjlp1(1),-1
83      102      dp(j)=dp(j)-gam(j+1)*dp(j+1)
84              do 103 j=mjlp1(1),netaml
85      103      phi(1,j)=phi(1,j)+dp(j)
86      c
87      c.... Y-sweep for 1 < i < nxi.
88      c
89          bet(2)=aa2
90          do 109 j=3,netaml
91              gam(j)=1./bet(j-1)
92      109      bet(j)=aa2-gam(j)
93              do 115 i=2,nximl
94              do 116 j=mjlp1(i),netaml
95                  erry(j)=ryxm(i)*phi(i-1,j)+ryxp(i)*phi(i+1,j)
96                      +phi(i,j+1)+phi(i,j-1)+aa2*phi(i,j)
97                  erra=abs(erry(j))
98                  if(erra .gt. errmx)then
99                      errmx=erra
100                     iermx=i
101                     jermx=j
102                 endif
103      116      sumerr=sumerr+erra
104                  dp(mjlp1(i))=-erry(mjlp1(i))/aa2
105                  do 117 j=mjlp2(i),netaml
106      117      dp(j)=(-erry(j)-dp(j-1))/bet(j-mj1(i)+1)
107                  do 118 j=netam2,mjlp1(i),-1
108      118      dp(j)=dp(j)-gam(j-mj1(i)+2)*dp(j+1)
109                  do 119 j=mjlp1(i),netaml
110      119      phi(i,j)=phi(i,j)+dp(j)
111      115      continue
112      c
113      c.... Y-sweep for i = nxi.
114      c
115          do 130 j=2,netaml
116              erry(j)=aal*phi(nximl,j)+phi(nxi,j+1)+phi(nxi,j-1)+aa2*phi(nxi,j)
117              erra=abs(erry(j))
118              if(erra .gt. errmx)then
119                  errmx=erra
120                  iermx=i
121                  jermx=j
122              endif
123      130      sumerr=sumerr+erra
124              dp(2)=-erry(2)/aa2
125              do 131 j=3,netaml
126      131      dp(j)=(-erry(j)-dp(j-1))/bet(j)
127              do 132 j=netam2,2,-1
128      132      dp(j)=dp(j)-gam(j+1)*dp(j+1)

```

```

129      do 133 j=2,netaml
130      133 phi(nxi,j)=phi(nxi,j)+dp(j)
131      c
132      c.... X-sweep for nj1 < j < neta.
133      c
134          bet(1)=aa4
135          gam(2)=aa3/bet(1)
136          bet(2)=aa2-ryxm(2)*gam(2)
137          do 199 i=3,nximl
138          gam(i)=ryxp(i)/bet(i-1)
139      199 bet(i)=aa2-gam(i)*ryxm(i)
140          gam(nxi)=ryxp(nxi)/bet(nximl)
141          bet(nxi)=aa2-aal*gam(nxi)
142          do 201 j=netaml,mj1p1(1),-1
143          errx(1)=aa3*phi(2,j)+phi(1,j+1)+phi(1,j-1)+aa4*phi(1,j)
144          sumerr=sumerr+abs(errx(1))
145          do 202 i=2,nximl
146          errx(i)=ryxm(i)*phi(i-1,j)+ryxp(i)*phi(i+1,j)
147          +phi(i,j+1)+phi(i,j-1)+aa2*phi(i,j)
148      202 sumerr=sumerr+abs(errx(i))
149          errx(nxi)=aal*phi(nximl,j)+phi(nxi,j+1)+phi(nxi,j-1)+aa2*
150          phi(nxi,j)
151          sumerr=sumerr+abs(errx(nxi))
152      c      dp(1)=-errx(1)/aa2
153          dp(1)=-errx(1)/aa4
154          do 203 i=2,nximl
155      203 dp(i)=(-errx(i)-ryxm(i)*dp(i-1))/bet(i)
156          dp(nxi)=(-errx(nxi)-aal*dp(nximl))/bet(nxi)
157          do 204 i=nximl,1,-1
158      204 dp(i)=dp(i)-gam(i+1)*dp(i+1)
159          do 205 i=1,nxi
160      205 phi(i,j)=phi(i,j)+dp(i)
161      201 continue
162      c
163          do 221 j=mj1(1),2,-1
164          do 222 i=mi2p1(j),nximl
165          errx(i)=ryxm(i)*phi(i-1,j)+ryxp(i)*phi(i+1,j)
166          +phi(i,j+1)+phi(i,j-1)+aa2*phi(i,j)
167      222 sumerr=sumerr+abs(errx(i))
168          errx(nxi)=aal*phi(nximl,j)+phi(nxi,j+1)+phi(nxi,j-1)+aa2*
169          phi(nxi,j)
170          sumerr=sumerr+abs(errx(nxi))
171          bet(mi2p1(j))=aa2
172          do 219 i=mi2p2(j),nximl
173          gam(i)=ryxp(i)/bet(i-1)
174      219 bet(i)=aa2-gam(i)*ryxm(i)
175          gam(nxi)=ryxp(nxi)/bet(nximl)
176          bet(nxi)=aa2-aal*gam(nxi)
177          dp(mi2p1(j))=-errx(mi2p1(j))/aa2
178          do 223 i=mi2p2(j),nxi
179      223 dp(i)=(-errx(i)-ryxm(i)*dp(i-1))/bet(i)
180          do 224 i=nximl,mi2p1(j),-1
181      224 dp(i)=dp(i)-gam(i+1)*dp(i+1)
182          do 225 i=mi2p1(j),nxi
183      225 phi(i,j)=phi(i,j)+dp(i)
184      221 continue
185      c
186          if (it.eq.itmx .or. it .eq. 1) then
187              write(6,901)it,sumerr,errmx,iermx,jermx
188              write(23,901)it,sumerr,errmx,iermx,jermx
189          endif
190      901 format('c it sumerr errmx ',i6,1p,11.3,e11.3,2i4)
191      c
192      9000 continue

```

193
194
195

c

return
end

```

1      subroutine cadi2(it1)
2      c
3      c.... ADI for coarse grid, excluding fine-grid region.
4      c.... Communicates with fine-grid through the boundary.
5      c.... Neumann condition at i=1 & nxi with d(phi) / d(x) = 0; cylindrical.
6      c.... Dirichlet condition at j=1 & neta.
7      c
8      include 'global.h'
9      c
10     write(6,349)ni1,ni2,nj1
11     write(23,349)ni1,ni2,nj1
12 349   format('ni1,ni2 nj1 ',3i4)
13     rdelyx=dely/delx
14     rdlyx2=rdelyx**2
15     aal=2.*rdlyx2
16     aa2=-2.*(rdlyx2+1.)
17     aa3=4.*rdlyx2
18     aa4=-2.*(2.*rdlyx2+1.)
19     c
20     do 9000 it=1,itmx
21     c
22     errmx=0.
23     sumerr=0.
24     c
25     c.... Y-sweep for i = 1.
26     c
27     do 100 j=2,nyfc1
28     erry(j)=aa3*phi(2,j)+phi(1,j+1)+phi(1,j-1)+aa4*phi(1,j)
29     erra=abs(erry(j))
30     if(erra.gt.errmx)then
31         errmx=erra
32         iermx=1
33         jermx=j
34     endif
35 100    sumerr=sumerr+erra
36     bet(2)=aa4
37     dp(2)=-erry(2)/aa4
38     do 101 j=3,nyfc1
39     gam(j)=1./bet(j-1)
40     bet(j)=aa4-gam(j)
41 101    dp(j)=(-erry(j)-dp(j-1))/bet(j)
42     do 102 j=nyfc1-1,2,-1
43 102    dp(j)=dp(j)-gam(j+1)*dp(j+1)
44     do 103 j=2,nyfc1
45 103    phi(1,j)=phi(1,j)+dp(j)
46     c
47     do 300 j=nyfc2,netam1
48     erry(j)=aa3*phi(2,j)+phi(1,j+1)+phi(1,j-1)+aa4*phi(1,j)
49     erra=abs(erry(j))
50     if(erra.gt.errmx)then
51         errmx=erra
52         iermx=1
53         jermx=j
54     endif
55 300    sumerr=sumerr+erra
56     bet(nyfc2)=aa4
57     dp(nyfc2)=-erry(nyfc2)/aa4
58     do 301 j=nyfc2+1,netam1
59     gam(j)=1./bet(j-1)
60     bet(j)=aa4-gam(j)
61 301    dp(j)=(-erry(j)-dp(j-1))/bet(j)
62     do 302 j=netam2,nyfc2,-1
63 302    dp(j)=dp(j)-gam(j+1)*dp(j+1)
64     do 303 j=nyfc2,netam1

```



```

65      303  phi(1,j)=phi(1,j)+dp(j)
66      c
67      c.... Y-sweep for 1 < i < nil.
68      c
69          bet(2)=aa2
70          do 109 j=3,nyfc1
71              gam(j)=1./bet(j-1)
72      109  bet(j)=aa2-gam(j)
73          do 110 i=2,nil-1
74              do 111 j=2,nyfc1
75                  erry(j)=ryxm(i)*phi(i-1,j)+ryxp(i)*phi(i+1,j)
76                  +phi(i,j+1)+phi(i,j-1)+aa2*phi(i,j)
77              erra=abs(erry(j))
78              if(erra .gt. errmx)then
79                  errmx=erra
80                  iermx=i
81                  jermx=j
82              endif
83      111  sumerr=sumerr+erra
84          dp(2)=-erry(2)/aa2
85          do 112 j=3,nyfc1
86      112  dp(j)=(-erry(j)-dp(j-1))/bet(j)
87          do 113 j=nyfc1-1,2,-1
88      113  dp(j)=dp(j)-gam(j+1)*dp(j+1)
89          do 114 j=2,nyfc1
90      114  phi(i,j)=phi(i,j)+dp(j)
91      110  continue
92      c
93          bet(nyfc2)=aa2
94          do 309 j=nyfc2+1,netam1
95              gam(j)=1./bet(j-1)
96      309  bet(j)=aa2-gam(j)
97          do 310 i=2,nxfc2-1
98              do 311 j=nyfc2,netam1
99                  erry(j)=ryxm(i)*phi(i-1,j)+ryxp(i)*phi(i+1,j)
100                 +phi(i,j+1)+phi(i,j-1)+aa2*phi(i,j)
101             erra=abs(erry(j))
102             if(erra .gt. errmx)then
103                 errmx=erra
104                 iermx=i
105                 jermx=j
106             endif
107      311  sumerr=sumerr+erra
108          dp(nyfc2)=-erry(nyfc2)/aa2
109          do 312 j=nyfc2+1,netam1
110      312  dp(j)=(-erry(j)-dp(j-1))/bet(j)
111          do 313 j=netam2,nyfc2,-1
112      313  dp(j)=dp(j)-gam(j+1)*dp(j+1)
113          do 314 j=nyfc2,netam1
114      314  phi(i,j)=phi(i,j)+dp(j)
115      310  continue
116      c
117      c.... Y-sweep for ni2 < i < nxfc2.
118      c
119          do 120 i=ni2+1,nxfc2-1
120          do 121 j=2,nyfc1
121              erry(j)=ryxm(i)*phi(i-1,j)+ryxp(i)*phi(i+1,j)
122              +phi(i,j+1)+phi(i,j-1)+aa2*phi(i,j)
123          erra=abs(erry(j))
124          if(erra .gt. errmx)then
125              errmx=erra
126              iermx=i
127              jermx=j
128          endif

```

```

129      121      sumerr=sumerr+erra
130          dp(2)=-erry(2)/aa2
131          do 122 j=3,nyfc1
132      122      dp(j)=(-erry(j)-dp(j-1))/bet(j)
133          do 123 j=nyfc1-1,2,-1
134      123      dp(j)=dp(j)-gam(j+1)*dp(j+1)
135          do 124 j=2,nyfc1
136      124      phi(i,j)=phi(i,j)+dp(j)
137      120      continue
138      c
139      c.... Y-sweep for nxfc2 =< i < nxi.
140      c
141          bet(2)=aa2
142          do 509 j=3,netaml
143          gam(j)=1./bet(j-1)
144      509      bet(j)=aa2-gam(j)
145          do 520 i=nxfc2,nximl
146          do 521 j=2,netaml
147          erry(j)=ryxm(i)*phi(i-1,j)+ryxp(i)*phi(i+1,j)
148              +phi(i,j+1)+phi(i,j-1)+aa2*phi(i,j)
149          erra=abs(erry(j))
150          if(erra .gt. errmx)then
151              errmx=erra
152              iermx=i
153              jermx=j
154          endif
155      521      sumerr=sumerr+erra
156          dp(2)=-erry(2)/aa2
157          do 522 j=3,netaml
158      522      dp(j)=(-erry(j)-dp(j-1))/bet(j)
159          do 523 j=netam2,2,-1
160      523      dp(j)=dp(j)-gam(j+1)*dp(j+1)
161          do 524 j=2,netaml
162      524      phi(i,j)=phi(i,j)+dp(j)
163      520      continue
164      c
165      c.... Y-sweep for i = nxi.
166      c
167          do 130 j=2,netaml
168          erry(j)=aal*phi(nximl,j)+phi(nxi,j+1)+phi(nxi,j-1)+aa2*phi(nxi,j)
169          erra=abs(erry(j))
170          if(erra .gt. errmx)then
171              errmx=erra
172              iermx=i
173              jermx=j
174          endif
175      130      sumerr=sumerr+erra
176          dp(2)=-erry(2)/aa2
177          do 131 j=3,netaml
178      131      dp(j)=(-erry(j)-dp(j-1))/bet(j)
179          do 132 j=netam2,2,-1
180      132      dp(j)=dp(j)-gam(j+1)*dp(j+1)
181          do 133 j=2,netaml
182      133      phi(nxi,j)=phi(nxi,j)+dp(j)
183      1100      continue
184      c
185      c.... X-sweep for nyfc2 <= j < neta.
186      c
187          bet(1)=aa4
188          gam(2)=aa3/bet(1)
189          bet(2)=aa2-ryxm(2)*gam(2)
190          do 199 i=3,nximl
191          gam(i)=ryxp(i)/bet(i-1)
192      199      bet(i)=aa2-gam(i)*ryxm(i)

```

```

193      gam(nxi)=ryxp(nxi)/bet(nximl)
194      bet(nxi)=aa2-aa1*gam(nxi)
195      do 201 j=netaml,nyfc2,-1
196      errx(1)=aa3*phi(2,j)+phi(1,j+1)+phi(1,j-1)+aa4*phi(1,j)
197      sumerr=sumerr+abs(errx(1))
198      do 202 i=2,nximl
199      errx(i)=ryxm(i)*phi(i-1,j)+ryxp(i)*phi(i+1,j)
200      +phi(i,j+1)+phi(i,j-1)+aa2*phi(i,j)
201      sumerr=sumerr+abs(errx(i))
202      errx(nxi)=aal*phi(nximl,j)+phi(nxi,j+1)+phi(nxi,j-1)+aa2*
203      phi(nxi,j)
204      sumerr=sumerr+abs(errx(nxi))
205      dp(1)=-errx(1)/aa4
206      do 203 i=2,nximl
207      dp(i)=(-errx(i)-ryxm(i)*dp(i-1))/bet(i)
208      dp(nxi)=(-errx(nxi)-aal*dp(nximl))/bet(nxi)
209      do 204 i=nximl,1,-1
210      dp(i)=dp(i)-gam(i+1)*dp(i+1)
211      do 205 i=1,nxi
212      phi(i,j)=phi(i,j)+dp(i)
213      201 continue
214      c
215      c.... X-sweep for nyfc1 >= j > 1.
216      c
217      do 211 j=nyfc1,2,-1
218      errx(1)=aa3*phi(2,j)+phi(1,j+1)+phi(1,j-1)+aa4*phi(1,j)
219      sumerr=sumerr+abs(errx(1))
220      do 212 i=2,nilm1
221      errx(i)=ryxm(i)*phi(i-1,j)+ryxp(i)*phi(i+1,j)
222      +phi(i,j+1)+phi(i,j-1)+aa2*phi(i,j)
223      212 sumerr=sumerr+abs(errx(i))
224      c      dp(1)=-errx(1)/aa2
225      dp(1)=-errx(1)/aa4
226      do 213 i=2,nilm1
227      213 dp(i)=(-errx(i)-ryxm(i)*dp(i-1))/bet(i)
228      do 214 i=nilm2,1,-1
229      214 dp(i)=dp(i)-gam(i+1)*dp(i+1)
230      do 215 i=1,nilm1
231      215 phi(i,j)=phi(i,j)+dp(i)
232      211 continue
233      c
234      bet(nxfc2)=aa2
235      do 419 i=nxfc2+1,nximl
236      gam(i)=ryxp(i)/bet(i-1)
237      419 bet(i)=aa2-gam(i)*ryxm(i)
238      gam(nxi)=ryxp(nxi)/bet(nximl)
239      bet(nxi)=aa2-aa1*gam(nxi)
240      do 441 j=nyfc2-1,nyfc1+1,-1
241      do 422 i=nxfc2,nximl
242      errx(i)=ryxm(i)*phi(i-1,j)+ryxp(i)*phi(i+1,j)
243      +phi(i,j+1)+phi(i,j-1)+aa2*phi(i,j)
244      422 sumerr=sumerr+abs(errx(i))
245      errx(nxi)=aal*phi(nximl,j)+phi(nxi,j+1)+phi(nxi,j-1)+aa2*
246      phi(nxi,j)
247      sumerr=sumerr+abs(errx(nxi))
248      dp(nxfc2)=-errx(nxfc2)/aa2
249      do 423 i=nxfc2+1,nxi
250      423 dp(i)=(-errx(i)-ryxm(i)*dp(i-1))/bet(i)
251      do 424 i=nximl,nxfc2,-1
252      424 dp(i)=dp(i)-gam(i+1)*dp(i+1)
253      do 425 i=nxfc2,nxi
254      425 phi(i,j)=phi(i,j)+dp(i)
255      441 continue
256      c

```

```

257      bet(ni2p1)=aa2
258      do 219 i=ni2p2,nxim1
259          gam(i)=ryxp(i)/bet(i-1)
260      219      bet(i)=aa2-gam(i)*ryxm(i)
261          gam(nxi)=ryxp(nxi)/bet(nxim1)
262          bet(nxi)=aa2-aal*gam(nxi)
263      do 221 j=nyfc1,2,-1
264      do 222 i=ni2p1,nxim1
265          errx(i)=ryxm(i)*phi(i-1,j)+ryxp(i)*phi(i+1,j)
266              +phi(i,j+1)+phi(i,j-1)+aa2*phi(i,j)
267      222      sumerr=sumerr+abs(errx(i))
268          errx(nxi)=aal*phi(nxim1,j)+phi(nxi,j+1)+phi(nxi,j-1)+aa2*
269              phi(nxi,j)
270          sumerr=sumerr+abs(errx(nxi))
271          dp(ni2p1)=-errx(ni2p1)/aa2
272      do 223 i=ni2p2,nxi
273      223      dp(i)=(-errx(i)-ryxm(i)*dp(i-1))/bet(i)
274          do 224 i=nxim1,ni2p1,-1
275      224      dp(i)=dp(i)-gam(i+1)*dp(i+1)
276          do 225 i=ni2p1,nxi
277      225      phi(i,j)=phi(i,j)+dp(i)
278      221      continue
279      c
280          if (it.eq.itmx .or. it .eq. 1) then
281              write(6,901)it1,it,sumerr,errmx,iermx,jermx
282              write(23,901)it1,it,sumerr,errmx,iermx,jermx
283          endif
284      901      format(' it sumerr errmx ',2i6,1pe11.3,e11.3,2i4)
285      c
286      9000      continue
287      c
288      c.... Calculate electric field.
289      c
290          emx=0.
291          do 10 i=1,nxim1
292              do 10 j=1,netaml
293                  ay=.5*(phi(i,j)+phi(i+1,j)-phi(i,j+1)-phi(i+1,j+1))/dely
294                  ax=.5*(phi(i,j+1)+phi(i,j)-phi(i+1,j+1)-phi(i+1,j))/delx
295                  ex(i,j)=ax
296                  ey(i,j)=ay
297                  eec(i,j)=sqrt(ax**2+ay**2)
298                  if(eec(i,j) .gt. emx)then
299                      emx=eec(i,j)
300                      iemx=i
301                      jemx=j
302                  endif
303      10      continue
304          write (6,200)iemx,jemx,emx,x(iemx),y(jemx)
305          write (23,200)iemx,jemx,emx,x(iemx),y(jemx)
306      200      format("max Electric field ",2i4,1pe11.3,2e11.3)
307      c
308          return
309      end

```

```

1      subroutine cadi20
2
3      c
4      c.... ADI for coarse grid, covering the whole region at beginning.
5      c.... Neumann condition at i=1 & nxi with d(phi) / d(x) = 0; cylindrical.
6      c.... Dirichlet condition at j=1 & neta.
7      c
8      include 'global.h'
9
10     c
11     c.... Find coarse-grid constants.
12     c
13     do 340 i=1,nxi
14     if(mask(i,1) .eq. 1)goto 341
15     340 continue
16     341 ni1=i
17     do 342 j=2,neta
18     if(mask(ni1,j) .ne. 1)goto 343
19     342 continue
20     343 nj1=j-1
21     do 344 i=ni1,nxi
22     if(mask(i,1) .ne. 1)goto 345
23     344 continue
24     345 ni2=i-1
25     nj1p1=nj1+1
26     nj1p2=nj1+2
27     ni1m1=ni1-1
28     ni1m2=ni1-2
29     ni2p1=ni2+1
30     ni2p2=ni2+2
31     write(6,349)ni1,nj1
32     write(23,349)ni1,ni2,nj1
33     349 format('ni1,ni2 nj1 ',3i4)
34     c
35     if(resume)return
36     c
37     c.... Initialize phi.
38     c
39     do 1000 i=1,nxi
40     phi(i,1)=0.
41     1000 phi(i,neta)=volts
42     do 1001 j=2,netam1
43     do 1001 i=1,nxi
44     phi(i,j)=(phi(i,1)*(neta-j)+phi(i,neta)*(j-1))/float(neta-1)
45     do 1002 i=ni1,ni2
46     do 1002 j=1,nj1
47     1002 phi(i,j)=0.
48     do 1003 i=ni1,ni2
49     do 1003 j=nj1p1,netam1
50     1003 phi(i,j)=(phi(i,nj1)*(neta-j)+phi(i,neta)*(j-nj1))/float(neta-nj1)
51     c
52     1004 rdelyx=dely/delx
53     rdlyx2=rdelyx**2
54     aa1=2.*rdlyx2
55     aa2=-2.*(rdlyx2+1.)
56     aa3=4.*rdlyx2
57     aa4=-2.*(2.*rdlyx2+1.)
58     c
59     do 9000 it=1,itmx
60     c
61     errmx=0.
62     sumerr=0.
63     c
64     c.... Y-sweep for i = 1.
65     c
66     do 100 j=2,netam1

```

```

65      erry(j)=aa3*phi(2,j)+phi(1,j+1)+phi(1,j-1)+aa4*phi(1,j)
66      erra=abs(erry(j))
67      if(erra .gt. errmx)then
68          errmx=erra
69          iermx=1
70          jermx=j
71      endif
72  100  sumerr=sumerr+erra
73      bet(2)=aa4
74      dp(2)=-erry(2)/aa4
75      do 101 j=3,netam1
76          gam(j)=1./bet(j-1)
77          bet(j)=aa4-gam(j)
78  101  dp(j)=(-erry(j)-dp(j-1))/bet(j)
79      do 102 j=netam2,2,-1
80  102  dp(j)=dp(j)-gam(j+1)*dp(j+1)
81      do 103 j=2,netam1
82  103  phi(1,j)=phi(1,j)+dp(j)
83      c
84      c.... Y-sweep for 1 < i < nil.
85      c
86          bet(2)=aa2
87          do 109 j=3,netam1
88              gam(j)=1./bet(j-1)
89  109  bet(j)=aa2-gam(j)
90          do 110 i=2,nil-1
91              do 111 j=2,netam1
92                  erry(j)=ryxm(i)*phi(i-1,j)+ryxp(i)*phi(i+1,j)
93                      +phi(i,j+1)+phi(i,j-1)+aa2*phi(i,j)
94                  erra=abs(erry(j))
95                  if(erra .gt. errmx)then
96                      errmx=erra
97                      iermx=i
98                      jermx=j
99                  endif
100  111  sumerr=sumerr+erra
101      dp(2)=-erry(2)/aa2
102      do 112 j=3,netam1
103  112  dp(j)=(-erry(j)-dp(j-1))/bet(j)
104      do 113 j=netam2,2,-1
105  113  dp(j)=dp(j)-gam(j+1)*dp(j+1)
106      do 114 j=2,netam1
107  114  phi(i,j)=phi(i,j)+dp(j)
108  110  continue
109      c
110      c.... Y-sweep for nil =< i =< ni2.
111      c
112          do 115 i=nil,ni2
113              do 116 j=nj1p1,netam1
114                  erry(j)=ryxm(i)*phi(i-1,j)+ryxp(i)*phi(i+1,j)
115                      +phi(i,j+1)+phi(i,j-1)+aa2*phi(i,j)
116                  erra=abs(erry(j))
117                  if(erra .gt. errmx)then
118                      errmx=erra
119                      iermx=i
120                      jermx=j
121                  endif
122  116  sumerr=sumerr+erra
123      dp(nj1p1)=-erry(nj1p1)/aa2
124      do 117 j=nj1p2,netam1
125  117  dp(j)=(-erry(j)-dp(j-1))/bet(j-nj1+1)
126      do 118 j=netam2,nj1p1,-1
127  118  dp(j)=dp(j)-gam(j-nj1+2)*dp(j+1)
128      do 119 j=nj1p1,netam1

```

```

129      119  phi(i,j)=phi(i,j)+dp(j)
130      115  continue
131      c
132      c.... Y-sweep for ni2 < i < nxi.
133      c
134          do 120 i=ni2+1,nximl
135              do 121 j=2,netaml
136                  erry(j)=ryxm(i)*phi(i-1,j)+ryxp(i)*phi(i+1,j)
137                      +phi(i,j+1)+phi(i,j-1)+aa2*phi(i,j)
138                  erra=abs(erry(j))
139                  if(erra.gt. errmx)then
140                      errmx=erra
141                      iermx=i
142                      jermx=j
143                  endif
144      121  sumerr=sumerr+erra
145          dp(1)=-erry(2)/aa2
146          do 122 j=3,netaml
147      122  dp(j)=(-erry(j)-dp(j-1))/bet(j)
148          do 123 j=netam2,2,-1
149      123  dp(j)=dp(j)-gam(j+1)*dp(j+1)
150          do 124 j=2,netaml
151      124  phi(i,j)=phi(i,j)+dp(j)
152      120  continue
153      c
154      c.... Y-sweep for i = nxi.
155      c
156          do 130 j=2,netaml
157              erry(j)=aal*phi(nximl,j)+phi(nxi,j+1)+phi(nxi,j-1)+aa2*phi(nxi,j)
158              erra=abs(erry(j))
159              if(erra.gt. errmx)then
160                  errmx=erra
161                  iermx=i
162                  jermx=j
163              endif
164      130  sumerr=sumerr+erra
165          dp(2)=-erry(2)/aa2
166          do 131 j=3,netaml
167      131  dp(j)=(-erry(j)-dp(j-1))/bet(j)
168          do 132 j=netam2,2,-1
169      132  dp(j)=dp(j)-gam(j+1)*dp(j+1)
170          do 133 j=2,netaml
171      133  phi(nxi,j)=phi(nxi,j)+dp(j)
172      c
173      c.... X-sweep for nj1 < j < neta.
174      c
175          bet(1)=aa4
176          gam(2)=aa3/bet(1)
177          bet(2)=aa2-ryxm(2)*gam(2)
178          do 199 i=3,nximl
179              gam(i)=ryxp(i)/bet(i-1)
180      199  bet(i)=aa2-gam(i)*ryxm(i)
181          gam(nxi)=ryxp(nxi)/bet(nximl)
182          bet(nxi)=aa2-aal*gam(nxi)
183          do 201 j=netaml,nj1p1-1
184              errx(1)=aa3*phi(2,j)+phi(1,j+1)+phi(1,j-1)+aa4*phi(1,j)
185              sumerr=sumerr+abs(errx(1))
186          do 202 i=2,nximl
187              errx(i)=ryxm(i)*phi(i-1,j)+ryxp(i)*phi(i+1,j)
188                  +phi(i,j+1)+phi(i,j-1)+aa2*phi(i,j)
189      202  sumerr=sumerr+abs(errx(i))
190          errx(nxi)=aal*phi(nximl,j)+phi(nxi,j+1)+phi(nxi,j-1)+aa2*
191              phi(nxi,j)
192          sumerr=sumerr+abs(errx(nxi))

```

```

193      c      dp(1)=-errx(1)/aa2
194      dp(1)=-errx(1)/aa4
195      do 203 i=2,nximl
196      203      dp(i)=(-errx(i)-ryxm(i)*dp(i-1))/bet(i)
197      dp(nxi)=(-errx(nxi)-aal*dp(nximl))/bet(nxi)
198      do 204 i=nximl,1,-1
199      204      dp(i)=dp(i)-gam(i+1)*dp(i+1)
200      do 205 i=1,nxi
201      205      phi(i,j)=phi(i,j)+dp(i)
202      201      continue
203      c
204      c.... X-sweep for nj1 >= j > 1.
205      c
206      do 211 j=nj1,2,-1
207      errx(1)=aa3*phi(2,j)+phi(1,j+1)+phi(1,j-1)+aa4*phi(1,j)
208      sumerr=sumerr+abs(errx(1))
209      do 212 i=2,nilml
210      errx(i)=ryxm(i)*phi(i-1,j)+ryxp(i)*phi(i+1,j)
211      +phi(i,j+1)+phi(i,j-1)+aa2*phi(i,j)
212      sumerr=sumerr+abs(errx(i))
213      c      dp(1)=-errx(1)/aa2
214      dp(1)=-errx(1)/aa4
215      do 213 i=2,nilml
216      213      dp(i)=(-errx(i)-ryxm(i)*dp(i-1))/bet(i)
217      do 214 i=nilm2,1,-1
218      214      dp(i)=dp(i)-gam(i+1)*dp(i+1)
219      do 215 i=1,nilml
220      215      phi(i,j)=phi(i,j)+dp(i)
221      211      continue
222      c
223      bet(ni2p1)=aa2
224      do 219 i=ni2p2,nximl
225      gam(i)=ryxp(i)/bet(i-1)
226      219      bet(i)=aa2-gam(i)*ryxm(i)
227      gam(nxi)=ryxp(nxi)/bet(nximl)
228      bet(nxi)=aa2-aal*gam(nxi)
229      do 221 j=nj1,2,-1
230      do 222 i=ni2p1,nximl
231      errx(i)=ryxm(i)*phi(i-1,j)+ryxp(i)*phi(i+1,j)
232      +phi(i,j+1)+phi(i,j-1)+aa2*phi(i,j)
233      222      sumerr=sumerr+abs(errx(i))
234      errx(nxi)=aal*phi(nximl,j)+phi(nxi,j+1)+phi(nxi,j-1)+aa2*
235      phi(nxi,j)
236      sumerr=sumerr+abs(errx(nxi))
237      dp(ni2p1)=-errx(ni2p1)/aa2
238      do 223 i=ni2p2,nxi
239      223      dp(i)=(-errx(i)-ryxm(i)*dp(i-1))/bet(i)
240      do 224 i=nximl,ni2p1,-1
241      224      dp(i)=dp(i)-gam(i+1)*dp(i+1)
242      do 225 i=ni2p1,nxi
243      225      phi(i,j)=phi(i,j)+dp(i)
244      221      continue
245      c
246      if (it.eq.itmx .or. it .eq. 1) then
247      write(6,901)it,sumerr,errmx,iermx,germx
248      write(23,901)it,sumerr,errmx,iermx,germx
249      endif
250      901      format(' it sumerr errmx ',i6,1p11.3,e11.3,2i4)
251      c
252      9000      continue
253      c
254      return
255      end

```



```

1      subroutine conplot(it1,aa,imin,imax,jmin,jmax,nregn
2      ,label,auto)
3
4      c
5      c.... CONPLOT: Contour plotter for rectangular uniform mesh.
6      c
7      include 'global.h'
8      parameter (nauto=20)
9      dimension aa(nxi,neta),ww(nxi,neta)
10     dimension autolevs(nauto)
11     character(*) label
12     logical auto
13
14     c.... Find min/max.
15     c
16     aamin= 1.e99
17     aamax=-1.e99
18
19     do 10 i=imin,imax
20     do 10 j=jmin,jmax
21     aamin=min(aa(i,j),aamin)
22     aamax=max(aa(i,j),aamax)
23
24     if (aamax-aamin.lt.1.e-3) return
25
26     c.... Load work array.
27     c
28     ii=0
29
30     do 15 i=imin,imax
31     ii=ij+1
32     jj=0
33     do 15 j=jmin,jmax
34     jj=jj+1
35     ww(ii,jj)=aa(i,j)
36
37     c.... Automatic scaling if requested.
38     c
39     if (auto) then
40     delta=(aamax-aamin)/float(nauto-1)
41     do 20 n=1,nauto
42     autolevs(n)=aamin+float(n-1)*delta
43     endif
44
45     c.... Label.
46     c
47     if (auto) then
48     write (lab,25) label,it1,nregn,aamin,aamax
49     format(a,i3,i2,": min=",lpe9.2," max=",e10.3)
50     else
51     lab=label
52     endif
53
54     c
55     ilen=1
56
57     do 30 i=len(lab),1,-1
58     if (lab(i:i).ne." ") then
59     ilen=i
60     go to 40
61     endif
62
63     30 continue
64     c
65     40 continue
66
67     call set(0.0,1.0,0.0,1.0,0.0,1.0,0.0,1.0,1)

```

```
65      call wtstr(0.5,0.95,lab(1:ilen),24,0,0)
66      c
67      c.... Set viewport and window.
68      c
69      call set(0.1,0.9,0.1,0.9,
70      . float(imin),float(imax),float(jmin),float(jmax),1)
71      c
72      c.... Draw grid.
73      c
74      call labmod("(1pe10.3)","(1pe10.3)",0,0,10,10,0,0,0)
75      call periml(10,2,10,2)
76      c
77      c.... Draw structure if necessary.
78      c
79      call msklplot(nregn)
80      c
81      c.... Draw contours.
82      c
83      if (auto) then
84          call conrec(ww,nxi,imax-imin+1,jmax-jmin+1,
85          . 0.,0.,0,-1,-1,0)
86      else
87          call conrec(ww,nxi,imax-imin+1,jmax-jmin+1,
88          . aclevs(1),aclevs(nclevs),-float(nclevs),-1,-1,0)
89      endif
90      c
91      c.... Frame advance.
92      c
93      call frame
94      c
95      c.... Done.
96      c
97      return
98      end
```

```

1      subroutine fadil(it1)
2      c
3      c.... ADI for fine grid, excluding ffine-grid region.
4      c.... Communicates with fine-grid through the boundary.
5      c.... Neumann condition at i=1 & nxi with d(phi) / d(x) = 0; cylindrical.
6      c.... Dirichlet condition at j=1 & neta.
7      c
8      include 'global.h'
9      c
10     rdelyx=delyf/delxf
11     rdlyx2=rdelyx**2
12     aa1=2.*rdlyx2
13     aa2=-2.*(rdlyx2+1.)
14     aa3=4.*rdlyx2
15     aa4=-2.*(2.*rdlyx2+1.)
16     c
17     do 9000 it=1,itmx
18     c
19     errmx=0.
20     sumerr=0.
21     c
22     c.... Y-sweep for i = 1.
23     c
24     do 300 j=nyff2,netaml
25     erry(j)=aa3*phif(2,j)+phif(1,j+1)+phif(1,j-1)+aa4*phif(1,j)
26     erra=abs(erry(j))
27     if(erra .gt. errmx)then
28         errmx=errra
29         iermx=1
30         jermx=j
31     endif
32 300 sumerr=sumerr+errra
33     bet(nyff2)=aa4
34     dp(nyff2)=-erry(nyff2)/aa4
35     do 301 j=nyff2+1,netaml
36     gam(j)=1./bet(j-1)
37     bet(j)=aa4-gam(j)
38 301 dp(j)=(-erry(j)-dp(j-1))/bet(j)
39     do 302 j=netam2,nyff2,-1
40     dp(j)=dp(j)-gam(j+1)*dp(j+1)
41 302 do 303 j=nyff2,netaml
42     phif(1,j)=phif(1,j)+dp(j)
43     c
44     c.... Y-sweep for 1 < i < nil.
45     c
46     do 110 i=2,nxff2-1
47     if(mj1fpl(i).lt.nxff1)then
48     bet(mj1fpl(i))=aa2
49     do 109 j=mj1fp2(i),nyff1
50     gam(j)=1./bet(j-1)
51 109 bet(j)=aa2-gam(j)
52     do 111 j=mj1fpl(i),nyff1
53     erry(j)=ryxfm(i)*phif(i-1,j)+ryxfp(i)*phif(i+1,j)
54         +phif(i,j+1)+phif(i,j-1)+aa2*phif(i,j)
55     erra=abs(erry(j))
56     if(erra .gt. errmx)then
57         errmx=errra
58         iermx=i
59         jermx=j
60     endif
61 111 sumerr=sumerr+errra
62     dp(mj1fpl(i))=-erry(mj1fpl(i))/aa2
63     do 112 j=mj1fp2(i),nyff1
64 112 dp(j)=(-erry(j)-dp(j-1))/bet(j)

```

```

65      do 113 j=nyff1-1,mj1fpl(i),-1
66      113      dp(j)=dp(j)-gam(j+1)*dp(j+1)
67      do 114 j=mj1fpl(i),nyff1
68      114      phif(i,j)=phif(i,j)+dp(j)
69      endif
70      110      continue
71      c
72      bet(nyff2)=aa2
73      do 309 j=nyff2+1,netam1
74      gam(j)=1./bet(j-1)
75      309      bet(j)=aa2-gam(j)
76      do 310 i=2,nxff2-1
77      do 311 j=nyff2,netam1
78      erry(j)=ryxfm(i)*phif(i-1,j)+ryxfp(i)*phif(i+1,j)
79      +phif(i,j+1)+phif(i,j-1)+aa2*phif(i,j)
80      erra=abs(erry(j))
81      if(erra .gt. errmx)then
82          errmx=erra
83          iermx=i
84          jermx=j
85      endif
86      311      sumerr=sumerr+erra
87      dp(nyff2)=-erry(nyff2)/aa2
88      do 312 j=nyff2+1,netam1
89      312      dp(j)=(-erry(j)-dp(j-1))/bet(j)
90      do 313 j=netam2,nyff2,-1
91      313      dp(j)=dp(j)-gam(j+1)*dp(j+1)
92      do 314 j=nyff2,netam1
93      314      phif(i,j)=phif(i,j)+dp(j)
94      310      continue
95      c
96      c.... Y-sweep for nxff2 =< i < nxi.
97      c
98      bet(2)=aa2
99      do 509 j=3,netam1
100     gam(j)=1./bet(j-1)
101     509     bet(j)=aa2-gam(j)
102     do 520 i=nxff2,nxim1
103     do 521 j=2,netam1
104     erry(j)=ryxfm(i)*phif(i-1,j)+ryxfp(i)*phif(i+1,j)
105     +phif(i,j+1)+phif(i,j-1)+aa2*phif(i,j)
106     erra=abs(erry(j))
107     if(erra .gt. errmx)then
108         errmx=erra
109         iermx=i
110         jermx=j
111     endif
112     521     sumerr=sumerr+erra
113     dp(2)=-erry(2)/aa2
114     do 522 j=3,netam1
115     522     dp(j)=(-erry(j)-dp(j-1))/bet(j)
116     do 523 j=netam2,2,-1
117     523     dp(j)=dp(j)-gam(j+1)*dp(j+1)
118     do 524 j=2,netam1
119     524     phif(i,j)=phif(i,j)+dp(j)
120     520     continue
121     c
122     goto 134
123     c
124     c.... Y-sweep for i = nxi.
125     c
126     135     do 130 j=2,netam1
127     erry(j)=aa1*phif(nxim1,j)+phif(nxi,j+1)+phif(nxi,j-1)
128     +aa2*phif(nxi,j)

```

```

129      erra=abs(erry(j))
130      if(erra .gt. errmx)then
131          errmx=erra
132          iermx=nxi
133          jermx=j
134      endif
135  130      sumerr=sumerr+erra
136      dp(2)=-erry(2)/aa2
137      do 131 j=3,netaml
138  131      dp(j)=(-erry(j)-dp(j-1))/bet(j)
139      do 132 j=netam2,2,-1
140  132      dp(j)=dp(j)-gam(j+1)*dp(j+1)
141      do 133 j=2,netaml
142  133      phif(nxi,j)=phif(nxi,j)+dp(j)
143      c
144      c.... X-sweep for nyff2 <= j < neta.
145      c
146  134      bet(1)=aa4
147      gam(2)=aa3/bet(1)
148      bet(2)=aa2-ryxfm(2)*gam(2)
149      do 199 i=3,nximl
150      gam(i)=ryxfp(i)/bet(i-1)
151  199      bet(i)=aa2-gam(i)*ryxfm(i)
152      gam(nxi)=ryxfp(nxi)/bet(nximl)
153      bet(nxi)=aa2-aal*gam(nxi)
154      do 201 j=netaml,nyff2,-1
155      errx(1)=aa3*phif(2,j)+phif(1,j+1)+phif(1,j-1)+aa4*phif(1,j)
156      sumerr=sumerr+abs(errx(1))
157      do 202 i=2,nximl
158      errx(i)=ryxfm(i)*phif(i-1,j)+ryxfp(i)*phif(i+1,j)
159      +phif(i,j+1)+phif(i,j-1)+aa2*phif(i,j)
160  202      sumerr=sumerr+abs(errx(i))
161      errx(nxi)=aal*phif(nximl,j)+phif(nxi,j+1)+phif(nxi,j-1)+aa2*
162      phif(nxi,j)
163      sumerr=sumerr+abs(errx(nxi))
164      dp(1)=-errx(1)/aa4
165      do 203 i=2,nximl
166  203      dp(i)=(-errx(i)-ryxfm(i)*dp(i-1))/bet(i)
167      dp(nxi)=(-errx(nxi)-aal*dp(nximl))/bet(nxi)
168      do 204 i=nxim2,1,-1
169  204      dp(i)=dp(i)-gam(i+1)*dp(i+1)
170      do 205 i=1,nximl
171  205      phif(i,j)=phif(i,j)+dp(i)
172  201      continue
173      c
174      c.... X-sweep for nyff1 >= j > 1.
175      c
176      bet(nxff2)=aa2
177      do 419 i=nxff2+1,nximl
178      gam(i)=ryxfp(i)/bet(i-1)
179  419      bet(i)=aa2-gam(i)*ryxfm(i)
180      gam(nxi)=ryxfp(nxi)/bet(nximl)
181      bet(nxi)=aa2-aal*gam(nxi)
182      do 441 j=nyff2-1,nyff1+1,-1
183      do 422 i=nxff2,nximl
184      errx(i)=ryxfm(i)*phif(i-1,j)+ryxfp(i)*phif(i+1,j)
185      +phif(i,j+1)+phif(i,j-1)+aa2*phif(i,j)
186  422      sumerr=sumerr+abs(errx(i))
187      errx(nxi)=aal*phif(nximl,j)+phif(nxi,j+1)+phif(nxi,j-1)+aa2*
188      phif(nxi,j)
189      sumerr=sumerr+abs(errx(nxi))
190      dp(nxff2)=-errx(nxff2)/aa2
191      do 423 i=nxff2+1,nxi
192  423      dp(i)=(-errx(i)-ryxfm(i)*dp(i-1))/bet(i)

```

```

193      do 424 i=nxim2,nxff2,-1
194      424      dp(i)=dp(i)-gam(i+1)*dp(i+1)
195      do 425 i=nxff2,nxim1
196      425      phif(i,j)=phif(i,j)+dp(i)
197      441      continue
198      c
199      do 221 j=nyff1,2,-1
200      bet(mi2fp1(j))=aa2
201      do 219 i=mi2fp2(j),nxim1
202      gam(i)=ryxfp(i)/bet(i-1)
203      219      bet(i)=aa2-gam(i)*ryxfm(i)
204      gam(nxi)=ryxfp(nxi)/bet(nxim1)
205      bet(nxi)=aa2-aal*gam(nxi)
206      do 222 i=mi2fp1(j),nxim1
207      errx(i)=ryxfm(i)*phif(i-1,j)+ryxfp(i)*phif(i+1,j)
208      +phif(i,j+1)+phif(i,j-1)+aa2*phif(i,j)
209      222      sumerr=sumerr+abs(errx(i))
210      errx(nxi)=aal*phif(nxim1,j)+phif(nxi,j+1)+phif(nxi,j-1)+aa2*
211      phif(nxi,j)
212      sumerr=sumerr+abs(errx(nxi))
213      dp(mi2fp1(j))=-errx(mi2fp1(j))/aa2
214      do 223 i=mi2fp2(j),nxi
215      223      dp(i)=(-errx(i)-ryxfm(i)*dp(i-1))/bet(i)
216      do 224 i=nxim2,mi2fp1(j),-1
217      224      dp(i)=dp(i)-gam(i+1)*dp(i+1)
218      do 225 i=mi2fp1(j),nxim1
219      225      phif(i,j)=phif(i,j)+dp(i)
220      221      continue
221      c
222      if (it.eq.itmx .or. it .eq. 1) then
223      write(6,901)it1,it,sumerr,errmx,iermx,jermx
224      write(23,901)it1,it,sumerr,errmx,iermx,jermx
225      endif
226      901      format('f it sumerr errmx ',2i6,1pe11.3,e11.3,2i4)
227      c
228      9000      continue
229      c
230      c.... Calculate electric field.
231      c
232      emx=0.
233      do 10 i=1,nxim1
234      do 10 j=1,netaml
235      by=.5*(phif(i,j)+phif(i+1,j)-phif(i,j+1)-phif(i+1,j+1))/delyf
236      bx=.5*(phif(i,j+1)+phif(i,j)-phif(i+1,j+1)-phif(i+1,j))/delxf
237      exf(i,j)=bx
238      eyf(i,j)=by
239      eec(i,j)=sqrt(bx**2+by**2)
240      if(eec(i,j) .gt. emx)then
241      emx=eec(i,j)
242      iemx=i
243      jemx=j
244      endif
245      10      continue
246      write (6,200)iemx,jemx,emx,xf(iemx),yf(jemx)
247      write (23,200)iemx,jemx,emx,xf(iemx),yf(jemx)
248      200      format("max Electric field ",2i4,1pe11.3,2e11.3)
249      c
250      return
251      end

```

```

1      subroutine fadi10
2
3      c
4      c.... Neumann condition at i=1 with d(phi) / d(x) = 0; cylindrical.
5      c.... Dirichlet condition at j=1 & neta and i=nxi.
6      c
7      include 'global.h'
8      c
9      if(resume)return
10     c
1004   rdelyx=delyf/delxf
11     rdlyx2=rdelyx**2
12     aa1=2.*rdlyx2
13     aa2=-2.*(rdlyx2+1.)
14     aa3=4.*rdlyx2
15     aa4=-2.*(2.*rdlyx2+1.)
16   c
17   do 9000 it=1,itmx
18   c
19     errmx=0.
20     sumerr=0.
21   c
22   c.... Y-sweep for i = 1.
23   c
24     do 100 j=mj1fp1(1),netaml
25     erry(j)=aa3*phif(2,j)+phif(1,j+1)+phif(1,j-1)+aa4*phif(1,j)
26     erra=abs(erry(j))
27     if(erra .gt. errmx)then
28       errmx=errra
29       iermx=1
30       jermx=j
31     endif
32   100   sumerr=sumerr+errra
33     bet(mj1fp1(1))=aa4
34     dp(mj1fp1(1))=-erry(mj1fp1(1))/aa4
35     do 101 j=mj1fp2(1),netaml
36     gam(j)=1./bet(j-1)
37     bet(j)=aa4-gam(j)
38   101   dp(j)=(-erry(j)-dp(j-1))/bet(j)
39     do 102 j=netam2,mj1fp1(1),-1
40     dp(j)=dp(j)-gam(j+1)*dp(j+1)
41   102   do 103 j=mj1fp1(1),netaml
42   103   phif(1,j)=phif(1,j)+dp(j)
43   c
44   c.... Y-sweep for 1 < i < nxi.
45   c
46     bet(2)=aa2
47     do 109 j=3,netaml
48     gam(j)=1./bet(j-1)
49   109   bet(j)=aa2-gam(j)
50     do 115 i=2,nxim1
51     do 116 j=mj1fp1(i),netaml
52     erry(j)=ryxfm(i)*phif(i-1,j)+ryxfp(i)*phif(i+1,j)
53     .      +phif(i,j+1)+phif(i,j-1)+aa2*phif(i,j)
54     erra=abs(erry(j))
55     if(erra .gt. errmx)then
56       errmx=errra
57       iermx=i
58       jermx=j
59     endif
60   116   sumerr=sumerr+errra
61     dp(mj1fp1(i))=-erry(mj1fp1(i))/aa2
62     do 117 j=mj1fp2(i),netaml
63   117   dp(j)=(-erry(j)-dp(j-1))/bet(j-mj1f(i)+1)
64     do 118 j=netam2,mj1fp1(i),-1

```

```

65      118  dp(j)=dp(j)-gam(j-mj1f(i)+2)*dp(j+1)
66      do 119 j=mj1fp1(i),netam1
67      119  phif(i,j)=phif(i,j)+dp(j)
68      115  continue
69      goto 134
70      c
71      c.... Y-sweep for i = nxi.
72      c
73      135  do 130 j=2,netam1
74      erry(j)=aa1*phif(nxim1,j)+phif(nxi,j+1)+phif(nxi,j-1)
75      .+aa2*phif(nxi,j)
76      erra=abs(erry(j))
77      if(erra .gt. errmx)then
78      errmx=erra
79      iermx=i
80      jermx=j
81      endif
82      130  sumerr=sumerr+erra
83      dp(2)=-erry(2)/aa2
84      do 131 j=3,netam1
85      131  dp(j)=(-erry(j)-dp(j-1))/bet(j)
86      do 132 j=netam2,2,-1
87      132  dp(j)=dp(j)-gam(j+1)*dp(j+1)
88      do 133 j=2,netam1
89      133  phif(nxi,j)=phif(nxi,j)+dp(j)
90      c
91      c.... X-sweep for nj1 < j < neta.
92      c
93      134  bet(1)=aa4
94      gam(2)=aa3/bet(1)
95      bet(2)=aa2-ryxfm(2)*gam(2)
96      do 199 i=3,nxim1
97      gam(i)=ryxfp(i)/bet(i-1)
98      199  bet(i)=aa2-gam(i)*ryxfm(i)
99      gam(nxi)=ryxfp(nxi)/bet(nxim1)
100     bet(nxi)=aa2-aa1*gam(nxi)
101     do 201 j=netam1,mj1fp1(1),-1
102     errx(1)=aa3*phif(2,j)+phif(1,j+1)+phif(1,j-1)+aa4*phif(1,j)
103     sumerr=sumerr+abs(errx(1))
104     do 202 i=2,nxim1
105     errx(i)=ryxfm(i)*phif(i-1,j)+ryxfp(i)*phif(i+1,j)
106     .+phif(i,j+1)+phif(i,j-1)+aa2*phif(i,j)
107     202  sumerr=sumerr+abs(errx(i))
108     errx(nxi)=aa1*phif(nxim1,j)+phif(nxi,j+1)+phif(nxi,j-1)+aa2*
109     .phif(nxi,j)
110     sumerr=sumerr+abs(errx(nxi))
111     c
112     dp(1)=-errx(1)/aa2
113     dp(1)=-errx(1)/aa4
114     do 203 i=2,nxim1
115     203  dp(i)=(-errx(i)-ryxfm(i)*dp(i-1))/bet(i)
116     dp(nxi)=(-errx(nxi)-aa1*dp(nxim1))/bet(nxi)
117     do 204 i=nxim2,1,-1
118     204  dp(i)=dp(i)-gam(i+1)*dp(i+1)
119     do 205 i=1,nxim1
120     205  phif(i,j)=phif(i,j)+dp(i)
121     201  continue
122     c
123     do 221 j=mj1f(1),2,-1
124     do 222 i=mi2fp1(j),nxim1
125     errx(i)=ryxfm(i)*phif(i-1,j)+ryxfp(i)*phif(i+1,j)
126     .+phif(i,j+1)+phif(i,j-1)+aa2*phif(i,j)
127     222  sumerr=sumerr+abs(errx(i))
128     errx(nxi)=aa1*phif(nxim1,j)+phif(nxi,j+1)+phif(nxi,j-1)+aa2*
     .phif(nxi,j)

```



```
129      sumerr=sumerr+abs(errx(nxi))
130      bet(mi2fp1(j))=aa2
131      do 219 i=mi2fp2(j),nxim1
132      gam(i)=ryxfp(i)/bet(i-1)
133      219 bet(i)=aa2-gam(i)*ryxfm(i)
134      gam(nxi)=ryxfp(nxi)/bet(nxim1)
135      bet(nxi)=aa2-aal*gam(nxi)
136      dp(mi2fp1(j))=-errx(mi2fp1(j))/aa2
137      do 223 i=mi2fp2(j),nxi
138      223 dp(i)=(-errx(i)-ryxfm(i)*dp(i-1))/bet(i)
139      do 224 i=nxim2,mi2fp1(j),-1
140      224 dp(i)=dp(i)-gam(i+1)*dp(i+1)
141      do 225 i=mi2fp1(j),nxim1
142      225 phif(i,j)=phif(i,j)+dp(i)
143      221 continue
144      c
145      if (it.eq.itmx .or. it .eq. 1) then
146      write(6,901)it,sumerr,errmx,iermx,jermx
147      write(23,901)it,sumerr,errmx,iermx,jermx
148      endif
149      901 format('f it sumerr errmx ',i6,1p11.3,e11.3,2i4)
150      c
151      9000 continue
152      c
153      return
154      end
```

```

1      subroutine fadi2(it1)
2
3      c.... ADI for fine grid, excluding ffine-grid region.
4      c.... Communicates with fine-grid through the boundary.
5      c.... Neumann condition at i=1 & nxi with d(phi) / d(x) = 0; cylindrical.
6      c.... Dirichlet condition at j=1 & neta.
7
8      include 'global.h'
9
10     c
11     write(6,349)nif1,nif2,njlf
12     write(23,349)nif1,nif2,njlf
13 349   format('nif1,nif2 njlf ',3i4)
14     rdelyx=delyf/delxf
15     rdlyx2=rdelyx**2
16     aal=2.*rdlyx2
17     aa2=-2.*(rdlyx2+1.)
18     aa3=4.*rdlyx2
19     aa4=-2.*(2.*rdlyx2+1.)
20
21     c
22     do 9000 it=1,itmx
23
24     c
25     errmx=0.
26     sumerr=0.
27
28     c.... Y-sweep for i = 1.
29     c
30     do 100 j=2,netaml
31     erry(j)=aa3*phif(2,j)+phif(1,j+1)+phif(1,j-1)+aa4*phif(1,j)
32     erra=abs(erry(j))
33     if(erra .gt. errmx)then
34         errmx=erra
35         iermx=1
36         jermx=j
37     endif
38 100    sumerr=sumerr+erra
39     bet(2)=aa4
40     dp(2)=-erry(2)/aa4
41     do 101 j=3,netaml
42     gam(j)=1./bet(j-1)
43     bet(j)=aa4-gam(j)
44 101    dp(j)=(-erry(j)-dp(j-1))/bet(j)
45     do 102 j=netaml-1,2,-1
46     dp(j)=dp(j)-gam(j+1)*dp(j+1)
47 102    do 103 j=2,netaml
48     phif(1,j)=phif(1,j)+dp(j)
49
50     c
51     c.... Y-sweep for 1 < i <= nxffl.
52     c
53     bet(2)=aa2
54     do 299 j=3,netaml
55     gam(j)=1./bet(j-1)
56     bet(j)=aa2-gam(j)
57 299    do 290 i=2,nxffl
58     do 291 j=2,netaml
59     erry(j)=ryxfm(i)*phif(i-1,j)+ryxfp(i)*phif(i+1,j)
60         +phif(i,j+1)+phif(i,j-1)+aa2*phif(i,j)
61     erra=abs(erry(j))
62     if(erra .gt. errmx)then
63         errmx=erra
64         iermx=i
65         jermx=j
66     endif
67 291    sumerr=sumerr+erra
68     dp(2)=-erry(2)/aa2

```

```

65      do 292 j=3,netaml
66      292  dp(j)=(-erry(j)-dp(j-1))/bet(j)
67      do 293 j=netaml-1,2,-1
68      293  dp(j)=dp(j)-gam(j+1)*dp(j+1)
69      do 294 j=2,netaml
70      294  phif(i,j)=phif(i,j)+dp(j)
71      290  continue
72      c
73      c.... Y-sweep for nxffl+1 < i < nifl.
74      c
75      c      bet(2)=aa2
76      c      do 109 j=3,nyffl
77      c      gam(j)=1./bet(j-1)
78      c109  bet(j)=aa2-gam(j)
79      do 110 i=nxffl+1,nifl-1
80      do 111 j=2,nyffl
81      erry(j)=ryxfm(i)*phif(i-1,j)+ryxfp(i)*phif(i+1,j)
82      +phif(i,j+1)+phif(i,j-1)+aa2*phif(i,j)
83      erra=abs(erry(j))
84      if(erra .gt. errmx)then
85          errmx=erra
86          iermx=i
87          jermx=j
88      endif
89      111  sumerr=sumerr+erra
90      dp(2)=-erry(2)/aa2
91      do 112 j=3,nyffl
92      112  dp(j)=(-erry(j)-dp(j-1))/bet(j)
93      do 113 j=nyffl-1,2,-1
94      113  dp(j)=dp(j)-gam(j+1)*dp(j+1)
95      do 114 j=2,nyffl
96      114  phif(i,j)=phif(i,j)+dp(j)
97      110  continue
98      c
99      c.... Y-sweep for nif2 < i < nxff2.
100     c
101     do 120 i=nif2+1,nxff2-1
102     do 121 j=2,nyffl
103     erry(j)=ryxfm(i)*phif(i-1,j)+ryxfp(i)*phif(i+1,j)
104     +phif(i,j+1)+phif(i,j-1)+aa2*phif(i,j)
105     erra=abs(erry(j))
106     if(erra .gt. errmx)then
107         errmx=erra
108         iermx=i
109         jermx=j
110     endif
111     121  sumerr=sumerr+erra
112     dp(2)=-erry(2)/aa2
113     do 122 j=3,nyffl
114     122  dp(j)=(-erry(j)-dp(j-1))/bet(j)
115     do 123 j=nyffl-1,2,-1
116     123  dp(j)=dp(j)-gam(j+1)*dp(j+1)
117     do 124 j=2,nyffl
118     124  phif(i,j)=phif(i,j)+dp(j)
119     120  continue
120     c
121     bet(nyff2)=aa2
122     do 309 j=nyff2+1,netaml
123     gam(j)=1./bet(j-1)
124     309  bet(j)=aa2-gam(j)
125     do 310 i=nxffl+1,nxff2-1
126     do 311 j=nyff2,netaml
127     erry(j)=ryxfm(i)*phif(i-1,j)+ryxfp(i)*phif(i+1,j)
128     +phif(i,j+1)+phif(i,j-1)+aa2*phif(i,j)

```

```

129      erra=abs(erry(j))
130      if(erra .gt. errmx)then
131          errmx=erra
132          iermx=i
133          jermx=j
134      endif
135      311 sumerr=sumerr+erra
136      dp(nyff2)=-erry(nyff2)/aa2
137      do 312 j=nyff2+1,netaml
138          312 dp(j)=(-erry(j)-dp(j-1))/bet(j)
139          do 313 j=netam2,nyff2,-1
140              313 dp(j)=dp(j)-gam(j+1)*dp(j+1)
141              do 314 j=nyff2,netaml
142                  314 phif(i,j)=phif(i,j)+dp(j)
143              310 continue
144          c
145      c.... Y-sweep for nxff2 =< i < nxi.
146      c
147          bet(2)=aa2
148          do 509 j=3,netaml
149              gam(j)=1./bet(j-1)
150          509 bet(j)=aa2-gam(j)
151          do 520 i=nxff2,nximl
152              do 521 j=2,netaml
153                  erry(j)=ryxfm(i)*phif(i-1,j)+ryxfp(i)*phif(i+1,j)
154                      +phif(i,j+1)+phif(i,j-1)+aa2*phif(i,j)
155                  erra=abs(erry(j))
156                  if(erra .gt. errmx)then
157                      errmx=erra
158                      iermx=i
159                      jermx=j
160                  endif
161          521 sumerr=sumerr+erra
162          dp(2)=-erry(2)/aa2
163          do 522 j=3,netaml
164              522 dp(j)=(-erry(j)-dp(j-1))/bet(j)
165              do 523 j=netam2,2,-1
166                  523 dp(j)=dp(j)-gam(j+1)*dp(j+1)
167                  do 524 j=2,netaml
168                      524 phif(i,j)=phif(i,j)+dp(j)
169              520 continue
170          c
171      c.... X-sweep for nyff2 <= j < neta.
172      c
173          bet(1)=aa4
174          gam(2)=aa3/bet(1)
175          bet(2)=aa2-ryxfm(2)*gam(2)
176          do 199 i=3,nximl
177              gam(i)=ryxfp(i)/bet(i-1)
178          199 bet(i)=aa2-gam(i)*ryxfm(i)
179              gam(nxi)=ryxfp(nxi)/bet(nximl)
180              bet(nxi)=aa2-aal*gam(nxi)
181              do 201 j=netaml,nyff2,-1
182                  errx(1)=aa3*phif(2,j)+phif(1,j+1)+phif(1,j-1)+aa4*phif(1,j)
183                  sumerr=sumerr+abs(errx(1))
184                  do 202 i=2,nximl
185                      errx(i)=ryxfm(i)*phif(i-1,j)+ryxfp(i)*phif(i+1,j)
186                          +phif(i,j+1)+phif(i,j-1)+aa2*phif(i,j)
187          202 sumerr=sumerr+abs(errx(i))
188          dp(1)=-errx(1)/aa4
189          do 203 i=2,nximl
190              203 dp(i)=(-errx(i)-ryxfm(i)*dp(i-1))/bet(i)
191              do 204 i=nxim2,1,-1
192                  204 dp(i)=dp(i)-gam(i+1)*dp(i+1)

```

```

193      do 205 i=1,nxim1
194      205  phif(i,j)=phif(i,j)+dp(i)
195      201  continue
196      c
197      do 231 j=nyff2-1,nyff1+1,-1
198      errx(1)=aa3*phif(2,j)+phif(1,j+1)+phif(1,j-1)+aa4*phif(1,j)
199      sumerr=sumerr+abs(errx(1))
200      do 232 i=2,nxff1
201      errx(i)=ryxfm(i)*phif(i-1,j)+ryxfp(i)*phif(i+1,j)
202      +phif(i,j+1)+phif(i,j-1)+aa2*phif(i,j)
203      232  sumerr=sumerr+abs(errx(i))
204      dp(1)=-errx(1)/aa4
205      do 233 i=2,nxff1
206      233  dp(i)=(-errx(i)-ryxfm(i)*dp(i-1))/bet(i)
207      do 234 i=nxff1-1,1,-1
208      234  dp(i)=dp(i)-gam(i+1)*dp(i+1)
209      do 235 i=1,nxff1
210      235  phif(i,j)=phif(i,j)+dp(i)
211      231  continue
212      c
213      c.... X-sweep for nyff1 >= j > 1.
214      c
215      do 211 j=nyff1,2,-1
216      errx(1)=aa3*phif(2,j)+phif(1,j+1)+phif(1,j-1)+aa4*phif(1,j)
217      sumerr=sumerr+abs(errx(1))
218      do 212 i=2,nif1m1
219      errx(i)=ryxfm(i)*phif(i-1,j)+ryxfp(i)*phif(i+1,j)
220      +phif(i,j+1)+phif(i,j-1)+aa2*phif(i,j)
221      212  sumerr=sumerr+abs(errx(i))
222      c      dp(1)=-errx(1)/aa2
223      dp(1)=-errx(1)/aa4
224      do 213 i=2,nif1m1
225      213  dp(i)=(-errx(i)-ryxfm(i)*dp(i-1))/bet(i)
226      do 214 i=nif1m2,1,-1
227      214  dp(i)=dp(i)-gam(i+1)*dp(i+1)
228      do 215 i=1,nif1m1
229      215  phif(i,j)=phif(i,j)+dp(i)
230      211  continue
231      c
232      bet(nxff2)=aa2
233      do 419 i=nxff2+1,nxim1
234      gam(i)=ryxfp(i)/bet(i-1)
235      419  bet(i)=aa2-gam(i)*ryxfm(i)
236      gam(nxi)=ryxfp(nxi)/bet(nxim1)
237      bet(nxi)=aa2-aal*gam(nxi)
238      do 441 j=nyff2-1,nyff1+1,-1
239      do 422 i=nxff2,nxim1
240      errx(i)=ryxfm(i)*phif(i-1,j)+ryxfp(i)*phif(i+1,j)
241      +phif(i,j+1)+phif(i,j-1)+aa2*phif(i,j)
242      422  sumerr=sumerr+abs(errx(i))
243      dp(nxff2)=-errx(nxff2)/aa2
244      do 423 i=nxff2+1,nxim1
245      423  dp(i)=(-errx(i)-ryxfm(i)*dp(i-1))/bet(i)
246      do 424 i=nxim2,nxff2,-1
247      424  dp(i)=dp(i)-gam(i+1)*dp(i+1)
248      do 425 i=nxff2,nxim1
249      425  phif(i,j)=phif(i,j)+dp(i)
250      441  continue
251      c
252      bet(nif2p1)=aa2
253      do 219 i=nif2p2,nxim1
254      gam(i)=ryxfp(i)/bet(i-1)
255      219  bet(i)=aa2-gam(i)*ryxfm(i)
256      gam(nxi)=ryxfp(nxi)/bet(nxim1)

```

```

257      bet(nxi)=aa2-aal*gam(nxi)
258      do 221 j=nyff1,2,-1
259      do 222 i=nif2p1,nxim1
260      errx(i)=ryxfm(i)*phif(i-1,j)+ryxfp(i)*phif(i+1,j)
261      +phif(i,j+1)+phif(i,j-1)+aa2*phif(i,j)
262      222 sumerr=sumerr+abs(errx(i))
263      dp(nif2p1)=-errx(nif2p1)/aa2
264      do 223 i=nif2p2,nxim1
265      223 dp(i)=(-errx(i)-ryxfm(i)*dp(i-1))/bet(i)
266      do 224 i=nxim2,nif2p1,-1
267      224 dp(i)=dp(i)-gam(i+1)*dp(i+1)
268      do 225 i=nif2p1,nxim1
269      225 phif(i,j)=phif(i,j)+dp(i)
270      221 continue
271      c
272      if (it.eq.itmx .or. it .eq. 1) then
273      write(6,901)it1,it,sumerr,errmx,iermx,jermx
274      write(23,901)it1,it,sumerr,errmx,iermx,jermx
275      endif
276      901 format(' it sumerr errmx ',2i6,1pe11.3,e11.3,2i4)
277      c
278      9000 continue
279      c
280      c.... Calculate electric field.
281      c
282      emx=0.
283      do 10 i=1,nxim1
284      do 10 j=1,netaml
285      ay=.5*(phif(i,j)+phif(i+1,j)-phif(i,j+1)-phif(i+1,j+1))/delyf
286      ax=.5*(phif(i,j+1)+phif(i,j)-phif(i+1,j+1)-phif(i+1,j))/delxf
287      exf(i,j)=ax
288      eyf(i,j)=ay
289      eec(i,j)=sqrt(ax**2+ay**2)
290      if(eec(i,j) .gt. emx)then
291      emx=eec(i,j)
292      iemx=i
293      jemx=j
294      endif
295      10 continue
296      write (6,200)iemx,jemx,emx,xf(iemx),yf(jemx)
297      write (23,200)iemx,jemx,emx,xf(iemx),yf(jemx)
298      200 format("max Electric field ",2i4,1pe11.3,2e11.3)
299      c
300      return
301      end

```

```

1      subroutine fadi20
2
3      c
4      c.... Neumann at i=1 (cylindrical r=0); Dirichlet at i=nxi.
5      c.... Dirichlet condition at j=1 & neta.
6      c.... Use for fine-grid.
7      c
8      include 'global.h'
9      c
10     write(6,449)nif1,nif2,nj1f
11     write(23,449)nif1,nif2,nj1f
12 449   format('nif1,nif2 nj1f ',3i4)
13     c
14     n111=1
15     rdelyx=delyf/delxf
16     rdlyx2=rdelyx**2
17     aa1=2.*rdlyx2
18     aa2=-2.*(rdlyx2+1.)
19     aa3=4.*rdlyx2
20     aa4=-2.*(2.*rdlyx2+1.)
21     c
22     do 9000 it=1,itmx
23     c
24     errmx=0.
25     sumerr=0.
26     c
27     c.... Y-sweep for i = 1.
28     c
29     do 100 j=2,netam1
30     erry(j)=aa3*phif(2,j)+phif(1,j+1)+phif(1,j-1)+aa4*phif(1,j)
31     erra=abs(erry(j))
32     if(erra .gt. errmx)then
33         errmx=erra
34         iermx=1
35         jermx=j
36     endif
37 100    sumerr=sumerr+erra
38     bet(2)=aa4
39     dp(2)=-erry(2)/aa4
40     do 101 j=3,netam1
41     gam(j)=1./bet(j-1)
42     bet(j)=aa4-gam(j)
43 101    dp(j)=(-erry(j)-dp(j-1))/bet(j)
44     do 102 j=netam2,2,-1
45 102    dp(j)=dp(j)-gam(j+1)*dp(j+1)
46     do 103 j=2,netam1
47     phif(1,j)=phif(1,j)+dp(j)
48     c
49     c.... Y-sweep for 1 < i < nil.
50     c
51     9001 bet(2)=aa2
52     do 109 j=3,netam1
53     gam(j)=1./bet(j-1)
54 109    bet(j)=aa2-gam(j)
55     c
56     do 115 i=2,nxim1
57     do 116 j=nj1p1(i),netam1
58     erry(j)=ryxfm(i)*phif(i-1,j)+ryxfp(i)*phif(i+1,j)
59     +phif(i,j+1)+phif(i,j-1)+aa2*phif(i,j)
60     erra=abs(erry(j))
61     if(erra .gt. errmx)then
62         errmx=erra
63         iermx=i
64         jermx=j
65     endif

```

```

65      116      sumerr=sumerr+erra
66      dp(nj1p1(i))=-erry(nj1p1(i))/aa2
67      do 117 j=nj1p2(i),netaml
68      117      dp(j)=(-erry(j)-dp(j-1))/bet(j-nj1(i)+1)
69      do 118 j=netam2,nj1p1(i),-1
70      118      dp(j)=dp(j)-gam(j-nj1(i)+2)*dp(j+1)
71      do 119 j=nj1p1(i),netaml
72      119      phif(i,j)=phif(i,j)+dp(j)
73      115      continue
74      c
75      c.... X-sweep for njlf < j < neta.
76      c
77      bet(1)=aa4
78      gam(2)=aa3/bet(1)
79      bet(2)=aa2-ryxfm(2)*gam(2)
80      do 199 i=3,nximl
81      gam(i)=ryxfp(i-1)/bet(i-1)
82      199      bet(i)=aa2-gam(i)*ryxfm(i)
83      gam(nxi)=ryxfp(nximl)/bet(nximl)
84      bet(nxi)=aa2-aal*gam(nxi)
85      do 201 j=netaml,nj1p1,-1
86      errx(1)=aa3*phif(2,j)+phif(1,j+1)+phif(1,j-1)+aa4*phif(1,j)
87      sumerr=sumerr+abs(errx(1))
88      do 202 i=2,nximl
89      errx(i)=ryxfm(i)*phif(i-1,j)+ryxfp(i)*phif(i+1,j)
90      +phif(i,j+1)+phif(i,j-1)+aa2*phif(i,j)
91      202      sumerr=sumerr+abs(errx(i))
92      c      dp(1)=-errx(1)/aa2
93      dp(1)=-errx(1)/aa4
94      do 203 i=2,nximl
95      203      dp(i)=(-errx(i)-ryxfm(i)*dp(i-1))/bet(i)
96      c      dp(nxi)=(-errx(nxi)-aal*dp(nximl))/bet(nxi)
97      do 204 i=nxim2,1,-1
98      204      dp(i)=dp(i)-gam(i+1)*dp(i+1)
99      do 205 i=1,nximl
100     205      phif(i,j)=phif(i,j)+dp(i)
101     201      continue
102     c
103     c.... X-sweep for njlf >= j > 1 for i between 1 & nilml ...
104     c
105     do 211 j=njlf,2,-1
106     errx(1)=aa3*phif(2,j)+phif(1,j+1)+phif(1,j-1)+aa4*phif(1,j)
107     sumerr=sumerr+abs(errx(1))
108     do 212 i=2,niilm1(j)
109     errx(i)=ryxfm(i)*phif(i-1,j)+ryxfp(i)*phif(i+1,j)
110     +phif(i,j+1)+phif(i,j-1)+aa2*phif(i,j)
111     212      sumerr=sumerr+abs(errx(i))
112     c      dp(1)=-errx(1)/aa2
113     dp(1)=-errx(1)/aa4
114     do 213 i=2,niilm1(j)
115     213      dp(i)=(-errx(i)-ryxfm(i)*dp(i-1))/bet(i)
116     do 214 i=niilm2(j),1,-1
117     214      dp(i)=dp(i)-gam(i+1)*dp(i+1)
118     do 215 i=1,niilm1(j)
119     215      phif(i,j)=phif(i,j)+dp(i)
120     211      continue
121     c
122     c.... .... and for i between ni2p1 & nxi.
123     c
124     do 221 j=njlf,2,-1
125     bet(ni2p1(j))=aa2
126     do 219 i=ni2p2(j),nximl
127     c      gam(i)=ryxfp(i)/bet(i-1)
128     gam(i)=ryxfp(i-1)/bet(i-1)

```



```

129      219      bet(i)=aa2-gam(i)*ryxfm(i)
130      gam(nxi)=ryxfp(nxi)/bet(nximl)
131      bet(nxi)=aa2-aal*gam(nxi)
132      do 222 i=nii2p1(j),nximl
133      errx(i)=ryxfm(i)*phif(i-1,j)+ryxfp(i)*phif(i+1,j)
134      +phif(i,j+1)+phif(i,j-1)+aa2*phif(i,j)
135      222      sumerr=sumerr+abs(errx(i))
136      dp(nii2p1(j))=-errx(nii2p1(j))/aa2
137      do 223 i=nii2p2(j),nximl
138      223      dp(i)=(-errx(i)-ryxfm(i)*dp(i-1))/bet(i)
139      do 224 i=nxim2,nii2p1(j),-1
140      224      dp(i)=dp(i)-gam(i+1)*dp(i+1)
141      do 225 i=nii2p1(j),nximl
142      225      phif(i,j)=phif(i,j)+dp(i)
143      221      continue
144      c
145      9005      if (it .eq. 1 .or. it.eq.itmx) then
146      write(6,901)it1,it,sumerr,errmx,iermx,jermx
147      write(23,901)it1,it,sumerr,errmx,iermx,jermx
148      endif
149      901      format(' it sumerr errmx ',2i6,1pelli.3,e11.3,2i4)
150      c
151      9000      continue
152      c
153      c.... Calculate electric field.
154      c
155      emx=0.
156      do 10 i=1,nximl
157      do 10 j=1,netaml
158      ay=.5*(phif(i,j)+phif(i+1,j)-phif(i,j+1)-phif(i+1,j+1))/delyf
159      ax=.5*(phif(i,j+1)+phif(i,j)-phif(i+1,j+1)-phif(i+1,j))/delxf
160      exf(i,j)=ax
161      eyf(i,j)=ay
162      eec(i,j)=sqrt(ax**2+ay**2)
163      if(eec(i,j) .gt. emx)then
164      emx=eec(i,j)
165      iemx=i
166      jemx=j
167      endif
168      10      continue
169      write (6,200)iemx,jemx,emx,xf(iemx),yf(jemx)
170      write (23,200)iemx,jemx,emx,xf(iemx),yf(jemx)
171      200      format("max Electric field ",2i4,1pelli.3,2e11.3)
172      return
173      c
174      c.... Plots.
175      c
176      18      do 14 j=1,neta
177      dum1(j)=phif(nxi,j)
178      14      dum2(j)=yf (j)
179      call sliceplt(dum2,dum1,neta,"Potential at RHS")
180      do 15 j=1,neta
181      dum1(j)=phif(1,j)
182      15      dum2(j)=yf (j)
183      call sliceplt(dum2,dum1,neta,"Potential at LHS")
184      do 16 i=1,nxi
185      dum1(i)=phif(i,1)
186      16      dum2(i)=xf (i)
187      call sliceplt(dum2,dum1,nxi,"Potential at BOTTOM")
188      do 17 i=1,nxi
189      dum1(i)=phif(i,neta)
190      17      dum2(i)=xf (i)
191      call sliceplt(dum2,dum1,nxi,"Potential at TOP")
192      c

```

193
194

return
end

```

1      subroutine fcadil
2
3      c
4      include 'global.h'
5      logical auto
6      data auto/.true./
7
8      c
9      call setmsk1
10
11     c
12     1004 rdelyx=dely/delx
13     rdlyx2=rdelyx**2
14     do 10 i=2,nxi
15     ryxp(i)=rdlyx2*(1.+0.5*delx/x(i))
16     ryxm(i)=rdlyx2*(1.-0.5*delx/x(i))
17     c
18     c.... Find fine-grid constants.
19     c
20     do 451 i=1,nxi
21     mj1f(i)=1
22     do 452 i=1,nxi
23     do 442 j=2,neta
24     if(maskf(i,j) .ne. 1)goto 443
25     442 continue
26     443 mj1f(i)=j-1
27     452 continue
28     do 453 i=1,nxi
29     mj1fp1(i)=mj1f(i)+1
30     453 mj1fp2(i)=mj1f(i)+2
31     nj10=1
32     do 454 i=1,nxi
33     if(mj1f(i).gt.nj10)nj10=mj1f(i)
34     nj10p1=nj10+1
35     nj10p2=nj10+2
36     c
37     do 346 j=1,neta
38     do 344 i=1,nxi
39     if(maskf(i,j) .ne. 1)goto 345
40     344 continue
41     345 mi2f(j)=i-1
42     mi2fp1(j)=mi2f(j)+1
43     mi2fp2(j)=mi2f(j)+2
44     346 continue
45     ni20=mi2f(1)
46     c
47     rdelyx=delyf/delxf
48     rdlyx2=rdelyx**2
49     do 12 i=2,nxi
50     ryxfp(i)=rdlyx2*(1.+0.5*delxf/xf(i))
51     12 ryxfm(i)=rdlyx2*(1.-0.5*delxf/xf(i))
52     c
53     c.... Find ffine-grid constants.
54     c
55     do 471 i=1,nxi
56     mj1ff(i)=1
57     do 472 i=1,nxi
58     do 482 j=2,neta
59     if(maskff(i,j) .ne. 1)goto 483
60     482 continue
61     483 mj1ff(i)=j-1
62     472 continue
63     do 473 i=1,nxi
64     mj1ffp1(i)=mj1ff(i)+1
65     473 mj1ffp2(i)=mj1ff(i)+2
66     c
67     do 366 j=1,neta

```

```

65      do 368 i=1,nxi
66      if(maskff(i,j) .ne. 1)goto 367
67      368 continue
68      367 mi2ff(j)=i-1
69      mi2ffp1(j)=mi2ff(j)+1
70      mi2ffp2(j)=mi2ff(j)+2
71      366 continue
72      c
73      rdelyx=delyff/delxff
74      rdlyx2=rdelyx**2
75      do 13 i=2,nxi
76      ryxffp(i)=rdlyx2*(1.+0.5*delxff/xff(i))
77      13 ryxffm(i)=rdlyx2*(1.-0.5*delxff/xff(i))
78      c
79      c.... Start ADI.
80      c
81      it1=0
82      call cadi10
83      if(.not. resume)then
84      call conplot(it1,phi,1,nxi,1,neta,1,
85      .      "Phi",.not.auto)
86      call fcbndl(0)
87      call fadi10
88      call conplot(it1,phif,1,nxi,1,neta,2,
89      .      "Phif",.not.auto)
90      c call conplot(it1,eec,1,nxim1,1,netam1,2,
91      c .      "Electric field", auto)
92      endif
93      c
94      do 100 it1=1,itmax
95      c
96      call ffbndl(it1)
97      call ffadil(it1)
98      if(mod(it1,2) .eq. 0 .or. it1 .eq. itmax)then
99      call conplot(it1,phiff,1,nxi,1,neta,3,
100     .      "Phiff",.not.auto)
101      call conplot(it1,eec,1,nxim1,1,netam1,3,
102     .      "Electric field", auto)
103      endif
104      c.... Feed back ffine-grid solution to fine-grid.
105      do 111 j=nyff1+1,nyff2-1
106      do 111 i=nxff1+1,nxff2-1
107      phif(i,j)=phiff(1+(i-nxff1)*mxff,1+(j-nyff1)*myff)
108      111 continue
109      call fadi1(it1)
110      if(mod(it1,2) .eq. 0 .or. it1 .eq. itmax)then
111      call conplot(it1,phif,1,nxi,1,neta,2,
112     .      "Phif",.not.auto)
113      call conplot(it1,eec,1,nxim1,1,netam1,2,
114     .      "Electric field", auto)
115      endif
116      c.... Feed back fine-grid solution to coarse-grid.
117      do 110 j=nyfc1+1,nyfc2-1
118      do 110 i=nxfc1,nxfc2-1
119      phi(i,j)=phif(1+(i-nxfc1)*mxfc,1+(j-nyfc1)*myfc)
120      110 continue
121      call cadi1(it1)
122      if(mod(it1,2) .eq. 0 .or. it1 .eq. itmax)then
123      call conplot(it1,phi,1,nxi,1,neta,1,
124     .      "Phi",.not.auto)
125      call conplot(it1,eec,1,nxim1,1,netam1,1,
126     .      "Electric field", auto)
127      endif
128      call fcbndl(it1)

```

```
129      call fadi1(it1)
130      c
131      100 continue
132      c
133      call conplot(it1,phif,1,nxi,1,neta,2,
134      .           "Phif",.not.auto)
135      call conplot(it1,eec,1,nximl,1,netaml,2,
136      .           "Electric field",      auto)
137      call ffbndl(it1)
138      call ffadi1(it1)
139      call conplot(it1,phiff,1,nxi,1,neta,3,
140      .           "Phiff",.not.auto)
141      call conplot(it1,eec,1,nximl,1,netaml,3,
142      .           "Electric field",      auto)
143      c
144      return
145      end
```

```

1      subroutine fcadi2
2
3      c
4      include 'global.h'
5      logical auto
6      data auto/.true./
7
8      c
9      call setmsk2
10
11     1004 rdelyx=dely/delx
12         rdlyx2=rdelyx**2
13         do 10 i=2,nxi
14             ryxp(i)=rdlyx2*(1.+0.5*delx/x(i))
15             ryxm(i)=rdlyx2*(1.-0.5*delx/x(i))
16         c
17         c.... Find fine-grid constants.
18         c
19         do 44 i=1,nxi
20             if(maskf(i,1).eq. 1)goto 441
21         440 continue
22         441 nif1=i
23             do 444 i=nif1,nxi
24                 if(maskf(i,1).ne. 1)goto 445
25             444 continue
26             445 nif2=i-1
27         c
28         do 451 i=1,nxi
29             njj1(i)=1
30             dc 452 i=nif1,nif2
31             do 442 j=2,neta
32                 if(maskf(i,j).ne. 1)goto 443
33             442 continue
34             443 njj1(i)=j-1
35             452 continue
36             do 453 i=1,nxi
37                 njj1p1(i)=njj1(i)+1
38                 453 njj1p2(i)=njj1(i)+2
39                 nj1f=1
40                 do 454 i=nif1,nif2
41                     if(njj1(i).gt.nj1f)nj1f=njj1(i)
42                     nj1fp1=nj1f+1
43                     nj1fp2=nj1f+2
44                     nif1m1=nif1-1
45                     nif1m2=nif1-2
46                     nif2p1=nif2+1
47                     nif2p2=nif2+2
48                     do 460 j=1,nj1f
49                         do 460 i=nif1,nif2
50                             if(maskf(i-1,j).eq.0 .and. maskf(i,j).eq.1)nii1(j)=i
51                             460 if(maskf(i,j).eq.1 .and. maskf(i+1,j).eq.0)nii2(j)=i
52                             do 461 j=1,nj1f
53                                 nii1m1(j)=nii1(j)-1
54                                 nii1m2(j)=nii1(j)-2
55                                 nii2p1(j)=nii2(j)+1
56                                 461 nii2p2(j)=nii2(j)+2
57                             c
58                             rdelyx=delyf/delxf
59                             rdlyx2=rdelyx**2
60                             do 12 i=2,nxi
61                                 ryxfp(i)=rdlyx2*(1.+0.5*delxf/xf(i))
62                                 ryxfm(i)=rdlyx2*(1.-0.5*delxf/xf(i))
63                             c
64                             c.... Find ffine-grid constants.
65                             c
66                             do 340 i=1,nxi

```

```

65      if(maskff(i,1) .eq. 1)goto 341
66      340 continue
67      341 niff1=i
68          do 344 i=niff1,nxi
69              if(maskff(i,1) .ne. 1)goto 345
70      344 continue
71      345 niff2=i-1
72      c
73          do 351 i=1,nxi
74      351      njjlf(i)=1
75              do 352 i=niff1,niff2
76                  do 342 j=2,neta
77                      if(maskff(i,j) .ne. 1)goto 343
78      342 continue
79      343 njjlf(i)=j-1
80      352 continue
81          do 353 i=1,nxi
82              njjlfpl(i)=njjlf(i)+1
83      353      njjlfpl(i)=njjlf(i)+2
84              njlff=1
85              do 354 i=niff1,niff2
86      354      if(njjlf(i) .gt. njlff)njlff=njjlf(i)
87                  njlffpl=njlff+1
88                  njlffp2=njlff+2
89                  niff1m1=niff1-1
90                  niff1m2=niff1-2
91                  niff2p1=niff2+1
92                  niff2p2=niff2+2
93                  do 360 j=1,njlff
94                      do 360 i=niff1,niff2
95                          if(maskff(i-1,j) .eq. 0 .and. maskff(i,j) .eq. 1)niif1(j)=i
96      360      if(maskff(i,j) .eq. 1 .and. maskff(i+1,j) .eq. 0)niif2(j)=i
97                          do 361 j=1,njlff
98                              niif1m1(j)=niif1(j)-1
99                              niif1m2(j)=niif1(j)-2
100                             niif2p1(j)=niif2(j)+1
101      361      niif2p2(j)=niif2(j)+2
102      c
103          rdelyx=delyff/delxff
104          rdlyx2=rdelyx**2
105          do 13 i=1,nxi
106              ryxffp(i)=rdlyx2*(1.+0.5*delxff/xff(i))
107      13      ryxffm(i)=rdlyx2*(1.-0.5*delxff/xff(i))
108      c
109      c.... Start ADI.
110      c
111          it1=0
112          call cadi20
113          if(.not. resume)then
114              call conplot(it1,phi,1,nxi,1,neta,1,
115                  "Equipotentials",.not.auto)
116              call fcbnd2(0)
117              call fadi20
118              call conplot(it1,phif,1,nxi,1,neta,2,
119                  "Equipotentials",.not.auto)
120              call conplot(it1,eec,1,nxim1,1,netam1,2,
121                  "Electric field", auto)
122          endif
123      c
124          do 100 it1=1,itmax
125      c
126          call ffbnd2(it1)
127          call ffadi2(it1)
128          if(mod(it1,4) .eq. 0 .or. it1 .eq. itmax)then

```

```

129      call conplot(itl,phiff,1,nxi,1,neta,3,
130      .          "Equipotentials",.not.auto)
131      call conplot(itl,eec,1,nximl,1,netaml,3,
132      .          "Electric field",      auto)
133      endif
134      c.... Feed back ffine-grid solution to fine-grid.
135      do 111 j=nyff1+1,nyff2-1
136      do 111 i=nxff1+1,nxff2-1
137      phif(i,j)=phiff(1+(i-nxff1)*mxff,1+(j-nyff1)*myff)
138      111 continue
139      call fadi2(itl)
140      if(mod(itl,4) .eq. 0 .or. itl .eq. itmax)then
141      call conplot(itl,phif,1,nxi,1,neta,2,
142      .          "Equipotentials",.not.auto)
143      call conplot(itl,eec,1,nximl,1,netaml,2,
144      .          "Electric field",      auto)
145      endif
146      c.... Feed back fine-grid solution to coarse-grid.
147      do 110 j=nyfc1+1,nyfc2-1
148      do 110 i=nxfc1,nxfc2-1
149      phi(i,j)=phif(1+(i-nxfc1)*mxfc,1+(j-nyfc1)*myfc)
150      110 continue
151      call cadi2(itl)
152      if(mod(itl,4) .eq. 0 .or. itl .eq. itmax)then
153      call conplot(itl,phi,1,nxi,1,neta,1,
154      .          "Equipotentials",.not.auto)
155      call conplot(itl,eec,1,nximl,1,netaml,1,
156      .          "Electric field",      auto)
157      endif
158      call fcbnd2(itl)
159      call fadi2(itl)
160      c
161      100 continue
162      c
163      call conplot(itl,phif,1,nxi,1,neta,2,
164      .          "Equipotentials",.not.auto)
165      call conplot(itl,eec,1,nximl,1,netaml,2,
166      .          "Electric field",      auto)
167      call ffbnd2(itl)
168      call ffadi2(itl)
169      call conplot(itl,phiff,1,nxi,1,neta,3,
170      .          "Equipotentials",.not.auto)
171      call conplot(itl,eec,1,nximl,1,netaml,3,
172      .          "Electric field",      auto)
173      c
174      return
175      end

```



```

1      subroutine fcbnd1(itl)
2
3      c
4      c.... Spline fit coarse grid phi solution to fine grid boundary.
5      c
6      include 'global.h'
7      real spl(ldum), sp2(ldum), sp3(ldum), xsp(ldum), phisp(ldum)
8      common /xxbnd/ spl, sp2, sp3, xsp, phisp
9      c
10     c.... Spline fit.
11     c
12     nsp=nxfc2-nxfc1+1
13     do 340 i=nxfc1,nxfc2
14     xsp(i-nxfc1+1)=x(i)
15     340 phisp(i-nxfc1+1)=phi(i,nyfc2)
16     call spline(nsp,xsp,phisp,spl,sp2,sp3)
17     do 345 i=1,nxi
18     345 phif(i,neta)=seval(nsp,xf(i),xsp,phisp,spl,sp2,sp3)
19     nsp=nyfc2-nyfc1+1
20     do 350 i=nyfc1,nyfc2
21     xsp(i-nyfc1+1)=y(i)
22     350 phisp(i-nyfc1+1)=phi(nxfc2,i)
23     call spline(nsp,xsp,phisp,spl,sp2,sp3)
24     do 355 i=1,neta
25     355 phif(nxi,i)=seval(nsp,yf(i),xsp,phisp,spl,sp2,sp3)
26     nsp=nxfc2-nxfc1+1
27     do 360 i=nxfc1,nxfc2
28     xsp(i-nxfc1+1)=x(i)
29     360 phisp(i-nxfc1+1)=phi(i,nyfc1)
30     call spline(nsp,xsp,phisp,spl,sp2,sp3)
31     do 365 i=1,nxi
32     365 if(maskf(i,1).ne.1)
33     .phif(i,1)=seval(nsp,xf(i),xsp,phisp,spl,sp2,sp3)
34     c
35     if(xl(2).gt.0.)then
36     if(itl.eq.0)then
37     nsp=nyfc2-nyfc1+1
38     do 370 i=nyfc1,nyfc2
39     xsp(i-nyfc1+1)=y(i)
40     370 phisp(i-nyfc1+1)=phi(1,i)
41     call spline(nsp,xsp,phisp,spl,sp2,sp3)
42     do 375 i=1,neta
43     375 if(maskf(1,i).ne.1)
44     .phif(1,i)=seval(nsp,yf(i),xsp,phisp,spl,sp2,sp3)
45     c.... Initialize phif.
46     if(.not. resume)then
47     ol=1./float(mxfc*myfc)
48     do 1105 j=nyfc1,nyfc2-1
49     do 1105 i=nxfc1,nxfc2-1
50     do 1105 il=1,mxfc
51     do 1105 jl=1,myfc
52     i2=1+(i-nxfc1)*mxfc+il
53     j2=1+(j-nyfc1)*myfc+jl
54     if(maskf(i2,j2).ne.1)
55     .phif(i2,j2)=(phi(i,j)*(mxfc-il)*(myfc-jl)+phi(i+1,j+1)*il*jl
56     .+phi(i+1,j)*il*(myfc-jl)+phi(i,j+1)*(mxfc-il)*jl)*ol
57     1105 continue
58     endif
59     endif
60     c
61     return
62     c
63     135 if(mod(itl,4).eq.0.or.itl.eq.itmax)then
64     do 14 j=1,neta
65     dum1(j)=phif(nxi,j)
66     dum2(j)=phif(1,j)

```

```
65      14      dum3(j)=yf (j)
66      call slicepl2(dum3,dum1,dum2,neta,"Potential at RHS(solid) LHS")
67      do 16 i=1,nxi
68      dum1(i)=phif(i,neta)
69      dum2(i)=phif(i,1)
70      16      dum3(i)=xf (i)
71      call slicepl2(dum3,dum2,dum1,nxi,"Potential at BOTTOM(solid) TOP")
72      endif
73      c
74      return
75      end
```

```

1      subroutine fcbnd2(it1)
2
3      c
4      c.... Spline fit coarse grid phi solution to fine grid boundary.
5      c
6      include 'global.h'
7      real sp1(ldum),sp2(ldum),sp3(ldum),xsp(ldum),phisp(ldum)
8      common /xxbnd/ sp1,sp2,sp3,xsp,phisp
9      c
10     c      if(xl(2) .gt. 0.)then
11     c      if(it1 .eq. 0)then
12     c      nsp=nyfc2-nyfc1+1
13     c      do 370 i=nyfc1,nyfc2
14     c      xsp(i-nyfc1+1)=y(i)
15     c      370 phisp(i-nyfc1+1)=phi(1,i)
16     c      call spline(nsp,xsp,phisp,sp1,sp2,sp3)
17     c      do 375 i=1,neta
18     c      phif(1,i)=seval(nsp,yf(i),xsp,phisp,sp1,sp2,sp3)
19     c.... Initialize phif.
20     c      if(.not. resume)then
21     c      do 1101 j=2,netam1
22     c      do 1101 i=2,nxim1
23     c      1101 if(maskf(i,j) .ne. 1)
24     c      .phif(i,j)=(phif(i,1)*(neta-j)+phif(i,neta)*(j-1))/float(neta-1)
25     c      do 1103 i=nif1,nif2
26     c      do 1103 j=njj1p1(i),netam1
27     c      1103 phif(i,j)=(phif(i,njj1(i))*(neta-j)+phif(i,neta)*(j-njj1(i)))
28     c      ./float(neta-njj1(i))
29     c      do 1104 i=2,nif1-1
30     c      do 1104 j=2,njlf
31     c      1104 phif(i,j)=phif(1,j)
32     c      ol=1./float(mxfc*myfc)
33     c      do 1105 j=nyfc1,nyfc2-1
34     c      do 1105 i=nxfc1,nxfc2-1
35     c      do 1105 il=1,mxfc
36     c      do 1105 jl=1,myfc
37     c      i2=1+(i-nxfc1)*mxfc+il
38     c      j2=1+(j-nyfc1)*myfc+jl
39     c      if(maskf(i2,j2) .ne. 1)
40     c      .phif(i2,j2)=(phi(i,j)*(mxfc-il)*(myfc-jl)+phi(i+1,j+1)*il*j1
41     c      .+phi(i+1,j)*il*(myfc-jl)+phi(i,j+1)*(mxfc-il)*jl)*ol
42     c      1105 continue
43     c      endif
44     c      endif
45     c
46     c.... Spline fit.
47     c
48     c      nsp=nxfc2-nxfc1+1
49     c      do 340 i=nxfc1,nxfc2
50     c      xsp(i-nxfc1+1)=x(i)
51     c      340 phisp(i-nxfc1+1)=phi(i,nyfc2)
52     c      call spline(nsp,xsp,phisp,sp1,sp2,sp3)
53     c      do 345 i=1,nxi
54     c      345 phif(i,neta)=seval(nsp,xf(i),xsp,phisp,sp1,sp2,sp3)
55     c      nsp=nyfc2-nyfc1+1
56     c      do 350 i=nyfc1,nyfc2
57     c      xsp(i-nyfc1+1)=y(i)
58     c      350 phisp(i-nyfc1+1)=phi(nxfc2,i)
59     c      call spline(nsp,xsp,phisp,sp1,sp2,sp3)
60     c      do 355 i=1,neta
61     c      355 phif(nxi,i)=seval(nsp,yf(i),xsp,phisp,sp1,sp2,sp3)
62     c      nsp=nxfc2-nxfc1+1
63     c      do 360 i=nxfc1,nxfc2
64     c      xsp(i-nxfc1+1)=x(i)
65     c      360 phisp(i-nxfc1+1)=phi(i,nyfc1)

```

```
65      call spline(nsp,xsp,phisp,spl,sp2,sp3)
66      do 365 i=1,nxi
67      365      if(maskf(i,1) .ne. 1)
68      .phif(i,1)=seval(nsp,xf(i),xsp,phisp,spl,sp2,sp3)
69      c
70      return
71      c
72      20      if(mod(iti,4) .eq. 0 .or. itl .eq. itmax)then
73      do 14 j=1,neta
74      dum1(j)=phif(nxi,j)
75      dum2(j)=phif(1,j)
76      14      dum3(j)=yf (j)
77      call slicepl2(dum3,dum1,dum2,neta,"Potential at RHS(solid) LHS")
78      do 16 i=1,nxi
79      dum1(i)=phif(i,neta)
80      dum2(i)=phif(i,1)
81      16      dum3(i)=xf (i)
82      call slicepl2(dum3,dum2,dum1,nxi,"Potential at BOTTOM(solid) TOP")
83      endif
84      c
85      return
86      end
```

```

1      subroutine ffadil(itl)
2
3      c
4      c.... Dirichlet at i=1 & nxi.
5      c.... Dirichlet condition at j=1 & neta.
6      c.... Use for ffine-grid,
7      c
8      include 'global.h'
9      c
10     rdelyx=delyff/delxff
11     rdlyx2=rdelyx**2
12     aal=2.*rdlyx2
13     aa2=-2.*(rdlyx2+1.)
14     aa3=4.*rdlyx2
15     aa4=-2.*(2.*rdlyx2+1.)
16
17     c
18     do 9000 it=1,itmx
19     c
20     errmx=0.
21     sumerr=0.
22     c
23     c.... Y-sweep for i = 1.
24     c
25     do 100 j=mj1ffp1(1),netam1
26     erry(j)=aa3*phiff(2,j)+phiff(1,j+1)+phiff(1,j-1)+aa4*phiff(1,j)
27     erra=abs(erry(j))
28     if(erra .gt. errmx)then
29         errmx=errra
30         iermx=1
31         jermx=j
32     endif
33     sumerr=sumerr+errra
34     bet(mj1ffp1(1))=aa4
35     dp(mj1ffp1(1))=-erry(mj1ffp1(1))/aa4
36     do 101 j=mj1ffp2(1),netam1
37     gam(j)=1./bet(j-1)
38     bet(j)=aa4-gam(j)
39     101 dp(j)=(-erry(j)-dp(j-1))/bet(j)
40     do 102 j=netam2,mj1ffp1(1),-1
41     102 dp(j)=dp(j)-gam(j+1)*dp(j+1)
42     do 103 j=mj1ffp1(1),netam1
43     phiff(1,j)=phiff(1,j)+dp(j)
44     c
45     c.... Y-sweep for 1 < i < nxi.
46     c
47     bet(2)=aa2
48     do 109 j=3,netam1
49     gam(j)=1./bet(j-1)
50     109 bet(j)=aa2-gam(j)
51     do 115 i=2,nxim1
52     do 116 j=mj1ffp1(i),netam1
53     erry(j)=ryxfrm(i)*phiff(i-1,j)+ryxffp(i)*phiff(i+1,j)
54     +phiff(i,j+1)+phiff(i,j-1)+aa2*phiff(i,j)
55     erra=abs(erry(j))
56     if(erra .gt. errmx)then
57         errmx=errra
58         iermx=i
59         jermx=j
60     endif
61     sumerr=sumerr+errra
62     116 dp(mj1ffp1(i))=-erry(mj1ffp1(i))/aa2
63     do 117 j=mj1ffp2(i),netam1
64     117 dp(j)=(-erry(j)-dp(j-1))/bet(j-mj1ff(i)+1)
65     do 118 j=netam2,mj1ffp1(i),-1
66     118 dp(j)=dp(j)-gam(j-mj1ff(i)+2)*dp(j+1)

```

```

65      do 119 j=mj1ffp1(i),netaml
66      119  phiff(i,j)=phiff(i,j)+dp(j)
67      115  continue
68      goto 134
69      c
70      c.... Y-sweep for i = nxi,
71      c
72      135  do 130 j=2,netaml
73      erry(j)=aa1*phiff(nxim1,j)+phiff(nxi,j+1)+phiff(nxi,j-1)
74      .+aa2*phiff(nxi,j)
75      erra=abs(erry(j))
76      if(erra .gt. errmx)then
77          errmx=erra
78          iermx=i
79          jermx=j
80      endif
81      130  sumerr=sumerr+erra
82      dp(2)=-erry(2)/aa2
83      do 131 j=3,netaml
84      131  dp(j)=(-erry(j)-dp(j-1))/bet(j)
85      do 132 j=netam2,2,-1
86      132  dp(j)=dp(j)-gam(j+1)*dp(j+1)
87      do 133 j=2,netaml
88      133  phiff(nxi,j)=phiff(nxi,j)+dp(j)
89      c
90      c.... X-sweep for nj1 < j < neta.
91      c
92      134  bet(1)=aa4
93      gam(2)=aa3/bet(1)
94      bet(2)=aa2-ryxffm(2)*gam(2)
95      do 199 i=3,nxim1
96      gam(i)=ryxffp(i)/bet(i-1)
97      199  bet(i)=aa2-gam(i)*ryxffm(i)
98      gam(nxi)=ryxffp(nxi)/bet(nxim1)
99      bet(nxi)=aa2-aa1*gam(nxi)
100     do 201 j=netaml,mj1ffp1(1),-1
101     errx(1)=aa3*phiff(2,j)+phiff(1,j+1)+phiff(1,j-1)+aa4*phiff(1,j)
102     sumerr=sumerr+abs(errx(1))
103     do 202 i=2,nxim1
104     errx(i)=ryxffm(i)*phiff(i-1,j)+ryxffp(i)*phiff(i+1,j)
105     .+phiff(i,j+1)+phiff(i,j-1)+aa2*phiff(i,j)
106     202  sumerr=sumerr+abs(errx(i))
107     errx(nxi)=aa1*phiff(nxim1,j)+phiff(nxi,j+1)+phiff(nxi,j-1)+aa2*
108     .phiff(nxi,j)
109     sumerr=sumerr+abs(errx(nxi))
110     c
111     dp(1)=-errx(1)/aa2
112     dp(1)=-errx(1)/aa4
113     do 203 i=2,nxim1
114     203  dp(i)=(-errx(i)-ryxffm(i)*dp(i-1))/bet(i)
115     dp(nxi)=(-errx(nxi)-aa1*dp(nxim1))/bet(nxi)
116     do 204 i=nxim2,1,-1
117     204  dp(i)=dp(i)-gam(i+1)*dp(i+1)
118     do 205 i=1,nxim1
119     205  phiff(i,j)=phiff(i,j)+dp(i)
120     201  continue
121     c
122     do 221 j=mj1ff(1),2,-1
123     do 222 i=mj2ffp1(j),nxim1
124     errx(i)=ryxffm(i)*phiff(i-1,j)+ryxffp(i)*phiff(i+1,j)
125     .+phiff(i,j+1)+phiff(i,j-1)+aa2*phiff(i,j)
126     222  sumerr=sumerr+abs(errx(i))
127     errx(nxi)=aa1*phiff(nxim1,j)+phiff(nxi,j+1)+phiff(nxi,j-1)+aa2*
128     .phiff(nxi,j)
129     sumerr=sumerr+abs(errx(nxi))

```

```

129      bet(mi2ffp1(j))=aa2
130      do 219 i=mi2ffp2(j),nxim1
131      gam(i)=ryxffp(i)/bet(i-1)
132      219 bet(i)=aa2-gam(i)*ryxffm(i)
133      gam(nxi)=ryxffp(nxi)/bet(nxim1)
134      bet(nxi)=aa2-aa1*gam(nxi)
135      dp(mi2ffp1(j))=-errx(mi2ffp1(j))/aa2
136      do 223 i=mi2ffp2(j),nxi
137      223 dp(i)=(-errx(i)-ryxffm(i)*dp(i-1))/bet(i)
138      do 224 i=nxim2,mi2ffp1(j),-1
139      224 dp(i)=dp(i)-gam(i+1)*dp(i+1)
140      do 225 i=mi2ffp1(j),nxim1
141      225 phiff(i,j)=phiff(i,j)+dp(i)
142      221 continue
143      c
144      if (it.eq.itmx .or. it .eq. 1) then
145      write(6,901)it1,it,sumerr,errmx,iermx,jermx
146      write(23,901)it1,it,sumerr,errmx,iermx,jermx
147      endif
148      901 format('ff it sumerr errmx ',2i6,1pelli.3,e11.3,2i4)
149      c
150      9000 continue
151      c
152      c.... Calculate electric field.
153      c
154      emx=0.
155      do 10 i=1,nxim1
156      do 10 j=1,netam1
157      by=.5*(phiff(i,j)+phiff(i+1,j)-phiff(i,j+1)-phiff(i+1,j+1))/delyff
158      bx=.5*(phiff(i,j+1)+phiff(i,j)-phiff(i+1,j+1)-phiff(i+1,j))/delx
159      exff(i,j)=bx
160      eyff(i,j)=by
161      eec(i,j)=sqrt(bx**2+by**2)
162      if(eec(i,j) .gt. emx)then
163      emx=eec(i,j)
164      iemx=i
165      jemx=j
166      endif
167      10 continue
168      write (6,200)iemx,jemx,emx,xff(iemx),yff(jemx)
169      write (23,200)iemx,jemx,emx,xff(iemx),yff(jemx)
170      200 format("max Electric field ",2i4,1pelli.3,2elli.3)
171      c
172      return
173      end

```

```

1      subroutine ffadi2(it1)
2
3      c
4      c.... Dirichlet at i=1 & nxi.
5      c.... Dirichlet condition at j=1 & neta.
6      c.... Use for ffine-grid,
7      c
8      include 'global.h'
9      c
10     write(6,449)niff1,niff2,nj1ff
11     write(23,449)niff1,niff2,nj1ff
12 449   format('niff1,niff2 nj1ff ',3i4)
13     c
14     n111=2
15     rdelyx=delyff/delx2
16     rdlyx2=rdelyx**2
17     aa1=2.*rdlyx2
18     aa2=-2.*(rdlyx2+1.)
19     aa3=4.*rdlyx2
20     aa4=-2.*(2.*rdlyx2+1.)
21
22     c
23     do 9000 it=1,itmx
24     c
25     errmx=0.
26     sumerr=0.
27     c
28     c.... Y-sweep for 1 < i < n11.
29     c
30 9001  bet(2)=aa2
31     do 109 j=3,netam1
32     gam(j)=1./bet(j-1)
33 109   bet(j)=aa2-gam(j)
34     do 115 i=2,nxim1
35     do 116 j=nj1fpl(i),netam1
36     erry(j)=ryxfrm(i)*phiff(i-1,j)+ryxfrm(i)*phiff(i+1,j)
37     +phiff(i,j+1)+phiff(i,j-1)+aa2*phiff(i,j)
38     erra=abs(erry(j))
39     if(erra .gt. errmx)then
40     errmx=erra
41     iermx=i
42     jermx=j
43     endif
44 116   sumerr=sumerr+erra
45     dp(nj1fpl(i))=-erry(nj1fpl(i))/aa2
46     do 117 j=nj1fpl2(i),netam1
47 117   dp(j)=(-erry(j)-dp(j-1))/bet(j-nj1f(i)+1)
48     do 118 j=netam2,nj1fpl(i),-1
49 118   dp(j)=dp(j)-gam(j-nj1f(i)+2)*dp(j+1)
50     do 119 j=nj1fpl(i),netam1
51 119   phiff(i,j)=phiff(i,j)+dp(j)
52 115   continue
53     c
54 9003  continue
55     c
56     c.... X-sweep for nj1ff < j < neta for n111 = 2.
57     c
58     bet(2)=aa2
59     do 1199 i=3,nxim1
60     gam(i)=ryxfrm(i-1)/bet(i-1)
61 1199  bet(i)=aa2-gam(i)*ryxfrm(i)
62     gam(nxi)=ryxfrm(nxim1)/bet(nxim1)
63     bet(nxi)=aa2-aa1*gam(nxi)
64     do 1201 j=netam1,nj1fpl,-1
65     do 1202 i=2,nxim1
66     errx(i)=ryxfrm(i)*phiff(i-1,j)+ryxfrm(i)*phiff(i+1,j)

```



```

65      +phiff(i,j+1)+phiff(i,j-1)+aa2*phiff(i,j)
66 1202 sumerr=sumerr+abs(errx(i))
67      dp(2)=-errx(2)/aa2
68      do 1203 i=3,nxim1
69 1203 dp(i)=(-errx(i)-ryxffm(i)*dp(i-1))/bet(i)
70      do 1204 i=nxim2,2,-1
71 1204 dp(i)=dp(i)-gam(i+1)*dp(i+1)
72      do 1205 i=2,nxim1
73 1205 phiff(i,j)=phiff(i,j)+dp(i)
74 1201 continue
75      c
76      c.... X-sweep for njlff >= j > 1 for i between 2 & nilm1 ...
77      c
78      do 1211 j=njlff,2,-1
79      do 1212 i=2,niiflml(j)
80      errx(i)=ryxffm(i)*phiff(i-1,j)+ryxffp(i)*phiff(i+1,j)
81      +phiff(i,j+1)+phiff(i,j-1)+aa2*phiff(i,j)
82 1212 sumerr=sumerr+abs(errx(i))
83      dp(2)=-errx(2)/aa2
84      do 1213 i=3,niiflml(j)
85 1213 dp(i)=(-errx(i)-ryxffm(i)*dp(i-1))/bet(i)
86      do 1214 i=niiflml2(j),2,-1
87 1214 dp(i)=dp(i)-gam(i+1)*dp(i+1)
88      do 1215 i=2,niiflml(j)
89 1215 phiff(i,j)=phiff(i,j)+dp(i)
90 1211 continue
91      c
92      c.... ... and for i between ni2p1 & nxi.
93      c
94      do 1221 j=njlff,2,-1
95      bet(niif2p1(j))=aa2
96      do 1219 i=niif2p2(j),nxim1
97      gam(i)=ryxffp(i-1)/bet(i-1)
98 1219 bet(i)=aa2-gam(i)*ryxffm(i)
99      gam(nxi)=ryxffp(nxi)/bet(nxim1)
100      bet(nxi)=aa2-aal*gam(nxi)
101      do 1222 i=niif2p1(j),nxim1
102      errx(i)=ryxffm(i)*phiff(i-1,j)+ryxffp(i)*phiff(i+1,j)
103      +phiff(i,j+1)+phiff(i,j-1)+aa2*phiff(i,j)
104 1222 sumerr=sumerr+abs(errx(i))
105      dp(niif2p1(j))=-errx(niif2p1(j))/aa2
106      do 1223 i=niif2p2(j),nxim1
107 1223 dp(i)=(-errx(i)-ryxffm(i)*dp(i-1))/bet(i)
108      do 1224 i=nxim2,niif2p1(j),-1
109 1224 dp(i)=dp(i)-gam(i+1)*dp(i+1)
110      do 1225 i=niif2p1(j),nxim1
111 1225 phiff(i,j)=phiff(i,j)+dp(i)
112 1221 continue
113      c
114 9005 if (it .eq. 1 .or. it.eq.itmx) then
115      write(6,901)it1,it,sumerr,errmx,iermx,iermx
116      write(23,901)it1,it,sumerr,errmx,iermx,iermx
117      endif
118 901 format(' it sumerr errmx ',2i6,1pe11.3,e11.3,2i4)
119      c
120 9000 continue
121      c
122      c.... Calculate electric field.
123      c
124      emx=0.
125      do 10 i=1,nxim1
126      do 10 j=1,netaml
127      ay=.5*(phiff(i,j)+phiff(i+1,j)-phiff(i,j+1)-phiff(i+1,j+1))/delyff
128      ax=.5*(phiff(i,j+1)+phiff(i,j)-phiff(i+1,j+1)-phiff(i+1,j))/delxff

```

```
129      exff(i,j)=ax
130      eyff(i,j)=ay
131      eec(i,j)=sqrt(ax**2+ay**2)
132      if(eec(i,j) .gt. emx)then
133          emx=eec(i,j)
134          iemx=i
135          jemx=j
136      endif
137      10  continue
138          write (6,200)iemx,jemx,emx,xff(iemx),yff(jemx)
139          write (23,200)iemx,jemx,emx,xff(iemx),yff(jemx)
140      200 format("max Electric field ",2i4,1pelli.3,2elli.3)
141      return
142      c
143      c.... Plots.
144      c
145      18  do 14 j=1,neta
146          dum1(j)=phiff(nxi,j)
147      14  dum2(j)=yff(j)
148          call sliceplt(dum2,dum1,neta,"Potential at RHS")
149          do 15 j=1,neta
150              dum1(j)=phiff(1,j)
151      15  dum2(j)=yff(j)
152          call sliceplt(dum2,dum1,neta,"Potential at LHS")
153          do 16 i=1,nxi
154              dum1(i)=phiff(i,1)
155      16  dum2(i)=xff(i)
156          call sliceplt(dum2,dum1,nxi,"Potential at BOTTOM")
157          do 17 i=1,nxi
158              dum1(i)=phiff(i,neta)
159      17  dum2(i)=xff(i)
160          call sliceplt(dum2,dum1,nxi,"Potential at TOP")
161      c
162      return
163      end
```

```

1      subroutine ffbnd1(itl)
2      c
3      c.... Spline fit fine grid phif solution to ffine grid boundary.
4      c
5      include 'global.h'
6      real spl(1dum),sp2(1dum),sp3(1dum),xsp(1dum),phisp(1dum)
7      common /xxbnd/ spl,sp2,sp3,xsp,phisp
8      c
9      if(resume .and. itl.eq.1)return
10     c
11     c.... Spline fit.
12     c
13     nsp=nxeff2-nxeff1+1
14     do 340 i=nxeff1,nxeff2
15     xsp(i-nxeff1+1)=xf(i)
16     340 phisp(i-nxeff1+1)=phif(i,nyff2)
17     call spline(nsp,xsp,phisp,spl,sp2,sp3)
18     do 345 i=1,nxi
19     345 phiff(i,neta)=seval(nsp,xf(i),xsp,phisp,spl,sp2,sp3)
20     nsp=nyff2-nyff1+1
21     do 350 i=nyff1,nyff2
22     xsp(i-nyff1+1)=yf(i)
23     350 phisp(i-nyff1+1)=phif(nxeff2,i)
24     call spline(nsp,xsp,phisp,spl,sp2,sp3)
25     do 355 i=1,neta
26     355 phiff(nxi,i)=seval(nsp,yf(i),xsp,phisp,spl,sp2,sp3)
27     nsp=nxeff2-nxeff1+1
28     do 360 i=nxeff1,nxeff2
29     xsp(i-nxeff1+1)=xf(i)
30     360 phisp(i-nxeff1+1)=phif(i,nyff1)
31     call spline(nsp,xsp,phisp,spl,sp2,sp3)
32     do 365 i=1,nxi
33     365 if(maskff(i,1) .ne. 1)
34     .phiff(i,1)=seval(nsp,xf(i),xsp,phisp,spl,sp2,sp3)
35     if(itl.eq.1)then
36     nsp=nyff2-nyff1+1
37     do 370 i=nyff1,nyff2
38     xsp(i-nyff1+1)=yf(i)
39     370 phisp(i-nyff1+1)=phif(nxeff1,i)
40     call spline(nsp,xsp,phisp,spl,sp2,sp3)
41     do 375 i=1,neta
42     375 if(maskff(1,i) .ne. 1)
43     .phiff(1,i)=seval(nsp,yf(i),xsp,phisp,spl,sp2,sp3)
44     c.... Initialize phiff.
45     if(.not. resume )then
46     o1=1./float(mxeff*myff)
47     do 1105 j=nyff1,nyff2-1
48     do 1105 i=nxeff1,nxeff2-1
49     do 1105 il=1,mxeff
50     do 1105 jl=1,myff
51     i2=1+(i-nxeff1)*mxeff+il
52     j2=1+(j-nyff1)*myff+jl
53     if(maskff(i2,j2) .ne. 1)
54     .phiff(i2,j2)=(phif(i,j)*(mxeff-il)*(myff-jl)+phif(i+1,j+1)*il*jl
55     .+phif(i+1,j)*il*(myff-jl)+phif(i,j+1)*(mxeff-il)*jl)*o1
56     1105 continue
57     endif
58     endif
59     c
60     if(mod(itl,4) .eq. 0 .or. itl .eq. itmax)then
61     do 14 j=1,neta
62     dum1(j)=phiff(nxi,j)
63     dum2(j)=phiff(1,j)
64     14 dum3(j)=yff(j)

```

```
65      call slicepl2(dum3,dum1,dum2,neta,"phiff at RHS(solid) LHS")
66      do 16 i=1,nxi
67          dum1(i)=phiff(i,neta)
68          dum2(i)=phiff(i,1)
69      16  dum3(i)=xff(i)
70          call slicepl2(dum3,dum2,dum1,nxi,"phiff at BOTTOM(solid) TOP")
71      endif
72      c
73      return
74      end
```

```

1      subroutine ffbnd2(it1)
2      c
3      c.... Spline fit fine grid phif solution to ffine grid boundary.
4      c
5          include 'global.h'
6          real spl(ldum),sp2(ldum),sp3(ldum),xsp(ldum),phisp(ldum)
7          common /xxbnd/ spl,sp2,sp3,xsp,phisp
8      c
9          if(resume .and. it1.eq.1)return
10     c
11     c.... Initialize phiff.
12     c
13         if(.not. resume .and. it1 .eq. 1)then
14             do 1101 j=2,netaml
15             do 1101 i=2,nximl
16     1101     if(maskff(i,j) .ne. 1)
17             .phiff(i,j)=(phiff(i,1)*(neta-j)+phiff(i,neta)*(j-1))/float(neta-1)
18             do 1103 i=niff1,niff2
19             do 1103 j=njjlfp1(i),netaml
20     1103     phiff(i,j)=(phiff(i,njjlf(i))*(neta-j)+phiff(i,neta)*(j-njjlf(i)))/
21             .float(neta-njjlf(i))
22             do 1104 i=2,niff1-1
23             do 1104 j=2,njlff
24     1104     phiff(i,j)=phiff(1,j)
25             ol=1./float(mxff*myff)
26             do 1105 j=nyff1,nyff2-1
27             do 1105 i=nxff1,nxff2-1
28             do 1105 il=1,mxff
29             do 1105 jl=1,myff
30             i2=1+(i-nxff1)*mxff+il
31             j2=1+(j-nyff1)*myff+jl
32             if(maskff(i2,j2) .ne. 1)
33             .phiff(i2,j2)=(phif(i,j)*(mxff-il)*(myff-jl)+phif(i+1,j+1)*il*jl
34             .+phif(i+1,j)*il*(myff-jl)+phif(i,j+1)*(mxff-il)*jl)*ol
35     1105     continue
36     c
37     c
38     c
39     c
40     c1105 continue
41     endif
42     c
43     c.... Spline fit.
44     c
45         nsp=nxff2-nxff1+1
46         do 340 i=nxff1,nxff2
47             xsp(i-nxff1+1)=xf(i)
48     340     phisp(i-nxff1+1)=phif(i,nyff2)
49             call spline(nsp,xsp,phisp,spl,sp2,sp3)
50             do 345 i=1,nxi
51     345     phiff(i,neta)=seval(nsp,xff(i),xsp,phisp,spl,sp2,sp3)
52             nsp=nyff2-nyff1+1
53             do 350 i=nyff1,nyff2
54             xsp(i-nyff1+1)=yf(i)
55     350     phisp(i-nyff1+1)=phif(nxff2,i)
56             call spline(nsp,xsp,phisp,spl,sp2,sp3)
57             do 355 i=1,neta
58     355     phiff(nxi,i)=seval(nsp,yf(i),xsp,phisp,spl,sp2,sp3)
59             nsp=nxff2-nxff1+1
60             do 360 i=nxff1,nxff2
61             xsp(i-nxff1+1)=xf(i)
62     360     phisp(i-nxff1+1)=phif(i,nyff1)
63             call spline(nsp,xsp,phisp,spl,sp2,sp3)
64             do 365 i=1,nxi
65     365     if(maskff(i,1) .ne. 1)

```

```
65      .phiff(i,1)=seval(nsp,xff(i),xsp,phisp,sp1,sp2,sp3)
66      nsp=nyff2-nyff1+1
67      do 370 i=nyff1,nyff2
68      xsp(i-nyff1+1)=yf(i)
69      370 phisp(i-nyff1+1)=phif(nxff1,i)
70      call spline(nsp,xsp,phisp,sp1,sp2,sp3)
71      do 375 i=1,neta
72      375 phiff(1,i)=seval(nsp,yff(i),xsp,phisp,sp1,sp2,sp3)
73      c
74      if(mod(it1,4) .eq. 0 .or. it1 .eq. itmax)then
75      do 14 j=1,neta
76      dum1(j)=phiff(nx1,j)
77      dum2(j)=phiff(1,j)
78      14 dum3(j)=yff(j)
79      call slicepl2(dum3,dum1,dum2,neta,"phiff at RHS(solid) LHS")
80      do 16 i=1,nxi
81      dum1(i)=phiff(i,neta)
82      dum2(i)=phiff(i,1)
83      16 dum3(i)=xff(i)
84      call slicepl2(dum3,dum2,dum1,nxi,"phiff at BOTTOM(solid) TOP")
85      endif
86      c
87      return
88      end
```

```

1      subroutine genmsh
2      c
3      c.... GENMSH: Mesh generator.
4      c
5          include 'global.h'
6      c
7      c.... Generate coarse mesh.
8      c
9          np=nxi*neta
10         npp=(nxi+1)*(neta+1)
11         delx=(xh(1)-xl(1))/float(nxi-1)
12         dely=(yh(1)-yl(1))/float(neta-1)
13         write (6,800) delx,dely
14         write (23,800) delx,dely
15     800   format("delx=",1pe10.3," dely=",e10.3)
16         do 10 i=1,nxi
17     10    x(i)=(i-1)*delx+xl(1)
18         do 11 j=1,neta
19     11    y(j)=(j-1)*dely+yl(1)
20         c
21         c.... Generate fine mesh.
22         c
23         delxf=(xh(2)-xl(2))/float(nxi-1)
24         delyf=(yh(2)-yl(2))/float(neta-1)
25         write (6,801) delxf,delyf
26         write (23,801) delxf,delyf
27     801   format("delxf=",1pe10.3," delyf=",e10.3)
28         do 20 i=1,nxi
29     20    xf(i)=(i-1)*delxf+xl(2)
30         do 21 j=1,neta
31     21    yf(j)=(j-1)*delyf+yl(2)
32         c
33         c.... Generate ffine mesh.
34         c
35         delxff=(xh(3)-xl(3))/float(nxi-1)
36         delyff=(yh(3)-yl(3))/float(neta-1)
37         write (6,802) delxff,delyff
38         write (23,802) delxff,delyff
39     802   format("delxff=",1pe10.3," delyff=",e10.3)
40         do 22 i=1,nxi
41     22    xff(i)=(i-1)*delxff+xl(3)
42         do 23 j=1,neta
43     23    yff(j)=(j-1)*delyff+yl(3)
44         c
45         c.... Find coarse-fine grids boundary.
46         c
47         do 30 j=1,neta
48             a1=abs(yl(2)-y(j))
49             a2=abs(yh(2)-y(j))
50             if(a1 .le. ck)nyfc1=j
51             if(a2 .le. ck)nyfc2=j
52     30    continue
53         do 32 i=1,nxi
54             a1=abs(xl(2)-x(i))
55             a2=abs(xh(2)-x(i))
56             if(a1 .le. ck)nxfc1=i
57             if(a2 .le. ck)nxfc2=i
58     32    continue
59         c
60         c.... Find ffine-fine grids boundary.
61         c
62         do 34 j=1,neta
63             a1=abs(yl(3)-yf(j))
64             a2=abs(yh(3)-yf(j))

```

```

65         if(a1 .le. ck)nyff1=j
66         if(a2 .le. ck)nyff2=j
67     34     continue
68         do 35 i=1,nxi
69             a1=abs(xl(3)-xf(i))
70             a2=abs(xh(3)-xf(i))
71             if(a1 .le. ck)nxff1=i
72             if(a2 .le. ck)nxff2=i
73     35     continue
74     c
75         mxfc=int(delx/delxf+fuzzfc)
76         myfc=int(dely/delyf+fuzzfc)
77         mxff=int(delxf/delxff+fuzzff)
78         myff=int(delyf/delyff+fuzzff)
79     c
80     c.... Check whether grids are on top of each other.
81     c
82         as=0.
83         do 33 i=nxfc1,nxfc2
84     33     as=as+abs(x(i)-xf(1+(i-nxfc1)*mxfc))
85         do 36 j=nyfc1+1,nyfc2-1
86     36     as=as+abs(y(j)-yf(1+(j-nyfc1)*myfc))
87         write(6,90)nxfc1,nxfc2,nyfc1,nyfc2,delx/delxf,dely/delyf,as
88         write(23,90)nxfc1,nxfc2,nyfc1,nyfc2,delx/delxf,dely/delyf,as
89     90     format('nxfc1,2 nyfc1,2 ',4i4,1pe9.2,2e9.2)
90         as=0.
91         do 37 i=nxff1,nxff2
92     37     as=as+abs(xf(i)-xff(1+(i-nxff1)*mxff))
93         do 38 j=nyff1+1,nyff2-1
94     38     as=as+abs(yf(j)-yff(1+(j-nyff1)*myff))
95         write(6,94)nxff1,nxff2,nyff1,nyff2,delxf/delxff,delyf/delyff,as
96         write(23,94)nxff1,nxff2,nyff1,nyff2,delxf/delxff,delyf/delyff,as
97     94     format('nxff1,2 nyff1,2 ',4i4,1pe9.2,2e9.2)
98     c
99     c.... Write parameters.
100    c
101        if(ntype.eq.2)then
102            write(23,91)xmas,ymas,radc
103            write(6,91)xmas,ymas,radc
104        elseif(ntype.eq.1)then
105            write(23,95)radc,height,width,angle
106            write(6,95)radc,height,width,angle
107            write(23,92)nxi,neta
108        endif
109     95     format('radc,height,width,angle ',1pe9.2,3e9.2)
110     91     format('xmas,ymas ',1pe9.2,3e9.2,' radc ',e9.2)
111        write(23,92)nxi,neta
112        write(6,92)nxi,neta
113     92     format('nxi,neta ',2i5)
114        write(23,93)xl,xh,yl,yh
115        write(6,93)xl,xh,yl,yh
116     93     format('xl,xh,yl,yh',6f6.3,6f5.1)
117    c
118        return
119    end

```



```
1      subroutine getinput
2      c
3      c.... GETINPUT: Gets namelist input from terminal.
4      c
5          include 'global.h'
6          data r0/0./,dr/0./
7      c
8          namelist /io/ itmax,itmx,volts,ntype,dump,fuzzfc,fuzzff,
9              .          xl,xh,yl,yh,radc,height,width,angle,
10             .          resume,xmas,ymas,newlevs,r0,dr
11      c
12          namelist /iolevs/ nclevs,aclevs
13      c
14      c.... Get run parameters.
15      c
16          write (6,io)
17          read (5,io)
18      c
19      c.... Get new contour levels if necessary.
20      c
21          if (newlevs) then
22              write (6,iolevs)
23              write (6,10) maxlevs
24          10      format("maxlevs=",i2)
25              read (5,iolevs)
26          endif
27      c
28      c.... Convert.
29      c
30          pi=4.0*atan(1.0)
31          angle=pi*angle/180.
32          if (r0.ne.0. .and. dr.ne.0.) then
33              xmas(1)=r0-0.5*dr
34              xmas(2)=r0+0.5*dr
35          endif
36      c
37      c.... Done.
38      c
39          return
40      end
```

```
1      subroutine msk1plot(nr)
2      c
3      c.... MASKPLOT: Plots grid mask boundary.
4      c
5          include 'global.h'
6          real xmk(nxi),ymk(nxi)
7          common /xxmk/ xmk,ymk
8          logical done
9          data done/.false./
10      c
11          do 100 i=1,nxi
12      100  xmk(i)=float(i)
13      c
14          if (ntype.eq.2 .and. .not.done) then
15              do 105 n=1,nxi
16                  mjl(n)=1
17                  mjlff(n)=njjl(n)
18      105  mjlff(n)=njjlff(n)
19              do 106 n=nil,ni2
20      106  mjl(n)=nj1
21              done=.true.
22          endif
23      c
24          if(nr.eq.1)then
25              do 101 i=1,nxi
26      101  ymk(i)=float(mjl(i))
27              else if(nr.eq.2)then
28                  do 102 i=1,nxi
29      102  ymk(i)=float(mjlff(i))
30              else if(nr.eq.3)then
31                  do 103 i=1,nxi
32      103  ymk(i)=float(mjlff(i))
33              endif
34      c
35          call dashdb(ishift(30840,1))
36          call getusv('LW',lw)
37          call setusv('LW',3*lw)
38          call curved(xmk,ymk,nxi)
39          call setusv('LW',lw)
40      c
41          return
42      end
```

```
1      subroutine msk2plot
2      c
3      c.... MASKPLOT: Plots [shaded] mask for coarse grid.
4      c
5      include 'global.h'
6      c
7      xmask(1)=float(nil)
8      ymask(1)=1.
9      xmask(2)=float(nil)
10     ymask(2)=float(nj1)
11     xmask(3)=float(ni2)
12     ymask(3)=float(nj1)
13     xmask(4)=float(ni2)
14     ymask(4)=1.
15     c
16     call dashdb(ishift(30840,1))
17     call getusv('LW',lw)
18     call setusv('LW',3*lw)
19     call curved(xmask,ymask,4)
20     call setusv('LW',lw)
21     c
22     return
23     end
```

```
1      subroutine msk2plt1
2      c
3      c.... MASKPLOT: Plots fine-grid mask boundary.
4      c
5      include 'global.h'
6      real xmk(nxi),ymk(nxi)
7      common /xxmk/ xmk,ymk
8      c
9      xmk(1)=float(nif1)
10     ymk(1)=1.
11     j=1
12     do 100 i=nif1,nif2
13     j=j+1
14     xmk(j)=float(i)
15     ymk(j)=float(njj1(i))
16     xmk(j)=float(nif2)
17     ymk(j)=1.
18     c
19     call dashdb(ishift(30840,1))
20     call getusv('LW',lw)
21     call setusv('LW',3*lw)
22     call curved(xmk,ymk,j)
23     call setusv('LW',lw)
24     c
25     return
26     end
```

```
1      subroutine msk2plt2
2
3      c
4      c.... MASKPLOT: Plots fine-grid mask boundary.
5      c
6      include 'global.h'
7      real xmk(nxi),ymk(nxi)
8      common /xxmk/ xmk,ymk
9      c
10     xmk(1)=float(niff1)
11     ymk(1)=1.
12     j=1
13     do 100 i=niff1,niff2
14     j=j+1
15     xmk(j)=float(i)
16     100 ymk(j)=float(njj1f(i))
17     xmk(j)=float(niff2)
18     ymk(j)=1.
19     c
20     call dashdb(ishift(30840,1))
21     call getusv('LW',lw)
22     call setusv('LW',3*lw)
23     call curved(xmk,ymk,j)
24     call setusv('LW',lw)
25     c
26     return
    end
```

```
1      subroutine readhdr(mode)
2      c
3      c.... READHDR: Reads file header for restarts.
4      c
5          include 'global.h'
6          character* 4 mode
7          character*17 line1
8      c
9      c.... Read header.
10     c
11         if (mode.eq."mesh") then
12             read(22,10) line1,np,ndummy
13             format(a/2x,i5/2x,i5/2x,i5/2x,i5)
14             stop
15         else
16             read(22)line1,ntype,xl,xh,yl,yh,xmas,ymas,radc,
17             .         height,width,angle
18             write(6,23)ntype
19             if(ntype.eq.2)then
20                 write(6,21)nxi,neta,xl,xh,yl,yh,xmas,ymas,radc
21             elseif(ntype.eq.1)then
22                 write(6,22)nxi,neta,xl,xh,yl,yh,radc,height,
23                 .         width,angle
24             endif
25         endif
26     c
27     c.... Send message.
28     c
29         write (6,20) line1
30         format("File format is: ",a)
31         format('nxi,neta,xl,xh,yl,yh,xmas,ymas,radc',2i5,1pe9.2,5e9.2,
32         .         11e9.2)
33         format('nxi,neta,xl,xh,yl,yh,radc,height,width,angle',2i5,
34         .         1pe9.2,15e9.2)
35         format('geometry type: ',i3)
36     c
37         np=nxi*neta
38         npp=(nxi+1)*(neta+1)
39     c
40     c.... Done.
41     c
42         return
43     end
```

```
1      subroutine readmesh(mode)
2      c
3      c.... READMESH: Reads mesh from file for restarts.
4      c
5          include 'global.h'
6          character*4 mode
7      c
8      c.... Read data.
9      c
10         read(22) (x (n),n=1,nxi)
11         read(22) (y (n),n=1,neta)
12         read(22) (xf (n),n=1,nxi)
13         read(22) (yf (n),n=1,neta)
14         read(22) (xff(n),n=1,nxi)
15         read(22) (yff(n),n=1,neta)
16      c
17      c.... Find upper & lower bounds for x & y: x0,x3,y0,y2.
18      c
19         x0=1.e33
20         x3=-1.e33
21         y0=1.e33
22         y2=-1.e33
23         do 402 i=1,nxi
24             if(x(i) .lt. x0)x0=x(i)
25         402     if(x(i) .gt. x3)x3=x(i)
26             do 404 i=1,neta
27                 if(y(i) .gt. y2)y2=y(i)
28         404     if(y(i) .lt. y0)y0=y(i)
29             write(6,403)x0,x3,y0,y2
30         403     format('bounds in x y: ',1pe11.3,3e11.3)
31             xf0=1.e33
32             xf3=-1.e33
33             yf0=1.e33
34             yf2=-1.e33
35             do 412 i=1,nxi
36                 if(xf(i) .lt. xf0)xf0=xf(i)
37         412     if(xf(i) .gt. xf3)xf3=xf(i)
38                 do 414 i=1,neta
39                     if(yf(i) .gt. yf2)yf2=yf(i)
40         414     if(yf(i) .lt. yf0)yf0=yf(i)
41             write(6,413)xf0,xf3,yf0,yf2
42         413     format('bounds in xf yf: ',1pe11.3,3e11.3)
43             xlen=x3-x0
44             ylen=y2-y0
45      c
46      c.... Done.
47      c
48         return
49     end
```

```
1      subroutine readsoln
2      c
3      c.... READSOLN: Reads solution previously written out for restarts.
4      c
5      include 'global.h'
6      c
7      c.... Read data.
8      c
9      read(22) (vphi(n),n=1,np)
10     read(22) (vphif(n),n=1,np)
11     read(22) (vphiff(n),n=1,np)
12     c
13     c.... Send message.
14     c
15     write (6,10) nxi,neta,np,eps,ck
16     10 format("FEAT dump read."/
17     .      "k=",i4," l=",i4," n=",i6/
18     .      "eps=",1pe10.3," ck=",e10.3)
19     c
20     c.... Done.
21     c
22     return
23     end
```



```
1      subroutine setdims
2
3      c
4      c.... SETDIMS: Sets derived dimensions.
5      c
6      include 'global.h'
7      c
8      nn=nxi*neta
9      nxim1=nxi-1
10     nxim2=nxi-2
11     nxim3=nxi-3
12     nxim4=nxi-4
13     netam1=neta-1
14     netam2=neta-2
15     netam3=neta-3
16     netam4=neta-4
17     c
18     return
19     end
```

```
1      subroutine setmskl
2
3      c
4      c.... Sets mask for type 1 structures.
5      c
6      include 'global.h'
7      c
8      do 39 i=1,nxi
9      do 39 j=1,neta
10     maskff(i,j)=0
11     maskf(i,j)=0
12     39   mask(i,j)=0
13     x0=radc*cos(angle)
14     y0=height-radc*(1.-sin(angle))
15     tgan=tan(angle)
16     h1=height-radc
17     rad2=radc**2
18
19     c
20     c.... Set mesh for structure.
21     c
22     do 40 i=1,nxi
23     do 40 j=1,neta
24     if(x(i).le.width)then
25     if(x(i).gt.x0)then
26     al=(y(j)-y0)*tgan+x(i)-x0
27     if(al.le.0.)then
28     mask(i,j)=1
29     phi(i,j)=0.
30     endif
31     else
32     if(y(j).le.y0)then
33     mask(i,j)=1
34     phi(i,j)=0.
35     else
36     al=x(i)**2+(y(j)-h1)**2
37     if(al.le.rad2)then
38     mask(i,j)=1
39     phi(i,j)=0.
40     endif
41     endif
42     endif
43     40   continue
44     do 41 i=1,nxi
45     do 41 j=1,neta
46     if(xf(i).le.width)then
47     if(xf(i).gt.x0)then
48     al=(yf(j)-y0)*tgan+xf(i)-x0
49     if(al.le.0.)then
50     maskf(i,j)=1
51     phif(i,j)=0.
52     endif
53     else
54     if(yf(j).le.y0)then
55     maskf(i,j)=1
56     phif(i,j)=0.
57     else
58     al=xf(i)**2+(yf(j)-h1)**2
59     if(al.le.rad2)then
60     maskf(i,j)=1
61     phif(i,j)=0.
62     endif
63     endif
64     endif
65     endif
66     endif
```

```
65      41      continue
66      do 42 i=1,nxi
67      do 42 j=1,neta
68      if(xff(i).le.width)then
69      if(xff(i).gt.x0)then
70      al=(yff(j)-y0)*tgan+xff(i)-x0
71      if(al.le.0.)then
72      maskff(i,j)=1
73      phiff(i,j)=0.
74      endif
75      else
76      if(yff(j).le.y0)then
77      maskff(i,j)=1
78      phiff(i,j)=0.
79      else
80      al=xff(i)**2+(yff(j)-h1)**2
81      if(al.le.rad2)then
82      maskff(i,j)=1
83      phiff(i,j)=0.
84      endif
85      endif
86      endif
87      endif
88      42      continue
89      c
90      return
91      end
```

```

1      subroutine setmsk2
2
3      c
4      c.... Sets mask for type 2 structures.
5      c
6      include 'global.h'
7      c
8      do 39 i=1,nxi
9      do 39 j=1,neta
10     maskff(i,j)=0
11     maskf(i,j)=0
12 39   mask(i,j)=0
13   c
14   c.... Set mesh for structure.
15   c
16     ymas2=ymas(2)-radc
17     do 40 i=1,nxi
18     do 40 j=1,neta
19     if(y(j).le. ymas(2) .and. y(j).ge. ymas(1) .and. x(i).le.
20     . xmas(2).and. x(i).ge. xmas(1))then
21     mask(i,j)=1
22     phi(i,j)=0.
23     endif
24 40   continue
25     do 41 i=1,nxi
26     do 41 j=1,neta
27     if(yf(j).le. ymas2 .and. yf(j).ge. ymas(1) .and. xf(i)
28     .le.xmas(2).and. xf(i).ge. xmas(1))then
29     maskf(i,j)=1
30     phif(i,j)=0.
31     endif
32 41   continue
33     do 42 i=1,nxi
34     do 42 j=1,neta
35     if(yff(j).le. ymas2 .and. yff(j).ge. ymas(1) .and. xff(i)
36     .le.xmas(2).and. xff(i).ge. xmas(1))then
37     maskff(i,j)=1
38     phiff(i,j)=0.
39     endif
40 42   continue
41     r2=radc**2
42     xml=xmas(1)+radc
43     xm2=xmas(2)-radc
44     ym2=ymas2+radc
45     do 50 i=1,nxi
46     do 50 j=1,neta
47     if(yf(j).le.ym2 .and. yf(j).ge.ymas2)then
48     if(xf(i).ge.xmas(1) .and. xf(i).le.xml)then
49     a2=(xf(i)-xml)**2+(yf(j)-ymas2)**2
50     if(a2.le.r2)then
51     maskf(i,j)=1
52     phif(i,j)=0.
53     endif
54     endif
55     if(xf(i).le.xmas(2) .and. xf(i).ge.xm2)then
56     a2=(xf(i)-xm2)**2+(yf(j)-ymas2)**2
57     if(a2.le.r2)then
58     maskf(i,j)=1
59     phif(i,j)=0.
60     endif
61     endif
62     if(xf(i).ge.xml .and. xf(i).le.xm2)then
63     maskf(i,j)=1
64     phif(i,j)=0.
65     endif

```

```
65      endif
66      50      continue
67      do 51 i=1,nxi
68      do 51 j=1,neta
69      if(yff(j).le.ym2 .and. yff(j).ge.ymas2)then
70      if(xff(i).ge.xmas(1) .and. xff(i).le.xml1)then
71      a2=(xff(i)-xml1)**2+(yff(j)-ymas2)**2
72      if(a2.le.r2)then
73      maskff(i,j)=1
74      phiff(i,j)=0.
75      endif
76      endif
77      if(xff(i).le.xmas(2) .and. xff(i).ge.xml2)then
78      a2=(xff(i)-xml2)**2+(yff(j)-ymas2)**2
79      if(a2.le.r2)then
80      maskff(i,j)=1
81      phiff(i,j)=0.
82      endif
83      endif
84      if(xff(i).ge.xml1 .and. xff(i).le.xml2)then
85      maskff(i,j)=1
86      phiff(i,j)=0.
87      endif
88      endif
89      51      continue
90      c
91      return
92      end
```

```
1      function seval(n, u, x, y, b, c, d)
2
3      c
4      c      this routine evaluates the cubic spline function
5      c      seval = y(i) + b(i)*(u-x(i)) + c(i)*(u-x(i))**2 + d(i)*(u-x(i))**3
6      c      where x(i) .lt. u .lt. x(i+1)
7      c      if u .lt. x(1) then i = 1 is used.
8      c      if u .gt. x(n) then i = n is used.
9      c      input:
10     c      n      - the number of data points
11     c      u      - the abscissa at which the spline is to be evaluated
12     c      x,y    - the arrays of data abscissas and ordinates
13     c      b,c,d  - arrays of spline coefficients computed by spline
14     c
15     c      if u is not in the same interval as the previous call, then a
16     c      binary search is performed to determine the proper interval.
17     c
18     c      save
19     c      real x(n), y(n), b(n), c(n), d(n)
20     c      data i/1/
21
22     c      if(i.ge.n) i = 1
23     c      if(u.lt.x(i)) go to 10
24     c      if(u.le.x(i+1)) go to 30
25     c      binary search
26     10  i = 1
27     20  j = n+1
28     20  k = (i+j)/2
29     28  if(u.lt.x(k)) j = k
30     29  if(u.ge.x(k)) i = k
31     30  if(j.gt.i+1) go to 20
32     c      evaluate spline
33     30  dx = u - x(i)
34     33  if(i.eq.n) dx = 0.
35     34  seval = y(i) + dx*( b(i) + dx*( c(i) + dx*( d(i) )))
36     c
37     c      return
38     c      end
```

```
1      subroutine slicepl2(ax,ay,ayl,npts,label)
2      c
3      c.... SLICEPLT: Slice plots (type 2).
4      c
5          include 'global.h'
6          dimension ax(1),ay(1),ayl(1)
7          character*(*) label
8      c
9      c.... Initialize.
10         ymax=-1.e99
11         ymin= 1.e99
12     c
13     c.... Find min/max.
14         do 10 i=1,npts
15             ymin=min(ay(i),ymin)
16             ymin=min(ayl(i),ymin)
17             ymax=max(ay(i),ymax)
18             10 ymax=max(ayl(i),ymax)
19     c
20         if(abs(ymax) .lt. ck)then
21             ymax=0.
22         else
23             ymax=ymax+0.1*abs(ymax)
24         endif
25     c
26         if(abs(ymin) .lt. ck)then
27             ymin=0.
28         else
29             ymin=ymin-0.1*abs(ymin)
30         endif
31     c
32     c.... Set viewport and window.
33         call set(0.1,0.9,0.1,0.9,ax(1),ax(npts),ymin,ymax,1)
34     c
35     c.... Plot.
36         call anotat(" $", " $",1,4,1,'$$$$$$$$$$$$$$$')
37         call displa(2,0,0)
38         call ezxy(ax,ay,npts,label/"$")
39         call anotat(" $", " $",1,4,1,'$'$'$'$'$'$'$'$'$'$')
40         call displa(1,0,0)
41         call ezxy(ax,ayl,npts," $")
42     c
43         return
44     end
```

```
1      subroutine sliceplt(ax,ay,npts,label)
2      c
3      c.... SLICEPLT: Slice plots (type 1).
4      c
5          include 'global.h'
6          dimension ax(1),ay(1)
7          character*(*) label
8      c
9      c.... Initialize.
10         ymin= 1.e99
11         ymax=-1.e99
12     c
13     c.... Find min/max.
14     c
15         do 10 i=1,npts
16             ymin=amin1(ay(i),ymin)
17             10  ymax=amax1(ay(i),ymax)
18     c
19         ymin=ymin-0.1*abs(ymin)
20         ymax=ymax+0.1*abs(ymax)
21     c
22         if (ymax-ymin.lt.1.e-14) return
23     c
24     c.... Set viewport and window.
25     c
26         call set(0.1,0.9,0.1,0.9,ax(1),ax(npts),ymin,ymax,1)
27     c
28     c.... Plot.
29     c
30         call anotat(" $", " $",1,4,1,'$$$$$$$$$$$$$$$')
31         call ezxy(ax,ay,npts,label//"$")
32     c
33     c.... Done.
34     c
35         return
36     end
```



```

1      subroutine spline(n, x, y, b, c, d)
2      c
3      c-----
4      c   the coefficients b(i), c(i), d(i), i=1,2,...,n are computed
5      c   for a cubic interpolating spline
6      c    $s(x) = y(i) + b(i)*(x-x(i)) + c(i)*(x-x(i))^2 + d(i)*(x-x(i))^3$ 
7      c   for x(i) .le. x .le. x(i+1)
8      c   input:
9      c   n - the number of data points or knots (n.ge.2)
10     c   x - the abscissas of the knots in strictly increasing order
11     c   y - the ordinates of the knots
12     c   output:
13     c   b,c,d - arrays of spline coefficients as defined above
14     c   using p to denote differentiation from the right
15     c   y(i) = s(x(i))
16     c   b(i) = sp(x(i))
17     c   c(i) = spp(x(i))/2
18     c   d(i) = spps(x(i))/6
19     c-----
20     c
21     save
22     real x(n),y(n),b(n),c(n),d(n)
23     c
24     nml = n-1
25     if(n.lt.2) stop 'spline error'
26     if(n.lt.3) go to 50
27     c   set up tridiagonal system
28     c   b = diagonal, d = offdiagonal, c = right hand side
29     d(1) = x(2) - x(1)
30     c(2) = (y(2) - y(1))/d(1)
31     do 10 i=2, nml
32         d(i) = x(i+1) - x(i)
33         b(i) = 2.*(d(i-1) + d(i))
34         c(i+1) = (y(i+1) - y(i))/d(i)
35         c(i) = c(i+1) - c(i)
36     10 continue
37     c   end conditions. third derivatives at x(1) and x(n)
38     c   obtained from divided differences
39     b(1) = -d(1)
40     b(n) = -d(n-1)
41     c(1) = 0.
42     c(n) = 0.
43     if(n.eq.3) go to 15
44     c(1) = c(3)/(x(4)-x(2)) - c(2)/(x(3)-x(1))
45     c(n) = c(n-1)/(x(n)-x(n-2)) - c(n-2)/(x(n-1)-x(n-3))
46     c(1) = c(1)*(d(1)**2)/(x(4)-x(1))
47     c(n) = -c(n)*(d(n-1)**2)/(x(n)-x(n-3))
48     c   forward elimination
49     15 do 20 i=2,n
50         t = d(i-1)/b(i-1)
51         b(i) = b(i) - t*d(i-1)
52         c(i) = c(i) - t*c(i-1)
53     20 continue
54     c   back substitution
55     c(n) = c(n)/b(n)
56     do 30 ib=1,nml
57         i = n-ib
58         c(i) = (c(i) - d(i)*c(i+1))/b(i)
59     30 continue
60     c   compute polynomial coefficients
61     b(n) = (y(n) - y(nml))/d(nml) + d(nml)*(c(nml) + 2.*c(n))
62     do 40 i=1,nml
63         b(i) = (y(i+1) - y(i))/d(i) - d(i)*(c(i+1) + 2.*c(i))
64         d(i) = (c(i+1) - c(i))/d(i)

```

```
65      c(i) = 3.*c(i)
66      40 continue
67      c(n) = 3.*c(n)
68      d(n) = d(n-1)
69      return
70
71      50 b(1) = (y(2)-y(1))/(x(2)-x(1))
72      c(1) = 0.
73      d(1) = 0.
74      b(2) = b(1)
75      c(2) = 0.
76      d(2) = 0.
77      return
78      c
79      end
```

```
1      subroutine wrdump
2      c
3      c.... WRDUMP: Writes out solution, etc. for diagnostic rerun.
4      c
5          include 'global.h'
6          character*17 linel
7      c
8      c.... Create file.
9          open (29,file=dumpfile,status='unknown',form='unformatted')
10     c
11     c.... Write header.
12         linel="FEAT v."//ivers
13         write(29) linel,ntype,xl,xh,yl,yh,xmas,ymas,radc,
14             height,width,angle
15     c
16     c.... Write data.
17         write(29) (x (n),n=1,nxi)
18         write(29) (y (n),n=1,neta)
19         write(29) (xf (n),n=1,nxi)
20         write(29) (yf (n),n=1,neta)
21         write(29) (xff(n),n=1,nxi)
22         write(29) (yff(n),n=1,neta)
23     c         write(29) (vphi(n),n=1,np)
24     c         write(29) (vphif(n),n=1,np)
25     c         write(29) (vphiff(n),n=1,np)
26         write(29) (vex(n),n=1,npp)
27         write(29) (vexf(n),n=1,npp)
28         write(29) (vexff(n),n=1,npp)
29         write(29) (vey(n),n=1,npp)
30         write(29) (veyf(n),n=1,npp)
31         write(29) (veyff(n),n=1,npp)
32         write(29) (mj1(n),n=1,nxi)
33         write(29) (mj1f(n),n=1,nxi)
34         write(29) (mj1ff(n),n=1,nxi)
35     c
36     c.... Close file.
37         close(29)
38     c
39     c.... Send message.
40         write (6,10)
41     10    format("Dump written.")
42     c
43     c.... Done.
44     c
45         return
46     end
```

```

47      program tpic
48      c
49      c=====
50      c
51      c.... TPIC: Test particle pusher using fields from FEAT.
52      c
53      c.... Alan Mankofsky (alan@mclapo.saic.com): original version (3/91)
54      c.... Doug Kirkpatrick (dougk@mclapo.saic.com): various mods (6-7/91)
55      c
56      c.... SAIC Applied Physics Operation
57      c.... McLean, VA 22102
58      c
59      c=====
60      c
61      include 'global.h'
62      character*5 idd
63      character*7 ivers
64      c
65      ivers="02Jul91"
66      c
67      c.... Send banner.
68      write (6,10) ivers
69      10  format("/TPIC v.",a7/)
70      c
71      c.... Get execute line.
72      c
73      narg=iargc()
74      c
75      if (narg.ne.1) then
76          write (6,20)
77      20  format("Bad execute line!")
78          stop
79      endif
80      c
81      call getarg(1,idd)
82      id=idd(1:4)
83      c
84      c.... Open files.
85      write (6,25) id//".dmp"
86      25  format("Opening dump file ",a)
87      open (22,file=id//".dmp",status="old",form="unformatted",err=900)
88      open (7,file=id//".out",status="new",form="formatted")
89      write (7,27) ivers,idd
90      27  format("TPIC v.",a," : run ",a/)
91      c
92      c.... Get input.
93      call input
94      c
95      c.... Read file.
96      call readhdr
97      call readmesh
98      call readsoln
99      c
100     c.... Close dump file.
101     close (22)
102     c
103     c.... Prestore constants.
104     c
105     qm=q/m
106     dth=0.5*dt
107     pi=4.0*atan(1.0)
108     c.... <aconst> corresponds to elementary charge over 10 A**2 area.
109     aconst=abs(q)/(1.0e-14)
110     c

```

```

111      dx(1)=(xh(1)-xl(1))/float(nximl)
112      dx(2)=(xh(2)-xl(2))/float(nximl)
113      dx(3)=(xh(3)-xl(3))/float(nximl)
114      dxmin=min(dx(1),dx(2),dx(3))
115      dxmax=max(dx(1),dx(2),dx(3))
116      dy(1)=(yh(1)-yl(1))/float(netaml)
117      dy(2)=(yh(2)-yl(2))/float(netaml)
118      dy(3)=(yh(3)-yl(3))/float(netaml)
119      dymin=min(dy(1),dy(2),dy(3))
120      dymax=max(dy(1),dy(2),dy(3))
121      c
122      write (6,50) dx,dy
123      write (7,50) dx,dy
124      50  format("dx=",1p,3e9.2/"dy=",3e9.2)
125      c
126      area(1)=dx(1)*dy(1)
127      area(2)=dx(2)*dy(2)
128      area(3)=dx(3)*dy(3)
129      c
130      c.... Fill in edges of meshes.
131      call edges
132      c
133      c.... Initialize particle emission sites.
134      call pinit
135      c
136      c.... Smooth fields at emission surface
137      call smooth
138      c
139      c.... Calculate emission data.
140      call premit
141      c
142      c.... Main loop.
143      100  call emit(ip)
144      if (ip.eq.0) then
145      go to 200
146      else
147      call push(ip)
148      endif
149      go to 100
150      c
151      c.... Initialize NCAR graphics.
152      200  call opngks
153      c
154      c.... Plots.
155      if (lscat) then
156      do 210 ig=1,3
157      210  call scatplot(pr,pz,nt+1,npmax,itkill,
158      .          xl(ig),xh(ig),yl(ig),yh(ig),
159      .          ig,"r-z trajectories",.true.)
160      call scatplot(pr,vr,nt+1,npmax,itkill,
161      .          xl(1),xh(1),0.0,0.0,
162      .          1,"Vr-r trajectories",.false.)
163      endif
164      call phase(nsites)
165      c
166      c.... Terminate NCAR graphics.
167      call clsgks
168      c
169      c.... Done.
170      stop
171      c
172      c.... Error trap.
173      900  write (6,910) id//".dmp"
174      910  format("Unable to open dump file ",a,".")

```

175		stop
176	c	
177		end

```
1  # TPIC makefile
2  # Alan Mankofsky, SAIC (alan@mclapo.saic.com)
3
4  OBJS = blkdat.o    edges.o    emit.o    input.o    maskplot.o  tpic.o \
5          pinit.o    push.o     readhdr.o  readmesh.o  readsoln.o  scatplot.o \
6          t.o        v.o        phase.o    premit.o    smooth.o
7
8  FFLAGS = -O
9  LIBS = -L/usr/local/lib -lncarg -lncarg_gks -lncarg_loc
10
11  tpic:    $(OBJS)
12          xlf -o tpic $(LIBS) $(OBJS)
13
14  clean:
15          rm -f tpic $(OBJS)
16
17  $(OBJS): global.h
```

```
1      block data
2
3      c
4      include 'global.h'
5
6      c
7      data q/-1.6022e-19/,m/9.1095e-31/
8      data dt/5.0e-16/,vmult/10.0/,phi/5.1/
9      data nsites/0/,wmin/1.e-8/,wmax/1.e10/
10     data xcell/0.9/,debug/.false./,wmult/0.01/
11     data lscat/.false./,dtxtal/1.0e-12/
12     data nsmooth/0/
13
14     c
15     end
```



```

1      subroutine edges
2
3      c
4      c.... EDGES: Fills in edges of meshes.
5      c
6      include 'global.h'
7      c
8      c.... Loop over grids.
9      do 1000 ig=1,3
10     c
11     c.... Mesh data.
12     c
13     rr(0 ,ig)=rr(1 ,ig)-dx(ig)
14     rr(nx1+1,ig)=rr(nx1,ig)+dx(ig)
15     zz(0 ,ig)=zz(1 ,ig)-dy(ig)
16     zz(neta+1,ig)=zz(neta,ig)+dy(ig)
17     c
18     c.... Boundary mask data (kludge).
19     c
20     njj(0 ,ig)=njj(1 ,ig)
21     njj(nx1+1,ig)=njj(nx1,ig)
22     c
23     c.... Bottom.
24     c
25     do 10 i=2,nx1m2
26     ddx=
27     . 0.5*(er(i+1,1,ig)-er(i-1,1,ig))
28     ddy=
29     . 0.5*(-er(i,3,ig)+4.0*er(i,2,ig)-3.0*er(i,1,ig))
30     er(i,0,ig)=er(i,1,ig)+ddx+ddy
31     ddx=
32     . 0.5*(ez(i+1,1,ig)-ez(i-1,1,ig))
33     ddy=
34     . 0.5*(-ez(i,3,ig)+4.0*ez(i,2,ig)-3.0*ez(i,1,ig))
35     10 ez(i,0,ig)=ez(i,1,ig)+ddx+ddy
36     c
37     ddx=
38     . 0.5*(-er(3,1,ig)+4.0*er(2,1,ig)-3.0*er(1,1,ig))
39     ddy=
40     . 0.5*(-er(1,3,ig)+4.0*er(1,2,ig)-3.0*er(1,1,ig))
41     er(1,0,ig)=er(1,1,ig)+ddx+ddy
42     ddx=
43     . 0.5*(-ez(3,1,ig)+4.0*ez(2,1,ig)-3.0*ez(1,1,ig))
44     ddy=
45     . 0.5*(-ez(1,3,ig)+4.0*ez(1,2,ig)-3.0*ez(1,1,ig))
46     ez(1,0,ig)=ez(1,1,ig)+ddx+ddy
47     c
48     ddx=
49     . -0.5*(-er(nx1m3,1,ig)+4.0*er(nx1m2,1,ig)-3.0*er(nx1m1,1,ig))
50     ddy=
51     . 0.5*(-er(nx1m1,3,ig)+4.0*er(nx1m1,2,ig)-3.0*er(nx1m1,1,ig))
52     er(nx1m1,0,ig)=er(nx1m1,1,ig)+ddx+ddy
53     ddx=
54     . -0.5*(-ez(nx1m3,1,ig)+4.0*ez(nx1m2,1,ig)-3.0*ez(nx1m1,1,ig))
55     ddy=
56     . 0.5*(-ez(nx1m1,3,ig)+4.0*ez(nx1m1,2,ig)-3.0*ez(nx1m1,1,ig))
57     ez(nx1m1,0,ig)=ez(nx1m1,1,ig)+ddx+ddy
58     c
59     c.... Top.
60     c
61     do 20 i=2,nx1m2
62     ddx=
63     . 0.5*(er(i+1,netam1,ig)-er(i-1,netam1,ig))
64     ddy=
65     . -0.5*(-er(i,netam3,ig)+4.0*er(i,netam2,ig)+3.0*er(i,netam1,ig))

```

```

65      er(i,neta,ig)=er(i,netaml,ig)+ddx+ddy
66      ddx=
67      . 0.5*(ez(i+1,netaml,ig)-ez(i-1,netaml,ig))
68      ddy=
69      . -0.5*(-ez(i,netam3,ig)+4.0*ez(i,netam2,ig)+3.0*ez(i,netaml,ig))
70 20    ez(i,neta,ig)=ez(i,netaml,ig)+ddx+ddy
71    c
72      ddx=
73      . 0.5*(-er(3,netaml,ig)+4.0*er(2,netaml,ig)-3.0*er(1,netaml,ig))
74      ddy=
75      . -0.5*(-er(1,netam3,ig)+4.0*er(1,netam2,ig)-3.0*er(1,netaml,ig))
76      er(1,neta,ig)=er(1,netaml,ig)+ddx+ddy
77      ddx=
78      . 0.5*(-ez(3,netaml,ig)+4.0*ez(2,netaml,ig)-3.0*ez(1,netaml,ig))
79      ddy=
80      . -0.5*(-ez(1,netam3,ig)+4.0*ez(1,netam2,ig)-3.0*ez(1,netaml,ig))
81      ez(1,neta,ig)=ez(1,netaml,ig)+ddx+ddy
82    c
83      ddx=
84      . -0.5*(-er(nxim3,netaml,ig)+4.0*er(nxim2,netaml,ig)-
85      . 3.0*er(nxim1,netaml,ig))
86      ddy=
87      . -0.5*(-er(nxim1,netam3,ig)+4.0*er(nxim1,netam2,ig)-
88      . 3.0*er(nxim1,netaml,ig))
89      er(nxim1,neta,ig)=er(nxim1,netaml,ig)+ddx+ddy
90      ddx=
91      . -0.5*(-ez(nxim3,netaml,ig)+4.0*ez(nxim2,netaml,ig)-
92      . 3.0*ez(nxim1,netaml,ig))
93      ddy=
94      . -0.5*(-ez(nxim1,netam3,ig)+4.0*ez(nxim1,netam2,ig)-
95      . 3.0*ez(nxim1,netaml,ig))
96      ez(nxim1,neta,ig)=ez(nxim1,netaml,ig)+ddx+ddy
97    c
98    c.... Left.
99    c
100      do 30 j=2,netam2
101      ddx=
102      . 0.5*(-er(3,j,ig)+4.0*er(2,j,ig)-3.0*er(1,j,ig))
103      ddy=
104      . 0.5*(er(1,j+1,ig)-er(1,j-1,ig))
105      er(0,j,ig)=er(1,j,ig)+ddx+ddy
106      ddx=
107      . 0.5*(-ez(3,j,ig)+4.0*ez(2,j,ig)-3.0*ez(1,j,ig))
108      ddy=
109      . 0.5*(ez(1,j+1,ig)-ez(1,j-1,ig))
110 30    ez(0,j,ig)=ez(1,j,ig)+ddx+ddy
111    c
112      ddx=
113      . 0.5*(-er(3,1,ig)+4.0*er(2,1,ig)-3.0*er(1,1,ig))
114      ddy=
115      . 0.5*(-er(1,3,ig)+4.0*er(1,2,ig)-3.0*er(1,1,ig))
116      er(0,1,ig)=er(1,1,ig)+ddx+ddy
117      ddx=
118      . 0.5*(-ez(3,1,ig)+4.0*ez(2,1,ig)-3.0*ez(1,1,ig))
119      ddy=
120      . 0.5*(-ez(1,3,ig)+4.0*ez(1,2,ig)-3.0*ez(1,1,ig))
121      ez(0,1,ig)=ez(1,1,ig)+ddx+ddy
122    c
123      ddx=
124      . 0.5*(-er(3,netaml,ig)+4.0*er(2,netaml,ig)-3.0*er(1,netaml,ig))
125      ddy=
126      . -0.5*(-er(1,netam3,ig)+4.0*er(1,netam2,ig)-3.0*er(1,netaml,ig))
127      er(0,netaml,ig)=er(1,netaml,ig)+ddx+ddy
128      ddx=

```

```

129      . 0.5*(-ez(3,netaml,ig)+4.0*ez(2,netaml,ig)-3.0*ez(1,netaml,ig))
130      ddy=
131      . -0.5*(-ez(1,netam3,ig)+4.0*ez(1,netam2,ig)-3.0*ez(1,netaml,ig))
132      ez(0,netaml,ig)=ez(1,netaml,ig)+ddx+ddy
133  c
134  c.... Right.
135  c
136      do 40 j=2,netam2
137      ddx=
138      . -0.5*(-er(nxim3,j,ig)+4.0*er(nxim2,j,ig)-3.0*er(nxim1,j,ig))
139      ddy=
140      . 0.5*(er(nxim1,j+1,ig)-er(nxim1,j-1,ig))
141      er(nxi,j,ig)=er(nxim1,j,ig)+ddx+ddy
142      ddx=
143      . -0.5*(-ez(nxim3,j,ig)+4.0*ez(nxim2,j,ig)-3.0*ez(nxim1,j,ig))
144      ddy=
145      . 0.5*(ez(nxim1,j+1,ig)-ez(nxim1,j-1,ig))
146  40  ez(nxi,j,ig)=ez(nxim1,j,ig)+ddx+ddy
147  c
148      ddx=
149      . -0.5*(-er(nxim3,1,ig)+4.0*er(nxim2,1,ig)-3.0*er(nxim1,1,ig))
150      ddy=
151      . 0.5*(-er(nxim1,3,ig)+4.0*er(nxim1,2,ig)-3.0*er(nxim1,1,ig))
152      er(nxi,1,ig)=er(nxim1,1,ig)+ddx+ddy
153      ddx=
154      . -0.5*(-ez(nxim3,1,ig)+4.0*ez(nxim2,1,ig)-3.0*ez(nxim1,1,ig))
155      ddy=
156      . 0.5*(-ez(nxim1,3,ig)+4.0*ez(nxim1,2,ig)-3.0*ez(nxim1,1,ig))
157      ez(nxi,1,ig)=ez(nxim1,1,ig)+ddx+ddy
158  c
159      ddx=
160      . -0.5*(-er(nxim3,netaml,ig)+4.0*er(nxim2,netaml,ig)-
161      . 3.0*er(nxim1,netaml,ig))
162      ddy=
163      . -0.5*(-er(nxim1,netam3,ig)+4.0*er(nxim1,netam2,ig)-
164      . 3.0*er(nxim1,netaml,ig))
165      er(nxi,netaml,ig)=er(nxim1,netaml,ig)+ddx+ddy
166      ddx=
167      . -0.5*(-ez(nxim3,netaml,ig)+4.0*ez(nxim2,netaml,ig)-
168      . 3.0*ez(nxim1,netaml,ig))
169      ddy=
170      . -0.5*(-ez(nxim1,netam3,ig)+4.0*ez(nxim1,netam2,ig)-
171      . 3.0*ez(nxim1,netaml,ig))
172      ez(nxi,netaml,ig)=ez(nxim1,netaml,ig)+ddx+ddy
173  c
174  c.... Corners.
175  c
176      ddx=
177      . 0.5*(-er(3,0,ig)+4.0*er(2,0,ig)-3.0*er(1,0,ig))
178      ddy=
179      . 0.5*(-er(0,3,ig)+4.0*er(0,2,ig)-3.0*er(0,1,ig))
180      er(0,0,ig)=0.5*(er(1,0,ig)+ddx+
181      . er(0,1,ig)+ddy)
182      ddx=
183      . 0.5*(-ez(3,0,ig)+4.0*ez(2,0,ig)-3.0*ez(1,0,ig))
184      ddy=
185      . 0.5*(-ez(0,3,ig)+4.0*ez(0,2,ig)-3.0*ez(0,1,ig))
186      ez(0,0,ig)=0.5*(ez(1,0,ig)+ddx+
187      . ez(0,1,ig)+ddy)
188  c
189      ddx=
190      . -0.5*(-er(nxim3,0,ig)+4.0*er(nxim2,0,ig)-3.0*er(nxim1,0,ig))
191      ddy=
192      . 0.5*(-er(nxi,3,ig)+4.0*er(nxi,2,ig)-3.0*er(nxi,1,ig))

```

```

193     er(nxi,0,ig)=0.5*(er(nximl,0,ig)+ddx+
194         er(nxi,1,ig)+ddy)
195     ddx=
196     . -0.5*(-ez(nxim3,0,ig)+4.0*ez(nxim2,0,ig)-3.0*ez(nximl,0,ig))
197     ddy=
198     . 0.5*(-ez(nxi,3,ig)+4.0*ez(nxi,2,ig)-3.0*ez(nxi,1,ig))
199     ez(nxi,0,ig)=0.5*(ez(nximl,0,ig)+ddx+
200         ez(nxi,1,ig)+ddy)
201     c
202     ddx=
203     . -0.5*(-er(nxim3,neta,ig)+4.0*er(nxim2,neta,ig)-
204         3.0*er(nximl,neta,ig))
205     ddy=
206     . -0.5*(-er(nxi,netam3,ig)+4.0*er(nxi,netam2,ig)-
207         3.0*er(nxi,netaml,ig))
208     er(nxi,neta,ig)=0.5*(er(nximl,neta,ig)+ddx+
209         er(nxi,netaml,ig)+ddy)
210     ddx=
211     . -0.5*(-ez(nxim3,neta,ig)+4.0*ez(nxim2,neta,ig)-
212         3.0*ez(nximl,neta,ig))
213     ddy=
214     . -0.5*(-ez(nxi,netam3,ig)+4.0*ez(nxi,netam2,ig)-
215         3.0*ez(nxi,netaml,ig))
216     ez(nxi,neta,ig)=0.5*(ez(nximl,neta,ig)+ddx+
217         ez(nxi,netaml,ig)+ddy)
218     c
219     ddx=
220     . 0.5*(-er(3,neta,ig)+4.0*er(2,neta,ig)-3.0*er(1,neta,ig))
221     ddy=
222     . -0.5*(-er(0,netam3,ig)+4.0*er(0,netam2,ig)-3.0*er(0,netaml,ig))
223     er(0,neta,ig)=0.5*(er(1,neta,ig)+ddx+
224         er(0,netaml,ig)+ddy)
225     ddx=
226     . 0.5*(-ez(3,neta,ig)+4.0*ez(2,neta,ig)-3.0*ez(1,neta,ig))
227     ddy=
228     . -0.5*(-ez(0,netam3,ig)+4.0*ez(0,netam2,ig)-3.0*ez(0,netaml,ig))
229     ez(0,neta,ig)=0.5*(ez(1,neta,ig)+ddx+
230         ez(0,netaml,ig)+ddy)
231     c
232     c.... Next grid.
233     1000 continue
234     c
235     c.... Done.
236     return
237     end

```

```

1      subroutine emit(ip)
2      c
3      c.... EMIT: Fowler-Nordheim emission from predetermined sites.
4      c
5          include 'global.h'
6          data np/0/
7          data truemin/1.e37/,truemax/-1.e37/,wav/0./,curtot/0./
8          save np
9      c
10     c.... Loop over sites.
11         do 500 isite=1,nsites
12     c
13     c.... Skip?
14         if (sites(isite,1).eq.-1) go to 500
15     c
16     c.... Store indices.
17         i=sites(isite,1)
18         j=sites(isite,2)
19     c
20     c.... Mark as done.
21         sites(isite,1)=-1
22     c
23     c.... Fowler-Nordheim emission.
24         ee=0.01*sqrt(exff(i,j)**2+eyff(i,j)**2)
25         yy=3.795e-4*sqrt(ee)/phi
26         vyy=v(yy)
27         tyy=t(yy)
28         f1=1.541e-6*ee**2/(phi*tyy**2)
29         f2=exp(-6.831e7*(sqrt(phi))**3*vyy/ee)
30         fj=f1*f2
31         if (fj.eq.0.) go to 500
32         dtfn=aconst/fj
33         dtem=dtfn+dtxtal
34         fj=aconst/dtem
35         cur=1.e4*fj*pi*(xff(i)+xff(i+1))*dx(3)
36         w=abs(cur*dt/q)
37     c
38     c.... Emit particle.
39     c
40         if (w.ge.wmin .and. w.le.wmax) then
41     c
42         xb(1)=0.
43         xb(2)=0.
44         xb(3)=0.5*(yff(j)+yff(j+1))
45         xb(4)=0.5*(xff(i)+xff(i+1))
46         xb(5)=w
47         if (debug) write (6,80) (xb(jp),jp=1,5)
48     80    format("Emitted particle: ",5(1pe10.3,1x))
49     c
50     c.... Loop over five subparticles spaced in spread pattern
51     c.... over cell that has been chosen for emission.
52     c
53         dkdx = xff(i+1) - xff(i)
54         dkdy = yff(j+1) - yff(j)
55     c
56         do 100 ipart=1,5
57         np=np+1
58         ip=np
59         if (ip.gt.npmax) then
60             write (6,90)
61             write (7,90)
62     90    format("Too many particles!")
63             stop
64         endif

```

```

65         if (ipart .eq. 1) then
66             pr(1,ip)=xb(4)
67             pz(1,ip)=xb(3)
68         elseif (ipart .eq. 2) then
69             pr(1,ip)=xb(4) - 0.4*dkdx
70             pz(1,ip)=xb(3) - 0.4*dkdy
71         elseif (ipart .eq. 3) then
72             pr(1,ip)=xb(4) - 0.4*dkdx
73             pz(1,ip)=xb(3) + 0.4*dkdy
74         elseif (ipart .eq. 4) then
75             pr(1,ip)=xb(4) + 0.4*dkdx
76             pz(1,ip)=xb(3) + 0.4*dkdy
77         else
78             pr(1,ip)=xb(4) + 0.4*dkdx
79             pz(1,ip)=xb(3) - 0.4*dkdy
80         endif
81         vr(1,ip)=0.
82         weight(ip)=w*0.2
83         truemin=min(truemin,weight(ip))
84         truemax=max(truemax,weight(ip))
85         wav=wav+weight(ip)
86     100     curtot=curtot+cur*0.2
87     c
88         return
89     c
90     endif
91     c
92     c.... Next site.
93     500     continue
94     c
95     c.... Flag for no particles emitted.
96     ip=0
97     c
98     c.... Diagnostics.
99         if (np.eq.0) then
100             write (6,510)
101             write (7,510)
102     510     format("No particles actually emitted!")
103             stop
104         else
105             write (6,520) np,truemin,truemax,wav/float(np),curtot
106             write (7,520) np,truemin,truemax,wav/float(np),curtot
107     520     format(/i4," particles actually emitted. "/
108             .      "truemin=",1pe10.3," truemax=",e10.3," wav=",e10.3,
109             .      " curtot=",e10.3)
110         endif
111     c
112     c.... Done.
113     return
114     end

```

```

1      parameter (nxi=501,neta=501,npmax=1000,nt=1600,maxsites=1000)
2      parameter (nbins=25)
3      parameter (nn=nxi*neta,nnp=(nxi+1)*(neta+1))
4      parameter (nxim1=nxi-1,nxim2=nxi-2,nxim3=nxi-3)
5      parameter (netam1=neta-1,netam2=neta-2,netam3=neta-3)
6
7      c
8      dimension xl(3),xh(3),yl(3),yh(3)
9      dimension xmas(2),ymas(2)
10     dimension dx(3),dy(3),area(3)
11
12     c
13     dimension x (0:nxi+1),y (0:neta+1)
14     dimension xf (0:nxi+1),yf (0:neta+1)
15     dimension xff(0:nxi+1),yff(0:neta+1)
16
17     c
18     dimension ex (0:nxi,0:neta),ey (0:nxi,0:neta)
19     dimension exf (0:nxi,0:neta),eyf (0:nxi,0:neta)
20     dimension exff(0:nxi,0:neta),eyff(0:nxi,0:neta)
21
22     c
23     dimension njl(0:nxi+1),njlf(0:nxi+1),njlff(0:nxi+1)
24
25     c
26     dimension xb(5),weight(npmax),itkill(npmax)
27
28     c
29     dimension pr(nt+1,npmax),pz(nt+1,npmax),vr(nt+1,npmax)
30
31     c
32     dimension sites(maxsites,2)
33     integer sites
34     dimension work(maxsites,2)
35
36     c
37     dimension vx (1),vy (1)
38     equivalence (vx,x),(vy,y)
39     dimension vxf (1),vyf (1)
40     equivalence (vxf,xf),(vyf,yf)
41     dimension vxff(1),vyff(1)
42     equivalence (vxff,xff),(vyff,yff)
43
44     c
45     dimension vex (1),vey (1)
46     equivalence (vex,ex),(vey,ey)
47     dimension vexf (1),veyf (1)
48     equivalence (vexf,exf),(veyf,eyf)
49     dimension vexff(1),veyff(1)
50     equivalence (vexff,exff),(veyff,eyff)
51
52     c
53     dimension er(0:nxi,0:neta,3),ez(0:nxi,0:neta,3)
54     equivalence (ex ,er(0,0,1)),
55     .           (exf ,er(0,0,2)),
56     .           (exff,er(0,0,3))
57     equivalence (ey ,ez(0,0,1)),
58     .           (eyf ,ez(0,0,2)),
59     .           (eyff,ez(0,0,3))
60
61     c
62     dimension rr(0:nxi+1,3),zz(0:neta+1,3)
63     equivalence (x ,rr(0,1)),
64     .           (xf ,rr(0,2)),
65     .           (xff,rr(0,3))
66     equivalence (y ,zz(0,1)),
67     .           (yf ,zz(0,2)),
68     .           (yff,zz(0,3))
69
70     c
71     dimension njj(0:nxi+1,3)
72     equivalence (njl ,njj(0,1)),
73     .           (njlf,njj(0,2)),
74     .           (njlff,njj(0,3))
75
76     c
77     common /misc/ xl,xh,yl,yh,xmas,ymas,q,m,qm,dt,dth,phi,

```

```
65      .          dx,dy,dxmin,dxmax,dymin,dymax,area,nsites,  
66      .          wmin,wmax,vmult,xcell,pi,debug,radc,height,  
67      .          width,angle,wmult,lscat,dtxtal,aconst,nsmooth  
68      real m  
69      logical debug,lscat  
70      c  
71      common /cmisc/ id  
72      character*4 id  
73      c  
74      common /xpoint/ x,xf,xff,y,yf,yff,  
75      .          ex,exf,exff,ey,eyf,eyff,  
76      .          nj1,nj1f,nj1ff,weight,work,  
77      .          xb,pr,pz,vr,sites,itkill
```



```
1      subroutine input
2      c
3      c.... INPUT: Gets TTY input.
4      c
5      include 'global.h'
6      c
7      namelist /io/ dt,wmin,wmax,phi,vmult,xcell,debug,
8      .            wmult,lscat,dtxtal,nsmooth
9      c
10     write (6,io)
11     read  (5,io)
12     c
13     write (7,io)
14     c
15     return
16     end
```

```
1      subroutine maskplot(ig)
2      c
3      c.... MASKPLOT: Plots grid mask boundary.
4      c
5      include 'global.h'
6      c
7      do 10 i=1,nxi
8      10  vex(i)=float(i)
9      c
10     do 20 i=1,nxi
11     20  vey(i)=float(njj(i,ig))
12     c
13     call set(0.1,0.9,0.1,0.9,1.0,float(nxi),1.0,float(neta),1)
14     call getusv('LW',lw)
15     call setusv('LW',4*lw)
16     call curve(vex,vey,nxi)
17     call setusv('LW',lw)
18     c
19     return
20     end
```

```

1      subroutine phase(np)
2
3      c
4      c.... PHASE: Vr-r phase space contour plot at top of system.
5      c....      Also computes emittance, sigmas, and epsilon.
6      c
7      include 'global.h'
8      dimension rhit(npmax),vhit(npmax),whit(npmax),xwhit(npmax)
9      dimension rbin(nbins),vbin(nbins),fbin(nbins,nbins)
10     character*36 line
11     common /conre4/ junk(5),ilab
12
13     c
14     c.... Initialize.
15     mm=0
16     top=yh(1)-0.5*dy(1)
17     ilab=0
18
19     c
20     c.... Get particle data at top.
21     do 10 ip=1,npmax
22     if (weight(ip).eq.0.) go to 10
23     do 5 it=1,itkill(ip)+1
24     if (pz(it,ip).lt.top .and. pz(it+1,ip).gt.top) then
25     mm=mm+1
26     rhit(mm)=0.5*(pr(it,ip)+pr(it+1,ip))
27     vhit(mm)=0.5*(vr(it,ip)+vr(it+1,ip))
28     whit(mm)=weight(ip)
29     c.... This spreads out the particle weight over 2*pi*r*(dr) at
30     c.... the location of the witness plate. The weight is now appropriate
31     c.... to an x-vx distribution for the calculation of emittance.
32     xwhit(mm)=weight(ip)/(2.0*pi*rhit(ip))
33     go to 10
34     endif
35
36     5 continue
37     10 continue
38
39     c
40     c.... Modified 6/91 (DAK): Calculation of x-vx edge emittance.
41     c.... Note that this is a kludge and will overestimate the emittance.
42     totw8 = 0.
43     do 11 ip=1,mm
44     totw8 = totw8 + whit(ip)
45     ip = mm+1
46     wght90 = totw8
47     12 ip = ip - 1
48     wght90 = wght90 - whit(ip)
49     if (wght90 .gt. (0.9*totw8)) go to 12
50     x90 = rhit(ip)
51     vx90 = vhit(ip)
52     write (6,14) x90,vx90
53     write (7,14) x90,vx90
54     14 format(" 90-percent x = ",1pe10.3," 90-percent vx = ",e10.3)
55
56     c
57     c.... Check.
58     write (6,15) mm
59     write (7,15) mm
60     15 format(i4," particles in phase space contour plot.")
61     if (mm.eq.0) return
62
63     c
64     c.... Initialize for extrema.
65     rmin= 1.e37
66     rmax=-1.e37
67     vmin= 1.e37
68     vmax=-1.e37
69
70     c
71     c.... Find extrema.
72     do 20 ip=1,mm

```

```

65      rmin=min(rhit(ip),rmin)
66      rmax=max(rhit(ip),rmax)
67      vmin=min(vhit(ip),vmin)
68      vmax=max(vhit(ip),vmax)
69      c
70      c.... Initialize for binning.
71      drbin=(rmax-rmin)/float(nbins-2)
72      dvbin=(vmax-vmin)/float(nbins-2)
73      rbinmin=rmin-0.5*drbin
74      vbinmin=vmin-0.5*dvbin
75      c
76      c.... Compute spatial and velocity bins.
77      do 30 i=1,nbins
78          rbin(i)=rbinmin+float(i-1)*drbin
79      30  vbin(i)=vbinmin+float(i-1)*dvbin
80      c
81      c.... Initialize contour array.
82      do 40 i=1,nbins
83          do 40 j=1,nbins
84      40  fbin(i,j)=0.
85      c
86      c.... Accumulate contour data.
87      do 50 ip=1,mm
88          ir=int((rhit(ip)-rbinmin)/drbin+0.001)+1
89          iv=int((vhit(ip)-vbinmin)/dvbin+0.001)+1
90          if (ir.le.0 .or. ir.ge.nbins .or.
91              iv.le.0 .or. iv.ge.nbins ) go to 50
92          fracr=(rhit(ip)-rbin(ir))/drbin
93          fracv=(vhit(ip)-vbin(iv))/dvbin
94          fbin(ir+1,iv+1)=fbin(ir+1,iv+1)+      fracr *      fracv *weight(ip)
95          fbin(ir ,iv )=fbin(ir ,iv )+(1.0-fracr)*(1.0-fracv)*weight(ip)
96          fbin(ir+1,iv )=fbin(ir+1,iv )+      fracr *(1.0-fracv)*weight(ip)
97          fbin(ir ,iv+1)=fbin(ir ,iv+1)+(1.0-fracr)*      fracv *weight(ip)
98      50  continue
99      c
100     c.... Label.
101     write (line,60) id,vmult
102     60  format("Vr-r phase space at top (",a4,"/",f5.1,"")
103     call set(0.0,1.0,0.0,1.0,0.0,1.0,0.0,1.0,1)
104     call wtstr(0.5,0.95,line,24,0,0)
105     c
106     c.... Set window and viewport.
107     call set(0.1,0.9,0.1,0.9,rbin(1),rbin(nbins),
108             vbin(1),vbin(nbins),1)
109     c
110     c.... Grid.
111     call labmod("(1pe10.3)","(1pe10.3)",0,0,10,10,0,0,0)
112     call periml(10,2,10,2)
113     c
114     c.... Contours.
115     call conrec(fbin,nbins,nbins,nbins,0.0,0.0,-10.0,-1,-1,0)
116     c
117     wsum =0.
118     rsum =0.
119     r2sum=0.
120     vrsum=0.
121     vr2sum=0.
122     vrrsum=0.
123     c
124     do 100 ip=1,mm
125     wsum =wsum +whit(ip)
126     rsum =rsum +whit(ip)*rhit(ip)
127     r2sum=r2sum +whit(ip)*rhit(ip)**2
128     vrsum =vrsum +whit(ip)*vhit(ip)

```

```
129      vr2sum=vr2sum+whit(ip)*vhit(ip)**2
130      100      vrrsum=vrrsum+whit(ip)*vhit(ip)*rhit(ip)
131      c
132      rsum =rsum /wsum
133      r2sum =r2sum /wsum
134      vrsum =vrsum /wsum
135      vr2sum=vr2sum/wsum
136      vrrsum=vrrsum/wsum
137      c
138      sigrr =r2sum-rsum**2
139      sigvv=vr2sum-vrsum**2
140      sigvr=vrrsum-vrsum*rsum
141      c
142      eps=4.0*sqrt(max(sigrr*siggv-sigvr**2,0.))
143      c
144      write (6,110) sigrr,siggv,sigvr,eps
145      write (7,110) sigrr,siggv,sigvr,eps
146      110      format("sigrr=",1pe10.3," siggv=",e10.3,
147      .          " sigvr=",e10.3," eps=",e10.3)
148      c
149      c..... Done.
150      return
151      end
```

```

1      subroutine pinit
2
3      c
4      c.... PINIT: Initializes particle emission sites.
5      c
6      include 'global.h'
7      data emax/0.,imax/0.,jmax/0/
8
9      c
10     do 100 i0=1,nximl
11
12     c
13     j0=nj1ff(i0)
14     i1=i0+1
15     j1=nj1ff(i1)
16
17     c
18     if      (j1.eq.j0) then
19         nsites=nsites+1
20         if (nsites.gt.maxsites) then
21             write (6,10)
22             format("Too many emission sites!")
23             stop
24         endif
25         sites(nsites,1)=i0
26         sites(nsites,2)=j0
27         eel=sqrt(exff(i0,j0)**2+eyff(i0,j0)**2)
28         if (eel.gt.emax) then
29             emax=eel
30             imax=i0
31             jmax=j0
32         endif
33     elseif (j1.gt.j0) then
34         do 20 jj=j0,j1-1
35             nsites=nsites+1
36             if (nsites.gt.maxsites) then
37                 write (6,10)
38                 stop
39             endif
40             sites(nsites,1)=i0
41             sites(nsites,2)=jj
42             eel=sqrt(exff(i0,jj)**2+eyff(i0,jj)**2)
43             if (eel.gt.emax) then
44                 emax=eel
45                 imax=i0
46                 jmax=jj
47             endif
48         20 continue
49     else
50         do 30 jj=j0-1,j1,-1
51             nsites=nsites+1
52             if (nsites.gt.maxsites) then
53                 write (6,10)
54                 stop
55             endif
56             sites(nsites,1)=i0
57             sites(nsites,2)=jj
58             eel=sqrt(exff(i0,jj)**2+eyff(i0,jj)**2)
59             if (eel.gt.emax) then
60                 emax=eel
61                 imax=i0
62                 jmax=jj
63             endif
64         30 continue
65     endif
66
67     c
68     100 continue
69     c

```

```
65      if (nsites.eq.0) then
66          write (6,110)
67      110      format("No emission sites!")
68          stop
69      else
70          write (6,120) nsites
71      120      format(i5," emission sites.")
72          write (6,130) 0.01*emax,imax,jmax
73          write (7,130) 0.01*emax,imax,jmax
74      130      format("Max ffE = ",lpe10.3," V/cm at (",i3,",",i3,")".)
75      endif
76      c
77      return
78      end
```

```

1      subroutine premit
2
3      c
4      c.... PREMIT: Calculates emission data.
5      c
6          include 'global.h'
7          data np/0/
8          data truemin/1.e37/,truemax/-1.e37/,wav/0./,curtot/0./
9      c
10     c.... Loop over sites.
11         do 500 isite=1,nsites
12     c
13     c.... Store indices.
14         i=sites(isite,1)
15         j=sites(isite,2)
16     c
17     c.... Fowler-Nordheim emission.
18         ee=0.01*sqrt(exff(i,j)**2+eyff(i,j)**2)
19         yy=3.795e-4*sqrt(ee)/phi
20         vyy=v(yy)
21         tyy=t(yy)
22         f1=1.541e-6*ee**2/(phi*tyy**2)
23         f2=exp(-6.831e7*(sqrt(phi))**3*vyy/ee)
24         fj=f1*f2
25         if (fj.eq.0.) go to 500
26         dtfn=aconst/fj
27         dtem=dtfn+dtxtal
28         fj=aconst/dtem
29         cur=1.e4*fj*pi*(xff(i)+xff(i+1))*dx(3)
30         w=abs(cur*dt/q)
31         if (debug) write (6,75) i,j,ee,yy,vyy,tyy,f1,f2,fj,cur,w
32     75     format(/"i=",i3," j=",i3," ee=",lpe10.3/
33         .      " yy=",e10.3," vyy=",e10.3," tyy=",e10.3/
34         .      " f1=",e10.3," f2=",e10.3," fj=",e10.3,
35         .      " cur=",e10.3," w=",e10.3)
36     c
37     c.... Accumulate data.
38         if (w.gt.0.) then
39             np=np+1
40             truemin=min(truemin,w)
41             truemax=max(truemax,w)
42             wav=wav+w
43             curtot=curtot+cur
44             if (abs(curtot).gt.1.e-3) then
45                 write (6,80)
46                 write (7,80)
47                 format("I .gt. 1.0e-3 A !")
48                 stop
49             endif
50         endif
51     c
52     c.... Next site.
53     500    continue
54     c
55     c.... Diagnostics.
56         if (np.eq.0) then
57             write (6,510)
58             write (7,510)
59             format("No particles to be emitted!")
60             stop
61         else
62             wav=wav/float(np)
63             write (6,520) np,truemin,truemax,wav,curtot
64             write (7,520) np,truemin,truemax,wav,curtot
65             format(/"Maximum of ",i4," particles to be emitted."/

```



```
65      .      "truemin=",lpe10.3," truemax=",e10.3," wav=",e10.3,  
66      .      " curtot=",e10.3)  
67      if (wmult.gt.0.) then  
68      wmin=wmult*wav  
69      write (6,530) wmin  
70      write (7,530) wmin  
71      530      format("wmin reset to ",lpe10.3)  
72      endif  
73      endif  
74      c  
75      c..... Done.  
76      return  
77      end
```

```

1      subroutine push(ip)
2      c
3      c.... PUSH: Particle pusher.
4      c
5      c.... Modified 7/1/91 (DAK): This is kludgy to get five particles per cell:
6      c.... emit(ip) counts up five particles, then push counts back five particles,
7      c.... then resets the ip counter back up by five...makes sense?
8      c
9      include 'global.h'
10     data ck/1.e-20/
11     c
12     c.... Set counter back by 5, etc.
13     ip = ip - 5
14     do 5000 nwptcl=1,5
15     ip = ip + 1
16     c
17     c.... Reset initial velocities to zero and xb-vector.
18     xb(1) = 0.
19     xb(2) = 0.
20     xb(3) = pz(1,ip)
21     xb(4) = pr(1,ip)
22     c
23     c.... Print.
24     c write (6,1) ip,xb(5)
25     1 format(/"Emitting particle ",i4," (w=",1pe10.3," ) ... ")
26     c
27     c.... Loop over timesteps.
28     idead = 0
29     do 1000 it=1,nt
30     if (idead .eq. 1) go to 1000
31     c
32     c.... Print.
33     c if (mod(it,100).eq.0 .and. .not.debug) write (6,5) it
34     5 format(i5," ... ",$)
35     c
36     c.... Which grid?
37     if (xb(4).ge.xl(3) .and. xb(4).le.xh(3) .and.
38     .   xb(3).ge.yl(3) .and. xb(3).le.yh(3)) then
39     ig=3
40     elseif (xb(4).ge.xl(2) .and. xb(4).le.xh(2) .and.
41     .   xb(3).ge.yl(2) .and. xb(3).le.yh(2)) then
42     ig=2
43     else
44     ig=1
45     endif
46     c
47     c.... Cell indices.
48     ix=int((xb(4)-xl(ig))/dx(ig)+0.501)
49     jx=int((xb(3)-yl(ig))/dy(ig)+0.501)
50     c
51     c.... Splitting coefficients.
52     xd=(xb(4)-0.5*(rr(ix,ig)+rr(ix+1,ig)))/dx(ig)
53     yd=(xb(3)-0.5*(zz(jx,ig)+zz(jx+1,ig)))/dy(ig)
54     if (abs(xd).gt.1.0 .or. abs(yd).gt.1.0) then
55     write (6,115) ip
56     115 format(/"Indexing problem: particle ",i4)
57     stop
58     endif
59     xm=1.0-xd
60     ym=1.0-yd
61     all=xm*ym
62     alr=xd*ym
63     aur=xd*yd
64     aul=xm*yd

```

```

65      c
66      c.... Interpolate fields (area-weighted for now).
67      pex=all*er(ix ,jx ,ig)+alr*er(ix+1,jx ,ig)+
68      .   aur*er(ix+1,jx+1,ig)+aul*er(ix ,jx+1,ig)
69      pey=all*ez(ix ,jx ,ig)+alr*ez(ix+1,jx ,ig)+
70      .   aur*ez(ix+1,jx+1,ig)+aul*ez(ix ,jx+1,ig)
71      c
72      c.... Debug.
73      if (debug) write (6,120) it,ig,ix,jx,xd,yd,pex,pey
74      120  format("*** it=",i4," ig=",i1," ix=",i3," jx=",i3/
75      . "xd=",1pe10.3," yd=",e10.3," pex=",e10.3," pey=",e10.3)
76      c
77      c.... Adaptive timestep.
78      dtdvel=xcell*min(abs(dx(ig)/(xb(2)+ck)),
79      .   abs(dy(ig)/(xb(1)+ck)))
80      dtdfor=min(sqrt(abs(xcell*dx(ig)/(qm*pex+ck))),
81      .   sqrt(abs(xcell*dy(ig)/(qm*pey+ck))))
82      dta=dtdvel*dtdfor/(dtdvel+dtdfor)
83      dtah=0.5*dta
84      c
85      c.... Debug.
86      if (debug) then
87      write (6,130) dtdvel,dtdfor,dta
88      130  format("dtdvel=",1pe10.3," dtdfor=",e10.3," dta=",e10.3)
89      write (6,131) xb(1),xb(2),xb(3),xb(4)
90      131  format("Before: ",4(1pe10.3,1x))
91      endif
92      c
93      c.... Advance velocities.
94      xb(1)=xb(1)+qm*pey*dta
95      xb(2)=xb(2)+qm*pex*dta
96      c
97      c.... Advance positions.
98      xb3h =xb(3)+xb(1)*dtah
99      xb(3)=xb(3)+xb(1)*dta
100     xb4h =xb(4)+xb(2)*dtah
101     xb(4)=xb(4)+xb(2)*dta
102     c
103     c.... Debug.
104     if (debug) write (6,132) xb(1),xb(2),xb(3),xb(4)
105     132  format("After: ",4(1pe10.3,1x))
106     c
107     c.... Save data.
108     pr(it+1,ip)=xb4h
109     pz(it+1,ip)=xb3h
110     vr(it+1,ip)=xb(2)
111     c
112     c.... Advanced mesh indices.
113     ix=int((xb(4)-xl(ig))/dx(ig)+0.001)+1
114     jx=int((xb(3)-yl(ig))/dy(ig)+0.001)+1
115     c
116     c.... Which grid?
117     if (xb(4).ge.xl(3) .and. xb(4).le.xh(3) .and.
118     .   xb(3).ge.yl(3) .and. xb(3).le.yh(3)) then
119         ig=3
120     elseif (xb(4).ge.xl(2) .and. xb(4).le.xh(2) .and.
121     .   xb(3).ge.yl(2) .and. xb(3).le.yh(2)) then
122         ig=2
123     else
124         ig=1
125     endif
126     c
127     c.... Kill particle?
128     if (xb(3).le.zz(njj(ix,ig),ig) .or.

```

```
129      .   xb(3).le.yl(1) .or. xb(3).ge.yh(1) .or.  
130      .   xb(4).le.xl(1) .or. xb(4).ge.xh(1)      ) then  
131      weight(ip)=weight(ip)*dta/dt  
132      itkill(ip)=it  
133      c   write (6,300) it,ig,ix,xb(3),jx,xb(4)  
134      300  format(/"Particle killed: it=",i4," ig=",i1/  
135      .   " ix=",i3," xb3=",1pe10.3," jx=",i3," xb4=",e10.3)  
136      c   write (6,310) njj(ix,ig),zz(njj(ix,ig),ig)  
137      310  format(" structure index=",i3," structure=",1pe10.3)  
138      idead = 1  
139      endif  
140      c  
141      c.... Next timestep.  
142      1000 continue  
143      c  
144      if (idead .eq. 1) go to 4000  
145      c  
146      c.... Particle still alive.  
147      weight(ip)=weight(ip)*dta/dt  
148      itkill(ip)=nt  
149      c  
150      c.... Diagnostic.  
151      write (6,2000) ip  
152      2000 format(/"Warning: particle ",i5," still alive.")  
153      write (6,2010) ix,xb(3),jx,xb(4)  
154      2010 format(" ix=",i3," xb3=",1pe10.3," jx=",i3," xb4=",e10.3)  
155      c  
156      4000 continue  
157      5000 continue  
158      c  
159      c.... Done.  
160      return  
161      end
```

```
1      subroutine readhdr
2      c
3      c.... READHDR: Reads/rescales FEAT file header.
4      c
5      include 'global.h'
6      character*17 line1
7      c
8      c.... Read header.
9      c      read (22) line1,idum,idum,xl,xh,y1,yh,xmas,ymas
10     read (22) line1,ntype,xl,xh,y1,yh,xmas,ymas,radc,
11     .      height,width,angle
12     c
13     c.... Rescale.
14     do 10 i=1,3
15     xl(i)=1.e-6*xl(i)
16     xh(i)=1.e-6*xh(i)
17     yl(i)=1.e-6*yl(i)
18     10  yh(i)=1.e-6*yh(i)
19     c
20     c.... Send message.
21     write (6,20) line1
22     20  format("File format is: ",a)
23     write (6,30) nxi,neta,xl,xh,y1,yh
24     write (7,30) nxi,neta,xl,xh,y1,yh
25     30  format("nxi=",i5," neta=",i5/
26     .      "xl=",1p,3e9.2," xh=",3e9.2/
27     .      "yl=",3e9.2," yh=",3e9.2)
28     c
29     c.... Done.
30     return
31     end
```

```
1      subroutine readmesh(mode)
2      c
3      c.... READMESH: Reads/rescales FEAT mesh from file.
4      c
5          include 'global.h'
6          character*4 mode
7      c
8      c.... Read data.
9          read (22) (x (n),n=1,nxi)
10         read (22) (y (n),n=1,neta)
11         read (22) (xf (n),n=1,nxi)
12         read (22) (yf (n),n=1,neta)
13         read (22) (xff(n),n=1,nxi)
14         read (22) (yff(n),n=1,neta)
15      c
16      c.... Rescale.
17          do 10 n=1,nxi
18              x (n)=1.e-6*x (n)
19              xf (n)=1.e-6*xf (n)
20          10  xff(n)=1.e-6*xff(n)
21              do 20 n=1,neta
22                  y (n)=1.e-6*y (n)
23                  yf (n)=1.e-6*yf (n)
24          20  yff(n)=1.e-6*yff(n)
25      c
26      c.... Done.
27          return
28      end
```

```
1      subroutine readsoln
2      c
3      c.... READSOLN: Reads/rescales FEAT solution previously written out.
4      c
5      include 'global.h'
6      c
7      c.... Read data.
8      c
9      write (6,5) "Skipping phi."
10     format(a)
11     read (22) (vex(n),n=1,nn)
12     read (22) (vex(n),n=1,nn)
13     read (22) (vex(n),n=1,nn)
14     c
15     write (6,5) "Reading Ex."
16     read (22) (vex (n),n=1,nnp)
17     read (22) (vexf (n),n=1,nnp)
18     read (22) (vexff(n),n=1,nnp)
19     c
20     write (6,5) "Reading Ey."
21     read (22) (vey (n),n=1,nnp)
22     read (22) (veyf (n),n=1,nnp)
23     read (22) (veyff(n),n=1,nnp)
24     c
25     write (6,5) "Reading boundary mask."
26     read (22) (nj1 (n),n=1,nxi)
27     read (22) (nj1f (n),n=1,nxi)
28     read (22) (nj1ff(n),n=1,nxi)
29     c
30     c.... Send message.
31     write (6,10)
32     10 format("RECADI dump read.")
33     c
34     c.... Rescale.
35     vv=1.e6*vmult
36     do 20 n=1,nnp
37     vex (n)=vv*vex (n)
38     vexf (n)=vv*vexf (n)
39     vexff(n)=vv*vexff(n)
40     vey (n)=vv*vey (n)
41     veyf (n)=vv*veyf (n)
42     20 veyff(n)=vv*veyff(n)
43     c
44     c.... Send message.
45     write (6,30)
46     30 format("Data rescaled.")
47     c
48     c.... Done.
49     return
50     end
```

```

1      subroutine scatplot(ax,ay,nt,np,itkill,xmin,xmax,ymin,ymax,
2      .                      ig,label,lbdry)
3
4      c
5      c.... SCATPLOT: Scatter plots.
6      c
7      dimension ax(nt,np),ay(nt,np),itkill(1)
8      character(*) label
9      logical lbdry
10
11     c
12     c.... Find extrema.
13     c
14     xxmin=xmin
15     xxmax=xmax
16
17     c
18     if (xxmin.eq.xxmax) then
19         xxmin= 1.0e37
20         xxmax=-1.0e37
21         do 10 ip=1,np
22             do 10 it=1,itkill(ip)+1
23                 xxmin=min(xxmin,ax(it,ip))
24                 xxmax=max(xxmax,ax(it,ip))
25             10
26         endif
27     c
28     yymin=ymin
29     yymax=ymax
30
31     c
32     if (yymin.eq.yymax) then
33         yymin= 1.0e37
34         yymax=-1.0e37
35         do 20 ip=1,np
36             do 20 it=1,itkill(ip)+1
37                 yymin=min(yymin,ay(it,ip))
38                 yymax=max(yymax,ay(it,ip))
39             20
40         endif
41     c
42     c.... Label.
43     c
44     ilen=1
45     do 30 i=len(label),1,-1
46         if (label(i:i).ne." ") then
47             ilen=i
48             go to 40
49         endif
50     30 continue
51     c
52     call set(0.0,1.0,0.0,1.0,0.0,1.0,0.0,1.0,1)
53     call wtstr(0.5,0.95,label(1:ilen),24,0,0)
54
55     c
56     c.... Cathode boundary.
57     if (lbdry) call maskplot(ig)
58
59     c
60     c.... Viewport and window.
61     call set(0.1,0.9,0.1,0.9,xxmin,xxmax,yymin,yymax,1)
62
63     c
64     c.... Grid.
65     call labmod("(1pe10.3)","(1pe10.3)",0,0,10,10,0,0,0)
66     call periml(10,2,10,2)
67
68     c
69     c.... Plot.
70     do 50 ip=1,np
71         call points(ax(1,ip),ay(1,ip),itkill(ip)+1,0,0)
72     50
73
74     c
75     c.... New frame.
76     call frame

```



```
65      c
66      c..... Done.
67      return
68      end
```

```
1      subroutine smooth
2      c
3      c.... SMOOTH: Smooths fields at emission surface.
4      c
5      include 'global.h'
6      c
7      c.... Return if no smoothing.
8      if (nsmooth.le.0) return
9      c
10     c.... Smooth <nsmooth> times.
11     do 100 m=1,nsmooth
12     c
13     c.... Copy to scratch.
14     do 10 i=1,nsites
15         work(i,1)=exff(sites(i,1),sites(i,2))
16     10  work(i,2)=eyff(sites(i,1),sites(i,2))
17     c
18     c.... Left endpoint.
19     exff(sites(1,1),sites(1,2))=
20     . 0.25*(3.0*work(1,1)+work(2,1))
21     eyff(sites(1,1),sites(1,2))=
22     . 0.25*(3.0*work(1,2)+work(2,2))
23     c
24     c.... Interior.
25     do 20 i=2,nsites-1
26         exff(sites(i,1),sites(i,2))=
27         . 0.25*(work(i-1,1)+2.0*work(i,1)+work(i+1,1))
28     20  eyff(sites(i,1),sites(i,2))=
29         . 0.25*(work(i-1,2)+2.0*work(i,2)+work(i+1,2))
30     c
31     c.... Right endpoint.
32     exff(sites(nsites,1),sites(nsites,2))=
33     . 0.25*(3.0*work(nsites,1)+work(nsites-1,1))
34     eyff(sites(nsites,1),sites(nsites,2))=
35     . 0.25*(3.0*work(nsites,2)+work(nsites-1,2))
36     c
37     c.... Next iteration.
38     100 continue
39     c
40     c.... Done.
41     return
42     end
```

```

1      function t(y)
2
3      c
4      c.... T: Fowler-Nordheim t(y).
5      c
6      real k0,k1,k2,k3,k4,k5
7      real l0,l1,l2,l3,l4,l5
8
9      c
10     data c0/ 1.000000000/
11     data c1/ 0.443251415/
12     data c2/ 0.062606012/
13     data c3/ 0.047573836/
14     data c4/ 0.017365064/
15
16     c
17     data d1/ 0.249983683/
18     data d2/ 0.092001800/
19     data d3/ 0.040696975/
20     data d4/ 0.005264496/
21
22     c
23     data k0/-1.449186516/
24     data k1/ 0.955487208/
25     data k2/ 0.437823717/
26     data k3/ 0.043249154/
27     data k4/ 0.011362799/
28     data k5/ 0.001263634/
29
30     c
31     data l0/-0.584130150/
32     data l1/-0.387793273/
33     data l2/ 0.233321796/
34     data l3/ 0.043868437/
35     data l4/ 0.007265463/
36     data l5/ 0.000381945/
37
38     c
39     if (y.lt.1.0) then
40         s=sqrt(1.0-y**2)
41         eta=(1.0-s)/(1.0+s)
42         x1=alog(1.0/eta)
43         x=      c0      +
44         .      eta      *(c1+d1*x1)+
45         .      eta**2*(c2+d2*x1)+
46         .      eta**3*(c3+d3*x1)+
47         .      eta**4*(c4+d4*x1)
48         t=x/(sqrt(1.0+eta))
49     else
50         x11=alog(2.0*y/(y+1.0))
51         x12=y/(y+1.0)
52         x=      k1+x11*l1 -x12*l0      +
53         .      (2.0*(k2+x11*l2)-x12*l1)/y      +
54         .      (3.0*(k3+x11*l3)-x12*l2)/y**2+
55         .      (4.0*(k4+x11*l4)-x12*l3)/y**3+
56         .      (5.0*(k5+x11*l5)-x12*l4)/y**4+
57         .      (      -x12*l5)/y**5
58         t=sqrt(2.0*y)*x/3.0
59     endif
60
61     c
62     return
63     end

```

```

1      function v(y)
2
3      c
4      c.... V: Fowler-Nordheim v(y).
5      c
6      real k0,k1,k2,k3,k4,k5
7      real l0,l1,l2,l3,l4,l5
8
9      c
10     data a0/ 1.000000000/
11     data a1/-1.329337308/
12     data a2/ 0.312530542/
13     data a3/ 0.038378000/
14     data a4/-0.009912374/
15     data a5/-0.011658860/
16
17     c
18     data b1/-0.750016317/
19     data b2/ 0.092013612/
20     data b3/-0.004906196/
21     data b4/-0.020665635/
22     data b5/-0.003571244/
23
24     c
25     data k0/-1.449186516/
26     data k1/ 0.955487208/
27     data k2/ 0.437823717/
28     data k3/ 0.043249154/
29     data k4/ 0.011362799/
30     data k5/ 0.001263634/
31
32     c
33     data l0/-0.584130150/
34     data l1/-0.387793273/
35     data l2/ 0.233321796/
36     data l3/ 0.043868437/
37     data l4/ 0.007265463/
38     data l5/ 0.000381945/
39
40     c
41     if (y.lt.1.0) then
42         s=sqrt(1.0-y**2)
43         eta=(1.0-s)/(1.0+s)
44         xl=alog(1.0/eta)
45         x=      a0      +
46         .      eta      *(a1+b1*xl)+
47         .      eta**2*(a2+b2*xl)+
48         .      eta**3*(a3+b3*xl)+
49         .      eta**4*(a4+b4*xl)+
50         .      eta**5*(a5+b5*xl)
51         v=x/(sqrt(1.0+eta))**3
52     else
53         xl=alog(2.0*y/(y+1.0))
54         x=y*(k0+xl*l0)      +
55         .      (k1+xl*l1)      +
56         .      (k2+xl*l2)/y      +
57         .      (k3+xl*l3)/y**2+
58         .      (k4+xl*l4)/y**3+
59         .      (k5+xl*l5)/y**4
60         v=sqrt(0.5*y)*x
61     endif
62
63     c
64     return
65     end

```

Appendix C

Final Report - GTEL

**Semiconductor-Metal Eutectic Composites
for Cold Cathode Applications**

**SEMICONDUCTOR-METAL EUTECTIC COMPOSITES
FOR COLD CATHODE APPLICATIONS**

Contract No. 21-910004-61

Prime Contract No. N00014-90-C-02118

Q.V. Nguyen and B.M. Ditchek

**Submitted to
Dr. Douglas A. Kirkpatrick
Science Application International Corporation
1710 Goodridge Drive
McLean, VA 22101**

**GTE Laboratories Incorporated
40 Sylvan Road
Waltham, MA 02254**

TABLE OF CONTENTS

Section		Page
1	Introduction	1
2	Historical Perspective and Background	3
3	SME Material Growth and Cold Cathode Fabrication	5
	3.1 SME Material Growth	5
	3.2 Etching Process	8
	3.3 Metallization	14
	3.4 Patterned Contacts	16
4	Fabrication of Microtubule Based on SME Materials	19
5	Cathode Characterization	21
	5.1 Si-TaSi ₂ Cathodes	21
	5.2 Si-WSi ₂ Cathodes	22
	5.3 W Microtubes	24
6	Conclusions	27
7	References	29

LIST OF FIGURES

Figure		Page
1	Photograph of a typical single-crystal (111) matrix Si-TaSi ₂ eutectic composite.	6
2	A transverse section of a Si-TaSi ₂ eutectic composite. Note the cellular arrangement of the TaSi ₂ rods.	6
3	Counts of TaSi ₂ rods in 85 μm square frame vs. position for wafers grown with seed and crucible rotation of (a) (+6, -6) rpm and (b) (0, 12) rpm, respectively.	7
4	Scanning electron micrographs of Si-based eutectics. The Si phase has been etched back to reveal the silicide phase.	9
5	(a), (b), and (c): Surface morphology of cathode wafers etched with different compositions of etchant.	10
6	Surface morphology of cathode surface etched with (1:10:3) solution at 5°C.	11
7	(a) Etching of Si with (1:10:3) solution at 5°C and (b) etching of TaSi ₂ with (1:10:3) solution at 5°C.	12
8	1-2 μm height sharp-pointed TaSi ₂ tips revealed by chemical etching.	13
9	4-5 μm height sharp-pointed TaSi ₂ tips revealed by chemical etching.	13
10	7-8 μm height sharp-pointed TaSi ₂ tips revealed by chemical etching.	14
11	Etching of Si with NaOCl-NaOH.	15
12	20 μm height sharp-pointed TaSi ₂ tips revealed by chemical etching.	15
13	Schematic diagram of patterned contact on Si-TaSi ₂ cold cathode.	17

14	SEM of the completed microtube emitters.	20
15	I-V characteristics of TaSi ₂ cold cathodes.	22
16	Surface morphology of etched WSi ₂ cold cathodes.	23
17	I-V characteristics of WSi ₂ cold cathodes.	23
18	I-V characteristics of cathode with microtube emitters.	25

1. INTRODUCTION

Semiconductor-metal eutectic (SME) composite materials are two phase materials prepared by the directional solidification of a melt through its liquid-solid transition temperature, called eutectic temperature. If the volume fraction of the metallic phase is low, this unidirectional solidification leads to the simultaneous separation of the phases into an aligned array of rod-shaped metallic fibers in the matrix of a semiconductor material. In the Si-TaSi₂ case, the directional solidification of the eutectic composition results in composites with over one million metallic TaSi₂ rods per square centimeter, each with a diameter of 1 μm embedded in the Si matrix.

Eutectic composites, because of their multipin structure, have long been considered for application as cold cathode emitters.^{1,2} They include refractory metal carbides in a NiCr matrix such as TaC, TiC, VC, etc., and oxide-metal composites such as UO₂-W, ZrO₂-W, etc. Among these materials, eutectic cold cathodes of tungsten pins in a matrix of uranium oxide have been the subject of the most extensive research. These eutectic cathodes tested in ultrahigh voltage yielded current densities of up to 20 A/cm² under dc conditions using small-area arrays with a density 10⁷ rods/cm². With larger arrays, current densities of 1.2 A/cm² and gross output currents of 20 mA were obtained.²

Multipin cold cathodes have also been fabricated using lithographic techniques. Spindt et al. prepared an array of molybdenum cones on a silicon wafer in a low-voltage emitter configuration.³ Initially the largest arrays were fabricated by wet chemical processes with 5000 pins at a package density of 6×10^5 pins/cm². When tested at high-voltage conditions, this multipin cathode achieved current densities of 8 A/cm² and maximum gross current of 5 mA in dc operation. Recently, with an improvement in fabricating process by using RIE instead of wet chemical etching to prevent the undercut of the SiO₂ layer, the emitter density of $1.5 \times 10^7/\text{cm}^2$ was obtained.⁴ An emission current density of up to 1000 A/cm² has been achieved with small arrays of tips, and 100 mA total emission was commonly produced with arrays 1 mm in diameter containing 10,000 tips. However, the inability of Spindt et al. to prepare uniform larger arrays by this process, and the thermal and mechanical instability of these structures, has limited the application of this approach to commercial products.

Thus, although both approaches developed cold cathodes that yielded attractive current densities, neither approach resulted in large gross currents.

Semiconductor-metal eutectic composite cold cathode materials are in many ways a hybrid between the Spindt-type photolithographically prepared cathode structure and the eutectic composite structures. SME materials, particularly those with a Si matrix, blend the best properties of both cathode groups. Like the other eutectic materials, the pins, fabricated without lithographic processing, are long and extend through the wafer. Also areas up to 45 cm^2 are expected using standard crystal growth processes. Since the matrix is single-crystal Si, it can be etched uniformly, so the emitter height can be accurately controlled. Furthermore, the Si-based eutectic is amenable to many processing procedures, such as lithography, thermal oxidation, metallization, and silicidation. Most importantly, the possibility of the epitaxial growth of high-quality Si layers on Si-TaSi₂ substrates holds the promise of integrability of these field emission array cathodes with conventional Si technology.⁵ The objective of this study has been to develop cold cathodes based on SME materials.

In this final report, our progress toward the development of SME materials for cold cathode application will be reviewed.

2. HISTORICAL PERSPECTIVE AND BACKGROUND

Field emission array (FEA) cathodes make use of the quantum mechanical tunneling of electrons from a metal surface to the vacuum. This process increases exponentially with the magnitude of the surface electric field, so sharp emitter tips which concentrate the field in a small area are employed. The emission process is described by the tunneling model of Fowler and Nordheim.⁶ This model relates the field emission current density, J , to the electric field at the surface, E , by

$$J = (aE^2/\phi t^2(y)) \exp(-b\phi^{3/2}f(y)/E), \quad (1)$$

where ϕ is the work function of the emitting surface, a and b are constants, and $f(y)$ and $t(y)$ are slowly varying functions of the field. In practice, the gross emission current, I , and the potential difference between the anode and cathode, V , are measured. One can substitute $J = I/A$ and $E = \beta V$ in Eq. (1), where A is the emitting area and β is the geometrical field enhancement factor at the emitting surface. β increases with decreasing radius of curvature. This gives

$$I = (Aa\beta V^2/\phi t^2(y)) \exp(-b\phi^{3/2}f(y)/\beta V). \quad (2)$$

The Fowler-Nordheim plot of $\log(I/V^2)$ as a function of V^{-1} allows the determination of ϕ or β if one of these is known.

From a practical standpoint, increased emission current density can be obtained by either increasing A or β , or decreasing ϕ . In multi-emitter arrays, it can also be enhanced by increasing the area tip density and uniformity, although when the pins become too dense, β is reduced.

In recent years, there has been substantial progress toward understanding the factors that affect the field concentration at the tips in FEA structures. The field enhancement factor, β , is related to the product of four primary factors:

- The radius of curvature of the exposed tip.
- The atomic scale surface roughness of the tip
- The height and aspect ratio of the exposed pins.
- The field reduction due to the presence of other pins.

In total, the four factors are expected to yield an enhancement factor of about 10^4 for a tip radius of curvature of 20 nm and interpin spacings and heights of about 5 μm .⁷

In historical perspective, the experimental study of field emission was very active with attempts to confirm the Fowler-Nordheim theory using various experimental techniques in the 1930s.^{8,9} From that time, the greatest achievement came from Spindt's work at Stanford Research Institute.³ His works led to the paper in 1976, which has been cited since by nearly every author in the field as evidence of the ability to fabricate devices of this type. However he and others have made only incremental improvements in the fabrication technology for field emission arrays. The microfabrication process required has not been reproducibly controlled to allow a commercial product based on this technology to be achieved.

Since 1990, work on ungated FEA cathodes using Si-based SME material has been carried out under a two-year DARPA-sponsored program, with the goal of obtaining the field emission array cathodes with macroscopic current densities greater than 100 A/cm² and electron beam brightness greater than 10⁶ A/cm² rad².

3. SME MATERIAL GROWTH AND COLD CATHODE FABRICATION

3.1 SME MATERIAL GROWTH

Si-TaSi₂ SME composite is grown from the melt by the Czochralski technique. The charge, composed of phosphorus-doped Wacker float zone Si with a carrier concentration in the mid 10^{14} cm⁻³ or less and Gallard-Schlesinger float zone Ta of 99.996% purity was melted in a quartz crucible surrounded by a graphite susceptor using RF heating. The Si seed was produced by growing from the same system. During growth, ultra-high-purity Ar was flowed through the quartz chamber. The seed and the crucible rotation can be independently controlled. After soaking period of 3 hr at a temperature of 1600°C, the melt temperature is reduced to ~1450°C and a Si seed is lowered and contacted with the melt, given time to thermally equilibrate, and then pulled up at the fixed rate of 20 cm/hr. The composite boule solidifies as the seed is pulled. This process of directional solidification yields the eutectic rod-like microstructure with the rods oriented along the growth direction.

As discussed below, to obtain reproducible smooth surface and the uniform pin height for cold cathode applications, a single crystalline Si matrix is required. Growth of a single-crystal matrix eutectic depends primarily on using the exact eutectic composition and minimizing impurities. The composition control is quite difficult due to the loss of Si as SiO during the soaking period and the melt back of the quartz crucible and the seed. However, with experience in proper balancing of the two effects, composite boules with a single-crystal matrix can be routinely grown. A photograph of a typical single-crystal matrix (111) boule is shown in Figure 1. The eutectic microstructure in a typical transverse section is shown in Figure 2. The figure shows that the rods in the eutectic are neither arranged in a regular array nor distributed in a strictly random pattern. They exhibit a kind of cellular structure. The interrod spacing in the cell walls is less than the average interrod spacing. Although this cellular structure of the rod distribution may have some effect on the emission uniformity under microscale, their effect on macroscale emission uniformity may be neglected because they are distributed nearly uniform across the wafers.

In the Czochralski crystal growth, thermal and forced convection currents are always produced by the seed/crucible rotation and the asymmetrical thermal distribution in the melt. This will cause temperature fluctuations and growth rate variations at the solid-liquid interface. As a result, the rod density distribution becomes nonuniform. To investigate this phenomena, the rod density distribution of the boules grown under different conditions was analyzed using the integrated

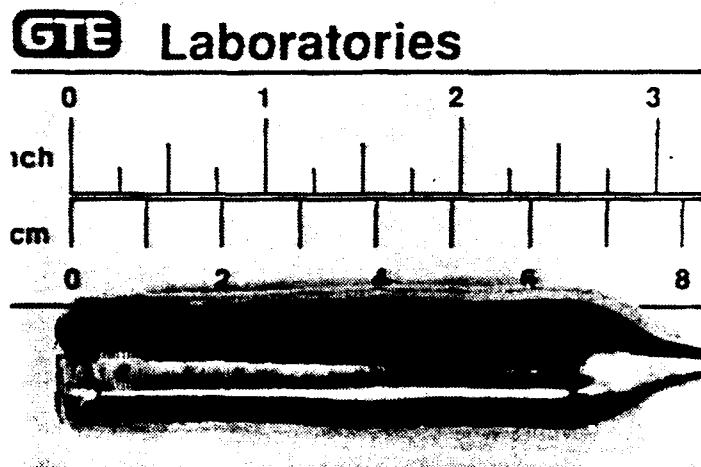


Figure 1. Photograph of a typical single-crystal (111) matrix Si-TaSi₂ eutectic composite.

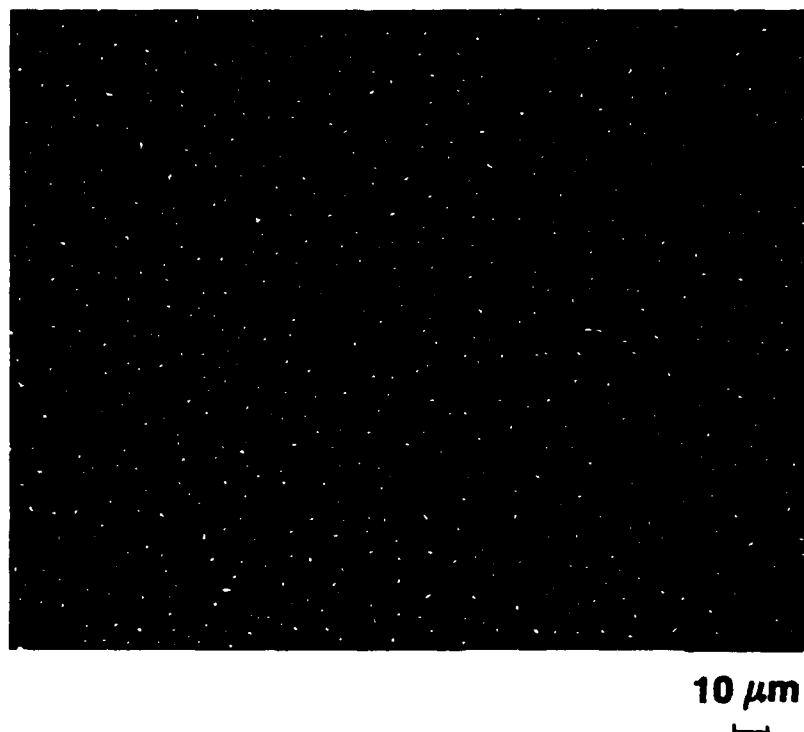


Figure 2. A transverse section of a Si-TaSi₂ eutectic composite. Note the cellular arrangement of the TaSi₂ rods.

SEM-Image analysis instrumentation. This consists of a JEOL JSM-840II SEM coupled with a Tracor Northern 5402/8502 Image Analysis system. The system was used primarily to count the number of rods in a given area, typically $85\text{ }\mu\text{m} \times 85\text{ }\mu\text{m}$.

Figures 3(a) and (b) show the counts of TaSi_2 rods in $85\text{ }\mu\text{m}$ square frames vs. the position for two wafers grown with seed/crucible counterrotation at 6 rpm and crucible rotation only at 12 rpm, respectively. It was found that by eliminating rotation of the seed, smaller variations of rod density were obtained. A wafer from a portion of a boule grown without seed rotation and crucible rotation of 12 rpm exhibited a mean rod count of 127.0 with a standard deviation of 6.85, compared to one grown with seed rotation of 6 rpm and crucible counterrotation of -6 rpm, which yielded a mean and standard deviation of 127.6 and 8.40, respectively. This indicates a clear decrease in the lateral variation in rod density of up to 30%.¹⁰ The effect of this improvement in the rod density distribution on the emission uniformity may be realized when comparing the emission current density of the cathodes fabricated from boules grown using both growth conditions or testing the emission at microscale, which is not available at this time.

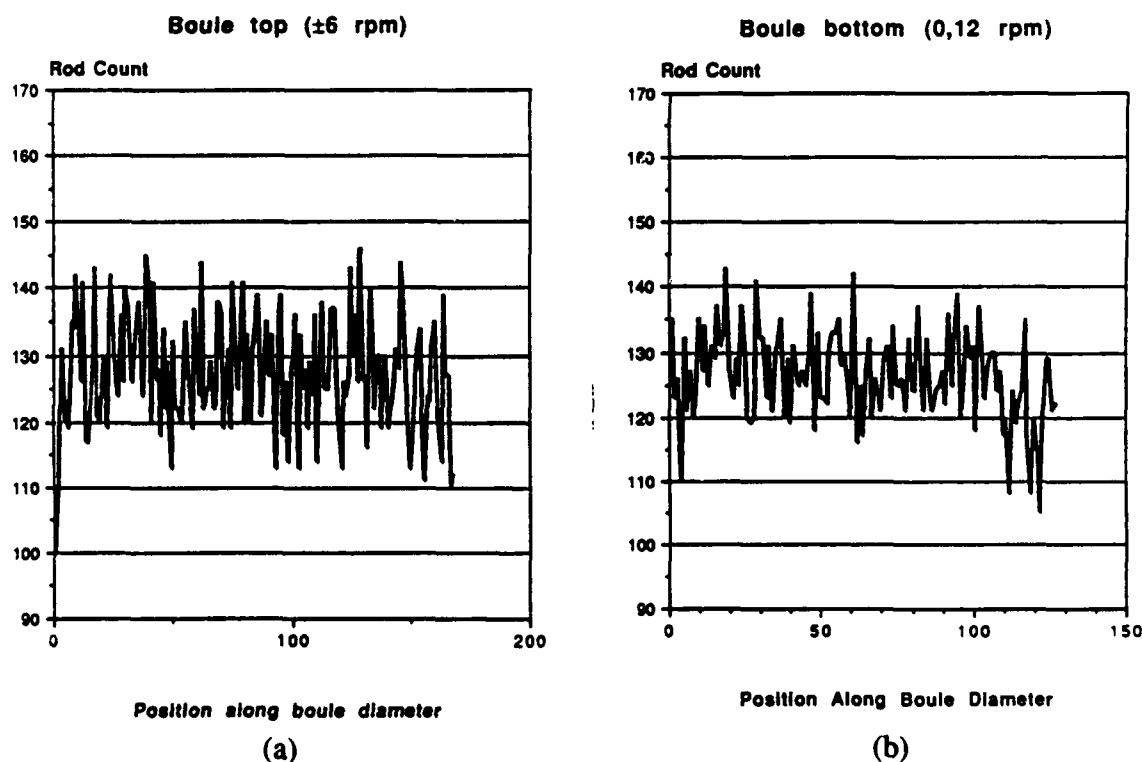


Figure 3. Counts of TaSi_2 rods in $85\text{ }\mu\text{m}$ square frame vs. position for wafers grown with seed and crucible rotation of (a) $(+6, -6)$ rpm and (b) $(0, 12)$ rpm, respectively.

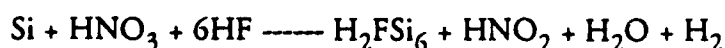
Appendix 1 is a summary of cathode wafers which were fabricated during the course of this study. Some wafers were tested at GTE Laboratories, and most of them were sent to Science Application International Corporation (SAIC) for characterization. All cathodes were fabricated from 8 boules. Boules TaSi₂-40, 47, and 84 were grown at seed and crucible counterrotation at 6 rpm; boules TaSi₂-86, 87, 90, 91, and 92 were grown with improved conditions, i.e., crucible rotation only at 12 rpm. Boules 40 and 47 have a p-type Si matrix, while all the rest have n-type. Boule TaSi₂-91 has a polycrystalline Si matrix grown at 30 cm/hr instead of 20 cm/hr to increase rod density.

In addition to Si-TaSi₂ eutectic, there exist many other Si-based eutectic composites. They included WSi₂, CoSi₂, ZrSi₂, CrSi₂, and NbSi₂. The microstructure of these composites grown from the melt at 10 cm/hr is shown in Figure 4. From this microphotograph, TaSi₂ and WSi₂ appeared to have separated silicide rods, which is important for cold cathode applications. However, many rods of WSi₂ have blade a shape rather than a rounded one and appear to be more irregular than that of TaSi₂. Although TaSi₂ was chosen for most of our experiments, WSi₂ cold cathodes have also been fabricated and tested, and the results will be discussed in Section 5.

3.2 ETCHING PROCESS

The first and most important step in fabricating the cold cathodes from the Si-based eutectic composite is etching to reveal silicide rods with sharp-pointed tips and with controlled height. The etching process was based on wet chemical techniques using a modified CF₄ solution, which is composed of hydrofluoric, nitric, and acetic acid. In general, the chemical reaction of this solution with Si is as follows:

- Si is oxidized by nitric acid to form SiO₂.
- Then the oxidation products are reacted with hydrofluoric acid to form soluble complex H₂FSi₆. All of these processes occur within a single etch mixture, resulting in the overall reaction¹¹



Acetic acid is used as a diluent. Although water can also be used for this purpose, acetic acid is preferred because using this diluent results in less dissociation of the nitric acid and hence in a higher concentration of the undissociated species. This preserves the oxidizing power of the nitric

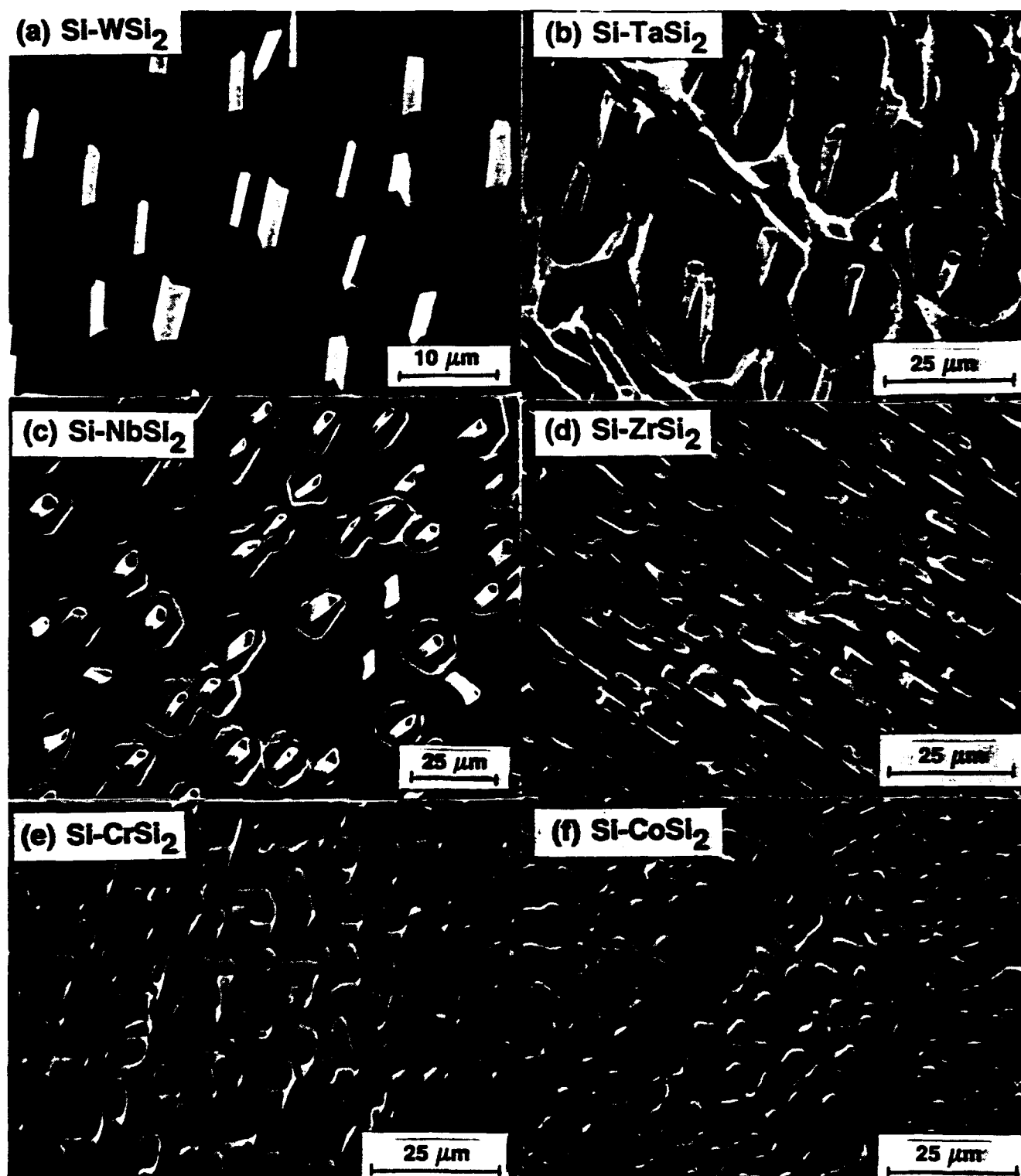


Figure 4. Scanning electron micrographs of Si-based eutectics. The Si phase has been etched back to reveal the silicide phase.

acid for a wider range of dilution than if water is used. Therefore the oxidizing power of the etchant tends to remain relatively constant during its operating life. The etching rate will depend on the removal reaction of SiO_2 with hydrofluoric acid and hence depend directly on hydrofluoric acid concentration in the etchant.

For cold cathode application, the etching process used to reveal silicide rods has to produce a smooth surface and uniform emitter height. First, a number of etchants with different composition were used to etch the composite wafers. Wafers were cut from the boule perpendicular to the growth axis, chemically polished to get a mirror-like surface, and then etched in solutions of (3:HF + 5:HNO₃ + 3:CH₃COOH), (3:HF + 10:HNO₃ + 3:CH₃COOH) and (1:HF + 10:HNO₃ + 3:CH₃COOH) for 20 s, 1 min, and 15 min at room temperature respectively. Surface morphology of the etched wafers is shown in Figure 5(a), (b), and (c). From these photographs it appears that increasing the HF/HNO₃ concentration ratio from 0.1 to 0.6 causes deep etch pits to develop on the cathode surface. Solutions with a lower HF/HNO₃ concentration ratio improves the surface smoothness. However, significantly decreasing this ratio causes the cathode surface to heavily oxidize and become very cloudy. The solution of (1:HF + 10:HNO₃ + 3:CH₃COOH) is an optimized etchant for surface smoothness, and is hereafter referred to as the (1:10:3) solution.

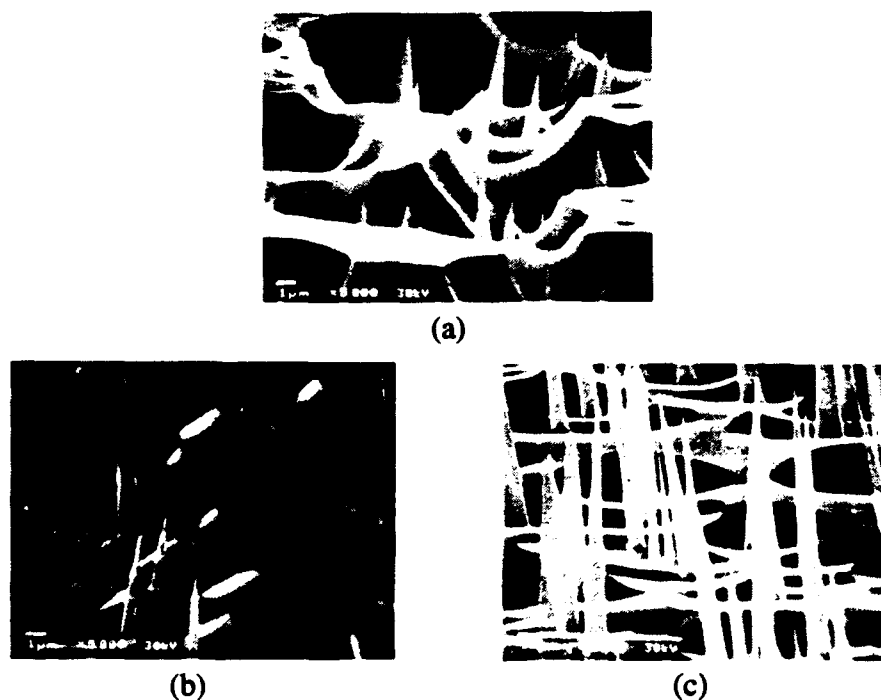


Figure 5. (a), (b), and (c): Surface morphology of cathode wafers etched with different compositions of etchant.

Further experiments were performed to investigate the influence of the etching temperature on the surface morphology. Wafers were etched with the optimized solution (1:10:3) at room temperature and at 5°C (mixing the solution in the ice bath for 15 min before etch) for 15 min and 20 min, respectively. Figure 6 and Figure 5(c) show that the surface morphology of the wafer etched at 5°C is completely smooth, without any shallow pits, compared with the wafer etched at room temperature.

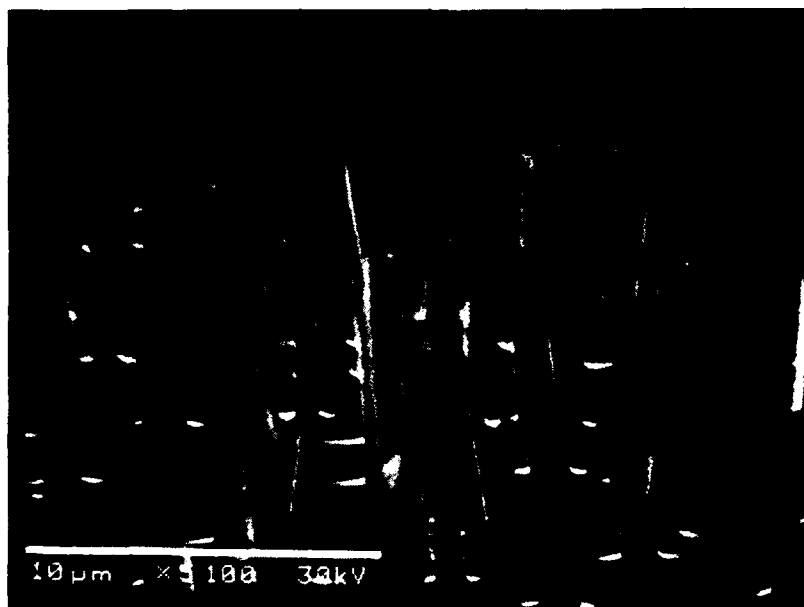


Figure 6. Surface morphology of cathode surface etched with (1:10:3) solution at 5°C.

The (1:10:3) solution also attacks the silicide, but at a much lower rate. Figures 7(a) and (b) show the etching rate of (1:10:3) solution at 5°C on Si and TaSi₂, respectively. From these results, the etching rate for Si is nearly 20 times higher than that for TaSi₂, which is about 25 nm/min. The average TaSi₂ rod diameter is about 1 μm, so to obtain the sharp-pointed emitter tips, etching time of 20 min is required to etch half diameter of the rods, which results in the TaSi₂ rod height of 10 μm.

In order to get different heights of sharp-pointed TaSi₂ emitter tips, we cannot simply reduce the etching time because with less than 20 min etching, the TaSi₂ rods are still blunt. Therefore different etchants have to be developed. To obtain less than 10 μm emitter tip height, etchants with selectivity ratios between Si and TaSi₂ smaller than 20 is necessary. It is known that the addition of sulfuric acid will accelerate the etching rate of TaSi₂, thus a number of etchants with

various concentrations of sulfuric acid were developed to obtain different rod heights of less than 10 μm . It is also worthwhile to note that due to the exothermic reaction of sulfuric acid with hydrofluoric and nitric acid, the etchant solution temperature and as the etching rate can be reduced with the mixing time. A summary of these etchants follows:

- (1:HF + 10:HNO₃ + 3:H₂SO₄) mixing 1 min at room temperature and etch for 20 s to obtain 1–2 μm height, as shown in Figure 8.
- (1:HF + 10:HNO₃ + 2:H₂SO₄) mixing 1 min and etch 2 min to obtain 4–5 μm height, as shown in Figure 9.
- (1:HF + 10:HNO₃ + 2:H₂SO₄) mixing 10 min and etch for 7 min to obtain 7–8 μm height, as shown in Figure 10.

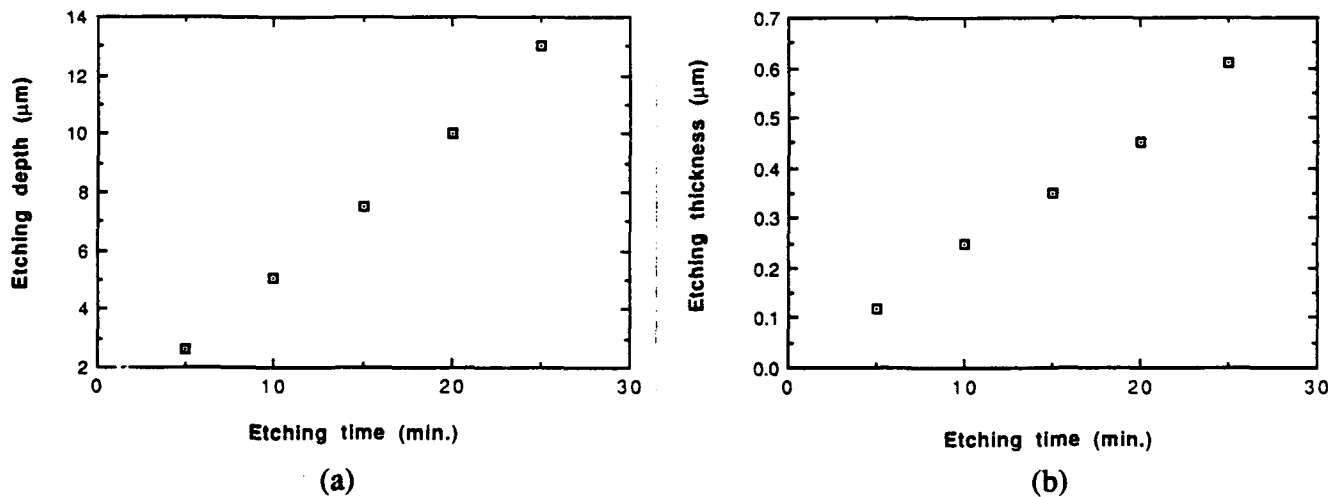


Figure 7. (a) Etching of Si with (1:10:3) solution at 5°C and (b) etching of TaSi₂ with (1:10:3) solution at 5°C.

In some applications, high β cold cathodes are required. It is known that the field enhancement factor, β , for this type of structure is approximately given by $\beta = h/r_c$, where h is the height of the tip and r_c is the tip radius of curvature.¹² Therefore high β cathodes can be made by using taller emitters (20–30 μm). To fabricate these cathodes, two-step etching is required. In the first step,

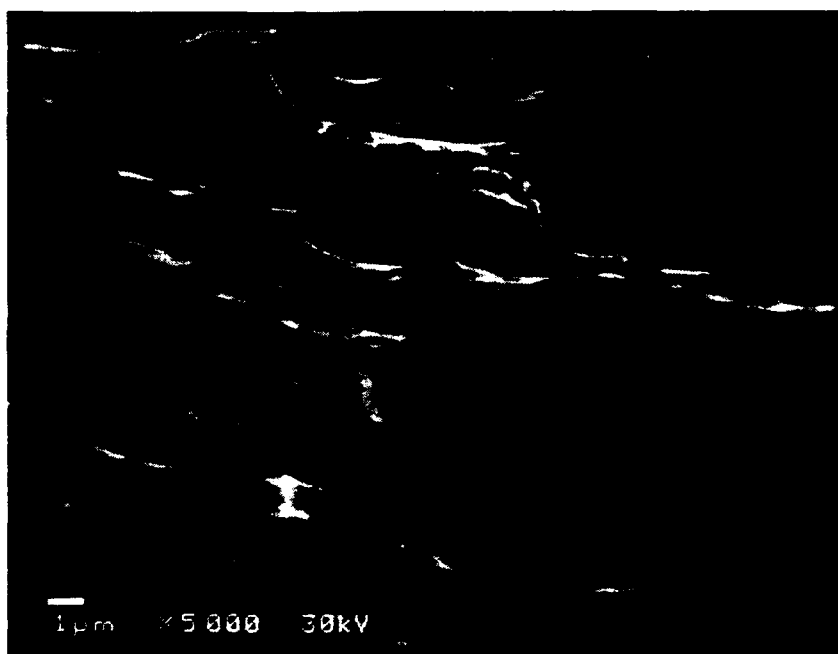


Figure 8. 1–2 μm height sharp-pointed TaSi_2 tips revealed by chemical etching.



Figure 9. 4–5 μm height sharp-pointed TaSi_2 tips revealed by chemical etching.

etching with one of the above-mentioned solutions to reveal sharp-pointed TaSi_2 tips and then etch in (1:5% NaOCl + 1:40% NaOH) at 85°C to remove Si. This etchant is an anisotropic etch, and it etches silicon only at an etching rate of $1\text{ }\mu\text{m}/\text{min}$, as shown in Figure 11. Due to the anisotropic properties of this etchant, in order to maintain the smooth surface, a high-quality single-crystalline matrix of Si is required. With a polycrystalline matrix, the wafer surface is composed of multigrain orientations which are etched at different rates; as a result, the surface becomes very rough. Figure 12 shows the cathode with $20\text{ }\mu\text{m}$ height TaSi_2 emitter tips etched in (1:10:3) solution for 20 min followed by etched in (NaOCl + NaOH) solution for 10 min more.



Figure 10. 7–8 μm height sharp-point TaSi_2 tips revealed by chemical etching.

3.3 METALLIZATION

Cathodes with thickness of 0.025 cm in many shapes and sizes, such as 1/8 in., 3/8 in. diameter, rectangular (1 mm \times 15 mm), and square (5 mm \times 5 mm), used in this program for testing were cored and cut from 1 in. diameter boule. Both sides of the wafers were lapped with alumina powder and finally polished with colloidal silica gel to get a mirror-like surface.

In the first two batches of cold cathodes sent to SAIC (see Appendix A), cathode wafers were directly bonded to the copper stub with Ag paint after etching. Emission testing results on these cathodes clearly indicated the problems associated with this contact. New metallization for the back side contact was then developed. In this metallization process, one side of the wafer is

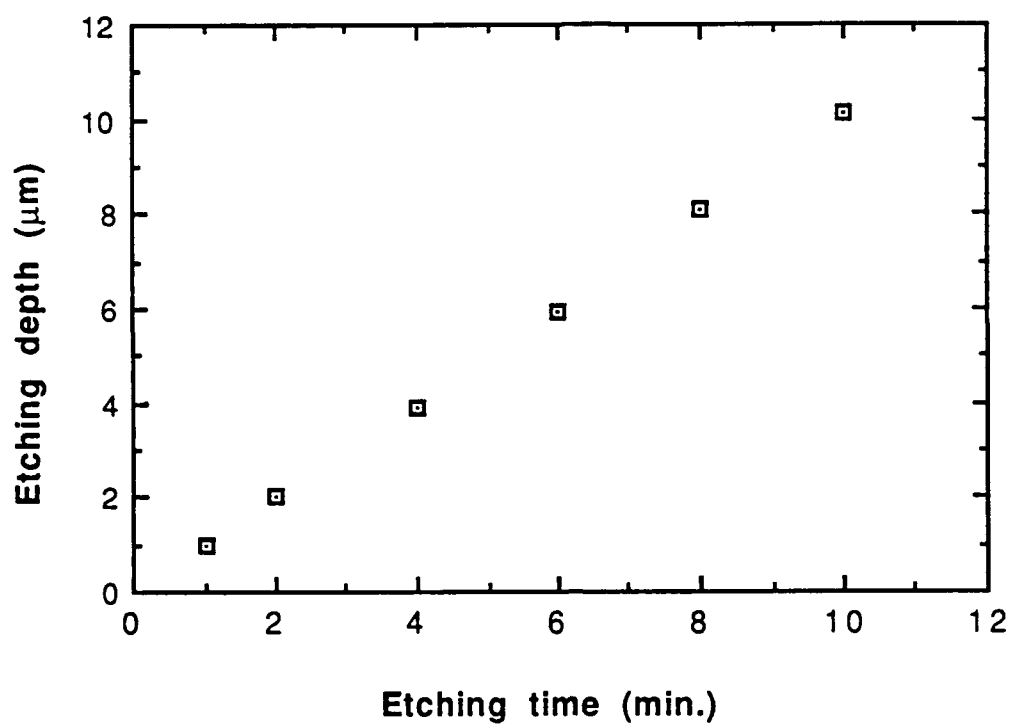


Figure 11. Etching of Si with NaOCl-NaOH.

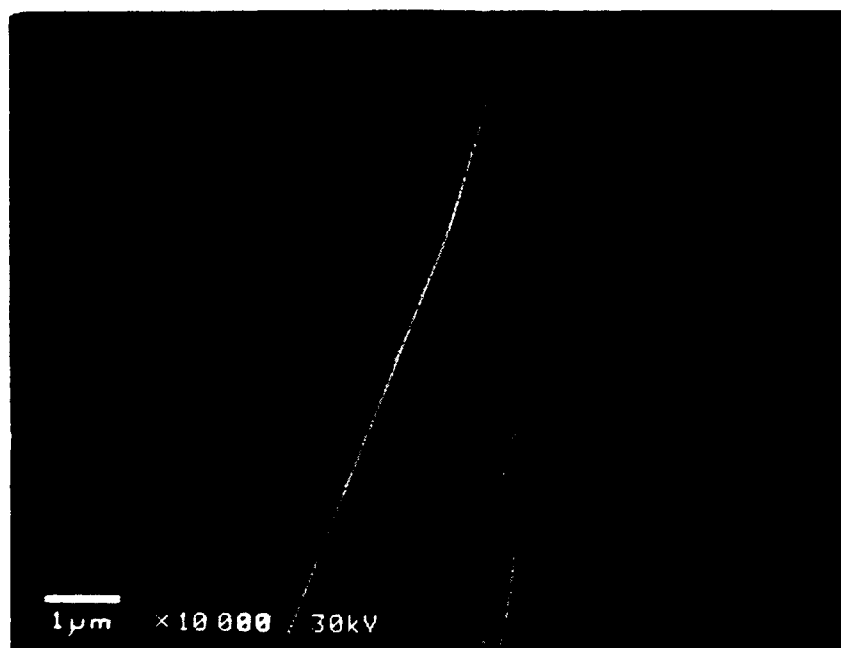


Figure 12. 20 μm height sharp-pointed TaSi₂ tips revealed by chemical etching.

successively coated with evaporated films of Ti (50 nm), Ni (150 nm), and Au (500 nm), and then annealed at 350°C for 15 min. This process produced very good contact to the TaSi₂ rods. Cathodes then were etched as discussed in Section 3.2 to obtain the desired emitter tips. All etchants used in this study do not attack gold contact on the back side, so that the etching process can be performed simply without the need to mask the contact metals. For the emission characterization, the Ti-Ni-Au face of the cathode wafer is soldered to a 0.95 cm diameter oxygen-free high-conductivity copper stub with 50/50 Pb/Sn solder, and this stub was inserted into the center of an anodized aluminum cathode holder.

In certain cases, cathodes and cathode assembly are subjected to a high-temperature annealing (~500°C) to obtain high vacuum level. The solder process using low melting point 50/50 Pb/Sn discussed above cannot be used. A metal brazing process was developed for fabrication of such high-temperature cathodes. One piece of brazing alloy InCuSil-15 (61.5% Ag + 24% Cu + 14.5% In) with exactly the same size cathode wafer and W stub is sandwiched between the cathode wafer and W stub. This assembly is placed inside the vacuum furnace with the W stub sitting on the brazing alloy piece and wafer so that its weight can push down the metal brazing when it is melted to adhere the wafer and W stub. The vacuum level during the brazing process is about 10⁻⁵ Torr. The temperature of the furnace is increased to 750°C at a ramping rate of 20°C/min and maintained at 750°C for 10 min, then cooled down to room temperature by free falling. This process also produced good contact to the TaSi₂ rods. The cathode wafer is then etched to reveal the TaSi₂ emitter tips. This etching process is also simply performed because the W stub and brazing alloy are not attacked by etching solutions.

3.4 PATTERNED CONTACTS

Patterned metal contacts on the back side of Si-TaSi₂ eutectic composite cathode wafers were fabricated to create multiple, individually addressable emission areas on each cathode. This arrangement would allow the use of this type of cathode in display applications or the simple fabrication of emission arrays of complex shape, as might be required for a distributed-cathode microwave amplifier where the electron sources are coupled to a waveguide.

The structure is shown in Figure 13. First, a dielectric silicon nitride layer with thickness of 1–2 μm and 1 μm thick Al layer are deposited on the back side of the wafer. Holes corresponding to the desired emitter areas are defined in the dielectric layer by photolithography and etching using the Al layer as an etching mask in the plasma etching process for silicon nitride. Then Al etch mask layer is removed by etching in the solution of (18:H₃PO₄ + 1:HNO₃ + 2:H₂O) for 5 min.

Metallization with Ti/Ni/Au, as discussed in Section 3.3, is applied to the entire back surface, but electrical contact is only made to the areas in the holes. The wafer is then etched in the usual manner to form the emitter elements on the front surface of the wafer.

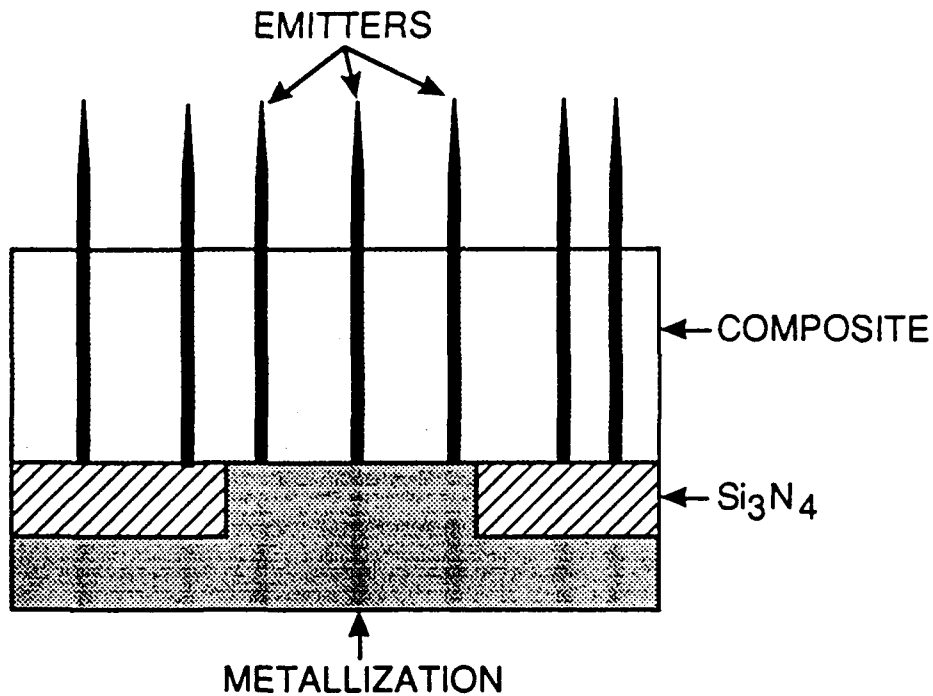


Figure 13. Schematic diagram of patterned contact on Si-TaSi₂ cold cathode.

Testing of the cathodes fabricated with the patterned contact of 10 mil dots on 40 mil centers by placing a phosphor screen directly in front of the cathode during operation shows clearly the emission pattern through the patterned contact.

4. FABRICATION OF MICROTUBULE BASED ON SME MATERIALS

In this section, the fabrication process for an alternative type of field-emission cathodes, sharp-edged microtubes, will be discussed. This type of field emission would be used rather than the sharp-pointed tips to increase emitting surface area, although somewhat decreasing the field concentration effect. Furthermore, microtubes have the advantage of producing smaller angular spreads in the momenta of the emitted electrons because the electric field inside the tube is parallel to its axis. Therefore, a large number of the emitted electrons are accelerated by the axial field, giving more uniform trajectories. As a result, beam brightness is improved, which is important for many applications requiring focused electron beams.

Efforts to make such field-emission cathodes have been reported.¹³ Emitters were made by metal-coated organically formed microtubes on a substrate. This process is complex and involves many difficulties, such as the tubes must be grown in uniform size and shape, and they must be aligned and mounted perpendicular to the conducting substrate with uniform height. The result was not encouraging.

Another factor that has a pronounced effect on the performance of field-emission cathodes is the surface work function of material used for emitters. To reduce the voltage necessary for a given current, the lowest work function material should be used. In the SME cathodes, emitter material has been grown inside the composite during the eutectic solidification process, and therefore in many cases, the low work function emitter materials were not obtained. A low work function material can be used to coat the previously formed emitters, however this method has drawbacks, for example, such a coating will be thin and easily damaged or it may be vaporized during cathode operation.

The process for microtube emitter fabrication based on Si-TaSi₂ is as follows:

- Start with Si-TaSi₂ composite substrate where TaSi₂ sharp-pointed tips protruded from the surface with the height of 10 μm by etching composite in (1:10:3) solution at 5°C.
- The sample is coated with 0.1 μm thick W layer by chemical vapor deposition. Next, a 10 μm thick photoresist layer is deposited, then 1–2 μm of this layer is removed to expose the tip of rods.

- W on the tip of rods is selectively removed by etching in the solution of (KH_2PO_4 , KOH , $\text{K}_3\text{Fe}(\text{CN})_6$, H_2O) to reveal TaSi_2 cores.
- TaSi_2 cores are etched down in HF solution to leave W microtubes, and then the photoresist layer is rinsed off. The wall thickness of the microtube can be further reduced by etching in (KH_2PO_4 , KOH , $\text{K}_3\text{Fe}(\text{CN})_6$, H_2O).

A scanning electron micrograph of the completed microtubes with a wall thickness of 150 nm is shown in Figure 14. Initial testing results on these microtube cathodes will be discussed in the Section 5.

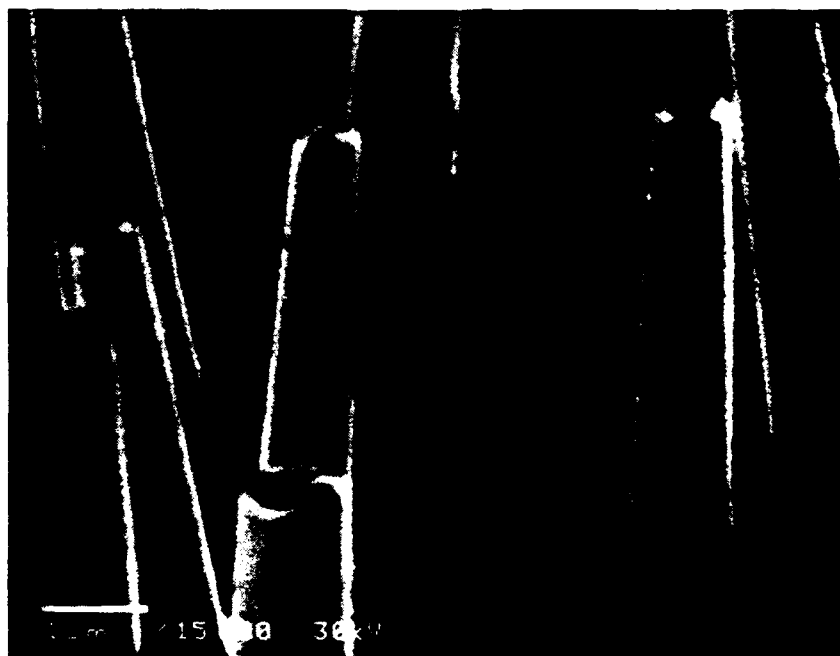


Figure 14. SEM of the completed microtube emitters.

5. CATHODE CHARACTERIZATION

5.1 Si-TaSi₂ CATHODES

The bulk of the characterization on cathodes fabricated from Si-TaSi₂ SME material has been performed at SAIC.¹⁴ To date, the following results have been obtained:

- Emission current density up to 75 A/cm² in the pulsed test of 1/8 in. cathodes.
- Modulation frequency up to 1.3 GHz.
- Uniform emission across the entire 0.95 cm diameter array.
- DC cathode lifetimes greater than 100 hr of operation in a background O₂ environment of 5×10^{-6} Torr.
- Turn on field less than 20 kV/cm.

In this report, characterization studies performed at GTE Laboratories on the cathodes fabricated from Si-TaSi₂, Si-WSi₂ and microtubule emitters are discussed. The current-voltage (I-V) characteristic data are obtained by applying a voltage between the cathode and a 1.5 cm diameter copper rod anode structure placed 1 mm away from the surface of the cathode. All measurements were performed under the vacuum pressure of $<10^{-8}$ Torr.

Figure 15 shows the measurement results from sample 8-1, cut from the boule TaSi₂-84 grown at 20 cm/hr and with seed and crucible rotation of 6 rpm in the opposite direction. This cathode is 0.95 cm in diameter and was etched with (1:10:3) solution at 5°C to obtain the rod height of 10 μ m. The plot $\log(I/V^2)$ against $1/V$ yields approximately straight-line characteristics for all data sets taken after successive burn-in at higher voltage. From the F-N equation (2) of Section 2, the slope and intercept of this plot yield the local field enhancement factor, β , and the emission area. The data sets obtained for β and emission area based on the surface work function of 4.5 eV are attached to Figure 15. Since the anode surface is larger than the cathode surface, the entire area of cathode surface is subjected to high electric field, and it can be calculated to be approximately 0.7 cm². The number of tips in the area of high field is approximately 1.1×10^6 . The emission area per tip is calculated to be 0.55–620 nm² based on emission area obtained from data set 2 and 4. The field enhancement factor, β , for the half-sphere emitter tip is given by

$\beta = h/r_c$, where h is the tip height and r_c is the tip radius of curvature. From the testing data of β and the tip height of $10\text{ }\mu\text{m}$, the radius curvature of the emitter tip is approximately $5.5\text{--}8.9\text{ nm}$. From the testing data of emission area, the radius curvature of $1.6\text{--}17\text{ nm}$ was obtained. The small value of radius curvature derived from data 2 may be due to some contamination on the tips at the initial testing which prevents some tips from emission. All other data sets give good agreement results for the field enhancement factor and emission area. On the other hand, the emission current of TaSi_2 cathodes obtained from data 5 is approximately 0.25 mA at 10 kV , which is corresponding to the emission current density of 0.35 mA/cm^2 provided that all emitter tips contributed to the emission.

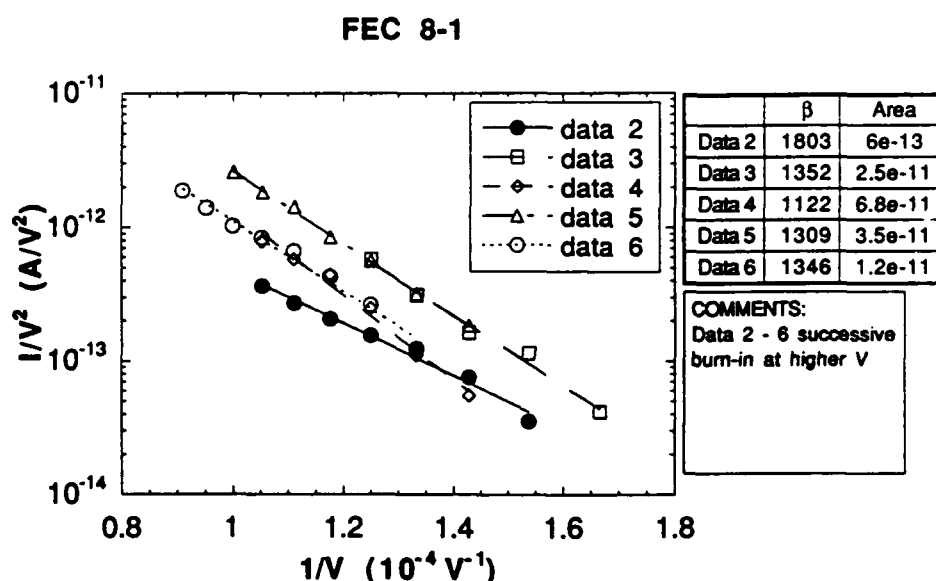


Figure 15. I-V characteristics of TaSi_2 cold cathodes.

5.2 Si- WSi_2 CATHODES

The cathode wafer was fabricated from the Si-WSi_2 polycrystalline boule using the same etching process for Si-TaSi_2 . A scanning electron micrograph of the etched Si-WSi_2 cathode is shown in Figure 16. The emitter rods have a blade structure. The etching process resulted in a rod height of $8\text{ }\mu\text{m}$ with sharp-pointed tips.

Testing of this cathode was performed in the same way as testing of the Si-TaSi_2 cathodes discussed above. Figure 17 shows 5 data sets taken after each burning time. The plots of $\ln(I/V^2)$ versus $1/V$ yield a straight line characteristic. Data 1 was taken after 3 hr burning at emission current of $200\text{ }\mu\text{A}$ and then left overnight inside the vacuum of $<10^{-8}\text{ Torr}$. The cathode turns on

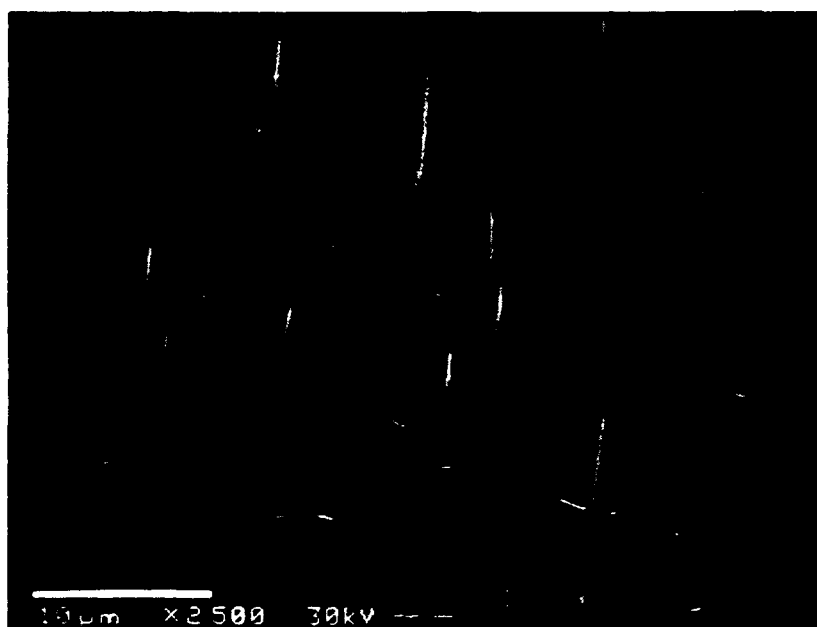


Figure 16. Surface morphology of etched WSi₂ cold cathodes.

17 - 1 Data - WSi cathode

	Data 1	Data 2	Data 3	Data 4	Data 5
BETA	1034.94	3113.91	1620.62	2077.92	1233.77
AREA	3.40685e-09	3.59236e-12	2.36041e-10	3.80950e-11	7.40336e-10

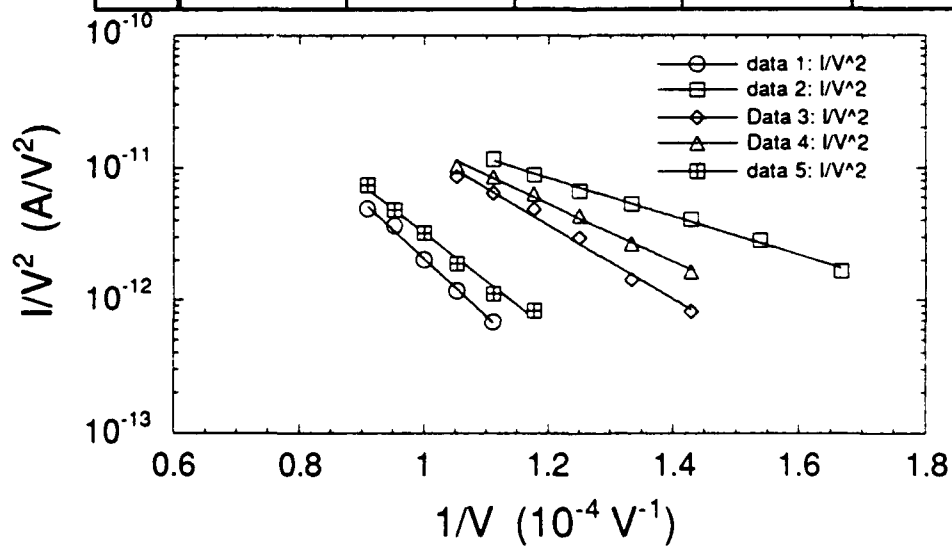


Figure 17. I-V characteristics of WSi₂ cold cathodes.

at 9 kV with emission current of 58 μA . Data 2 was taken after the cathode is subjected to 5–7 hr burning at the emission current of 250 μA and excursions up to 5.5 mA. This data set shows improvement in the emission current density. The emission current of 1.24 mA at voltage of 9 kV was obtained. Data 3 and 4 were taken after cooling for 30 min, with increasing and decreasing voltage, respectively. Data 4 shows better performance compared with data 3. This may be due to the short-term thermal effects which are associated with the increasing voltage. Data 5 was taken after cooling overnight. This data set is similar to data 1. This unstable behavior of the cathode after burning may have been due to arcing or evaporation, which destroyed the sharpest/highest (i.e., highest β) tips, leaving lower β tips to emit next, or due to the chemistry of the WSi_2 tips. Further studies are necessary to understand this behavior of WSi_2 cathodes.

5.3 W MICROTUBES

The initial attempts to test W microtubes in our test station failed because the microtube emitters cannot be turned on at 15 kV, our power supply limit. Therefore LaB_6 layer with thickness of 100 Å was deposited on the W layer to fabricate LaB_6 microtubes. With the low work function of 3 eV compared with 4.5 eV of W, these microtubes may be turned on at lower field. Figure 18 shows the testing results. The plots of $\ln(I/V^2)$ versus $1/V$ for all 5 data sets have a straight-line characteristic. From the F/N equation, the field enhancement factor and emission area for each testing time are calculated, and the results are shown in Figure 18. Data 1 is the initial testing, the cathode turned on at 5 kV with the emission current of 75 μA . This result clearly indicates the effect of low work function of LaB_6 . During testing some arcing occurred. Data 2 was taken immediately after arcing, and then the cathode was tested after it was left overnight inside the vacuum chamber of 10^{-8} Torr without burning (data 3). The cathode degraded slowly and then showed some improvements after 1.5 hr burning at 250 μA (data 4). Data 5 was taken after arcing at 1 mA; the field enhancement factor reduced nearly half of the initial value. The emission current of 0.9 mA at 9.5 kV was obtained. Examination of the cathode after testing revealed that the color of the LaB_6 layer changed from dark blue to almost the color of W.

This result indicated that using the deposition process for LaB_6 , it is not simple to obtain high-quality and stable film for field emission applications. However, with further improvements to the fabrication process for W microtubes to control the tube height and wall thickness, this may result in a promising new cathode material.

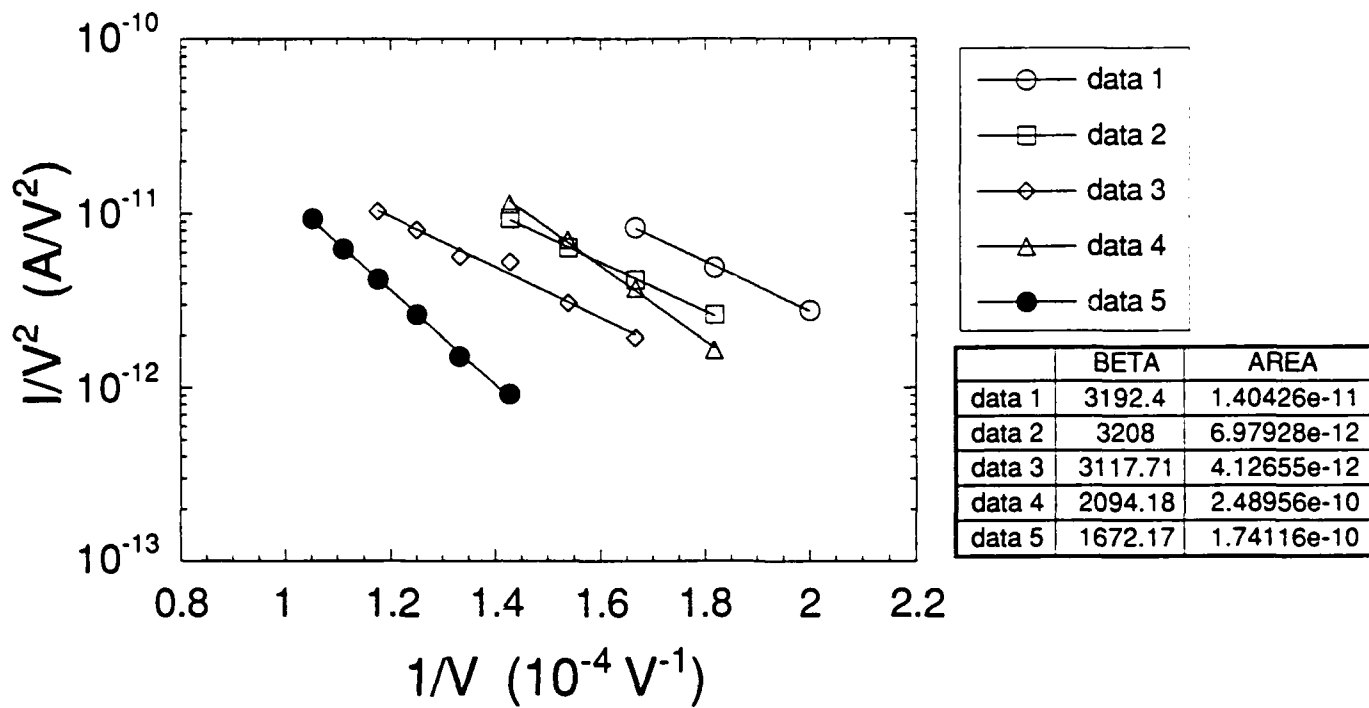


Figure 18. I-V characteristics of cathode with microtube emitters.

6. CONCLUSIONS

Rapid progress in the development of fabrication processes such as well-controlled chemical etching and contact metallization for Si-based eutectic composite cold cathodes has resulted in the demonstration of vacuum field emission devices with promising performance and characteristics. The linearity of the Fowler-Nordheim plots for all cathodes developed in this program verifies that the field emission is a primary mechanism for electron emission from these materials. The initial testing results on Si-TaSi₂ cathodes indicated the emission current density of 0.35 mA/cm² measured at 10 kV.

The cathodes based on Si-WSi also showed good characteristics with higher emission current density, however the unstable behavior of these cathodes during burning suggests the problems associated with emitter tips, such as shape/height in this system, and more efforts are needed to understand and improve performance of these cathodes.

The fabrication process for microtube emitters based on SME materials developed during the course of this program is a promising technique to produce high brightness and high current cathodes. With further efforts to improve the uniformity of the microtube height and wall thickness, high-performance cathodes based on microtube emitters could be realized.

7. REFERENCES

1. F.H. Plomp, in the Proceedings of the Fifth European Congress on Electron Microscopy, Sept 1972, Manchester (Institute of Physics, Bristol, 1973), p. 2.
2. J.K. Cochran, A.T. Chapman, R.K. Feeney, and D.N. Hill, in the 1980 International Electron Devices Meeting, Technical Digest (IEEE, Piscataway, NJ, 1980), p. 462.
3. C.A. Spindt, I. Brodie, L. Humphrey, and E.R. Westerberg, J. Appl. Phys. 47, 5248 (1976).
4. C.A. Spindt, C.E. Holland, A. Rosengreen, and I. Brodie, IEEE Trans. on Electron Devices 38, 2355 (1991).
5. M. Levinson, M. Tabasky, C. Sung, G. Hamill, D.H. Matthiesen, K. Ostreicher, and B.M. Ditchek, Appl. Phys. Lett. 58, 2815 (1991).
6. R. H.Fowler and L. Nordheim, Proc. R. Soc. London A 119, 173 (1928).
7. L.W. Swanson and L.C. Crouser, Phys. Rev. 163, 622 (1967).
8. E.W. Muller, Z. Physik, 102, 734 (1936).
9. E.W. Muller, Phys. Rev. 102, 618 (1956).
10. Q.V. Nguyen, T.R. Middleton, J. Hefter, and B.M. Ditchek, AACG Crystal Growth Conference, Fallen Leaf Lake, CA (1991) pg.12.
11. H. Robbins and B. Schwartz, J. Electrochem. Soc. 107, 108 (1960).
12. H.G. Kosmahl, IEEE Trans. Electron Devices 38, 1534 (1991).
13. D.A. Kirkpatrick, A.C. Ting, P.E. Schoen, W.B. Stockton, R. Pice, S. Baral, B. Kahn, J.M. Schnur, M. Levinson, and B.M. Ditchek, Proc. 15th Int. Conf. on Vacuum Electron., Los Alamos, NM (1990).

14. D.A. Kirkpatrick, G.L. Bergeron, M.A. Czarnaski, J.J. Hickman, M. Levinson, Q.V. Nguyen, and B.M. Ditchek, Appl. Phys. Lett. 59, 2094 (1991).

APPENDIX A

FIELD EMISSION CATHODE SUMMARY

Sample No.	Reference	Material	Diam(cm)	Etch	Pin hgt(μm)	Coating	Bond/Mount	Tes	Comments	Shipped
Sample No.	Reference	Material	Diam(cm)	Etch	Pin hgt(μm)	Coating	Bond/Mount	Tes	Comments	Shipped
7388-19-1	7388-19	SiTa47	0.95	mod. CP4	5 - 8	none	Ag plymd/Cu	no		SAIC 8/24/90
7388-19-2	7388-19	SiTa47	0.95	mod. CP4	5 - 8	Si-100A	Ag plymd/Cu	no		SAIC 8/24/90
7388-19-3	7388-19	SiTa47	0.95	mod. CP4	5 - 8	Si-100A	Ag plymd/Cu	no		SAIC 8/24/90
7388-19-4	7388-19	SiTa47	0.95	mod. CP4	5 - 8	Au-100A	Ag plymd/Cu	no		SAIC 8/24/90
7388-19-5	7388-19	SiTa47	0.95	mod. CP4	5 - 8	Au-100A	Ag plymd/Cu	no		SAIC 8/24/90
7388-23-1	7388-23	SiTa40	0.95	NaHP/NaOH	10 - 20	none	Ag plymd/Cu	no	pitted surface	SAIC 10/1/90
7388-23-2	7388-23	SiTa40	0.95	NaHP/NaOH	10 - 20	Au -100A	Ag plymd/Cu	no	pitted surface	SAIC 10/1/90
7388-23-3	7388-23	SiTa40	0.95	NaHP/NaOH	10 - 20	Si -100A	Ag plymd/Cu	no	pitted surface	SAIC 10/1/90
7388-23-4	7388-23	SiTa40	0.95	NaHP/NaOH	15 - 30	Au -100A	Ag plymd/Cu	no	pitted surface	SAIC 10/1/90
7388-23-5	7388-23	SiTa40	0.95	NaHP/NaOH	15 - 30	Si -100A	Ag plymd/Cu	no	pitted, wax res back	SAIC 10/1/90
3 - 1		SiTa84	0.95	NaHP/NaOH	~20	none	TiNiAu/none	no	unmounted	SAIC 11/29/90
3 - 2		SiTa84	0.95	NaHP/NaOH	~20	none	TiNiAu/none	no	unmounted	SAIC 11/29/90
3 - 3		SiTa84	0.95	NaHP/NaOH	~20	none	TiNiAu/PbSn/Cu	no	mounted	SAIC 12/4/90
3 - 4		SiTa84	0.95	NaHP/NaOH	~20	none	TiNiAu/PbSn/Cu	no	mounted	SAIC 12/4/90
3 - 5		SiTa84	0.95	NaHP/NaOH	~20	none	TiNiAu/PbSn/Cu	no	mounted	SAIC 12/4/90
4 - 1	7434-37	SiTa84	0.95	NHP/NOH+CP4	~20	none	TiNiAu/none	no	Remetallized after etch	SAIC 1/29/91
4 - 2	7434-37	SiTa84	0.95	NHP/NOH+CP4	~20	none	TiNiAu/none	no	because too-thin metal	SAIC 1/29/91
4 - 3	7434-37	SiTa84	0.95	NaHP/NaOH	~20	none	TiNiAu/none	no	came off.	SAIC 1/29/91
4 - 4	7434-37	SiTa84	0.95	NaHP/NaOH	~20	none	TiNiAu/none	no		SAIC 1/29/91
4 - 5	7434-37	SiTa84	0.95	NaHP/NaOH	~20	none	TiNiAu/none	no		SAIC 1/29/91
5 - 1	7434-47	SiTa84	0.95	cold CP4	6 - 10	none	TiNiAu/PbSn/Cu	no	few small pits,	SAIC 3/7/91
5 - 2	7434-47	SiTa84	0.95	cold CP4	6 - 10	none	TiNiAu/PbSn/Cu	no	r(tip) < 250 A	SAIC 3/7/91
5 - 3	7434-47	SiTa84	0.95	cold CP4	6 - 10	none	TiNiAu/PbSn/Cu	no		SAIC 3/7/91
5 - 4	7434-47	SiTa84	0.95	cold CP4	6 - 10	none	TiNiAu/none	no		SAIC 3/7/91
5 - 5	7434-47	SiTa84	0.95	cold CP4	6 - 10	none	TiNiAu/none	no		SAIC 3/7/91
6 - 1	7434-52	SiTa84	0.318	cold CP4	6 - 10	none	TiNiAu/PbSn/Cu	no	1/8" diam.	SAIC 3/20/91
6 - 2	7434-52	SiTa84	0.318	cold CP4	6 - 10	none	TiNiAu/PbSn/Cu	no		SAIC 3/20/91

Sample No.	Reference	Material	Diam(cm)	Etch	Pin hgt(μ m)	Coating	Bond/Mount	Res	Comments	Shipped
6 - 3	7434-52	SiTa84	0.318	cold CP4	6 - 10	none	TiNiAu/PbSn/Cu	no		SAIC 3/20/91
6 - 4	7434-52	SiTa84	0.318	cold CP4	6 - 10	none	TiNiAu/PbSn/Cu	no		SAIC 3/20/91
6 - 5	7434-52	SiTa84	0.318	cold CP4	6 - 10	none	TiNiAu/PbSn/Cu	no		SAIC 3/20/91
7 - 1	7434-53	SiTa84	0.95	cold CP4	6 - 10	none	TiNiAu/PbSn/Cu	no	Patterned with 20 mil d	SAIC 3/20/91
7 - 2	7434-53	SiTa84	0.95	cold CP4	6 - 10	none	TiNiAu/PbSn/Cu	no	in contact metal.	SAIC 3/20/91
7 - 3	7434-53	SiTa84	0.95	cold CP4	6 - 10	none	TiNiAu/none	no		SAIC 3/20/91
7 - 4	7434-53	SiTa84	0.95	cold CP4	6 - 10	none	TiNiAu/none	no		SAIC 3/20/91
8 - 1	7434-54	SiTa84	0.95	cold CP4	6 - 10	none				
8 - 2	7434-54	SiTa84	0.95	cold CP4	6 - 10	none				
8 - 3	7434-54	SiTa84	0.95	cold CP4	6 - 10	none				
8 - 4	7434-54	SiTa84	0.95	cold CP4	6 - 10	none				
8 - 5	7434-54	SiTa84	0.95	cold CP4	6 - 10	none				
9 - 1	7434-60	SiTa84	0.95	cold CP4	6 - 10	none	none	no		SAIC 5/21/91
9 - 2	7434-60	SiTa84	0.95	cold CP4	6 - 10	none	none	no		SAIC 5/21/91
9 - 3	7434-60	SiTa84	0.95	cold CP4	6 - 10	none	none	no		SAIC 5/21/91
9 - 4	7434-60	SiTa84	0.95	cold CP4	6 - 10	none	none	no		SAIC 5/21/91
9 - 5	7434-60	SiTa84	0.95	cold CP4	6 - 10	none	none	no		SAIC 5/21/91
9 - 6	7434-60	SiTa84	0.95	cold CP4	6 - 10	none	none	no		SAIC 5/21/91
9 - 7	7434-60	SiTa84	0.95	cold CP4	6 - 10	none	none	no		SAIC 5/21/91
9 - 8	7434-60	SiTa84	0.95	cold CP4	6 - 10	none	none	no		SAIC 5/21/91
9 - 9	7434-60	SiTa84	0.95	cold CP4	6 - 10	none	none	no		SAIC 5/21/91
9 - 10	7434-60	SiTa84	0.95	cold CP4	6 - 10	none	none	no		SAIC 5/21/91
10 - 1	7434-60	SiTa84	0.95	NaHP/NaOH	≤ 25	none	none	no		SAIC 5/21/91
10 - 2	7434-60	SiTa84	0.95	NaHP/NaOH	≤ 25	none	none	no		SAIC 5/21/91
10 - 3	7434-60	SiTa84	0.95	NaHP/NaOH	≤ 25	none	none	no		SAIC 5/21/91
10 - 4	7434-60	SiTa84	0.95	NaHP/NaOH	≤ 25	none	none	no		SAIC 5/21/91
10 - 5	7434-60	SiTa84	0.95	NaHP/NaOH	≤ 25	none	none	no		SAIC 5/21/91
11 - 1	7434-74	SiTa90	0.318	cold CP4	6 - 10	none	TiNiAu/PbSn/Cu	no		SAIC 7/30/91

Sample No.	Reference	Material	Diam(cm)	Etch	Pin hgt(μ m)	Coating	Bond/Mount	Tes	Comments	Shipped
11 - 2	7434-74	SiTa90	0.318	cold CP4	6 - 10	none	TiNiAu/PbSn/Cu	no		SAIC 7/30/91
11 - 3	7434-74	SiTa90	0.318	cold CP4	6 - 10	none	TiNiAu/PbSn/Cu	no		SAIC 7/30/91
11 - 4	7434-74	SiTa90	0.318	cold CP4	6 - 10	none	TiNiAu/PbSn/Cu	no		SAIC 7/30/91
11 - 5	7434-74	SiTa90	0.318	cold CP4	6 - 10	none	TiNiAu/PbSn/Cu	no		SAIC 7/30/91
12 - 1		SiTa87	0.95	NaHP/NaOH	20-30	none	TiNiAu/PbSn/Cu	yes	for plasma expt's	
12 - 2		SiTa87	0.95	NaHP/NaOH	20-30	none	TiNiAu/PbSn/Cu		edge has poly in both	
13 - 1	7434-81	SiTa87	0.95	tube process	6 - 7	W	TiNiAu/PbSn/Cu	no	500 A W tubes	SAIC 8/22/91
13 - 2	7434-81	SiTa87	0.95	tube process	6 - 7	W	TiNiAu/PbSn/Cu	no	500 A W tubes	SAIC 8/22/91
13 - 3	7434-81	SiTa87	0.95	tube process	5 - 8	W	TiNiAu/PbSn/Cu	no	1000 A W tubes	SAIC 8/22/91
13 - 4	7434-81	SiTa87	0.95	tube process		W	TiNiAu/PbSn/Cu	yes	1000 A W tubes	
13 - 5	7434-81	SiTa87	0.95	tube process		W	TiNiAu/PbSn/Cu	no	1000 A W tubes	
14 - 1		SiTa86	0.13x1.3	NaHP/NaOH		none	TiNiAu	no	rectangular for CFA	SAIC 9/13/91
14 - 2		SiTa86	0.13x1.3	NaHP/NaOH		none	TiNiAu	no	rectangular for CFA	SAIC 9/13/91
14 - 3		SiTa86	0.13x1.3	NaHP/NaOH		none	TiNiAu	no	rectangular for CFA	SAIC 9/13/91
14 - 4		SiTa86	0.13x1.3	NaHP/NaOH		none	TiNiAu	no	rectangular for CFA	SAIC 9/13/91
14 - 5		SiTa86	0.13x1.3	NaHP/NaOH		none	TiNiAu	no	rectangular for CFA	SAIC 9/13/91
14 - 6		SiTa86	0.13x1.3	NaHP/NaOH		none	TiNiAu	no	rectangular for CFA	SAIC 9/13/91
15 - 1		SiTa84	0.95	cold CP4	8 - 10	none	TiNiAu/PbSn/Cu	no		SAIC 10/17/91
15 - 2		SiTa84	0.95	cold CP4	8 - 10	none	TiNiAu/PbSn/Cu	no		SAIC 10/17/91
15 - 3		SiTa84	0.95	cold CP4	8 - 10	none	TiNiAu/PbSn/Cu	no		SAIC 10/17/91
15 - 4		SiTa84	0.95	cold CP4	8 - 10	none	TiNiAu/PbSn/Cu	no		SAIC 10/17/91
15 - 5		SiTa84	0.95	cold CP4	8 - 10	none	TiNiAu/PbSn/Cu	no		SAIC 10/17/91
16 - 1		SiTa86	0.13x1.3	NaHP/NaOH		none	TiNiAu	no	rectangular for CFA	SAIC 10/17/91
16 - 2		SiTa86	0.13x1.3	NaHP/NaOH		none	TiNiAu	no	rectangular for CFA	SAIC 10/17/91
16 - 3		SiTa86	0.13x1.3	NaHP/NaOH		none	TiNiAu	no	rectangular for CFA	SAIC 10/17/91
16 - 4		SiTa86	0.13x1.3	NaHP/NaOH		none	TiNiAu	no	rectangular for CFA	SAIC 10/17/91
16 - 5		SiTa86	0.13x1.3	NaHP/NaOH		none	TiNiAu	no	rectangular for CFA	SAIC 10/17/91
16 - 6		SiTa86	0.13x1.3	NaHP/NaOH		none	TiNiAu	no	rectangular for CFA	SAIC 10/17/91

Sample No.	Reference	Material	Diam(cm)	Etch	Pin hgt(μ m)	Coating	Bond/Mount	Test	Comments	Shipped
17 - 1		SIW	0.95	cold CP4	8	none	TiNiAu/PbSn/Cu	yes		
17 - 2		SIW	0.95	cold CP4	8	none	TiNiAu/PbSn/Cu			
17 - 3		SIW	0.95	cold CP4	8	none	TiNiAu/PbSn/Cu			
18 - 1		SiTa	0.95	cold CP4	8 - 10	none	InCuSi/W	no	brazed mount	SAIC 12/11/91
18 - 2		SiTa	0.95	cold CP4	8 - 10	none	InCuSi/W	no	brazed mount	SAIC 12/11/91
19 - 1			0.95	microtube		LaB6/W	TiNiAu/PbSn/Cu	no	chipped on mounting	
19 - 2			0.95	microtube		w/LaB6	TiNiAu/PbSn/Cu	yes		
20 - 1		SiTa89	0.95	cold CP4	8 - 10	none	TiNiAu	no		SAIC 2/25/92
20 - 2		SiTa89	0.95	cold CP4	8 - 10	none	TiNiAu	no		SAIC 2/25/92
20 - 3		SiTa89	0.95	cold CP4	8 - 10	none	TiNiAu	no		SAIC 2/25/92
20 - 4		SiTa89	0.95	cold CP4	8 - 10	none	TiNiAu	no		SAIC 2/25/92
20 - 5		SiTa89	0.95	cold CP4	8 - 10	none	TiNiAu	no		SAIC 2/25/92
21 - 1		SiTa90	0.318	cold CP4	8 - 10	none	TiNiAu	no		SAIC 2/25/92
21 - 2		SiTa90	0.318	cold CP4	8 - 10	none	TiNiAu	no		SAIC 2/25/92
21 - 3		SiTa90	0.318	cold CP4	8 - 10	none	TiNiAu	no		SAIC 2/25/92
21 - 4		SiTa90	0.318	cold CP4	8 - 10	none	TiNiAu	no		SAIC 2/25/92
21 - 5		SiTa90	0.318	cold CP4	8 - 10	none	TiNiAu	no		SAIC 2/25/92
22 - 1		SiTa86	0.5x0.5	cold CP4	8 - 10	none	TiNiAu	no		SAIC 2/25/92
22 - 2		SiTa86	0.5x0.5	cold CP4	8 - 10	none	TiNiAu	no		SAIC 2/25/92
22 - 3		SiTa86	0.5x0.5	cold CP4	8 - 10	none	TiNiAu	no		SAIC 2/25/92
22 - 4		SiTa86	0.5x0.5	cold CP4	8 - 10	none	TiNiAu	no		SAIC 2/25/92
12 cathodes		SiTa90	0.318	Unetched		none	TiNiAu	no		SAIC 2/25/92
15 cathodes		SiTa89	0.95	Unetched		none	TiNiAu	no		SAIC 2/25/92
23 - 1		SIW 1	0.95	cold CP4	8 - 10	none	TiNiAu	no		SAIC 3/11/92

FIELD EMISSION CATHODE SUMMARY

GTE LABORATORIES INCORPORATED

Sample No.	Reference	Material	Diam (cm)	Etch	Pin hgt (μ m)	Coating	Bond/Mount	Test	Comments	Shipped
23 - 2		SiW 1	0.95	Cold CP4	8 - 10	None	TiNiAu	No		SAIC 3/11/92
23 - 3		SiW 1	0.95	Cold CP4	8 - 10	None	TiNiAu	No		SAIC 3/11/92
36 cathodes		SiTa 90	0.318	None		None	TiNiAu	No		SAIC 5/5/92
36 cathodes		SiTa 90	0.318	None		None	None	No		SAIC 5/5/92
18 cathodes		SiTa 89	0.95	None		None	None	No		SAIC 5/5/92
17 cathodes		SiTa 89	0.95	None		None	TiNiAu	No		SAIC 5/5/92
Boule 91									Polycrystal matrix grown at 30 cm/hr	SAIC 5/5/92
Boule 92									Single-crystal matrix	SAIC 5/5/92